



HAL
open science

Les groupes de galaxies: apport des effets de lentillage gravitationnel

Rémi Cabanac

► **To cite this version:**

Rémi Cabanac. Les groupes de galaxies: apport des effets de lentillage gravitationnel. Cosmologie et astrophysique extra-galactique [astro-ph.CO]. Université de Toulouse, 2020. tel-03086579

HAL Id: tel-03086579

<https://hal.science/tel-03086579>

Submitted on 6 Jan 2021

HAL is a multi-disciplinary open access archive for the deposit and dissemination of scientific research documents, whether they are published or not. The documents may come from teaching and research institutions in France or abroad, or from public or private research centers.

L'archive ouverte pluridisciplinaire **HAL**, est destinée au dépôt et à la diffusion de documents scientifiques de niveau recherche, publiés ou non, émanant des établissements d'enseignement et de recherche français ou étrangers, des laboratoires publics ou privés.

Habilitation à Diriger les Recherches

**Les groupes de galaxies:
apport des effets de lentillage
gravitationnel**

Rémi Cabanac

Institut de Recherche en Astrophysique et Planétologie
Université de Toulouse - CNRS

3 décembre 2020

Résumé

Les groupes de galaxies sont des entités auto gravitantes de masses entre $10^{12} M_{\odot}$ et $10^{14} M_{\odot}$. Les groupes de galaxies contiennent la majorité des galaxies de l'Univers et leur échelle physique les rends à la fois sensibles aux effets cosmologiques de formation et d'évolution des structures et aux effets causés par la matière baryonique (mécaniques, chimiques, dynamiques et rayonnants), c'est-à-dire, les vents et les explosions d'étoiles, la rétroaction des noyaux actifs de galaxies, la friction du milieu intragroupe. Ce sont donc des laboratoires idéaux pour confronter la cosmologie à l'Univers local. Ce manuscrit propose une revue de nos connaissances théoriques et observationnelles sur les groupes de galaxies avec une emphase particulière sur les groupes détectés par effet de lentilles fort et faible.

Avant-propos et remerciements

L'habilitation à diriger les recherches est un exercice très particulier dans la vie d'un chercheur. Certains l'approchent avec un ennui consommé et une certaine dose de scepticisme sur son utilité. Pour ma part, Sans aller jusqu'à qualifier l'expérience d'enthousiasmante, j'ai fait le choix de profiter de l'occasion pour approfondir mes connaissances dans certains domaines que, par manque de temps et souci d'efficacité, je laissais à l'expertise de mes collaborateurs. C'est en particulier le cas des thèmes abordés au chapitre 2. J'ai trouvé passionnant de voir l'état de l'art en modélisation et le chemin qui nous reste à parcourir pour prétendre comprendre l'univers dans lequel nous vivons. Le métier de chercheur est décidément une aventure digne de celle des premiers explorateurs de notre monde depuis XVI^e siècle. C'est également avec un certain pincement de coeur que j'ai dû laisser de côté, une partie de mes recherches passées, celles que je ne pouvais décentement pas raccrocher au thème choisi sans introduire un sentiment d'artifice dans la cohérence du manuscrit. C'est le cas de mon travail sur les miroirs liquides, les galaxies à sursaut de formation d'étoiles, les météores, l'alignement à grande échelle des quasars, la construction de la première bibliothèque de spectres stellaires haute résolution UVES et enfin mes contributions à l'observation au Pic du Midi à travers la direction du Télescope Bernard Lyot. La vie est faite de choix, c'est ainsi.

Au terme de ce travail de rédaction par essence solitaire, le constat le plus important est que mon travail n'aurait pas été possible sans l'apport d'un très grand nombre de personnes sans lesquelles rien de tout cela n'aurait vu le jour. Je voudrais donc remercier mes collègues du GAHEC et plus largement de l'IRAP pour des discussions stimulantes, mes collaborateurs de l'OMP, d'Euclid, du LAM, du SL2S, du CFHT, du VLT, et de l'IAP pour leur aides, éclairages, partage de connaissances, stimulations intellectuelles diverses. Je voudrais remercier mes collègues de l'équipe de la licence de Physique, Chimie, Astronomie, Météorologie et Environnement de Tarbes pour m'avoir permis de goûter aux joies et exigences de l'enseignement. Je voudrais remercier mes collaborateurs Post-docs, thésitif, masters et licences pour m'avoir enseigné la patience et surtout l'humilité. Je voudrais tout spécialement remercier mes collègues et amis du Pic du Midi et du Télescope Bernard Lyot avec qui j'ai le privilège de travailler et qui m'ont montré la force d'une équipe qui contribue à un projet de façon complémentaire. Je voudrais enfin remercier mon épouse et mes enfants pour leur soutien, leur confiance et leur amour.

Table des matières

Résumé	i
Avant-Propos et remerciements	iii
Table des figures	vii
Liste des tableaux	ix
1 Introduction : pourquoi s'intéresser aux groupes de galaxies ?	1
1.1 Une très brève histoire de l'univers	1
1.2 Deux difficultés : définition et détection	5
1.2.1 Une définition floue	5
1.2.2 Une détection difficile	5
1.3 La zoologie des groupes de galaxies	7
1.3.1 Le Groupe Local et les groupes de l'univers local ($z < 0.01$)	7
1.3.2 Les groupes compacts de l'univers local	7
1.3.3 Les groupes fossiles	9
1.3.4 Les groupes lentilles	10
1.4 Pourquoi étudier les groupes de galaxies ?	12
1.4.1 Chainon indispensable de la formation des structures	12
1.4.2 La formation hiérarchique des structures	13
1.4.3 La formation des étoiles dans les galaxies	13
La physique stellaire	13
La formation des étoiles dans les galaxies	14
L'enrichissement chimique des galaxies	15
La formation stellaire à l'échelle du cosmos	16
1.5 Les amas de galaxies	19
1.5.1 Les observables	19
1.5.2 Les relations d'échelle	20
1.5.3 Les déviations aux relations d'échelle	22
1.6 Les groupes sont des laboratoires de physique	23
2 Un regard théorique sur les groupes de galaxies	27
2.1 La formation des objets dans l'univers	27
2.1.1 Premiers principes : les hypothèses fondamentales de la cosmologie contemporaine	27
2.1.2 De l'univers homogène à l'univers inhomogène : une petite histoire de contrastes	29
L'univers homogène	29

	Nucléosynthèse et fond de rayonnement cosmologique	31
	L'univers inhomogène	32
	La formation des objets denses dans l'univers	34
	Epoque de formation des galaxies, groupes et amas	37
2.1.3	Modèles d'évolution des objets : galaxies et amas de galaxies	38
	Simulations numériques et prédictions physiques	38
2.2	La physique baryonique des groupes	41
2.2.1	Absence de courants froids dans les groupes : la rétroaction des noyaux de galaxies actives	43
2.2.2	Balayage par pression dynamique (Ram pressure stripping)	44
2.2.3	Rétroaction des sursauts de formation d'étoile	45
	Calcul analytique de l'impact des vents de supernovas	45
	Simulations hydrodynamiques sur l'impact des vents de supernovas	51
2.3	Conclusion	56
3	Lentilles dans les groupes	57
3.1	Introduction	57
3.1.1	Principes physiques	57
3.1.2	Equation des lentilles	58
3.1.3	Modélisation des lentilles	59
3.1.4	Détection des lentilles	62
	Les projets	62
	Les techniques de détection	68
3.2	Le Strong Lensing Legacy Survey	95
4	Perspectives de recherches	257
4.1	programmes d'observation	257
4.2	Projets de recherches spécifiques	265
4.2.1	Recherches avec le Strong Lensing Legacy Survey	265
4.2.2	Recherches sur les techniques de détection	265
4.2.3	Recherches avec l'échantillon de groupes d'Euclid	265
4.2.4	Recherches instrumentales	266
5	Conclusion	267
	Bibliographie	271

Table des figures

1.1	Nucléosynthèse initiale	2
1.2	Carte du fond de rayonnement cosmologique	3
1.3	Equation d'état de l'énergie noire	4
1.4	Carte du Groupe Local	8
1.5	Groupe fossile	10
1.6	Groupes lentilles	12
1.7	Histoire de la formation stellaire	18
1.8	Deux amas caractéristiques	20
1.9	Lois d'échelles dans les amas	23
1.10	Déviations aux lois d'échelle dans les amas	24
2.1	P_k observé	34
2.2	Sondage 2dF	35
2.3	Redshift de formation des objets	38
2.4	La simulation à n-corps Ushuu	39
2.5	La simulation à n-corps Ushuu	40
2.6	Exemples de résultats d'Illustris	42
2.7	galaxies méduses	46
2.8	Diagramme de formation des galaxies en présence de supernovas	50
2.9	EAGLE : Fonction de masses stellaires des galaxies	53
2.10	EAGLE : relation Luminosité X vs Température X	54
2.11	Illustris : prédictions de densités de formation d'étoiles Cosmique en fonction du redshift	55
2.12	FABLE : Fonction de masses stellaires et gaz	55
3.1	Schéma géométrique de l'effet de lentille	58
3.2	Exemple de configurations canoniques d'images produites par lentillage	61
3.3	Modèle de masse de Abell 2744	62
4.1	Masse des lentilles-groupes détectables par Euclid	261
4.2	Les grands télescopes sols	263

Liste des tableaux

2.1	Paramètres cosmologiques de la mission Planck	29
2.2	Propriétés physiques des jets astrophysiques d'objets cosmologiques	43
3.1	Tableau des principaux catalogues de lentilles	64
4.1	Table synoptique des grands observatoires à venir.	264

Chapitre 1

Introduction : pourquoi s'intéresser aux groupes de galaxies ?

Note liminaire : Dans la suite de ce texte, nous adopterons le point "." comme signe décimal de séparation des unités et des fractions (résolution 10 de la 22e CGPM, 2003¹) et suivrons les conventions usuelles de notation des unités du Système International. Par défaut nous utiliserons pour notre univers les valeurs des paramètres cosmologiques du modèle de concordance, Λ CDM², cités au tableau 1.1. En particulier les valeurs physiques suivront la convention $H_0 = 68 h \text{ km} \cdot \text{s}^{-1} \cdot \text{Mpc}^{-1}$, où $h = h_{68} = 1$, $\Omega_m = 0.31$, $\Omega_\Lambda = 0.69$ et $\Omega_k = 0$.

1.1 Une très brève histoire de l'univers

La somme des connaissances scientifiques contemporaines sur la cosmogonie, science née il y a à peine un siècle, ne peut que forcer l'admiration des plus sceptiques sur la puissance prédictive et interprétative de la physique. En un siècle nous sommes passés d'un univers-île de taille indéterminé, peuplé d'étoiles et de mytérieuses nébuleuses (à la Kapteyn et Shapley), à un modèle de concordance établissant les paramètres cosmologiques régissant l'évolution de l'univers à quelques pourcents près sur 13.8 milliards d'années, et cela, avec une économie stupéfiante de moyens. En effet, La physique s'appuyant sur une théorie métrique de la gravitation (la relativité générale), un principe cosmologique d'homogénéité et d'isotropie des lois physiques, relativement logique et vérifiée jusqu'à des époques reculées (Chand, H. et al. 2004) et surtout des observations de plus en plus fines permettant de fixer les conditions de l'univers à différentes époques, est parvenue à construire un modèle cohérent, si on accepte que la majeure partie de l'univers est invisible, sous forme de matière et d'énergie sombres³, les reliquats étant de la matière

1. <https://www.bipm.org/fr/CGPM/db/22/10/>

2. Le modèle Λ CDM est détaillé au chapitre 2, il s'agit du modèle dominé par une énergie noire constante Λ , et d'une composante de matière noire non-baryonique et non-collisionnelle baptisée Cold Dark Matter (CDM).

3. La question de savoir si ces hypothétiques composantes sombres sont un indice d'une crise de la cosmologie moderne se pose de façon de plus en plus prégnante en 2020. Un certain nombre de théories métriques, voire des théories davantage exotiques, tentant de prédire les observations sans composantes sombres forment un domaine disciplinaire entier. Comme le dit Michael Turner de l'Université de Chicago : "extraordinary claims demand extraordinary evidence". Dans le reste de cette thèse, nous accepterons sans la remettre en question que l'hypothèse de l'existence de composantes sombres est la plus simple et la plus puissante aujourd'hui pour interpréter les observations.

baryonique (les baryons sont des hadrons, c'est-à-dire des particules composées de combinaisons de 3 quarks+anti-quarks, dans le jargon de la cosmologie le mot baryon est synonyme de proton ou neutron).

D'autre part, les observations nous montrent un univers en expansion depuis sa naissance, dont la composante baryonique, seule composante observable directement, évolue dans le temps. La structuration de cette matière baryonique dans l'univers passe par une phase de formation des premiers noyaux d'atomes. Cette phase appelée nucléosynthèse initiale (Coc & Vangioni 2017) produit les premiers noyaux légers à partir des neutrons, des protons et des électrons, dont la proportion est finement définie par l'équilibre entre sections efficaces, densités et le refroidissement de l'univers en expansion. Les modèles de nucléosynthèse initiale reproduisent bien les abondances mesurées des noyaux atomiques (He, D) relatives à l'hydrogène, le lithium (Li) est plus complexe à modéliser.

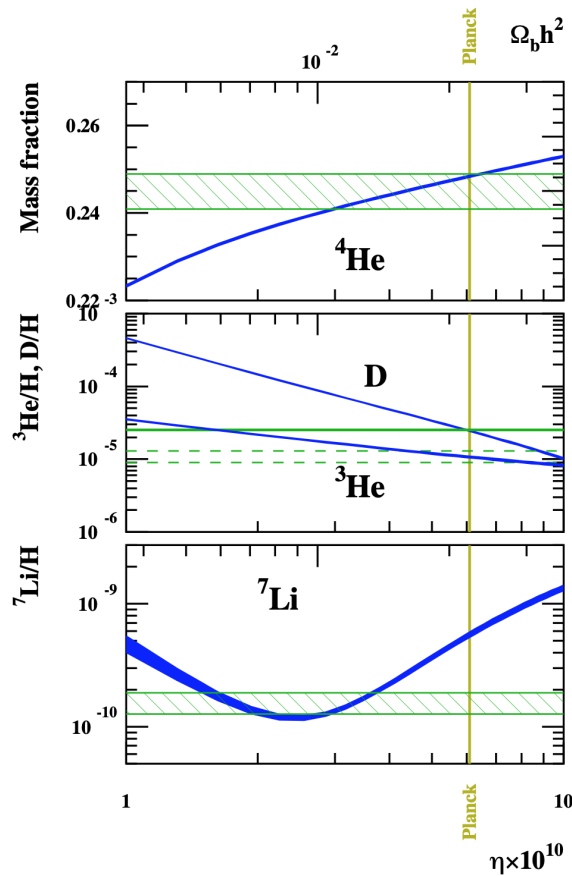


FIGURE 1.1 – Nucléosynthèse initiale : abondance prédite et mesurée en fraction de masse des noyaux atomiques (Li, He, D) par rapport à la quantité d'hydrogène en fonction du rapport nombre de photons au nombre de baryons η (Coc & Vangioni 2017). Les valeurs d'abondances mesurées (bandes horizontales vertes) contraignent fortement le rapport du nombre de photons au nombre de baryons à $\eta = N_{\text{baryons}}/N_{\text{photons}} = 6 \times 10^{-10}$ pour le deutérium. Comme on connaît bien le nombre de photons de l'Univers, qui correspond à peu de chose près au nombre de photons du fond de rayonnement cosmologique, nous avons une contrainte forte sur le nombre maximal de baryons dans l'Univers. La ligne beige verticale est la mesure de densité baryonique déduite des données du rayonnement de fond micro-onde de la mission Planck, données indépendante. La correspondance entre modèle et données observationnelles avec l'abondance de deutérium est phénoménale.

Les valeurs d'abondances stellaires mesurées dans des galaxies considérées comme proche des valeurs primordiales (bande vertes horizontales sur la Figure 1.1) contraignent fortement le rapport du nombre de photons au nombre de baryons à $\eta = N_{\text{baryons}}/N_{\text{photons}} =$

6×10^{-10} . On connaît bien le nombre de photons de l'univers, qui correspond à peu de chose près au nombre de photons du fond de rayonnement cosmologique, nous avons donc une contrainte forte sur le nombre maximal de baryons dans l'univers. Et ce nombre est très inférieur à la densité totale nécessaire pour créer les galaxies, groupes et amas observés autour de nous.

La relativité générale et les observations faites jusqu'ici nous enseignent par ailleurs que la matière de l'univers se comporte comme un fluide sans torsion. Ce fluide s'est aggloméré sous l'action de la gravité, partant (Fig 1.2) d'une distribution gaussienne des fluctuations de densité aux échelles où la gravité agit linéairement sur la matière, mesurée à un âge de 380 000 ans au moment de la combinaison des électrons et protons. Ces conditions initiales observées montrent que le contraste de densité à cette époque était faible, la donnée observable est le contraste de température et l'effet Sachs-Wolff aux grandes échelles, ainsi que les fluctuations adiabatiques aux petites échelles, relie le contraste de densité au contraste de température ($\Delta\rho/\rho \propto \Delta T/T < 10^{-4}$ où T est la température de corps noir du fond de rayonnement cosmologique émis à ce moment là et ρ la densité de matière) indiquant que l'univers naissant était très homogène.

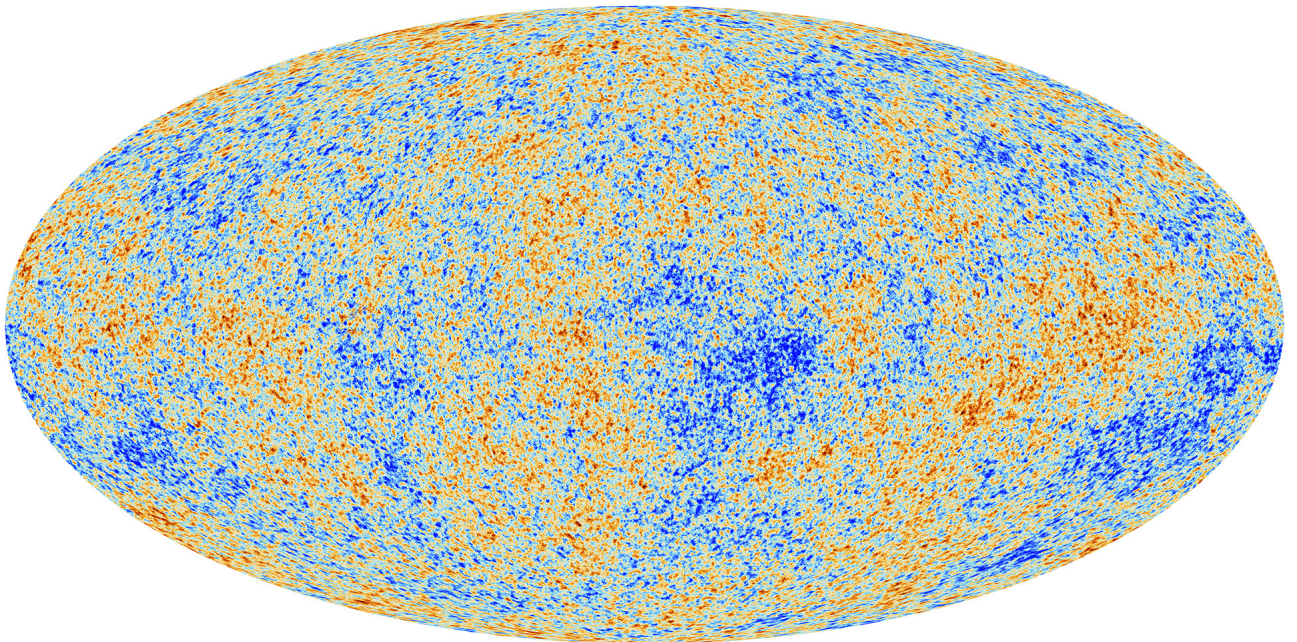


FIGURE 1.2 – Carte du fond de rayonnement cosmologique émis quand l'univers était âgé de 380 000 ans et observé ici par la sonde Planck (ESA). Le code couleur indique la température mesurée. Le contraste entre les zones les plus chaudes (en rouge) et les zones les plus froides (en bleu) est $\Delta T/T < 10^{-4}$ indiquant que l'univers naissant était très homogène.

Partant de ces conditions initiales, l'univers se refroidissant au cours des milliards d'années qui ont suivi, les puits de potentiels gravitationnels ont concentré la matière baryonique, jusqu'à ce que les effets non-linéaires dominent complètement les effondrements aux petites échelles ($< \sim 10\text{Mpc}$), produisant la richesse observée d'étoiles, de gaz, de poussière, de galaxies, d'amas de galaxies, ainsi que la structure à grande échelle (cf Figure 2.2).

Enfin, à l'aube du troisième millénaire, un faisceau d'observations indépendantes (Carroll et al. 1992), puis des mesures directes d'expansion (Riess et al. 1998; Perlmutter et al. 1999; Betoule et al. 2014), ont montré que l'expansion accélérerait et qu'une interprétation

simple d'un point de vue théorique de cette accélération était une énergie sombre d'effet inverse à la gravitation Frieman et al. (2008). Observation également confirmée par les missions spatiales WMAP et Planck.

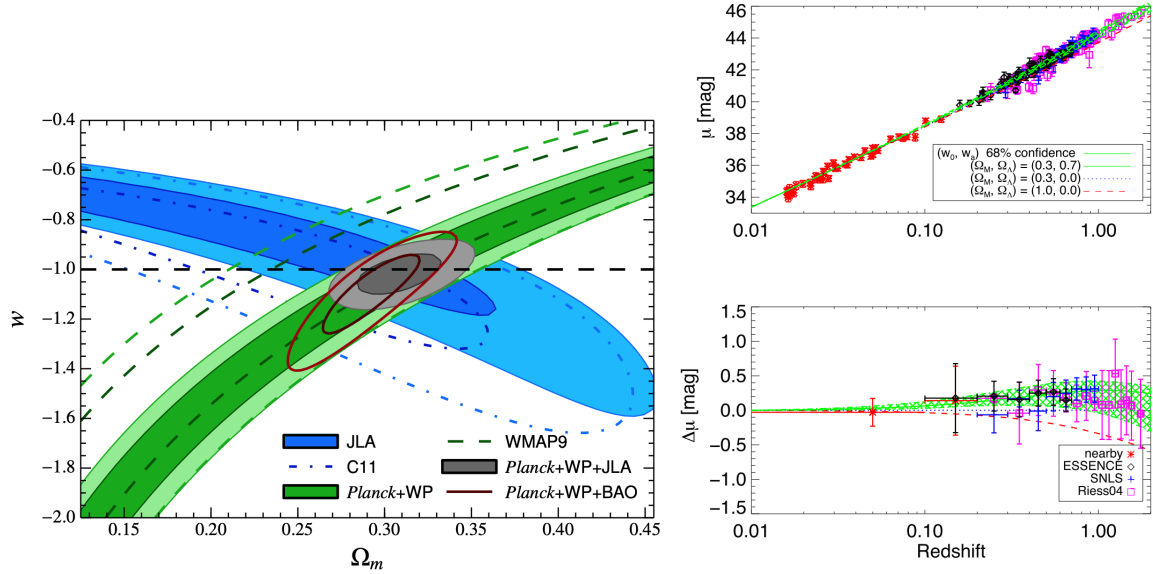


FIGURE 1.3 – A gauche, ellipses de vraisemblance de l’ajustement d’une constante cosmologique (paramétrisée ici par l’équation d’état w , cf chapitre 2) conjointement au paramètre de densité Ω_m , pour les sondes combinées indépendantes, la valeur $w = -1$ correspond à une énergie noire constante, tiré de Betoule et al. (2014). A droite, mesure du paramètre de Hubble par 4 équipes, utilisant les supernovas de type Ia comme chandelle standard. Les données sont les mieux ajustées par un univers Λ CDM, tiré de Frieman et al. (2008).

Nous vivons donc, semble-t-il, à une époque étrange où la physique nous impose de faire l’hypothèse que la majeure partie de la densité d’énergie de notre univers est invisible.

Si l’objet de la cosmologie est de reconstruire l’histoire causale des observations de la matière baryonique des origines à nos jours à l’aide des lois physiques à notre disposition afin de comprendre, à l’échelle de l’univers, d’où l’on vient et de prédire où l’on va, nous nous intéresserons dans ce texte à une petite brique de la cosmologie observationnelle et à une échelle particulière de l’agglomération de la matière baryonique, celle des groupes de galaxies. Nous aborderons tout d’abord ce que nous enseignent les observations sur les groupes de galaxies, puis dans le chapitre 2, la théorie de formation des groupes de galaxies. Le chapitre 3 présentera l’apport des observations de lentillage gravitationnel aux échelles des groupes de galaxies. Le chapitre 4 ouvrira la perspective des futures missions spatiales dans l’observation de lentillage par les groupes de galaxies en particulier les missions JWST⁴, Euclid⁵, CSST⁶ et WFIRST⁷ et les grands observatoires au sol LSST⁸, E-ELT⁹, SKA¹⁰.

4. <https://www.jwst.nasa.gov/>
 5. <https://sci.esa.int/web/euclid/home>
 6. <https://arxiv.org/abs/1901.04634>
 7. <https://wfirst.gsfc.nasa.gov/>
 8. <https://www.lsst.org/>
 9. <https://www.eso.org/public/teles-instr/elt/>
 10. <https://www.skatelescope.org/>

Mais la toute première étape dans notre découverte des groupes de galaxies commence forcément par l'énoncé de leur définition. C'est l'objet de la section suivante.

1.2 Deux difficultés : définition et détection

1.2.1 Une définition floue

La définition la plus simple des groupes de galaxies est apophatique : les groupes de galaxies ne sont ni des galaxies, ni des amas de galaxies. Cette définition, très courante dans la littérature, engendre une difficulté à laquelle font face les études des groupes de galaxies parce qu'elle recouvre une grande diversité d'objets sous le vocable "groupe de galaxies" et qu'elle impose de clarifier la sous-classe de groupes de galaxies étudiée à chaque étude. Nous n'échapperons pas à cette exigence dans les chapitres suivants, mais dans un premier temps nous proposons de faire un rapide tour d'horizon de la zoologie très diverse des groupes de galaxies avec une approche naturelle à la fois physique et généraliste, celle de classer les groupes de galaxies par leur masse. La seule hypothèse requise par cette classification est, bien évidemment, que les groupes de galaxies sont des objets auto-gravitants. L'avantage de cette définition ouverte est de broser le tableau le plus large possible des groupes de galaxies et de leur potentiel scientifique.

La définition apophatique fixe naturellement les extrema de masses des groupes de galaxies. Les galaxies étant définies comme les objets virialisés de masse totale inférieure à $M_{\text{galaxie}} < 10^{12} M_{\odot}$ et les amas de galaxies comme les ensembles de galaxies de masse supérieure à $M_{\text{amas}} > 10^{14} M_{\odot}$, les groupes de galaxies occupent donc, par défaut, un intervalle de masse de 2 ordres de grandeur, compris entre $10^{12} M_{\odot} < M_{\text{groupe}} < 10^{14} M_{\odot}$, avec une masse "signature" autour de $M_{\text{groupe}} \sim 10^{13} M_{\odot}$.

Aux deux frontières, la séparation est plutôt floue. Il n'y a pas vraiment de différence entre les galaxies les plus massives souvent entourées de compagnons de plus faible masse et les groupes de galaxies les moins massifs ≤ 4 individus. A l'autre extrémité les groupes de galaxies massifs d'une centaine de membres sont souvent classifiés dans la catégorie des petits amas. La plupart des analyses théoriques encore aujourd'hui considèrent que la notion de groupes de galaxies n'a pas de fondement physique très solide, les incluant plutôt dans un continuum de masse allant des galaxies aux amas, ou dans la queue de faible masse de la distribution statistique des amas de galaxies.

A contrario et comme nous le verrons dans le chapitre sur la formation des structures, on peut affirmer que la quasi totalité des galaxies massives, visibles aujourd'hui et dans un lointain passé, appartiennent à des groupes de galaxies. Ne serait-ce que par leur nombre et leur formation ancienne, les groupes de galaxies méritent que l'on s'y intéresse spécifiquement.

1.2.2 Une détection difficile

Une deuxième difficulté, de nature observationnelle, a freiné la recherche sur les groupes de galaxies ; la difficulté de les identifier de façon non équivoque sur le ciel profond, sur un intervalle de masse de 2 ordres de magnitude. En effet, à l'exception des objets très minoritaires avec une signature claire (e.g. groupes compacts, Hickson 1994, groupes fossiles ou massifs en X, Ponman et al. 1994; Mulchaey 2000, ou lentilles gravitationnelles, Cabanac et al. 2007), la détection de groupes par méthode amis-d'amis (Friend-of-friends) initiée par Turner & Gott (1976) et Huchra & Geller (1982) sur des échantillons photométriques

ou spectroscopiques est entachée d'incomplétude et d'impureté (voir les discussions détaillées de Duarte & Mamon 2015). La difficulté de détection est à deux niveaux, d'une part les groupes de faible masse sont difficilement repérables en tant qu'objets, c'est-à-dire par méthode dynamique, ou par sur-densité projetée sur le ciel. Comment être sûr à 100% qu'une sur-densité de galaxies sur le ciel n'est pas une concentration fortuite d'objets et que les objets sont bien liés par la gravité ? D'autre part, et cette difficulté affecte également les groupes massifs et les amas, comment être sûr que les galaxies à courte distance angulaire ou de redshift d'une sur-densité font bien partie du volume confiné par la gravité, autrement dit, sont-ils bien des membres du groupe. La contamination de galaxies non-membres, mal classifiées, peut atteindre 30% des galaxies d'un groupe (Duarte & Mamon 2015) .

Ces difficultés ont desservi le domaine de recherche sur les groupes de galaxies jusqu'à l'avènement de grands sondages cosmographiques du ciel profond (e.g. 2dFGRS, Colless et al. 2001, 6dFGRS, Jones et al. 2009, SDSS, Abazajian et al. 2009; Tago et al. 2010, GAMA, Hopkins et al. 2013) permettant la définition d'échantillons statistiques significatifs, tout en quantifiant les biais de détections systématiques. Un travail de fond de comparaison des algorithmes disponibles (Old et al. 2014, 2015) laisse entrevoir une amélioration significative des performances. Les derniers algorithmes sélectionnés pour la mission Euclid ; AMICO, un algorithme utilisant un filtre adaptatif dans l'espace des densités, magnitudes et redshifts photométriques (Bellagamba et al. 2017) et PZWAV¹¹, fondé sur une combinaison de probabilité dans l'espace des redshifts combiné à un filtre spatial à ondelettes (Gonzalez, priv com¹²) sont optimisés pour les données de faible signal-à-bruit et montrent une bonne combinaison de complétude et pureté sur les modèles simulés (Adam et al. 2019). Enfin, il est probable que dans ce domaine comme ailleurs, les méthodes d'apprentissage profond (Chollet et al. 2018¹³ et Gorbunov et al. 2017) finiront par supplanter les autres méthodes de détection et de caractérisation des groupes de galaxies (quelques exemples d'utilisation d'apprentissage profond sur la classification et morphologie de galaxies ; Huertas-Company et al. 2015; González et al. 2018; Domínguez Sánchez et al. 2018; Huertas-Company et al. 2019; Fischer et al. 2019; Cheng et al. 2020; Barchi et al. 2019; Khan et al. 2019; Hausen & Robertson 2019, détection de lentilles fortes ; Lanusse et al. 2018; Metcalf et al. 2019; Bom et al. 2019, modélisation de lentilles Hezaveh et al. 2017 identification de sources ponctuelles ; Sadr et al. 2018, séparation et fusion de galaxies ; Boucaud et al. 2019; Pearson et al. 2019; Burke et al. 2019, mesure de paramètres dans les galaxies ; Tuccillo et al. 2018; Boucaud et al. 2019; Dobbels et al. 2019 et amas de galaxies ; Ntampaka et al. 2019; Ho et al. 2019; Shen & Bekki 2020, extractions de paramètres à partir de données spectrales Jankov & Prochaska 2018; Zhao et al. 2019; Zhang et al. 2019; Leung & Bovy 2019; Muthukrishna et al. 2019, images de synthèse de sondages profonds Smith & Geach 2019¹⁴).

11. Les codes AMICO et PZWAV sont disponibles à travers la collaboration Euclid au site gitlab.euclid-sgs.uk/PF-LE3-CL/DET_CL_PZWAV

12. <http://www.sexten-cfa.eu/images/stories/conferenze2014/buildingclusters/talks/gonzalez.pdf>

13. <http://ascl.net/1806.022>

14. <http://ascl.net/1907.029>

1.3 La zoologie des groupes de galaxies

Les groupes de galaxies étant très divers, un peu de taxonomie est de rigueur pour en clarifier le paysage.

1.3.1 Le Groupe Local et les groupes de l'univers local ($z < 0.01$)

(Karachentsev & Kashibadze 2006; Makarov & Karachentsev 2011; Tully 2015))

Le groupe auquel la Voie Lactée appartient est un peu l'archétype des groupes de galaxies de faible masse dont la détection et la qualification, même à une distance de quelques dizaines de mégaparsec devient problématique. Il représente également un exemple symptomatique de la quantité abyssale d'informations perdues sur ce type d'objet à des distances même faibles. Pourtant, le Groupe Local est bien confiné gravitationnellement (la vitesse relative entre les galaxies massives étant $\Delta v = -123 \text{ km} \cdot \text{s}^{-1}$). Il est formé de deux galaxies massives, la Voie Lactée et la galaxie d'Andromède et d'une grosse cinquantaine de galaxies naines connues (en constante augmentation avec les progrès des moyens techniques), pour une masse totale de $M_{\text{GL}} = 1.29 \pm 0.14 \times 10^{12} M_{\odot}$.

De même, l'échantillon de 395 groupes de l'univers proche, appartenant tous au superamas local ou à son environnement proche, sont majoritairement des groupes de moins de 10 galaxies dont la dispersion de vitesse est $\sigma_{\text{groupe}} \leq 100 \text{ km} \cdot \text{s}^{-1}$. Il est intéressant de noter que la densité moyenne mesurée sur ce volume (rayon $\sim 40\text{-}45 \text{ Mpc}$) est de $\Omega_{\text{m}0} = 0.08 \pm 0.02$, soit 25 %, du paramètre de densité de matière mesuré par Planck (cf chapitre suivant). Il semble que nous vivions dans une zone de faible densité. Tant pis pour le principe copernicien...

1.3.2 Les groupes compacts de l'univers local

(Hickson 1994)

Les groupes compacts décrits par Hickson (1982) sont une sous-catégorie de groupes de faible masse, très compacts, souvent en interaction ou fusion, la plupart locaux, de galaxies brillantes répondant aux critères de sélection suivants :

1. $n \geq 4$ et $m_{\text{min}} \leq m_{\text{max}} + 3$. n est le nombre de membres, m_{min} et m_{max} sont les magnitudes du membre le plus faible, et le plus brillant.
2. $D \geq 3R_{\text{C}}$. R_{C} , est le rayon du cercle le plus petit incluant le centre de toutes les galaxies membres. D est la distance du centre de R_{C} à la galaxie non-membre la plus proche.
3. $\bar{\mu}_{\text{G}} < 26$. $\bar{\mu}_{\text{G}}$ est la brillance de surface moyenne dans le cercle R_{C} .

Hickson a trouvé 100 groupes dans les plaques du Palomar Observatory Sky Survey, mais 32 ont été disqualifiés comme des superpositions fortuites de plusieurs sous-groupes dans la ligne de visée. Mamon (1986) affirme qu'en dehors des objets montrant des signes directs d'interactions (morphologies perturbées, ponts de matière, queues de marées), les groupes compacts de Hickson tels que sélectionnés ne sont pas de véritables objets physiques.

Dans le but de créer un échantillon complet dans l'univers local et physiquement motivé, une recherche par Díaz-Giménez et al. (2018) à partir de l'échantillon de 500 000

Local Group and nearest galaxies

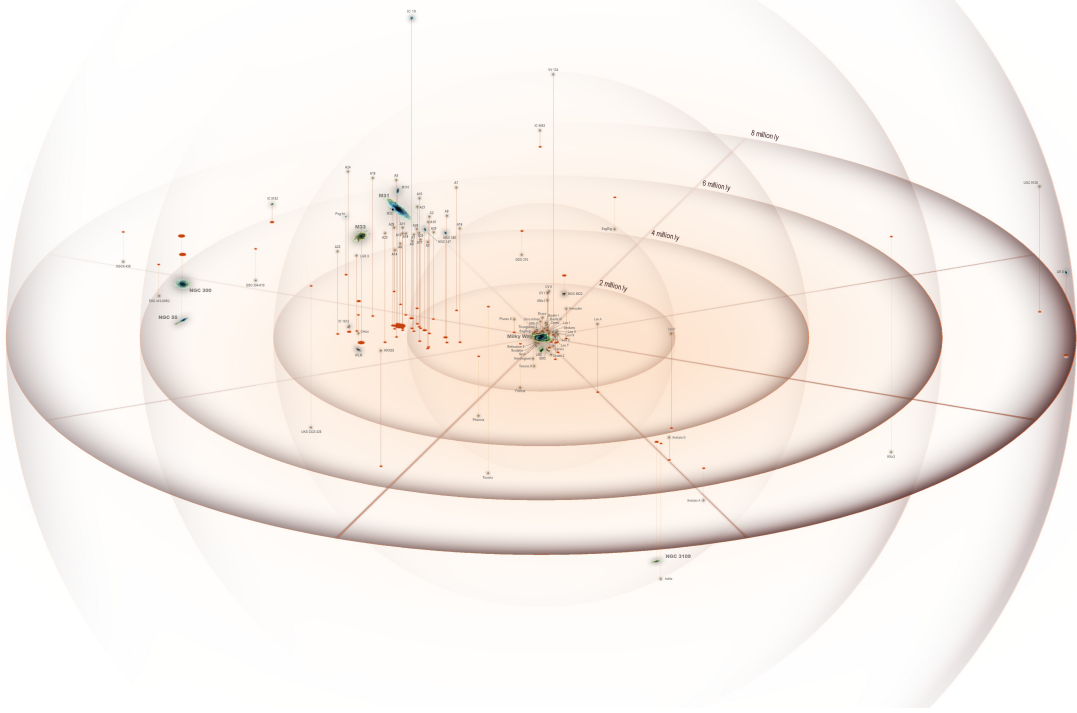


FIGURE 1.4 – Carte du Groupe Local.

galaxies extraites du SDSS DR12¹⁵, dont Tempel et al. (2017) a extrait des groupes en interaction, a permis de compléter l'échantillon à plus de 406 groupes compacts avec un critère additionnel sur l'intervalle de vitesse radiale,

$$\Delta v_{i,\text{med}} = c \frac{|z_i - z_{\text{med}}|}{1 + z_{\text{med}}} \leq 1000 \text{ km} \cdot \text{s}^{-1},$$

où z_i est le redshift de la galaxie testée et z_{med} est le redshift médian du groupe considéré. Confirmant l'intuition de Mamon, la singularité originelle de ces groupes compacts qui était leur dispersion de vitesse élevée, posant une question sur leur stabilité, ou leur masse totale, disparaît avec ce nouvel échantillon, qui montre une dispersion de vitesses ($\sigma_v \simeq 236 \pm 16 \text{ km} \cdot \text{s}^{-1}$) assez proche des mesures moyennes sur les groupes de galaxies et des rapports masse/luminosité cohérents avec les modèles de formation CDM ($M/L \simeq 100\text{-}150 M_\odot/L_\odot$). Notons que la mesure de la masse totale de ces groupes n'est pas aisée (Girardi et al. 2002; Proctor et al. 2015). L'hypothèse que ces systèmes sont virialisés n'est pas robuste. La masse contenue à l'intérieur d'un rayon de sur-densité de 200 fois la densité critique M_{200} , est souvent prise comme

$$M_{200} = \frac{3}{G} \sigma_{200}^2 R_{200} \quad (1.1)$$

où σ_{200} est la dispersion de vitesse dans un rayon de R_{200} et

$$R_{200} = \frac{\sqrt{3}\sigma}{10H(z)} \text{ Mpc}. \quad (1.2)$$

15. <https://www.sdss.org/dr12>

On réécrit souvent la définition de la masse comme

$$\log(M_{200}) = 3 \log(\sigma_{200}) + 6.24 - \log[\sqrt{\Omega_m(1+z)^3 + \Omega_\Lambda}]. \quad (1.3)$$

Sachant que localement à $z < 0.1$, le dernier terme est négligeable.

1.3.3 Les groupes fossiles

(Barnes 1989; Ponman et al. 1994; Jones et al. 2003; D’Onghia et al. 2005; Aguerri et al. 2011)

Les groupes fossiles, objets d’une riche bibliographie récente, sont des groupes montrant un halo d’émission X brillant ($L_X \gtrsim 5 \times 10^{34} h^{-2} \text{ W}$). Ils sont dominés par une galaxie massive elliptique très évoluée. La différence de magnitude entre les deux membres les plus brillants du groupe, Δm_{12} , doit être d’au moins 2 magnitudes en bande r . En outre, ces deux galaxies doivent se situer à la moitié du rayon viriel projeté r_{vir} . Ces critères de choix assurent que (i) l’émission X ne peut pas venir d’une galaxie isolée, (ii) la friction dynamique fera tomber les galaxies massives au centre du halo dans un temps inférieur au temps de Hubble, (iii) l’occurrence statistique de cette configuration pour une fonction de luminosité classique est très faible (Jones et al. 2003). L’identification des groupes fossiles impose bien évidemment l’existence de données X. Les premiers sondages systématiques ont utilisé la mission ROSAT à travers le projet WARPS¹⁶ (Wide Angle ROSAT Pointed Survey; Scharf et al. 1997). Ces premières études ont permis de fixer la densité de ce type d’objets à $\rho_{\text{FG}}(L \geq L_X \text{ pour } 0.5\text{-}2 \text{ keV}) \simeq 1.6 \pm 0.8 \times 10^{-6} h^3 \text{ Mpc}^{-3}$, c’est-à-dire à peu près 2 à 4 fois plus nombreux que les groupes compacts et environ 10 fois plus que la somme des amas massifs et amas pauvres ayant $L_X > 10^{35} \text{ W}$ dont ils pourraient être les progéniteurs des galaxies centrales. Une connection entre groupes fossiles et les groupes compacts massifs à $z > 0.14$ est aussi possible (Mendes de Oliveira & Carrasco 2007; Irwin et al. 2015). Les études récentes, notamment le projet FOGO¹⁷ (FOssil Group Origin; Aguerri et al. 2011, Zarattini et al. 2014 et références incluses.), incluent le suivi optique de 34 groupes fossiles Santos et al. (2007) extraits du SDSS DR5¹⁸, pour une densité de $\rho_{\text{FG}} \simeq 2.5 \pm 1.5 \times 10^{-6} h^3 \text{ Mpc}^{-3}$ jusqu’à un redshift de $z < 0.5$.

Il existe deux scénarios aujourd’hui proposés pour expliquer la formation des groupes fossiles. Le premier (baptisé "fusion") propose une fusion rapide à haut redshift de galaxies massives dans un halo CDM particulièrement compact (D’Onghia et al. 2005) expliquant l’absence de galaxies intermédiaires entre la galaxies géante centrale et les autres membres du groupe. Le second (baptisé "groupe raté") propose que la galaxie centrale s’est formée par un effondrement monolithique de la sur-densité dès l’origine, sans aucune présence de galaxies L^* , donc sans fusion majeure (Mulchaey & Zabludoff 1999). Il sera difficile de trouver quel scénario est le plus probable tant que l’on aura pas d’observations en X de groupes fossiles en formation à $z > 1$, bien que les études récentes de synthèse spectrale des galaxies centrales des groupes fossiles pointent plutôt sur le scénario "fusion" (Corsini et al. 2018) et qu’il semble que certaines fusions puissent être davantage tardives (von Benda-Beckmann et al. 2008).

16. <http://www.ifa.hawaii.edu/ebeling/clusters/WARPS.html>

17. <https://slideplayer.com/slide/6014778>

18. <https://www.sdss.org/dr5>

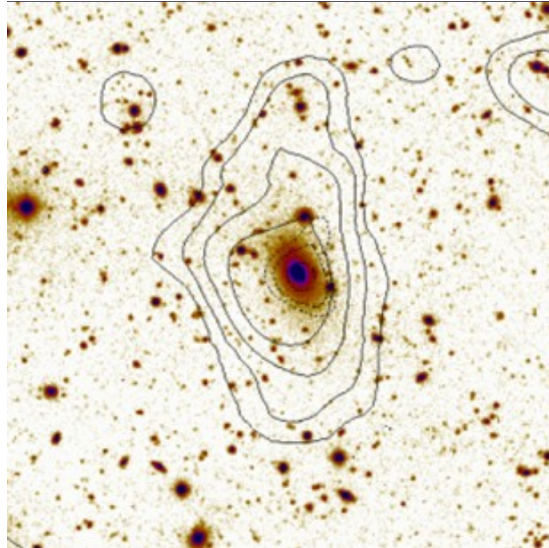


FIGURE 1.5 – Premier groupe fossile identifié : RX J1340.6+4018, image d’une arcmin de côté ; $z = 0.17$, les isophotes montrent la contrepartie X ($L_X = 2.4 \times 10^{36} h^{-2} W$, $M (< R = 1,62h^{-1} \text{ Mpc}) = 2.1 \times 10^{13} h^{-1} M_\odot$ et $M/L \sim 130_{-40}^{+130} M_\odot/L_\odot$ (Ponman et al. 1994).

Les dernières études s’appuyant sur les données du sondage XMM-LSS¹⁹ Pacaud et al. (2007) couvrant 3 deg^2 du CFHT-LS²⁰ (final release) retrouvent de façon indépendante que sur les 129 objets X détectés jusqu’à $z \leq 0.6$, $22 \pm 6\%$ sont des groupes fossiles (Gozaliasl et al. 2014), mais ils relâchent les critères de sélection à la fois sur le flux X et la différence de magnitude entre les deux membres les plus brillants ($L_X \gtrsim 2.8 \times 10^{34} h^{-2} W$) et $\Delta m_{12} > 1.7$. Leur étude suggère que Δm_{12} est un continuum dont les groupes fossiles occupent l’extrême. Ce continuum semble même être un bon indicateur pour tester les recettes semi- analytiques de formation d’étoiles et d’effets physiques d’évolution divers (effets rétroactifs d’AGN, supernovae). Plutôt que des recettes semi-analytiques, Il est bien entendu préférable de construire et tester des modèles hydrodynamiques comme Illustris ou New Horizon (Vogelsberger et al. 2013; Dubois et al. 2014; Teyssier 2015) (cf chapitre 2), quand ils sont disponibles, parce qu’ils modélisent les objets physiques à partir des premiers principes de façon cohérente sans greffer de modèles phénoménologiques (ou presque, cf chapitre 2).

1.3.4 Les groupes lentilles

(Cabanac et al. 2007; Limousin et al. 2009; More et al. 2012; Stark et al. 2013)

Une dernière catégorie de groupe de galaxies est apparue ces quinze dernières années, les groupes de galaxies détectés par lentillages gravitationnels forts. Il ne s’agit pas d’une caractéristique intrinsèque liée aux groupes eux-mêmes, puisque tous les types de groupes de galaxies se retrouvent dans les groupes lentilles. Cette famille de groupes fera l’objet d’un chapitre particulier de cette thèse, nous ne ferons ici qu’une description succincte du phénomène. Depuis la découverte de la première lentille forte (quasar binaire, Walsh et al.

19. <http://cosmosdb.iasf-milano.inaf.it:8080/XMM-LSS/>

20. www.cfht.hawaii.edu/Science/CFHTLS/

1979), toute la phénoménologie des lentilles gravitationnelles a été explorée et exploitée, au gré des progrès techniques, à la fois au sol et dans l'espace (par exemple Wambsganss 1998; Meylan et al. 2006; Treu 2010; Bartelmann 2010; Kneib & Natarajan 2011; Bartelmann & Maturi 2017; Mandelbaum 2018) . Il existe peu de domaine de l'astrophysique qui ne soit touché par cette propriété spatio-temporelle de la lumière passant à travers un milieu dense et trouvant une interprétation élégante dans la relativité générale. Comme tous les phénomènes de lentillage gravitationnel, la probabilité d'observer un événement dépend de deux facteurs : la densité de masse projetée sur le ciel de l'objet d'avant-plan (appelé la lentille), et la géométrie de la lentille et de l'objet d'arrière-plan (appelé source). On classe généralement le lentillage dans trois sous-classes :

- Le microlentillage, qui est un effet temporel variable et rapide, amplifiant le flux d'une source passant fortuitement derrière une microlentille,
- le lentillage faible qui change la forme et le flux des sources autour des lentilles de façon linéaire (voire statistique).
- le lentillage fort, formellement défini quand la magnification $\mu > 1$, qui produit des effets spectaculaires de mirages sous forme de grand arcs et de multiplication d'images sur une même source.

Les deux derniers effets sont spatiaux et ne varient pas de façon significative dans le temps (à l'échelle humaine) parce que les mouvements propres des lentilles et des sources sont négligeables en regard des distances dans la ligne de visée. Les variations de flux observées sont dues à des variations intrinsèques de la source (par exemple un quasar) et des effets superposés de microlentillage. Le domaine qui nous intéresse ici est l'effet de lentille gravitationnel fort par des galaxies, groupes ou amas de galaxies. Si les effets de lentillage sont aléatoires et ne favorisent pas particulièrement une échelle plutôt qu'une autre, certaines configurations sont plus facilement détectables. En l'occurrence, les amas de galaxies denses, rares, mais occupant une surface projetée significative sur le ciel et les galaxies massives isolées, très nombreuses, ont commencé à être observés à partir des années 1980 (quasars lentillés Kochanek et al. 1999; Myers et al. 2003 pour les amas Soucail et al. 1987; Fort et al. 1993; Gladders et al. 2002; Sharon et al. 2019, pour les galaxies isolées Blandford et al. 1989; dell'Antonio & Tyson 1996; Bolton et al. 2006), il a fallu attendre les premiers sondages photométriques profonds du ciel couvrant une surface de quelques degrés carrés pour voir apparaître les premiers groupes lentilles (Cabanac et al. 2007; Estrada et al. 2007; Kubo et al. 2009, 2010; Bayliss et al. 2011; More et al. 2012; Stark et al. 2013).

La donnée principale qu'apporte le lentillage gravitationnel à l'astrophysique contemporaine est la mesure de la masse totale dans la ligne de visée d'un objet. Plus le nombre de contraintes est grand (nombre d'arcs en fonction du rayon) plus la connaissance de cette masse totale s'affine (profil, sous-structures). Le lentillage fort fournit des mesures uniques du centre des sur-densités cosmiques, c'est-à-dire des zones dominées par les baryons dans les galaxies ou dans les zones fortement non-linéaires au centre des groupes et amas. Cette mesure est complémentaire des analyses à plus grandes échelles que peut apporter le lentillage faible. Le plus grand défi qui se pose au domaine du lentillage fort est la rareté du phénomène et la difficulté d'une part de collecter un échantillon statistiquement significatif, et d'autre part d'en bien connaître les effets de sélection.

Aujourd'hui, on connaît environ un millier de lentilles galaxies-galaxies, elles peuvent être assimilées à des groupes de faible masse, une centaine de groupes massifs de masse intermédiaire et quelques dizaines d'amas. Dans les années à venir, on peut s'attendre



FIGURE 1.6 – Quelques exemples des groupes de galaxies détectés dans le CFHTLS, Les rayons d'Einstein de ces groupes sont entre 5 et 10 arcsec (Cabanac et al. 2007; More et al. 2012).

à une moisson de candidats à toutes les échelles avec les sondages KiDS²¹ (1000 deg²; Spiniello et al. 2018; Petrillo et al. 2019) et Dark Energy Survey²² (5000deg²; Diehl et al. 2017; Treu et al. 2018), sans oublier, bien entendu le Large Synoptic Survey Telescope (LSST²³) ou la mission spatiale Euclid²⁴.

1.4 Pourquoi étudier les groupes de galaxies ?

1.4.1 Chainon indispensable de la formation des structures

Nous l'avons mentionné, les groupes de galaxies occupent un espace flou entre des objets physiques mieux définis, pourquoi dès lors dépenser de l'énergie à les étudier ? Outre la raison tautologique, qui ne convaincra que les astrophysiciens, que tout objet du ciel mérite qu'on s'y intéresse, une partie de la réponse se trouve dans les modèles d'évolution hiérarchique des structures (voir chapitre 2).

Les groupes de galaxies sont un chaînon essentiel de notre compréhension de l'histoire de

21. <http://kids.strw.leidenuniv.nl/>

22. <https://www.darkenergysurvey.org/>

23. <https://sites.google.com/view/lsst-stronglensing>

24. <https://euclid.cnes.fr/fr> ou <https://www.euclid-ec.org/> ou <http://sci.esa.int/euclid/>

la formation stellaire au sein des sur-densités et de la construction des grandes structures parce qu'ils occupent l'échelle où la physique baryonique rencontre les phénomènes cosmologiques.

Dans les galaxies, on ne voit pratiquement que la physique des baryons en action locale, mais on ne voit pas les conséquences de cette physique sur l'univers local²⁵, ni les effets d'expansion, d'accélération des composantes noires. Du côté des halos massifs, dans les amas de galaxies, on voit les conséquences de l'effondrement CDM dans leur profil, et le centre des amas montre les effets rémanents de processus physiques. Mais ces effets ont largement été effacés lors de la fusion des groupes au centre du puit de potentiel de l'amas, pendant la virialisation.

Pour observer et modéliser tous les processus physiques en jeu, de provenance baryonique et CDM, il faut aller dans les groupes de galaxies qui couvrent l'intervalle de masses intermédiaires des halos. C'est dans ces halos intermédiaires qui se sont effondrés à un moment de l'histoire de l'univers où la formation stellaire battait son plein que nous pouvons étudier le détail de l'émergence des processus physiques dans leur globalité et observer leur évolution en fonction de la masse et du redshift des halos. Les groupes de galaxies sont donc une des clefs de notre compréhension de l'histoire de la formation stellaire et de la formation des grandes structures de l'univers.

1.4.2 La formation hiérarchique des structures

En quelques mots, la théorie d'évolution des structures (voir chapitre 2), totalement dominée par la matière sombre non-baryonique (Cold Dark Matter, CDM) nous enseigne que les objets les plus petits se sont formés en premier dans notre univers, puis les objets de masse intermédiaire et enfin les grandes structures se sont formées en dernier, elles sont en train de se former encore aujourd'hui (voir par exemple Avila-R eese 2006; Peter & Uzan 2012). En d'autres termes, les amas de galaxies se forment de groupes de galaxies déjà assemblés qui se forment eux-mêmes de galaxies formées à des redshifts plus élevés. Ce processus d'effondrement est linéaire sur les grandes échelles, mais de plus en plus non-linéaire aux petites échelles, celle des galaxies. En parallèle à cet effondrement linéaire qui dépend entièrement de la distribution en densité de la matière noire non-baryonique (CDM), se construit la masse stellaire à partir du gaz primordial. Cette émergence de la masse baryonique chaude et rayonnante dans les puits de potentiels gravitationnels, c'est-à-dire la formation des étoiles dans les galaxies est la seule phase qu'on peut observer et qui occupe les astrophysiciens extragalactiques depuis cent ans.

1.4.3 La formation des étoiles dans les galaxies

La physique stellaire

On connaît assez bien, aujourd'hui, les grandes lignes de l'évolution stellaire, les modèles théoriques interprètent bien les observations des étoiles dans notre galaxie et dans les galaxies voisines assez proches pour que l'on puisse encore séparer les étoiles entre elles. Notons cependant que les premières phases (naissance des systèmes stellaires) et surtout les dernières phases de vie des étoiles (phases géante et asymptotique) pendant lesquelles

25. même si l'existence de halo de matière sombre, dont les vitesses de rotation plates des disques des galaxies sont un indice robuste, ont un impact astrophysique sur la vitesse de création de la masse stellaire à l'échelle cosmique

les étoiles dominant la lumière des galaxies ne sont pas encore parfaitement connues. C'est même la principale source d'erreur des modèles de synthèse spectrale (Bruzual & Charlot 2003). Nous ne ferons pas de revue de la physique stellaire, de nombreuses monographies sont disponibles, rappelons seulement les faits importants pour l'interprétation des observations et la modélisation de la formation des étoiles dans l'histoire de l'univers.

- L'évolution stellaire nous enseigne que les étoiles ont une durée de vie t_* inversement proportionnelle à leur masse M_* . $t_* \simeq (M_*/M_\odot)^{-2.3} t_\odot$, où t_\odot et M_\odot sont la durée de vie et la masse du soleil. Une étoile de 10 masses solaires a une durée de vie $t_* \simeq 0.005 t_\odot$, c'est-à-dire 5 millions d'années.
- La luminosité des étoiles de la séquence principale L_* est reliée à leur masse M_* par $L_* \simeq (M_*/M_\odot)^{3.3} L_\odot$.
- Pendant les phases de géante rouge et branche asymptotique (Asymptotic Giant Branch, AGB) qui durent typiquement 10% de la vie d'une étoile, leur luminosité augmente d'un facteur 1000 pour les étoiles de la masse du soleil et sub-solaire et d'un facteur 10 pour les étoiles massives.
- Les étoiles les plus massives perdent $\sim 5\%$ de leur masse au cours de leur courte vie sur la séquence principale. C'est beaucoup moins que ce que l'on pensait jusque dans les années 90. Ces pertes de masses dépendent de leur composition chimique (Smith 2014), de leur champ magnétique (voir les proceedings Balona et al. 2003, la revue Donati & Landstreet 2009 et tous les travaux produits avec l'instrument Narval²⁶ au Pic du midi)
- Les deux tiers des étoiles se trouvent dans des systèmes binaires, ou multiples. L'évolution de ces étoiles dépend de leur environnement. La physique stellaire en est encore à ses balbutiements sur les modèles de perte de masse des systèmes binaires.
- La quantité et la composition du gaz éjecté à la fin de la vie des étoiles dépend de façon critique de leur masse, de leur métallicité et de leur binarité.

Chacun de ses points a un impact quand on cherche à définir le rôle des baryons dans l'évolution de la masse stellaire des débuts de l'univers à aujourd'hui. L'état de nos connaissances sur l'évolution stellaire nous appelle à la plus grande prudence et humilité quand on cherche à extrapoler l'évolution d'objets du début de l'univers où aucune observation n'existe (Smith 2014).

La formation des étoiles dans les galaxies

D'un point de vue physique les étoiles se forment dans les galaxies en suivant un processus multi-échelle suivant cinq étapes. L'accrétion de gaz sur des disques depuis des galaxies satellites ou le milieu intergalactique (Mpc); le refroidissement de ce gaz pour former une phase neutre (kpc); la formation de nuages moléculaires ($\sim 10-100$ pc); la fragmentation et accrétion de ce gaz en structures plus dense (~ 1 pc) et en coeur proto-stellaires (~ 0.1 pc); et finalement en étoiles et systèmes planétaires (R_\odot et \sim UA). Nos connaissances de ces phases de formation restent encore lacunaires aujourd'hui, une approche unifiée pour comprendre la formation stellaire doit inclure des contraintes observationnelles et astrophysiques sur l'efficacité de la formation stellaire et les fonctions de masse à partir d'études aux plus petites échelles, en parallèle d'une compréhension des processus initiant et régulant la formation des nuages aux échelles des galaxies. Le lecteur est renvoyé aux revues détaillées de Kennicutt (1998) et Kennicutt & Evans (2012).

26. <https://tbl.omp.eu/observer-au-tbl/publications/>

L'enrichissement chimique des galaxies

Les processus thermonucléaires ayant lieu au centre des étoiles, leur permettant de d'équilibrer la gravitation et de briller, créent les éléments chimiques plus lourds que le béryllium et lithium (${}^7\text{Be}$, ${}^7\text{Li}$), c'est la nucléosynthèse stellaire, dont l'article fondateur est Burbidge, Burbidge, Fowler, Hoyle (1957) alias B2FH. Une partie de ces éléments est éjectée à la fin de la vie des étoiles en fonction de leur masse et enrichissent le milieu inter-stellaire des galaxies et le milieu intra-amas, génération après génération. Ces processus sont à la base de l'évolution chimique des galaxies.

Un modèle d'évolution chimique d'une galaxie a besoin de cinq ingrédients de base pour aboutir. (i) des conditions initiales (ii) le résultat de l'évolution stellaire en terme de composition et masse des éjectas en fonction du temps (iii) une fonction de masse initiale donnant le taux de formation des étoiles en fonction de leur masse (iv) un modèle de taux de formation d'étoiles en fonction du temps, de la masse, densité, température et dynamique du gaz (v) des hypothèses sur la contribution de propriétés influant globalement l'évolution en dehors des étoiles. Voyons chacun des ingrédients.

- (i) Conditions initiales : on prend en général les conditions primordiales après la nucléosynthèse initiale
- (ii) Résultat de l'évolution stellaire : est dicté par la physique stellaire
- (iii) Fonction de masse initiale : La fonction de masse initiale (IMF) des étoiles définit la distribution du taux de formation d'étoiles en fonction de leur masse. Cette fonction est généralement paramétrée par une loi ou une combinaison de lois de puissance ou une fonction log-normale (Salpeter 1955; Kroupa 2002; Chabrier 2003). Son universalité dans le temps et dans l'espace reste un objet de débat en 2020. Localement, le principe d'Occam nous pousse à conjecturer l'universalité de l'IMF, mais il semble que les IMF déduites d'observations à haut redshift montrent un excès d'étoiles massives (Zhang et al. 2018).
- (iv) Modèle de taux de formation d'étoiles : Au premier ordre la formation d'étoiles est proportionnelle à la densité de gaz disponible. Les observations montrent que la formation d'étoiles dans les galaxies localement n'est pas facilement modélisable par une loi continue, mais est plutôt dominée par de brefs sursauts de formation à des périodes non-prédictibles.
- (v) Effets environnementaux : les fusions de galaxies, les effets de marée, la pression de rayonnement sur le gaz, causée par un sursaut violent de formation à l'échelle de la galaxies, sont autant d'effets environnementaux pouvant influencer de façon majeure sur l'évolution de la formation d'étoile.

Ainsi, les étoiles que nous observons dans notre Galaxie aujourd'hui sont un reflet fossile biaisé de l'histoire de la formation des étoiles au cours des 13,8 milliards d'années passées. La grande partie des témoins, c'est-à-dire des étoiles massives, a disparu, a été ré-injectée dans les générations suivantes d'étoiles sous forme d'évolution chimique et ce sur plusieurs générations. Comprendre cet enchaînement de générations stellaires est compliqué par l'impact des rétroactions évolutives d'une génération stellaire à l'autre.

Une source additionnelle d'information provient des orbites stellaires. Par exemple notre Galaxie est connue de façon détaillée depuis la mission GAIA ²⁷ (Gaia Collaboration et al. 2016, 2018), qui nous a donné la position et le mouvement propre d'un milliard d'étoiles. Cette connaissance nous permet de retracer l'histoire détaillée de la formation

27. <http://gea.esac.esa.int/archive/>

de notre Galaxie par cannibalisations successives de galaxies naines. Pour les autres galaxies de notre univers local ou lointain, on ne dispose pas de ces informations détaillées, toutefois, on peut tenter de reconstruire une histoire de formation stellaire par diverses méthodes.

Si on dispose d'une information dynamique sur les étoiles dans la galaxie considérée, par exemple avec un spectrographe intégral de champ où chaque pixel donne un spectre de l'objet (par exemple l'instrument MUSE²⁸ au VLT) on peut faire des modèles chémo-dynamiques d'évolution (par exemple Guérou et al. 2016; Zhu et al. 2016).

Si on ne dispose que d'un seul spectre intégrant toute la lumière de la galaxie observée, la synthèse de population stellaire est la méthode la plus répandue (Bruzual & Charlot 2003; Cid Fernandes et al. 2005; González Delgado et al. 2005; Mathis et al. 2006), elle consiste à reconstruire le spectre observé en combinant les spectres des étoiles le composant, faisant une série d'hypothèses sur l'âge des étoiles de la galaxie, ainsi que diverses propriétés intégrées (extinction interstellaire, métallicité, poussière).

Si on connaît la distribution d'énergie spectrale (Spectra Energy Distribution, ou SED) de la galaxie considérée, on peut essayer de modéliser la SED avec des codes de transfert de rayonnement incluant des paramètres supposés réalistes pour l'émission des composants baryoniques (étoiles, poussière, gaz froid et chaud) par exemple le code CIGALE²⁹, (Boquien et al. 2019; Chevallard & Charlot 2016).

Rappelons que ces modélisations sont des problèmes inverses qui ont une infinité de solution. Par conséquent, choisir la "meilleure" solution parmi une multitude requiert des hypothèses simplifiant le problème et un traitement probabiliste.

La formation stellaire à l'échelle du cosmos

La formation stellaire à l'échelle du cosmos est abordée de façon détaillée par Maddau & Dickinson (2014). Replacer les modèles d'évolution stellaire des galaxies dans une perspective cosmologique et construire un scénario cohérent n'est pas chose aisée. Si les observations, parcellaires, des galaxies avec le redshift ne donnent pas encore suffisamment de détails pour faire émerger des modèles détaillés, on peut cependant s'appuyer sur une variété de traceurs de formation d'étoiles sensibles à différentes masses stellaires, âges et détectables à différents redshifts afin de donner une vision globale de la formation stellaire au cours de l'histoire du cosmos (Kennicutt & Evans 2012).

Les traceurs observationnels de formation d'étoiles dans l'univers lointain :

- le continu UV à 150, 230 ou 280 nm trace les étoiles très jeunes. Supposant une IMF de type Salpeter, et un sursaut de formation d'étoile unique, le continu UV à 150 nm diminue de 10^{-2} pour une population âgée de 10^8 ans, et de 10^{-3} à 10^{-6} en 10^9 ans, pourtant la moitié de l'énergie lumineuse produite sur 10 milliards d'années vient des premières 100 millions d'années. Cette forte sensibilité à l'âge fait du continu UV un excellent traceur de la formation d'étoiles massives avec une résolution temporelle de 10^7 ans, en augmentant proportionnellement à la longueur d'onde mesurée. Ce traceur couvre le domaine visible dans l'intervalle $1.5 < z < 4$ et proche infrarouge au-delà. Un défaut majeur de ce traceur est le fait que la majeure partie de la formation stellaire jeune se produit dans des nuages moléculaires riches

28. <https://www.eso.org/sci/facilities/paranal/instruments/muse/overview.html>

29. <https://cigale.lam.fr/>

en poussière. Ainsi, même des galaxies sélectionnées sur leur émission UV (par exemple les galaxies Lyman-Break, Steidel et al. 2003) sont riches en poussière et en moyenne 80% de leur émission UV est ré-émise en infrarouge (Reddy et al. 2012).

- l'émission infrarouge moyen (MIR) et lointain (FIR) provient de l'émission UV absorbée et ré-émise sans extinction. On définit la luminosité L_{IR} mesurée entre 8-1000 μm . On l'interprète comme une fraction directe de l'émission de la formation d'étoile. Cependant, cette luminosité peut également provenir de noyau actif de galaxie (AGN), ou d'étoiles vieilles, en particulier l'émission MIR. Comme cette observation est rarement directe on ajuste des modèles d'émission de poussière qui dépendent de plusieurs composants avec des tailles, densités et températures variées et l'étalonnage des données MIR est entaché d'incertitude. L'émission infrarouge moyen ($< 30 \mu\text{m}$) a été observée par la mission *Spitzer*³⁰ jusqu'à des redshifts de $z \approx 2$. Mais son interprétation est plus complexe que l'émission infrarouge lointain, où la mission *Herschel*³¹ a apporté une grande sensibilité pour les objets émettant dans la bande 60-100 μm à redshift $z < 4$, mais avec une résolution limitée ($\sim 30''$).
- Indicateurs d'émission nébulaire. Il existe des émissions nébulaires classiques de la formation stellaire (Osterbrock & Ferland 2006), notamment H α 656.3 nm, H β 486.1 nm, Paschen α 1875 nm et les lignes d'émissions des régions d'hydrogène ionisé HII. [OII] 372.7 nm, [OIII] 500.7 nm. La raie Ly α 121,6 nm étant résonnante son analyse est complexe.

Les observations : A l'aide des traceurs de formation stellaire, on peut reconstituer l'histoire de formation des étoiles dans l'univers. Les grands sondages ayant permis d'extraire cette information ces dernières années sont les sondages profonds multi-fréquence effectués avec les télescopes spatiaux (HST, *Herschel*, *Spitzer*) et au sol; GOODS³², COSMOS³³, CANDELS³⁴, AEGIS³⁵, et le suivi radio associé NOAO Deep Wide Field Survey³⁶. Le nerf de la guerre de ces observations est relié à la capacité à suivre les galaxies avec des spectrographes. Historiquement, les capacités de suivi spectroscopique ont toujours été réduites. Jusqu'à aujourd'hui, la communauté astronomique n'a pas réussi à converger vers le financement d'un télescope spécialisé en spectroscopie. Souhaitons que le projet en cours MSE³⁷ trouve le financement qu'il mérite. En attendant, les grands projets de suivi spectroscopique ont utilisé les instruments multi-objets à leur disposition, 2dFGRS³⁸, VIMOS VLT Deep Survey, VUDS³⁹ et bien entendu les données de la mission *GALEX*⁴⁰. L'ensemble de ces données font émerger une image assez robuste de la construction de la masse stellaire dans l'univers, celle de la figure 1.7 (Madau & Dickinson 2014), voir également Heavens et al. (2004).

30. <http://www.spitzer.caltech.edu/>

31. <http://sci.esa.int/herschel/>

32. <http://www.stsci.edu/science/goods/DataProducts/>

33. <http://cosmos.astro.caltech.edu/page/astronomers>

34. http://arcoiris.ucolick.org/candels/data_access/Latest_Release.html

35. <https://aegis.ucolick.org/>

36. <https://www.noao.edu/noao/noaodeep/index.html>

37. <https://mse.cfht.hawaii.edu/>

38. <http://www.2dfgrs.net/>

39. <http://cesam.lam.fr/cesamdata/data.php>

40. <http://www.galex.caltech.edu/>

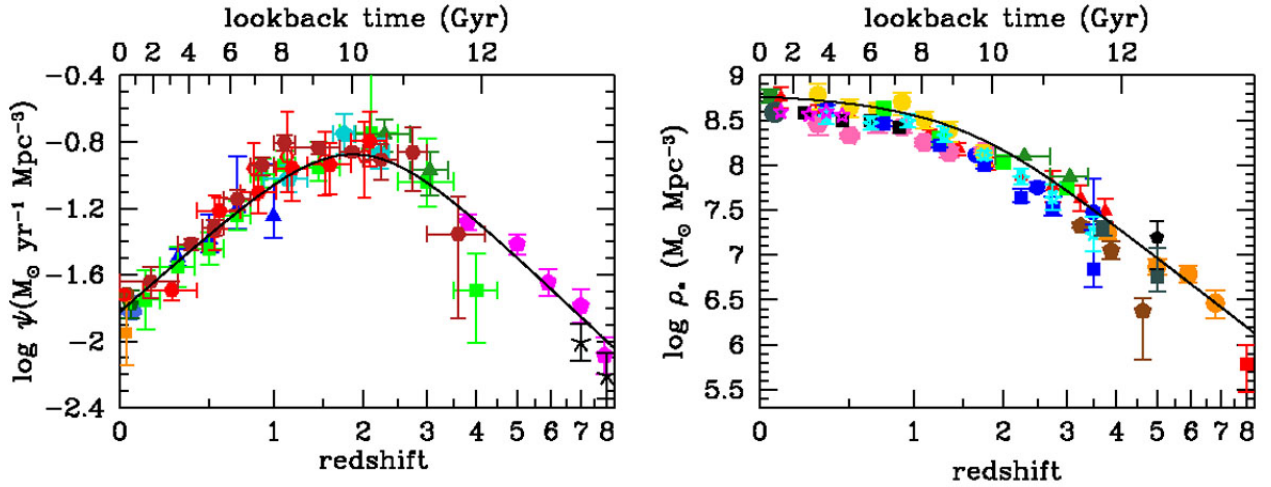


FIGURE 1.7 – Histoire de formation stellaire depuis les débuts de l’univers, en terme de taux de formation $\log \psi$ en $M_{\odot}/\text{an}/\text{Mpc}^3$ (à gauche), et de densité totale d’étoiles $\log \rho_*$ en M_{\odot}/Mpc^3 (à droite). Ces mesures sont extraites de champs profonds observés par les missions Spitzer, Herschel et HST. Le taux de formation d’étoiles monte rapidement des origines jusqu’il y a 11 milliards d’année, connaît un plateau sur environ 3 milliards d’années, puis s’éteint graduellement d’un facteur dix jusqu’à aujourd’hui. La densité totale du nombre d’étoiles est une mesure intégrée du taux de formation. Elle nous dit que la quasi totalité des étoiles de notre univers ont été formées dans les 5 premiers milliards d’années de l’Univers ($z > 1$) (Madau & Dickinson 2014).

Les modèles numériques : Dans une perspective cosmologique, les modèles numériques CDM nous offrent une vision où il apparaît que la formation des étoiles se fait au coeur même des halos CDM où la matière baryonique se concentre. La matière baryonique en domine d’ailleurs complètement le budget énergétique. On y applique les lois de la physique (hydrodynamique et transfert de rayonnement) pour interpréter la création des étoiles à l’aide de simulations numériques de plus en plus raffinées (cf chapitre suivant). Ainsi, les régions de formation d’étoiles des proto-galaxies et les galaxies sont-elles complètement dominées par la matière baryonique, même si les régions les plus excentrées des galaxies montrent des anomalies orbitales exigeant la présence de plus en plus dominante de CDM.

A l’échelle cosmologique, les modélisateurs sont obligés de faire confiance à des paramétrisations des phénomènes physiques en jeu dans la formation stellaire en fonction des observables à grande échelle dans les modèles globaux d’évolution. Ces modèles semi-analytiques peuvent être ajustés sur des observations (Cole et al. 1994, 2000; Somerville & Primack 1999) rendant leur valeur prédictive relativement faible, ou sur des modèles hydrodynamiques, davantage réalistes, mais encore très loin de la résolution nécessaire afin de prendre en compte la physique de formation stellaire locale.

La formation des étoiles dans les galaxies à l’échelle du cosmos est ramenée à un système de régulation simple et fonctionne comme un moteur alimenté par un carburant dont la disponibilité est sujette à des effets physiques variés, couplés entre eux et dont

l'impact a pu varier dans l'histoire de l'univers. Le taux de formation d'étoiles dépend de la quantité de gaz disponible. La disponibilité réelle de ce gaz est difficile à observer et complexe à modéliser (Kennicutt & Evans 2012). Elle dépend d'effets physiques internes aux galaxies, des conditions physiques du gaz (densité, fragmentation, température, turbulence, etc.), mais aussi d'effets externes (on parle d'effets d'environnement).

Parmi les effets positifs pour la formation stellaire on peut citer la dynamique de l'effondrement des structures à très grande échelle (on parle de courants froids ou courant de refroidissement, "cooling flows" dans la littérature, e.g. Fabian 1994; McDonald et al. 2018) et à l'échelle des groupes et des amas. Cette dynamique génère des courants de gaz extragalactique froid vers les puits de potentiels, courants qui semblent être l'effet dominant au début de l'univers (e.g. Springel & Hernquist 2003). On peut également citer la fusion de galaxies entre elles, telle qu'on semble l'observer dans les groupes fossiles, l'injection locale de gaz par recyclage des atmosphères stellaires.

En fait, les processus d'effondrement du gaz sont tellement efficaces que les modèles numériques doivent trouver des moyens de les ralentir. Les premiers modèles de formation prédisaient que la majeure partie des étoiles devait se former à $z \gtrsim 5$ en contradiction avec les observations.

Parmi les effets négatifs (rétroaction ou feedback en jargon anglais) ralentissant la formation stellaire, les modélisateurs ont évoqués la pression dynamique (ram pressure Gallagher 1978; Abadi et al. 1999; Vollmer et al. 2001; Ebeling et al. 2014; Ayromlou et al. 2019) et les effets de marées au sein des amas, le harcèlement des galaxies naines (galaxy harassment Moore et al. 1996), les vents stellaires, les supernovae, l'éjection de gaz moléculaire par les jets du trou noir super massif au centre des galaxies.

La prise en compte réaliste des effets de rétroaction locaux exigent une connaissance fine des processus mécaniques et thermiques en jeu, notamment la dissipation turbulente du gaz et la physique des chocs du milieu interstellaire (Renaud 2018; Cousin et al. 2019). Les observations les plus récentes montrent que les effets physiques sur le gaz jouent autant au sein des galaxies que dans le milieu intra-groupe Alatalo et al. (2015), et dans les amas de galaxies, par exemple, l'observation des galaxies méduses (Jachym et al. 2019).

1.5 Les amas de galaxies

Au-delà des groupes massifs de galaxies, on retrouve les amas de galaxies, objets virialisés ou en voie de virialisation les plus massifs de l'univers, dont la présente section présente les caractéristiques principales qui seront également celles des groupes les plus massifs.

1.5.1 Les observables

Les amas de galaxies observés montrent des propriétés à travers le spectre électromagnétique maintenant bien connues (Kravtsov & Borgani 2012).

Les amas de galaxies massifs Abell (1958), dans la figure 1.8 il s'agit d'Abell 1689, montrent :

- une émission stellaire dans les galaxies et autour des galaxies qu'on appelle lumière intra-amas (Intra-Cluster Light en jargon anglais; ICL). Cette émission stellaire provient presque exclusivement d'étoiles vieilles. On n'observe pratiquement pas de formation d'étoiles dans les amas aujourd'hui.

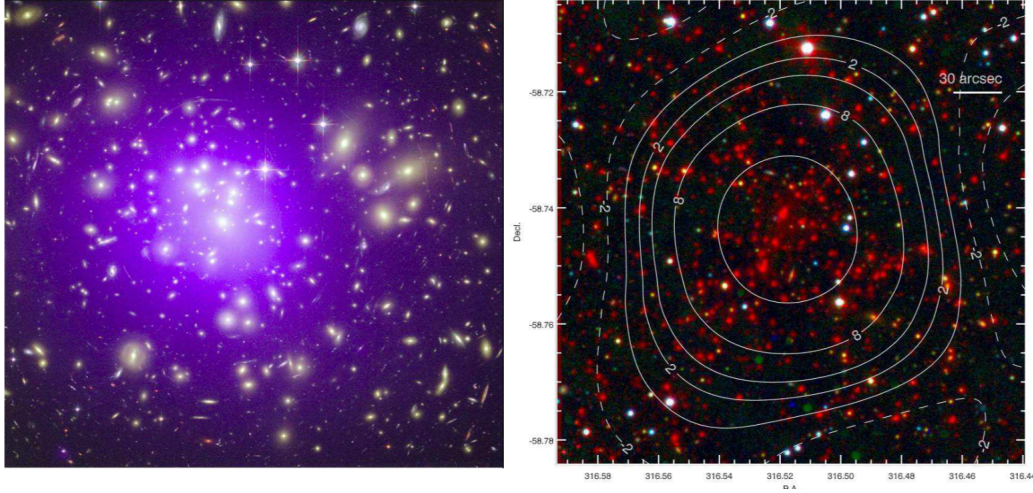


FIGURE 1.8 – A gauche, image de l’amas d’Abell 1689 à redshift $z = 0.18$, $M_{200} = 1.8^{+0.4}_{-0.3} \times 10^{15} h_{70}^{-1} M_{\odot}$, en bleu, l’émission diffuse du gaz X (mission *Chandra*), en jaune, les galaxies avec vieilles populations stellaires (mission *HST*) et en arrière plan de nombreux arcs de sources gravitationnellement magnifiées, cf chapitre 3. A droite, l’amas SPT-CL J2106-5844 à $z = 1.133$, $M_{200} \approx 1.3 \times 10^{15} h_{70}^{-1} M_{\odot}$, détecté par son effet Sunyaev-Zel’dovich (effet compton inverse des électrons du gaz X sur les photons du rayonnement fossile). Les galaxies en rouges sont imagées avec le télescope Magellan⁴¹, les contours de signifiacnce de l’effet Sunyaev-Zel’dovich proviennent du South Pole Telescope⁴². L’image couvre 2.4 Mpc de côté en distance physique transverse. Cité par Kravtsov & Borgani (2012).

- une émission de gaz X chaud qu’on appelle milieu intra-amas chaud (Intra-Cluster Medium ; ICM). Ce plasma diffus à des températures $\sim 10^8$ K n’est pas associé à des galaxies individuelles même si ses propriétés et celle des galaxies sont corrélées, par exemple leurs masses (Lin et al. 2012). Il contient la majeure partie de la masse baryonique de l’amas (Fig. 1.10).
- un effet Sunyaev-Zel’dovich sur le fond radio micro-onde (Figure 1.8 à droite)
- et pour certains un effet de lentillage gravitationnel sur les sources d’arrière-plan (Figure 1.8 à gauche).

1.5.2 Les relations d’échelle

L’ensemble des amas montrent des relations d’échelle (Giodini et al. 2013). Ces relations sont le résultat de la physique de formation des amas et de leur évolution. Le paradigme de formation hiérarchique CDM offre un cadre interprétatif puissant pour les expliquer (Kaiser 1986). Si la gravité domine les processus, les modèles auto-similaires entre les propriétés de base des amas et leur masse totale en résultent. Un modèle est dit auto-similaire si une sous-partie de l’objet qu’il décrit est une version d’échelle de l’objet entier. En terme mathématique, une fonction auto-similaire répond à $f(x) = f(\alpha x)$. Les lois de puissance, $f(x) = x^n$, sont auto-similaires.

Ainsi par exemple, le spectre de puissance des fluctuations de masse dans l’univers répond à $P(k) \propto k^n$ et la variance de la masse des fluctuations σ^2 est proportionnelle à $\sigma^2 \sim k^3 P(k) \propto r^{-(n+3)} \propto M^{-\frac{n+3}{3}}$, où les deux dernières proportionnalités viennent du fait que $k \propto r^{-1}$ et $M \propto r^3$. Donc l’amplitude des fluctuations σ est une loi de puissance fonction de la masse ou de la taille des objets. Elle est donc auto-similaire. De plus les fluctuations grandissent dans le temps comme $\sigma(M, t) \propto (1+z)^{-1} M^{-\frac{(n+3)}{6}}$, jusqu’à une

limite non-linéaire (voir chapitre 2) quand $\sigma \simeq 1$. Poser $\sigma = 1$ nous permet d'obtenir l'échelle de masse non-linéaire $M_{\text{NL}} \propto (1+z)^{-\frac{6}{(n+3)}}$. Le rapport M/M_{NL} est lui-même auto-similaire avec le redshift (Giodini et al. 2013), ce qui a pour conséquence que les propriétés des halos et leur abondances dans deux structures qui ont le même M/M_{NL} , sont les mêmes.

Parmi les structures à grande échelle, on s'attend à ce que les amas et les groupes soient auto-similaires (Kaiser 1986). Cela est vrai également pour le gaz présent dans ces structures, dans des conditions d'effondrement non-dissipatives. On peut prédire la forme de ses relations auto-similaires de façon assez simple. Deux relations sont particulièrement importantes, la relation Luminosité-Température X et la relation Masse-Température X.

La relation Masse-Température X découle du fait que deux halos auto-similaires formés au même moment doivent avoir la même densité, c'est-à-dire $M_{\delta_z} R_{\delta_z}^{-3} = \text{constant}$, où R_{δ_z} est le rayon au contraste de densité δ_z (voir chapitre 2). D'une part, la masse M_{δ_z} vient directement du volume de la sphère de surdensité δ_z ; $M_{\delta_z} = \frac{4}{3}\pi \delta_z \rho_{\text{crit},0} E^2(z) R_{\delta_z}^3$, où $E(z) \equiv \frac{H(z)}{H_0} = [\Omega_m(1+z)^{-3} + (1 - \Omega_m - \Omega_\Lambda)(1+z)^{-2} + \Omega_\Lambda]^{1/2}$ décrit l'évolution du paramètre de Hubble avec le redshift z . D'autre part, un amas de galaxie est dit virialisé, c'est-à-dire en équilibre hydrostatique quand le gradient de pression s'équilibre avec la gravité. Dans ce cas, la température du gaz est un bon estimé de la profondeur du puit de potentiel et de la masse virielle de l'amas : $T_{\text{gaz}} \propto GM/R \propto R_{\text{vir}}^2$, où R_{vir} est le rayon viriel. Ces trois équations mènent à la première loi d'échelle :

$$M_{\delta_z} \propto T_{\text{gaz}}^{3/2}. \quad (1.4)$$

La deuxième loi d'échelle reliant la luminosité X, qui est une observable, à la température du gaz, s'obtient en assumant que l'émission provient principalement d'électrons relativistes chauffés à des températures de $\sim 10^7 - 10^8$ K. Les électrons émettent du bremsstrahlung thermique, dont l'émissivité ϵ (densité volumique de luminosité) pour un plasma de métallicité solaire à cette température est $\epsilon \simeq 2.4 \times 10^{-29} T_{\text{gaz}}^{1/2} \rho_{\text{gaz}}^2 \text{ J}\cdot\text{m}^{-3}\cdot\text{s}^{-1}$, où on assume que les électrons et les ions sont à l'équilibre thermique. À l'aide de l'équation 1.4, on trouve la relation entre luminosité X et masse virielle : $L_X \approx \epsilon R^3 \approx T_{\text{gaz}}^{1/2} \rho_{\text{gaz}}^2 R^3 \approx T_{\text{gaz}}^{1/2} f_{\text{gaz}}^2 M_{\text{tot}} \approx f_{\text{gaz}}^2 T_{\text{gaz}}^2$, où f_{gaz}^2 est la fraction de gaz définie par $M_{\text{gaz}}/M_{\text{tot}}$. Comme le scénario auto-similaire prédit que la fraction de gaz est constante, on trouve la deuxième loi d'échelle :

$$L_X \propto T_{\text{gaz}}^2. \quad (1.5)$$

Les équations 1.4 et 1.5 sont les relations d'échelle de base entre les propriétés X dans les amas de galaxies, prédites par les modèles auto-similaires. Si on observe des entorses à ces relations, cela ne peut venir que d'effets dissipatifs non-négligables en regard des effets de la gravité. De plus les valeurs des exposants de ces équations sont des conséquences de la forme du spectre de fluctuation CDM (voir chapitre 2). Ces relations sont donc contraignantes.

Une dernière quantité est intéressante à dériver S , l'entropie des amas (Voit 2005), $S = k_B T_{\text{gaz}}/n_e^{2/3}$, où k_B est la constante de Boltzmann. Les relations d'échelles déjà dérivées nous permettent de relier l'entropie à la masse, $S \propto T_{\text{gaz}} \propto M_{\text{tot}}^{2/3}$. Il existe de nombreuses relations d'échelle dont les plus populaires sont données ci-dessous, en

introduisant un facteur F_z , combinant cosmologie et redshift, $F_z = E_z \times (\delta_z/\delta_{z=0})^{1/2}$:

$$\begin{aligned} L_X &\propto F_z T_{\text{gaz}}^2, \\ L_X &\propto F_z^{7/3} M_{\text{tot}}^{4/3}, \\ L_X &\propto F_z^{9/5} Y_X^{4/5}, \\ M_{\text{tot}} &\propto F_z^{-1} T_{\text{gaz}}^{3/2}, \\ M_{\text{tot}} &\propto F_z^{-2/5} Y_X^{3/5}, \\ M_{\text{gaz}} &\propto F_z^{-1} T_{\text{gaz}}^{3/2}, \\ S &\propto F_z^{-4/3} T_{\text{gaz}}, \end{aligned}$$

où $Y_X \equiv M_{\text{gaz}} \times T_X$. Rappelons que toutes ces relations n'ont de sens qu'à l'équilibre hydrostatique, et seul le centre des amas est à l'équilibre. Quand on s'éloigne vers l'extérieur les équilibres thermiques et hydrostatiques ne sont plus respectés⁴³. La figure 1.9 montre un certain nombre de ces lois d'échelle.

1.5.3 Les déviations aux relations d'échelle

De fait, les observations montrent bien que si les processus gravitationnels dans la formation des amas locaux, massifs et relaxés sont dominants dans un intervalle spécifique de rayon ($0.15R_{500}-R_{500}$), les déviations sont nombreuses tant à l'extérieur des amas que dans le centre et que ces déviations s'accroissent aux faibles masses, bien que peu d'observations sur les groupes soient disponibles encore aujourd'hui (Kundert et al. 2015; Chiu et al. 2016; Ebrahimpour et al. 2018). La figure 1.10 montre quatre exemples de déviation de l'auto-similarité au centre des amas. La densité électronique à un rayon donné dans les amas (à gauche) devrait être constante en fonction de la température X mesurée au facteur d'expansion près. Cela se vérifie au rayon R_{500} . Mais la densité électronique est clairement variable en fonction de la température au centre des amas. De même, la luminosité bolométrique en fonction du paramètre $Y_X \equiv M_{\text{g},500} T_X$ devrait suivre une loi d'échelle, ce qui est effectivement le cas (figure au centre). Cependant, quand on fait cette analyse en excluant le centre des amas (figure la plus à droite), l'écart-type de la distribution des points autour de la relation linéaire est beaucoup plus petit. Dans la partie basse de la figure 1.10, on affiche à gauche l'entropie du gaz en fonction de la température pour des amas et des groupes, nous avons vu à la section précédente que la solution autosimilaire impose que $S \propto T_X$ (représenté par la ligne pointillée), or le meilleur ajustement dévie de cette ligne, les groupes montrent une entropie plus élevée que le modèle auto-similaire. Enfin la figure en bas à droite, montre la luminosité L_X en fonction de la température pour un ensemble d'amas et groupes, la ligne bleue indique le modèle auto-similaire tandis que la ligne rouge montre le meilleur ajustement pour les groupes, ici encore ce sont les groupes qui semblent montrer une déviation à l'auto-similarité. Ces exemples militent pour l'existence d'effets physiques, au-delà de la simple influence de la gravité au centre des amas. Ces effets qui font dévier les relations d'échelle semblent s'accroître dans les groupes.

Les simulations numériques (cf chapitre 2) ne sont pas encore assez résolues pour comprendre les déviations des lois d'échelles. Elles commencent juste à aborder la question (e.g. Robson & Dav 2020).

43. Nagai et al. (2007) montrent que l'on peut retrouver les masses et profil des amas même s'ils ne sont pas relaxés

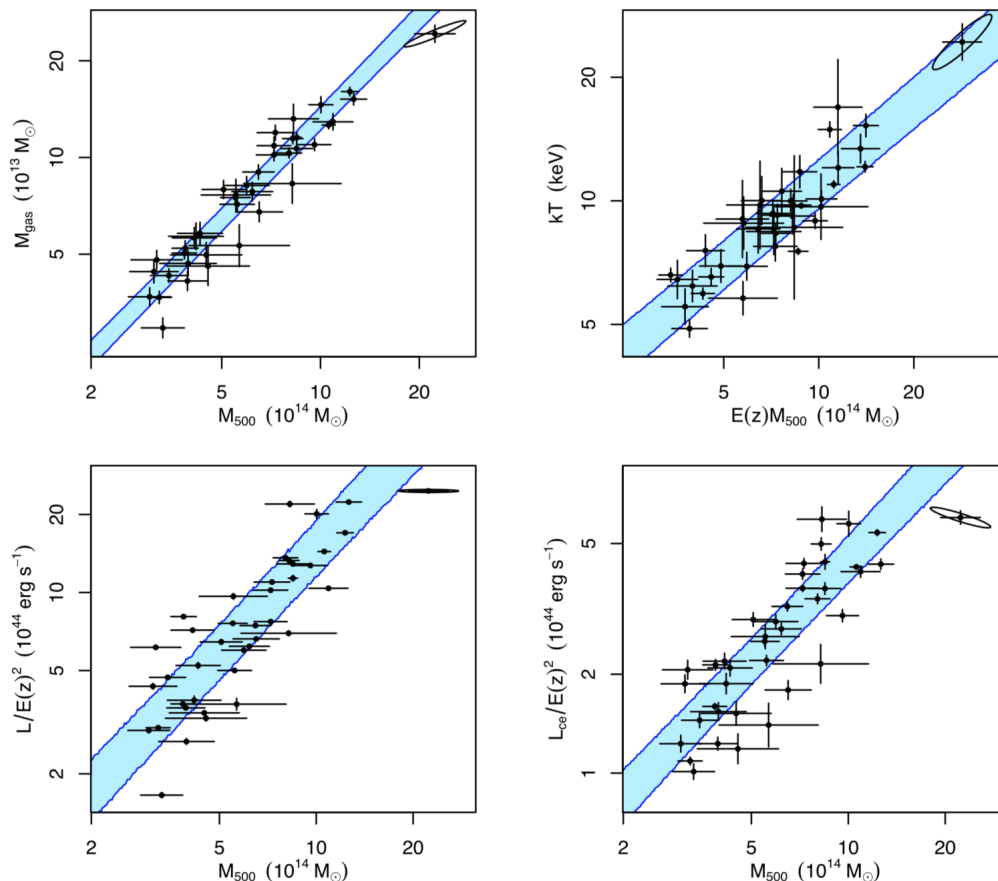


FIGURE 1.9 – D’en haut à gauche à en bas à droite sont exprimées les relations entre masse du gaz M_{gaz} , température kT , luminosité L en bande X et cette même luminosité avec le centre de l’amas exclu L_{ce} (rayon $< 0.15R_{500}$), en fonction de la masse totale de l’amas jusqu’à un rayon de surdensité 500, M_{500} . Les luminosités sont normalisées par $E^{-2}(z)$, l’évolution du paramètre de Hubble avec le redshift (voir texte pour la définition de $E(z)$). Les zones bleutées dénotent l’enveloppe de 1σ de la distribution autour de modèles auto-similaires correspondants aux équations 1.4 et 1.5. Les points sont un échantillon de 40 amas massifs et relaxés et l’ellipse de covariances des erreurs est donnée pour l’amas le plus massif de l’échantillon. (tiré de Mantz et al. 2016).

1.6 Les groupes sont des laboratoires de physique

Le fait que les relations d’échelle se fragilisent avec les masses de plus en plus faible des amas, c’est à dire, parmi les groupes de galaxies peut être dû à deux raisons. La première, est observationnelle, la deuxième est physique. En effet, l’observation des groupes de galaxies est plus difficile à une distance donnée que celle des amas. L’équivalent d’un biais de Malmquist⁴⁴ où les groupes les plus brillants et les plus denses seraient sur-représentés dans les échantillons observés. En effet, les groupes semblent montrer un excès de L_X et une entropie S plus élevée en regard de leur masse que celle attendue dans le modèle autosimilaire. L’ambiguïté ne pourra être levée qu’avec les futures générations de satellite X (mission ATHENA⁴⁵) qui permettront d’établir des échantillons limités en volumes à

44. Le biais de Malmquist est une surestimation de la magnitude moyenne d’un échantillon limité par la magnitude apparente, provoqué par la suppression artificielle des objets faibles (Malmquist 1922).

45. Advanced Telescope for High-ENergy Astrophysics : <https://sci.esa.int/web/athena/home> ou <https://athena.cnes.fr/fr> ou <https://www.the-athena-x-ray-observatory.eu/>

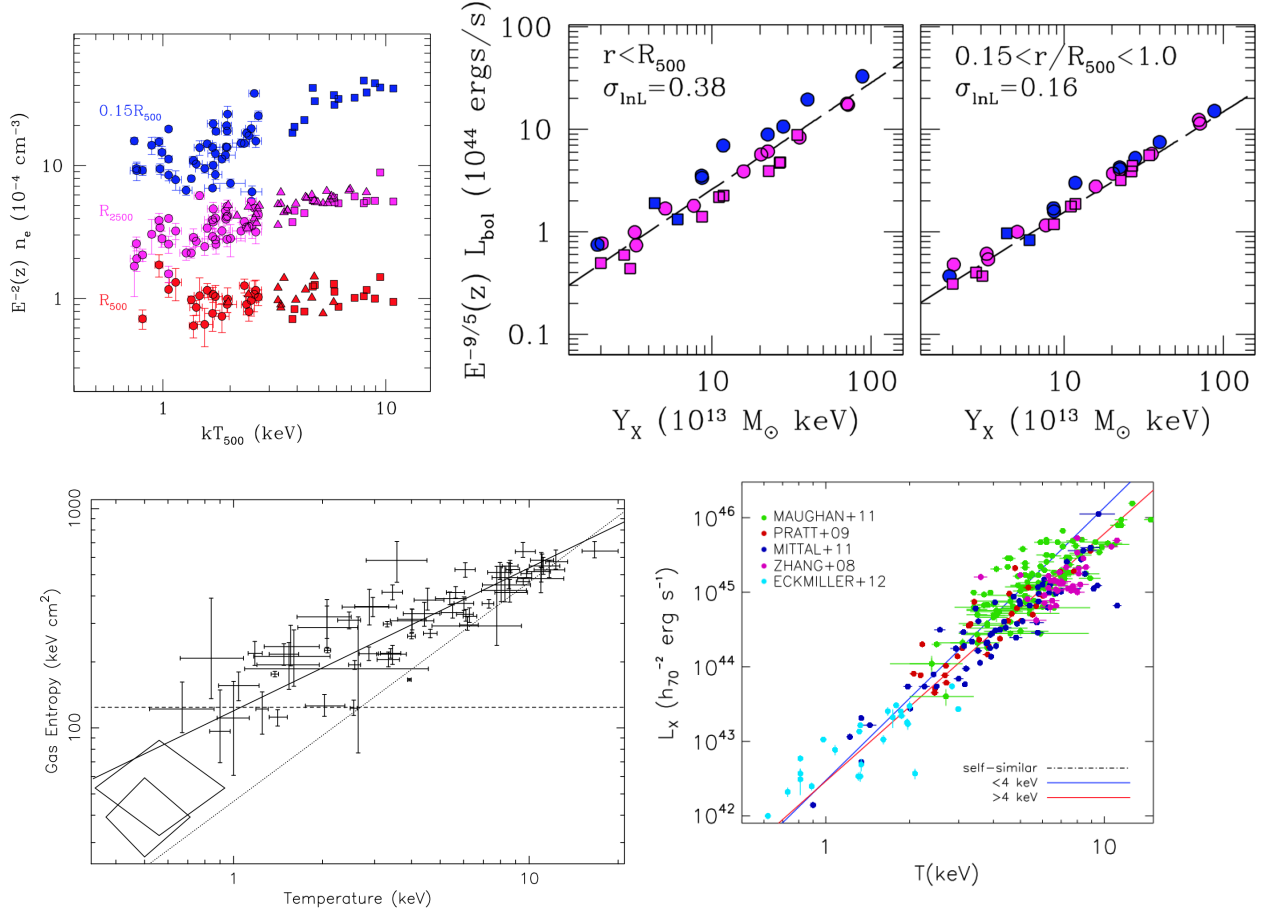


FIGURE 1.10 – En haut à gauche, la densité électronique n_e , mesurée à $0.15R_{500}, R_{2500}, R_{500}$ en fonction de la température ICM à R_{500} , normalisée par $E(z)$ l'évolution du paramètre de Hubble avec le redshift (voir texte pour la définition de $E(z)$), donc l'échelle attendue de la définition des rayons auxquels les densités sont mesurées. Les données des carrés et ronds viennent de la mission *Chandra* et les triangles de la mission *XMM-Newton*. A droite, la luminosité bolométrique L_{bol} en fonction du paramètre $Y_X \equiv M_{g,500}T_X$ où T_X est la température ajustée sur le spectre entre $(0.15 - 1) R_{500}$. Les données viennent du sondage XMM-Newton Cluster Structure Survey. En haut au centre les L_{bol} sont ajustées sur $(0-1) R_{500}$. En haut à droite, les L_{bol} sont ajustées sur $(0.15-1) R_{500}$, donc excluent les centres. $\sigma_{\text{ln}L}$ indique l'écart-type de L_{bol} à Y_X constant. Les symboles bleus (magentas) sont des amas au coeur froid (non-refroidi). Les carrés (ronds) sont classés comme relaxés (non-relaxés). Cité par Kravtsov & Borgani (2012). En bas à gauche, l'entropie du gaz en fonction de la température à R_{200} , données tirées de Ponman et al. (2003), pour des amas et groupes de galaxies, la ligne pointillée indique le modèle autosimilaire et la ligne pleine le meilleur ajustement. En bas à droite, la luminosité L_X en fonction de la température T_X de groupes et amas citée par Giodini et al. (2013), la ligne bleue superposée à la ligne pointillée indique le modèle autosimilaire, et la ligne rouge le meilleur ajustement.

des redshifts $z \sim 0.5$.

La deuxième raison physique est que les groupes sont des laboratoires de physique baryonique, et les déviations des relations d'échelle sont des indices forts que les effets dus strictement à la gravité ne dominant plus totalement le comportement global des objets. Cette deuxième raison ouvre des perspectives beaucoup plus intéressantes que la première et nous développerons les conséquences de cette deuxième hypothèse dans le reste de cette thèse.

Dans le deuxième chapitre, nous reviendrons sur la physique de formation des structures, et les effets de la structuration des baryons. Dans le troisième chapitre nous décrirons la physique des effets de lentillage gravitationnel et l'apport des observations de groupes de galaxies à travers cet effet. Enfin, le quatrième chapitre abordera l'avenir des observations des effets de lentillage gravitationnel à travers les missions spatiales en préparation, Euclid, CSSO, JWST et WFIRST.

Chapitre 2

Un regard théorique sur les groupes de galaxies

2.1 La formation des objets dans l'univers

2.1.1 Premiers principes : les hypothèses fondamentales de la cosmologie contemporaine

En 2020, la somme des observations faites à travers le spectre électro-magnétique principalement, à la fois au sol et depuis l'espace, et, dans une moindre mesure, à travers des vecteurs de l'information davantage exotiques (rayons cosmiques, neutrinos, ondes gravitationnelles), nous donne une description de plus en plus fine de notre univers. De ces observations émergent des interactions physiques fondamentales (nucléaires forte et faible, électromagnétisme et relativité générale) qui permettent l'élaboration de modèles numériques interprétatifs contraignants. Cela nous permet notamment de modéliser la genèse et l'évolution de la matière et du rayonnement depuis les tous premiers instants de l'univers (âge $\approx 10^{-43}$ s) jusqu'à aujourd'hui (âge = $4,35 \times 10^{17} \pm 6,6 \times 10^{14}$ s, alias $13,797 \pm 0,023$ Ga pour un paramètre de Hubble-Lemaître de $H_0 = 67,36 \pm 0,54 \text{ km}\cdot\text{s}^{-1}\cdot\text{Mpc}^{-1}$, Planck Collaboration et al. 2018, tableau 2) sur des distances allant de l'échelon sub-atomique ($\approx 10^{-15}$ m) à l'échelon extragalactique ($\approx 10^{26}$ m).

Il n'est pas inutile de revoir rapidement l'état de ces connaissances pour situer le contexte et l'intérêt de la recherche sur les groupes de galaxies. Rappelons simplement en préambule (Davis & Lineweaver 2004) que le paradigme fondamental de la cosmologie contemporaine fait l'hypothèse que l'univers obéit localement à la relativité restreinte (testée) et globalement à la relativité générale¹

Les modèles d'évolution cosmologique s'appuient aussi sur le principe copernicien (stipulant que nous n'occupons pas une place privilégiée dans l'univers) associé à l'hypothèse d'isotropie (les propriétés de l'espace-temps sont les mêmes dans toutes les directions)².

1. Cette hypothèse, testée localement, ne peut pas être testée globalement par définition, mais un certain nombre d'observations extra-galactiques prédites sont compatibles avec la relativité générale, dont l'observation de pulsar binaire; Weisberg & Taylor 2004, les ondes gravitationnelles Abbott et al. 2016). Or si, comme Imré Lakatos le suggérait, on admet que les meilleures théories sont celles dont le pouvoir prédictif est le plus riche, nous sommes forcés d'admettre en paraphrasant Churchill que la relativité générale est la pire des théories à l'exception de toutes les autres.

2. L'homogénéité de l'univers reste toute relative sur des volumes de quelques dizaines de Mpc de rayon (cf section 1.3.1), la validité de l'hypothèse doit se comprendre sur des échelles où l'expansion domine la gravitation ($R > \sim 1\text{Gpc}$). Il est intéressant de rappeler la controverse des années 90 sur la forme

Ces deux hypothèses combinées équivalent au principe cosmologique pour l'univers *observable*. Ces grands principes permettent de dériver les équations du champs gravitationnel d'un tel univers empli de fluide cosmologique contenant diverses composantes (où la vitesse de la lumière est exprimée en unité naturelle $c=1$ partout dans le document),

$$\mathcal{R}_{\mu\nu} = -8\pi G(\mathcal{T}_{\mu\nu} - \frac{1}{2}\mathcal{T}g_{\mu\nu}) + \Lambda g_{\mu\nu} \quad (2.1)$$

où $\mathcal{R}_{\mu\nu}$ est le tenseur de Ricci, $\mathcal{T}_{\mu\nu}$ est le tenseur énergie-impulsion d'un fluide parfait, et Λ est la constante cosmologique. Le tenseur énergie impulsion homogène et isotrope d'un fluide parfait se définit par sa pression p et sa densité ρ , constantes dans le temps cosmique,

$$\mathcal{T}^{\mu\nu} = (\rho + p)u^\mu u^\nu - pg^{\mu\nu}, \quad (2.2)$$

dont la trace \mathcal{T} donne $\mathcal{T} = \mathcal{T}^\mu_\mu = (\rho + p)$. La métrique décrivant un univers homogène et isotrope est celle de Friedmann-Lemaître-Robertson-Walker,

$$ds^2 = dt^2 - a^2(t) \left[\frac{dr^2}{1 - kr^2} + r^2 d\theta^2 + r^2 \sin^2\theta d\phi^2 \right], \quad (2.3)$$

où r, θ, ϕ sont les coordonnées spatiales comobiles, t est le temps cosmique, et l'expansion est exprimée par le facteur d'échelle $a(t)$ ($a_0 = 1$, l'indice 0 indique ici et dans le reste du document la valeur d'un paramètre aujourd'hui), k est le paramètre de courbure de l'espace tridimensionnel ($k = 0$ pour un espace plat, ce qui semble être le cas de notre univers après la mission Planck³ $|\Omega_k| < 0.005$, $k > 0$ dans un univers sur-critique et $k < 0$ dans un univers sous-critique).

La combinaison des équations 2.1 à 2.3 donnent les équations de Friedmann-Lemaître, décrivant le mouvement d'un fluide cosmologique parfait, homogène et isotrope

$$H^2 \equiv \left(\frac{\dot{a}}{a}\right)^2 = \frac{8\pi G\rho}{3} - \frac{k}{a^2} + \frac{\Lambda}{3} \quad (2.4)$$

$$\frac{\ddot{a}}{a} = -\frac{4\pi G}{3}(\rho + 3p) + \frac{\Lambda}{3} \quad (2.5)$$

où $H(z) \equiv \dot{a}/a$ est le paramètre de Hubble-Lemaître (aujourd'hui $H_0 = 67,74 \pm 0,46 \text{ km}\cdot\text{s}^{-1}\cdot\text{Mpc}^{-1}$).

On peut ajouter que l'observation des objets dans notre univers est sujette au rougissement de la lumière interprétée comme une mesure directe de l'augmentation du facteur d'échelle a , telle que

$$\frac{\lambda_o}{\lambda_e} = 1 + z = a^{-1}(t_e), \quad (2.6)$$

où λ_o et λ_e sont les longueurs d'ondes observée et émise, z est le rougissement (redshift). Ainsi, le facteur d'échelle se paramétrise directement dans les équations par la mesure du redshift qui est un observable. L'intervalle infinitésimal de temps cosmique s'exprime quant à lui comme

$$dt = \frac{dz}{(1+z)H(z)}. \quad (2.7)$$

autosimilaire de la structure à grande échelle de l'univers local bien décrit par des densités fractionnaires propres aux fractales (Sylos Labini et al. 1998) et de solutions d'accélération possible dans des univers inhomogènes (Ellis 2008; Célérier 2012; Cosmai et al. 2019).

3. <http://pla.esac.esa.int>

Le lecteur intéressé trouvera une description complète du modèle standard dans de nombreuses monographies, par exemple, Kolb & Turner (1990); Peter & Uzan (2012); Peebles (1993); Peacock (1999) et articles de revue (Carroll et al. 1992; Frieman et al. 2008).

De nombreuses questions se posent aux physiciens en lien avec l'émergence des interactions fondamentales et avec les tests de la relativité générale et de la mécanique quantique, voir par exemple Hansson (2015). Comme une bonne partie de ces questions, fascinantes à bien des égards, ne sont pas, aujourd'hui, réfutables au sens "popperien" du terme, nous nous concentrerons plutôt sur phases postérieures à la recombinaison de l'histoire de l'univers pendant lesquelles la matière et le rayonnement s'organisent. Ces phases de l'histoire de l'univers sont déjà accessibles aux observations et recèlent elles-mêmes leur lot d'énigmes sur lesquelles nous reviendrons.

TABLE 2.1 – Paramètres du modèle d'Univers Λ CDM, dérivé de la mission Planck publié en 2018 (Planck Collaboration et al. 2018).

Paramètre	(définition)	Valeurs pour Λ CDM-Base 68% intervalle de confiance
$\Omega_b h^2$	(paramètre de densité baryons)	$0,0224 \pm 0,0001$
$\Omega_c h^2$	(paramètre de densité CDM)	$0,120 \pm 0,001$
Ω_m	(paramètre de densité matière totale)	$0,315 \pm 0,007$
Ω_k	(paramètre de courbure)	$0,001 \pm 0,002$
n_s	(exposant du spectre scalaire de puissance)	$0,965 \pm 0,004$
$100\theta_*$	(échelle acoustique angulaire)	$1,0411 \pm 0,0003$
H_0	(paramètre de Hubble $\text{km}^{-1} \cdot \text{s}^{-1} \cdot \text{Mpc}^{-1}$)	$67,4 \pm 0,5$
σ_8	(amplitude des fluctuations à 8Mpc)	$0,811 \pm 0,006$
τ	(profondeur optique réionisation)	$0,054 \pm 0,007$
w_0	(paramètre équation d'état énergie noire)	$-1,03 \pm 0,03$
N_{eff}	(nombre de famille de neutrinos)	$2,99 \pm 0,17$
$\sum m_\nu$	(masse des neutrinos)	$< 0,12 \text{ eV}$

2.1.2 De l'univers homogène à l'univers inhomogène : une petite histoire de contrastes

L'histoire de la matière dans notre univers peut se résumer à une histoire de l'évolution des contrastes de densité sous les effets combinés et antagonistes de la gravitation et de l'expansion aux échelles dominées par le fluide cosmologique, auxquels s'ajoutent les effets de plus en plus dominants de la matière baryonique autour des pics de densité de matière localement.

L'univers homogène

Le modèle le plus probable (baptisé Λ CDM), dit de concordance, fait émerger notre univers dans une phase chaude, dense et quasi-homogène de matière et de rayonnement dont le comportement à grande échelle est décrit par une métrique de Friedmann-Lemaître-Robertson-Walker et une équation de conservation de l'énergie s'exprimant

comme

$$\nabla_\mu \mathcal{T}^{\mu\nu} = 0, \quad (2.8)$$

qui, combinée aux équations 2.4 et 2.5, mène à

$$\dot{\rho} + 3(\rho + p)H = 0, \quad (2.9)$$

où ρ et p sont les densités et pressions totales de toutes les composantes, c'est-à-dire simplement la somme algébrique des densité et pression de chaque composante, $\sum_i w_i$ et $\sum_i p_i$, $\dot{\rho}$ est la dérivé temporelle de la densité, H le paramètre de Hubble-Lemaître. L'équation d'état de la matière relie la pression et la densité par

$$p = w\rho, \quad (2.10)$$

où w est le paramètre de l'équation d'état. $w = 0$ pour une matière sans pression, $w = 1/3$ pour le rayonnement et $w = -1$ pour une énergie sombre sous forme de constante cosmologique Λ . Dans le cas le plus général, l'équation d'état peut varier au cours du temps cosmique et la relation entre ρ_i et w_i est donc

$$\rho_i \propto \exp \left[3 \int_0^z [1 + w_i(z)] d \ln(1 + z) \right]. \quad (2.11)$$

où z est le redshift. Les trois cas les plus courants donnés plus haut pour des valeurs constantes de w sont, pour la matière $\rho_M \propto (1 + z)^3$, le rayonnement $\rho_R \propto (1 + z)^4$, et la constante cosmologique $\rho_\Lambda = -p_\Lambda = -\Lambda/(8\pi G)$. Une dernière paramétrisation permet d'exprimer les équations de Friedmann sous forme adimensionnelle. Soit

$$\Omega_i = \frac{8\pi G \rho_i}{3H^2}, \quad \Omega_\Lambda = \frac{\Lambda}{3H^2}, \quad \Omega_k = \frac{k(1 + z)^2}{H^2}, \quad (2.12)$$

On obtient

$$\sum_i \Omega_i + \Omega_\Lambda + \Omega_k = 1, \quad (2.13)$$

ce qui se traduit en injectant l'équation de conservation de l'énergie,

$$\left(\frac{H}{H_0} \right)^2 = \sum \Omega_{i0} (1 + z)^{3(1+w_i)} + \Omega_{k0} (1 + z)^2 + \Omega_{\Lambda 0}. \quad (2.14)$$

L'indice 0 indique la valeur du paramètre aujourd'hui. Les différentes composantes de la matière couvrent une grande variété possible de cas ; la matière baryonique Ω_B , la matière noire Ω_{CDM} , le rayonnement Ω_γ , les neutrinos Ω_ν , ou toute autre espèce exotique.

Dans le modèle de concordance (Frieman et al. 2008), l'univers a connu dans son histoire deux phases d'expansion (trois si on inclut la phase d'inflation encore théorique avec un paramètre de Hubble-Lemaître constant aux premiers instants après le big bang $10^{-34} < \text{âge} < 10^{-32}$ s) selon l'équation d'état des composantes énergétiques variées dont l'univers est rempli. Une expansion décélérée d'abord dominée par le rayonnement, puis la matière, suivie d'une expansion accélérée dans les derniers 5 Ga, dominée par l'énergie sombre.

Nucléosynthèse et fond de rayonnement cosmologique

Une des conséquences de l'expansion de l'univers et de son refroidissement est l'existence d'une série de réactions nucléaires gouvernées par la thermodynamique des collisions (nucléosynthèse initiale) menant à une série de prédictions observables sur l'abondance des éléments légers au début de l'univers. Cette abondance des éléments primitifs est fixée notamment par le rapport entre baryons et photons (pour 3 familles de neutrinos) $\eta \approx 6 \times 10^{-10}$. Cette abondance teste aussi la valeur de constantes fondamentales (structure fine, constante de gravitation). Les mesures d'abondance primordiale des éléments sont devenues un outil puissant de test de la physique et de l'astrophysique. La mission Planck est la dernière d'une longue série à contraindre les conditions initiales et la combinaison des électrons et protons produisant massivement un fond de photons cosmologiques (Planck Collaboration et al. 2016, 2018).

Une deuxième conséquence du refroidissement de l'univers est un épisode de combinaison des électrons avec les protons qui ne dépend que de la température et du taux de réaction $p + e \leftrightarrow H + \gamma$. Le calcul n'est qu'un cas particulier de l'évolution thermodynamique d'une fonction de distribution à l'équilibre à partir de l'équation de Boltzmann relativiste (Peter & Uzan 2012). La résolution de cette équation donne, à l'équilibre, l'équation de Saha,

$$\frac{n_e n_p}{\bar{n}_e \bar{n}_p} = \frac{n_\gamma n_H}{\bar{n}_\gamma \bar{n}_H}, \quad (2.15)$$

où $n_i = \bar{n}_i \exp(-\mu_i/T)$. L'introduction de la fraction d'ionisation $X_e = n_e/(n_p + n_H)$ donne une solution de la forme

$$\frac{X_e^2}{1 - X_e} = \left(\frac{m_e T}{2\pi} \right)^{3/2} \frac{\exp[-(E_I/T)]}{n_b}, \quad (2.16)$$

où $E_I = m_e + m_p - m_H = 13,6 \text{ eV}$ est l'énergie d'ionisation de l'hydrogène. La température des photons est $T = 2.275(1+z) \text{ K}$, et la densité des baryons est $n_b = \eta n_{\gamma 0} (1+z)^3 \text{ cm}^{-3}$. Ces définitions réinjectées dans l'équation précédente permettent de l'exprimer comme,

$$\log \left(\frac{X_e^2}{1 - X_e} \right) = 20,98 - \log [\Omega_{b0} h^2 (1+z)^{3/2}] - \frac{25163}{1+z}. \quad (2.17)$$

Tous les termes de cette équation sont connus ($\Omega_{b0} h^2 = 0.02242 \pm 0.00014$, Planck 2018), on peut donc évaluer la fraction d'ionisation de l'univers en fonction du redshift. Cette équation montre que la fraction d'ionisation chute abruptement entre $z = 1400$ et $z = 1000$ de $X_e = 0,6$ à $0,0003$. Le découplage des photons avec les protons intervient très vite avec la chute de la densité électronique du milieu. Le calcul exact de la surface de dernière diffusion relève de la dynamique de la recombinaison. On peut montrer qu'elle intervient à un redshift de $z \approx 1100$ (Farhang et al. 2011) avec une profondeur de $\Delta z \approx 200$. La mission Planck ne montre aucune déviation du modèle standard.

Parmi les multiples apports de l'analyse du fond de rayonnement cosmologique, celui qui nous intéresse le plus est notre capacité à sonder l'état de l'univers, son homogénéité c'est-à-dire la répartition spatiale et l'amplitude des fluctuations de matière, à un temps très reculé (la période de combinaison correspond à un âge de l'univers de ~ 380000 ans). Les missions spatiales passées (COBE, WMAP) ont déjà montré une grande homogénéité de l'univers à toutes les échelles linéaires. Le fond de rayonnement fossile nous permet de fixer les conditions initiales d'évolution des structures à partir du spectre de puissance initial mesuré.

L'univers inhomogène

La section précédente nous a montré comment la relativité générale offre une solution élégante aux observations d'une expansion d'un fluide homogène aux échelles cosmologiques. Cependant, cette théorie ne tient pas compte des effets locaux de surdensités qui émergent de la période d'inflation (Bardeen et al. 1983). Les surdensités δ locales, définies par l'écart à la moyenne $\bar{\rho}_m$,

$$\delta = \frac{\rho(x) - \bar{\rho}_m}{\bar{\rho}_m} \quad (2.18)$$

sont décrites sous forme de spectre de puissance $P(k)$ (voir chapitre 9 de Kolb & Turner 1990 pour une définition des quantités en jeu).

Pour interpréter l'existence des grandes structures dans le domaine linéaire des fluctuations, il convient de développer une théorie des perturbations relativistes (Peter & Uzan 2012) pour les phases de l'univers denses et chaudes. Pour les phases froides, dominée par la matière, ce qui semble être le cas des composantes dominantes dans notre univers pendant la plus grande partie de son histoire, l'approximation newtonienne suffit. En outre, pour tout ce qui concerne les limites non-linéaires, c'est-à-dire la quasi-totalité des objets observables (galaxies, groupes de galaxies et amas de galaxies), un développement non-linéaire est nécessaire dont une méthode perturbative est donnée par Bernardeau et al. (2002). Pour les sur-densités extrêmes des galaxies et amas, seule une analyse numérique pourra proposer des solutions "réalistes".

Les faits généraux principaux des développements théoriques sont,

1. Le spectre des fluctuations initiales est gaussien et isotrope dans les modèles les plus simples ; Bartolo et al. 2004 (ce que semble confirmer Planck Collaboration et al. 2018, laissant une ouverture à des non-gaussiannités marginales Planck Collaboration et al. 2014).
2. Le spectre de puissance de fluctuations de densité $P(k)$ gaussien (prédit par les modèles simples d'inflation) est proportionnel à k^n , il est le même dans toutes les directions.
3. La quantité de matière nécessaire à la création des structures baryoniques visibles de l'univers observable excède très largement la quantité de matière baryonique présente dans l'univers (fixé par la nucléosynthèse initiale par le rapport $\eta = n_\gamma/n_b \approx 6 \times 10^{-10}$.) De plus des calculs de transfert de rayonnement dans le plasma primordial Silk (1968), montrent que les fluctuations optiquement épaisses sont détruites par la pression de rayonnement, inhibant la création des objets de masse inférieure à $5 \times 10^{11} M_\odot$. Cela est bien évidemment réfuté par les observations.
4. L'existence des structures massives observées aujourd'hui peut s'expliquer remarquablement bien par l'existence d'une matière noire non-relativiste, non-collisionnelle, et sans pression (Cold Dark Matter) dominant le budget de matière dans l'univers. Expliquer l'évolution des structures revient à expliquer l'évolution de cette composante⁴.

4. D'autres avenues possibles consistent à remplacer la théorie métrique de la gravitation par une nouvelle loi s'appliquant à grande échelle. Un exemple est la théorie Teves (Bekenstein 2011), généralisant une théorie modifiée de la gravitation (Milgrom 1983, 2019), ou explorer des modèles exotiques fondés sur une discrétisation de l'espace-temps (Verlinde 2017; Milgrom & Sanders 2016; Nottale 2011). Ce domaine de recherche est en plein essor, mais va très au-delà de ma compréhension de béotien.

La théorie canonique d'évolution des perturbations linéaires a été testée avec succès sur les observations. On comprend et interprète bien le comportement des contrastes de densité du régime linéaire depuis les débuts de l'univers à aujourd'hui en terme d'évolution du potentiel gravitationnel de la thermodynamique du fluide cosmologique et du facteur d'échelle de l'univers. Cette évolution est complexe. Elle dépend de la taille des fluctuations (super-Hubble; $>$ horizon ou sous-Hubble; $<$ horizon), du mode de ces fluctuations (adiabatique ou isocourbure), de l'équation d'état (dominée par la matière ou le rayonnement). Une théorie complète doit tenir compte de toutes les composantes (matière, baryonique, non-baryonique, rayonnement, couplage matière-rayonnement) pour produire un spectre de puissance réaliste. L'évolution du spectre de puissance, qui dépend de tous ces facteurs, est intégrée dans une fonction de transfert $T(k, a)$,

$$T(k, a) = \frac{\delta(k, a)}{\delta(k, a = a_i)D(a)}, \quad (2.19)$$

où $\delta(k, a)$ est le contraste de densité nombre d'onde k et facteur d'échelle a , l'indice i indique les conditions initiales, $D(a)$ est la fonction de croissance définie par

$$D(a) = \frac{5}{2} \frac{H(a)}{H_0} \Omega_{m0} \int_0^a \frac{a'}{[a'H(a')/H_0]^3}, \quad (2.20)$$

C'est $D(a)$ qui caractérise la modification du spectre initial sous l'effet de l'évolution. Le spectre de puissance observé $P_\delta(k, a_0)$ sera alors

$$P_\delta(k, a_0) = P_\delta(k, a_i)T^2(k, a_0) \quad (2.21)$$

La fonction de transfert se comporte qualitativement comme suit en fonction du nombre d'onde k autour d'une valeur pivot où la matière et le rayonnement ont une densité d'énergie égale.

$$k_{eq} = H_0 \sqrt{2 \frac{\Omega_{m0} a_0}{a_{eq}}} = 0,07 \Omega_{m0} h^2 \text{ Mpc}^{-1}, \quad k_{eq}^{-1} = \frac{14}{\Omega_{m0} h^2} \text{ Mpc}, \quad a_{eq}^{-1} = 1 + z_{eq} \simeq 2,4 \times 10^4 h^2 \quad (2.22)$$

Pour ($k \ll k_{eq}$), $T(k, a_0) \sim 1$, pour ($k \gg k_{eq}$), $T(k, a_0) \sim (k_{eq}/k)^2$. La fonction de transfert dépend également du type de fluctuation (adiabatique ou isocourbure). Mais les résultats de Planck montrent que des fluctuations adiabatiques provenant d'un champ scalaire simple expliquent le spectre observé. La fonction de transfert se paramétrise alors dans le cas d'un modèle CDM adiabatique par

$$T(x) = \frac{\ln(1 + 2,34x)}{2,34x} [1 + 3,89x + (16,1x)^2 + (5,46x)^3 + (6,71x)^4]^{-1/4}, \quad (2.23)$$

avec $x = k/(\Omega_{m0} h^2)$.

La figure 2.1 montre une synthèse du spectre de puissance des fluctuations sur 5 ordres de grandeurs. A partir de traceurs mesurés aujourd'hui. L'ajustement théorique (ligne rouge) des échelles les plus non-linéaires ($k \gtrsim 0.1h \text{ Mpc}^{-1}$) n'est possible qu'à l'aide d'un mapping fondé sur des simulations numériques. Il est à prendre avec précaution.

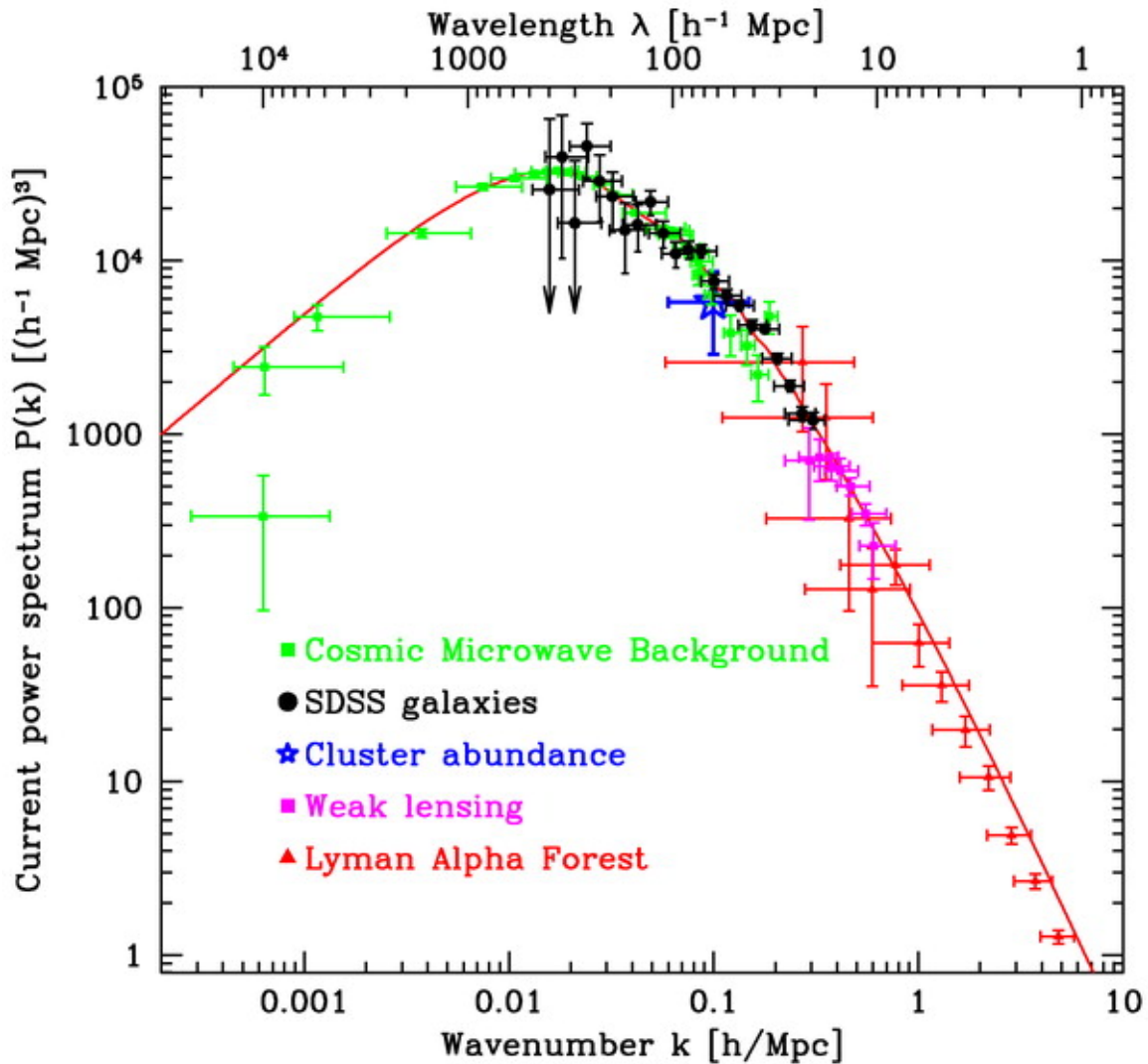


FIGURE 2.1 – spectre de puissance de la matière incluant toutes les composantes observables du fond de rayonnement cosmologique $k < 0,01$ [h/Mpc], à la forêt Lyman- α (Tegmark et al. 2004).

La formation des objets denses dans l'univers

Les galaxies, les groupes de galaxies et les amas de galaxies, c'est-à-dire la quasi-totalité des objets observables de l'univers (excluant les très grandes structures proches de l'homogénéité) appartiennent tous au régime non-linéaire. Les équations d'évolution de la matière sont donc non-linéaires dans leur cas.

On utilise souvent le paramètre σ_8 , la variance du spectre des perturbations dans un volume de 8 Mpc^{-1} comme signature de l'échelle de début des non-linéarités.

$$\sigma_8 \equiv \left(\frac{3}{4\pi R_8^3} \int_{x \leq R_8} \delta x d^3x \right)^2 \quad (2.24)$$

Pour comprendre le régime non-linéaire, il est important de déterminer quand une échelle entre dans ce régime. Plus une fluctuation de taille donnée entre tôt dans l'horizon, plus elle est amplifiée, la conséquence est que les petites structures (galaxies) entrent dans

le régime non-linéaire les premières et sont donc les plus anciennes. Les structures de plus en plus grandes entrent dans le régime non-linéaire de plus en plus tard. C'est un mécanisme hiérarchique.

Au moment de l'égalité matière-rayonnement, l'amplitude des perturbations est typiquement de 10^{-5} , les petites structures entrent dans le domaine non-linéaire pour $\delta_{CDM}(k, t) \sim 1$. Au même moment, l'univers à plus grande échelle reste très homogène. Le processus d'effondrement continue sur des échelles de plus en plus grandes. Les petites structures fusionnent en proto-galaxies, puis en galaxies de plus en plus grosses, puis en groupes et finalement en amas de galaxies. L'échelle de non-linéarité aujourd'hui est de l'ordre de 50 Mpc, c'est-à-dire la taille de super-amas, les structures les plus grandes sont des ensembles de super-amas (cf Laniakea Tully et al. 2014), ainsi que des filaments de galaxies et des vides de l'ordre de l'échelle de non-linéarité. L'univers ressemble donc à une éponge homogène à très grande échelle (cf fig 2.2).

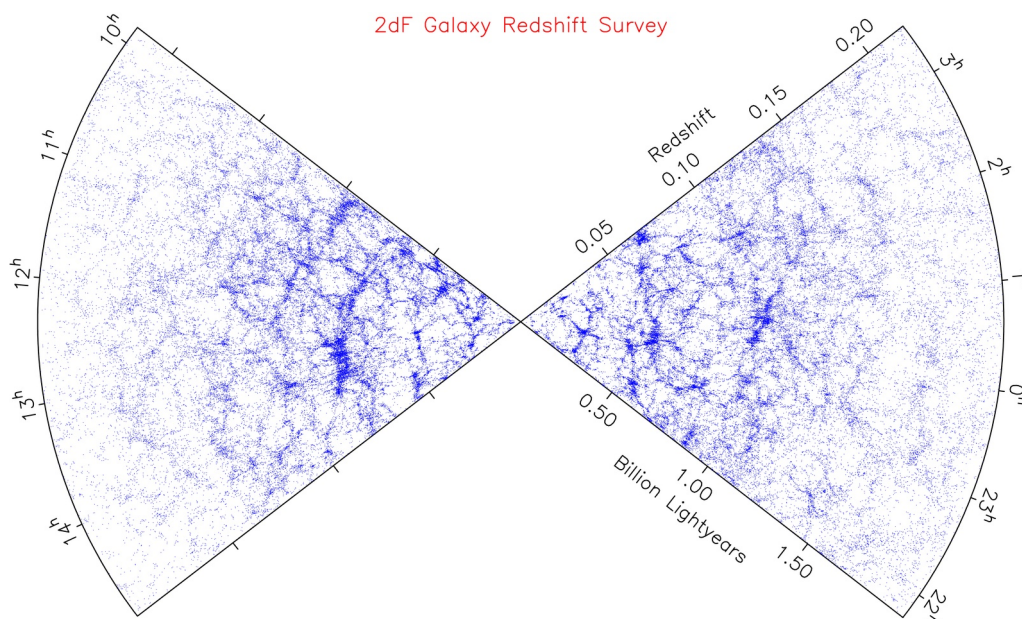


FIGURE 2.2 – Sondage 2dF de la structure à grande échelle des galaxies. <http://www.2dfgrs.net/>. L'interprétation de ces cartes n'est pas triviale, car l'échantillon est souvent dominé par des biais systématiques subtils. Mais les études statistiques de répartition des galaxies (autocorrélation à deux points, trois points) confirment localement les prédictions du modèle de concordance, notamment les effets de résonances dans le plasma primordial (appelées Baryon Acoustic Oscillations dans le jargon des cosmologistes) prédites de longue date (Peebles & Yu 1970) et qui impriment une structure spatiale dans la distribution des galaxies (Percival et al. 2007).

Nous devons maintenant aborder la physique d'effondrement gravitationnel. Le cas analytique sphérique reste une bonne approche qualitative pour comprendre le processus, mais le détail des phénomènes physiques passent par des simulations numériques. Pour le modèle analytique simple, les vitesses et les densités justifient une approximation newtonienne. L'évolution temporelle d'une sphère de rayon r peut se paramétriser comme

$$r = A(1 - \cos \theta) \quad t = A(\theta - \sin \theta). \quad (2.25)$$

θ est le paramètre de phase de l'effondrement. Les équations de mouvement, $\ddot{r} = -GM/r^2$ impliquent que $A^3 = GMB^2$. La sphère s'effondre en un point en un temps $t_c = t(2\pi) = 2\pi B$ et la densité moyenne de la sphère est $\rho_{int} = 3M/(4\pi r^3)$, alors que la densité de l'espace-temps en dehors de la zone gravitationnellement confinée est $\rho_{ext} = (6\pi Gt^2)^{-1}$. Le contraste de densité $\delta = \rho_{int}/\rho_{ext} - 1$. Au début de l'effondrement, $\theta \ll 1$ et $r(t)$ est simplement

$$r(t) \simeq \frac{A}{2} \left(\frac{6t}{B} \right)^{2/3} \left[1 - \frac{1}{20} \left(\frac{6t}{B} \right)^{2/3} \right]. \quad (2.26)$$

Le contraste de densité linéaire augmente donc comme $\delta_{lin} \propto t^{2/3} \simeq \frac{3}{20} \left(\frac{6t}{B} \right)^{2/3}$ conformément au régime linéaire. Ce modèle simple nous permet de décomposer l'effondrement en trois étapes.

1. *Le découplage de l'expansion* : La sur-densité est gravitationnellement liée. Son expansion maximale est atteinte pour $\theta = \pi$ (i.e. $t = \pi B$ et $r = 2A$), moment à partir duquel elle se découple de l'expansion de l'univers. Le contraste de densité à ce moment-là est $\delta = [(A/2)(6t/B)^{2/3}]^3 r^{-3} \sim 5.6$ au lieu de la valeur prédite par le régime linéaire ($\delta_{lin} \sim 1.06$).
2. *l'effondrement gravitationnel* : cet effondrement aboutit à une singularité si aucun autre mécanisme n'intervient, à $\theta = 2\pi$. Cet effondrement commence à partir de $\delta_{lin} \simeq 1.69$.
3. *La virialisation* : Des mécanismes dissipatifs convertissent l'énergie cinétique en mouvement thermique, la sphère atteint un régime stationnaire et stabilise son rayon. C'est le théorème du viriel qui fixe le contraste de densité $V = -2K$, où V est l'énergie potentielle et K l'énergie cinétique. On dérive un contraste final de l'ordre de $1 + \delta_{vir} \simeq 178\Omega^{-0.7}$.

La méthode de base (dite eulérienne) pour résoudre les évolutions de densité de façon numérique consiste à résoudre les équations de conservation thermodynamique d'un univers en expansion en présence d'un potentiel gravitationnel déterminé par l'équation de Poisson. Dans un espace en expansion, on introduit les variables comobiles de position \mathbf{x} et vitesse \mathbf{u} (vectorielles) telles que

$$r(t) = a(t)\mathbf{x}, \quad (2.27)$$

où $a(t)$ est le facteur d'échelle et le champ de vitesse est donné par

$$v(t) = \dot{r} = Hr + \mathbf{u} \quad (2.28)$$

où $\mathbf{u} = a\dot{\mathbf{x}}$ est la vitesse propre. Les équations de conservation classique (dans l'approximation Newtonienne) pour un fluide de densité ρ , de pression P dans un potentiel gravitationnel Φ s'écrivent alors

$$\dot{\rho}(x, t) + 3H\rho(x, t) + \frac{1}{a} \nabla_x [\rho(x, t)u(x, t)] = 0, \quad (2.29)$$

$$\dot{u}(x, t) + Hu(x, t) + \frac{1}{a}(u \cdot \nabla_x)u(x, t) = -\frac{1}{a} \nabla_x \Phi(x, t) - \frac{1}{a\rho} \nabla_x P(x, t). \quad (2.30)$$

Le potentiel gravitation est donné par

$$\Delta\Phi = \Delta 4\pi G\bar{\rho}a^2(t)\delta \quad \Leftrightarrow \quad \Phi(x, t) = -G\bar{\rho}a^2(t) \int d^3x' \frac{\delta(x', t)}{|x - x'|}, \quad (2.31)$$

où δ est le contraste de densité défini comme une perturbation autour de la densité moyenne

$$\rho = \bar{\rho}(t)[1 + \delta(x, t)]. \quad (2.32)$$

Si bien que les équations de conservation peuvent se ré-écrire en fonction de $\delta(x, t)$ et de ses dérivées en prenant deux conditions limites raisonnables, $\delta \ll 1$ et $(ut/d)^2 \ll \delta$, où d est une longueur de cohérence de perturbation, impliquant que les gradients de densité sont faibles :

$$\ddot{\delta} + 2H\dot{\delta} = \frac{c_s^2}{a^2}\Delta\delta + 4\pi G\bar{\rho}\delta, \quad (2.33)$$

où c_s est la vitesse du son. On trouve que la longueur de Jeans λ_J , définie dans le cas statique comme $\lambda_J \equiv c_s \sqrt{\frac{\pi}{G\bar{\rho}}}$, dépend ici du temps via la densité moyenne $\bar{\rho}(t)$.

Epoque de formation des galaxies, groupes et amas

Intéressons nous maintenant à l'époque de formation des halos CDM ayant produits les galaxies, groupes et amas (Avila-R eese 2006). On peut calculer le redshift d'effondrement d'une sur-densité dans le cas Λ CDM (Padmanabhan 1993),

$$\delta(z_{col}) = \delta_0 D(z_{col}) = \delta_{c0} \quad \text{avec} \quad \delta_{c0} = 1,686 \Omega_{m0}^{0,0055}, \quad (2.34)$$

$$D(z) = \frac{g(z)}{g(z_0)(1+z)}, \quad (2.35)$$

Avec :

$$g(z) \simeq \frac{5}{2} \left[\Omega_m^{4/7} - \Omega_\Lambda + \left(1 + \frac{\Omega_m}{2}\right) \left(1 + \frac{\Omega_\Lambda}{70}\right) \right]^{-1} \quad (2.36)$$

$$\Omega_m = \frac{\Omega_{m0}(1+z)^3}{\Omega_\Lambda + \Omega_{m0}(1+z)^3} \quad (2.37)$$

$$\Omega_\Lambda = \frac{\Omega_\Lambda}{\Omega_\Lambda + \Omega_{m0}(1+z)^3} \quad (2.38)$$

Ces équations couplées au modèle sphérique d'effondrement, nous permettent de relier la masse des sur-densités et leur redshift d'effondrement. La figure 2.3 (gauche) donne cette masse pour trois valeurs de sur-densité exprimée comme la valeur du pic de variance $\delta_0 = n\sigma_m$ avec $n = 1, 2, 3$. Les galaxies de masse ($M \sim 10^8$ - $10^{13} M_\odot$) correspondant aux halos de $1\sigma_m$ s'effondrent à un redshift de $z \leq 3.5$ tandis que les halos de la taille des groupes de galaxies ($M \sim 10^{13}$ - $10^{14} M_\odot$) sont plus rares (sur-densité à 2σ) et s'effondrent plutôt à $z \leq 1.5$, les halos de la taille des amas de galaxies (sur-densité à 3σ) s'effondrent à partir de $z \leq 0.5$, ce modèle suggère donc que la plupart des amas observés aujourd'hui ne sont pas virialisés. La figure 2.3 (droite) donne la fonction de masse des halos CDM, i.e. le nombre attendu d'objets de masse en unité de M_\odot par les modèles de Press-Schechter affinés par Sheth et al. (2001). Ce modèle montre une loi de puissance à faible masse et une coupure exponentielle pour des redshifts croissants. Cette coupure est liée au spectre de puissance des fluctuations. On voit que l'évolution est sensible pour des halos massifs ($\geq 10^{14} M_\odot$) aux décalages $z \leq 1$. C'est la raison pour laquelle l'abondance des amas de galaxies donne un test robuste des théories de formation des structures.

Insistons sur le fait que si les théories linéaires et les approches perturbatives permettent de prédire les fonctions de densité des amas avec le redshift, ainsi qu'un ensemble

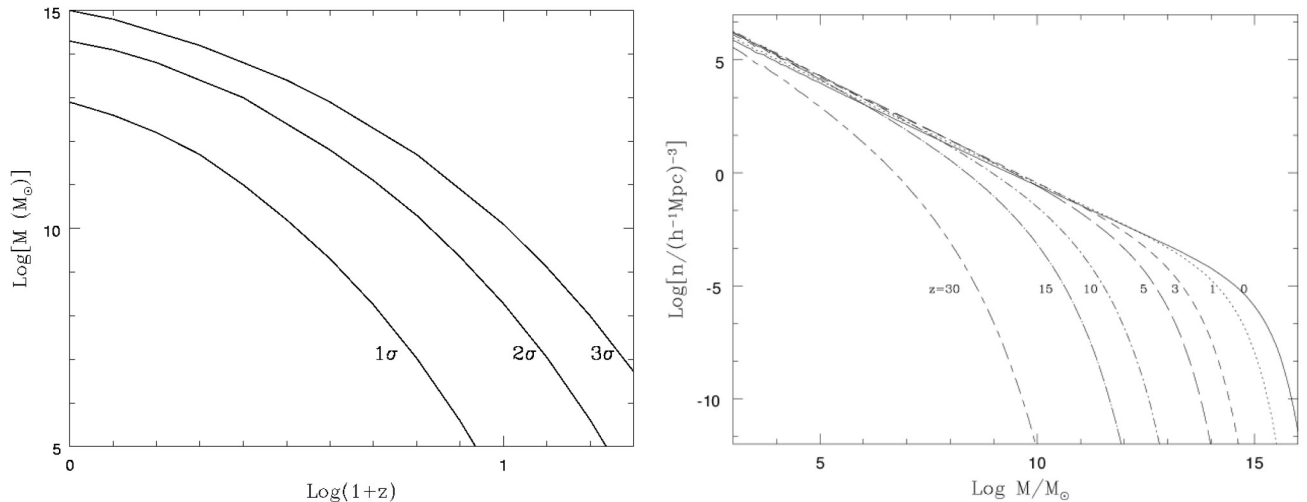


FIGURE 2.3 – (gauche) Redshifts d’effondrement de surdensités sphériques pour 1, 2 et $3\sigma (= \sigma_m)$, pour une cosmologie Λ CDM avec $\sigma_8 = 0.9$. Les galaxies de masse ($M \sim 10^8$ - $10^{13} M_\odot$) correspondant aux halos de $1\sigma_m$ s’effondrent à un redshift de $z \leq 3.5$ tandis que les halos de la taille des groupes de galaxies ($M \sim 10^{13}$ - $10^{14} M_\odot$) sont plus rares et s’effondrent plutôt à $z \leq 1.5$, les halos de la taille des amas de galaxies à $z \leq 0.5$. (droite) Fonction de masse des halos CDM donnant le nombre d’objets attendus pour une masse et un redshift donné d’après Avila-Rese (2006) sur un modèle de Sheth et al. (2001).

de lois d’échelle dans la partie extérieure des amas, en revanche, elles ne sont d’aucune utilité pour sonder les paramètres physiques fins comme les profils de densité des objets, les formes des objets au coeur des puits de potentiel gravitationnel. Dans ces cas particuliers, on doit recourir aux simulations numériques.

2.1.3 Modèles d’évolution des objets : galaxies et amas de galaxies

Simulations numériques et prédictions physiques

Seules les simulations numériques permettent d’approcher le comportement fin des surdensités non-linéaires. Le domaine des calculs numériques est celui qui a le plus avancé dans les dernières décennies. Les premières simulations à n-corps se concentraient sur la résolution des orbites ou du champ de vitesses (par méthode Lagrangienne ou Eulérienne) du fluide CDM discrétisé, mais utilisaient des méthodes phénoménologiques (méthodes semi-analytiques) pour relier les puits de potentiels CDM aux objets baryoniques observés avec les inconvénients associés (e.g. Somerville & Primack 1999; Cole et al. 2000; Guo et al. 2011). La simulation la plus résolue à ce jour est Ushuu⁵ (Ishiyama et al. 2020), dans une boîte de $2h^{-1}$ Gpc de côté avec 12300^3 particules de $3.27 \times 10^8 h^{-1} M_\odot$ pour la version grand volume et 6400^3 particules dans une boîte de $140h^{-1}$ Mpc de côté, avec une masse de $8.97 \times 10^5 h^{-1} M_\odot$ pour la version à très haute résolution (cf Figure 2.4 et 2.5).

La puissance actuelle des calculateurs permet non-seulement d’inclure les comportements gravitationnels du fluide CDM, mais également d’inclure l’hydrodynamique du fluide baryonique incluant un grand nombre d’effets physiques observables directement dans le calcul (Springel 2010; Schaye et al. 2010; Vogelsberger et al. 2014; Dubois et al. 2014; Schaye et al. 2015; Teyssier 2015; Khandaï et al. 2015) qui peuvent donc être

5. <http://skiesanduniverses.org/>

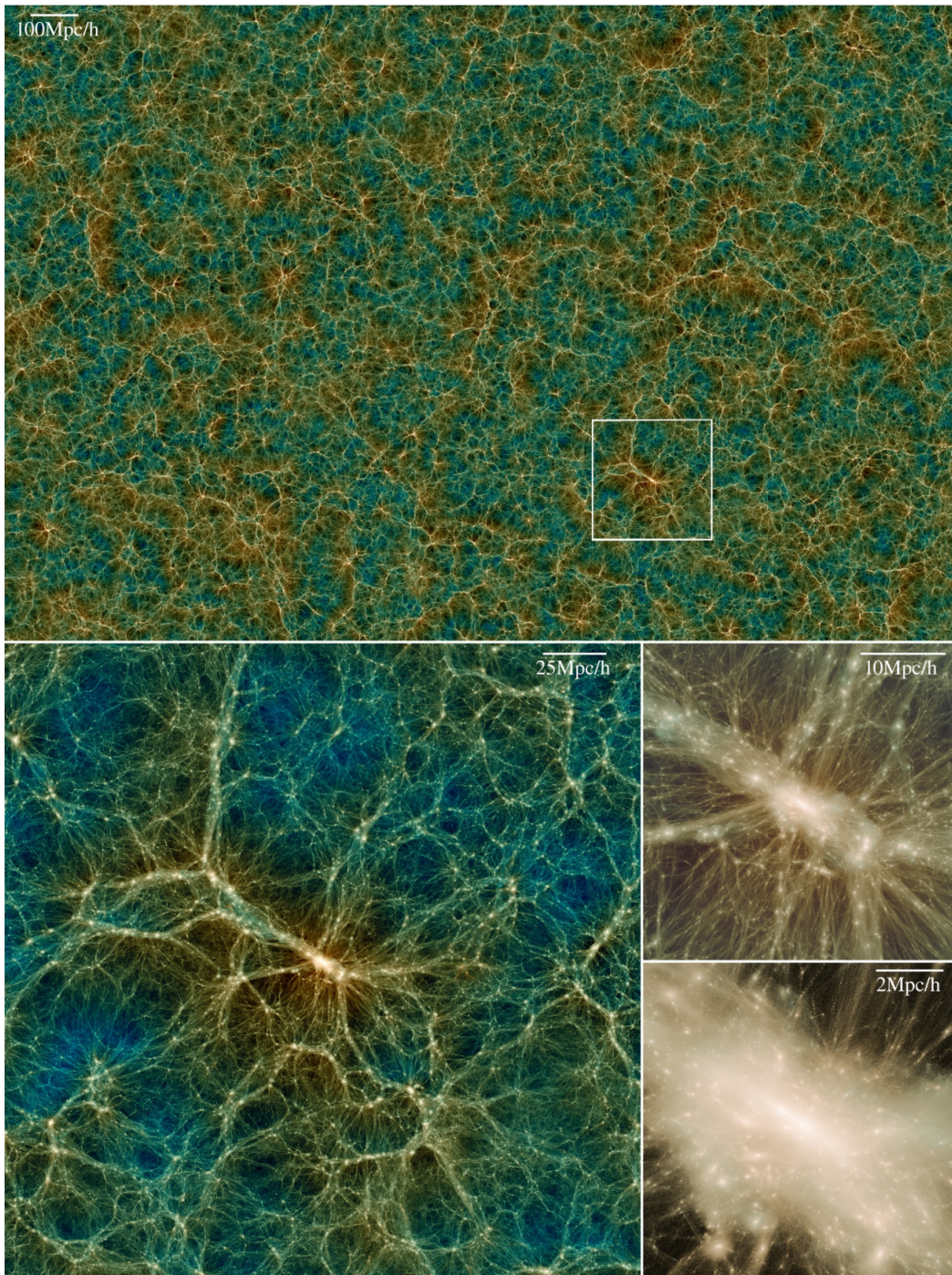


FIGURE 2.4 – tiré de Ishiyama et al. 2020, la figure montre la simulation CDM Uchuu simulation à $z = 0$. En haut, le cadre montre une coupe de $2000h^{-1} \text{ Mpc} \times 1333h^{-1} \text{ Mpc} \times 25h^{-1} \text{ Mpc}$. Les trois panneaux du bas sont des zooms variés du halo encadré, de gauche à droite $250, 38, 9.4h^{-1} \text{ Mpc}$.

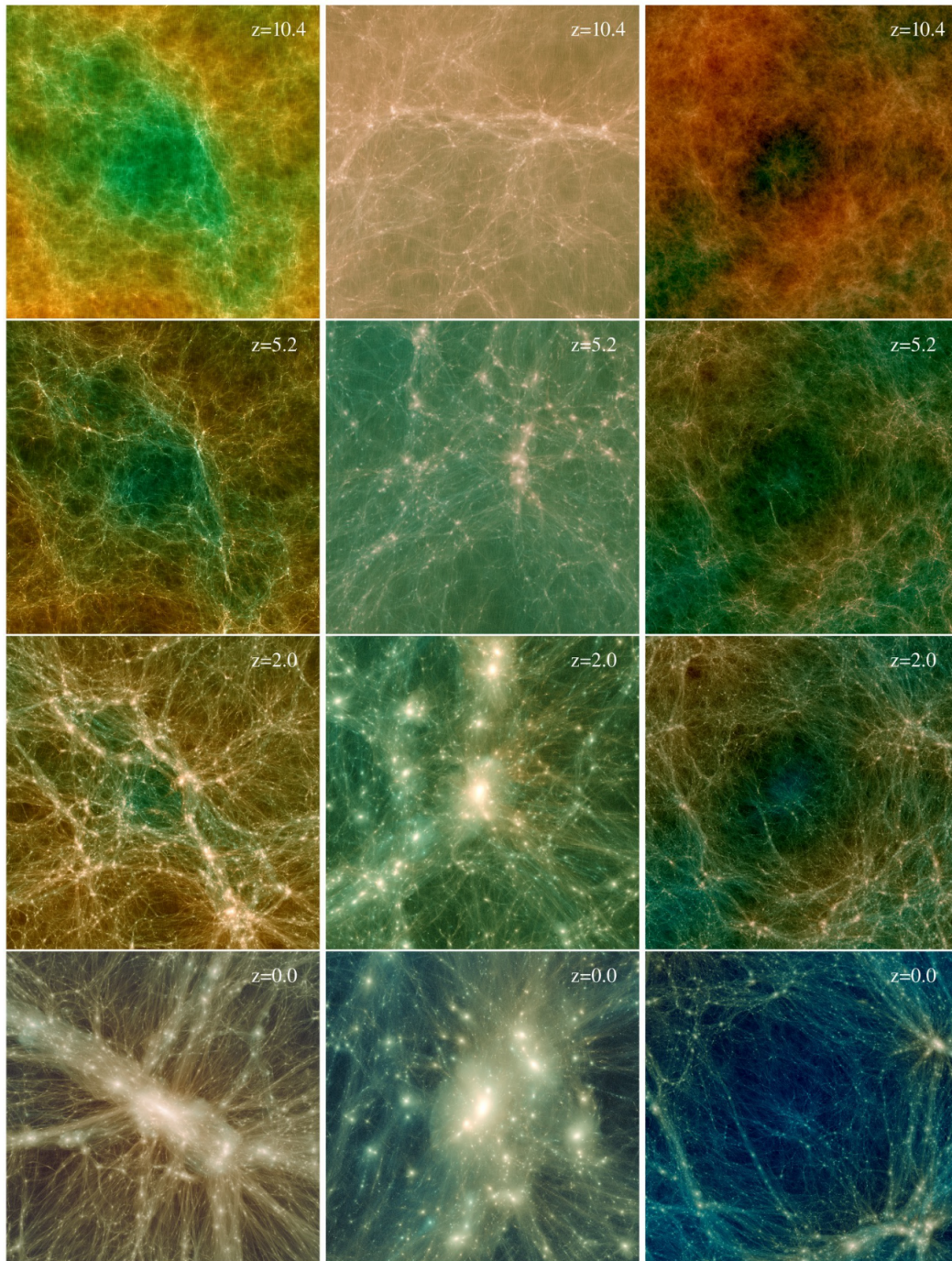


FIGURE 2.5 – tiré de Ishiyama et al. 2020, Evolution de trois sous-régions de la simulation Ushuu à haute résolution pour des redshifts de haut en bas . $z = 10.4, 5.2, 2.0$, et 0. Gauche : Le plus grand halo de la simulation. Centre : Un halo de la taille de Notre Galaxie. Droite : une région sous-dense sélectionnée dans Ushuu. Les tailles sont de $38, 2.3, 35h^{-1}$ Mpc.

confrontés aux observations. Les effets physiques introduits dans les simulations incluent : la formation d'étoiles, les processus de refroidissements radiatifs primordiaux et via les raies métalliques (pour le gaz chaud X), les effets d'évolution stellaire et enrichissement chimique fondés sur la synthèse de populations stellaires (pour comparer avec des observables de l'univers local), la rétroaction causée par les étoiles, la rétroaction causée par les noyaux actifs de galaxies, l'impact des champs magnétiques, le transfert radiatif, l'impact des rayons cosmiques, la conduction thermique (les références des publications qui prennent en compte ces effets sont dans Vogelsberger et al. 2014). Par exemple, les simulations Illustris⁶ incluent (Vogelsberger et al. 2013) le refroidissement du gaz X par rayonnement (courants froids), la rétroaction énergétique des trous noirs supermassifs et des supernovae, l'évolution stellaire, l'enrichissement en métaux et pertes de masse de gaz par les étoiles et les effets à proximité des noyaux de galaxies actives.

Les simulations hydrodynamiques (ici Illustris pris pour exemple) couvrent maintenant des volumes cosmologiques non-négligeables de l'ordre de la centaine de Mpc (à une résolution de l'ordre de 50pc), partant de conditions initiales proches du début de l'univers $z \sim 100$. Pour autant, la résolution des simulations numériques les plus puissantes reste ridiculement faible en regard de la réalité physique de la formation des étoiles, avec des particules "élémentaires" CDM d'une taille de quelques millions de masses solaires et des particules "élémentaires" de gaz de l'ordre du million de masses solaires. La dérivation physique complète des phénomènes, notamment liés aux mécanismes de formation stellaire dans les nuages de gaz où la turbulence joue un rôle dans la fragmentation et le refroidissement du gaz interstellaire (par exemple Renaud 2018; Cousin et al. 2019), aux trous noirs supermassifs (Vogelsberger et al. 2013), contient des paramètres libres ajustés sur des mesures observées de taux de formation d'étoiles sur des simulations locales de plus haute résolution. Elles restent donc d'une certaine manière liées à des lois semi-analytiques, mais s'appuyant sur des modèles physiques et non des lois phénoménologiques.

La figure 2.6 montre les résultats impressionnants du projet Illustris, où la distribution des halos de matière sombre est connectée au gaz chaud, ce qui permet de calculer les observables multi-longueurs d'onde des objets dans un intervalle de redshifts $z = 0 - 100$.

2.2 La physique baryonique des groupes

Nous avons vu dans le premier chapitre que les galaxies sont dominées par les effets de la matière baryonique, de même ces effets perturbent largement le centre des amas. la question que nous abordons dans cette section est quels effets physiques ont un impact évolutif global sur des groupes (profil, rayon, composition, métallicité) ainsi que sur leur membres (morphologie, dynamique, composition, gradients). Les effets à grande échelle en jeu dans les groupes sont souvent de même nature que ceux des amas. La question a été étudiée en détail d'un point de vue théorique dans une littérature trop riche pour être abordée exhaustivement ici. Mais les modèles numériques commencent à nous permettre d'identifier les phénomènes dominants que nous nous contenterons de voir rapidement : la rétroaction des noyaux de galaxies actives, la pression dynamique du milieu intra-amas et la rétroaction des sursauts de formation d'étoiles.

6. <http://www.illustris-project.org>

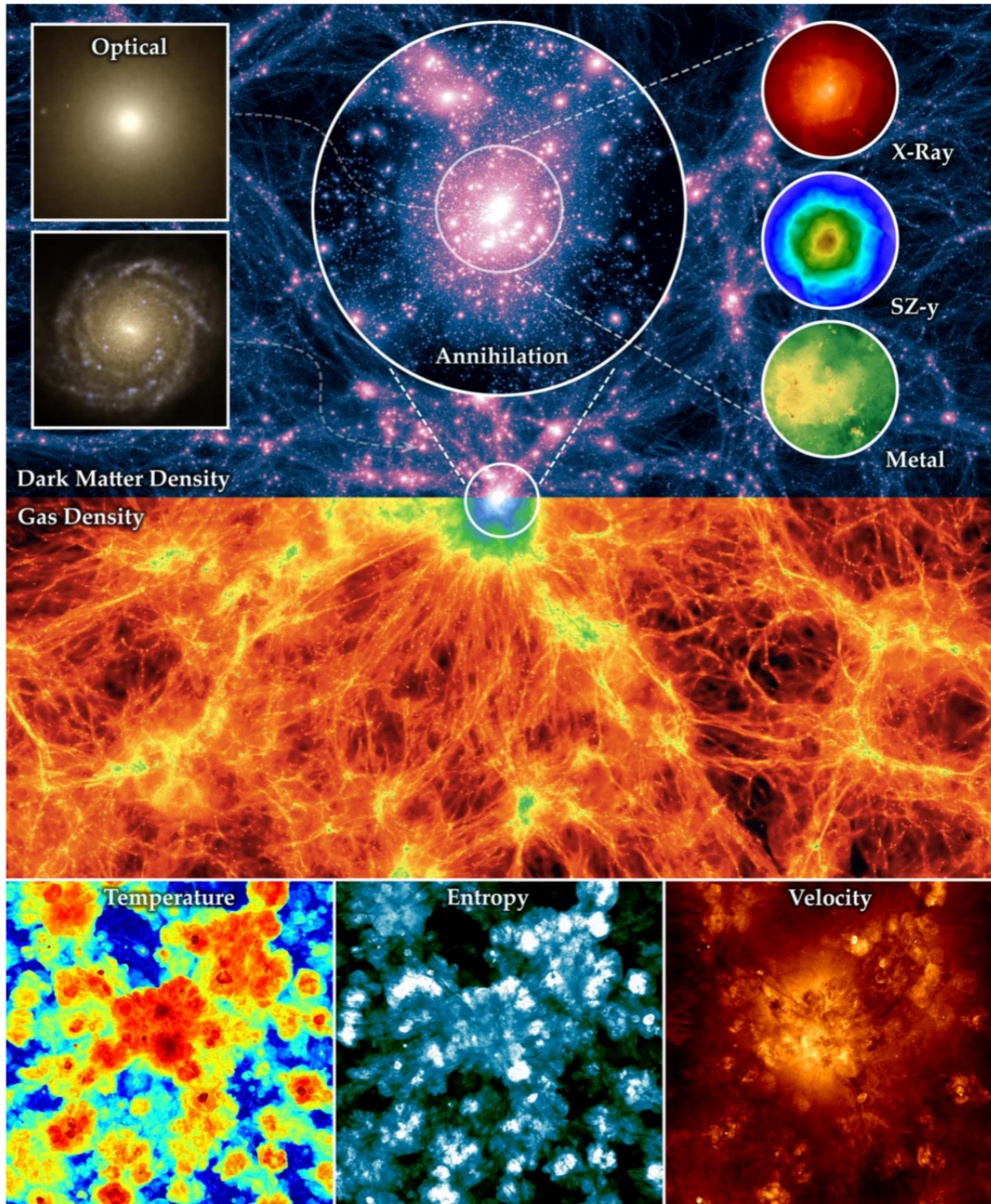


FIGURE 2.6 – illustration de la puissance des simulations numériques combinant, simulation gravitationnelle à n -corps (CDM) et hydrodynamique du gaz. Ici le projet Illustris <http://www.illustris-project.org>, faites pour un univers Λ CDM de paramètres $\Omega_m = 0,2726$, $\Omega_\Lambda = 0,7274$, $\Omega_b = 0,0456$, $\sigma_8 = 0,809$, $n_s = 0.963$, et $H_0 = 100 h \text{ km s}^{-1} \text{ Mpc}^{-1}$ avec $h = 0,704$.

2.2.1 Absence de courants froids dans les groupes : la rétroaction des noyaux de galaxies actives

Parmi les effets de rétroaction positive, le rôle des noyaux actifs de galaxies par les jets astrophysiques a été proposé par Silk & Rees (1998) et revu récemment par Soker (2016) sur les aspects théoriques et par Gaspari et al. (2011b,a), numériquement, et le colloque *Reality and myths of AGN Feedback*, Oct 3028, Leiden, (Husemann & Harrison 2018) a fait le point théorique et observationnel sur nos connaissances. La table 2.2 tirée de Soker (2016) compile les propriétés physiques des jets et l'impact de leur mécanismes pour les amas de galaxies et les galaxies. La troisième colonne de la table donne les mêmes propriétés pour les explosions de supernovas (SN) de type II, elle n'est mentionnée que parce que l'explosion des supernovas elle-même est une source importante d'énergie cinétique dans le milieu intergalactique et intra-amas, mais que l'origine de l'explosion des SN soit des jets ou non ne nous concerne pas ici.

TABLE 2.2 – Propriétés physiques (à un ordre de magnitude près) des jets astrophysiques pour deux types d'échelles et d'objets bornant les groupes de galaxies tirée de Soker (2016). Energie typique : pour un épisode. Masse typique, Taille : du gaz ambiant concerné. Temps : typique de durée du jet. Abbreviations et acronymes : R_a est le rayon typique de l'objet accrétant, Φ_a l'amplitude du potentiel gravitationnel à sa surface (unité de c ou $1000 \text{ km}\cdot\text{s}^{-1}$). R_{res} : rayon typique du réservoir de gaz acrétable, Φ_{res} énergie nécessaire à l'expulsion du réservoir (par unité de masse) en unité de $1000 \text{ km}\cdot\text{s}^{-1}$. MIA : milieu intra-amas; TN : trou noir; TNSM : trou noir supermassif; $M_{TN} - \sigma$ est la corrélation qui lie la masse du TNSM à la vitesse de dispersion des étoiles dans une galaxie.

Propriété	Amas de galaxies	Formation des galaxies	SN type II
Energie (J)	10^{53}	10^{52}	10^{44}
Masse (M_\odot) 10^{12}	10^{11}	10	
Taille; R_{res}	100 kpc	10 kpc	10^7 m
$-\Phi_{res}$	$1000 \text{ km}\cdot\text{s}^{-1}$	$300 \text{ km}\cdot\text{s}^{-1}$	$10\,000 \text{ km}\cdot\text{s}^{-1}$
Temps	$10^7\text{-}10^8 \text{ a}$	$10^7\text{-}10^8 \text{ a}$	1-3 s
T_{bulle} (K)	$10^9\text{-}10^{10}$	$10^9\text{-}10^{10}$	10^{10}
$T_{ambiante}$ (K)	$10^7\text{-}10^8$	$10^6\text{-}10^7$	10^9
Objet compact	trou noir supermassif	trou noir supermassif	trou noir/étoile neutron
Masse (M_\odot)	$10^8\text{-}10^{10}$	$10^6\text{-}10^9$	1-50
R_a (m)	$10^{11}\text{-}10^{14}$	$10^9\text{-}10^{12}$	$10^6/10^7$
$-\Phi_a$	c	c	$(0.1\text{-}1)c$
$-\Phi_a/\Phi_{res}$	10^5	10^6	100
Effets du jet	Chauffe le MIA	expulse le gaz	explosion
Rôle du jet	maintien température MIA	$M_{TN} - \sigma$	énergie explosion \approx liaison
Observables	Bulles dans le gaz X gaz froids	perte massive de gaz	explosion
Conséquences	refroidissement rapide	accroissement TNSM et formation étoiles	TN et GRB
Importance	Crucial dans courants froids	très commun, non-crucial	plausible avec neutrinos
Consensus ?	oui	oui	encore débattu

Le modèle classique des courants froids (Fabian 1994, 2012) et (McNamara & Nulsen 2012) prédit que le gaz primordial qui s'est réchauffé pendant la phase d'effondrement gravitationnel se refroidit par rayonnement, son entropie décroît donc localement et le gaz froid est comprimé par le gaz chaud l'entourant, provoquant un courant froid subsonique vers le centre du potentiel gravitationnel. Le déplacement de gaz est estimé à

$$\dot{M} \simeq \frac{2}{5} \frac{\mu m_p}{k_B T} L_X, \quad (2.39)$$

où L_X est la luminosité X, μ le poids moléculaire moyen, m_p la masse du proton et k_B la constante de Boltzmann. Pour une luminosité X typique ($\approx 10^{36}$ W), cette relation prédit un courant de plusieurs dizaines de masses solaires par an. Un tel courant n'est pas observé dans les groupes, en revanche les observations X de XMM et Chandra montrent des cavités dans le gaz X corrélées à la présence de lobes radio. Rafferty et al. (2008) parmi d'autres montrent une loi d'échelle entre le nombre de cavités et la puissance du noyau actif central. Gaspari et al. (2011b,a) montrent par des simulations hydrodynamiques 3D d'AGN dans un amas puis un groupe de galaxie typiques (Abell 1795 et NGC 5044), que la rétroaction d'un jet non-relativiste sur l'environnement est suffisante pour expliquer l'absence de courants froids dans les groupes. Le mécanisme physique de rétroaction lui-même n'est pas connu. Plusieurs mécanismes peuvent être invoqués :

- le premier, baptisé Cold Feedback, consiste à activer une rétroaction seulement quand le gaz refroidit à une température très basse dans une région proche du noyau. Habituellement, la majeure partie du gaz refroidit à proximité du centre de l'amas ou du groupe. Une fraction ϵ de l'énergie de masse au repos du gaz froid $\Delta M_{cool}c^2$ est injecté en énergie cinétique dans une masse de gaz chaud proche de l'AGN M_{act} dont la vitesse devient $v_{jet} = (2\epsilon\Delta M_{cool}c^2/M_{act})^{1/2}$, pour une énergie de jet $E_k^{jet} = M_{act}v_{jet}^2 = \epsilon\Delta M_{cool}c^2$. On remarque évidemment que le paramètre ϵ (entre 10^{-4} et 10^{-2}) va dicter la fréquence et l'amplitude de la rétroaction. En pratique la rétroaction se fait par sursauts ponctuels et violents.
- le deuxième, appelé mécanisme de Bondi, lie la rétroaction à la masse du trou noir supermassif par $\dot{M}_{Bondi} = 4\pi(GM_{TN})^2\rho_0/c_{s0}^3$, où M_{TN} est la masse du trou noir, ρ_0 est la densité de gaz dans un volume proche du trou noir (mais en pratique la résolution des simulations fixe une limite beaucoup plus grande $r_0 < 5$ kpc), c_{s0} est la vitesse du son dans la même région. La vitesse du jet produite devient $v_{jet} = (2\epsilon\dot{M}_{Bondi}\Delta t c^2/M_{act})^{1/2}$. En pratique l'efficacité de ce mécanisme est 10 à 100 fois plus grande que le premier ($\epsilon \sim 0.1$) et il donne une base physique à une rétroaction continue pour un AGN de faible puissance.
- d'autres recettes purement phénoménologiques sont également utilisées cf Gaspari et al. (2011b).

Il semble que les mécanismes de rétroaction dans les groupes exigent une plus grande finesse que dans les amas. Ainsi, la rétroaction Cold Feedback explique bien la rétroaction dans les intra-amas, alors qu'un mécanisme de type Bondi explique mieux la rétroaction dans les groupes. Il convient de rappeler deux points, d'une part la résolution des simulations (de l'ordre de quelques kpc) est encore beaucoup trop faible pour se convaincre que le modèle de Bondi est bien compris physiquement, d'autre part, les phénomènes continus sont rares en astrophysique et la plupart des jets sont intermittents. Il est donc probable que les rétroactions combinent des effets continus et intermittents. Ces études montrent bien que les phénomènes physiques dans les groupes ne peuvent pas être une simple translation d'échelle des amas.

2.2.2 Balayage par pression dynamique (Ram pressure stripping)

Cet effet physique (Hester 2006), observé dans les amas de galaxies, est un balayage du gaz des galaxies dont les orbites traversent le centre des amas par le milieu intra-amas. Décrit par Gunn & Gott (1972) pour la première fois, Gunn & Gott proposent une relation

simple pour déterminer quand le gaz de la galaxie est balayé :

$$\rho_{\text{ICM}} v_{\text{sat}}^2 > 2\pi G \sigma_* \sigma_{\text{gaz}}. \quad (2.40)$$

Le terme de gauche est la pression dynamique du milieu intra-amas de densité ρ_{ICM} sur une galaxie de mouvement à une vitesse v_{sat} . Le terme de droite est la pression du milieu intergalactique où σ_* et σ_{gaz} sont les densités de surface du disque. Si la densité du milieu intra-amas dépasse un certain seuil, la pression exercée sur le gaz de la galaxie balaye son gaz. Une condition analytique proche pour le balayage complet du gaz chaud d'une galaxie est donnée dans (Hester 2006),

$$\rho_{\text{ICM}} v_{\text{sat}}^2 > \rho_{0,\text{sat}} K_B T / \mu m_p, \quad (2.41)$$

où $\rho_{0,\text{sat}}$ est la densité du gaz chaud K_B , la constante de Boltzmann, T la température du gaz et μm_p est la masse moléculaire moyenne du gaz.

Cet effet très largement observé dans les amas, indirectement en HI (Giovanelli & Haynes 1985; Cayatte et al. 1994), et directement en H- α (Yoshida et al. 2008) est aussi à l'origine des *galaxies méduses* (voir figure 2.7), exemple de pression dynamique extrême (Ebeling et al. 2014; Poggianti et al. 2017).

Une étude détaillée de Hester (2006) analyse les paramètres en jeu dans le balayage dynamique et montre que le balayage dynamique existe à des degrés divers dans les groupes de galaxies. Les simulations hydrodynamiques expliquent très bien les processus physiques et les évolutions morphologiques des galaxies dans les amas et groupes de galaxies (e.g. Steinhauser et al. 2016). La figure 2.7 (bas) résume l'impact du balayage pour des galaxies de masses variées dans des amas et groupes.

2.2.3 Rétroaction des sursauts de formation d'étoile

Un des effets les plus marquants de la rétroaction dans les galaxies est la rétroaction des sursauts de formation d'étoiles sur le milieu interstellaire et intra-amas. Le lecteur est invité à visionner une des simulations d'Illustris, e.g. `illustris_comparison_adiabatic.mp4` montrant l'effet comparé d'une évolution sans rétroaction et d'une évolution avec rétroaction. L'effet de la formation stellaire est des plus frappants, il s'apparente à un feu d'artifice d'expulsions de gaz des galaxies vers le milieu intra-amas, sur des distances de plusieurs Mpc.

Il existe une riche littérature sur la rétroaction des supernovae depuis l'article pionnier de Dekel & Silk (1986), qui a, entre autre, étudié l'effet des supernovae sur les galaxies naines, Efstathiou (1992) propose que l'effet de rétroaction principal par photoionisation est de supprimer la formation d'étoile, Madau et al. (2001) suggèrent que la rétroaction permet d'enrichir en métaux le gaz primordial très tôt dans l'histoire de l'univers. Les travaux les plus récents s'appuient sur des simulations hydrodynamiques de plus en plus raffinées (e.g. tests de prescriptions phénoménologiques Kay et al. 2002, Smith et al. 2018 testent des modèles physiques de transfert énergétique entre SN et milieux, Tollet et al. 2019 étudient les différentes phases gazeuses des échelles interstellaires jusqu'à plusieurs rayons de viriel des amas, Lucas et al. 2020 s'intéressent à l'impact local de la rétroaction sur les nuages moléculaires denses).

Calcul analytique de l'impact des vents de supernovae

Les grandes lignes de la rétroaction par les sursauts de formation stellaire (principalement des supernovae) sont les suivants, tout comme pour les noyaux actifs de galaxies,

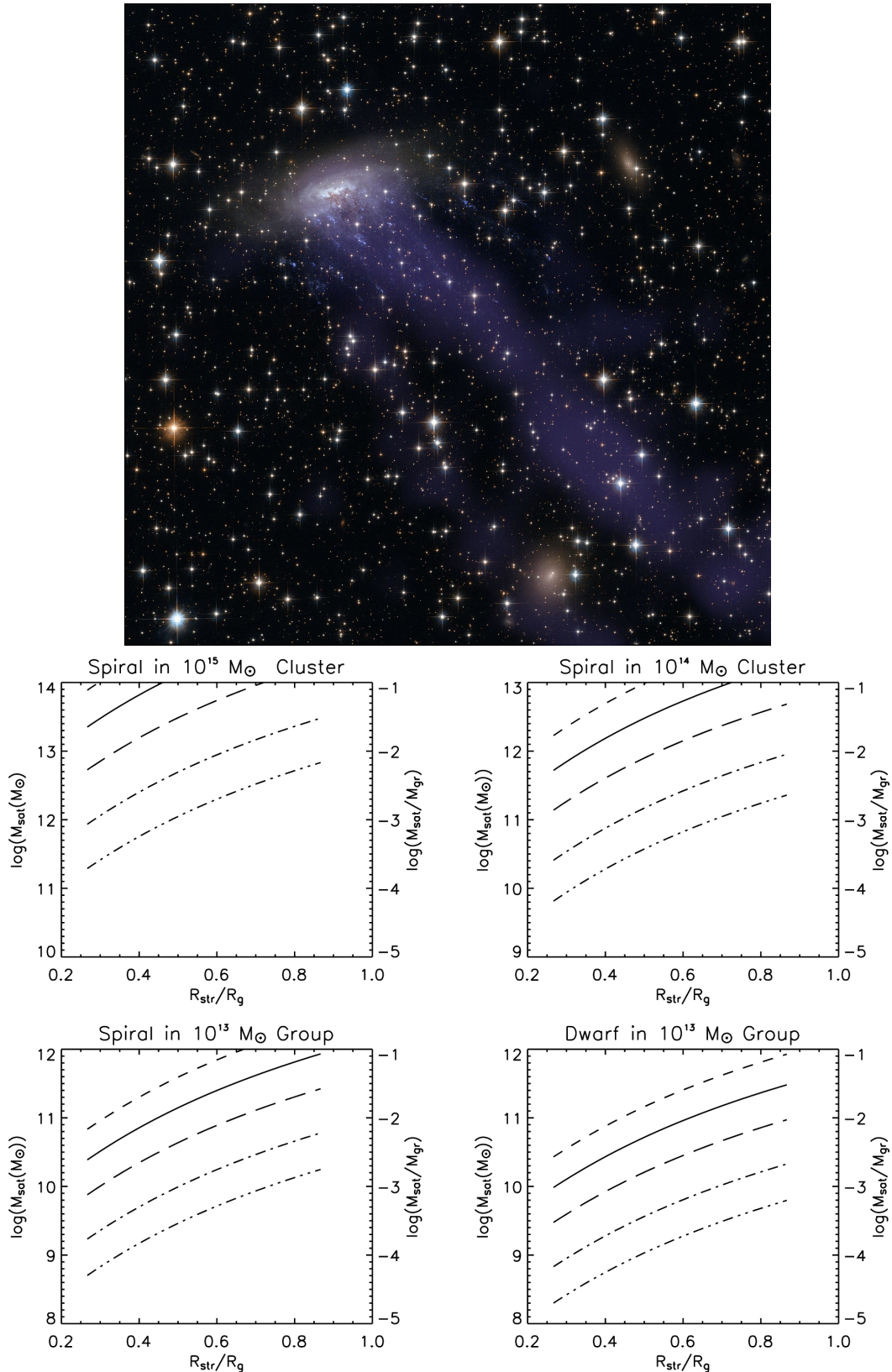


FIGURE 2.7 – Haut : ESO 137-001 est un exemple remarquable de pression dynamique. C'est une spirale de l'amas Abell 3627. En traversant le centre de l'amas, à une vitesse de $2000 \text{ km}\cdot\text{s}^{-1}$, elle perd son gaz chaud créant une longue queue de 80 kpc, ainsi qu'un chapelet de régions HII autour d'étoiles jeunes formées dans la perturbation, données combinées de HST et Chandra <https://chandra.harvard.edu/photo/2014/eso137/>. Bas : La masse à partir de laquelle une galaxies perd son gaz en passant dans un amas/groupe. En ordonnées $\text{Log}(M_{\text{sat}}/M_{\odot})$ est le logarithme de la masse du totale de la galaxie satellite. En abscisses R_{str}/R_g est le rayon, ramené au rayon total de la galaxie, au-delà duquel le gaz est balayé. Les quatre panneaux montrent des cas typiques de masses et les lignes des graphiques présentent différentes orbites de la galaxie dans l'amas paramétré par S_{orbit} , le périastre de l'orbite de la galaxie. Pour tous les cadres, de haut en bas $S_{\text{orbit}} = 0.25, 0.35, 0.5, 0.75, 1$ (Hester 2006).

la rétroaction peut-être thermique (via le rayonnement) et n'est efficace que si le milieu est optiquement épais, ou bien elle peut-être mécanique et la question est de savoir quels mécanismes transfèrent l'énergie cinétique vers le gaz. La physique de l'évolution du rémanent de supernova est décrite dans Dekel & Silk (1986) section IV. La question à laquelle Dekel et Silk essaient de répondre est dans quelle zone du plan densité de gaz n , température du gaz T (ou vitesse virielle du gaz v), une rétroaction de supernovae va provoquer une perte de gaz dans les galaxies ?

Je reproduis ici cette démonstration parce qu'elle place le cadre des travaux contemporains. Les équations et recettes sont toutes données en unité cgs ($1 \text{ erg} = 10^{-7} \text{ J}$). Le gaz est expulsé si l'énergie transmise au gaz par les supernovas lui donne une vitesse supérieure à la vitesse d'échappement. On définit la condition d'échappement paramétrée dans le plan n, v (n en cm^{-3}) par

$$E(n, v) > M_g v^2, \quad (2.42)$$

où M_g est la masse de gaz expulsée.

L'évolution standard d'un rémanent de supernova (dans la suite RSN) dans un milieu interstellaire uniforme passe par deux phases, adiabatique et radiative. Dans la phase adiabatique, les pertes dues au rayonnement sont négligeables, la majeure partie du gaz est balayée dans une fine coquille derrière le front de l'onde de choc en expansion. Le rayon de cette coquille à un temps t après l'explosion est donné par

$$R_s = \times 10^{15} \epsilon_{51}^{1/5} n^{-1/5} t^{2/5} \text{ cm}, \quad (2.43)$$

où $\epsilon_{51} = 1$ pour $\mathcal{E}_0 = \epsilon_{51} 10^{51} \text{ erg}$ l'énergie initiale du RSN, n est la densité d'hydrogène en cm^{-3} (en supposant une abondance d'hélium primordial de $Y = 0.25$). t est le temps en seconde. La majeure partie de l'énergie ($\sim 72\%$) est sous forme de chaleur, où la température juste à la limite du choc est

$$T_s \simeq 2.14 \times 10^{20} \epsilon_{51}^{2/5} n^{-2/5} t^{-6/5} \text{ K}. \quad (2.44)$$

Pour les métallicités faibles de $Z \approx 0.01$, typiques des galaxies naines, les courants froids dans les fourchettes $6 \times 10^4 \text{ K} < T < 6 \times 10^5 \text{ K}$ sont dominés par des émissions He^+ , $\text{Ly-}\alpha$ et raies d'oxygène dont l'effet combiné peut être approximé par

$$\Lambda(T) = 3 \times 10^{-18} \lambda T^{-1} n^2 \text{ erg} \cdot \text{cm}^{-3} \cdot \text{s}^{-1}, \quad (2.45)$$

où le paramètre λ est fonction de la métallicité, $\lambda = 1$ pour $Z = 0.01$ et λ augmente avec Z . Assumant que le gaz est confiné dans une coquille d'épaisseur $(\pi/3)R_s^3$, et utilisant les équations ci-dessus, on peut calculer la perte par rayonnement en fonction du temps avec

$$\mathcal{E}_{\text{loss}}(t) = \int_0^t \Lambda(t) (\pi/3) R_s^3(t) dt = 5.9 \times 10^7 \lambda \epsilon_{51}^{1/5} n^{9/5} t^{17/5} \text{ erg}. \quad (2.46)$$

Le temps de transition de la phase d'expansion adiabatique à la phase d'expansion radiative t_{rad} peut être défini comme le temps où le RSN a rayonné une fraction significative de son énergie initiale. Par exemple Dekel et Silk prennent une perte de $3/4 \mathcal{E}_0$. Ce temps est donné par

$$t_{\text{rad}} = 1.4 \times 10^5 \lambda^{-5/17} \epsilon_{51}^{4/17} t^{-9/17} \text{ an}. \quad (2.47)$$

Substituant ce temps dans l'équation 2.44 nous permet d'obtenir une température effectivement proche de $T_s \approx 10^5 \text{ K}$ au moment où la plus grande partie de l'énergie a été émise par rayonnement, justifiant l'équation de taux de refroidissement de l'équation 2.45.

La phase d'expansion radiative voit le RSN s'étendre de façon isotherme, balayant le gaz tout en conservant sa quantité de mouvement, comme un chasse-neige. Seulement une fraction de l'énergie initiale est encore disponible, principalement sous forme de chaleur dans le gaz très chaud laissé derrière l'onde de choc. Ce gaz se refroidit par expansion adiabatique. La quantité de cette énergie thermique est estimée à $\mathcal{E} \approx 0.22\epsilon_0(R_s/R_{\text{rad}})^{-2}$, où $R_{\text{rad}} = R_s(t_{\text{rad}})$ est donné par l'équation 2.43.

La relation entre R_s et le t en phase radiative s'obtient par calcul numérique, $R_s \propto t^{0.31}$, ce qui permet de déduire pour l'énergie $\mathcal{E} \propto t^{-0.62}$. Donc on peut écrire que l'énergie nette injectée dans le gaz par une seule supernova à un temps t comme

$$\mathcal{E}(t) = \begin{cases} \epsilon_0 - \epsilon_{\text{loss}}(t), & t < t_{\text{rad}}, \\ 0.22(t/t_{\text{rad}})^{-0.62}, & t > t_{\text{rad}}. \end{cases} \quad (2.48)$$

L'injection cumulée d'énergie de $N_s(t)$ supernovas est donné simplement par l'intégrale

$$\mathcal{E}(t) = \int_0^{N_s(t)} \epsilon(t - t_*) dN_s(t_*). \quad (2.49)$$

La grande part de l'énergie vient pratiquement exclusivement des étoiles massives, donc le cycle est très court et l'explosion des supernovas peut-être considérée comme instantanée après la naissance. Le nombre d'explosions par unité de masse d'étoiles formées est noté $\nu = 10^{-35}\nu_{50}g^{-1}$, où $\nu_{50} = 1$ pour un taux d'une supernova pour $50 M_\odot$ d'étoiles, et $\nu_{50} = 1/2$ est la valeur de actuelle de notre Galaxie. Il s'en suit, si le taux de formation d'étoiles \dot{M}_* est constant, que le nombre de RSN est

$$N_s(t) = \nu \dot{M}_* t, \quad (2.50)$$

donc

$$\mathcal{E}(t) = \dot{M}_* \nu \int_0^t \epsilon(t') dt'. \quad (2.51)$$

L'énergie injectée dans le gaz se réécrit donc

$$\mathcal{E}(t) = \dot{M}_* \nu \epsilon_0 t_{\text{rad}} f(t), \quad (2.52)$$

où le paramètre sans unité $f(t)$ couvre les phases d'expansion adiabatique et radiative

$$f(t) = \begin{cases} (t/t_{\text{rad}})[1 - 0.14(t/t_{\text{rad}})^{17/5}], & t \leq t_{\text{rad}}, \\ 0.86 + 0.58[(t/t_{\text{rad}})^{0.38} - 1], & t > t_{\text{rad}}. \end{cases} \quad (2.53)$$

Si les durées considérées sont de l'ordre de t_{rad} , alors f est proche de l'unité.

Si on choisit un taux de formation d'étoiles non pas constant, mais relié à des quantités physiques de la galaxie, par exemple :

$$\dot{M}_* = M_g / (\tau t_{\text{ff}}), \quad (2.54)$$

avec M_g masse de gaz dans la galaxie, t_{ff} temps de chute libre du gaz (ff = free fall) et le paramètre τ fixe le taux, maximal à $\tau = 1$. La section précédente nous montre que $t_{\text{ff}} = (6\pi G\rho)^{-1/2}$ et la masse de gaz est $M_g = gM$, où le paramètre g module la masse M . Alors,

$$t_{\text{ff}} = 1.9 \times 10^{-7} g^{1/2} n^{-1/2} \text{ an}. \quad (2.55)$$

Avec le taux naturel défini en 2.54 et introduit dans l'équation 2.52, la condition d'échappement de l'équation 2.42 définit une *vitesse critique* en-dessous de laquelle le balayage du gaz est possible,

$$v^2 < v_{\text{crit}}^2 = 2f\epsilon_0(\nu/\tau)(t/t_{\text{ff}}). \quad (2.56)$$

En comparant les équations 2.47 et 2.55, on voit que le rapport $(t_{\text{rad}}/t_{\text{ff}}) \sim 0.01$ est pratiquement indépendant de la densité n ou de la vitesse v . La vitesse critique est

$$v_{\text{crit}} = 123f^{1/2}\lambda^{-5/34}\epsilon_{51}^{21/34}(\nu_{50}/\tau)^{1/2}g^{-1/4}n^{-1/68}\text{ km} \cdot \text{s}^{-1}, \quad (2.57)$$

où la valeur exacte de f n'est pas encore déterminée. Pour la trouver, on assume que l'énergie disponible pour balayer le gaz est l'énergie du RSN au moment où il couvre une partie substantielle du volume du gaz et donc peut affecter une large fraction du gaz. Le temps de recouvrement t_{ov} associé doit être trouvé en résolvant l'équation suivante

$$\begin{aligned} R^3 &= \int_0^{N_s(t_{\text{ov}})} R_s^3(t_{\text{ov}} - t_*) dN_s(t_*) \\ &= \dot{M}_* \nu \int_0^{\text{ov}} R_s^3(t') dt', \end{aligned} \quad (2.58)$$

où R est le rayon de la galaxie. Résolvant cette équation pour t_{ov} donne,

$$t_{\text{ov}} = \begin{cases} 2 \times 10^5 \epsilon_{51}^{-0.27} (\frac{\nu_{50}}{\tau})^{-0.45} g^{0.23} n^{-0.41} \text{ an}, & t_{\text{ov}} \leq t_{\text{rad}}, \\ 1.9 \times 10^5 \epsilon_{51}^{-0.34} (\frac{\nu_{50}}{\tau})^{-0.52} g^{0.26} n^{-0.39} [1 + \frac{0.14 \epsilon_{51}^{1.12} (\nu_{50}/\tau)}{\lambda^{0.65} g^{0.5} n^{0.27}}]^{0.52} \text{ an}, & t_{\text{ov}} > t_{\text{rad}}. \end{cases} \quad (2.59)$$

Tant que le temps de recouvrement est plus court que le début de la phase radiative, i.e. $t_{\text{ov}} \leq t_{\text{rad}}$ on a donc

$$t_{\text{ov}}/t_{\text{rad}} = 1.4\lambda^{0.29}\epsilon_{51}^{-0.51}(\frac{\nu_{50}}{\tau})^{-0.45}g^{0.23}n^{0.12}, \quad (2.60)$$

Ainsi, si la formation d'étoiles est rapide ($\tau \sim 1$), alors $t_{\text{ov}} \approx t_{\text{rad}}$ avec une dépendance faible sur la densité n . La conséquence de ce calcul est que la plupart des RSM vont se recouvrir entre eux pendant qu'ils sont encore en phase adiabatique (ce sont les "explosions" vues dans la simulation d'Illustris). La densité (appelée *critique*) pour laquelle $t_{\text{ov}} = t_{\text{rad}}$ est dérivée par l'équation 2.60 mise à l'unité, i.e., $n_c = 0.06\lambda^{-2.42}\epsilon_{51}^{4.25}(\nu_{50}/\tau)^{3.75}g^{-1.92}$. Substituant t_{ov} dans l'équation 2.53 nous permet d'obtenir

$$f = \begin{cases} \frac{1.4\lambda^{0.29}g^{0.23}n^{0.12}}{\epsilon_{51}^{0.51}(\nu_{50}/\tau)^{0.45}} [1 - \frac{0.41\lambda^{0.99}g^{0.78}n^{0.41}}{\epsilon_{51}^{1.7}(\nu_{50}/\tau)^{1.53}}] & n \leq n_c, \\ 0.28 + \frac{0.64\lambda^{0.11}g^{0.1}n^{0.053}}{\epsilon_{51}^{0.22}(\nu_{50}/\tau)^{-0.2}} [1 + \frac{0.14\epsilon_{51}^{1.12}(\nu_{50}/\tau)}{\lambda^{0.65}g^{0.5}n^{0.27}}]^{0.20}, & n > n_c. \end{cases} \quad (2.61)$$

Ces valeurs pour f nous permettent finalement de dériver la vitesse critique v_{crit} en les substituant dans l'équation 2.57. On obtient pour $n \leq n_c$

$$v_{\text{crit}} = 144\epsilon_{51}^{0.36}(\nu_{50}/\tau)^{0.27}g^{-0.13}n^{0.045} \left[1 - \frac{0.41\lambda^{0.99}g^{0.78}n^{0.41}}{\epsilon_{51}^{1.7}(\nu_{50}/\tau)^{1.53}} \right]^{1/2} \text{ km} \cdot \text{s}^{-1}, \quad (2.62)$$

Ainsi la vitesse critique est $v_{\text{crit}} = 144\text{ km} \cdot \text{s}^{-1}$ à $n = n_c$ et $v_{\text{crit}} \propto n^{0.045}$ pour $n \ll n_c$. Pour $n > n_c$ la dépendance est encore plus faible avec $v_{\text{crit}} \propto n^{0.012}$ quand $n \gg n_c$.

Cette démonstration permet de construire un diagramme des zones de balayage du gaz dans les galaxies en fonction de leur masse (Figure 2.8). Dans le plan n (densité)- v (vitesse

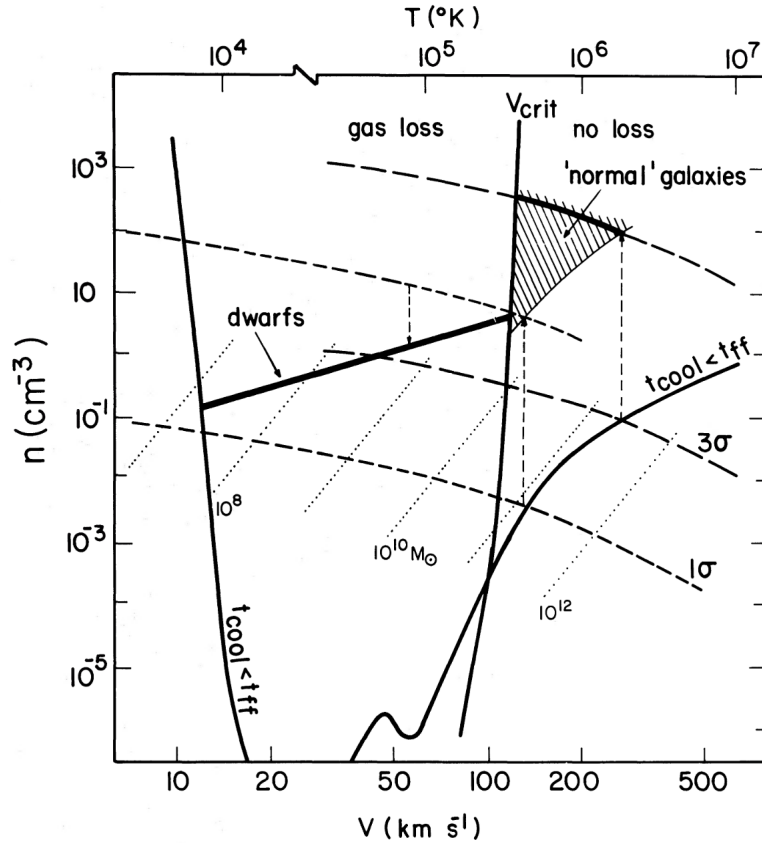


FIGURE 2.8 – Ce diagramme résume l'analyse de Dekel & Silk (1986), sur la masse des galaxies et le balayage du gaz dans le plan densité n - (vitesse virielle V / température T). La ligne marquée $t_{\text{cool}} < t_{\text{ff}}$ dénote la zone au-dessus de laquelle le gaz peut s'effondrer pour former des étoiles. Elle est calculée à partir du gaz primordial en supposant que la fraction initiale est de 10% de la densité totale de masse. La ligne presque verticale dénotée v_{crit} a été calculée au-dessus. Une protogalaxie ayant $v > v_{\text{crit}}$ utilisera la majorité de son gaz pour former les étoiles (zone "no loss"), tandis qu'une galaxie de plus faible masse avec $v > v_{\text{crit}}$ verra la totalité de son gaz expulsée après le premier (et donc dernier) sursaut de formation d'étoile par les vents de son cortège de supernovas (zone "gas loss"). Les lignes pointillées correspondent à des masses constantes d'objets auto-gravitants dénotées en M_{\odot} à chaque ligne. Les lignes discontinues dénotées $1-3\sigma$ sont des lignes sont reliées à l'amplitude des perturbations $\delta M/M$ et peuvent être ignorées dans la discussion qui nous intéresse.

virielle/température), la ligne marquée $t_{\text{cool}} < t_{\text{ff}}$ dénote la zone au-dessus de laquelle le gaz peut s'effondrer pour former des étoiles. Elle est calculée à partir du gaz primordial en supposant que la fraction initiale est de 10% de la densité totale de masse. La ligne presque verticale dénotée v_{crit} a été calculée au-dessus. Une protogalaxie ayant $v > v_{\text{crit}}$ utilisera la majorité de son gaz pour former les étoiles (zone "no loss" dans la Figure 2.8), tandis qu'une galaxie de plus faible masse avec $v > v_{\text{crit}}$ verra la totalité de son gaz expulsée après le premier (et donc dernier) sursaut de formation d'étoile par les vents de son cortège de supernovas (zone "gas loss" dans la Figure 2.8). Les lignes pointillées correspondent à des masses constantes d'objets auto-gravitants dénotées en M_{\odot} à chaque ligne. Les lignes discontinues dénotées $1-3\sigma$ sont des lignes sont reliées à l'amplitude des perturbations $\delta M/M$ et peuvent être ignorées dans la discussion qui nous intéresse.

Le calcul de Dekel et Silk semble montrer également que les sursauts de formation d'étoiles de la galaxie centrale auront assez d'énergie pour balayer également le gaz chaud des galaxies satellites dans le milieu intra-groupe.

Simulations hydrodynamiques sur l'impact des vents de supernovas

Les simulations hydrodynamiques des 20 dernières années ont permis de faire progresser notre connaissance de la microphysique en jeu dans les rétroactions de la formation d'étoiles sur le milieu interstellaire et dans les groupes. Reprenons à notre compte l'analyse de Schaye et al. (2015).

Les étoiles peuvent injecter énergie et quantité de mouvement dans le milieu interstellaire à travers les vents (énergie cinétique et quantité de mouvement), le rayonnement (énergie thermique) et les supernovas (les trois à la fois). Ces processus sont particulièrement importants pour les étoiles massives, et par conséquent de vie courte. Si la formation d'étoiles est intense, la rétroaction associée peut générer des expulsions à grande échelle dans les galaxies. Les simulations hydrodynamiques de taille cosmologique ont traditionnellement du mal à produire des rétroactions efficaces, telles que requises pour égaler les masses, tailles et flux de gaz observés. Si l'énergie est injectée sous forme thermique, elle tend à rapidement se diffuser sans produire de vents. Ce problème de sur-refroidissement (*overcooling problem*) est en général attribué au manque de résolution à petite échelle des simulations. Si les simulations ne contiennent pas de nuages de gaz froids et denses, alors la formation d'étoiles n'est pas assez grumeleuse et l'énergie de rétroaction est trop diffuse. De plus, comme la majeure partie du gaz se situe en réalité dans ces gaz froids du milieu interstellaire, les simulations qui ignorent cette composante froide surestiment par conservation de masse les composantes chaudes diffuses du gaz. Une autre source d'erreur s'ajoute au problème d'après Schaye et al. (2015), l'énergie est distribuée sur un trop grand intervalle de masse stellaire. En effet, pour une fonction de masse initiale standard, il y a environ une supernova par $100 M_{\odot}$ d'étoiles produites dans un sursaut de formation instantanée et, en réalité, toute l'énergie mécanique associée est initialement déposée dans quelques masses solaires d'éjectas, menant à des températures initiales très élevées (e.g. 2×10^8 K si 10^{44} J sont déposées dans $10 M_{\odot}$ de gaz). En revanche, dans les simulations hydrodynamiques qui distribuent l'énergie produite par une particule stellaire sur les voisins hydrodynamiques, le rapport entre la masse chauffée et la masse de la population du sursaut de formation instantanée est beaucoup plus grand que un. Cette inconsistance dans le rapport de masse induit que la température maximale du gaz directement chauffé est beaucoup plus basse qu'en réalité, et par conséquent que son temps de refroidissement est beaucoup trop court. Comme le rapport entre les particules hydrodynamiques et les particules étoiles est indépendant de la résolution, au premier ordre ce problème est indépendant de la résolution. Au deuxième ordre, une plus haute résolution aide parce que la rétroaction thermique peut tout de même générer des courants vers l'extérieur si le temps de refroidissement est grand comparé au temps de relaxation à vitesse du son à travers l'élément de résolution, et ce temps de relaxation diminue avec une augmentation de la résolution (mais seulement $\propto m_g^{1/3}$).

Le problème de manque de résolution à petite échelle requiert la fabrication de modèles physiques moyennant le comportement à échelles non-résolues, appelés *subgrid models* dans la littérature. Ces modèles sont requis pour générer les vents galactiques sur de grands volumes des simulations cosmologiques. Quatre types de recette sont utilisées :

- Injecter de l'énergie sous forme cinétique (Navarro & White 1993; Springel & Hernquist 2003; Dubois et al. 2014) en supprimant ponctuellement les forces hydrodynamiques agissant sur les particules de vent (Springel & Hernquist 2003). C'est le cas d'Illustris (Vogelsberger et al. 2013), Feedback Acting on Baryons in Large-scale Environments (FABLE; citealtHenden2018), Horizon (Dubois et al. 2014), MassiveBlack-II (Khandai et al. 2015) .

- couper le refroidissement radiatif de l'éjecta (Stinson et al. 2006; Wang et al. 2015). C'est le cas de Numerical Investigation of a Hundred Astrophysical Objects (NIHAO Wang et al. 2015).
- découpler explicitement les différentes phases thermiques pour injecter l'énergie thermique dans le gaz (Keller et al. 2014), c'est le cas de
- et générer une rétroaction thermique stochastique (Dalla Vecchia & Schaye 2012). C'est le cas de EAGLE Schaye et al. (2015) et Cluster-EAGLES récemment (Barnes et al. 2017).

Nous ne plongerons pas dans le détail des méthodes qui nous emmènerait trop loin de l'objet de cette section. Mais nous relèverons quelques points d'Illustris et EAGLE illustrant les défauts, qualités et la dépendance des résultats sur les choix de ces modèles physiques non-résolus.

EAGLE :

La recette de Dalla Vecchia & Schaye (2012) consiste à restituer l'énergie avec une rétroaction simple et globale des effets stellaires par une injection thermique stochastique dans la composante gazeuse hydrodynamique. En pratique il s'agit d'augmenter la température des particules hydrodynamiques de gaz sur une base statistique, d'une valeur ΔT , la proportion des particules est fixée par l'énergie délivrée par l'explosion des supernovas (30 millions d'années après le sursaut de formation), avec un paramètre ajustable f_{th} fixant la fraction d'énergie réellement injectée. La valeur $f_{\text{th}} = 1$ correspond à une énergie de 8.73×10^{14} J par kg de masse stellaire formée (correspondant à l'énergie d'une supernova; 10^{44} J, pour une fonction de masse initiale de Chabrier (2003), assumant que les étoiles de masses 6-100 M_{\odot} explosent). La valeur $\Delta T = 10^{7.5}$ K est fixée par les considérations entropiques sur la densité de gaz. En rendant la rétroaction stochastique, les auteurs peuvent contrôler la quantité d'énergie par rétroaction en fixant l'énergie moyenne par unité de masse stellaire formée. Cette énergie moyenne est calibrée sur l'énergie totale par unité de masse stellaire nécessaire pour reproduire la fonction de masses stellaires de la galaxie observée. Cette recette peut surestimer la quantité d'énergie nécessaire à la rétroaction parce que la perte par rayonnement des étoiles produites dans les régions de gaz chaud peut-être surestimée. Enfin, pour les galaxies massives c'est la rétroaction des AGN qui contrôle l'efficacité de formation des galaxies. Surestimer les pertes radiatives de la rétroaction stellaire, aura pour effet de surestimer l'efficacité nécessaire de la rétroaction AGN pour compenser. La figure 2.9 montre l'ajustement d'EAGLE aux données, et la comparaison avec Illustris sur la fonction de masse stellaire des galaxies. Comme EAGLE est ajusté à cet observable, il suit assez fidèlement le profil observé tout comme les recettes phénoménologiques semi-analytiques (à gauche), les simulations Illustris et MassiveBlack-II ont davantage de difficulté à produire les fonctions de masses alors qu'elles ont également été calibrées sur les données (à droite). Les données viennent du sondage Galaxy And Mass Assembly (GAMA; Baldry et al. 2012) et SDSS (Li & White 2009). Davantage intéressant que les observables ajustés, sont les prédictions d'EAGLE sur les données non ajustées, le lecteur est référé à la publication de Schaye et al. (2015) pour l'ensemble des prédictions, nous soulignerons ici une belle prédiction de la loi de Tully-Fisher, ainsi qu'une bonne compatibilité des métallicités en fonction des masses des galaxies pour les galaxies massives, avec une surestimation des abondances d'oxygène de 0.5 dex, légèrement au-dessus de l'erreur observationnelle ($\sim 1-2\sigma$). La figure 2.10 montre la prédiction d'EAGLE pour la loi L_X-T_X , où la simulation standard a tendance à surestimer la luminosité X pour une température donnée pour les amas, alors que les groupes

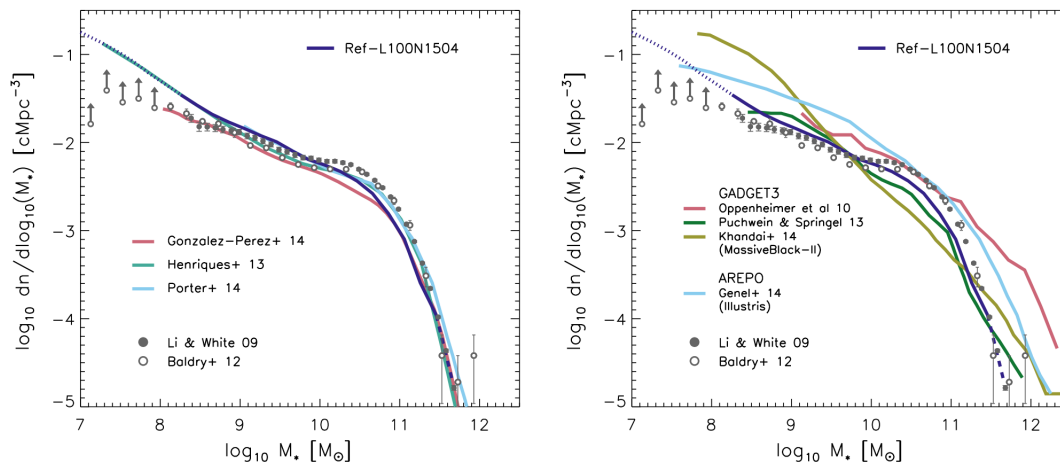


FIGURE 2.9 – Fonction de masses stellaires des galaxies observée sur Galaxy And Mass Assembly (GAMA; Baldry et al. 2012) et SDSS (Li & White 2009) et comparaison entre l’ajustement des modèles semi-analytiques et EAGLE (à gauche) et entre des simulations hydrodynamiques cosmologiques citées dans le texte et l’ajustement d’EAGLE. Tous les modèles ont été ramenés à la même fonction de masse initiale (Chabrier 2003). La courbe EAGLE est pointillée là où les galaxies sont formées de moins de 100 particules. A part Oppenheimer et al., toutes les simulations incluent également une rétroaction AGN. A part MassiveBlack-II, tous les modèles ont été étalonnés sur les données. L’accord est évidemment bon pour EAGLE et les modèles semi-analytiques. EAGLE est meilleur que les autres simulations hydrodynamiques.

sont plutôt bien prédits.

Illustris :

La formation des galaxies et les effets de rétroactions dans la simulation hydrodynamique cosmologique Illustris sont décrits en détail dans un papier de Vogelsberger et al. (2013). Les auteurs font l’hypothèse que tous les phénomènes physiques qui influent sur le milieu interstellaire, par exemple la turbulence, les instabilités thermiques, la conduction thermique, la formation des gaz moléculaires et les processus d’évaporation, atteignent un état d’équilibre auto-régulé qui peut se modéliser par une équation d’état effective. La température du milieu peut donc être modélisée par une fonction de la densité seulement. La formation d’étoiles est produite de façon stochastique au-dessus d’une densité de gaz ($\rho_{\text{SFR}} = 0.13 \text{ cm}^{-3}$) avec une échelle de temps ajustée aux observations ($t_{\text{SFR}} = 2.2 \times 10^9$ ans) le tout utilisant une fonction de masse initiale de type Chabrier (2003). Les processus de formation d’étoiles calquent ceux des simulations hydrodynamiques de plus haute résolution de MUGS (McMaster Unbiased Galaxy Simulations; Stinson et al. 2013) qui reproduisent bien les observations de Notre Galaxie (population stellaire, métallicité, composantes dynamiques des disques).

De cette formation d’étoiles découle toute la chaîne de rétroactions stellaires sur le milieu gazeux dont la métallicité, le nombre de supernovas et par conséquent la rétroaction cinétique des RSN. Les modèles de vents stellaires sont construits en fonction du taux de formation d’étoiles en sélectionnant une fraction de masse (proportionnelle à la dispersion des vitesses CDM locales), sous forme de particules voyageant dans l’espace sans interaction hydrodynamique et finalement déposées (masse, métaux et énergie thermique) dans le milieu interstellaire et intergalactique quand un critère de temps maximal de voyage ou de densité est atteint. Ces méthodes numériques permettent de mieux ajuster les rétroactions indépendamment des contraintes hydrodynamiques tout en réduisant

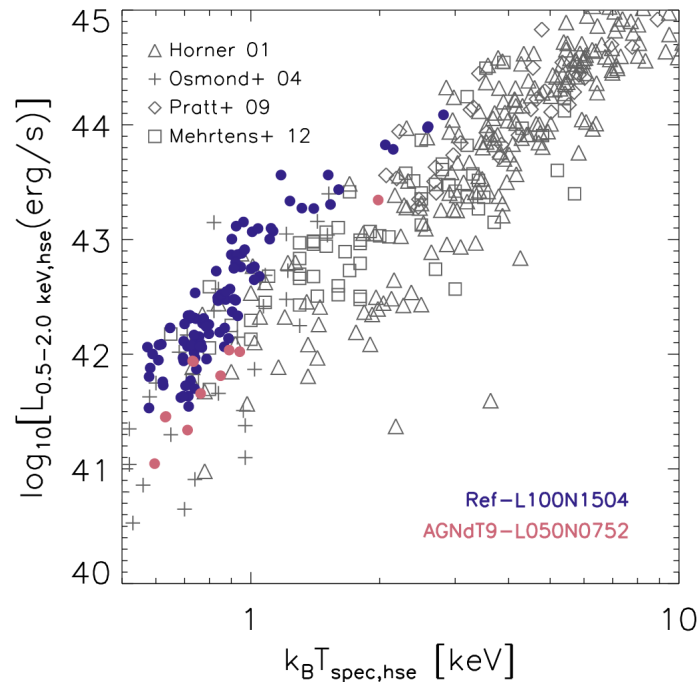


FIGURE 2.10 – La luminosité L_X dans l’intervalle 0.5-2.0 keV en fonction de la température T_X à $z = 0$. Seuls les points pour lesquels $M_{500} > 10^{13} M_\odot$ sont montrés. Les points gris sont des observations de la composante X du programme Group Evolution Multiwavelength Study (GEMS, Osmond & Ponman 2004), des données du satellite ASCAT (Horner 2001), des données du sondage XMM-XCS (Mehrtens et al. 2012), et des données REXCESS (Pratt et al. 2009). Le modèle EAGLE de référence (points bleus) prédit des luminosités X trop grandes pour les amas au-dessus de $T_X > 1$ keV. La simulation dédiée AGN est compatible avec les données.

les biais causés par la sous-résolution des simulations. La Figure 2.11 montre l’impact des différents paramètres de rétroactions (incluant stellaires et AGN) sur le taux de formation d’étoiles et des mesures de l’univers local.

Autres simulations hydrodynamiques :

Les autres simulations hydrodynamiques publiées dans la littérature utilisent des méthodes assez proches pour injecter une rétroaction stellaire dans leur espace hydrodynamique, avec des différences à la marge. Henden et al. (2018) avec FABLE reprend le même code AREPO qu’Illustris avec une modification de la fraction des particules de gaz éjectées (30% sont converties en énergie thermique) pour éviter une recondensation trop rapide sur les disques. Cet artifice donne fraction de masse stellaire et de gaz à l’échelle des groupes sensiblement différente de celle d’Illustris comme le montre la figure 2.12. Cela pointe une fois de plus sur le fait que la physique en jeu dans les groupes n’est pas encore bien comprise, ni bien prise en compte dans les simulations de trop faible résolution. Tollet et al. (2019) a produit une simulation identifiant cinq phases gazeuses (gaz froid dans les galaxies, i.e. milieu interstellaire froid, gaz froid à l’extérieur des galaxies mais dans le halo CDM, i.e. gaz froid circumgalactique, gaz chaud dans les galaxies, i.e. milieu interstellaire chaud, gaz chaud à l’extérieur des galaxies mais dans le halo CDM, i.e. gaz chaud circumgalactique, et le gaz à l’extérieur du halo CDM, dans le milieu intergalactique) et suit ces composantes pas à pas au cours des simulations.

Plusieurs auteurs se sont appuyés sur les simulations d’Illustris pour tenter de pro-

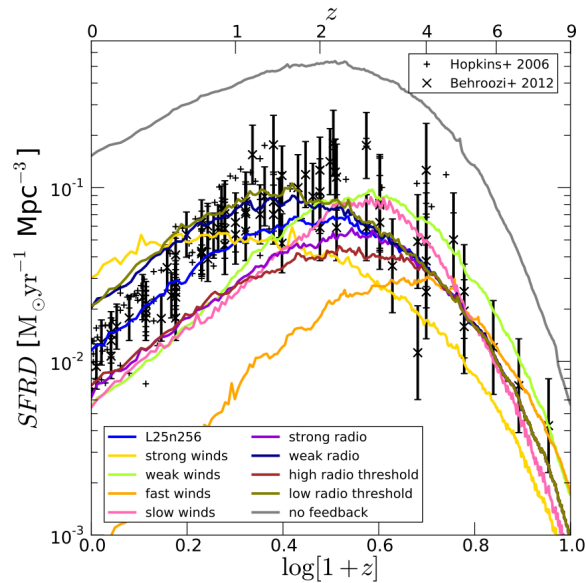


FIGURE 2.11 – Densité de formation d'étoiles Cosmique en fonction du redshift tiré de Vogelsberger et al. (2013). Les données observées viennent de compilations faites par Hopkins & Beacom (2006); Behroozi et al. (2013). L'impact de différentes prescription de vent est bien visible. Doubler la vitesse du vent (line 'faster winds') mène à une forte suppression de la formation d'étoiles. Augmenter l'énergie globale des vents ('stronger winds') mène à une surproduction d'étoiles à des époques récentes. L'impact de la rétroaction AGN n'a pas autant d'effet sur la formation stellaire que la rétroaction stellaire.

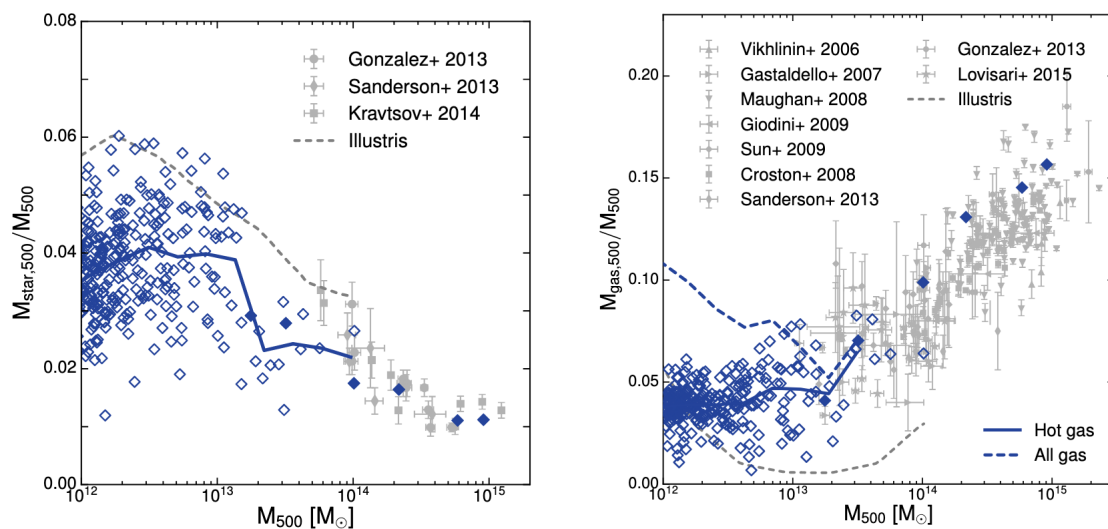


FIGURE 2.12 – Fonction de masses stellaires (gauche) et de gaz (droite) extraite de FABLE (Henden et al. 2018). Gauche : la fraction de masses stellaires dans un rayon R_{500} en fonction de la masse des halos à $z = 0$. Les losanges sont les halos simulés à des résolutions diverses (haute résolution à faible masse) dont la ligne solide montre la valeur moyenne, la ligne pointillée montre la même valeur tirée d'Illustris. Les symboles avec barres d'erreur sont des observations diminuées de 24% pour adapter la fonction de masses initiale à celle de Chabrier (cf références in Henden et al. 2018). Droite : la fraction de masses sous forme de gaz dans un rayon de R_{500} en fonction de la masse des halos à $z = 0$. La légende des lignes et symboles est la même qu'à gauche. Les phases gazeuses froides et multiphase ne sont pas incluses car biaisées par les simulations FABLE. On voit que les deux simulations FABLE et Illustris prédisent des fonctions de masses sensiblement différentes pour les groupes de galaxies, indice que le détail de la physique en jeu dans les groupes n'est pas encore bien compris et hors de portée des simulations aujourd'hui.

duire des relations observables des groupes et les comparer avec les sondages récents. Raouf et al. (2016) puis Kundert et al. (2017) ont étudié les caractéristiques des groupes produits par Illustris. Même si le nombre de groupes compacts, en particulier les groupes fossiles est surestimé par Illustris. La simulation hydrodynamique offre des pistes évolutives intéressantes par rapport aux recettes purement phénoménologiques. Raouf et al. (2016) montre qu'Illustris pointe vers un lien évolutif fort entre les masses des trous noirs centraux et l'état de relaxation des groupes. Les groupes les plus évolués d'Illustris ont également un milieu intra-groupe plus chaud, tous cela est conforme aux dernières observations. Kundert et al. (2017) étudient l'origine des groupes fossiles et la différence entre ceux-ci et les groupes normaux. Illustris ne montre pas de différence dans la formation des deux types de groupes, mais pointe vers une différenciation assez tardive entre les deux types, causée par un arrêt de l'accrétion dans le cas des groupes fossiles. Cette différence explique entièrement pour Illustris les observables.

De l'aveu même des spécialistes des simulations numériques, les modèles utilisés pour expliciter la physique complexe à des sous-résolutions restent très insuffisants pour encapsuler les effets non-linéaires qui en découlent (Ohlin et al. 2019; Keller & Kruijssen 2020; Lucas et al. 2020). Les incohérences entre les observations des objets de faible masse, galaxies naines (les plus difficiles à simuler) et les observables des galaxies les plus massives resteront hors de portée des simulations cosmologiques et même des simulations à l'échelles des galaxies car les résolutions de l'ordre du parsec sont nécessaires à la modélisation rigoureuse des effets de turbulence et de transfert de rayonnement robuste.

2.3 Conclusion

Ce chapitre nous a montré que les connaissances sur les processus physiques en jeu dans les groupes de galaxies ont fortement progressé ces dernières années. D'une part la formation des groupes de galaxies est expliquée par la théorie classique de la formation des structures de l'univers en expansion, comme un effondrement hiérarchique du fluide cosmique dominé par une matière sombre CDM et soumis aux équations d'Einstein, dont le spectre de puissance des fluctuations de densités est gaussien. D'autre part, la physique baryonique explique bien l'histoire de la formation des étoiles dans les galaxies et les observations des différentes phases de la matière dans les milieux à des échelles allant du parsec au mégaparsec. Cependant, si les grandes lignes de cette histoire commencent à être comprises, des points d'ombre perdurent. Les mécanismes de rétroactions ont probablement tous été identifiés, mais leur articulation reste floue. Aujourd'hui encore nous n'avons pas la moindre observation directe de la matière sombre non-baryonique. Les modèles nous enseignent que la frontière entre la physique baryonique et la cosmologie se situe quelque part entre le milieu circumgalactique des galaxies des groupes et le milieu intra-groupe qui se dilue dans les structures filamentaires des galaxies à grande échelle.

Plus que jamais aujourd'hui l'échelle des groupes offre une opportunité unique de mieux comprendre le lien entre l'univers cosmologique et l'univers baryonique des galaxies. L'astronomie reste une science fondamentalement ancrée sur les observations permettant de réfuter les expériences par la pensée que sont les modèles analytiques théoriques et les simulations numériques. Les chapitres suivants se tourneront résolument vers les observations en présentant à la fois les progrès permis par les sondages du ciel profond du début de XIXe siècle et les promesses des prochaines missions spatiales.

Chapitre 3

Les effets de lentilles dans les groupes de galaxies

3.1 Introduction

Comme nous l'avons vu en section 1.2.2 de l'introduction de ce manuscrit, la détection d'échantillons non-biaisés de groupes de galaxies est rendue difficile à faible masse par une double difficulté, d'une part la faible densité sur le ciel les groupes rend difficile à détecter et d'autre part, une fois détectés, il n'est toujours évident d'établir qu'une sur-densité sur le ciel n'est pas totalement fortuite. Il existe pourtant une méthode de détection qui nous assure que l'objet détecté présente une densité surfacique importante dans la ligne de visée ; le lentillage gravitationnel fort. Les lentilles gravitationnelles, font l'objet d'études théoriques depuis les débuts de la relativité générale, (cf ; l'excellente revue historique de Valls-Gabaud 2009) et observationnelles depuis plus de quarante ans (cf. section 1.3.4). Le lecteur intéressé pourra consulter les ouvrages de référence de Schneider et al. (1992) et les articles de revues sur *Annual Review on Astronomy & Astrophysics* (Blandford & Narayan 1992; Paczyński 1996; Mellier 1999; Refregier 2003; Treu 2010; Gaudi 2012; Mandelbaum 2018) et la revue très complète de Kneib & Natarajan (2011) sur les applications du lentillage gravitationnel à l'échelle des amas (et groupes de galaxies).

Notre propos dans ce chapitre ne touche qu'une petite partie du domaine, celui des lentilles fortes mettant en jeu des galaxies lentilles et des groupes de galaxies lentilles. Par ailleurs, les amas lentilles font l'objet depuis des années d'une grande diversité de travaux, à la fois en modélisation et observation e.g. MACS : Massive Cluster Survey (Ebeling et al. 2001), CLASH : Cluster Lensing And Supernova with Hubble¹ (Postman et al. 2012), HFF : Hubble Frontier Field Survey² (Lotz et al. 2017), qui font l'objet de campagnes de suivi multi-longueur d'onde.

3.1.1 Principes physiques

Sans réécrire les manuels de lentilles gravitationnelles, il me semble important de rappeler les grands principes derrière les effets physiques du lentillage en reprenant les conventions de Kneib & Natarajan (2011). Rappelons tout d'abord que l'Univers est

1. <https://www.stsci.edu/postman/CLASH/>

2. <https://outerspace.stsci.edu/display/HPR/HST+Frontier+Fields>

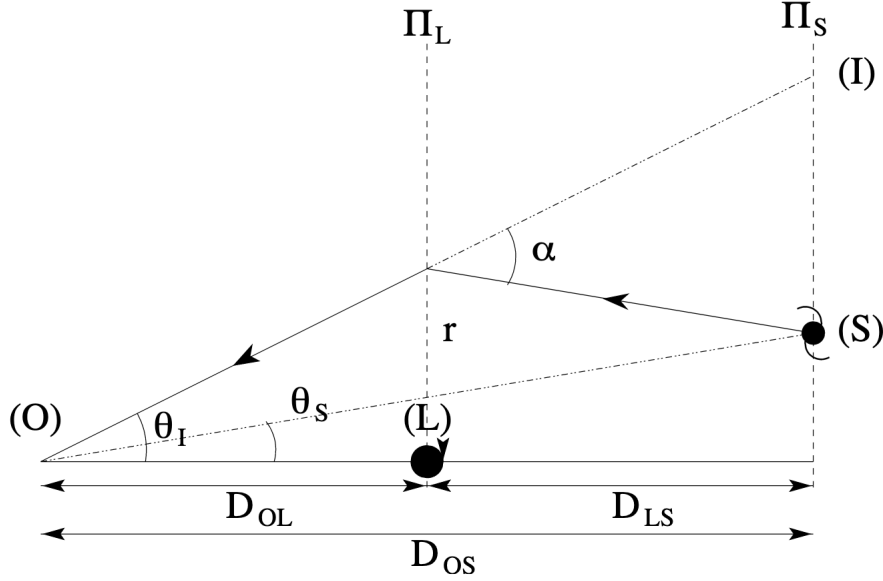


FIGURE 3.1 – Schéma géométrique classique de l'effet de lentille explicitant les angles et les distances en jeu dans l'équation des lentilles. À droite, la source (S), à gauche l'observateur (O), au centre la lentille déflectrice (L). Les distances D_{OS} , D_{OL} , D_{LS} sont des distances-luminosité. Π_L , Π_S sont les plans image et source. r la distance angulaire au centre de la lentille. θ_S , θ_I et α les angles.

assumé homogène et isotrope sur les distances en jeu dans le lentillage des amas, i.e. L .

$$L \sim \frac{c}{\sqrt{G\bar{\rho}}} \sim 2 \text{ Gpc} \quad (3.1)$$

où c est la vitesse de la lumière, G la constante gravitationnelle, $\bar{\rho}$ est la densité moyenne de l'Univers. La métrique qui décrit le mouvement des particules est donc la métrique de Friedmann-Lemaître-Robertson-Walker

$$ds^2 = c^2 dt^2 - a^2(t) \left(\frac{dr^2}{1 - kr^2} + r^2 d\theta^2 + r^2 \sin^2 \theta d\varphi^2 \right), \quad (3.2)$$

où $a(t)$ est le facteur d'échelle et k la courbure. Cette métrique est localement perturbée par la présence d'une masse dense où la solution de Schwarzschild donne la forme de la métrique dans la limite des champs faibles (toujours respectée en lentillage de groupes et d'amas) $\Phi \ll c^2$:

$$ds^2 = \left(1 + \frac{2\Phi}{c^2} \right) c^2 dt^2 - \left(1 - \frac{2\Phi}{c^2} \right) dr^2, \quad (3.3)$$

où Φ est le potentiel gravitationnel de la distribution de masse considérée.

3.1.2 Equation des lentilles

Prenant une configuration classique type illustré Figure 3.1, l'équation des lentilles est

$$\vec{\theta}_I = \vec{\theta}_S + \frac{D_{LS}}{D_{OS}} \vec{\alpha}(\vec{\theta}_I). \quad (3.4)$$

L'angle de déflexion $\vec{\alpha}$, mesuré localement sur $\vec{\theta}_I$ dépend de la perturbation de masse locale sur l'espace-temps. Les photons suivent des géodésiques nulle $ds^2 = 0$. L'équation

3.3 donne la durée du voyage t_T pour un chemin donné fonction de $\vec{\alpha}$. Le principe de Fermat établit que la lumière suit des chemins de durée stationnaire (i.e. $dt_t/d\vec{\theta}_I = \vec{0}$), il s'en suit sur $\vec{\alpha}$ en fonction du potentiel gravitationnel local newtonien³,

$$\vec{\alpha}(\vec{\theta}_I) = \frac{2}{c^2} \frac{D_{\text{LS}}}{D_{\text{OS}}} \vec{\nabla}_{\vec{\theta}_I} \phi_N^{2D}(\vec{\theta}_I), \quad (3.5)$$

où ϕ_N^{2D} est le potentiel gravitationnel newtonien projeté dans le plan de la lentille. Combinant les équations 3.4 et 3.5 on trouve *l'équation des lentilles* dans le régime de lentille mince, qui est toujours valide pour les lentilles amas et groupes isolés.

$$\vec{\theta}_S = \vec{\theta}_I - \frac{2\mathcal{E}}{c^2} \vec{\nabla} \phi_N^{2D}(\vec{\theta}_I) = \vec{\theta}_I - \vec{\nabla} \varphi(\vec{\theta}_I). \quad (3.6)$$

φ est le potentiel de la lentille, version normalisée du potentiel newtonien, et le facteur $\mathcal{E} = D_{\text{LS}}/D_{\text{OS}}$ dépend des redshifts de la lentille z_L et de la source z_S et des paramètres cosmologiques Ω_m et Ω_Λ . \mathcal{E} mesure l'efficacité d'une lentille sur une source, il ne dépend pas du paramètre de Hubble H_0 . En revanche, le cas le plus simple de lentille mince ne tient plus si plusieurs sur-densités apparaissent dans la ligne de visée à des redshifts divers. Dans ce cas, la solution suivra le formalisme davantage généraliste de Pyne & Birkinshaw (1996).

3.1.3 Modélisation des lentilles

Les équations fondamentales sont en général modélisées comme une transformation de formes d'un plan source (S) à un plan image (I). Dans le cas d'une seule lentille, le Hessien de cette transformation (aussi appelé la matrice de magnification) relie au premier ordre un *pixel* de la source du plan image ($d\vec{\theta}_I$) vers le plan source ($d\vec{\theta}_S$) de la façon suivante

$$\frac{d\vec{\theta}_S}{d\vec{\theta}_I} = \mathcal{A}^{-1} = \begin{pmatrix} 1 - \partial_{xx}\varphi & -\partial_{xy}\varphi \\ -\partial_{xy}\varphi & 1 - \partial_{yy}\varphi \end{pmatrix} = \begin{pmatrix} 1 - \partial_{rr}\varphi & -\partial_r(\frac{1}{r}\partial_\theta\varphi) \\ -\partial_r(\frac{1}{r}\partial_\theta\varphi) & 1 - \frac{1}{r}\partial_r\varphi - \frac{1}{r^2}\partial_{\theta\theta}\varphi \end{pmatrix}, \quad (3.7)$$

où les deux dernières expressions de l'équation donnent les composants en coordonnées cartésiennes puis polaires. Il s'agit de la matrice de magnification \mathcal{A}^{-1} également exprimées selon les paramètres $\kappa = \Delta\varphi/2 \equiv$ convergence, et $\vec{\gamma} = (\gamma_1, \gamma_2) = \gamma_1 + i\gamma_2 \equiv$ cisaillement,

$$\mathcal{A}^{-1} = \begin{pmatrix} 1 - \kappa - \gamma_1 & -\gamma_2 \\ -\gamma_1 & 1 - \kappa + \gamma_1 \end{pmatrix} = (1 - \kappa) \left[\begin{pmatrix} 1 & 0 \\ 0 & 1 \end{pmatrix} + \frac{\gamma}{1 - \kappa} \begin{pmatrix} 1 & 0 \\ 0 & -1 \end{pmatrix} \right], \quad (3.8)$$

où κ et γ sont les normes. Le dernier terme de l'équation s'interprète comme suit, la déformation lentille se compose d'une composante isotrope $(1 - \kappa)$ et cisaillement réduit $\gamma/(1 - \kappa) \equiv g$ est anisotrope, dont l'orientation est définie par l'angle θ_{shear}

$$\tan 2\theta_{\text{shear}} = \frac{2\partial_{xy}\varphi}{\partial_{yy}\varphi - \partial_{xx}\varphi}. \quad (3.9)$$

3. La condition $\Phi \ll c^2$ permet de faire tous les traitements en formalisme newtonien sans perte de généralité

Les normes et les composantes sont données par

$$\gamma_1 = \frac{1}{2}(\partial_{xx}\varphi - \partial_{yy}\varphi) \quad (3.10)$$

$$\gamma_2 = \partial_{xy}\varphi \quad (3.11)$$

$$\gamma = \frac{1}{2}\sqrt{(\partial_{xx}\varphi - \partial_{yy}\varphi)^2 + (2\partial_{xy}\varphi)^2} \quad (3.12)$$

$$\kappa = \frac{\Sigma}{\Sigma_{\text{crit}}} \quad (3.13)$$

Σ_{crit} est la densité surfacique critique,

$$\Sigma_{\text{crit}} \simeq 1.62 \left(\frac{H_0}{70 \text{ km} \cdot \text{s}^{-1} \text{Mpc}^{-1}} \right) \left(\frac{D_{\text{OS}}}{D_{\text{LS}}} \right) \left(\frac{c/H_0}{D_{\text{OL}}} \right) \text{ kg} \cdot \text{m}^{-2}. \quad (3.14)$$

Dernier concept important pour analyse les modèles des lentilles, les lignes critiques et les caustiques. La magnification μ d'une lentille est définie en fonction de la convergence et du cisaillement :

$$\mu^{-1} = \det(\mathcal{A}^{-1}) = (1 - \kappa)^2 - \gamma^2 = (1 - \kappa)^2(1 - g^2). \quad (3.15)$$

On voit immédiatement que la magnification devient infinie quand un des deux termes de droite est nul ce qui définit deux lignes critiques fermées. Ces deux lignes critiques définies dans le plan image se transforment en deux lignes caustiques dans le plan source. Ce sont dans les zones proches de ces lignes critiques que les images auront une amplification suffisante pour être visible. La ligne critique extérieure amplifie tangentiellement et la ligne critique intérieure amplifie radialement.

La Figure 3.2, tirée de Kneib & Natarajan (2011), montre la phénoménologie d'une lentille simple isolée pour différentes configurations. Le plan source visible (cadre S) montre 10 positions de la source dénotées 1 à 10, relativement à la lentille (montrée au cadre I) dont les lignes caustiques sont montrées au cadre (S) et les lignes critiques aux cadres 1 à 10. La lentille est une galaxie isolée avec un profil de masse elliptique. Les arc images apparaissent toujours près des lignes critiques. Les configurations montrées les plus typiques sont aux cadres 3 et 4; des arcs radiaux, aux cadres 5 à 7; une configuration de pointe (*cusp* en jargon technique), au cadre 8; la fameuse croix d'Einstein, aux cadres 4, 9 et 10; une configuration de bascule (*fold* en jargon).

Les équations présentées dans cette section permettent de faire des modèles de densités projetées de lentilles, parfois très complexes, dont la finesse dépend directement de la résolution des données disponibles et dans une moindre mesure des mesures de redshifts des sources d'arrière-plan. Un exemple de modélisation fine est montrée à la figure 3.3. On voit un des 5 amas observés pour le Hubble Frontier Field Survey et modélisé par Jauzac et al. (2015).

La reconstitution de modèles de masse à partir d'observations est un problème inverse admettant une infinité de solution. En pratique, la modélisation est aujourd'hui effectuée avec des codes qui automatisent la recherche de modèles ajustés avec des hypothèses probables sur la forme des sources et des lentilles, réduisant la dimensionalité du problème. La plupart des codes proposent des méthodes bayésiennes s'appuyant sur une inférence de type chaîne de Markov aléatoire (Markov Chain Monte Carlo)⁴ dont la convergence est fixée par une règle de vraisemblance.

4. Une implémentation populaire en python par exemple <https://github.com/dfm/emcee> et documentation associée <https://emcee.readthedocs.io/en/stable/>

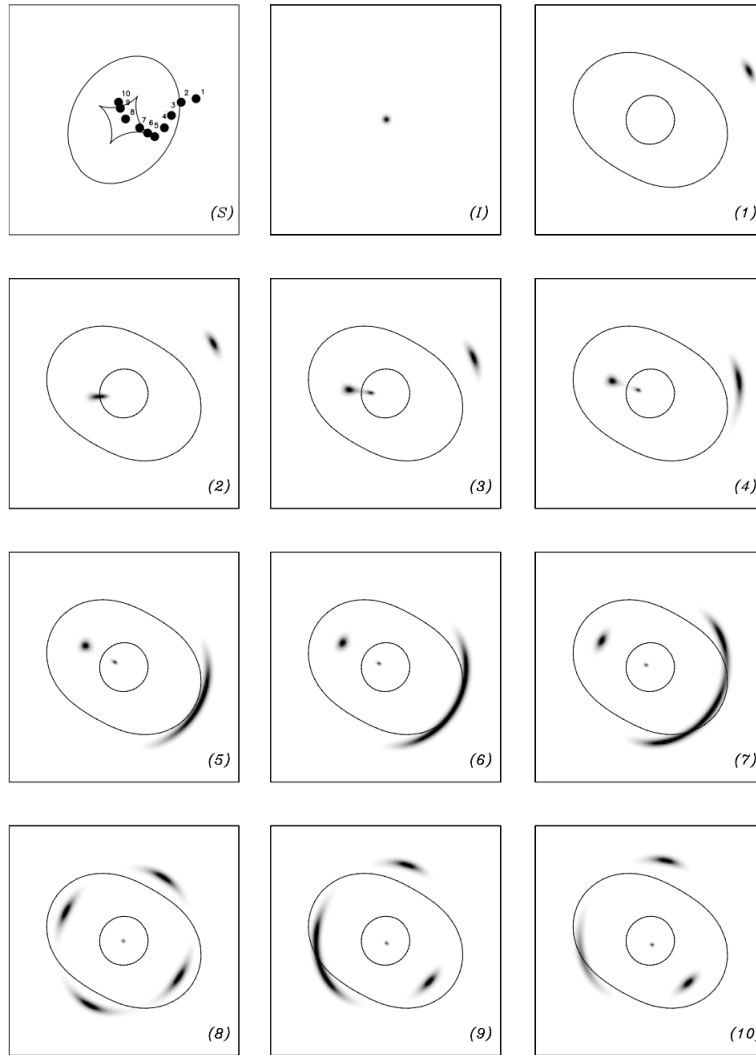


FIGURE 3.2 – Le plan source visible (cadre S) montre 10 positions de la source dénotées 1 à 10, relativement à la lentille (montrée au cadre I) dont les lignes caustiques sont montrées au cadre (S) et les lignes critiques aux cadres 1 à 10. La lentille est une galaxie isolée avec un profil de masse elliptique. Les arc images apparaissent toujours près des lignes critiques. Les configurations les plus typiques sont (3) ; arc radial, (5 à 7) cusp, (8) croix d'Einstein (4, 9 et 10) fold. Tiré de Kneib & Natarajan (2011)

Il existe aujourd'hui un grand nombre de codes publics de modélisation de lentilles gravitationnelles. Depuis la revue de Lefor et al. (2013), de nouveaux codes en Python, d'installation logicielle simple et de plus en plus automatisés ont été publiés, parmi les plus robustes, flexibles et maintenus :

- lenstronomy : <https://github.com/sibirrer/lenstronomy> (Birrer & Amara 2018)
- AutoLens : <https://pypi.org/project/autolens/> (Nightingale et al. 2018)
- LENSED : <https://glenco.github.io/lensed/> (Tessore et al. 2016)
- lenstool : <https://projets.lam.fr/projects/lenstool> (Kneib et al. 1996; Jullo et al. 2007; Jullo & Kneib 2009)
- gravlens : <http://www.physics.rutgers.edu/~keeton/gravlens/2012WS/> (Keeton 2001)

Ces codes permettent d'ajuster, d'optimiser des modèles de lentilles en fonction d'images données en entrée (géométrie des positions et flux des images pour lenstool et gravlens,

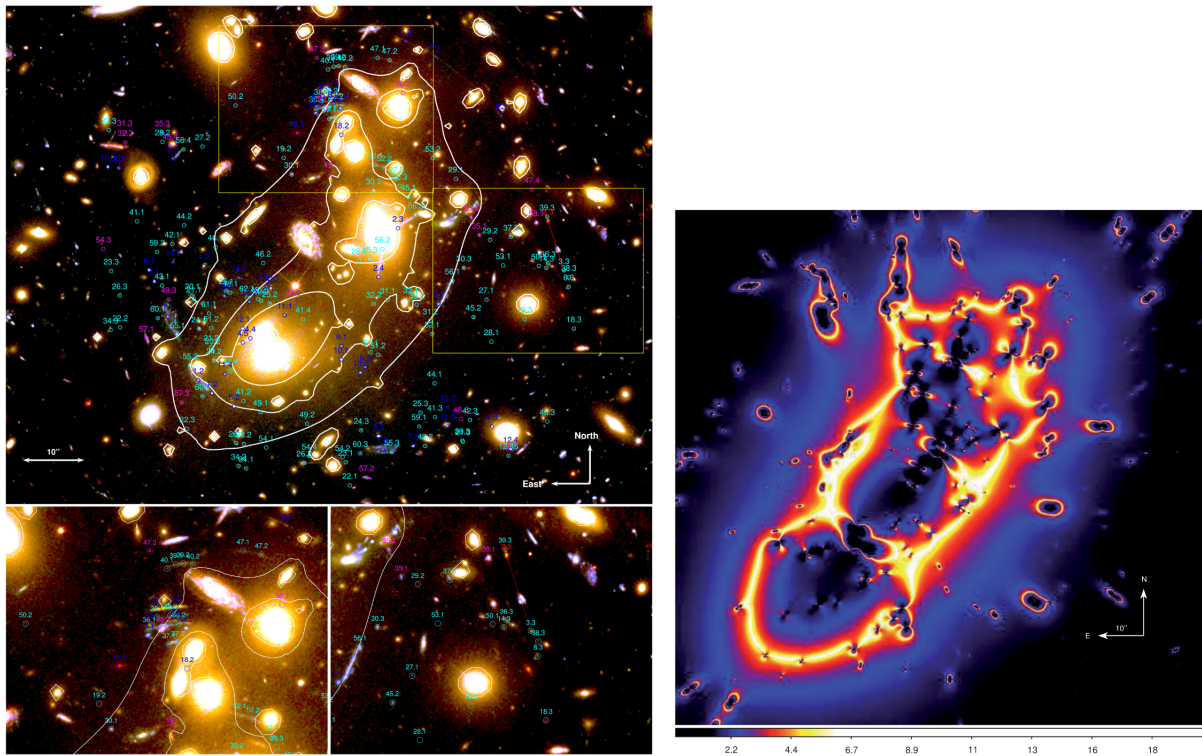


FIGURE 3.3 – (Gauche) Mosaique d’images du télescope spatial Hubble sur l’amas Abel 2744 en bandes $F814W$, $F606W$ et $F435W$. Des 180 images multiples des 61 sources d’arrière-plan, identifiées en cyan, bleu et magenta, 152 ont été utilisées pour établir un modèle de lentille. Les lignes blanches continues sont les contours du meilleur ajustement de la masse du modèle de lentille forte. (Droite) carte de magnification obtenue des contraintes des images de gauche pour une source à $z_S = 9$. Le nombre important de contraintes permet aux auteurs de dériver une masse totale par effet de lentille dans un rayon de 200 kpc à une précision 1% près, soit $M_{\text{lens}} = 2.162 \pm 0.005 \times 10^{14} M_{\odot}$. Tirés de Jauzac et al. (2015)

carte 2D de brillance de surface des images pour lenstronomy , AutoLens et LENSED) en utilisant des profils de densité paramétriques, ou des modèles non-paramétriques et fournissent en sortie le meilleur modèle de masse totale de la lentille, des cartes de magnification et de cisaillement et pour lenstronomy et AutoLens une tentative de reconstruction de la morphologie de la source d’arrière-plan à partir des images.

3.1.4 Détection des lentilles

Les projets

Après les années pionnières de découvertes des premiers arcs gravitationnels (Soucaill et al. 1987) et le suivi systématique des amas massifs (Abell), la chasse aux lentilles était lancée. Jusqu’aux années 2000, les candidats lentilles fortes étaient majoritairement détectés de façon visuelle sur les images profondes d’objets extragalactiques, souvent par hasard (e.g. CASTLE⁵ Kochanek et al. 1999 et Cabanac et al. 2005), avec l’exception des quasars multiples dont la typologie permettait d’effectuer des recherches systématiques mais simples dans les catalogues, comme le sondage Cosmic Lens All-Sky Survey⁶ (Myers et al. 2003). Mais les découvertes restaient très en deçà des prédictions statistiques qui

5. <https://www.cfa.harvard.edu/castles/>

6. <http://www.aoc.nrao.edu/smyers/class.html>

donnaient à penser que des milliers de lentilles à toutes les échelles attendaient d'être découvertes (Oguri 2006).

La possibilité de détecter des groupes de galaxies lentilles est, pour ainsi dire, née avec le développement des détecteurs CCD grand champs en astronomie dans les années 1990, permettant de paver le ciel très efficacement dans des bandes photométriques à des sensibilités inconnues jusque là. Le deuxième facteur limitant du domaine des lentilles étant la résolution, il a fallu de surcroît attendre le développement de ces imageurs grand-champ dans des sites d'exception comme le Mauna Kea sur l'île d'Hawaï, avec le Canada-France Hawaii Legacy Survey ⁷ (CFHTLS :) utilisant l'instrument MegaCam ⁸. Les grands sondages ont permis de faire un premier bond dans cette recherche avec les publications successives du Sloan Digital Sky Survey (SDSS ⁹ : Abazajian et al. 2009; Tago et al. 2010 et des sondages spectroscopiques (e.g. 2dFGRS, Colless et al. 2001, 6dFGRS, Jones et al. 2009).

Avant de donner une liste des projets de détection des lentilles gravitationnelles, nous pointons le lecteur sur la Master Lens Database ¹⁰ qui regroupe les efforts internationaux pour détecter les lentilles, à la fois sur des grands programmes et celles découvertes par hasard (Orphan Lens). Établir une liste exhaustive est difficile dans le contexte évolutif très rapide. L'arrivée prochaine de milliers de candidats avec les sondes spatiales (principalement Euclid) rendra cet exercice encore davantage ardu et peut-être vain désormais. Toujours est-il que la somme des efforts consentis sur la recherche des lentilles gravitationnelles fortes abouti à ca. 2500 lentilles, en ignorant les nombreux doublons d'un projet à l'autre, la plupart étant des lentilles galaxie-galaxie. C'est-à-dire, encore fort peu, si on considère la grande diversité des échelles et l'inhomogénéité des échantillons, pour pouvoir faire des études statistiques fines avec les échantillons existants. Cependant, les premières études incluant quelques dizaines de lentilles du même type, ont tout de même permis d'apporter des débuts de réponses sur les profils de masse totale et leur évolution entre les lentilles locales $z \leq 0.3$ et les lentilles à redshifts plus élevés $z \geq 0.5$. Ce sont les projets SLACS combiné au projet LSD et SL2S (voir Tableau 3.1) pour les lentilles galaxie-galaxie qui ont démontré que les galaxies lentilles ont des profils isothermes qui n'évoluent pas énormément entre $0 < z < 1$ (voir la revue de Treu 2010). Pour les groupes de galaxies, le seul sondage permettant une détection de quelques dizaines de groupes homogènes est le CFHTLS avec le SL2S, dont la section suivante donne les résultats les plus saillants.

7. <https://www.cfht.hawaii.edu/Science/CFHTLS/cfhtlsfinalreleaseexecsummary.html>

8. <https://www.cfht.hawaii.edu/Instruments/Imaging/MegaPrime/>

9. <https://www.sdss.org>

10. <http://admin.masterlens.org/index.php>

TABLE 3.1 – Tableau des principaux catalogues de lentilles

Nom	Nombre	Masses [M_{\odot}]	Lien	Référence	Commentaires
BELLS	36	10^{11} - 10^{12}	-	Brownstein et al. (2012)	Sondage BOSS/SDSSIII : Détection spectroscopique à la SLACS, lentilles galaxies-galaxies entre $0.4 < z < 0.7$. Candidats confirmés par images HST
BELLS GALLERY	17	10^{11}	-	Shu et al. (2016)	BELLS GALaxy-Ly α Emitter sYstems : continuation de BELLS sur les galaxies Lyman Alpha du SDSS III.
CASSOWARY	53	10^{11} - 10^{15}	CASSOWARY	Stark et al. (2013)	Cambridge And Sloan Survey Of Wide ARcs in the skY : lentilles galaxies à amas massifs $z > 0.5$ dans le SDSS.
CASTLE	100	10^{11} - 10^{12}	CASTLE	Kochanek et al. (1999)	Lentilles galaxies-galaxies et QSO-galaxies détectées en optique dans le ciel entier par hasard.
CFHTLS-SL2S	170	10^{11} - 10^{15}	CFHTLS	Cabanac et al. (2007)	cf section 3.2
C82 LS	15	10^{12} - 10^{13}	-	cf. SPACEWARPS	Anupreeta More et Gabriel Caminha ont détecté des candidats lentilles dans les 170 deg ² du CS82 avec MegaCam au CFHT
CLASH	8	10^{14} - 10^{15}	CLASH	(Postman et al. 2012)	Cluster Lensing And Supernova survey with Hubble : lentilles amas.
CLASS	16	10^{11} - 10^{12}	CLASS	(Myers et al. 2003)	Cosmic Lens All-Sky Survey : Sources radio à spectre plat. 16 000 objets ciblés, 30 sec chaque, puis filtrés avec des observations haute résolution Merlin and VLBI pour sélectionner les lentilles (VLA et Jodrell Bank).
COSMOS	18	10^{11} - 10^{12}	COSMOS	Faure et al. (2008)	Le sondage COSMOS fait 2 deg ² avec HST/ACS, multi longueur d'onde. Lentilles galaxies-galaxies.
DES	~ 500	10^{12} - 10^{13}	DES	Jacobs et al. (2019)	Dark Energy survey : sondage du ciel de l'hémisphère Sud 5000 deg ² .

continuation sur la page suivante ...

... continuation de la page précédente

Nom	Nombre	Masses [M_{\odot}]	Lien	Référence	Commentaires
DLS	~ 10	10^{13}	DLS	Kubo (2007)	Deep Lens Survey : couvre 20 deg ² en imagerie <i>BVRz</i> . Un seeing moyen $\simeq 1''$ en limite la sensibilité. Détecte des groupes massifs.
EELs	1-5	10^{12}	-	Auger et al. (2011)	Early-type Early-type Lenses : sondage spectroscopique à la SLACS et BELLS mais dont la source a un spectre elliptique. Sous-échantillon du SLACS.
EGS	10	10^{12}	AEGIS	Marshall et al. (2009)	Extended Groth Strip / DEEP2 Survey : sondage HST WFPC2 et ACS avec suivi spectroscopique Keck DEIMOS. lentilles galaxie-galaxie.
GLQ-GAIA	22	10^{11} - 10^{12}	GLQ	Lemon et al. (2019)	Gravitationally lensed quasars in Gaia : ciel entier, recherche de QSO multiples dans l'échantillon astrométrique ; combiné avec PanSTARRS et WISE.
GEMS	10	10^{11} - 10^{12}	GEMS	More et al. (2011)	Galaxy Evolution from Morphology and SEDs : recherche systématique dans l'Extended Chandra Deep Field South (ECDFS), avec images couleurs de HST ACS GEMS avec $z < 1.1$
H-ATLAS	80	10^{11} - 10^{12}	H-ATLAS	Negrello et al. (2017)	Herschel Astrophysical Terahertz Large Area Survey : sondage submillimétrique de 600deg ² . détection de galaxies lentilles sur critère de luminosité à 500 μm .
HE survey	7	10^{11} - 10^{12}	Hamburg-ESO	Wisotzki et al. (1996)	Hamburg-ESO survey : lentilles QSO brillantes $mag_B < 17.5$. spectroscopie avec prisme objectif. 1000deg ² .
HERMES Lens	9	10^{11} - 10^{12}	HERMES	Wardlow et al. (2012)	Herschel Multi-tiered Extragalactic Survey 95deg ² du sondage submillimétrique dont les lentilles sont détectés par les sources brillantes, et lentilles par suivi HST et spectroscopique à l'IRAM.

continuation sur la page suivante ...

... continuation de la page précédente

Nom	Nombre	Masses [M_{\odot}]	Lien	Référence	Commentaires
HOLISMOKES	330	10^{12} et +	PanSTARRS	Canameras et al. (2020)	Recherche sur $30\,000\text{deg}^2$ du Panoramic Survey Telescope And Rapid Response Système avec préselection par réseau de neurones CNN et sélection visuelle. lentilles dominées par des candidats galaxie-galaxies ($0.1 < z < 0.7$).
JVAS	5	10^{11} - 10^{12}	JVAS	King et al. (2002)	Jodrell/VLA Astrometric Survey : sondage précurseur de CLASS.
LinKS	89	10^{11} - 10^{14}	KIDS	Petrillo et al. (2019)	Lens in Kilo-Degree Survey ; sondage dans les bandes <i>griz</i> de 1000deg^2 . Lentilles découvertes par réseau neuronal (CNN).
MACS-Lens	16	10^{14} - 10^{15}	MACS	Ebeling et al. (2001)	Massive Cluster Survey : sondage d'amas détectés en X.
OLS	5	10^{11} - 10^{12}	-	Willis et al. (2006)	Optimal Line-of-Sight Lens Survey : sondage à la SLACS sur des candidats SDSS.
RCS2 SL	60	10^{11} - 10^{14}	-	Anguita et al. (2012)	Red-Sequence Cluster Survey 2 : sondage en imagerie bande <i>ugriz</i> de 820deg^2 . Lentille galaxie-galaxie et galaxie-groupe
SBAS	10	10^{13} - 10^{14}	-	Wiesner et al. (2012)	Sloan Bright Arcs Survey : recherche systématique d'arcs brillants parmi des elliptiques et amas du SDSS. Sources à $z = 0.4$ -2.9.
SGAS	32	10^{13} - 10^{15}	-	Bayliss et al. (2011)	Sloan Giant Arc Survey : assez proche de SBAS. Suivis nombreux en spectroscopie.
SLACS	50	10^{11} - 10^{12}	SLACS	Bolton et al. (2006)	Sloan Lens ACS Survey. Sondage spectroscopique dans le Sloan, lentilles galaxie-galaxies apr construction $z < 1$, suivi HST.
SOGRAS	8	10^{14}	-	Furlanetto et al. (2013)	SOAR Gravitational Arc Survey : suivi spectroscopie de 47 amas massifs dans CS82.
SPACEWARPS	59	10^{11} - 10^{13}	SPACEWARPS	More et al. (2016)	Space Warps est un projet de science citoyenne combinant des images de CS82 et CFHT-LS sur 130deg^2 .

continuation sur la page suivante ...

... continuation de la page précédente

Nom	Nombre	Masses [M_{\odot}]	Lien	Référence	Commentaires
SPT	100	10^{11}	SPT	Rotermund et al. (2020)	South Pole Telescope : sondage submillimétrique de 87 deg^2 au pôle sud. Les sources surbrillantes sont des candidates lentilles ($0.1 < z < 1.4$).
SQLS	81	10^{13} - 10^{15}	SQLS	Inada et al. (2012)	Sloan Digital Sky Survey Quasar Lens Search : QSOs lentilles avec large séparation angulaire dans le SDSS
STRIDES	7	10^{11} - 10^{12}	STRIDES	Treu et al. (2018)	The STRong lensing Insights into the Dark Energy Survey : suivi de candidats lentilles dans DES.
SuGOHI	250-500	10^{12} - 10^{14}	-	Jaelani et al. (2020)	Survey of Gravitationally-lensed Objects in HSC Imaging : candidats groupes détectés visuellement. 1114 deg^2 .
SWELLS	24	10^{11}	-	Treu et al. (2011)	SDSS WFPC2 Edge-on Late-type Lens Survey : campagne de suivi de galaxies à disques vues de côté dans le SDSS, à la SLACS.
UKIDSS	6	10^{11} - 10^{12}	UKIDSS	Jackson et al. (2012)	UKIRT Infrared Deep Sky Survey : sondage de 7500 deg^2 en bandes JHK pour QSO lentilles

Les techniques de détection

Les techniques contemporaines de détection se tournent résolument vers des solutions semi-automatiques en préparation des grands relevés qui fourniront des centaines de milliers, voire des millions de candidats lentilles à filtrer. Ces solutions consistent à appliquer des méthodes de filtrage des images à analyser avec des algorithmes permettant de réduire la dimensionalité du problème et d'extraire un échantillon aussi complet que possible, mais dont la pureté est de quelques pourcents, puis de visualiser l'échantillon considéré, via, pourquoi pas, un projet de type science citoyenne (Citizen Science, e.g. www.spacewarps.org). Les derniers travaux collaboratifs sur les meilleurs algorithmes de filtrage, dont le papier Metcalf et al. (2019) reproduit ci-dessous, pointent systématiquement vers les méthodes d'apprentissage profonds, que ce soient des réseaux de neurones convolutifs, des analyses PCA ou des méthodes vectorielles SVM (Hartley et al. 2017). Soulignons que le tendon d'Achille des réseaux de neurones convolutifs réside dans la supervision des modèles par un ensemble massif de données. D'une part, l'étiquetage de dizaines de milliers de lentilles est impraticable et d'autre part, la fabrication de simulations fussent-elles les plus réalistes possibles, biaisera forcément la détection des candidats, empêchant même la découverte de candidats lentilles rares, donc non présents dans l'échantillon simulé. Il est probable que les réseaux de neurones non-supervisés de type auto-encodeur seront de plus en plus utilisés pour la classification de données réelles (Cheng et al. 2020) car ils permettent d'éviter un étiquetage initial.

The Strong Gravitational Lens Finding Challenge

R. Benton Metcalf^{1,2*}, M. Meneghetti², Camille Avestruz^{3,4,5,**}, Fabio Bellagamba^{1,2}, Clécio R. Bom^{6,7}, Emmanuel Bertin⁸, Rémi Cabanac⁹, F. Courbin¹², Andrew Davies²², Etienne Decencière¹⁰, Rémi Flamary¹¹, Raphael Gavazzi⁸, Mario Geiger¹², Philippa Hartley¹³, Marc Huertas-Company¹⁴, Neal Jackson¹³, Colin Jacobs²³, Eric Jullo¹⁵, Jean-Paul Kneib¹², Léon V. E. Koopmans¹⁶, François Lanusse¹⁷, Chun-Liang Li¹⁸, Quanbin Ma¹⁸, Martin Makler⁷, Nan Li¹⁹, Matthew Lightman¹⁵, Carlo Enrico Petrillo¹⁶, Stephen Serjeant²², Christoph Schäfer¹², Alessandro Sonnenfeld²¹, Amit Tagore¹³, Crescenzo Tortora¹⁶, Diego Tuccillo^{10,14}, Manuel B. Valentín⁷, Santiago Velasco-Forero¹⁰, Gijs A. Verdoes Kleijn¹⁶, and Georgios Vernardos¹⁶

¹ Dipartimento di Fisica & Astronomia, Università di Bologna, via Gobetti 93/2, 40129 Bologna, Italy

² INAF-Osservatorio Astronomico di Bologna, via Ranzani 1, 40127 Bologna, Italy

³ Enrico Fermi Institute, The University of Chicago, Chicago, IL 60637 U.S.A.

⁴ Kavli Institute for Cosmological Physics, The University of Chicago, Chicago, IL 60637 U.S.A.

⁵ Department of Astronomy & Astrophysics, The University of Chicago, Chicago, IL 60637 U.S.A.

⁶ Centro Federal de Educação Tecnológica Celso Suckow da Fonseca, CEP 23810-000, Itaguaí, RJ, Brazil

⁷ Centro Brasileiro de Pesquisas Físicas, CEP 22290-180, Rio de Janeiro, RJ, Brazil

⁸ Institut d'Astrophysique de Paris, Sorbonne Université, CNRS, UMR 7095, 98 bis bd Arago, 75014 Paris, France.

⁹ IRAP, Université de Toulouse, CNRS, UPS, Toulouse, France.

¹⁰ MINES Paristech, PSL Research University, Centre for Mathematical Morphology, 35 rue Saint-Honore, Fontainebleau, France

¹¹ Laboratoire Lagrange, Université de Nice Sophia-Antipolis, Centre National de la Recherche Scientifique,

¹² Institute of Physics, Laboratory of Astrophysics, Ecole Polytechnique Fédérale de Lausanne (EPFL), Observatoire de Sauverny, 1290 Versoix, Switzerland

¹³ Jodrell Bank Centre for Astrophysics, School of Physics & Astronomy, University of Manchester, Oxford Rd, Manchester M13 9PL, UK Observatoire de la Côte d'Azur, Parc Valrose, 06108 Nice, France

¹⁴ LERMA, Observatoire de Paris, CNRS, Université Paris Diderot, 61, Avenue de l'Observatoire F-75014, Paris, France

¹⁵ Aix Marseille Université, CNRS, LAM (Laboratoire d'Astrophysique de Marseille) UMR 7326, 13388, Marseille, France

¹⁶ Kapteyn Astronomical Institute, University of Groningen, Postbus 800, 9700 AV, Groningen, The Netherlands

¹⁷ McWilliams Center for Cosmology, Department of Physics, Carnegie Mellon University, Pittsburgh, PA 15213, USA

¹⁸ School of Computer Science, Carnegie Mellon University, Pittsburgh, PA 15213, USA

¹⁹ School of Physics and Astronomy, Nottingham University, University Park, Nottingham, NG7 2RD, UK

²⁰ JPMorgan Chase, Chicago, IL 60603 U.S.A.

²¹ Kavli IPMU (WPI), UTIAS, The University of Tokyo, Kashiwa, Chiba 277-8583, Japan

²² School of Physical Sciences, The Open University, Walton Hall, Milton Keynes, MK7 6AA, UK

²³ Centre for Astrophysics and Supercomputing, Swinburne University of Technology, P.O. Box 218, Hawthorn, VIC 3122, Australia

March 21, 2019

ABSTRACT

Large-scale imaging surveys will increase the number of galaxy-scale strong lensing candidates by maybe three orders of magnitudes beyond the number known today. Finding these rare objects will require picking them out of at least tens of millions of images, and deriving scientific results from them will require quantifying the efficiency and bias of any search method. To achieve these objectives automated methods must be developed. Because gravitational lenses are rare objects, reducing false positives will be particularly important. We present a description and results of an open gravitational lens finding challenge. Participants were asked to classify 100,000 candidate objects as to whether they were gravitational lenses or not with the goal of developing better automated methods for finding lenses in large data sets. A variety of methods were used including visual inspection, arc and ring finders, support vector machines (SVM) and convolutional neural networks (CNN). We find that many of the methods will be easily fast enough to analyse the anticipated data flow. In test data, several methods are able to identify upwards of half the lenses after applying some thresholds on the lens characteristics such as lensed image brightness, size or contrast with the lens galaxy without making a single false-positive identification. This is significantly better than direct inspection by humans was able to do. Having multi-band, ground based data is found to be better for this purpose than single-band space based data with lower noise and higher resolution, suggesting that multi colour data is crucial. Multi-band space based data will be superior to ground based data. The most difficult challenge for a lens finder is differentiating between rare, irregular and ring-like face-on galaxies and true gravitational lenses. The degree to which the efficiency and biases of lens finders can be quantified largely depends on the realism of the simulated data on which the finders are trained.

1. Introduction

Strong gravitational lenses are rare cases in which a distant galaxy or quasar is aligned so closely with a foreground galaxy or cluster of galaxies that the gravitational field of the foreground object creates multiple, highly distorted images of the background object. The first strong lens was discovered in 1979 by Walsh et al. (1979) and since then several hundred of them have been found. When the lens is an individual galaxy and the source a quasar, there are two, four or five distinct images of the source. The time-delay between images, the magnification ratios between images and the image positions can all be used to model the mass distribution of the lens and measure cosmological parameters. When the lens is a cluster of galaxies the images of background galaxies are multiplied and distorted into many thin arcs. When the lens is an individual galaxy and the background source also a galaxy, the lensed images can take the form of a partial or complete ring seen around or through the lens galaxy, an *Einstein ring*.

Strong lenses have to date provided very valuable scientific information. They have been used to study how dark matter is distributed in galaxies and clusters (e.g. Kochanek 1991; Cohn et al. 2001; Koopmans & Treu 2002; Rusin et al. 2003; Koopmans & Treu 2003; Wayth et al. 2005; Dye & Warren 2005; Vegetti & Koopmans 2009; Tessore et al. 2016) and to measure the Hubble constant and other cosmological parameters (e.g. Refsdal 1964; Blandford & Narayan 1992; Witt et al. 2000; Suyu et al. 2013; Treu & Marshall 2016). Their magnification has been used as a natural telescope to observe otherwise undetectable objects at high redshift (e.g. Marshall et al. 2007; Bellagamba et al. 2017; Shu et al. 2016). They have put limits on the self interaction of dark matter and on the theory of gravitation (Markevitch et al. 2004). Through microlensing they have been used to study the structure of quasars (Morgan et al. 2008; Poindexter et al. 2008; Blackburne et al. 2011). To expand on this wealth of information we must study more lenses. The first step in doing this is to find more of these rare objects.

So far, less than a thousand lenses have been found in total across many heterogeneous data sets. The Square Kilometer Array (SKA)¹, the Large Synoptic Survey Telescope (LSST)² and the Euclid space telescope³ are expected to increase the number of potential lenses by orders of magnitude (Oguri & Marshall 2010; Collett 2015; SLWhitePaper 2017; McKean et al. 2015). For example it is estimated that there will be approximately 200,000 observable galaxy-galaxy lenses in the Euclid data set among tens of billions of potential objects. These surveys will bring a new era for strong lensing where large relatively well defined samples of lenses will be possible. It will also require handling much larger quantities of data than has been customary in this field.

Up to this point, the most widely used method for finding lenses in imaging surveys has been by visual inspection of candidates that have been selected on the basis of luminosity and/or colour. This has been done in the radio (Browne et al. 2003) and in the visible with space and

ground based data (Jackson 2008; Faure et al. 2008; Sygnet et al. 2010; Pawase et al. 2014). A related method pioneered by the SPACE WARPS project (Marshall et al. 2016; More et al. 2016; Geach et al. 2015) has been to crowd source the visual inspection through an online platform. These efforts have proved very fruitful, but they deal with orders of magnitude fewer candidates and lenses than will be necessary in the future. Dealing with such large quantities of data will not be practical for any visual inspection approach. In addition, the efficiency and detection bias of human inspection methods are difficult to rigorously quantify.

Spectroscopic searches for galaxy scale lenses have also been done by looking for high redshift stellar lines in the spectra of lower redshift large galaxies. Notably this was done in the Sloan Lens ACS (SLACS) survey, producing a relatively well defined and pure sample of Einstein ring lenses (Willis et al. 2006; Bolton et al. 2006; Brownstein et al. 2012; Smith et al. 2015). New spectrographs such as the Dark Energy Spectroscopic Instrument (DESI) (DESI Collaboration et al. 2016) and Subaru Prime Focus Spectrograph (PFS) (Tamura et al. 2016) have the potential to greatly expand spectroscopic lens searches. However, spectroscopy is telescope-time consuming and for the foreseeable future we are not likely to have spectroscopic surveys that cover anywhere near the number of objects as the planned imaging surveys.

Some automated algorithms have been developed in the past to detect lenses by their morphology in images. These have been designed to detect arc-like features (Alard 2006; Seidel & Bartelmann 2007; Bom et al. 2017) and rings (Gavazzi et al. 2014; Joseph et al. 2014). They have been applied to survey data and found of order 200 lenses (Cabanac et al. 2007; More et al. 2012; Paraficz et al. 2016).

Marshall et al. (2009) pioneered an automated technique for finding Einstein ring type lenses that uses a lens modelling code to fit a model to all candidates and picks out the ones that fit the model well (see also Sonnenfeld et al. 2017). This approach has the attractive feature that it distinguishes lenses from non-lenses by their similarity to what we expect a lens to look like and priors can be put on the model parameters that are physically motivated, unlike the next category of finders below. Challenges arise in making the modelling fast and automatic enough to handle large data sets while allowing it to be flexible enough to find unusual lens configurations. The YattaLens entrant to this challenge was of this type.

More recently, machine learning techniques that have become widely used in the fields of computer image processing and artificial intelligence have been applied to this and other problems in astronomy; in particular, artificial neural networks (ANNs), support vector machines (SVM), and logistic regression. SVMs and some logistic regression methods belong to the family of reproducing kernel Hilbert Space methods. They learn from a training set how to classify objects using features given by predefined kernel functions. ANNs, and a popular variant convolutional neural networks (CNNs), are even more flexible in learning directly from a training set which features are the most important for distinguishing categories of objects. These have been used widely for such tasks as handwriting and facial recognition. In astronomy, these families of algorithms are beginning to be used for categorising galaxy morphologies (Dieleman et al. 2015), photometric redshifts (Cavuoti et al. 2017; Sadeh et al. 2016; Samui & Samui Pal 2017), super-

* E-mail: robertbenton.metcalf@unibo.it

** Provost's Postdoctoral Scholar at the University of Chicago

¹ <http://skatelescope.org/>

² <https://www.lsst.org/>

³ <https://www.euclid-ec.org/>

nova classification (Lochner et al. 2016) and the lens finding problem (Petrillo et al. 2017; Jacobs et al. 2017; Ostrovski et al. 2017; Bom et al. 2017; Hartley et al. 2017).

Given the future of this field, with large amounts of data coming soon and many new ideas emerging, it is timely to stage a series of challenges to stimulate new work, determine what can realistically be done in lens finding and get a better idea of the strengths and weaknesses of different methods. The long term goal is to get a set of algorithms that can handle Euclid, LSST or SKA data sets and produce high purity and high completeness lens samples with well defined efficiency or selection. We anticipate further challenges in the future in which the realism of the data simulations will become progressively better. Here we have chosen to concentrate on galaxy/small group scale lenses where the background source is a galaxy because we feel that this is where the most progress can be made and the scientific return is the highest, but QSO lens and cluster/group lens challenges may follow.

The paper is organised as follows. The form of the challenge and its rules are described in the next section. The methods used to simulate mock images of galaxies and gravitational lenses are described in Section 3. In Section 4, each of the methods that were used to solve the challenge are briefly described. We discuss the metrics used to evaluate entries in Section 5.1. The performance of each of the methods is presented in Section 5.2. Finally, in Section 6, we conclude with a discussion of what was learned and how methods can be improved in the future.

2. The Challenge

The challenge was in fact two separate challenges that could be entered independently. One was designed to mimic a single band of a future imaging data set from a satellite survey such as Euclid. The other was designed to mimic ground based data with multiple bands, roughly modeled on the Kilo-Degree Survey (KiDS)⁴ (de Jong et al. 2013). In neither case were the simulated images meant to precisely mock these surveys, but the surveys were used as guides to set noise levels, pixel sizes, sensitivities, and other parameters.

In each case, a training set of 20,000 images in each band was provided for download at any time along with a key giving some properties of the object including whether it was a gravitational lens. Each image was 101×101 pixels. These specifications were not of particular significance except that the image size would encompass almost all galaxy-galaxy lenses and that the number of images (including ones with and without noise, lens and source which were needed for later analysis) was not too large. The participants were free to download these sets and train their algorithms on them. To enter the contest, the participants needed to register with a team name at which point they would be given a unique key and the address of a test data set. These data sets contained 100,000 candidates. In the case of the multi-band ground-based set this was 400,000 images. The participants had 48 hours to upload a classification of all candidates consisting of a score between 0 and 1, 0 signifying the lowest confidence that it is a lens and 1 signifying the highest. This ranking could have been a simple binary (0 or 1) classification or it could have been a continuous range

of numbers representing the probability of being a lens or it could have been a finite number of confidence levels. The challenge was opened on November 25, 2016 and closed on February 5, 2017.

3. The simulations

Creating the mock images started with a cosmological N-body simulation, in this case the Millennium simulation (Boylan-Kolchin et al. 2009). A catalogue of dark matter halos and galaxies within a light-cone was constructed within the Millennium Observatory project (Overzier et al. 2013). The challenge sets were based on a 1.6 sq.deg. light cone extending out to redshift $z = 6$ using all the simulation snapshots. The halos were found with a friends-of-friends algorithm and characterised by a total mass, size and half mass radius. They included subhalos of larger halos. The halos were populated with galaxies based on their merger history using the semi-analytic model (SAM) of Guo et al. (2011).

The halo catalogue was read into the GLAMER lensing code (Metcalf & Petkova 2014; Petkova et al. 2014) to do all the ray-tracing. Within this code a Navarro, Frenk & White (NFW) (Navarro et al. 1996) profile is fit to the three parameters given above to represent the dark matter component of the lens. The halos are projected onto a series of 20 lens planes and the deflection angle at any point on each plane are calculated by summing the effects of all the halos with a hybrid tree method. In this way the halos have the mass, concentration and clustering properties from the N-body simulation, but within each strong lens the mass resolution is not limited by the original simulation, but follows the analytic mass profile. An additional mass component that will be discussed later is added to each halo to represent the stellar mass.

With GLAMER we identify and map out all the caustics within the light-cone for 33 source planes – $z=1$ to 3 in intervals of 0.1 and 3 to 6 in intervals of 0.25. We take every caustic that corresponded to a critical curve with an Einstein radius larger than 1.5 times the resolution of the final images. The Einstein radius is estimated here and in all that follows as $R_{\text{ein}} = \sqrt{A_{\text{ein}}/\pi}$ where A_{ein} is the angular area within the critical curve.

In the light cone there are many thousands of caustics for the higher source redshifts. These lenses could be used as is, but we wanted to produce a much larger number with more randomness. For each caustic we identify the lens plane with the highest convergence and identify all the halos within a three dimensional distance of 0.5 Mpc from the centre of the critical curve and on this and its neighbouring lens planes. This collection of halos is then used as the lens and rotated to produce more random lenses. It contains all the sub-halos and nearby companion halos, but not the large scale structure surrounding it.

To model the background objects that are lensed we use sources from the Hubble Ultra Deep Field (UDF) that have been decomposed into shapelet functions to remove noise. This is the same set of images as used in Meneghetti et al. (2008, 2010) (see also Plazas et al. 2019). There are 9,350 such sources with redshifts and separate shapelet coefficients in 4 bands.

To construct a mock lens, first a caustic on the highest redshift source plane is selected. This is done in order of Einstein area, but all the critical curves are used more than

⁴ <http://kids.strw.leidenuniv.nl/>

once. Since every lens with a caustic at a lower redshift will have a caustic at the highest redshift this is a selection from all of the caustics in the light-cone. The lens is extracted as explained above and rotated randomly in three dimensions. A source is selected at random from the shapelet catalogue subject to a magnitude limit in a reference band. The redshift of the UDF source is used as the source redshift. If the source is at a lower redshift than the lens or within $\Delta z = 0.4$ another random source is selected.

The furthest point in the caustic is found from its own centre and the source is placed randomly within 3 times this distance. This is a somewhat arbitrary length designed to be a compromise between producing only very clear strong lenses, because all the sources are right in the centre of the caustic, and making the process inefficient because most of the sources are too far away from the caustic to produce clear lenses. If the source positions were taken completely at random the fraction of clear lenses would be very low.

The visible galaxies associated with the lens must also be simulated. There are too few bright galaxies in the UDF catalogue to make enough mock lens galaxies for this purpose. Instead, for most of the lenses, we used an analytic model for the surface brightness of these galaxies. The Millennium Observatory provides parameters for the galaxies that inhabit the dark matter halos using the semi-analytic galaxy formation models of Guo et al. (2011). The parameters used here were the total magnitude, the bulge-to-disc ratio, the disc scale height and the bulge effective radius. The magnitude and bulge-to-disc ratio are a function of the pass band. Each galaxy is given a random orientation and inclination angle between 0 and 80°. The disc is exponential with no vertical height which is why the inclination is limited to 80°. The bulge is represented by an elliptical Sérsic profile with an axis ratio randomly sampled between 0.5 and 1. The Sérsic index, n_s , is given by

$$\log(n_s) = 0.4 \log \left[\max \left(\frac{B}{T}, 0.03 \right) \right] + 0.1x \quad (1)$$

where $\frac{B}{T}$ is the bulge to total flux ratio and x is a uniform random number between -1 and 1. This very approximately reproduces the observed correlation between these quantities (Graham 2001).

In addition to the basic disc and bulge models we introduce some spiral arms. The surface brightness of the discs are given by

$$S(\theta, r) = e^{-r/R_h} [1 + A \cos(N_a \theta + \phi_r)] , \quad (2)$$

$$\phi_r = \alpha \log(2r/R_h) + \phi_d$$

where R_h is the scale height of the disc. The phase angle of the arms, ϕ_d , is chosen at random. The parameters A , α and N_a are chosen from distributions that are judged by eye to produce realistic galaxies. The bulge is also perturbed from a perfect Sérsic profile by multiplying the surface brightness by

$$1 + \sum_{n=1}^6 a_n \cos(n\theta + \phi_n) \quad (3)$$

where ϕ_n is a random phase. The coefficients are picked randomly from between -0.002 and 0.002.

These foreground galaxies are rotated in three dimensions with the halos of the lens each time a random lens is produced so that they remain in the same positions relative

to the mass. All the random parameters are also reassigned with every realisation of the lens.

These images of the foreground galaxies are not intended to reproduce the true population of galaxies, but only to be sufficiently irregular to make them difficult to fit to a simple analytic model that might make them unrealistically easy to distinguish from a foreground plus a lensed image. As will be discussed later, more realistic models will be needed in the future and are a subject of current investigation.

To represent the mass of the galaxies we make a gridded map of the surface brightness at 3 times the resolution of the final image. The surface brightness map is converted into a mass map within GLAMER by assuming a uniform mass-to-light ratio of 1.5 times solar in the reference band. These mass maps are added to the NFW dark matter halos discussed before to make the total lens mass distribution. The deflections caused by the mass maps are calculated by Fast Fourier Transform (FFT) and added to the halos' deflections for the ray tracing.

The code is able to produce any combination of foreground galaxies, lensed image and noise that is desired. For the training set, an image of the total lens with noise, an image of the foreground galaxies with noise and image of the lensed background source without noise were provided. For the test sets only the final images were provided to participants although all the information was stored for analysing the challenge entries.

3.1. Space-based

The space-based datasets were meant to roughly mimic the data quality which is expected from observations by the Euclid telescope in the visible channel. To this end, the pixel size was set to 0.1 arcsec and a Gaussian PSF was applied with a FWHM of 0.18 arcsec. The Gaussian PSF is clearly a simplified model, but a realistic treatment of the PSF is outside the scope of this paper. The reference band for background and foreground galaxies was SDSS i , which is overlapping with the broader Euclid VIS band. The realisation of the mock images followed the same procedure described in Grazian et al. (2004) and Meneghetti et al. (2008). As a result, the noise follows a Gaussian distribution with a realistic width and is uncorrelated between pixels. Characteristics of the instrument, filter and exposure times were taken from the Euclid Red Book (Laureijs et al. 2011).

In the challenge set the limiting magnitude for background sources was 28 in i . 60% of the cases had no background source and were thus labelled as non-lenses.

3.2. Ground-based

For the ground-based images four bands (SDSS u, g, r , and i) were simulated. The reference band was r . For the challenge set, 85% of the images were made with purely simulated images as outlined above and the other 15% used actual images taken from a preliminary sample of bright galaxies directly from the KiDS survey. Lensed source images were added to these real images at the same rate as for the mock images, in this case 50%. No attempt was made to match the halo masses to the observed galaxies in these cases. These real images were added for more realism and so that, by comparing the results for real and mock

images, we can evaluate how realistic our simulations are in this context. There were about 160,000 of these stamps from KiDS.

The KiDS survey provided a representative PSF map in each band that was applied to all mock images. The pixel size in this case was 0.2 arcsec. Weight maps for the KiDS images were also provided. Some of these had masked regions from removed stars, cosmic rays, and bad pixels. For the mock images the noise was simulated by adding normally distributed numbers with the variance given by the weight maps. The weight maps were also randomly rotated and flipped. This resulted in many of the images having large masked regions in them.

By chance one of the original KiDS images appears to have been a lens. When an additional lensed source was added this made a double lens or "jackpot" lens (Gavazzi et al. 2008).

4. Lens finding methods

There were 24 valid entries into the challenge which are listed in Table 1. There were a variety of different methods used and participants came from a variety of different backgrounds, most were professional astronomers, but there were also entries from researchers outside of the field.

The following sections contain short descriptions of the lens finding methods that were used in the challenge. Each sub-section refers to a team which gave a separate entry. We have grouped the methods into four categories according to the type of method used. The Receiver Operating Characteristic (ROC) curve and the area under this curve are referred to in these sections. The ROC is defined in Section 5.1 where methods for evaluating the entries is discussed. A reader unfamiliar with the ROC might want to refer to that section.

4.1. Visual inspection

4.1.1. Manchester1/Manchester2 (Jackson, Tagore)

All images (a total of 100000) were examined for each of the space- and ground-based datasets. This was done by two observers; AT (Amit Tagore) examined 30000 images in each case and NJ (Neal Jackson) examined 70000. Observation was carried out over a 48-hour period, at the rate of 5000/hr (NJ) and 2500/hr (AT). The overall results, in terms of area under the ROC (see Section 5.1) curves, were very similar for both observers. The space-based challenge produced areas of 0.800 and 0.812 for NJ and AT respectively, and the ground-based challenge yielded 0.891 and 0.884.

The Python scripts used for manual examination of multiple images are available on GitHub⁵ and are described in more detail in Hartley et al. (2017). For one-colour data such as the space-based training set, the images are individually colour-scaled using square-root scaling. The bright limit of the colour-scale is determined from the pixel values in a rectangle comprising the inner ninth of the image area, with the limit being chosen as the n th centile of the pixel values in this area. Values between $n = 95$ and $n = 98$ give optimum results, judging by experiments on the training set. The number of images in each grid was also optimised

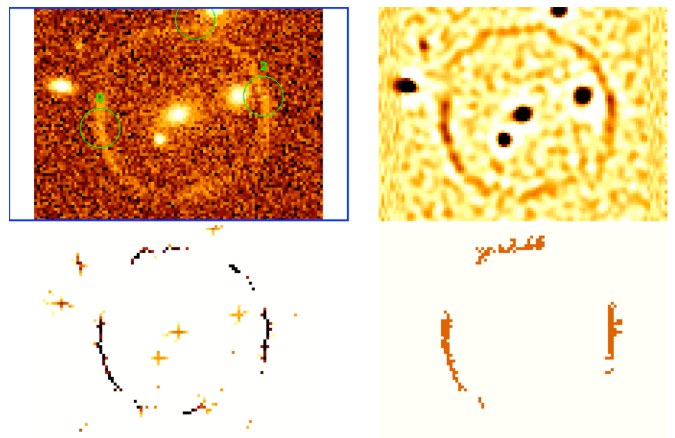


Fig. 1. (GAHEC IRAP) From top-left to bottom right, 1) a simulated arc extracted from the strong lensing challenge in which an tuned Arcfinder selects 3 candidates (green circles), 2) the smoothed image on which pixel wise elongation is computed, 3) the resulting elongated pixels after threshold, 4) the set of pixels selected for the computation of arc candidate properties.

using the training set, with 16×8 or 8×4 giving good results on one-colour data. For three-colour data, such as the ground-based challenge data, the individual bands for each object are colour-scaled and then combined into an RGB image. In this case 8×4 grids were used for examination, due to the generally lower resolution of the images. The script also allows the user to adjust the colour-scale in real time when examining and marking images, and records the image name corresponding to the image within which the cursor resides at the time any key is pressed, together with the key.

Images were classified by both observers into 5 categories, ranging from 0 (no evidence of any lensed objects in the image) to 4 (certain lenses). For both observers, the rate of false positives in the "certain" lenses was between 0.1% and 0.3%. The exception was the ground-based imaging for one observer, where a 4.6% rate resulted mainly from a single decision to allow a false-positive "double lens" which occurred repeatedly throughout the data at different orientations. The false-negative rate among the class-0 identifications was similar for both observers, at around 25% for the space-based images and 20% for the ground-based.

4.2. Arc-Finders

These methods seek to identify gravitationally lensed arcs and differentiate between them and other objects such as spiral arms and edge on spirals using their width, colour, curvature and other pre-selected criterion.

4.2.1. GAHEC IRAP (Cabanac)

Arcfinder (Alard 2006; Cabanac et al. 2007; More et al. 2012) illustrated in Figure 1, is a fast linear method that computes a pixel wise elongation parameter (ratio of first-order moments in a n -pix window oriented in proper reference frame) for all pixels of mexican-hat-smoothed FITS images. Arcfinder then extracts contiguous pixels above a given background and computes the candidate arc's length, width, area, radius of curvature and peak surface brightness. A final thresholding is set to maximize purity over

⁵ <https://github.com/nealjackson/bigeye>

Name	type	authors	section
1 AstrOmatic	Space-Based	Bertin	4.4.1
2 GAHEC IRAP	Space-Based	Cabanac	4.2.1
3 CAS Swinburne Melb	Ground-Based	Jacobs	4.4.8
4 ALL-star	Ground-Based	Avestruz, N. Li & Lightman	4.3.2
5 Manchester1	Space-Based	Jackson & Tagore	4.1.1
6 CMU-DeepLens-Resnet-Voting	Space-Based	Ma, Lanusse & C. Li	4.4.5
7 Manchester SVM	Ground-Based	Hartley & Flamary	4.3.1
8 CMU-DeepLens-Resnet	Space-Based	Francois Lanusse, Ma, C. Li & Ravanbakhsh	4.4.5
9 CMU-DeepLens-Resnet-Voting	Ground-Based	Ma, Lanusse & C. Li	4.4.5
10 YattaLensLite	Space-Based	Sonnenfeld	4.2.2
11 NeuralNet2	Space-Based	Davies & Serjeant	4.4.7
12 CAST	Ground-Based	Roque De Bom, Valentín & Makler	4.4.4
13 CMU-DeepLens-Resnet-ground3	Ground-Based	Lanusse, Ma, Ravanbakhsh & C. Li	4.4.5
14 GAMOCLASS	Space-Based	Huertas-Company, Tuccillo, Velasco-Forero & Decenci�ere	4.4.3
15 LASTRO EPFL (CNN)	Space-Based	Geiger, Sch�afer & Kneib	4.4.2
16 Manchester SVM	Space-Based	Hartley & Flamary	4.3.1
17 CMU-DeepLens-Resnet-aug	Space-Based	Ma, Lanusse, Ravanbakhsh & C. Li	4.4.5
18 LASTRO EPFL	Ground-Based	Geiger, Sch�afer & Kneib	4.4.2
19 CAST	Space-Based	Bom, Valentín & Makler	4.4.2
20 AstrOmatic	Ground-Based	Bertin	4.4.1
21 ALL-now	Space-Based	Avestruz, N. Li & Lightman	4.3.2
22 Manchester2	Ground-Based	Jackson & Tagore	4.1.1
23 YattaLensLite	Ground-Based	Sonnenfeld	4.2.2
24 Kapteyn Resnet	Space-Based	Petrillo, Tortora, Kleijn, Koopmans & Vernardos	4.4.6

Table 1. Entries to the challenges. Descriptions of the methods are in the sections listed on the right.

completeness on a few typical arcs of the dataset. For the current strong lensing challenge, arcfinder was tuned to detect long and narrow arcs, and was optimized on a subset of 1000 simulated images with a grid covering a range of elongation windows and arc areas. A python wrapper allows users to change parameters in a flexible way and run the arcfinder C code from the linux command line. Arcfinder took a couple of hours to run on the entire dataset with some overheads due to the dataset format. The code is publicly available at <https://github.com/rcabanac/arcfinder>.

4.2.2. YattaLens Lite (Sonnenfeld)

YattaLensLite is a simpler version of the algorithm YattaLens (Sonnenfeld et al. 2017), modified to meet the time constraints of the challenge. YattaLensLite subtracts a model surface brightness profile describing the lens galaxy from the g -band image, then runs SExtractor to detect tangentially elongated or ring-shaped objects, which are interpreted as lensed images. In the ground-based challenge, the model lens surface brightness profile is obtained by taking a rescaled version of the i -band image. The difference in colour between lens and source usually allows the lensed images to still be detectable after the lens subtraction process. However, in order to avoid subtracting off the lensed images in systems with similar colours between lens and source, we radially truncate the model lens surface brightness. The model lens light is truncated at the smallest radius between the position where the surface brightness is comparable to the sky background level, or the position of a positive radial gradient in surface brightness, if detected.

In the space-based challenge, it is not possible to separate lens and source based on colour, because only data in one band is provided. The lens light model then is produced by taking a centrally-inverted image and then using the

same truncation prescription used with ground-based data. The central inversion step is taken to reduce the chances of subtracting flux from lensed images, which are in general not centrally symmetric as opposed to typical lens galaxies.

In the full version of YattaLens, a lens modeling step is performed to improve the purity of the sample. However, such a procedure is too time consuming and was not performed in this challenge.

4.3. Machine Learning Methods that use pre-selected features

These are methods that classify the objects by making linear or nonlinear boundaries in a feature space. The features are properties of the image and are typically chosen by the user with a combination of knowledge, intuition, and trial-and-error. Using the training set, the optimal boundaries are found according to a criterion that depends on the method. The machine learns how to use the features best for distinguishing between lenses and non-lenses.

4.3.1. Manchester-SVM (Hartley, Flamary)

A Support Vector Machine (SVM) is a supervised machine learning method which uses labelled training data to determine a classification model (see e.g., Vapnik (1979), Cortes & Vapnik (1995) and Burges (1998)). A preprocessing stage first extracts a set of useful features from input samples, before projecting each sample as a vector into a high-, possibly infinite-dimensional space. The model then separates classes of data by maximising the margin between a defining hyperplane and a set of so-called support-vectors at the inner edge of each class. The process of classification is computationally inexpensive since the optimisation depends only on the dot products of the support vector subset. Feature extraction, however, requires both an extensive



Fig. 2. Example of our feature extraction procedure used to transform a ring. The image on the right shows the response of a set of Gabor filters after convolution with a polar transformed image of an Einstein ring. The strongest response is seen in the orientation perpendicular to the radial direction and at the frequency most closely matching that of the ring.

exploration of the feature space during the development of a model, and potentially intensive computer resources in order to transform the original samples. Our full method is described in detail in Hartley et al. (2017) and was developed using the Python *scikit-learn* and *scikit-image* packages (Pedregosa et al. 2011; van der Walt et al. 2014).

During our development of an SVM classifier for lens finding, feature extraction initially involved the decomposition of each image into a set of objects, using SExtractor (Bertin & Arnouts 1996) and GALFIT (Peng et al. 2002) to recover and subtract objects iteratively. This method had previously been used in a static algorithm approach which assigned points according to the morphological properties of each image (see Joseph et al. 2014). Lensed-like objects displaying, for example, greater ellipticity and tangential elongation were awarded more points. Since the SVM operates in a fixed dimensional space, properties of individual objects were collapsed into a fixed set describing the mean and variance of morphological properties of all the objects within an image. After training an SVM using these features we recorded a modest separation of lens and non-lens classes.

An alternative approach was to design a set of Gabor filters to be applied to each sample. The Gabor kernel is described by a sinusoidal function multiplied by a Gaussian envelope. We discard the imaginary part of the function to leave, in two-dimensional space:

$$G_c[i, j] = B e^{-\frac{(i^2 + j^2)}{2\sigma^2}} \cos\left[\frac{2\pi}{\lambda}(i \cos \theta + j \sin \theta)\right], \quad (4)$$

where harmonic wavelength λ , Gaussian spread σ and orientation θ define the operation performed on each point i, j in an image. Such a kernel is a popular image processing choice for edge detection and texture classification (e.g. Petkov & Kruizinga 1997; Feichtinger & Strohmer 1998) and is thought to mimic some image processing functions of the mammalian brain (Jones & Palmer 1987).

Our final feature extraction procedure first applied a polar transform to each image in order to exploit the edge detection of the Gabor filter, picking out tangential components typical of galaxy-galaxy lensing. Each image was then convolved with several Gabor filters of varying frequency and rotation (see Fig. 2). Stability selection methods were used to investigate the classification performance using different combinations of filters. The responses for each Gabor filter when applied to each image were measured by calculating statistical moments for each filtered image. These moments formed our final input data on which the SVM

could be trained and applied. We used brute-force optimisation methods to select a non-linear SVM containing radial basis function (RBF) kernel and tuned a small set of regularisation hyperparameters to achieve good generalisation performance. During training and testing, our final and best scores achieved when testing on the training data were an area under the ROC curve of 0.88 for the space set and 0.95 for the ground set. Classification was performed using a modest desktop PC.

4.3.2. ALL (Avestruz, Li, Lightman)

The ALL team methodology is detailed in Avestruz et al. (2017). The pipeline was originally developed to automatically classify strong lenses in mock HST and LSST data generated with code described in Li et al. (2016) and Collett (2015). We apply exactly the same steps for the single-band data for Euclid, but modify the feature extraction step for the four-band KIDS data. We summarize the steps below.

Tools from *Scikit-learn* (Pedregosa et al. 2012) are used and some minimal image preprocessing is performed. First, we replace masked pixels with the average of surrounding pixels, then enhance contrast in the image by taking the normalized log of pixel values. The next step consists of a feature extraction stage, where our feature vector is a *histogram of oriented gradients* (HOG) (Dalal & Triggs 2005) that quantifies edges in the image. HOG has three main parameters that determine the binning and resolution of edges captured by the features. The result is a one dimensional feature vector corresponding to the magnitude of oriented gradients across the image. With the KIDS data, we extract a feature vector for each of the four bands and concatenate the vectors to create a final feature vector for each object that we use to train a model classifier.

We use *Logistic Regression* (LR) to train a classifier model. LR requires a parameter search over the regression coefficient, C_{LogReg} . The parameters from both the feature extractor, HOG, and the linear classifier, LR, contain parameters that we optimize for peak model performance. We use *GridSearchCV* from *Scikit-learn* to select cross-validated parameters for HOG parameters and a subset of C_{LogReg} values with 20% of the test images provided. We then run a finer parameter search over C_{LogReg} , splitting the test images into 80% training and 20% test to avoid overfitting the data. We use the best parameters to then train the entire dataset for the final model classifier that we used to evaluate the competition data.

4.4. Convolutional Neural Networks

Since Convolutional Neural Networks (CNNs) are central to many of the methods that will be described later, here we provide a brief general description of them. A CNN (Fukushima 1980; Lecun et al. 1998) is a multi-layer feed-forward neural network model, which is particularly well-suited for processing natural images. With the very recent advances of the *Deep Learning* framework (LeCun et al. 2015), models based on CNN architectures have reached or even surpassed human accuracy in image classification tasks (He et al. 2015a).

The fundamental building block of a CNN is the *convolutional layer*. This element applies a set of convolution filters on an input image to produce a series of so-called *fea-*

ture maps. The coefficients of these filters are free parameters that are learned by the model. The notation $n \times n - n_c$ will signify a convolutional layer using filters of size $n \times n$ pixels and outputting n_c feature maps. In typical architectures, the size of these convolution filters is kept small (i.e. 3x3 or 5x5 pixels) to limit the complexity of the model.

Similarly to conventional fully-connected neural networks, convolution layers are typically followed by an element-wise activation function, which allows for the modelling of complex functional forms by introducing nonlinearities in the model. Classical choices for activation functions include the sigmoid-shaped logistic function (or just sigmoid) $f(x) = 1/(1 + \exp(-x))$ or the hyperbolic tangent function $f(x) = \tanh(x)$. However, much of the success of Deep Learning is due to the introduction of activation functions that do not saturate (become very close to one with very small derivatives), allowing for the efficient training of very deep architectures. The most common choice in modern deep learning models is the simple ReLU activation (for rectified linear unit) (Nair & Hinton 2010) defined as $f(x) = \max(x, 0)$. A closely related common alternative is the ELU activation (for Exponential Linear Unit) (Clevert et al. 2015) defined as

$$f(x) = \begin{cases} x & \text{if } x \geq 0 \\ e^x - 1, & \text{otherwise} \end{cases}, \quad (5)$$

which often leads to better results in practice.

Because the filters used in convolution layers are typically just a few pixels in size, to capture features on larger scales, CNNs rely on a multi-resolution approach by interleaving convolutional layers with *pooling layers*, which apply a downsampling operation to the feature maps. The most common downsampling schemes are the max-pooling and average pooling strategies, which downsample an input image by taking respectively the maximum or average values within a given region (e.g. 2x2 patches for a downsampling of factor 2).

A CNN architecture is therefore a stack of convolution layers and pooling layers, converting the input image into an increasing number of feature maps of progressively coarser resolution. The final feature maps can capture information on large scales and can reach a high-level of abstraction. To perform the classification itself from these feature maps, the CNN is typically topped by a fully-connected neural network outputting the class probability of the input image.

For a binary classification problem such as the one involved in strong lens detection, the training is performed by optimizing the weights of the model so that it minimizes the *binary cross-entropy* :

$$S = - \sum_{n=1}^N y[n] \log \hat{y}[n] + (1 - y[n]) \log(1 - \hat{y}[n]), \quad (6)$$

where N is the number of training instances, $y \in \{0, 1\}$ is the true class of the image and $\hat{y} \in [0, 1]$ is the class probability predicted by the model. This optimization is usually performed by a Stochastic Gradient Descent (SGD) algorithm or its variants (e.g. ADAM (Kingma & Ba 2014), Adagrad (Duchi et al. 2011), RMSprop (Tieleman & Hinton 2012), or accelerated gradients (Nesterov 1983)). SGD updates the model iteratively by taking small gradient steps over randomly selected subsamples of the training set (so called *mini-batches*). All the CNN-based methods presented

in this work rely on the ADAM optimisation algorithm, which also uses past gradients from previous iterations to adaptively estimate lower-order moments. Empirically it has been found that in many problems ADAM converges faster than SGD (Ruder 2016).

Neural networks often suffer from overfitting to the training set. A common way to mitigate this is to use a regularisation scheme. For example, the Dropout regularisation technique (Hinton et al. 2012; Srivastava et al. 2014a), were a certain percentage of the neurons and their connections are randomly dropped from the neural network. This regularisation techniques reduces overfitting by preventing complex co-adaptations of neurons on training data.

Training multi-layer neural networks with gradient descent based approaches can be very challenging. One of the main reasons behind this is the effect of *vanishing gradients*: it has been empirically observed that in many multi-layer neural networks the gradients in higher-level (further from the image) layers often become too small to be effective in gradient descent based optimisation. Another difficulty is that the distribution of each layer's inputs changes during training as the parameters of the previous layers change. These issues make it difficult to find the best learning rates.

Batch normalisation layers (Ioffe & Szegedy 2015) are one way of addressing these challenges. Let the activities of a given neuron in a mini-batch be denoted by x_1, \dots, x_m . The batch normalisation layers i) calculate the empirical mean ($\mu = \frac{1}{m} \sum_{i=1}^m x_i$) and variance ($\sigma^2 = \frac{1}{m} \sum_{i=1}^m (x_i - \mu)^2$) of the neural activities using the mini-batch data, ii) standardise the neuron activities to make them zero mean with unit variance, that is $\hat{x}_i = (x_i - \mu)/\sigma$, iii) linearly transform these activities with adjustable parameters $\beta, \gamma \in \mathbb{R}$: $y_i = \gamma \hat{x}_i + \beta$. Here y_i denotes the output after applying the batch normalisation layer on the neuron with activities x_i . It has been empirically demonstrated that batch normalisation can often accelerate the training procedure and help mitigate the above described challenges.

There are many variations on these techniques and concepts some of which are represented in the following descriptions of particular methods.

4.4.1. AstrOmatic (Bertin)

The lens detector is based on a CNN, trained with the provided training datasets. The CNN is implemented in Python, using the TensorFlow framework⁶. Both ground multichannel and space monochannel image classifiers have the exact same CNN architecture.

The network itself consists of three convolutional layers (11x11-32, 5x5-64 and 3x3-64), followed by two fully-connected layers (256 and 64 neurons) and an output softmax layer. The first five layers use the ELU activation function, which in our tests led to significantly faster convergence compared to ReLU and even SoftPlus activation. Dropout regularization is applied to both convolutional and fully connected layers, with “keep” probabilities $p = 2/3$ and $p = 1/2$, respectively.

Prior to entering the first convolutional layer, input image data are rescaled and the dynamic-range compressed with the function $f(x) = \text{arcsinh}(10^{11}x)$, and bad pixels are simply set to 0. Data augmentation (increasing the amount of training data by modifying and reusing it) is performed

⁶ <http://www.tensorflow.org/>

in the form of random up-down and left-right image flipping, plus $k\pi/2$ rotations, where k is a random integer in the $[0, 3]$ range. Additionally, a small rotation with random angle θ is applied, involving bicubic image resampling, the angle θ is drawn from a Gaussian distribution with mean $\mu = 0$ and standard deviation $\sigma_\theta = 5^\circ$. No attempt was made to generate and randomize bad pixel masks in the data augmentation process.

The CNN weights are initialized to random values using a truncated Gaussian distribution with mean $\mu = 0$ and standard deviation $\sigma = 0.05$. The network is trained on a Titan-X “Pascal” nVidia GPU using the ADAM gradient-based optimizer during 800 epochs, with an initial learning rate $\eta(t = 0) = 10^{-3}$ and a learning rate decay $\eta(t + 1)/\eta(t) = 0.99$, where t is the epoch. Because of a lack of time, tests were limited to assessing the basic classification performance on a subset of the of 1,000 images/daticubes, using the 19,000 others for training.

4.4.2. LASTRO EPFL (Geiger, Schäfer)

We used a CNN (Fukushima 1980; Lecun et al. 1998) with a simple architecture of 12 layers (inspired by (Dieleman et al. 2016)), see table 2. To avoid the problem of the data flow distribution getting out of the comfort zone of the activation functions (“Internal Covariate Shift”), we used a mix of normalization propagation (Arpit et al. 2016) (without the constraint on the weights but a proper initialization) and batch normalization (Ioffe & Szegedy 2015) (slowly disabled over the iterations). As activation function, we used a scaled and shifted ReLU, defined as

$$\frac{1}{\sqrt{\pi - 1}}(\sqrt{2\pi} \max(0, x) - 1), \quad (7)$$

to satisfy the properties required by the normalization propagation. Our batch normalization implementation computes the mean of the activation function $\bar{\mu}_i$ using the following equation

$$\bar{\mu}_i \leftarrow (1 - \eta) \bar{\mu}_{i-1} + \eta \mu_i(\text{batch}). \quad (8)$$

$\bar{\mu}_i$ is computed using the mean value μ_i over the batch in combination with the previous mean $\bar{\mu}_{i-1}$ using an inertia value η set to 1 at the beginning and decaying with the iterations. For the training, the 20,000 provided images were split into two sets, 17,000 for training and 3k for validation. Each iteration of the gradient descent (more precisely ADAM (Kingma & Ba 2015)) minimizes the cross entropy,

$$\begin{cases} -\log(p) & \text{if the image is a true lens} \\ -\log(1 - p) & \text{if the image is a nonlens} \end{cases}, \quad (9)$$

where p is the output of the neural network, computed over a batch of 30 images, 15 lenses and 15 nonlenses, picked from the training set. The small batches with only 30 images were easier to handle computationally but added more noise to the gradient which we considered negligible due to there being only two classes to classify.

To augment the training set, each image of the batch is transformed with a random transformation of the dihedral group (rotations of 90 degrees and mirrors), its pixel values multiplied by a factor picked between 0.8 and 1.2 and shifted by a random value between -0.1 and 0.1 . To

prevent the overfitting, we used some dropout (Srivastava et al. 2014b) (with a keeping probability decreasing with the iterations). The masked regions of the ground based images are handled by simply setting them to zero. Each final prediction is made of the product of the predictions of the 8 transformations of the image by the dihedral group. The architecture is implemented in Tensorflow⁷. Our code is accessible on github⁸. Additional details can be found in Schaefer et al. (2017).

4.4.3. GAMOCLASS (Tuccillo, Huertas-Company, Velasco-Forero, Decenci ere)

GAMOCLASS is a CNN based classifier. We used the full training data set in the proportion of 4/5 for training and 1/5 for validation. The training images were labelled with 1 if showing strong lensing and 0 otherwise. Our CNN gives as output a probability $[0,1]$ of the input image being a strongly lensed system. The final architecture of our model is illustrated in Fig. 3. The input image (101x101 pixels) is first processed by a 2D convolution layer with a 3x3 filter size, then subsampled by a 3x3 max pooling layer. Another two identical units follow, with a growing dimensionality of the output space in the convolution, for a total of 3 convolutional layers and 3 max pooling layers. Each of these convolutional layers is followed by a ReLU step. The output of these units is then processed through a single fully-connected layer followed by a dropout layer, and, finally, by a one-neuron fully connected layer with sigmoid activation functions. For the classification problem we used the binary cross-entropy cost function and found the weights using ADAM (Kingma & Ba 2014) optimization method. The use of the ADAM optimizer improved the learning rate compared to tests with stochastic gradient descent (SGD). In order to increase the size of the training set and make the model invariant to specific transformations, we perform these data augmentation steps: 1) we introduce random rotations of the image in the range $[0, 180^\circ]$, using a reflection fill mode to keep constant the size of the images; 2) the images are randomly shifted of 0.02 times the total width of the image; 3) the images are randomly flipped horizontally and vertically.

During the training we initialize the weights of our model with random normal values and we “warm up” the training of the CNN for 25 epochs, using an exponential decay rate (10^{-6}) (Huang et al. 2016) and then a starting learning rate of 0.001. Then the network was trained using an early stopping method, and for a maximum number of 300 epochs. The early stopping method is an effective method of preventing overfitting and consists in stopping the training if a monitored quantity does not improve for a fixed number (called *patience*) of training epochs. The quantity that we monitored was the *accuracy* of the classification of the validation sample. The best architecture was trained over 220 epochs with a parameter of patience equal to 20. We implemented our code in the Keras framework (Chollet 2015) on top of Theano (Bastien et al. 2012). Our architecture converges with a classification accuracy of 91% on the validation sample. We further evaluated the performance of our classifier calculating the ROC (see Section 5.1) curve of the classifier, i.e. the True Positive Rate

⁷ <http://tensorflow.org/>

⁸ <https://github.com/antigol/lensfinder-euclid>

Layer type	shape	activation	# parameters
convolutional 4x4	$101 \times 101 \times 1/4 \rightarrow 98 \times 98 \times 16$	rectifier	$256/1'024 + 16$
convolutional 3x3	$98 \times 98 \times 16 \rightarrow 96 \times 96 \times 16$	rectifier	$2'304 + 16$
max pool /2	$96 \times 96 \times 16 \rightarrow 48 \times 48 \times 16$	-	-
batch normalization	$48 \times 48 \times 16$	-	$16 + 16$
convolutional 3x3	$48 \times 48 \times 16 \rightarrow 46 \times 46 \times 32$	rectifier	$4'608 + 32$
convolutional 3x3	$46 \times 46 \times 32 \rightarrow 44 \times 44 \times 32$	rectifier	$9'216 + 32$
max pool /2	$44 \times 44 \times 32 \rightarrow 22 \times 22 \times 32$	-	-
batch normalization	$22 \times 22 \times 32$	-	$32 + 32$
convolutional 3x3	$22 \times 22 \times 32 \rightarrow 20 \times 20 \times 64$	rectifier	$18'432 + 64$
convolutional 3x3	$20 \times 20 \times 64 \rightarrow 18 \times 18 \times 64$	rectifier	$36'864 + 64$
max pool /2	$18 \times 18 \times 64 \rightarrow 9 \times 9 \times 64$	-	-
batch normalization	$9 \times 9 \times 64$	-	$64 + 64$
dropout	$9 \times 9 \times 64$	-	-
convolutional 3x3	$9 \times 9 \times 64 \rightarrow 7 \times 7 \times 128$	rectifier	$73'728 + 128$
dropout	$7 \times 7 \times 128$	-	-
convolutional 3x3	$7 \times 7 \times 128 \rightarrow 5 \times 5 \times 128$	rectifier	$147'456 + 128$
batch normalization	$5 \times 5 \times 128$	-	$128 + 128$
dropout	$5 \times 5 \times 128$	-	-
fully-connected	$5 \times 5 \times 128 \rightarrow 1024$	rectifier	$3'276'800 + 1'024$
dropout	1024	-	-
fully-connected	$1024 \rightarrow 1024$	rectifier	$1'048'576 + 1'024$
dropout	1024	-	-
fully-connected	$1024 \rightarrow 1024$	rectifier	$1'048'576 + 1'024$
batch normalization	1024	-	$1'024 + 1'024$
fully-connected	$1024 \rightarrow 1$	sigmoid	$1'024 + 1$
Total	-	-	$\approx 5'674'000$

Table 2. LASTRO EPFL architecture

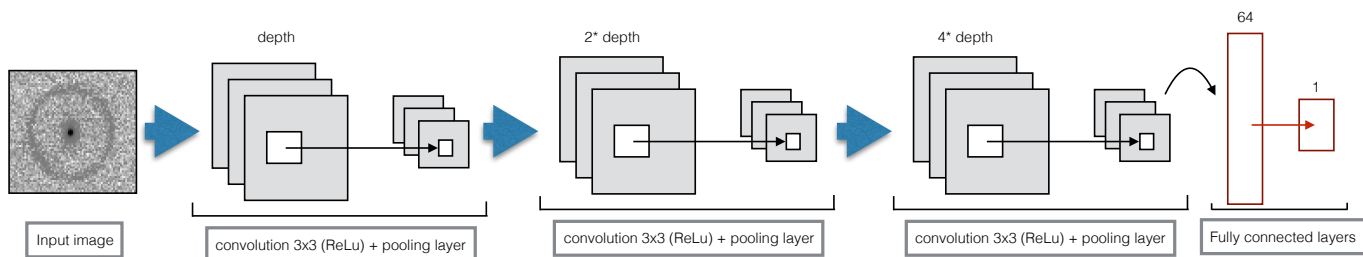


Fig. 3. GAMOCLASS schematic

(TPR) against the False Positive Rate. We reached a TPR higher than the 90% with a FPR < 8%.

4.4.4. CAST (Bom, Valentín, Makler)

The CBPF Arc Search Team (CAST) tested several arc-finding schemes with CNNs at their core. For both the space-based and ground-based samples we used a simple preprocessing phase to enhance the objects in the images to check to see if this improved the automated arc detection with the CNN. We chose a contrast adjustment with 0.1% pixel saturation and apply a low pass band Wiener filter (Wiener 1964) to reduce the effect of the noise.

We used a native CNN from Matlab⁹, which has Convolutional 2D layers with 20 5x5 filters. This CNN can work either with one or three input images, representing greyscale

⁹ <https://www.mathworks.com/products/matlab.html>, <https://www.mathworks.com/help/nnet/convolutional-neural-networks.html>

and colour images. We employed different strategies for the two samples available for the challenge, which involve combinations of the available bands running in one or more CNN, using or not the preprocessing, and combining the output with the aid of other machine learning methods. In each case we used the simulations made available for the challenge both to train and to validate the results and we used the area under the ROC (see Section 5.1) to determine which combination of methods gives the best result. We selected 90% of the images, chosen randomly, for the training and 10% to validate. We repeated the process 10 times to avoid bias due to a specific choice of training/validation set and to define an uncertainty in our ROC.

For the space-based data set we tested only two configurations: i) using the CNN straightforwardly for classification and ii) with the preprocessing described above. We found that the results, accounting for the uncertainties, were clearly superior in terms of the area under the ROC with the preprocessing. Therefore, this is the configuration we used for the challenge entry.

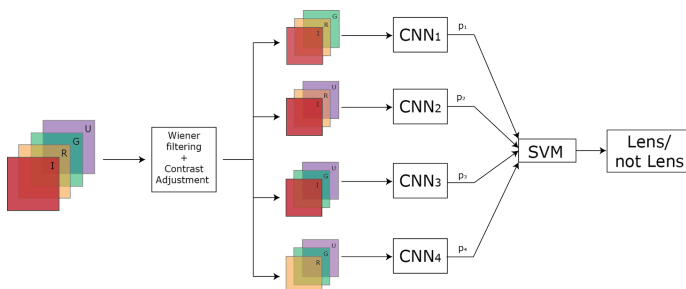


Fig. 4. CAST Lens finder pipeline for the ground based sample. Illustration of the chosen architecture for the CAST search in the case of ground-based simulated images.

As mentioned above, the CNN we used can take 3 colour images as input. To use the information on the 4 available bands, we needed to either combine 2 of the 4 bands to end up with 3 bands for a single RGB CNN (configuration I below) or we use multiple CNNs (configuration II to VI below). To combine the outputs of several CNNs we use a Support Vector Machine (SVM; see e.g. Rebenrost et al. 2014) also implemented in Matlab. The SVM is used to combine the outputs p_i of the several CNNs (configurations II, III, IV and VI). Instead of using only p_i as inputs to the SVM we also tested providing the SVM with image features obtained by the CNN (feature maps, configuration V) as inputs. In all cases we tested with and without the preprocessing

A more detailed description of each configuration tested is presented below:

- I. Combination of bands r and i with the average between bands u and g . Use one CNN for classification.
- II. Creation of 1 CNN for each band (total of 4). The 4 outputs are used as input to a SVM classifier which returns the final classification p .
- III. Combination into 4 different combinations of bands: RGB $\rightarrow (u, g, r)$, (u, g, i) , (u, r, i) and (g, r, i) . One CNN for each combination of bands and then use of the output score as input to an SVM classifier.
- IV. Average of bands in different combinations RGB $\rightarrow (ug, r, i)$, (u, gr, i) and (u, g, ri) . The outputs of these 3 CNNs are inputs to a SVM classifier.
- V. Use of CNN-activations (CNN feature maps) as inputs to a SVM classifier, using same combinations of bands of III. The output of each CNN is used as input to a SVM classifier.
- VI. Use of wiener filter and contrast adjustment on each band, then using the resulting images in the same architecture as in (III).

For the ground based cases, the three configurations with highest area under ROC were III, IV and VI. Although the areas are very similar between IV and VI the last one is superior in the low fake positives end. Thus, for the Strong Lensing Challenge in the ground base sample, we used configuration VI. This final scheme is illustrated in figure 4.

The area under ROC, in both space based configurations were, in general, smaller than in the multi-band case, which suggests how the CNNs are sensitive to colour information to find strong lensing. Particularly, ground base configuration II used one CNN per band and has the similar area under ROC as our best single band configuration.

4.4.5. CMU DeepLens (Lanusse, Ma, Li, Ravanbakhsh)

CMU DeepLens is based on a residual network (or *resnet*) architecture (He et al. 2015a), a modern variant of CNNs which can reach much greater depths (over 1000 layers) while still gaining accuracy. We provide a short overview of our model below but a full description of our architecture can be found in Lanusse et al. (2018).

Much like conventional CNNs, resnets are based on convolutional and pooling layers. However, resnet differ from CNNs by the introduction of so-called shortcut connections bypassing blocks of several convolutional layers. As a result, instead of learning the full mapping from their input to their output these residual blocks only have to learn the difference to the identity transformation. In practice, this difference allows residual networks to be trained even for very deep models. For a more thorough description of this architecture, we refer the interested reader to Section 2.3 of Lanusse et al. (2018).

Our baseline model is composed of a first 7×7 -32 convolutional layer which can accommodate either single-band or multi-band images. The rest of the model is composed of 5 successive blocks, each block being made of 3 resnet units (specifically, pre-activated bottleneck residual units (He et al. 2016)). At each block, the signal is downsampled by a factor 2 and the number of feature maps is in turn multiplied by 2. The model is topped by an average-pooling layer followed by a single fully-connected sigmoid layer with a single output. Apart from the final layer, we use the ELU (Exponential Linear Unit) activation throughout. The weights of the model are initialized using random normal values, following the strategy advocated in He et al. (2015a).

Training was performed using the ADAM optimizer with mini-batches of size 128 over 120 epochs, with an initial learning rate of $\alpha = 0.001$, subsequently decreased by a factor 10 every 40 epochs. This multi-step training procedure is important to progressively refine the model parameters and achieve our final accuracy.

We adopt a minimal pre-processing strategy for the input images, removing the mean image and normalising by the noise standard deviation σ in each band, this statistic being evaluated over the whole training set. In addition, we clip extreme values above 250σ to limit the dynamic range of the input. Bad-pixels are simply set to 0 after this pre-processing step.

Given the relatively small training set preventing overfitting is an important consideration. In our final model, we combine several data augmentation strategies: random rotations (in the range $[-90, 90^\circ]$), random mirroring along both axes, and random resizing (by a small factor in the range $[0.9, 1]$).

The architecture presented above is the one that lead to our best results in both branches of the challenge, i.e. CMU-DeepLens-Resnet for space-based and CMU-DeepLens-Resnet-ground3 for ground-based. We also submitted results for two variants of this baseline model, named -aug and -Voting. The first variant introduced several data-augmentation schemes, including the ones mentioned above and the addition of Gaussian noise to the input images. We found however that the introduction of noise was not necessary as the other methods were enough to prevent overfitting. The second variant was used to explore a voting strategy between three different models. These models dif-

ferred by the type of residual blocks (bottleneck vs wide) and by their handling of missing pixels (setting to 0 or to the median value of the image). The predictions of the best 2 out of 3 models were then averaged to produce the final classification probability.

Our model is implemented using the `Theano`¹⁰ and `Lasagne`¹¹ libraries. On an Nvidia Titan Xp GPU, our full training procedure requires approximately 6 hours on the ground-based challenge, but classification of the whole testing set is performed in a couple of minutes. Finally, in the interest of reproducible research, our code is made publicly available on GitHub¹². This repository also contains a notebook detailing how to reproduce our challenge submission.

4.4.6. Kapteyn Resnet (Petrillo, Tortora, Vernardos, Kleijn, Koopmans)

Our lens-finder is based on a CNN, following the strategy adopted recently in (Petrillo et al. 2017). We decide to treat the problem as a three-class classification problem where the classes are *non-lenses*, *clear lenses* and *dubious lenses*. We define the *dubious lenses* as the lenses with lensing features with less than 160 pixels and the *clear lenses* those with more than 160 pixels belonging to the lensed source. This choice is motivated by the fact that specializing the network in recognizing different classes could lead to a more robust classification. In addition, in a hypothetical application of the method to real data from a survey, this could be a way to select the most blatant lenses.

The CNN is implemented in Python 2.7 using the open-source libraries `LASAGNE`¹³ and `THEANO`¹⁴ (Theano Development Team 2016). The training of the CNN is executed on a GeForce GTX 760 in parallel with the data augmentation performed on the CPU using the `SCIKIT-IMAGE`¹⁵ package (Van der Walt et al. 2014).

We used the CNN architecture called Resnet described in (He et al. 2015b) with three stacks of residual blocks of 5 layers. The output layer is composed by three units. Each unit gives as an output a number between 0 and 1 that represents, respectively, the probability of being a *non-lens*, a *dubious lens*, a *certain lens*. We then collapsed one of the classes into another to give a binary classification : 0 when a source is classified as a *non-lens* and a 1 when is classified as a *clear lens* or as a *dubious lens*. This choice did not allow for building a continuous ROC (see Section 5.1) curve but only a binary one. The final submission was produced by averaging the values of the predictions from three CNNs with the same architecture.

The training image files were preprocessed with the software `STIFF`¹⁶ which automatically converts the fits files to grey-scale TIFF images operating a non-linear intensity transformations to enhance the low-brightness features of the image. Due to memory limitations we down-sampled the images to 84 by 84 pixels. We augmented the training images in the following way: i) random rotation of 90, 180 or 270 degrees; ii) random shift in both x and y direction be-

tween -2 and +2 pixels; iii) 50% probability of horizontally flipping the image. Finally, the image border is cropped in order to have 80 by 80 pixel input images.

The network is trained by minimizing the categorical cross-entropy loss function

$$L = - \sum_j t_j \log p_j \quad (10)$$

where the t_j and p_j are respectively the label and the prediction for the class j . The minimization is done via mini-batch stochastic gradient descent with ADAM updates (Kingma & Ba 2014). We used a batch size of 56 and performed 46000 gradient updates. We started with a learning rate of 4×10^{-4} , decrease it to 4×10^{-5} after 35000 updates and to 4×10^{-6} after 43000 updates. The weights of each filter are initialized from a random normal distribution with variance $2/n$ where n is the number of inputs of the unit and a mean of zero (He et al. 2015a). We use L2-norm regularization with $\lambda = 9 \times 10^{-3}$.

4.4.7. NeuralNet2 (Davies, Serjeant)

Our lens finder included wavelet prefiltering. The image was convolved with the Mallat wavelet with a kernel size of 4 in both the horizontal and vertical directions, then combined and compared to the original image to make the input image; input image = $\sqrt{H^2 + V^2}$. This prefiltering was performed to emphasise the edges in the images. It was found to improve the results compared to the CNN without this pre-filter. The CNN had 2 convolution layers each containing $3 \times 3 - 32$ filters, incorporating dropout and max-pooling, and then 3 dense fully-connected layers to classify each image. The network was trained on 18000 of the 20000 training images; training took 15 epochs and was completed once the validation loss was minimised. The training was validated on the remaining 2000 images. Validation loss was calculated using binary cross entropy

$$\mathcal{L} = \sum_{i=1}^n [y_i \log(p_i) + (1 - y_i) \log(1 - p_i)] \quad (11)$$

where \mathcal{L} is the loss function, n is the number of inputs, y_i is the true value of the i^{th} input, and p_i is the predicted value for the i^{th} input from the network. A perfect loss of 0 was generated once every predicted value matched the true value for every input. The network was made and trained in Python 2.7 using the open-source libraries `THEANO` and `KERAS`¹⁷. A more developed version of our lens finder will appear in Davies, Bromley and Serjeant (in preparation).

4.4.8. CAS Swinburne (Jacobs)

Our model is a CNN-based classifier. The architecture of our network was simple, similar to that of AlexNet (Krizhevsky et al. 2012), with three 2D convolutional layers (with kernel sizes 11, 5, and 3), and two fully-connected layers of 1024 neurons each. The activation function after each convolutional layer was a ReLU. After each convolution we employed a 3×3 max pooling layer. To avoid over-fitting, we included a dropout layer of 0.5 after each of the two fully-connected layers. We implemented our network using

¹⁷ <https://github.com/keras-team/keras>

¹⁰ <http://deeplearning.net/software/theano/>

¹¹ <https://github.com/Lasagne/Lasagne>

¹² <https://github.com/McWilliamsCenter>

¹³ <http://github.com/Lasagne/Lasagne/>

¹⁴ <http://deeplearning.net/software/theano/>

¹⁵ <http://scikit-image.org/>

¹⁶ <http://www.astromatic.net/software/stiff>

the Keras python framework (Chollet 2015) and Theano (Bastien et al. 2012).

The training set was augmented with three rotations, and 20% of the images were reserved for validation. The training set consisted of 4-band FITS files of simulated lenses and non-lenses. We imported the training set into HDF5 database files. The data was normalised on import, such that the mean value of the data cube, across all bands, is zero and the standard deviation is one, i.e. $X' = (X - \mu) / \sigma$; the dynamic range was not altered. We also include batch normalisation step after the first convolution, which normalises the outputs of this layer to the same range ($\mu = 0$, $\sigma = 1$). This has been shown empirically to aid in more rapid convergence of the training process.

The training process using a categorical cross-entropy loss function, and a stochastic gradient descent optimizer with an initial learning rate of 0.01, learning rate decay of 10^{-6} , and Nesterov momentum (Nesterov 1983) of 0.9. Training converged (validation loss stopped decreasing) after approximately 30 epochs.

We note that experiments indicated that training on 4-band FITS data, as opposed to RGB images produced from the fits files, resulted in improved validation accuracy, of order a few percent.

5. Results

In this section we summarize the analysis of the submissions. In Section 5.1 we discuss how to judge a classifier in this particular case and define some metrics of success. The results for all the submissions are given in Section 5.2.

5.1. Figures of merit

In deriving a good figure of merit for evaluating lens finding algorithms one needs to take into account the particular nature of this problem. The traditional method for evaluating a classification algorithm is with the receiver operating characteristic curve, or ROC curve. This is a plot of the true positive rate (TPR) versus the false positive rate (FPR). In this case these are defined as

$$\text{TPR} = \frac{\text{number of true lenses classified as lenses}}{\text{total number of true lenses}} \quad (12)$$

$$\text{FPR} = \frac{\text{number of non-lenses classified as lenses}}{\text{total number of non-lenses}} \quad (13)$$

The classifier generally gives a probability of a candidate being a lens, p , in which case a threshold is set and everything with p greater is classified as a lens and everything smaller is classified as not a lens. The TPR and FPR are then plotted as a curve parametrised by this threshold. At $p = 1$ all of the cases are classified as non-lenses and so $\text{TPR} = \text{FPR} = 0$ and at $p = 0$ all of the cases are classified as lenses so $\text{TPR} = \text{FPR} = 1$. These points are always added to the ROC curve. If the classifier made random guesses then the ratio of lenses to non-lenses would be the same as the ratio of the number of cases classified as lens to the number of cases classified as non-lenses and so $\text{TPR} = \text{FPR}$. The better a classifier is the smaller the FPR and the larger the TPR so the further away from this diagonal line it will be. When a classifier provides only a binary classification or a discrete ranking, the ROC connects the endpoints to the discrete points found by using each rank as a threshold.

A common figure of merit for a classifier is the area under the ROC (**AUROC**). This evaluates the overall ability of a classifier to distinguish between cases. This was the criterion on which the challenge participants were told to optimise. However, in the case of gravitational lensing this is not the only thing, and not the most important thing, to consider. Gravitational lenses are rare events, but to improve the discrimination and training of the classifiers the fraction of lenses in test and training sets are boosted to something around half. In these circumstances it is important to consider the absolute number of cases that will be misclassified when the fraction of true cases is closer to what is expected in the data.

If the rates of false positives and false negatives remain the same in real data the contamination of the sample will be

$$\frac{\text{FP}}{\text{TP}} \approx \frac{\text{FPR}}{\text{TPR}} \left(\frac{\text{number of non-lenses in sample}}{\text{number of lenses in sample}} \right). \quad (14)$$

Since only about one in a thousand objects will be a lens (perhaps somewhat more depending on pre-selection) the contamination will be high unless the FPR is much less than the TPR. For this reason we consider some additional figures of merit.

The **TPR₀** will be defined as the highest TPR reached, as a function of p threshold, before a single false positive occurs in the test set of 100,000 cases. This is the point where the ROC meets the $\text{FPR} = 0$ axis. This quantity highly penalizes classifiers with discrete ranking which often get $\text{TPR}_0 = 0$ because their highest classification level is not conservative enough to eliminate all false positives. We also define **TPR₁₀** which is the TPR at the point where less than ten false positives are made. If the TP rate is boosted from the FPR by a factor of 1,000 in a realistic data set this would correspond to about a 10% contamination.

In addition to these considerations, the performance of a classifier is a function of many characteristics of the lens system. It might be that one classifier is good at finding systems with large Einstein radii and incomplete arcs, but not as good at finding small complete Einstein rings that are blended with the light of the lens galaxy. Also a lens may have a source that is too faint to be detected by any algorithm or is too far from the lens to be very distorted, but will be classified as a lens in the test dataset. We do not impose a definitive arc/ring magnification, brightness or surface brightness limit for a system to be considered a lens because we want to include these “barely lensed” objects to test the limits of the classifiers. As we will see, if one restricts the objectives to detecting only lensed images with surface brightness above some threshold, for example, the “best” algorithm might change and the TPR will change. For this reason we plot the AUROC, TPR_0 and TPR_{10} as a function of several variables for all the entries. This is done by removing all the lenses that do not exceed the threshold and then recalculating these quantities, while the number of non-lenses remains the same.

5.2. Performance of the methods

Table 3 shows the AUROC, TPR_0 and TPR_{10} for the entries in order of AUROC and dataset type. It can be seen that CMU-DeepLens-Resnet-ground3 had the best AUROC for the ground-based set and LASTRO EPFL the best for the

Name	type	AUROC	TPR ₀	TPR ₁₀	short description
CMU-DeepLens-Resnet-ground3	Ground-Based	0.98	0.09	0.45	CNN
CMU-DeepLens-Resnet-Voting	Ground-Based	0.98	0.02	0.10	CNN
LASTRO EPFL	Ground-Based	0.97	0.07	0.11	CNN
CAS Swinburne Melb	Ground-Based	0.96	0.02	0.08	CNN
AstrOmatic	Ground-Based	0.96	0.00	0.01	CNN
Manchester SVM	Ground-Based	0.93	0.22	0.35	SVM / Gabor
Manchester2	Ground-Based	0.89	0.00	0.01	Human Inspection
ALL-star	Ground-Based	0.84	0.01	0.02	edges/gradients and Logistic Reg.
CAST	Ground-Based	0.83	0.00	0.00	CNN / SVM
YattaLensLite	Ground-Based	0.82	0.00	0.00	SExtractor
LASTRO EPFL	Space-Based	0.93	0.00	0.08	CNN
CMU-DeepLens-Resnet	Space-Based	0.92	0.22	0.29	CNN
GAMOCCLASS	Space-Based	0.92	0.07	0.36	CNN
CMU-DeepLens-Resnet-Voting	Space-Based	0.91	0.00	0.01	CNN
AstrOmatic	Space-Based	0.91	0.00	0.01	CNN
CMU-DeepLens-Resnet-aug	Space-Based	0.91	0.00	0.00	CNN
Kapteyn Resnet	Space-Based	0.82	0.00	0.00	CNN
CAST	Space-Based	0.81	0.07	0.12	CNN
Manchester1	Space-Based	0.81	0.01	0.17	Human Inspection
Manchester SVM	Space-Based	0.81	0.03	0.08	SVM / Gabor
NeuralNet2	Space-Based	0.76	0.00	0.00	CNN / wavelets
YattaLensLite	Space-Based	0.76	0.00	0.00	Arcs / SExtractor
All-now	Space-Based	0.73	0.05	0.07	edges/gradients and Logistic Reg.
GAHEC IRAP	Space-Based	0.66	0.00	0.01	arc finder

Table 3. The AUROC, TPR₀ and TPR₁₀ for the entries in order of AUROC.

space-based set. The order is different if TPR₀ is used to rank the entries as seen in table 4. Here Manchester SVM and CMU-DeepLens-Resnet get the best scores.

Figures 5 and 6 show the ROC curves for all the entries. We note that ROC curves for the ground-based challenge (figure 6) are uniformly better than those for the space-based challenge (figure 5). This is because of the importance of colour information in discriminating lensed arcs from pieces of the foreground lens galaxy.

In addition, figure 7 shows the ROC curves for only the ground-based images where an actual KiDS image was used (see Section 3.2). It can be seen that the classifiers do uniformly less well on this subset. This indicates that the simulated galaxy images are different from the real ones and that the classifiers are able to distinguish fake foreground galaxies from lenses more easily than from real galaxies. Some methods are more affected by this than others, but none seem to be immune, not even the human classification. This is perhaps not unexpected, but does show that the simulated lenses need to be improved before the raw numbers can be directly used to evaluate the performance of a classifier on real data.

Figures 8 and 9 show the AUROC, TPR₀, TPR₁₀ and fraction of lenses as a function of a lower cutoff on the Einstein radius (area). There is also a vertical dotted line that indicates where no more than 100 lenses in the test sample had larger Einstein radii. Beyond this point one should be suspicious of small number statistics. When deriving the distribution of Einstein radii from data these curves would need to be used to correct for detection bias. It can be seen that CMU-DeepLens-Resnet, Manchester1, Manchester SVM and GAMOCCLASS obtain significantly higher TPR₀ and TPR₁₀ for larger Einstein radii. Manchester1 is the human inspection method. In some cases the TPR₀'s are above 50% of the lenses that meet this criterion. Re-

member that many of the so called lenses are very dim or there is no significant arc because the source position is well outside the caustic. If an additional requirement was placed on the definition of a lens, such as the brightness of the arc being above a threshold, the TPRs would go up.

Figures 10 and 11 are the same except that the flux in the lensed images is used as the threshold. We count only the flux in pixels with flux over one σ of the background. In some cases one can see an abrupt rise in the TPRs at some flux threshold. CMU-DeepLens-Resnet in particular reaches a TPR₀ above 75% for the brightest $\sim 10\%$ of the lenses.

A lensed image can be bright without being visibly distorted as in the case of unresolved images. Figures 12 and 13 use the number of pixels in the lensed image(s) that are over one σ of the background. In this case also some classifiers show an abrupt improvement when the image is required to be larger than some threshold. Interestingly in some cases the TPRs go down with lensed image size after reaching a peak. This could be because they are not differentiating the arcs from companion galaxies as well in this regime. There were also cases where the arc intersects with the borders of the image that might cause them to be missed.

Figures 14 and 15 investigate how the flux contrast between the foreground objects and the lensed source affects the classifiers. Interestingly some methods' TPRs go up with this quantity and some go down. We have not yet found any clear explanation for this variety of behaviours.

The two human inspectors, NJ and AT, got significantly different scores on the ground based test set with individual AUROCs of 0.88 and 0.902 and TPR₁₀s of 0.01 and 0.06 respectively. They did not inspect the same images however so differences cannot be considered conclusive, but it does suggest that different inspectors will have different detection efficiencies and biases.

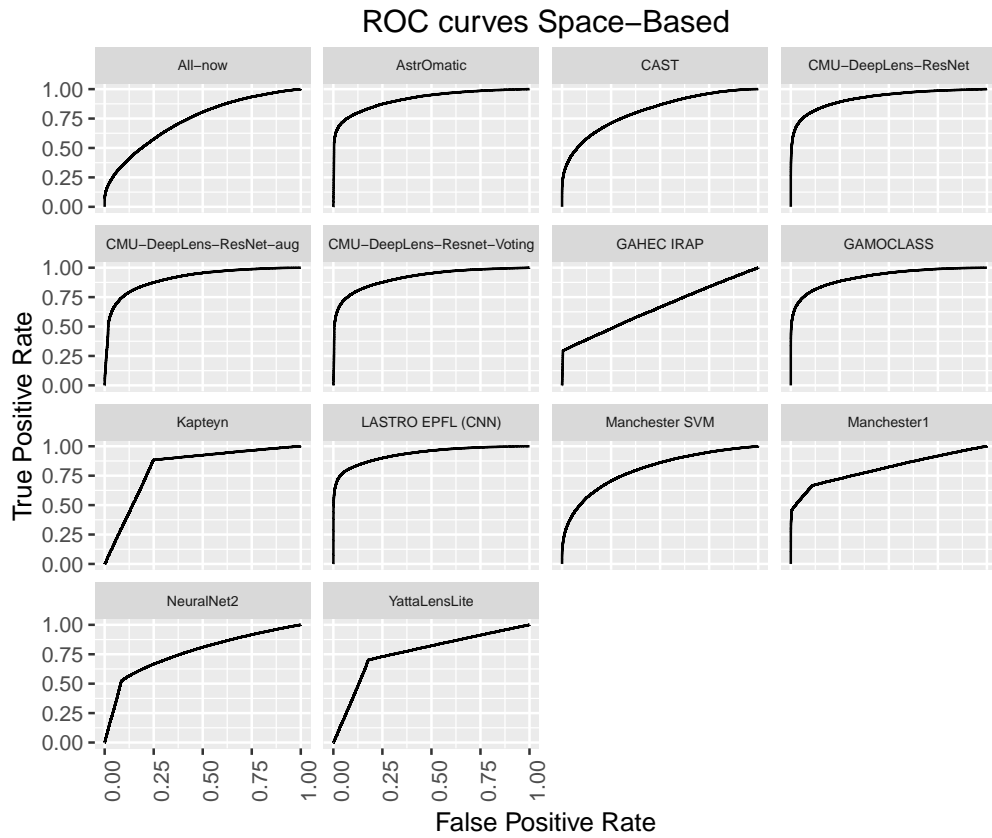


Fig. 5. ROC curves for the space-based entries.

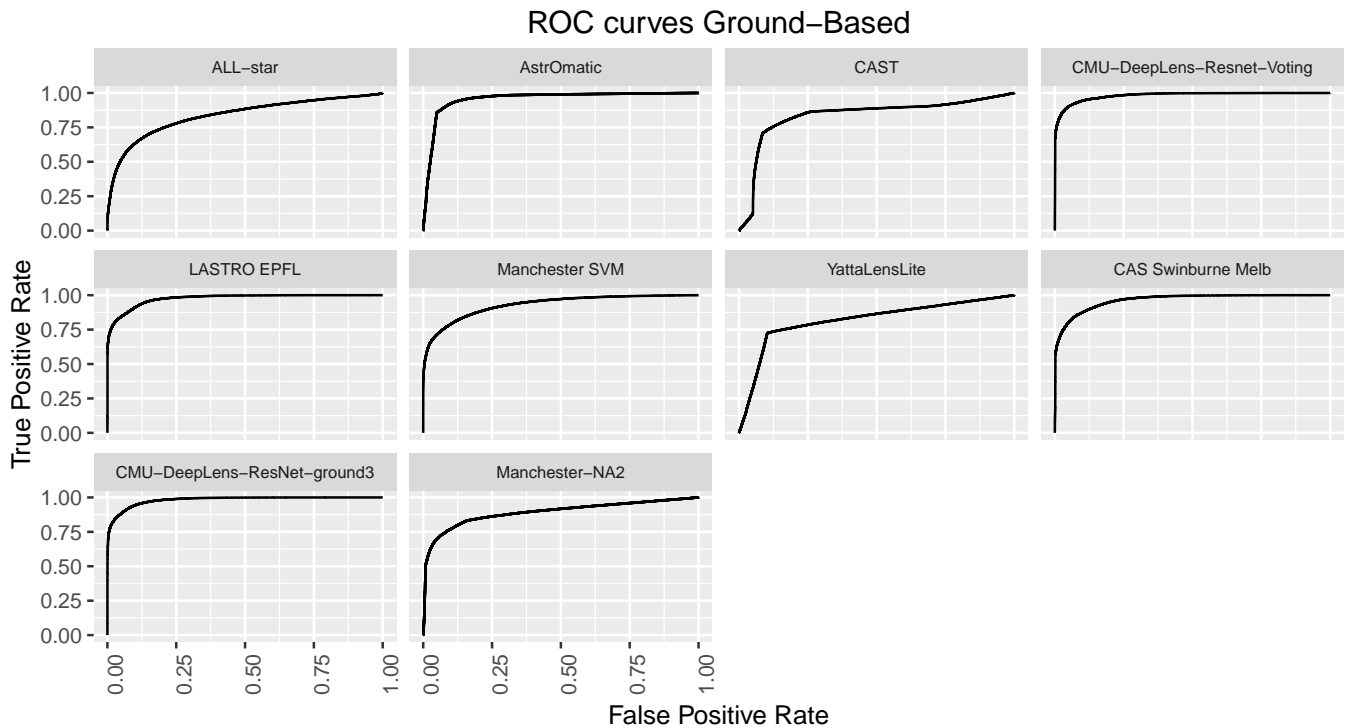


Fig. 6. ROC curves for the ground-based entries. Notice that these are generally better than in figure 8 indicating that colour information is an important discriminant.

Name	type	AUROC	TPR ₀	TPR ₁₀	short description
Manchester SVM	Ground-Based	0.93	0.22	0.35	SVM / Gabor
CMU-DeepLens-Resnet-ground3	Ground-Based	0.98	0.09	0.45	CNN
LASTRO EPFL	Ground-Based	0.97	0.07	0.11	CNN
CMU-DeepLens-Resnet-Voting	Ground-Based	0.98	0.02	0.10	CNN
CAS Swinburne Melb	Ground-Based	0.96	0.02	0.08	CNN
ALL-star	Ground-Based	0.84	0.01	0.02	edges/gradients and Logistic Reg.
Manchester2	Ground-Based	0.89	0.00	0.01	Human Inspection
YattaLensLite	Ground-Based	0.82	0.00	0.00	SExtractor
CAST	Ground-Based	0.83	0.00	0.00	CNN / SVM
AstrOmatic	Ground-Based	0.96	0.00	0.01	CNN
CMU-DeepLens-Resnet	Space-Based	0.92	0.22	0.29	CNN
GAMOCCLASS	Space-Based	0.92	0.07	0.36	CNN
CAST	Space-Based	0.81	0.07	0.12	CNN
All-now	Space-Based	0.73	0.05	0.07	edges/gradients and Logistic Reg.
Manchester SVM	Space-Based	0.80	0.03	0.07	SVM / Gabor
Manchester1	Space-Based	0.81	0.01	0.17	Human Inspection
LASTRO EPFL	Space-Based	0.93	0.00	0.08	CNN
GAHEC IRAP	Space-Based	0.66	0.00	0.01	arc finder
AstrOmatic	Space-Based	0.91	0.00	0.01	CNN
Kapteyn Resnet	Space-Based	0.82	0.00	0.00	CNN
CMU-DeepLens-Resnet-aug	Space-Based	0.91	0.00	0.00	CNN
CMU-DeepLens-Resnet-Voting	Space-Based	0.91	0.00	0.01	CNN
NeuralNet2	Space-Based	0.76	0.00	0.00	CNN / wavelets
YattaLensLite	Space-Based	0.76	0.00	0.00	Arcs / SExtractor

Table 4. The AUROC, TPR₀ and TPR₁₀ for the entries in order of TPR₀.

6. Conclusions and discussion

A large variety of lens finding methods were tested on simulated images that were developed separately. Based on figures 8 and 9, we found that some methods could recover more than 50% of the lenses above a lensed image brightness or size threshold without a single false positive out of 100,000 candidates. If the data closely resembled the simulations we would already have reasonably good methods whose efficiency and biases can be quantitatively characterized.

We have done a fairly good job of determining that lenses can be identified in a population of fairly "normal" galaxies. It is the rare "abnormal" objects that pose the greatest challenge. When real KiDS data was used in the simulations the classifiers were all less accurate and it was only human inspection that found the one jackpot lens (a double Einstein ring with two background sources) in the data. Things like ring galaxies, tidal tails in merging galaxies and irregular galaxies can be mistaken for lenses and were not well represented in the simulated data. Accurately reproducing these objects will be an objective of future work. This might be done by including more real images in the challenge or images based on real images with some random elements added.

It was surprising to some of the authors how well CNN and SVM methods did relative to human inspection. These methods find differences in the classes of images that are not obvious to a human and can classify things as lenses with high confidence where a human would have doubt. This ability comes with some danger of over fitting to the training set however. The distinguishing characteristics might only be a property of simulated data and not of real data. In principle, SVM methods might potentially mitigate this somewhat because with them one can choose which features to use based on knowledge of the properties of irregular

galaxies or ring galaxies for example. This has yet to be shown however. Methods based on fitting with a lens modelling code (Marshall et al. 2009; Sonnenfeld et al. 2017) might also help to mitigate this problem. The confidence one will have in the machine learning methods is really limited by the confidence one has in the realism of the simulations. It might be useful in the future to have a challenge without a training set. This might more clearly reveal the presence of over-fitting. It would also be useful to include more real images or images more closely based on real images.

When initiating this project we had a concern that current methods would be too slow or require too much human intervention to handle large data sets. Happily this seems not to be a problem with most of the automatic methods. The CNN and SVM codes take some time to train, but once trained they are very fast in classifying objects. Billions of objects can be easily handled.

Another lesson is that colour information is very important. Even with lower noise levels, higher resolution, a simpler PSF and no masking, the lenses in the space-based set were harder to find than the lenses in the ground-based set (see figures 5 and 6). Having multiple bands clearly makes a significant difference. Euclid will have several infrared bands with lower resolution than the visible images that were not included in the challenge. Even rather low resolution information from another instrument or telescope when combined with higher resolution data in one band might significantly improve the detection rates. Combining ground based data, such as LSST, with space based data, such as Euclid, would likely boost the detection rates by factors of several.

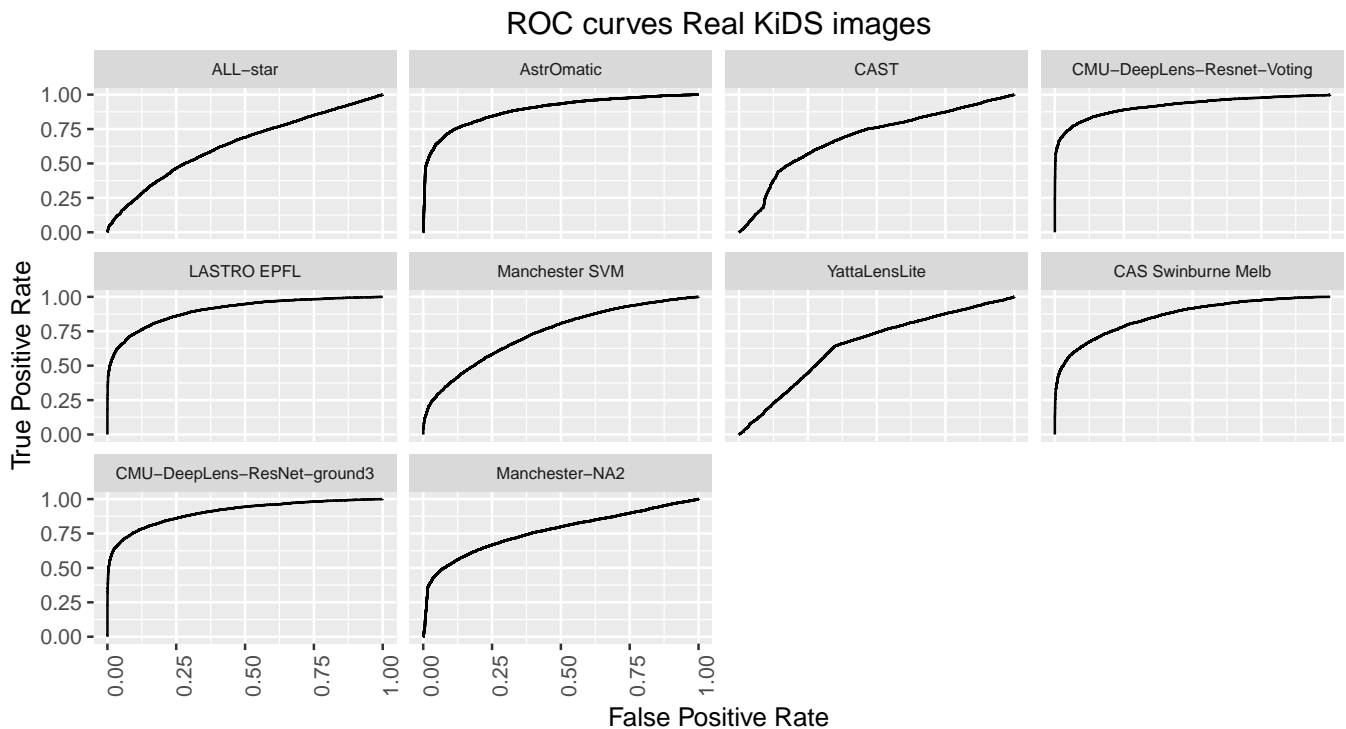


Fig. 7. ROC curves for the ground-based entries including only the cases with authentic images taken from the KiDS survey. It can be seen that in all cases these are lower than in figure 6.

Acknowledgements

AS was supported by World Premier International Research Center Initiative (WPI Initiative), MEXT, Japan. RBM's research was partly part of project GLENCO, funded under the European Seventh Framework Programme, Ideas, Grant Agreement n. 259349. AT acknowledges receipt of an STFC postdoctoral research assistantship. We thank the International Space Science Institute (ISSI) for hosting and funding our workshop.¹⁸ JPK and CS acknowledge support from the ERC advanced grant LIDA and the ESA-NPI grant 491-2016. CA acknowledges support from the Enrico Fermi Institute at the University of Chicago, and the University of Chicago Provost's Office. NL would like to thank the funding support from NSFC, grant no.11503064, and Shanghai Natural Science Foundation, grant no. 15ZR1446700. This work was also supported in part by the Kavli Institute for Cosmological Physics at the University of Chicago through grant NSF PHY-1125897 and an endowment from the Kavli Foundation and its founder Fred Kavli. LVEK, CEP, CT and GV are supported through an NWO-VICI grant (project number 639.043.308). GVK acknowledges financial support from the Netherlands Research School for Astronomy (NOVA) and Target. Target is supported by Samenwerkingsverband Noord Nederland, European fund for regional development, Dutch Ministry of economic affairs, Pieken in de Delta, Provinces of Groningen and Drenthe.

¹⁸ <http://www.issibern.ch/>

References

- Alard C., 2006, ArXiv Astrophysics e-prints,
 Arpit D., Zhou Y., Kota B. U., Govindaraju V., 2016, International Conference on Machine Learning (ICML)
 Avestruz C., Li N., Lightman M., Collett T. E., Luo W., 2017, preprint, ([arXiv:1704.02322](https://arxiv.org/abs/1704.02322))
 Bastien F., Lamblin P., Pascanu R., Bergstra J., Goodfellow I. J., Bergeron A., Bouchard N., Bengio Y., 2012, Theano: new features and speed improvements, Deep Learning and Unsupervised Feature Learning NIPS 2012 Workshop
 Bellagamba F., Tessore N., Metcalf R. B., 2017, MNRAS, 464, 4823
 Bertin E., Arnouts S., 1996, AAPS, 117, 393
 Blackburne J. A., Pooley D., Rappaport S., Schechter P. L., 2011, ApJ, 729, 34
 Blandford R. D., Narayan R., 1992, ARA& A, 30, 311
 Bolton A. S., Burles S., Koopmans L. V. E., Treu T., Moustakas L. A., 2006, ApJ, 638, 703
 Bom C. R., Makler M., Albuquerque M. P., Brandt C. H., 2017, A& A, 597, A135
 Boylan-Kolchin M., Springel V., White S. D. M., Jenkins A., Lemson G., 2009, MNRAS, 398, 1150
 Browne I. W. A., Wilkinson P. N., Jackson N. J. F., et al., 2003, MNRAS, 341, 13
 Brownstein J. R., et al., 2012, ApJ, 744, 41
 Burges C. J., 1998, Data Mining and Knowledge Discovery, 2, 121
 Cabanac R. A., et al., 2007, A& A, 461, 813
 Cavuoti S., Amaro V., Brescia M., Vellucci C., Tortora C., Longo G., 2017, MNRAS, 465, 1959
 Chollet F., 2015, keras, <https://github.com/fchollet/keras>
 Clevert D.-A., Unterthiner T., Hochreiter S., 2015, preprint, ([arXiv:1511.07289](https://arxiv.org/abs/1511.07289))
 Cohn J. D., Kochanek C. S., McLeod B. A., Keeton C. R., 2001, ApJ, 554, 1216
 Collett T. E., 2015, ApJ, 811, 20
 Cortes C., Vapnik V., 1995, Machine Learning, 20, 273
 DESI Collaboration et al., 2016, preprint, ([arXiv:1611.00036](https://arxiv.org/abs/1611.00036))
 Dalal N., Triggs B., 2005, IEEE Computer Society Conference on Computer Vision and Pattern Recognition

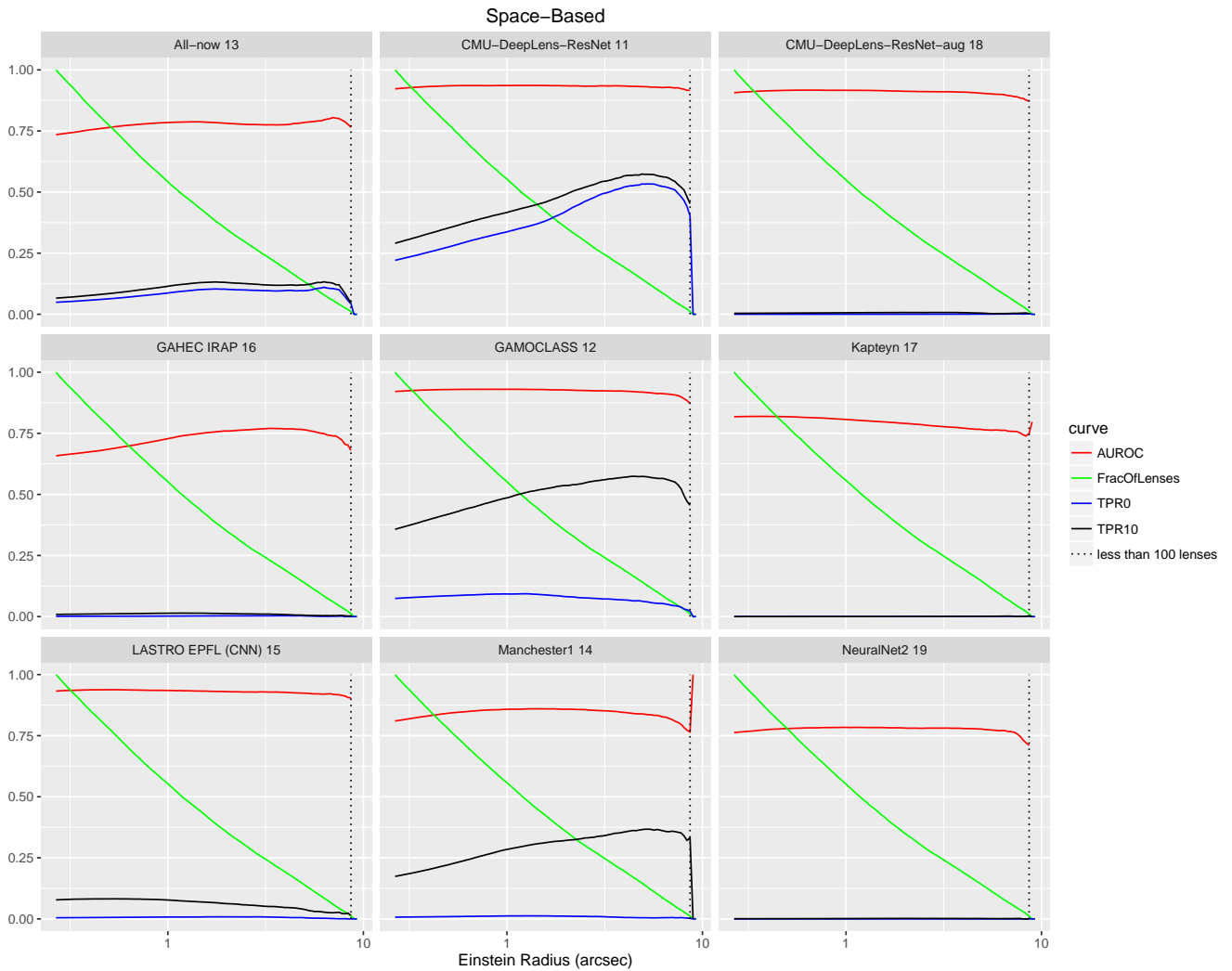


Fig. 8. The AUROC, TPR_0 , TPR_{10} and the fraction of lenses in the test sample after discarding the lenses with Einstein radii larger than the number indicated on the x-axis. The vertical dotted lines indicate where no more than 100 lenses in the test sample had larger Einstein radii. Beyond this point one should be suspicious of small number statistics.

Dieleman S., Willett K. W., Dambre J., 2015, MNRAS, 450, 1441
 Dieleman S., De Fauw J., Kavukcuoglu K., 2016, International Conference on Machine Learning (ICML)
 Duchi J., Hazan E., Singer Y., 2011, Journal of Machine Learning Research, 12, 2121
 Dye S., Warren S. J., 2005, ApJ, 623, 31
 Faure C., Kneib J.-P., Covone G., Tasca L., et al., 2008, ApJS, 176, 19
 Feichtinger H. G., Strohmer T., eds, 1998, Gabor Analysis and Algorithms. Applied and Numerical Harmonic Analysis, Birkhäuser
 Fukushima K., 1980, Biological Cybernetics, 36, 193
 Gavazzi R., Treu T., Koopmans L. V. E., Bolton A. S., Moustakas L. A., Burles S., Marshall P. J., 2008, ApJ, 677, 1046
 Gavazzi R., Marshall P. J., Treu T., Sonnenfeld A., 2014, ApJ, 785, 144

Geach J. E., et al., 2015, MNRAS, 452, 502
 Graham A. W., 2001, AJ, 121, 820
 Grazian A., Fontana A., De Santis C., Galozzi S., Giallongo E., Di Pangrazio F., 2004, PASP, 116, 750
 Guo Q., et al., 2011, MNRAS, 413, 101
 Hartley P., Flamary R., Jackson N., Tagore A. S., Metcalf R. B., 2017, Monthly Notices of the Royal Astronomical Society, 471, 3378
 He K., Zhang X., Ren S., Sun J., 2015a, in 2015 IEEE International Conference on Computer Vision (ICCV). IEEE, pp 1026–1034 (arXiv:1502.01852), doi:10.1109/ICCV.2015.123, <http://arxiv.org/abs/1502.01852><http://ieeexplore.ieee.org/document/7410480/>
 He K., Zhang X., Ren S., Sun J., 2015b, CoRR, abs/1512.03385
 He K., Zhang X., Ren S., Sun J., 2016, preprint, pp 1–15 (arXiv:1603.05027)

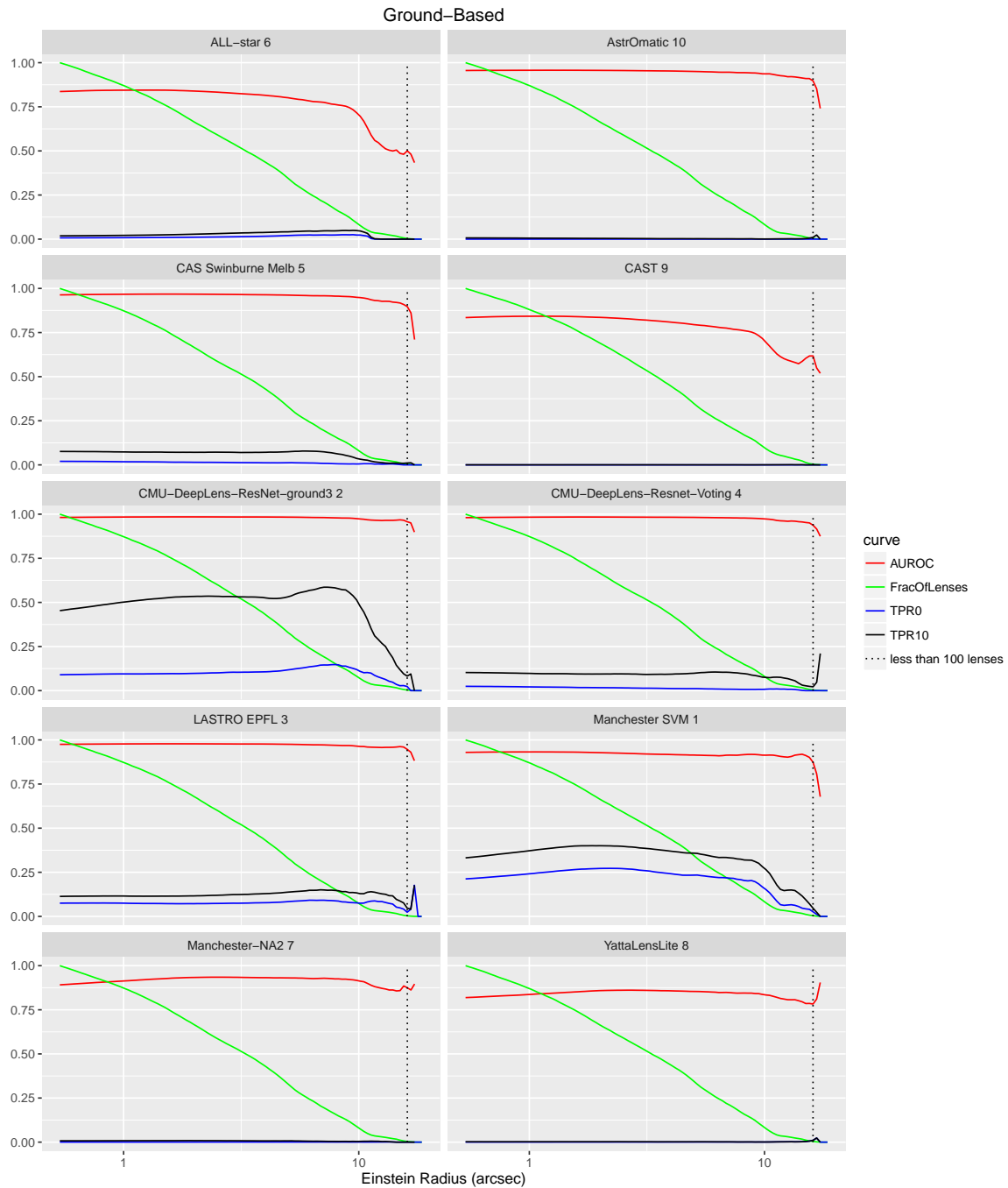


Fig. 9. Same as figure 8, but for ground-based entries. The AUROC, TPR_0 , TPR_{10} and the fraction of lenses in the test sample after discarding the lenses with Einstein radii larger than the number indicated on the x-axis. The vertical dotted lines indicate where no more than 100 lenses in the test sample had larger Einstein radii.

Hinton G. E., Srivastava N., Krizhevsky A., Sutskever I., Salakhutdinov R. R., 2012, preprint, (arXiv:1207.0580)
Huang G., Sun Y., Liu Z., Sedra D., Weinberger K. Q., 2016, CoRR, abs/1603.09382
Ioffe S., Szegedy C., 2015, Journal of Machine Learning Research
Jackson N., 2008, MNRAS, 389, 1311
Jacobs C., Glazebrook K., Collett T., More A., McCarthy C., 2017, MNRAS, 471, 167
Jones J. P., Palmer L. A., 1987, Journal of Neurophysiology, 58, 1233
Joseph R., et al., 2014, A&A, 566, A63
Kingma D. P., Ba J., 2014, preprint, (arXiv:1412.6980)
Kingma D. P., Ba J., 2015, International Conference on Learning Representations
Kochanek C. S., 1991, ApJ, 373, 354
Koopmans L. V. E., Treu T., 2002, ApJ, 568, L5

Koopmans L. V. E., Treu T., 2003, ApJ, 583, 606
Krizhevsky A., Sutskever I., Hinton G. E., 2012, in Pereira F., Burges C. J. C., Bottou L., Weinberger K. Q., eds., Advances in Neural Information Processing Systems 25. Curran Associates, Inc., pp 1097–1105
Lanusse F., Ma Q., Li N., Collett T. E., Li C.-L., Ravanbakhsh S., Mandelbaum R., Poczós B., 2018, MNRAS, 473, 3895
Laureijs R., et al., 2011, preprint, (arXiv:1110.3193)
LeCun Y., Bengio Y., Hinton G., 2015, Nature, 521, 436
Lecun Y., Bottou L., Bengio Y., Haffner P., 1998, Proceedings of the IEEE, 86, 2278
Li N., Gladders M. D., Rangel E. M., Florian M. K., Bleem L. E., Heitmann K., Habib S., Fasel P., 2016, ApJ, 828, 54
Lochner M., McEwen J. D., Peiris H. V., Lahav O., Winter M. K., 2016, ApJS, 225, 31

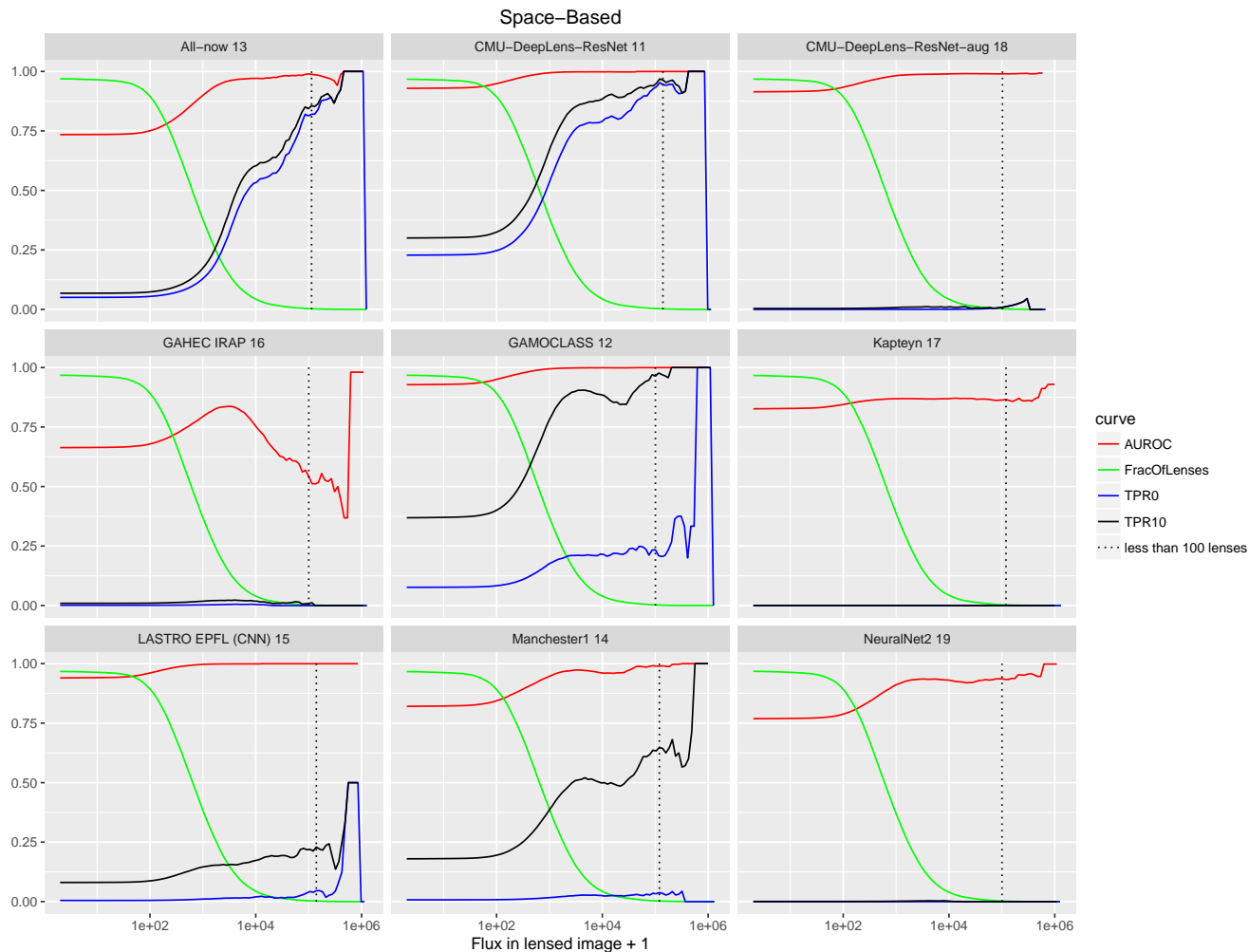


Fig. 10. The AUROC, TPR_0 , TPR_{10} and the fraction of lenses in the space-based test sample after discarding the lenses with fluxes within the pixels that are above 1σ in the lensed source as indicated on the x-axis. The vertical dotted lines indicate where no more than 100 lenses in the test sample had larger Einstein radii.

Markevitch M., Gonzalez A. H., Clowe D., Vikhlinin A., Forman W., Jones C., Murray S., Tucker W., 2004, *The Astrophysical Journal*, 606, 819
 Marshall P. J., et al., 2007, *ApJ*, 671, 1196
 Marshall P. J., Hogg D. W., Moustakas L. A., Fassnacht C. D., Bradač M., Schrabback T., Blandford R. D., 2009, *ApJ*, 694, 924
 Marshall P. J., Verma A., More A., Davis C. P., et al., 2016, *MNRAS*, 455, 1171
 McKean J., et al., 2015, *Advancing Astrophysics with the Square Kilometre Array (AASKA14)*, p. 84
 Meneghetti M., et al., 2008, *A&A*, 482, 403
 Meneghetti M., Rasia E., Merten J., Bellagamba F., Ettori S., Mazzotta P., Dolag K., Marri S., 2010, *A&A*, 514, A93
 Metcalf R. B., Petkova M., 2014, *MNRAS*, 445, 1942
 More A., Cabanac R., More S., Alard C., Limousin M., Kneib J.-P., Gavazzi R., Motta V., 2012, *ApJ*, 749, 38

More A., Verma A., Marshall P. J., More S., et al., 2016, *MNRAS*, 455, 1191
 Morgan C. W., Kochanek C. S., Dai X., Morgan N. D., Falco E. E., 2008, *ApJ*, 689, 755
 Nair V., Hinton G. E., 2010, *Proceedings of the 27th International Conference on Machine Learning*, pp 807–814
 Navarro J. F., Frenk C. S., White S. D. M., 1996, *ApJ*, 462, 563
 Nesterov Y., 1983, *Doklady ANSSSR (translated as Soviet.Math.Docl.)*, 269, 543
 Oguri M., Marshall P. J., 2010, *MNRAS*, 405, 2579
 Ostrovski F., McMahon R. G., Connolly A. J., et al., 2017, *MNRAS*, 465, 4325
 Overzier R., Lemson G., Angulo R. E., Bertin E., Blaizot J., Henriques B. M. B., Marleau G.-D., White S. D. M., 2013, *MNRAS*, 428, 778
 Paraficz D., et al., 2016, *A&A*, 592, A75

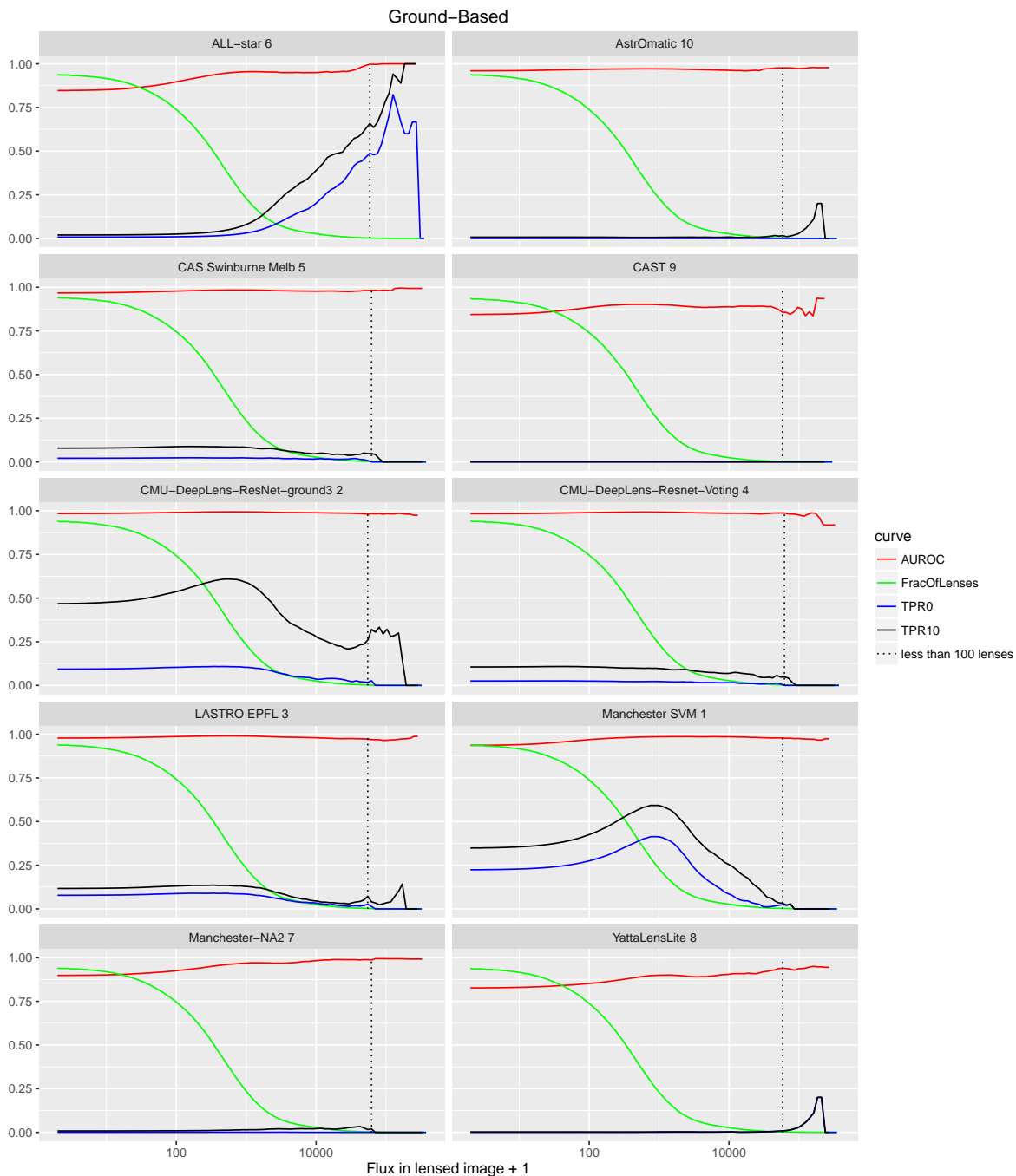


Fig. 11. Same as figure 10, but for ground-based entries.

Pawase R. S., Courbin F., Faure C., Kokotanekova R., Meylan G., 2014, *MNRAS*, 439, 3392
 Pedregosa F., et al., 2011, *Journal of Machine Learning Research*, 12, 2825
 Pedregosa F., et al., 2012, preprint, ([arXiv:1201.0490](https://arxiv.org/abs/1201.0490))
 Peng C. Y., Ho L. C., Impey C. D., Rix H.-W., 2002, *AJ*, 124, 266
 Petkov N., Kruizinga P., 1997, *Computational Models of Visual Neurons Specialised in the Detection of Periodic and Aperiodic Oriented Visual Stimuli: Bar and Grating Cells*
 Petkova M., Metcalf R. B., Giocoli C., 2014, *MNRAS*, 445, 1954
 Petrillo C. E., et al., 2017, *MNRAS*, 472, 1129
 Plazas A. A., Meneghetti M., Maturi M., Rhodes J., 2019, *MNRAS*, 482, 2823
 Poindexter S., Morgan N., Kochanek C. S., 2008, *ApJ*, 673, 34
 Reberntrost P., Mohseni M., Lloyd S., 2014, *PhysRevL*, 113, 130503
 Refsdal S., 1964, *MNRAS*, 128, 307
 Ruder S., 2016, *An overview of gradient descent optimization algorithms*, <https://arxiv.org/abs/1609.04747>

Rusin D., et al., 2003, *ApJ*, 587, 143
 SLWhitePaper 2017, ?, 0, 0
 Sadeh I., Abdalla F. B., Lahav O., 2016, *PASP*, 128, 104502
 Samui S., Samui Pal S., 2017, *New A*, 51, 169
 Schaefer C., Geiger M., Kuntzer T., Kneib J., 2017, preprint, ([arXiv:1705.07132](https://arxiv.org/abs/1705.07132))
 Seidel G., Bartelmann M., 2007, *A&A*, 472, 341
 Shu Y., et al., 2016, *ApJ*, 833, 264
 Smith R. J., Lucey J. R., Conroy C., 2015, *MNRAS*, 449, 3441
 Sonnenfeld A., et al., 2017, preprint, ([arXiv:1704.01585](https://arxiv.org/abs/1704.01585))
 Srivastava N., Hinton G., Krizhevsky A., Sutskever I., Salakhutdinov R., 2014a, *Journal of Machine Learning Research*, 15, 1929
 Srivastava N., Hinton G., Krizhevsky A., Sutskever I., Salakhutdinov R., 2014b, *Journal of Machine Learning Research*, 15, 1929
 Suyu S. H., et al., 2013, *ApJ*, 766, 70
 Sygnet J. F., Tu H., Fort B., Gavazzi R., 2010, *A&A*, 517, A25
 Tamura N., et al., 2016, in *Ground-based and Airborne Instrumentation for Astronomy VI*. p. 99081M ([arXiv:1608.01075](https://arxiv.org/abs/1608.01075)), doi:10.1117/12.2232103

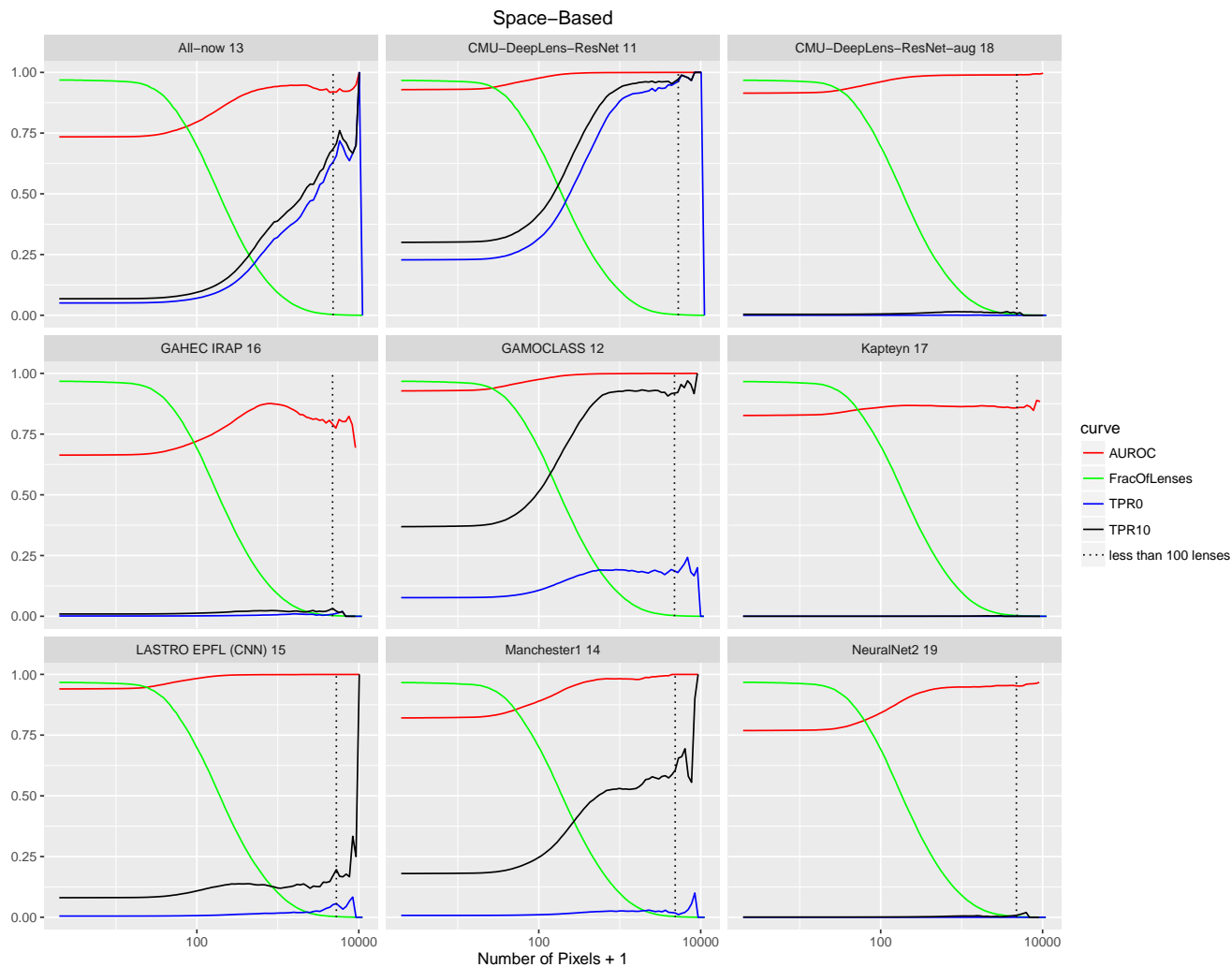


Fig. 12. The AUROC, TPR_0 , TPR_{10} and the fraction of lenses as a function of the lens image size for the space-based test set. The x-axis is the number of pixels that are above 1σ in the lensed source only image. This is an indication of the lensed arcs' size. The vertical dotted lines indicate where no more than 100 lenses in the test sample had larger Einstein radii.

Tessore N., Bellagamba F., Metcalf R. B., 2016, MNRAS, 463, 3115
 Theano Development Team 2016, arXiv e-prints, abs/1605.02688
 Tieleman T., Hinton G., 2012, Root Mean Square Propagation. Divide the gradient by a running average of its recent magnitude. COURSE-ERA: Neural Networks for Machine Learning, http://www.cs.toronto.edu/~tijmen/csc321/slides/lecture_slides_lec6.pdf
 Treu T., Marshall P. J., 2016, A& ARv, 24, 11
 Van der Walt S., Schönberger J. L., Nunez-Iglesias J., Boulogne F., Warner J. D., Yager N., Gouillart E., Yu T., 2014, PeerJ, 2, e453
 Vapnik V. N., 1979, Estimation of Dependences Based on Empirical Data [in Russian]. Nauka, USSR
 Vegetti S., Koopmans L. V. E., 2009, MNRAS, 392, 945
 Walsh D., Carswell R. F., Weymann R. J., 1979, Natur., 279, 381
 Wayth R. B., Warren S. J., Lewis G. F., Hewett P. C., 2005, MNRAS, 360, 1333

Wiener N., 1964, Extrapolation, interpolation, and smoothing of stationary time series: with engineering applications. Technology press books in science and engineering, Technology Press of the Massachusetts Institute of Technology, <https://books.google.com.br/books?id=A6QgAAAAMAAJ>
 Willis J. P., Hewett P. C., Warren S. J., Dye S., Maddox N., 2006, MNRAS, 369, 1521
 Witt H. J., Mao S., Keeton C. R., 2000, ApJ, 544, 98
 de Jong J. T. A., Verdoes Kleijn G. A., Kuijken K. H., Valentijn E. A., 2013, Experimental Astronomy, 35, 25
 van der Walt S., et al., 2014, PeerJ, 2, e453

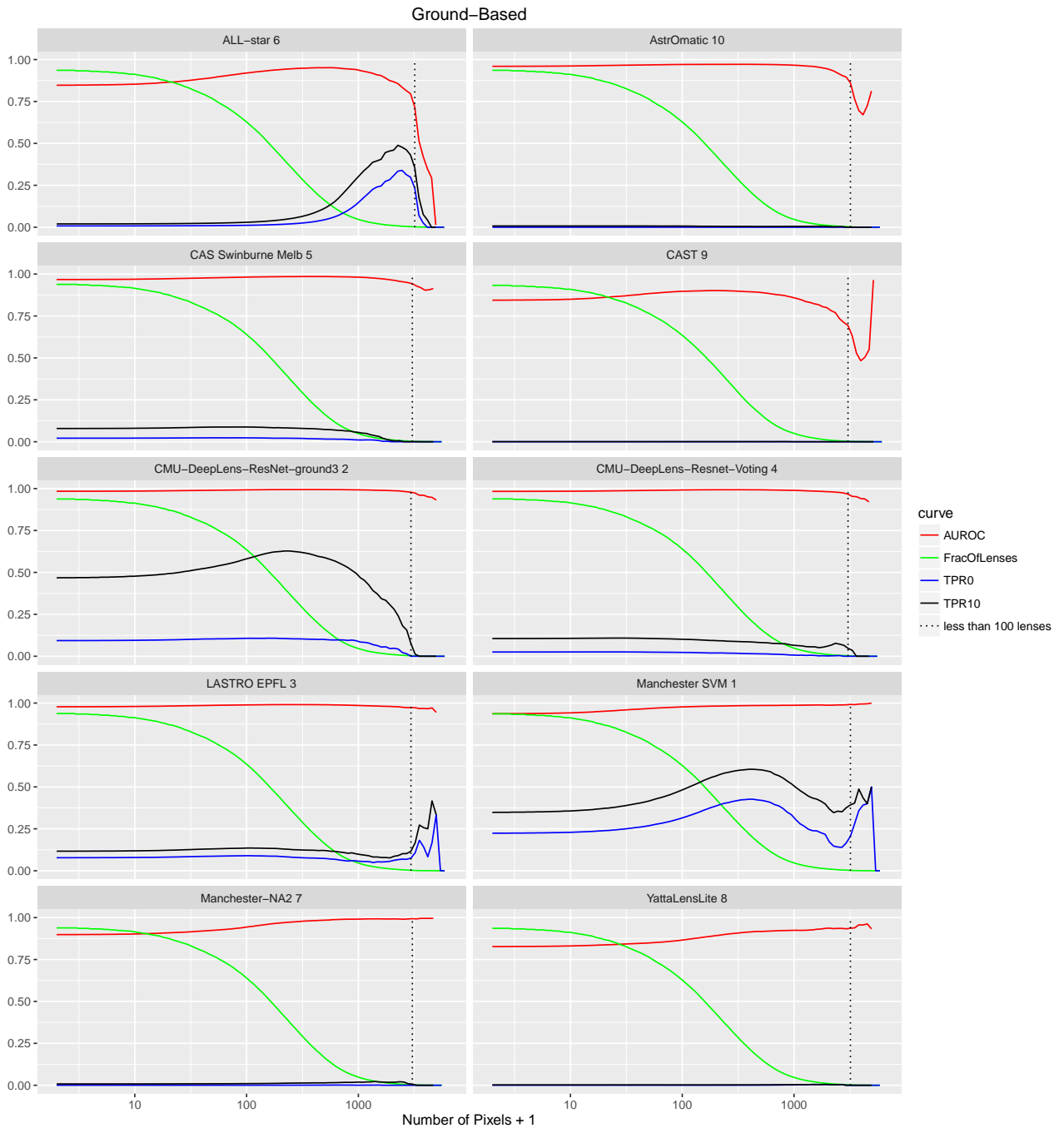


Fig. 13. Same as figure 12, but for ground-based entries.

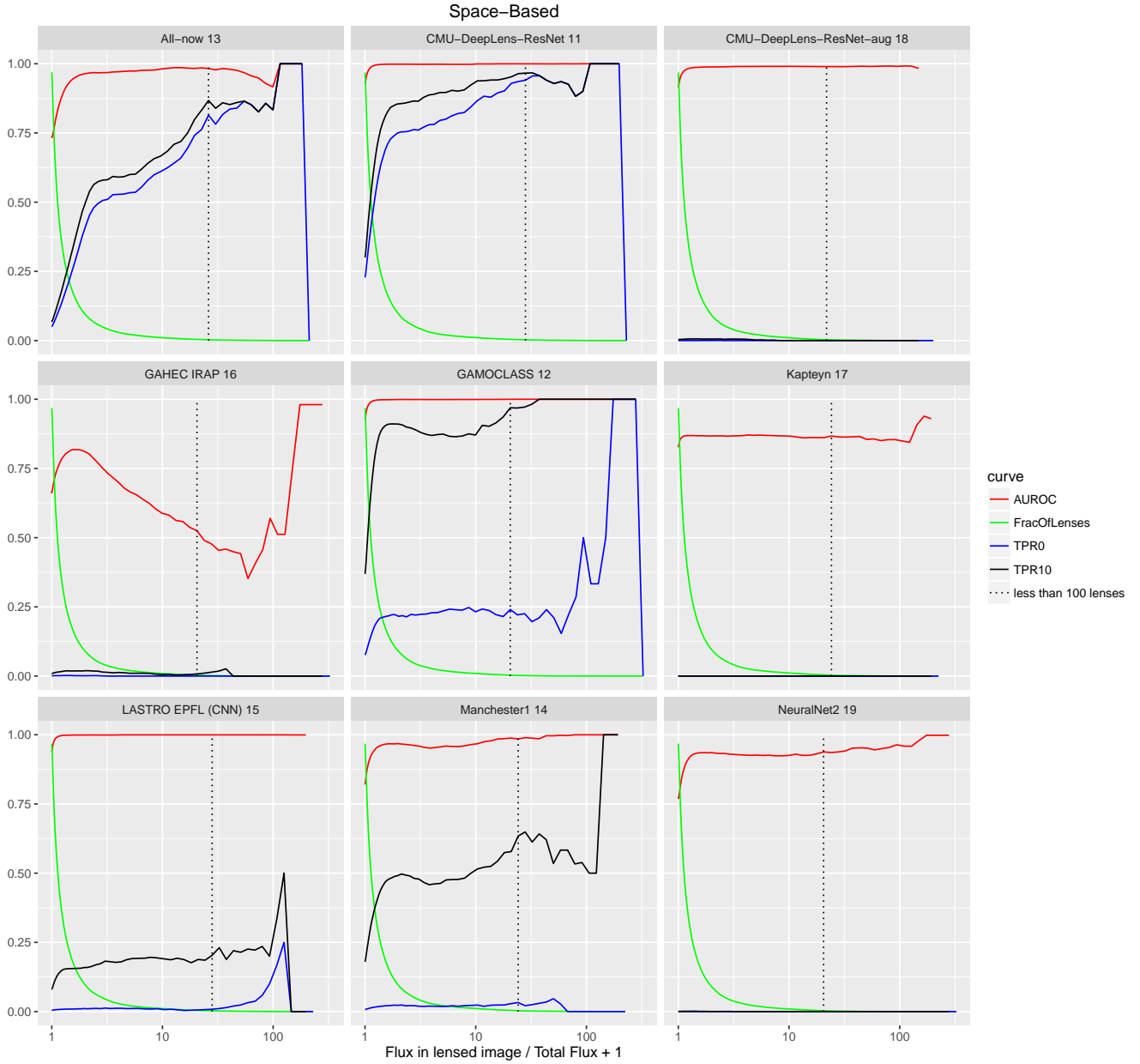


Fig. 14. Same as figure 14, but here the x-axis is the ratio of the flux coming from the lensed source to the total flux in the image in the index band. This is for the space-based test set.

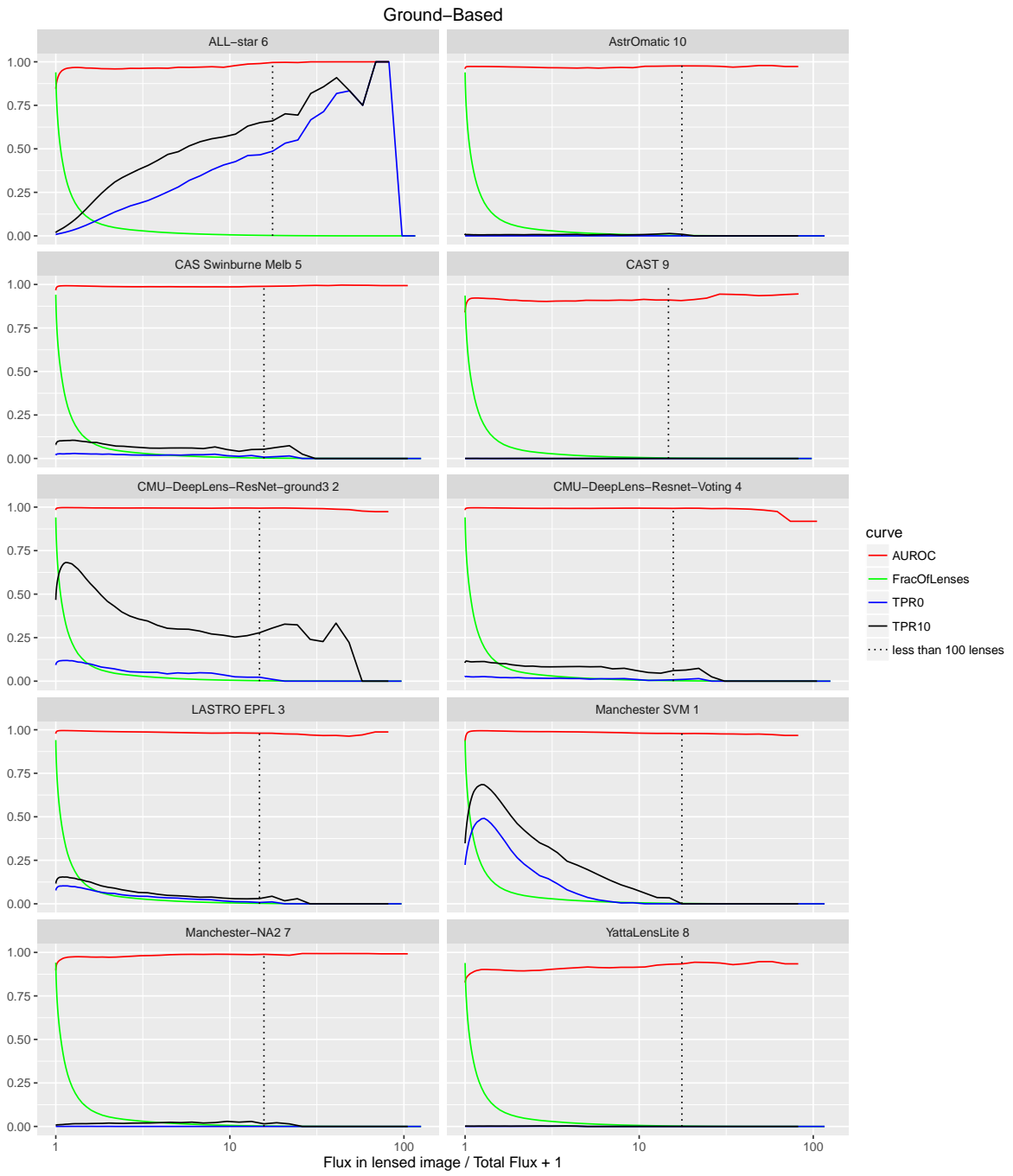


Fig. 15. Same as figure 14, but for ground-based entries.

3.2 Le Strong Lensing Legacy Survey

Cette section reproduit une série d'articles publiés sur les groupes détectés par lentillage gravitationnel dans le Canada-France-Hawaii Legacy Survey de 2007 à 2019. Ils couvrent la détection et l'étude générale de l'échantillon (Cabanac et al. 2007; More et al. 2012). Les modélisations détaillées des groupes ayant un suivi haute-résolution avec HST (Limousin et al. 2008; Muñoz et al. 2013; Foëx et al. 2013). Les analyses combinées des groupes ayant des observations spectroscopiques (Limousin et al. 2010; Verdugo et al. 2011, 2014; Gastaldello et al. 2014; Verdugo et al. 2016)

The CFHTLS strong lensing legacy survey

I. Survey overview and T0002 release sample[★]

R. A. Cabanac¹, C. Alard², M. Dantel-Fort², B. Fort³, R. Gavazzi⁴, P. Gomez⁵, J. P. Kneib⁶,
O. Le Fèvre⁶, Y. Mellier^{3,2}, R. Pello⁴, G. Soucail⁴, J. F. Sygnet³, and D. Valls-Gabaud^{1,4,7}

¹ Canada-France-Hawaii Telescope, 65-1238 Mamalahoa Hw., Kamuela, Hawaii 96743, USA
e-mail: cabanac@cft.hawaii.edu

² Observatoire de Paris, LERMA, CNRS-UMR8112, 61 avenue de l'Observatoire, 75014 Paris, France

³ Institut d'Astrophysique de Paris, CNRS-UMR7095 and Université Pierre et Marie Curie, 98bis boulevard Arago, 75014 Paris, France

⁴ Laboratoire d'Astrophysique de Toulouse-Tarbes, CNRS-UMR5572 and Université Paul Sabatier Toulouse III, 14 avenue Édouard Belin, 31400 Toulouse, France

⁵ Gemini Observatory Northern Operations Center, 670 N. A'ohoku Place, Hilo, Hawaii 96720, USA

⁶ Laboratoire d'Astrophysique de Marseille, traverse du Siphon, BP 8, 13376 Marseille Cedex 12, France

⁷ Observatoire de Paris, GEPI, CNRS-UMR8111, 5 place Jules Janssen, 92195 Meudon Cedex, France

Received 12 June 2006 / Accepted 5 September 2006

ABSTRACT

Aims. We present data from the CFHTLS Strong Lensing Legacy Survey (SL2S). Due to the unsurpassed combined depth, area and image quality of the Canada-France-Hawaii Legacy Survey it is becoming possible to uncover a large, statistically well-defined sample of strong gravitational lenses which spans the dark halo mass spectrum predicted by the concordance model from galaxy to cluster haloes.

Methods. We describe the development of several automated procedures to find strong lenses of various mass regimes in CFHTLS images.

Results. The preliminary sample of about 40 strong lensing candidates discovered in the CFHTLS T0002 release, covering an effective field of view of 28 deg² is presented. These strong lensing systems were discovered using an automated search and consist mainly of gravitational arc systems with splitting angles between 2 and 15 arcsec. This sample shows for the first time that it is possible to uncover a large population of strong lenses from galaxy groups with typical halo masses of about 10¹³ h⁻¹ M_⊙. We discuss the future evolution of the SL2S project and its main scientific aims for the next 3 years, in particular our observational strategy to extract the hundreds of gravitational rings also present in these fields.

Key words. gravitational lensing – surveys – cosmology: dark matter – galaxies: fundamental parameters – galaxies: clusters: general – galaxies: halos

1. Introduction

The observation of gravitational lensing effects produced by mass concentrations is a powerful tool to directly probe dark matter haloes and their interplay with visible mass (Schneider et al. 1992; Blandford & Narayan 1992; Miralda-Escude & Lehar 1992; Mellier 2002; Kneib et al. 2003). Both strong and weak lensing regimes are therefore widely used to explore the dark matter distribution properties, either from observations of individual cases (Warren et al. 1996; Cabanac et al. 2005; Willis et al. 2006) or from statistical analyses of large samples of lensed galaxies or quasars (for a comprehensive review Mellier & Meylan 2005).

On galaxy scales, ongoing lens surveys are now providing reliable descriptions of galaxies and a clearer understanding of the key issues regarding the star and dark matter distributions. As pointed out by Rusin et al. (2003) and Rusin & Kochanek (2005), using a large sample of well-studied strong lenses, it is possible to describe galaxy structure and the transition between the inner stellar matter-dominated and the outer dark matter-dominated galaxy haloes, without being sensitive to the mass-sheet degeneracy. It complements the galaxy-galaxy lensing methods that explore galaxy haloes on much larger scales (Hoekstra et al. 2004; Seljak et al. 2005). Detailed lens studies have led to an observational technique based on spectroscopic selection of compact lensing galaxy candidates (Hall et al. 2000; Hewett et al. 2000) that was fully exploited by Bolton et al. (2006); Treu et al. (2005); Koopmans et al. (2006) and Willis et al. (2006). Using the large spectroscopic data base of the SDSS, Bolton et al. (2006) have identified and studied a first set of 20 rings (which are merged compact multiple arc systems) among a total sample of 120 candidates. The first analysis of this Sloan Lens ACS (SLACS) data has provided a better description of the structural parameters of isolated galaxy lenses at low

[★] Based on observations obtained with MegaPrime/MegaCam, a joint project of CFHT and CEA/DAPNIA, at the Canada-France-Hawaii Telescope (CFHT) which is operated by the National Research Council (NRC) of Canada, the Institut National des Sciences de l'Univers of the Centre National de la Recherche Scientifique (CNRS) of France, and the University of Hawaii. This work is based in part on data products produced at TERAPIX and the Canadian Astronomy Data Centre as part of the Canada-France-Hawaii Telescope Legacy Survey, a collaborative project of NRC and CNRS.

redshift than multiply-imaged quasars (Treu et al. 2005; Koopmans et al. 2006). Moreover, their study of the fundamental plane of E/SO galaxies improves on earlier work (Kochanek et al. 2000) by combining a standard dynamical analysis with the strong lens constraints. This allows them to break the degeneracy between anisotropy of the stellar velocity tensor and the lens gravitational potential (for a similar approach Miralda-Escude 1995). They also showed that the lens galaxies of the SLACS sample nicely follow the E/S0 fundamental plane, being only slightly skewed towards the more massive objects. However, the SLACS is limited to small rings ($<3''$) by the aperture of the spectrograph fibers and to nearby lenses ($z_{\max}(\text{lens}) < 0.5$, $z_{\max}(\text{source}) < 0.8$; cutoff of the SDSS spectroscopic follow-up, and SLACS selection criteria). An extension of the method to larger redshifts should enlarge the sample significantly and will benefit from the higher efficiency of strong lensing at redshift ~ 0.5 for galaxy sources at redshift above 1. Such ongoing efforts by Willis et al. (2006) push $z_{\max}(\text{source}) < 1.3$.

Because clusters of galaxies are more complex systems than galaxies alone, it is not yet clear to what extent systematics, projection and selection effects hamper a reliable description of cluster size haloes. While the number of cluster-size haloes can in principle be derived from weak lensing studies (Hettterscheidt et al. 2005), the detailed description of the cluster halo structures and of their light versus mass distribution properties is still uncertain. Ground-based+HST observations and strong+weak lensing analyses of individual or samples of clusters of galaxies seem to indicate that more complex radial profiles (NFW like or power law with a flat core) than singular isothermal are required to fit the lensing data (Kneib et al. 2003; Gavazzi et al. 2003; Broadhurst et al. 2005). However for giant arcs in clusters of galaxies, large optically selected samples of strong lensing groups of galaxies are not available yet. The Red-sequence Cluster Survey (Gladders et al. 2003) is a first attempt to systematically find strong lensing around clusters and groups of galaxies. But their relatively low detection sensitivity has led to the discovery of only eight cluster-like structures at $z > 0.64$ over a 90 sq. degree field.

A key issue is to understand the transition between galaxy-scale to cluster-scale halo structures. Quasar lenses and gravitational arcs have mostly probed two regimes of halo masses: galaxies and clusters of galaxies, but bring only weak constraints on the intermediate mass range ($10^{12} - 10^{14} M_{\odot}$) which is important for the assembly of large scale structures (Kochanek et al. 2001; Grant et al. 2004; Fassnacht et al. 2005; Mathews et al. 2005; Oguri 2006). The study of groups of galaxies in the CNOC survey using weak lensing by Parker et al. (2005) yielded the first constraints of their averaged mass-to-light ratios but nothing on their inner structures or on whether groups are self-similar.

In summary, no homogeneous sample of strong lenses have been built so far that covers the full dark matter halo mass spectrum because of the lack of a large, deep sky survey with a sub-arc-second seeing. We will demonstrate here that with the CFHT Legacy Survey (CFHTLS), due to its combined depth, area and image quality of the data, we are able to find strong lensing systems around a wide mass spectrum of structures. Indeed, the three $7 \times 7\text{-deg}^2$ wide patches together with the four $1 \times 1\text{-deg}^2$ deep patches of CFHTLS allow us to build up a large sample of strong galaxy-, group-, and cluster-scale lenses with a well-defined selection function and sampling variance, as well as to explore halo properties at different depths and redshifts.

In order to do this, a set of automated procedures has been developed to detect various types of strong lensing events. It has been successfully tested on the T002 release. We present in this

paper a preliminary sample built with these selection procedures. Although these procedures are not yet fully optimized, we can nevertheless uncover within the CFHTLS a large population of “group lenses”, a new class of lenses with multiple image separation of 2 to $7''$. We also show that it is possible to implement a dedicated procedure to recover gravitational rings with Einstein radii below $2''$. The CFHTLS Strong Lensing Legacy Survey (SL2S) should allow us to extract the whole lensing mass spectrum from galaxies to clusters of galaxies, in a homogeneous and statistically well-defined procedure.

The paper is organized as follows: Sect. 2 summarizes the present state of the CFHTLS and the data used in this preliminary study. Section 3 presents the SL2S project itself with a brief discussion of the automated search procedures, as well as the first results obtained for group lenses. A full description of the selection procedures will be provided elsewhere. Sections 4 and 5 discuss the future of the project.

Throughout the paper we use a flat Λ CDM cosmology ($\Omega_m = 0.3$, $\Omega_{\Lambda} = 0.7$), all observables are computed with $H_0 = 70 h \text{ km s}^{-1} \text{ Mpc}^{-1}$ and magnitudes are given in the AB system unless specified otherwise.

2. The Canada-France-Hawaii telescope legacy survey

2.1. Description

The Canada-France-Hawaii Telescope Legacy Survey (CFHTLS) is a major photometric survey of more than 450 nights over 5 years (started on June 1st, 2003) using the wide field imager MegaPrime which covers ~ 1 square degree on the sky, with a pixel size of $0.186''$. The project is comprehensively described in <http://www.cfht.hawaii.edu/Science/CFHTLS/> and links therein. The CFHTLS has two components aimed at extragalactic studies: a very Deep component made of 4 pencil-beam fields of 1 deg^2 and a Wide component made of 3 mosaics covering 170 deg^2 in total, both in 5 broadband filters. The data are pre-reduced at CFHT with the Elixir pipeline¹ which removes the instrumental artefacts in individual exposures. The CFHTLS images are then evaluated, astrometrically calibrated, photometrically inter-calibrated, resampled and stacked by the Terapix group at the Institut d’Astrophysique de Paris (IAP) and finally archived at the Canadian Astronomy Data Centre (CADC). Terapix also provides weightmap images, quality assessments meta-data for each stack as well as mask files that mask straylight, saturated stars and defects on each image. The preliminary SL2S sample presented here is based on the T002 release (July 2005), corresponding to data obtained between June 1st, 2003 and Nov. 22nd, 2004. A detailed description of this release is given at the Terapix web site <http://terapix.iap.fr> and the Terapix T002 release document (Mellier et al 2005: <http://terapix.iap.fr/IMG/pdf/Newterapixdoc.pdf>). The T002 release includes 40 stacked fields in the Wide survey observed in broadband g' , r' and i' filters, and a stack of the 4 Deep fields in the 5 bands, for a total area of 44 deg^2 , or ca. 28 deg^2 of unmasked area, i.e. area not contaminated by instrumental artefacts from bright stars (internal reflections, bleeding). Table 1 summarizes the main characteristics of the data used in the paper. The 4 Deep fields are much deeper, with an average seeing ranging from $1.0''$ in u^* to $0.85''$ in z' . The Wide survey is presently available in 3 filters only with an

¹ <http://www.cfht.hawaii.edu/Instruments/Elixir/>

Table 1. CFHTLS: Terapix T0002 release (July 2005).

Deep fields	Magnitudes Limits ¹				
	u^*	g'	r'	i'	z'
D1	26.4	26.3	26.1	25.9	24.9
D2	26.1	25.8	25.8	25.4	24.3
D3	25.8	26.3	26.3	25.9	24.7
D4	26.2	26.3	26.3	25.7	24.9
Wide fields	Average Magnitudes Limits ¹				
W1	–	25.5	24.5	24.5	–
W2	–	25.4	24.7	24.6	–
W3	–	25.7	25.0	24.6	–
W1 area (unmasked)	20 (11.4) deg ²				
W2 area (unmasked)	8 (5.0) deg ²				
W3 area (unmasked)	12 (9.0) deg ²				

¹ 50% completeness limit in AB mag (AB to Vega $u^* - 0.35$, $g' + 0.09$, $r' - 0.17$, $i' - 0.40$, $z' - 0.55$).

average seeing of $1.0''$ in g' and $0.9''$ in r' and i' . But not surprisingly, the Wide survey is more suited to our strong lensing selection processes, because of its wide angular coverage.

2.2. Strong lensing number predictions

In this paper we call a *ring* any compact system of arcs where multiple images merge into a single ring-like image surrounding the deflector; all other types of multiple systems are either called (giant) *arcs* or *arcllets*. The previous observations of QSO lenses and the results from the most recent simulations (lensing optical depths) give good estimates of number densities of lenses associated at various deflecting halo masses (i.e. for splitting angles) (Oguri 2006, Figs. 9 and 10, and Table 1). Typically, for any giant arc detected in a cluster, we expect about 4 times more arc(et)s systems in haloes corresponding to group masses, and 20 times more gravitational rings associated with lens galaxy haloes (assuming equivalent detection limit and angular magnification factor in all cases). We will see below that the preliminary number of group-lenses, based on the first (beta) version of the arc detection software, is found to be $\sim 0.5 \text{ deg}^{-2}$ in the CFHTLS data. Extrapolating Oguri's distribution to the total area of the CFHTLS Wide component (170 deg²) yields ~ 75 group arcs, ~ 400 galaxy rings, and ~ 20 cluster arcs. The number of lenses will be very small per Megacam field whatever the deflector mass regime (cluster, group or galaxy). Their detection is therefore very challenging as the lensed features are hidden within a huge number of faint background galaxies. The only way to find them efficiently is to use well-defined automated procedures (e.g. see Lenzen et al. 2004). In practice such an approach has already been proposed for some large numerical simulations of lensing configurations, mostly in simulated samples of clusters of galaxies (Horesh et al. 2005).

3. Automated software for strong lensing candidate detection

One of the goals of the SL2S is to provide a complete and homogeneous sample of strong lenses with known detection efficiency with regard to a series of observational parameters. This goal requires us not only to develop a comprehensive series of simulations taking into account the most common biases such as seeing, PSF variation, crowding, limiting magnitude, surface brightness, and arc length/radius/thickness distribution, but also

requires us to automate the detection procedures. We are thus currently developing three complementary algorithms covering various regimes of strong lensing. The first one is a gravitational *ARC* detector (mostly for groups and clusters). The second is a detector of compact *RING* candidates (which will then require either spectroscopic or higher resolution images for confirmations). The third one is a *MULTIPLY* detector, aimed at detecting peculiar and rare multiple arclet systems that cannot be recognized by the *ARC* detector. This includes badly resolved multiple image systems or configurations which may form in potential saddles. The software selects multiple image configurations based only on generic properties like color, distance, flux ratio and shear orientation, if any, and the geometric distribution of multiple images. However we have not yet been able to optimize this procedure on ground-based images so the *MULTIPLY* detector will not be addressed further.

3.1. ARC detector

Giant arcs are in principle the most straightforward images to identify and detect through direct pattern recognition (Lenzen et al. 2004; Seidel & Bartelmann 2006). They are known to occur around massive clusters ($>10^{14} h^{-1} M_{\odot}$) and show radii up to $\sim 40''$ in very luminous X-ray clusters (see for example the spectacular case of A 1689 Broadhurst et al. 2005). When arcs appear around groups of galaxies, their radii are five to ten times smaller and the seeing makes them more difficult to identify from ground-based imaging. A full description of the technique overcoming this difficulty is given in Alard (2006). Briefly, the arc-detector algorithm detects elongated structures and analyzes the local properties of these structures. Elongated objects are defined as very narrow objects along one direction with a width nearly equal to the size of the seeing. We model the elongated arc(let)s structures as small rectilinear objects having the width of the seeing along one direction, and 3 times this width in the other direction. This condition sets the detection threshold below an Einstein radius of $3''$ for an arc angular aperture of about 60° . Each object in the image is decomposed in a series of contiguous elements aligned along the tangential direction of the elongated structure. The full object is re-constructed by associating the areas covered by the different elements. Once a set of pixels is associated with the object, we compute its general properties, size, color, curvature, etc. To ease the pattern recognition the routine also requires both the $g' - i'$ color and surface brightness of the elongated objects to be constant. Finally we produce a catalogue of candidates and a set of associated color images for visual inspection according to a selected set of parameters that fully describes the detection procedure.

The *ARC* detector is very efficient at detecting extremely faint arcs over a large range of splitting angles and will be used in subsequent CFHTLS releases (cf. Table 2).

3.2. RING detector

The ring detector is aimed at detecting compact rings around centers of isolated galaxies ($<10^{13} h^{-1} M_{\odot}$). Most of the ring radii are in the range $0.5\text{--}2.0''$ and rings are usually hidden within the deflector. Seeing and intrinsic galaxy morphologies, like dust lanes and face-on spirals, make the ring detection challenging. We use an “object-oriented” routine, *RING*, that will be described in a future paper (Gavazzi et al., in preparation). Presently, we focus on the 4 Deep fields that have been observed in 5 filters and for which photometric redshift catalogs

Table 2. CFHTLS-SL2S Terapix T0002 release (July 2005).

Name	RA (J2000) h min s	Dec (J2000) ° ' ''	u^*	g'	AB mag ^d r'	i'	z'	Arc radius ^b arcsec	z_{ens}^c	Comments ^d
SL2SJ021258-051809	02 12 58.114	-05 18 09.17	21.86 ± 0.02	20.73 ± 0.01	19.51 ± 0.01	18.77 ± 0.01	18.42 ± 0.01	1.8 ± 0.2	0.650	W1 (2) arc
SL2SJ021301-043605	02 13 01.862	-04 36 05.46	23.93 ± 0.07	21.47 ± 0.01	20.29 ± 0.01	18.96 ± 0.01	18.41 ± 0.01	3 ± 0.5	0.650	W1 (2) arc
SL2SJ021308-053726	02 13 08.693	-05 37 26.11	21.96 ± 0.03	20.12 ± 0.01	18.87 ± 0.01	18.33 ± 0.01	17.97 ± 0.01	2.5 ± 0.3	0.300	W1 (2) vis
SL2SJ021311-041015	02 13 11.261	-04 10 15.98	24.98 ± 0.31	23.82 ± 0.09	23.10 ± 0.07	22.35 ± 0.04	22.14 ± 0.09	2.4 ± 0.1	0.725	W1 (2) arc
SL2SJ021408-053532	02 14 08.038	-05 35 32.30	22.67 ± 0.04	20.97 ± 0.01	19.58 ± 0.01	18.83 ± 0.01	18.43 ± 0.01	6 ± 1	0.495	W1 (1) arc
SL2SJ021411-040502	02 14 11.212	-04 05 02.90	23.02 ± 0.06	22.20 ± 0.02	21.04 ± 0.01	19.95 ± 0.01	19.54 ± 0.01	1.7 ± 0.1	0.735	W1 (1) arc
SL2SJ021416-050315	02 14 16.579	-05 03 15.51	23.23 ± 0.06	22.25 ± 0.02	21.26 ± 0.01	20.75 ± 0.01	20.29 ± 0.01	2.8 ± 0.3	0.300	W1 (1) arc
SL2SJ021613-061858	02 16 13.991	-06 18 58.91	22.61 ± 0.06	21.92 ± 0.02	20.97 ± 0.02	19.88 ± 0.01	19.54 ± 0.01	1.2 ± 0.1	0.750	W1 (2) arc
SL2SJ021737-051329	02 17 37.232	-05 17 37.232	22.23 ± 0.03	21.37 ± 0.01	20.62 ± 0.01	19.68 ± 0.01	19.17 ± 0.01	1.4 ± 0.1	0.67	W1 (1) arc
SL2SJ021807-051536	02 18 07.440	-05 15 36.16	23.48 ± 0.08	22.82 ± 0.03	22.18 ± 0.03	21.60 ± 0.02	21.10 ± 0.02	2.7 ± 0.5	0.70	W1 (1) arc
SL2SJ021932-053135	02 19 32.029	-05 31 35.46	26.08 ± 0.79	23.97 ± 0.06	22.24 ± 0.03	21.16 ± 0.01	20.81 ± 0.04	3.5 ± 0.3	0.755	W1 (2) arc
SL2SJ021956-052759 ^e	02 19 56.409	-05 27 59.08	21.58 ± 0.03	20.48 ± 0.01	19.30 ± 0.01	18.71 ± 0.01	18.45 ± 0.01	2.7 ± 0.1	0.5	W1 (1) arc
SL2SJ022315-062904	02 23 15.303	-06 29 04.92	22.59 ± 0.07	22.32 ± 0.01	20.11 ± 0.01	19.22 ± 0.01	18.91 ± 0.01	2.5 ± 0.3	0.95	W1 (1) arc
SL2SJ022345-042402	02 23 45.401	-04 24 02.16	21.14 ± 0.01	19.70 ± 0.01	18.57 ± 0.01	17.99 ± 0.01	17.71 ± 0.01	3 ± 1	0.495	W1 (2) arc
SL2SJ022532-045100	02 25 31.990	-04 51 00.22	21.60 ± 0.01	20.94 ± 0.01	20.61 ± 0.01	19.44 ± 0.01	19.11 ± 0.01	2.0 ± 0.2	0.495	D1 (2) vis/ring
SL2SJ022914-065940	02 29 14.265	-06 59 40.36		22.20 ± 0.03	21.07 ± 0.02	19.96 ± 0.01		1.9 ± 0.1	0.900	W1 (2) arc
SL2SJ023011-055023	02 30 11.647	-05 50 23.64		19.65 ± 0.01	18.17 ± 0.01	17.51 ± 0.01		3.0 ± 0.5	0.575	W1 (2) arc
SL2SJ085446-012137 ^f	08 54 46.000	-01 21 37.000		20.00 ± 0.01	18.44 ± 0.01	18.00 ± 0.01		4.9 ± 0.2	0.35	W2 (1)
SL2SJ090407-005952	09 04 07.915	-00 59 52.75		21.28 ± 0.02	20.44 ± 0.01	19.44 ± 0.01		1.9 ± 0.1	0.750	W2 (1) arc
SL2SJ100009+022455	10 00 09.700	+02 24 55.00	23.89 ± 0.05	21.63 ± 0.01	20.22 ± 0.01	19.42 ± 0.01	19.23 ± 0.01	2.4 ± 0.2	0.505	D2 (2) arc
SL2SJ100012+022015	10 00 12.600	+02 20 15.00	23.22 ± 0.05	21.37 ± 0.01	19.89 ± 0.01	19.24 ± 0.01	18.94 ± 0.01	0.6 ± 0.1	0.284	D2 (1) vis
SL2SJ100013+022249	10 00 13.900	+02 22 49.00	22.58 ± 0.05	20.55 ± 0.01	19.19 ± 0.01	18.57 ± 0.01	18.29 ± 0.01	1.6 ± 0.1	0.256	D2 (1) vis
SL2SJ100018+023845 ^g	10 00 18.400	+02 38 45.00	>26.1	25.68 ± 0.28	23.59 ± 0.05	22.75 ± 0.03	22.43 ± 0.07	1.3 ± 0.1	0.6?	D2 (1) vis
SL2SJ100056+021226	10 00 56.700	+02 12 26.00	22.69 ± 0.04	20.75 ± 0.01	19.30 ± 0.01	18.64 ± 0.01	18.32 ± 0.01	1.9 ± 0.1	0.256	D2 (1) vis
SL2SJ100148+022325	10 01 48.100	+02 23 25.00	22.98 ± 0.05	20.97 ± 0.01	19.47 ± 0.01	18.83 ± 0.01	18.52 ± 0.01	1.6 ± 0.2	0.284	D2 (1) vis
SL2SJ100208+021422	10 02 08.500	+02 14 22.00	23.90 ± 0.08	22.03 ± 0.01	20.63 ± 0.01	19.99 ± 0.01	19.65 ± 0.01	1.7 ± 0.2	0.256	D2 (1) vis
SL2SJ100211+021139 ^h	10 02 11.200	+02 11 39.00	25.56 ± 0.33	24.12 ± 0.07	22.37 ± 0.02	21.08 ± 0.01	20.29 ± 0.01	3.4 ± 0.2	0.54	D2 (1) vis
SL2SJ100216+022955	10 02 16.800	+02 29 55.00	27.05 ± 1.27	22.88 ± 0.03	21.28 ± 0.01	20.11 ± 0.01	19.68 ± 0.01	1.7 ± 0.2	0.52	D2 (1) vis
SL2SJ100221+023440	10 02 21.100	+02 34 40.00	23.57 ± 0.06	21.57 ± 0.01	20.06 ± 0.01	19.39 ± 0.01	19.05 ± 0.01	0.6 ± 0.2	0.256	D2 (1) vis
SL2SJ141447+544703 ^h	14 14 45.498	+54 47 00.03		21.35 ± 0.03	19.59 ± 0.01	18.33 ± 0.01		14 ± 1	0.75	W3 (1) vis/arc
SL2SJ141558+523955	14 15 58.182	+52 39 55.92		21.45 ± 0.01	19.77 ± 0.01	18.60 ± 0.01		4.6 ± 0.2	0.75	W3 (1) vis/arc
SL2SJ141807+524924	14 18 07.966	+52 49 24.28	22.42 ± 0.04	20.43 ± 0.01	19.00 ± 0.01	18.39 ± 0.01	18.08 ± 0.01	4 ± 0.5	0.256	D3 (2) vis

^a AB mag as given in the official release, SExtractor Best Magnitudes, (AB to Vega $u^* - 0.35$, $g' + 0.09$, $r' - 0.17$, $i' - 0.40$, $z' - 0.55$).

^b Arc radii are computed from LensTool program (Kneib 2001).

^c z_{ens} : Best photometric redshift given by HyperZ, taking into account all available filters and $E(B - V)$ (Pello 2006, priv. comm.).

^d Comments: CFHTLS component, Numbers refer to: (1) Good quality candidate based on visual inspection (2) Potential candidate based on visual inspection, Detection method: arc = arc detector,

^e vis = visual, ring = ring detector.

^f The bright arc of this candidate is around a secondary peak (Fig. 2). If confirmed, it is a good example of an enhanced convergence in a dense field with presence of sub-halos.

^g Massive cluster lens.

^h Compact and red candidate (u dropouts) in the field of COSMOS. Its photometric redshift is not well-constrained because the source contaminates the deflector. For SL2S100018, the source has

a best $z_{\text{phot}} \sim 4.2$.

ⁱ Massive system with a bright radial arc.

Table 2. continued.

Name	RA (J2000) h min s	Dec (J2000) ° ' "	u^*	g'	r'	i'	z'	Arc radius ^b arcsec	z_{lens}^c	Comments ^d
SL2SJ141912+532612 ⁱ	14 19 12.000	+53 26 12.00	22.27 ± 0.02	20.94 ± 0.01	19.56 ± 0.01	20.02 ± 0.01	10–17 ± 0.5	0.65	W3 (1) vis/arc	
SL2SJ142028+521303	14 20 28.799	+52 13 03.54	22.51 ± 0.03	20.65 ± 0.01	20.26 ± 0.01	20.02 ± 0.01	2.7 ± 0.3	0.344	W3 (2) arc	
SL2SJ142031+525822 ^j	14 20 31.811	+52 58 22.16	22.53 ± 0.04	20.95 ± 0.01	19.48 ± 0.01	18.48 ± 0.01	1.7 ± 0.2	0.300	D3 (1) vis	
SL2SJ142032+530107	14 20 32.147	+53 01 07.13	22.98 ± 0.04	22.20 ± 0.01	21.58 ± 0.01	20.44 ± 0.01	1.6 ± 0.2	0.74	W3 (2) vis	
SL2SJ142057+530843 ^j	14 20 57.684	+53 08 43.81	>25.8	>26.3	25.92 ± 0.53	23.23 ± 0.06	8.0 ± 1.0	0.622	D3 (2) vis	
SL2SJ142207+531013	14 22 07.611	+53 10 13.88	21.46 ± 0.01	20.64 ± 0.01	19.87 ± 0.01	19.40 ± 0.01	1.5 ± 0.2	0.310	D3 (2) ring	
SL2SJ142209+524652	14 22 09.268	+52 46 52.42	21.15 ± 0.01	19.87 ± 0.01	18.75 ± 0.01	17.99 ± 0.01	3.5 ± 0.5	0.189	D3 (1) vis	
SL2SJ142258+512440	14 22 58.343	+51 24 40.79	22.83 ± 0.02	21.77 ± 0.03	20.89 ± 0.01	19.99 ± 0.01	1.9 ± 0.1	0.87	W3 (2) arc	
SL2SJ143001+554647 ^k	14 30 01.000	+55 46 47.00	21.93 ± 0.02	20.59 ± 0.01	19.70 ± 0.01	19.70 ± 0.01	5.5 ± 1	0.695	W3 (1) vis/arc	
SL2SJ143140+553323	14 31 40.000	+55 33 23.00	21.81 ± 0.02	20.09 ± 0.01	19.45 ± 0.01	19.45 ± 0.01	3.1 ± 0.7	0.655	W3 (1) vis	
SL2SJ143141+513143	14 31 41.829	+51 31 43.71	22.86 ± 0.02	21.38 ± 0.02	20.46 ± 0.01	20.46 ± 0.01	3.9 ± 0.2	0.85	W3 (1) arc	

^a AB mag as given in the official release, SExtractor Best Magnitudes, (AB to Vega $u^* - 0.35$, $g' + 0.09$, $r' - 0.17$, $i' - 0.40$, $z' - 0.55$).

^b Arc radii are computed from LensTool program (Kneib 2001).

^c z_{lens} : Best photometric redshift given by HyperZ, taking into account all available filters and $E(B - V)$ (Pello 2006, priv. comm.).

^d Comments: CFHTLS component, Numbers refer to: (1) Good quality candidate based on visual inspection (2) Potential candidate based on visual inspection, Detection method: arc = arc detector,

vis = visual, ring = ring detector.

ⁱ Other name RCS1419.2+5326 ($z_{\text{spectro}} = 0.64$; Gladders et al. 2003), HST imaging available in F814W; HST proposal 10626, PI Loh. This system shows at least three arcs at 10, 14.5, and 17".

^j HST imaging available in F606W and F814W from the Groth Strip Survey (Simard et al. 2002; Vogt et al. 2005), probably a tidal tail.

^k Massive cluster lens with fold arc.

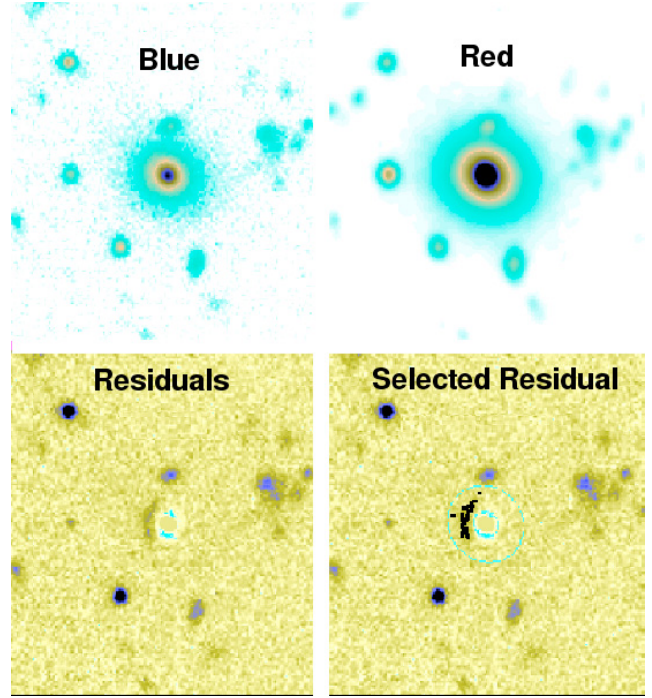


Fig. 1. Schematics of the ring detection procedure (here SL2SJ100013+022249). The candidates are selected from CFHTLS ellipticals (top). $g' - i'$ color images reveal strong residual signal (bottom).

are built. These catalogs include a photometric redshift estimate, the best fit spectral type and information on the absolute magnitudes in different spectral bands. Selecting all objects catalogued as E/S0 galaxies, the routine filters out the large scale light distribution of the deflectors, using $g' - \alpha \times i'$ color vignettes. When the profile of the potential deflector does not depend much on color, or when the deflector profile is smooth on large scales, the deflector is subtracted cleanly and any residual comes from a superimposed smaller-scale anisotropy. The routine selects the lens candidates based on the computed residuals above sky noise in the range 0.8–2.5" (Fig. 1). We are currently optimizing the method with a sample of 10 lens candidates common to the COSMOS field and the CFHTLS-D2 field. The first results are encouraging: most of the rings with radii larger than 0.8" seem to be recovered. However the method has two limitations. First, any ring candidate smaller than the seeing radius is lost. Second, the procedure is a good filtering method, efficient in removing massive ellipticals that are not lenses, but still produces false candidates among S0 galaxies. Therefore a final eyeball selection is currently still required to select good candidates.

The resulting candidates will need confirmation by spectroscopic identification of both the redshift of the lens and the lensed galaxy. In addition, high-resolution spectroscopy will help determine to the lens stellar velocity dispersion, and higher resolution images, using for example the *Hubble Space Telescope*, will allow us to address the lens modelling with high accuracy. Thus, the method is mostly able to select, among a large number of massive ellipticals, a small sample of good strong lensing candidates.

3.3. Lens modelling

A large number of algorithms of gravitational lens modelling are available (e.g. Kneib et al. 1993; Saha & Williams 1997;

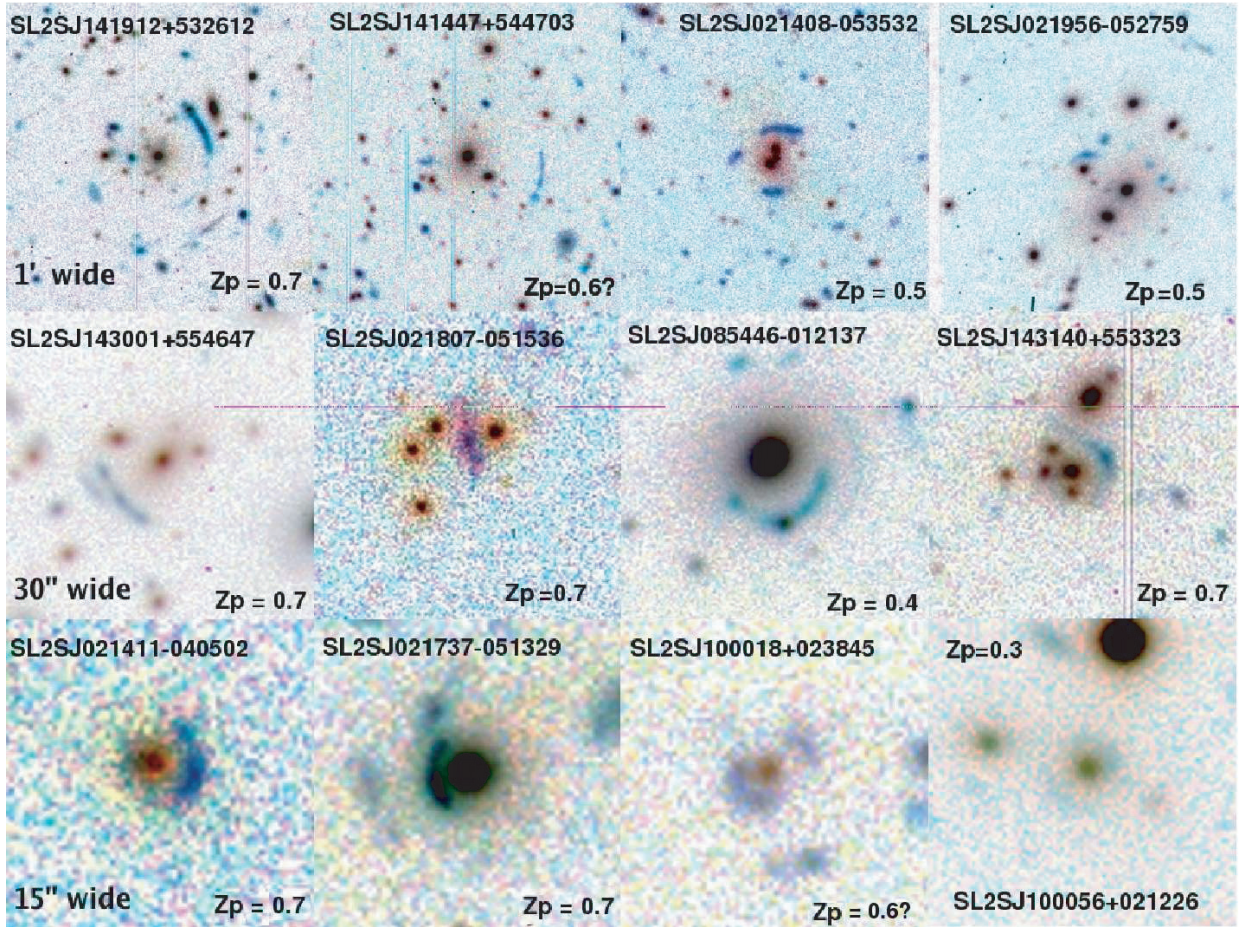


Fig. 2. RGB ($i'g'u^*$) mosaic of SL2S candidates showing the three regimes probed by the sample. Top examples show $1'$ -wide vignettes of SL2S cluster lenses ($>10^{13} h^{-1} M_{\odot}$). Middle examples show $30''$ -vignettes of SL2S intermediate mass lenses (galaxy groups; $\sim 10^{13} h^{-1} M_{\odot}$). Bottom line shows $15''$ -wide vignettes of Einstein rings around single galaxy lenses ($<10^{13} h^{-1} M_{\odot}$). The estimated photometric redshift for the deflector is marked.

Keeton 2001; Warren & Dye 2003; Brewer & Lewis 2006). It is clearly beyond the scope of this paper to review them. Our team has developed many parametric and non-parametric codes, using a variety of optimization algorithms to model the full spectrum of the mass regimes, therefore mostly adapted to the CFHTLS-SL2S sample.

4. Preliminary sample from the T0002 release

4.1. Description of the sample

The preliminary analysis of the CFHTLS T0002 release led to the discovery of 43 candidate strong lenses listed in Table 2. Most of the CFHTLS-SL2S candidates that we present here were extracted using the arc detector, which turned out to be very efficient irrespective of the arc size or the lens environment. The list also contains 10 rings first identified in the COSMOS field and then recovered in the CFHTLS-D2 data. Hence, this preliminary sample is considered a feasibility study for the SL2S project, demonstrating that a wide mass range will be uncovered by the CFHTLS-SL2S. This sample should not be used for quantitative statistical studies.

In the current selection process, the automated software extracts a list of candidates and creates color images of each of them for subsequent visual inspection. The SL2S database (<http://www.cfht.hawaii.edu/~cabanac/SL2S/>) is presently under construction and includes for each

system the magnitudes of the lens, its photometric redshift estimates, using either the latest version of the HyperZ code (Bolzonella et al. 2000), or LePhare, a code based on a Bayesian approach (Ilbert et al. 2006). A few geometrical properties for the lensed source (arc radius, magnitudes when known) are also included. Table 2 summarizes these measurements for our preliminary sample.

4.2. Global properties of the sample

Although this sample is not yet complete, we already see three classes, split according to their arc radius, hence to their mass regime. A detailed mass classification will only be possible when spectroscopic redshifts of the lenses and the sources are known, and when high-resolution imaging yields accurate lens modeling.

- The most conspicuous class includes giant arcs with radii $>7''$. In the T0002 release sample, this class contains 4 candidates, detected over an effective area of 28 sq. degrees. By simple extrapolation, one can expect to find about 15–20 of these giant arcs in the complete CFHTLS 170 deg^2 (equivalent to about 100 deg^2 unmasked clear sky). The top line of Fig. 2 mosaic shows the 4 giant arcs with arc radii $>7''$. Usually such features appear in massive clusters often associated with strong X-ray emission.

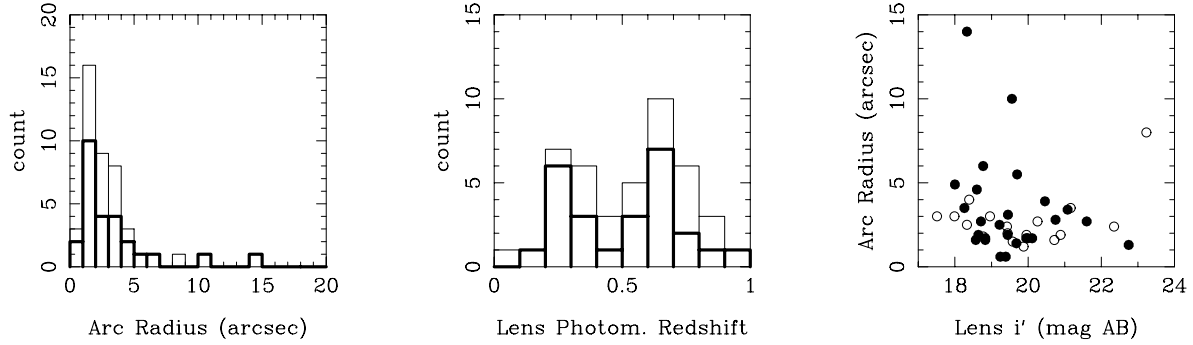


Fig. 3. T0002 release sample basic characteristics: Arc radius histogram (*left*), deflector/lens redshift histogram (*middle*). Arc radius versus central galaxy i' magnitude of the deflector/lens (*right*). Thick lines and filled circles correspond to quality 1 candidates. Thin lines and open circles correspond to quality 2 candidates (cf. text and Table 2).

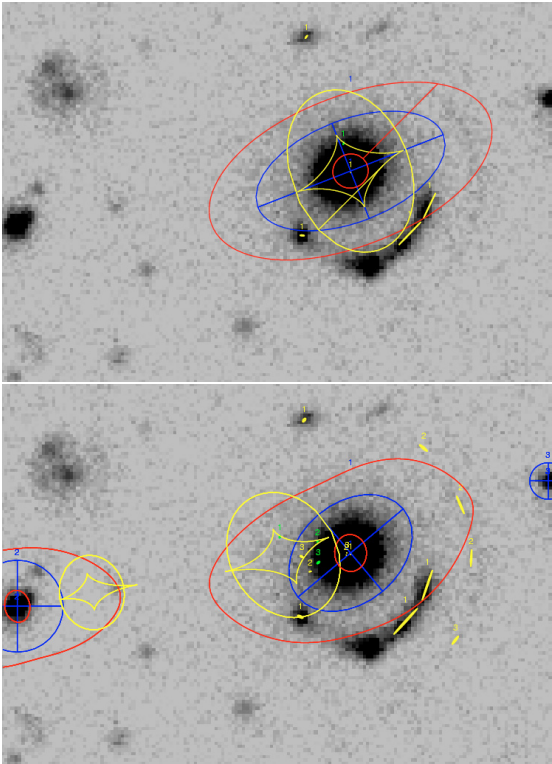


Fig. 4. *Top*: simple modelling of SL2SJ085446-012137 using LensTool (Kneib 1993, <http://www.oamp.fr/cosmology/lenstool/>) where only the central galaxy is used as a deflector. The source near the upper cusp of the radial critical line divides into 4 virtual images, three on the south half and one in the north. *Bottom*: same lens with a more complex modelling including surrounding galaxies as potential sources of shear. High-resolution imaging and surface brightness information will allow one to remove part of the degeneracy of lens models.

galaxy, or of rings around an isolated elliptical galaxy. As an illustration, Fig. 4 shows the possible influence of the external shear due to group members on the main arc modeling for the lens SL2SJ085446-012137. Only HST imaging will allow us to reduce these degeneracies.

- The third class is made up of compact ring candidates commonly associated with isolated galaxies, with ring radii $< 3''$. This class is expected to be the most populated one. If we follow Oguri's predictions (2006) we expect the presence of about 100 rings in the T0002 Wide survey release by a simple scaling between the intermediate mass lenses and the galaxy mass lenses. If we exclude the 10 rings identified in the COSMOS field (D2) using HST imaging and detected a posteriori in the CFHTLS data, there are only 12 extra candidates detected in our sample. This shows that appropriate detection of ring candidates is not yet fully operational and requires more developments and tests, along the lines described in Sect. 3.2. The bottom line of Fig. 2 shows a selection of the few compact arc or ring candidates already identified.

The photometric redshift histograms of the deflectors of the total sample (thin line) and almost undisputable candidates (thick line) (Fig. 3) show a wide distribution up to $z \sim 1$. Ilbert et al. (2006) claim that LePhare Bayesian photometric redshifts are accurate to $\sigma_{\Delta z} \sim 0.05$, with only 4% of so-called catastrophic errors, i.e. when $\sigma_{\Delta z} > 0.15$, for objects brighter than $i_{AB} < 24$, based on the 5 CFHTLS colors. However, photometric redshifts of almost all the lenses detected in the Wide survey are determined from 3 photometric colors only (g', r', i') and should be taken with caution, as the expected rate of catastrophic errors increases to $\sim 20\%$. The observed bimodal distribution with a peak about $z = 0.3$ and another around $z = 0.6$ could be a statistical fluctuation or a real effect due to the fact that for the limiting magnitude of the CFHTLS Wide survey the distribution of sources is expected to peak just above $z \sim 0.6$. A better determination of the photometric redshifts, including near-IR data, or a spectroscopic measurement through a dedicated spectroscopic follow-up are planned to derive the observed redshift distribution of the sample. With an average lens redshift $z \sim 0.5$ the SL2S will go beyond the SLACS and will provide a galaxy and group sample able to probe the evolution of mass at higher redshift. Figure 3 also shows the expected loose correlation between arc radius and lens apparent magnitude in i' band, suggesting that the CFHTLS is not strongly biased in any mass regime, but seems, on the contrary, to be sensitive to the complete parameter space.

- The second class of lenses is mostly made of intermediate mass deflectors, showing arc radii in the range $3-7''$. We found 13 such candidates (8 additional candidates with radii $\sim 2.5''$ which might belong to small groups) in the CFHTLS T0002 release (~ 75 are expected over the complete survey). The middle line of Fig. 2 shows a selection of these intermediate mass candidates. They represent the largest sample of intermediate mass lens detected so far and the CFHTLS-SL2S seems to be particularly efficient at detecting this class of lenses. The lens modeling of groups might be more complex than the modeling of giant arcs in clusters of galaxies, often dominated by a bright central

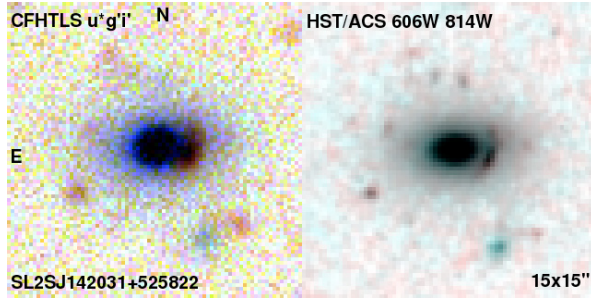


Fig. 5. *Left:* CFHTLS RGB ($i'g'u^*$) image of the candidate SL2SJ142031+525822. *Right:* HST RGB (814W-606W-600W) image of the same field clearly showing a bright arc akin to lensing distortion but a spectrum is needed to confirm that the arc is indeed at a higher redshift and not a star-forming spiral arm or a merging galaxy.

4.3. Notes on selected candidates

SL2SJ021408-053532: A bright system of fold arcs around a compact group of three galaxies at $z_{\text{phot}} \sim 0.5$ (Fig. 2), absolute B magnitude $M_B = -22.4$, and a homogeneous population of galaxies with similar color within $2'$.

SL2SJ021411-040502: Typical example of a compact ring candidate around a galaxy in a loose group or cluster at $z_{\text{phot}} \sim 0.7$. These cases seem to be common in the CFHTLS and might provide interesting constraints on the sub-structure of DM haloes.

SL2SJ100013+022249: This is an example of a compact lensing candidate which does not appear very clearly in CFHTLS imaging, but stands out in the HST cosmos field, and the CFHT normalized $g' - i'$ image (Fig. 1).

SL2SJ141912+532612: This massive cluster showing multiple arcs is not a new detection. Gladders et al. (2003) already discovered the same lensing cluster called RCS1419.2+5326 within the Red Cluster Sequence survey. The photometric redshift of SL2SJ141912+532612 is $z_l = 0.65$ based on 3 colors only ($g'r'i'$) but is remarkably similar to the spectroscopic redshift of RCS1419.2+5326 $z_{\text{spectro}} = 0.64$. HST imaging in F814W is available; HST proposal 10626, PI Loh. This system shows at least three arcs at 10, 14.5, and 17'' (Fig. 2).

SL2SJ142031+525822: Example of a relatively compact arc/ring candidate at $z_{\text{phot}} \sim 0.3$ (and likely higher), the confirmation of which typically requires a spectroscopic follow-up in addition to higher-resolution imaging. This candidate fortunately falls within the Groth Strip Survey and has already been imaged with HST/ACS in $F606W$ and $F814W$ (Simard et al. 2002; Vogt et al. 2005). Figure 5 shows $1 \times 1'$ RGB images of the CFHTLS ($i'g'u^*$) and HST (814W-606W-600W). This candidate is particularly interesting for the large ellipticity the deflector, a rare occurrence among isolated strong lenses.

SL2SJ142209+524652: This candidate is a very extended arc surrounding a compact group of two galaxies at $z_{\text{phot}} \sim 0.2$ and offers a very unorthodox lensing configuration.

SL2SJ143140+553323 Example of lensing by two groups occupying the same line of sight at $z_{\text{phot}} \sim 0.5-0.6$, and having a discernable impact on the lensing distortion with a fold arc and a potential saddle pair.

5. Discussion

5.1. Dark matter distribution in galaxy groups

Only a handful of galaxy groups associated with strong lenses are known, mostly as an environmental association with a galaxy lens (Grant et al. 2004; Fassnacht et al. 2005; Auger et al. 2006). In such cases the group reveals its presence because it produces an external shear acting as a perturbation in the lens modeling. But so far almost no lenses with image splitting between 3 and 7 arcsec have been observed corresponding to halo masses of $M_{\text{halo}} \gtrsim 10^{13} h^{-1} M_{\odot}$, except the “historical” double quasar Q 0957+561 (Walsh et al. 1979); this system is centered in a giant elliptical galaxy embedded in a poor cluster of galaxies at redshift 0.36 (Angonin-Willaime et al. 1994), and recently the 2 lensed quasars of the SDSS (Oguri et al. 2005).

There are several important reasons to study groups. 60% of the galaxies belong to groups which play a key role in the assembly of structures. Merging processes in groups can have a strong effect on the star formation rate and probably on the growth of the super massive black hole that lies in their dominant ellipticals. Much work has been done in recent years using large surveys of groups in the SDSS spectroscopic data base (Weinmann et al. 2006), within the DEEP survey (Coil et al. 2006) and/or with X-ray surveys (Miles et al. 2004, GEMS survey). These first results did not succeed in giving a definitive picture of the average group mass profile, the relation between the light and total mass distribution, or the relation between the different galaxy type fractions (segregation effect as observed in clusters).

Part of the problem lies in the fact that sub-structures of simulated DM haloes can be very complex and the definition of a DM halo center is scale dependent. Strong lensing arcs in the center of group haloes can provide a unique measure of the total projected density profile, where dynamical estimates only provide constraints on the baryonic mass with the strong assumption that groups are virialized systems.

Recent weak shear analyses have been done by roughly stacking two classes of groups detected in the CNOC2 spectroscopic galaxy survey in order to derive structural and M/L properties (Möller et al. 2002; Parker et al. 2005). They found that very poor groups with a mean velocity dispersion of 200 km s^{-1} have an average Einstein radius of about $1''$ (very similar to single massive ellipticals) while the most massive groups with a velocity dispersion close to 300 km s^{-1} have properties more similar to clusters. It also appears that a total mass of $10^{13} h^{-1} M_{\odot}$ might correspond to a transition mass scale for the M/L ratio and the related star formation rate.

X-ray observations have also revealed that there is a peculiar class of old groups dominated by a bright elliptical galaxy that probably formed at an early time in the universe (D’Onghia et al. 2005; Ulmer et al. 2005). Likewise, Guimarães et al. (2005) used the QSO magnification bias in the 2dF Galaxy Redshift Survey to measure a surprisingly high lensing signal, suggesting that some groups are more massive than expected.

The SL2S group sample is well adapted to address these questions.

5.2. Searching a large sample of gravitational rings

Based on our simple extrapolations, CFHTLS Einstein rings will clearly outnumber all the already existing galaxy lens samples. Once fully optimised, the SL2S ring detection procedure will provide ca. 400 rings in the 170 deg^2 of the CFHTLS wide survey. Even if we restrict ourselves to a more conservative number of ~ 300 robust SL2S systems, confirmed with HST imaging, it will increase the present known sample by a factor of 3 over a large redshift range 0.3–1. Thus a comprehensive statistical analysis of this class of lenses will be possible, looking for variations as a function of cosmic time and galaxy luminosity, type and environment, and extending the results of the SLACS on the evolution of the E/S0 fundamental plane and the M/L ratio of normal galaxies, following their pioneering method of combined spectroscopy-based dynamical analysis and lens modelling.

6. Conclusion

We have presented the guidelines of the CFHTLS Strong Lensing Legacy Survey, a survey aimed at detecting all the lensed features in the CFHTLS data for the study of the dark matter halo distributions from isolated galaxies to groups and large clusters up to a redshift of 1. A series of three automated softwares are being developed: an arc detector mainly focused on giant arcs and arclets, a ring detector for the detection of compact Einstein rings and a multiplet detector optimized in multiplet images showing generic lensing properties irrespective of the deflector's light. The preliminary sample is based on the CFHTLS T0002 release and led to the discovery of ca. 40 candidates spanning the complete mass range (the current release, T0003, increases the sample by 50%. The best candidates will be followed up by HST in Cycle 15, snapshot program 10876). An unexpectedly large number of intermediate mass deflectors akin to galaxy groups is present in this sample. We therefore expect to address many questions related to galaxy group physics through the project, like the mass profile transition between cluster-like NFW and galaxy-like isothermal profiles, dark matter substructures in intermediate mass haloes, star formation processes and their feedback in the inter-galactic medium, and stellar mass assembly with redshift. Moreover, although the detection procedure is not yet fully optimised, we expect to uncover and study the most abundant population of rings, known to be present in the CFHTLS images. This will allow us to extend the work of the SLACS team to higher redshifts for a better understanding of the dark matter distribution and impact of baryon cooling in galaxy haloes, and the evolution of the Fundamental Plane and mass assembly of isolated galaxies.

By the end of the survey (2008), we expect to build a sample of about 500 lenses with well-controlled selection effects. This will allow us to investigate the probability distribution of lens splitting angles across the whole lens mass range from galaxies to clusters. Following the pioneering work of Kochanek & White (2001), the studies by Ofek et al. (2003) and more recently Oguri (2006) demonstrate how crucial it is to have a large observational sample to be able to make meaningful comparisons with simulations. The CFHTLS-SL2S is likely to become the most complete survey of strong lenses available for many years.

Acknowledgements. The SL2S collaboration would like to thank P. Petitjean for sharing his MegaCam dataset prior to publication, and Cécile Faure and the COSMOS team for sharing their Einstein ring candidates in CFHTLS D2. This work also uses Groth Strip Survey data obtained or processed with support of the National Science Foundation grants AST 95-29028 and AST 00-71198.

References

- Alard, C. 2006, [arXiv:astro-ph/0606757]
 Angonin-Willaime, M.-C., Soucail, G., & Vandierriest, C. 1994, *A&A*, 291, 411
 Auger, M. W., Fassnacht, C. D., Abrahamse, A. L., Lubin, L. M., & Squires, G. K. 2006, [arXiv:astro-ph/0603448]
 Blandford, R. D., & Narayan, R. 1992, *ARA&A*, 30, 311
 Bolton, A. S., Burles, S., Koopmans, L. V. E., Treu, T., & Moustakas, L. A. 2006, *ApJ*, 638, 703
 Bolzonella, M., Miralles, J.-M., & Pelló, R. 2000, *A&A*, 363, 476
 Brewer, B. J., & Lewis, G. F. 2006, *ApJ*, 637, 608
 Broadhurst, T., Benítez, N., Coe, D., et al. 2005, *ApJ*, 621, 53
 Cabanac, R. A., Valls-Gabaud, D., Jaunsen, A. O., Lidman, C., & Jerjen, H. 2005, *A&A*, 436, L21
 Coil, A. L., Gerke, B. F., Newman, J. A., et al. 2006, *ApJ*, 638, 668
 D'Onghia, E., Sommer-Larsen, J., Romeo, A. D., et al. 2005, *ApJ*, 630, L109
 Fassnacht, C., Lubin, L., McKean, J., et al. 2005, in *IAU Symp.*, ed. Y. Mellier, & G. Meylan, 311
 Gavazzi, R., Fort, B., Mellier, Y., Pelló, R., & Dantel-Fort, M. 2003, *A&A*, 403, 11
 Gladders, M. D., Hoekstra, H., Yee, H. K. C., Hall, P. B., & Barrientos, L. F. 2003, *ApJ*, 593, 48
 Grant, C. E., Bautz, M. W., Chartas, G., & Garmire, G. P. 2004, *ApJ*, 610, 686
 Guimarães, A. C. C., Myers, A. D., & Shanks, T. 2005, *MNRAS*, 362, 657
 Hall, P. B., Yee, H. K. C., Lin, H., et al. 2000, *AJ*, 120, 1660
 Hettterscheidt, M., Erben, T., Schneider, P., et al. 2005, *A&A*, 442, 43
 Hewett, P. C., Warren, S. J., Willis, J. P., Bland-Hawthorn, J., & Lewis, G. F. 2000, in *Imaging the Universe in Three Dimensions*, ed. W. van Breugel, & J. Bland-Hawthorn, *ASP Conf. Ser.*, 195, 94
 Hoekstra, H., Yee, H. K. C., & Gladders, M. D. 2004, *ApJ*, 606, 67
 Horesh, A., Ofek, E. O., Maoz, D., et al. 2005, *ApJ*, 633, 768
 Ilbert, O., Arnouts, S., McCracken, H. J., et al. 2006, [arXiv:astro-ph/0603217]
 Keeton, C. R. 2001, *ApJ*, submitted [arXiv:astro-ph/0102340]
 Kneib, J. P., Mellier, Y., Fort, B., & Mathez, G. 1993, *A&A*, 273, 367
 Kneib, J.-P., Hudelot, P., Ellis, R. S., et al. 2003, *ApJ*, 598, 804
 Kochanek, C. S., & White, M. 2001, *ApJ*, 559, 531
 Kochanek, C. S., Falco, E. E., Impey, C. D., et al. 2000, *ApJ*, 543, 131
 Kochanek, C. S., Keeton, C. R., & McLeod, B. A. 2001, *ApJ*, 547, 50
 Koopmans, L. V. E., Treu, T., Bolton, A. S., Burles, S., & Moustakas, L. A. 2006, [arXiv:astro-ph/0601628]
 Lenzen, F., Schindler, S., & Scherzer, O. 2004, *A&A*, 416, 391
 Mathews, W. G., Faltenbacher, A., Brighenti, F., & Buote, D. A. 2005, *ApJ*, 634, L137
 Mellier, Y. 2002, *Space Sci. Rev.*, 100, 73
 Mellier, Y., & Meylan, G., eds. 2005, *Gravitational Lensing Impact on Cosmology (S225)*
 Miles, T. A., Raychaudhury, S., Forbes, D. A., et al. 2004, *MNRAS*, 355, 785
 Miralda-Escude, J. 1995, *ApJ*, 438, 514
 Miralda-Escude, J., & Lehar, J. 1992, *MNRAS*, 259, 31P
 Möller, O., Natarajan, P., Kneib, J.-P., & Blain, A. W. 2002, *ApJ*, 573, 562
 Ofek, E. O., Rix, H.-W., & Maoz, D. 2003, *MNRAS*, 343, 639
 Oguri, M. 2006, *MNRAS*, 367, 1241
 Oguri, M., Inada, N., Hennawi, J. F., et al. 2005, *ApJ*, 622, 106
 Parker, L. C., Hudson, M. J., Carlberg, R. G., & Hoekstra, H. 2005, *ApJ*, 634, 806
 Rusin, D., & Kochanek, C. S. 2005, *ApJ*, 623, 666
 Rusin, D., Kochanek, C. S., Falco, E. E., et al. 2003, *ApJ*, 587, 143
 Saha, P., & Williams, L. L. R. 1997, *MNRAS*, 292, 148
 Schneider, P., Ehlers, J., & Falco, E. E. 1992, *Gravitational Lenses XIV* (Berlin, Heidelberg, New York: Springer-Verlag), also *Astronomy and Astrophysics Library*
 Seidel, G., & Bartelmann, M. 2006, [arXiv:astro-ph/0607547]
 Seljak, U., Makarov, A., Mandelbaum, R., et al. 2005, *Phys. Rev. D*, 71, 043511
 Simard, L., Willmer, C. N. A., Vogt, N. P., et al. 2002, *ApJS*, 142, 1
 Treu, T., Ellis, R. S., Liao, T. X., & van Dokkum, P. G. 2005, *ApJ*, 622, L5
 Ulmer, M. P., Adami, C., Covone, G., et al. 2005, *ApJ*, 624, 124
 Vogt, N. P., Koo, D. C., Phillips, A. C., et al. 2005, *ApJS*, 159, 41
 Walsh, D., Carswell, R. F., & Weymann, R. J. 1979, *Nature*, 279, 381
 Warren, S. J., & Dye, S. 2003, *ApJ*, 590, 673
 Warren, S. J., Hewett, P. C., Lewis, G. F., et al. 1996, *MNRAS*, 278, 139
 Weinmann, S. M., van den Bosch, F. C., Yang, X., & Mo, H. J. 2006, *MNRAS*, 366, 2
 Willis, J. P., Hewett, P. C., Warren, S. J., Dye, S., & Maddox, N. 2006, *MNRAS*, 369, 1521

THE CFHTLS–STRONG LENSING LEGACY SURVEY (SL2S): INVESTIGATING THE GROUP-SCALE LENSES WITH THE SARCS SAMPLE*

A. MORE^{1,2}, R. CABANAC^{3,4}, S. MORE¹, C. ALARD⁵, M. LIMOUSIN^{2,6}, J-P. KNEIB², R. GAVAZZI⁵, AND V. MOTTA⁷

¹ Kavli Institute for Cosmological Physics, University of Chicago, 5640 S. Ellis Ave., Chicago, IL 60637, USA; anupreeta@kicp.uchicago.edu

² Laboratoire d'Astrophysique de Marseille, Université d'Aix-Marseille & CNRS, UMR7326, 38 rue Frédéric Joliot Curie, F-13013 Marseille, France

³ Université de Toulouse, UPS-OMP, IRAP, Tarbes, France

⁴ CNRS, IRAP, 57, Ave. d'Azereix, F-65000 Tarbes, France

⁵ Institut d'Astrophysique de Paris, 98 Bis Boulevard Arago, F-45014 Paris, France

⁶ Dark Cosmology Centre, Niels Bohr Institute, University of Copenhagen, Juliane Maries Vej 30, DK-2100 Copenhagen, Denmark

⁷ Departamento de Física y Astronomía, Universidad de Valparaíso, Avenida Gran Bretaña 1111, Valparaíso, Chile

Received 2011 September 7; accepted 2012 January 31; published 2012 March 20

ABSTRACT

We present the Strong Lensing Legacy Survey–ARCS (SARCS) sample compiled from the final T0006 data release of the Canada–France–Hawaii Telescope Legacy Survey (CFHTLS) covering a total non-overlapping area of 159 deg². We adopt a semi-automatic method to find gravitational arcs in the survey that makes use of an arc-finding algorithm. The candidate list is pruned by visual inspection and ranking to form the final SARCS sample. This list also includes some serendipitously discovered lens candidates which the automated algorithm did not detect. The SARCS sample consists of 127 lens candidates which span arc radii $\sim 2''$ – $18''$ within the unmasked area of ~ 150 deg². Within the sample, 54 systems are promising lenses among which, we find 12 giant arcs (length-to-width ratio ≥ 8). We also find two radial arc candidates in SL2SJ141447+544704. From our sample, we detect a systematic alignment of the giant arcs with the major axis of the baryonic component of the putative lens in concordance with previous studies. This alignment is also observed for all arcs in the sample and does not vary significantly with increasing arc radius. The mean values of the photometric redshift distributions of lenses corresponding to the giant arcs and all arcs sample are at $z \sim 0.6$. Owing to the large area and depth of the CFHTLS, we find the largest sample of lenses probing mass scales that are intermediate to cluster and galaxy lenses for the first time. We compare the observed image separation distribution (ISD) of our arcs with theoretical models. A two-component density profile for the lenses which accounts for both the central galaxy and the dark matter component is required by the data to explain the observed ISD. Unfortunately, current levels of uncertainties and degeneracies accommodate models both with and without adiabatic contraction. We also show the effects of changing parameters of the model that predict the ISD and that a larger lens sample might constrain relations such as the concentration–mass relation, mass–luminosity relation, and the faint-end slope of the luminosity function.

Key words: dark matter – gravitational lensing: strong – methods: data analysis – surveys

Online-only material: color figures

1. INTRODUCTION

Gravitational lensing is the deflection of light coming from distant sources in the universe, due to the gravitational potential of intervening structures (see reviews, e.g., Blandford & Narayan 1986, 1992; Kochanek 2006). The last decade has seen the rise of a wide variety of applications of strong lensing such as the study of distant lensed galaxies with unprecedented magnification (e.g., Impellizzeri et al. 2008; Swinbank et al. 2009; Zitrin & Broadhurst 2009; Richard et al. 2011), the constraints on substructure within lensing halos (e.g., More et al. 2009a; Suyu & Halkola 2010; Vegetti et al. 2010a, 2010b), accurate measurements of the Hubble constant (e.g., Coles 2008; Suyu et al. 2010), constraints on the stellar initial mass function (e.g., Treu et al. 2010; Ferreras et al. 2010; Sonnenfeld et al. 2011), constraints on the slope of the inner density profile of the lensing halos (e.g., Treu & Koopmans 2002a, 2002b; Koopmans & Treu 2003; Koopmans et al. 2006; More et al. 2008; Barnabè et al.

2009; Koopmans et al. 2009), and estimation of the fraction of dark matter in galaxy-scale halos (e.g., Gavazzi et al. 2007; Jiang & Kochanek 2007; Grillo et al. 2010; Faure et al. 2011; More et al. 2011a; Ruff et al. 2011).

Although strong lensing is a rare event, several surveys covering a wide sky area and deep enough imaging across different wavelengths have resulted in the discovery of over 200 strong lens systems at galaxy scales from surveys such as, the Great Observatories Origins Deep Survey (Fassnacht et al. 2004), Cosmic Evolution Survey (COSMOS; Faure et al. 2008; Jackson 2008), Mediu Deep Survey (Ratnatunga et al. 1999), the Cosmic Lens All Sky Survey (CLASS; Myers et al. 2003), and the Sloan Lens ACS Survey (SLACS; Bolton et al. 2006) and about a few dozen lens systems at cluster scales such as, the Extended Medium Sensitivity Survey (EMSS; Luppino et al. 1999), the MAssive Cluster Survey (MACS; Ebeling et al. 2001), the Las Campanas Distant Cluster Survey (LCDCS; Zaritsky & Gonzalez 2003), and the Red sequence Cluster Survey (RCS; Gladders et al. 2003, henceforth G03). Large imaging and spectroscopic surveys enable us to probe statistical properties of both dark matter and baryonic matter or constrain cosmological parameters with high accuracy. For instance, on galaxy scales, the SLACS sample has been used to study the average density profiles of lens galaxies up to redshift of ~ 0.3 (e.g., Koopmans et al. 2006; Gavazzi et al. 2007;

* Based on observations obtained with MegaPrime/MegaCam, a joint project of CFHT and CEA/DAPNIA, at the Canada–France–Hawaii Telescope (CFHT) which is operated by the National Research Council (NRC) of Canada, the Institut National des Science de l'Univers of the Centre National de la Recherche Scientifique (CNRS) of France, and the University of Hawaii. This work is based in part on data products produced at TERAPIX and the Canadian Astronomy Data Centre as part of the Canada–France–Hawaii Telescope Legacy Survey, a collaborative project of NRC and CNRS.

Koopmans et al. 2009; Auger et al. 2010), Falco et al. (1999) used the CfA-Arizona Space Telescope LEns Survey (CASTLES; Muñoz et al. 1998) sample to measure the mean extinction due to the interstellar medium of the lens galaxies, Mediavilla et al. (2009) estimated the fraction of mass in compact objects within lens galaxies from the CASTLES, and Wyithe (2004) constrained the bright end of the quasar luminosity function from the absence of lensed quasars at high redshift in the Sloan Digital Sky Survey (SDSS). On cluster scales, G03 found that the observed abundance of giant arcs from the RCS is too high to be consistent with the predictions from the current standard cosmological model (see also Bartelmann et al. 1998; Li et al. 2005, 2006) and Zitrin et al. (2011) found some discrepancy between the predictions from the standard model and the observed distribution of Einstein radii from the MACS sample. However, the magnitude of these differences has been mitigated with subsequent studies (e.g., Horesh et al. 2005; Meneghetti et al. 2011).

As discussed above, the majority of the surveys in the past have primarily focused on studying galaxy-scale or cluster-scale structures. As a result, matter distribution in galaxies and galaxy clusters is relatively well studied via both strong and weak lensing. A further improvement in our understanding has come from the use of complementary methods to lensing such as stellar kinematics, satellite kinematics, and X-ray scaling relations. In contrast, little is known about galaxy groups which are intermediate to galaxies and galaxy clusters, typically corresponding to masses of 10^{12} – $10^{14} M_{\odot}$. Relatively fewer investigations have been carried out with galaxy groups, e.g., study of the intra-group medium with a very low redshift X-ray sample (Helsdon & Ponman 2000), study of mass-to-light ratios with the Canadian Network for Observational Cosmology 2 sample (Parker et al. 2005), study of the faint end of the luminosity function of nearby compact groups (Krusch et al. 2006), study of the concentration–mass (c – M) relation from SDSS (Mandelbaum et al. 2008) via weak lensing, study of colors and star formation (e.g., Balogh et al. 2009, 2011), study of the scaling relations of X-ray selected groups (Rines & Diaferio 2010), and study of baryon fractions from the Two Micron All Sky Survey (Dai et al. 2010). Since studies of groups are limited, we still do not have a detailed understanding of matter distribution, formation, and evolution of galaxy groups. Being one of the important components in the hierarchical assembly of structures in the universe, galaxy groups are much more massive than galaxy-scale halos and are concentrated enough to act as lenses. Furthermore, since galaxy groups are quite abundant compared to massive structures like galaxy clusters, the probability of finding group-scale lenses is also large. Hence, lensing can be successfully used to study group-scale halos.

The Strong Lensing Legacy Survey (SL2S; Cabanac et al. 2007) is a survey from the Canada–France–Hawaii Telescope Legacy Survey (CFHTLS). The design of CFHTLS allows us to find large sample of group-scale lenses, which can be studied in detail upto high redshifts, for the first time. The SL2S is as a precursor to wide-field imaging surveys such as the Dark Energy Survey, Large Synoptic Survey Telescope, and Euclid. A combined study of SL2S galaxy-scale lenses with the SLACS sample have been used to show mild evolution of the slope of the average density profile of galaxies (Ruff et al. 2011) which is constrained by the strong lensing and stellar dynamics techniques. Disk galaxies are also a relatively less studied population especially at high redshifts. An automated search for

edge-on disk lenses from the SL2S resulted in 18 candidates, out of which three to five are expected to be real lenses (Sygnet et al. 2010). A subset of the SL2S groups have been studied in detail using a combination of techniques such as strong lensing, group dynamics, weak lensing to probe the density profiles of the lensing groups (e.g., Limousin et al. 2009; Thanjavur et al. 2010; Verdugo et al. 2011).

In this paper, we present the SL2S-ARCS (SARCS) sample from the final T0006 release of the CFHTLS. In Section 2, we give an overview of the survey and procedure of sample selection, describe details of the algorithm, ARCFINDER (Alard 2006), and present the final sample. In Section 3, we discuss some statistical results using the final sample. In Section 4, we summarize the survey and our main findings.

2. THE CFHTLS–SL2S-ARCS SAMPLE

In this section, we give a brief overview of the survey from which we derive the lens sample. This is followed by a description of the semi-automatic process of selecting the candidates in the final sample. We also discuss how the algorithm, ARCFINDER works and the modifications implemented in the new ARCFINDER. Last, we present the final sample and report duplicate detections of some candidates from other surveys.

2.1. Survey Overview

CFHTLS is a photometric survey made with the Canada–France–Hawaii Telescope (CFHT) in five optical bands ($u^*g'r'i'z'$) using the wide-field imager MegaPrime with a field of view of 1 deg^2 on the sky and a pixel size of $0''.186$. The WIDE and DEEP components of the CFHTLS are designed to carry out extragalactic research. These components are ideal for searching strong lens systems. The SL2S sample is compiled from the CFHTLS-WIDE encompassing a combined area of 171 deg^2 and CFHTLS-DEEP encompassing a combined area of 4 deg^2 . However, taking into account the masked and overlapping areas, the effective area of the survey is 150.4 deg^2 (146.9 deg^2 for WIDE and 3.5 deg^2 for DEEP). The WIDE consists of four fields, W1, W2, W3, and W4. Field W1 has the largest sky coverage of 63.65 deg^2 . Fields W2 and W4 have similar sky coverages of 20.32 deg^2 and 20.02 deg^2 , respectively.⁸ Field W3 has a sky coverage of 42.87 deg^2 and is more than twice as large as W2 and W4. DEEP also consists of four fields, D1 (located within the W1 field), D2, D3, and D4. Each of the deep fields covers an area of 1 deg^2 . The DEEP images are produced in two image stacks D-25 and D-85. The former consists of 25% of the best seeing images and the latter consists of 85% of the best seeing images. We use the D-25 images for searching lens candidates. Among the WIDE fields, g -band imaging is the deepest of all bands with a limiting magnitude of 25.47 and a mean seeing of $0''.78$ whereas the g -band imaging of DEEP fields has nearly 10 times deeper exposures than the WIDE fields and the median seeing is $\sim 0''.7$. The zero point to convert flux to AB magnitude for all bands is 30. Further details of the T0006 release, which is the first complete release of the WIDE and DEEP, can be found on Terapix Web site.⁹

2.2. Sample Selection

The SL2S lens sample is compiled using two algorithms: RINGFINDER and ARCFINDER. The former aims at detecting

⁸ These numbers are estimated from http://terapix.iap.fr/cplt/table_syn_T0006.html.

⁹ <http://terapix.iap.fr/cplt/T0006-doc.pdf>

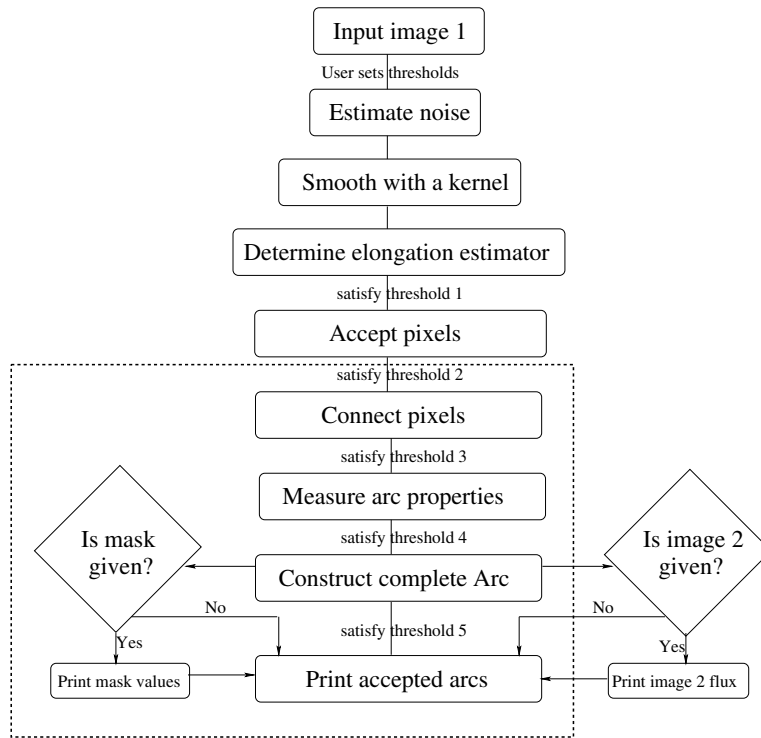


Figure 1. Flowchart showing the ARCFINDER algorithm.

galaxy-scale lenses by using color information. The SL2S RINGS sample will be presented and discussed in a separate paper (R. Gavazzi et al., in preparation). Here, we focus on the SARCS sample created with the help of ARCFINDER, followed by visual inspection and screening of the candidates.

We define the SARCS sample such that lens systems with arc radius (R_A) $\gtrsim 2''$ belong to the sample. The radius of the arc is defined as the distance of the lensed image from the putative lens galaxy which is roughly the Einstein radius. Typically, lensing halos with Einstein radius larger than $2''$ are very massive lenses with significant contribution from the environment of the primary lensing galaxy. Thus, the SARCS sample predominantly consists of group to cluster-scale lenses. Lens systems with $R_A < 2''$, typically, form part of the RINGS sample. We note that a few lens systems are common to both SL2S samples since the cut on R_A is not a sharp limit imposed by the algorithms.

The SARCS sample from CFHTLS is compiled in a three-step process. The first step is to run the arc-detection algorithm called ARCFINDER. We choose to run the ARCFINDER on the g -band image since most of the lensed images correspond to galaxies with high star formation that have little emission at redder wavelengths. Also, focusing on the g band prevents us from detecting high-redshift g -dropouts. However, we plan to search for g -dropout arcs which are brighter in the i band. These results will be presented in a separate paper.

At the end of the first step, we produce a list of arc candidates with various parameters. The next step is applying a cutoff on arc properties such as the area, the peak flux count, and the radius of curvature, and rejecting candidates within masked area. These cuts allow a significant reduction in false detections at the cost of losing some real arc candidates. In the third step, visual inspection and classification are carried out to grade the quality of the candidates. Note that the final SARCS sample consists of

candidates that are detected by the ARCFINDER and/or by visual inspection.

2.3. Automatic Detection of Arcs: ARCFINDER

With the advent of several large imaging surveys, searching for lens systems visually is a subjective and time-expensive exercise which may not be easily repeatable. Hence, several algorithms have been devised in the last few years to automate the process of lens detection as much as possible. The algorithms, usually, focus on a specific target population, for example, algorithms to detect the lensed sources such as quasars via the quasar time variability (Kochanek et al. 2006) based on the difference imaging technique of Alard & Lupton (1998), spectrum-based algorithms such as the one used by Bolton et al. (2004) to form the SLACS sample following the technique of Warren et al. (1996) or lens-modeling robots that assesses the probability of a bright red galaxy being a lens (Marshall et al. 2009). Since groups to cluster-scale lenses form arc-like lensed images, there are a few arc-finders in the literature (e.g., Lenzen et al. 2004; Horesh et al. 2005; Seidel & Bartelmann 2007) that aim at detecting elongated arc-like images.

The ARCFINDER (Alard 2006) is a generic algorithm that can be used to detect elongated and curved features in an image. The algorithm uses pixel intensities from a standard FITS image to trace the structure of a feature. Multiple thresholds are applied to the structural properties of the feature to select an arc candidate. The reader is referred to Alard (2006) for the details of the algorithm. Below, we describe the algorithm along with some modifications implemented in the newer version (V2.0), which is used to compile the SARCS sample.

We show a flowchart to illustrate the various steps involved in the algorithm (see Figure 1) and step through an example of a mock arc image (see Figure 2).

1. We run the ARCFINDER on images of 19354×19354 pixels, which corresponds to a single MEGACAM pointing. For

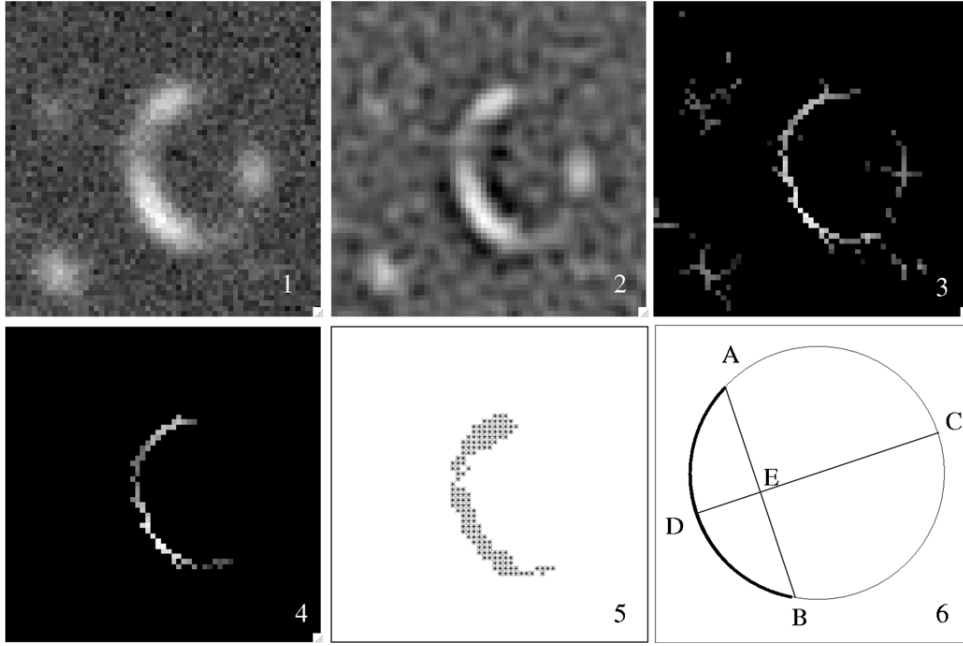


Figure 2. Outputs of ARCFINDER at various stages of the execution (panels 1–5) using a mock arc image. Panel 1: original image with the mock arc; panel 2: smoothed image; panel 3: (disconnected) pixels with elongation estimator values higher than a threshold; panel 4: connected pixels above thresholds that belong to the arc; and panel 5: the reconstructed shape of the final arc. The image is $11''3$ on a side. Schematic diagram for measuring length of an arc (panel 6).

such large images, the assumption of Gaussian distribution for the noise holds well. Assuming a Gaussian distribution for the noise in the input image (panel 1 of Figure 2), the noise σ is calculated in the first step. Most of the arcs are unresolved with the ground-based telescopes like CFHT and are limited by the size of the point-spread function (PSF).

2. Convolution of the image with a smoothing kernel, with a size of the order of the PSF, can help damp the noise and enhance the detection of arcs. Hence, the input image is smoothed with a Mexican-hat filter in the next step (panel 2 of Figure 2).

The Mexican-hat bandpass filter with scale b is given by

$$M(x, y) = e^{-\bar{r}^2} - 0.5e^{-\frac{\bar{r}^2}{2}}, \quad (1)$$

where $b^2 = 3$ pixels and

$$\bar{r} = \frac{\sqrt{x^2 + y^2}}{b}. \quad (2)$$

3. Now, we define a local estimator of elongation for every pixel in the smoothed image. This is calculated by using the flux from all pixels within a window centered on every pixel. The size of the window is chosen to be a few times the PSF size. We consider a square window of side W centered on the pixel at (x, y) . Using the second-order moments of brightness distribution within the window, the local direction of the elongation of the feature is calculated. This direction is then used to align the feature along the x -axis to determine the local axis ratio, similar to a length-to-width ratio, within the window. The elongation estimator is defined as follows:

$$Q(x, y) = \frac{1}{W} \frac{F_X}{F_{Y_{\max}}}, \quad (3)$$

Table 1

Thresholds used in the Final Selection of the SARCS Candidates	
Step	Parameters and Thresholds
Smooth	$W = 9, b^2 = 3.0$
Detect	$W = 11, \text{Th1} = 11 * 0.75\sigma$
Connect	$W = 9, \text{Th2} = 1.25$
	$W = 9, \text{Th4} = 0.5\text{S1}, 0.3\text{S2}$
Properties	Final Thresholds
Area	$55 < A < 500$ (pixel)
Peak counts	< 50 (ADU s^{-1})
Mean counts	$2\sigma < \text{SB} < 50$ ($\text{ADU s}^{-1} \text{ pixel}^{-1}$)
Length	> 7 (pixel)
Width	$1.5 \leq w \leq 8$ (pixel)
Curvature	$r_c < 100$ and $r_c > 1000$ (pixel)

Notes. W is the window size in pixels. Th1, Th2, and Th4 imply thresholds 1, 2, and 4, respectively. S1 and S2 imply intermediate mean counts of candidates in the input and smoothed images, respectively.

where F_X is the integrated flux of the single central row of pixels and $F_{Y_{\max}}$ is the maximum of the integrated flux values calculated from single columns of pixels within the window. If F_X and $F_{Y_{\max}}$ are above $(W+1)0.75\sigma$ (threshold 1 in Figure 1 and Table 1), then the estimator $Q(x, y)$ is assigned to the pixel (x, y) at the center of the window or else the pixel is assigned a value of 0. Likewise, the estimator is calculated for every pixel in the image (see panel 3 of Figure 2).

4. In the following step, we attempt to connect the pixels that possibly belong to the candidate arc. A pixel is accepted if the estimator value from the image in panel 3 is > 1.25 (threshold 2 in Figure 1 and Table 1). The estimator is set to 0 as soon as a pixel is connected in the prior step to avoid repetitive checking of connected pixels. Iterating the above steps over the image allows tracing of the primary shape of the arc. If the number of connected pixels is more than 10

(threshold 3) then the properties of arcs such as the length, peak flux, and surface brightness are calculated. Panel 4 shows the image with connected pixels, which, for the case at hand, consists of one candidate only. The estimator is particularly suited for recovering pixels along the length of the arc. In order to connect the pixels along the width of the arc, we use the input and smoothed images (panels 1 and 2, respectively). Using arcs with length >7 pixels, we apply surface brightness thresholds on pixel values from images in panels 1 and 2 in order to accept pixels belonging to the arc (threshold 4; see Figure 1 and Table 1) and construct the arc fully.

5. In the last step, if the candidate arc satisfies thresholds on the arc properties such as the width (≥ 1.5 and ≤ 8 pixels), area (>25 pixels), surface brightness ($>2\sigma$), and peak flux (<500 ADU s^{-1} pixel $^{-1}$) which correspond to threshold 5 in Figure 1, then the arc is accepted (see panel 5 in Figure 2).
6. In the following, we describe how the arc properties are measured. The area of the arc is the total number of pixels belonging to the final arc. The length of the arc is calculated by assuming that the candidate arc is similar to an arc of a circle. We first find the extreme ends of the arc, connect them with a chord labeled AB in panel 6 of Figure 2. From the midpoint E of chord AB, we draw a line perpendicular to the chord and find its intersection D with the arc. The lengths ED and AB uniquely identify the circle to which the arc belongs and as well as the length of the arc. The width of the arc is defined as the ratio of the area to the length of the arc. The radius of the circle going through the arc is used as a proxy for the curvature of the arc.

In the algorithm, the use of a second image at another wavelength and a mask file are optional. The algorithm, in its current version, merely prints the values of the pixels belonging to the candidate arc from the image 2 and/or the mask file, if provided. This allows us to optionally screen the candidate arcs based on their color and/or masking information. For the SARCS sample, we made use of the mask option only and further restricted the parameter space of the output list of arcs by introducing more strict cuts on some of the arc properties. Table 1 lists the final set of thresholds which are satisfied by the SARCS candidates detected by ARCFINDER.

The components enclosed by the dashed line in Figure 1 are the sections of the algorithm that have been improved. This includes the way in which the pixels belonging to the arc are connected and the way the properties of the arcs are measured. In the earlier version of the algorithm, a candidate arc is accepted at the final stage only if it satisfies a certain threshold on the curvature of the arc. This feature has been removed and the option of using mask information is introduced in the V2.0. The values for all the different thresholds are tuned from an initial sample of CFHTLS arcs, found visually or from the previous version of ARCFINDER, based on an early release of the data. Furthermore, all the thresholds can now be set during the execution of the algorithm.

The ARCFINDER V2.0 finds ~ 1.5 times more detections, most of which arise due to spikes and halos near stars. However, the use of masks removes these false detections, thereby making the number of detections comparable to or less than the output of the earlier version. The modified ARCFINDER is over three times faster than the earlier version. We have also recently parallelized the algorithm, which enables us to achieve even faster computation on shared memory platforms. The ARCFINDER V2.0 is available upon request to the author.

Finally, we note that the existing algorithms are far from perfect and almost always require manual intervention. Attempts to increase the completeness of the sample almost always leads to a corresponding increase in the rate of false positives. In light of these issues, citizen science projects such as the Galaxy Zoo (Lintott et al. 2008) might be a better tool, for the time being, in identifying lens systems not detected by the algorithms. These projects, in turn, could be used to calibrate and improve existing algorithms. We are currently pursuing the feasibility of such a project.

2.4. SARCS Sample

After the automatic detection and screening, about 1000 candidates deg^{-2} are visually inspected. This is reduced to a total sample of 413 candidates, which is further considered for ranking by three people. The individually assigned ranks are from 1 to 4 with 1 being the least likely to 4 being the almost certain lens system. We present the 127 lens candidates which are ranked 2 or higher (average of the ranks by three people) and which have $R_A \gtrsim 2''$. All of the 127 candidates¹⁰ are listed in Table 2, which gives the ID, lens position, lens magnitudes in AB, lens redshifts with 1σ uncertainties, arc radii, ranks, the type indicating whether the candidates are primarily detected via the ARCFINDER and the field name in which the candidate is located. For the calculation of arc radii in physical units, we use flat cosmology with following parameters $(\Omega_m, \Omega_\Lambda, H_0) = (0.3, 0.7, 100 \text{ km s}^{-1} \text{ Mpc}^{-1})$. The symbol A stands for detection by ARCFINDER and V implies that a candidate is found serendipitously. A total of 54 candidates are good-to-best systems (that is, a rank of 3 and above) and are shown in Figures 3 and 4. Out of the total sample, 27 systems have been or are being followed up for further analyses (see Table 3) and most of them are confirmed lens systems, 5 systems are very likely lenses and rest of the 96 are possible lenses. Table 3 does not report information about any archival data on any of the lens candidates.

One of the deep fields, D2, has an overlap with the COSMOS (Scoville et al. 2007), a photometric survey of 1.8 deg^2 in the *I* band (limiting magnitude of 26.5) with the Advanced Camera Survey (ACS) on board the *Hubble Space Telescope* (HST). We find two of the SARCS candidates common to the lens sample of COSMOS (Faure et al. 2008). The SARCS candidates with IDs SA78 and SA83 are known COSMOS candidates and the rest of the six candidates within the COSMOS field are new (see Table 2 with field labeled as D2). For comparison, we also show the ACS images of the SARCS candidates in Figure 5 from the COSMOS archive. The W3 field overlaps with one of the 22 individual fields of the RCS survey which covers a combined area of $\sim 90 \text{ deg}^2$. The overlapping RCS field has a lensing cluster, RCS 1419.2+5326 at $z = 0.64$. This cluster is also detected in the SARCS sample identified by SA102 (see Table 2).

3. RESULTS AND DISCUSSION

In the following subsections, we describe the main findings from the SARCS sample and constraints on average properties of the lens population using statistical properties of the arcs. Note that many of the lens candidates are not confirmed lenses yet and hence the results should be taken as indicative. First, based on the photometric redshifts of the lenses, we study the lens redshift distribution. Subsequently, we discuss about the abundance of

¹⁰ High-resolution images of these systems are made available at http://kicp.uchicago.edu/~anupreeta/sarcs_sample.

Table 2
Characteristics of Lens Candidates from the SARCS Sample

ID	R.A.	Decl.	g	r	i	z_{phot}	R_A		Rank	Type	Field
	(hms)	(dms)	(mag)	(mag)	(mag)		($''$)	(h^{-1} kpc)			
SA1	02:01:21.89	-09:15:15.09	22.06	20.58	19.90	0.46 ± 0.02	2.2	9.0	2.0	A	W1
SA2	02:02:10.50	-11:09:11.68	19.79	18.48	17.80	0.48 ± 0.02	5.0	20.9	3.7	A	W1
SA3	02:02:38.87	-06:34:56.12	20.89	19.91	19.54	0.37 ± 0.03	2.2	7.9	2.0	A	W1
SA4	02:03:02.84	-08:21:14.25	21.96	20.57	19.99	0.14 ± 0.07	2.4	4.1	2.0	V	W1
SA5	02:03:12.61	-10:47:07.95	22.02	20.55	19.52	0.62 ± 0.03	3.0	14.3	2.3	V	W1
SA6	02:03:20.43	-07:34:50.78	21.69	20.36	19.45	0.59 ± 0.03	5.0	23.2	3.3	A	W1
SA7 ^m	02:03:49.98	-09:42:53.51	17.84	16.73	16.18	0.25 ± 0.02	5.0	13.7	3.3	A	W1
SA8	02:04:54.51	-10:24:02.48	19.52	18.18	17.68	0.33 ± 0.02	10.8	35.9	2.7	A	W1
SA9	02:05:03.15	-11:05:46.63	21.54	20.17	19.16	0.62 ± 0.03	3.3	15.7	3.0	V	W1
SA10	02:06:48.47	-06:57:01.33	20.95	19.60	18.90	0.49 ± 0.06	3.2	13.5	3.0	A	W1
SA11	02:08:15.66	-07:24:57.81	21.98	20.55	19.49	0.62 ± 0.02	4.3	20.4	2.0	A	W1
SA12	02:08:16.87	-09:36:52.69	22.16	20.85	19.60	0.74 ± 0.03	3.4	17.4	3.7	A	W1
SA13	02:08:41.61	-07:01:28.07	19.85	18.70	18.20	0.29 ± 0.03	3.5	10.7	2.0	V	W1
SA14	02:09:29.33	-06:43:11.26	20.47	19.15	18.57	0.45 ± 0.02	3.2	12.9	3.7	A	W1
SA15	02:09:57.67	-03:54:57.08	21.41	19.98	19.27	0.43 ± 0.03	3.9	15.3	2.3	V	W1
SA16	02:10:26.57	-04:46:41.59	21.77	20.79	20.24	0.55 ± 0.03	1.9	8.5	2.0	A	W1
SA17	02:10:51.59	-03:52:52.64	21.79	20.84	19.91	0.73 ± 0.04	1.9	9.7	2.0	V	W1
SA18	02:11:08.66	-10:12:13.86	19.81	18.44	17.89	0.38 ± 0.02	2.0	7.3	2.3	A	W1
SA19	02:11:18.49	-04:27:29.20	23.13	22.48	21.43	1.19 ± 0.07	3.5	20.3	3.3	A	W1
SA20	02:12:20.52	-09:38:44.10	23.48	22.18	20.88	0.77 ± 0.03	2.4	12.4	2.0	A	W1
SA21 ^G	02:13:24.52	-07:43:54.82	24.11	23.73	23.18	0.80 ± 0.16	2.8	14.7	4.0	V	W1
SA22	02:14:08.07	-05:35:32.39	20.98	19.42	18.69	0.48 ± 0.02	7.1	29.7	4.0	A	W1
SA23 ^G	02:14:11.24	-04:05:02.71	22.11	20.92	19.88	0.74 ± 0.04	1.9	9.7	4.0	A	W1
SA24	02:15:23.03	-07:36:23.56	23.64	22.08	20.89	1.05 ± 0.02	3.7	21.0	2.7	A	W1
SA25	02:15:52.36	-07:21:01.32	21.50	20.06	19.29	0.48 ± 0.02	2.8	11.7	2.0	A	W1
SA26 ^m	02:16:04.66	-09:35:06.65	21.68	20.26	19.09	0.69 ± 0.02	16.4	81.6	2.7	V	W1
SA27 ^{mG}	02:16:24.03	-09:57:39.09	17.29	16.35	15.90	0.18 ± 0.02	2.8	5.9	3.3	A	W1
SA28	02:16:31.19	-07:31:57.13	21.90	20.89	19.80	0.86 ± 0.04	2.4	12.9	2.3	A	W1
SA29	02:16:46.84	-09:18:16.74	21.73	20.53	19.48	0.72 ± 0.03	2.4	12.1	2.5	V	W1
SA30	02:16:49.25	-07:03:23.80	21.04	19.54	18.85	0.45 ± 0.02	5.6	22.6	3.7	A	W1
SA31 ^m	02:17:23.76	-10:15:50.30	18.68	17.53	17.03	0.27 ± 0.02	3.2	9.3	2.3	V	W1
SA32	02:17:39.56	-10:33:19.93	22.94	22.05	21.04	1.05 ± 0.05	1.9	10.8	2.3	A	W1
SA33 ^m	02:18:07.29	-05:15:36.16	22.54	21.21	20.18	0.42 ± 0.03	2.4	9.3	3.7	V	W1
SA34	02:18:14.39	-10:06:02.30	21.20	20.57	20.27	0.46 ± 0.03	2.8	11.4	2.0	A	W1
SA35	02:19:09.86	-04:01:43.32	21.43	19.95	19.27	0.45 ± 0.02	4.3	17.3	2.3	A	W1
SA36	02:19:56.42	-05:27:59.21	20.48	19.38	18.84	0.35 ± 0.04	3.0	10.4	3.0	V	W1
SA37	02:20:43.11	-10:52:16.45	22.81	21.68	20.48	0.79 ± 0.03	2.2	11.5	2.7	A	W1
SA38	02:20:56.43	-07:43:11.71	22.91	21.56	20.51	0.71 ± 0.03	2.4	12.1	2.3	A	W1
SA39	02:21:51.18	-06:47:32.66	21.34	20.18	19.16	0.72 ± 0.03	5.2	26.3	4.0	V	W1
SA40	02:23:15.41	-06:29:06.40	21.20	20.02	19.21	0.55 ± 0.06	1.9	8.5	3.0	A	W1
SA41	02:23:18.33	-10:58:48.46	21.57	20.29	19.53	0.52 ± 0.04	6.1	26.6	2.0	A	W1
SA42	02:24:00.92	-03:46:25.83	23.12	22.04	20.92	0.98 ± 0.05	2.6	14.5	2.7	A	W1
SA43	02:24:05.01	-04:47:07.00	20.00	18.68	18.10	0.36 ± 0.04	4.3	15.1	2.0	A	D1
SA44	02:24:34.96	-04:11:35.02	24.01	23.03	22.06	0.68 ± 0.04	1.9	9.4	2.7	V	D1
SA45	02:24:35.26	-04:01:57.86	22.49	21.21	20.13	1.13 ± 0.07	3.5	20.1	2.0	V	D1
SA46	02:24:39.06	-04:00:45.16	20.75	19.33	18.62	0.43 ± 0.05	3.2	12.6	3.0	V	D1
SA47	02:24:59.25	-04:01:03.77	24.05	22.83	21.70	0.80 ± 0.04	1.9	10.0	3.0	V	D1
SA48: ^G	02:25:11.04	-04:54:33.54	18.72	17.57	17.03	0.33 ± 0.01	2.8	9.3	3.7	A	D1
SA49	02:25:38.74	-04:03:20.36	22.09	20.64	19.52	0.62 ± 0.06	4.3	20.4	2.0	A	D1
SA50	02:25:46.13	-07:37:38.52	20.99	19.50	18.60	0.54 ± 0.02	5.8	25.8	4.0	V	W1
SA51	02:26:07.15	-04:27:26.26	19.36	18.44	17.97	0.17 ± 0.05	3.7	7.5	2.0	V	D1
SA52	02:27:20.22	-07:49:20.19	21.31	19.81	19.00	0.53 ± 0.03	2.1	9.3	2.0	V	W1
SA53	02:27:59.21	-09:07:29.86	20.71	19.87	19.42	0.55 ± 0.03	3.9	17.5	2.0	A	W1
SA54	02:28:32.05	-09:49:45.44	20.25	18.74	18.07	0.45 ± 0.02	6.3	25.4	2.7	V	W1
SA55	02:29:17.36	-05:54:05.54	19.67	18.30	17.73	0.38 ± 0.03	2.6	9.5	3.0	A	W1
SA56	02:30:39.96	-03:50:28.06	22.36	21.89	21.32	0.27 ± 0.02	2.1	6.1	2.0	A	W1
SA57	02:31:06.46	-05:55:04.63	21.68	20.20	19.46	0.52 ± 0.03	3.7	16.1	2.0	A	W1
SA58	02:32:23.77	-08:50:38.37	22.05	20.76	20.09	0.46 ± 0.04	2.6	10.6	2.0	A	W1
SA59	02:33:07.05	-04:38:38.21	21.56	20.66	19.62	0.79 ± 0.03	1.9	9.9	2.0	A	W1
SA60	02:35:01.61	-09:58:32.76	21.78	20.24	19.07	0.70 ± 0.03	4.7	23.5	2.7	A	W1
SA61	08:48:23.66	-04:07:15.29	21.17	19.63	18.85	0.51 ± 0.02	7.4	32.0	2.7	A	W2
SA62	08:50:07.72	-01:23:53.30	22.23	20.92	20.35	0.37 ± 0.04	3.5	12.5	2.7	A	W2
SA63	08:52:07.18	-03:43:16.28	20.91	19.33	18.61	0.48 ± 0.02	5.0	20.9	3.3	V	W2
SA64	08:52:08.36	-04:05:28.36	21.62	20.26	19.59	0.43 ± 0.03	2.4	9.4	2.0	A	W2
SA65	08:54:25.14	-03:14:53.11	24.89	24.53	22.84	0.98 ± 0.10	1.9	10.6	2.7	A	W2
SA66 ^m	08:54:46.55	-01:21:37.08	19.34	17.88	17.28	0.48 ± 0.11	4.8	20.1	4.0	A	W2

Table 2
(Continued)

ID	R.A.	Decl.	g	r	i	z_{phot}	R_A		Rank	Type	Field
	(hms)	(dms)	(mag)	(mag)	(mag)		($''$)	(h^{-1} kpc)			
SA67	08:55:59.92	-04:09:17.76	21.06	19.60	18.90	0.45 ± 0.02	2.1	8.5	3.0	A	W2
SA68	08:57:26.91	-02:42:26.64	19.91	18.44	17.80	0.42 ± 0.02	2.8	10.8	2.3	A	W2
SA69	08:57:35.96	-01:01:12.55	21.03	20.57	20.29	0.05 ± 0.23	2.4	1.6	2.3	A	W2
SA70	08:57:49.10	-01:13:00.73	19.99	18.81	18.26	0.29 ± 0.03	3.9	11.9	2.0	A	W2
SA71 ^m	08:58:48.83	-02:39:25.79	19.16	18.23	17.83	0.36 ± 0.10	3.7	13.0	3.0	V	W2
SA72	08:59:14.55	-03:45:14.85	22.01	20.75	19.67	0.74 ± 0.03	4.5	23.0	4.0	A	W2
SA73 ^m	08:59:54.54	-01:32:13.39	20.87	19.47	18.85	0.66 ± 1.06	4.3	21.0	2.0	A	W2
SA74	09:00:50.10	-02:30:54.15	20.52	19.23	18.65	0.36 ± 0.02	3.2	11.3	2.0	V	W2
SA75	09:02:20.42	-02:30:57.28	22.76	21.97	21.41	0.63 ± 0.04	3.0	14.4	2.3	A	W2
SA76 ^G	09:04:07.97	-00:59:52.85	22.03	21.18	20.22	0.77 ± 0.04	2.4	12.4	3.3	A	W2
SA77	09:05:29.75	-02:03:17.70	20.94	19.47	18.80	0.42 ± 0.02	2.4	9.3	2.0	A	W2
SA78 ^C	09:59:39.17	+02:30:43.98	22.72	21.20	19.92	0.74 ± 0.06	3.2	16.4	3.0	V	D2
SA79	09:59:42.43	+02:29:56.10	23.10	21.64	20.32	0.76 ± 0.04	3.5	18.1	3.0	V	D2
SA80	09:59:55.98	+02:19:01.79	23.30	22.19	21.06	1.00 ± 0.04	2.4	13.5	3.3	A	D2
SA81	10:01:33.74	+02:21:35.35	21.96	20.71	20.08	0.69 ± 0.05	3.0	14.9	2.0	V	D2
SA82	10:01:47.79	+02:22:06.55	22.92	21.44	20.20	0.69 ± 0.05	3.5	17.4	2.7	V	D2
SA83 ^C	10:02:11.22	+02:11:39.46	23.64	22.02	20.77	0.89 ± 0.05	2.6	14.1	4.0	V	D2
SA84	10:02:11.67	+02:29:55.24	22.81	21.55	20.56	0.77 ± 0.05	1.9	9.9	3.0	A	D2
SA85	10:02:14.85	+02:37:36.47	23.51	22.20	21.15	0.65 ± 0.05	2.1	10.2	3.0	V	D2
SA86	13:56:49.33	+55:27:07.00	20.41	18.86	18.21	0.46 ± 0.03	3.7	15.1	2.5	A	W3
SA87	13:57:25.48	+53:17:43.96	20.52	19.03	18.15	0.54 ± 0.02	3.5	15.6	3.0	A	W3
SA88	13:59:47.26	+55:35:37.57	23.40	22.63	21.57	0.87 ± 0.04	2.2	11.9	2.3	A	W3
SA89	14:00:40.17	+56:07:49.41	20.47	19.08	18.48	0.42 ± 0.03	3.7	14.3	3.0	A	W3
SA90	14:01:10.46	+56:54:20.51	20.89	19.42	18.57	0.53 ± 0.03	3.7	16.3	3.7	A	W3
SA91	14:01:44.90	+53:02:09.62	22.01	20.50	19.61	0.56 ± 0.03	3.0	13.6	3.7	A	W3
SA92 ^G	14:01:56.39	+55:44:46.78	20.79	19.40	18.70	0.50 ± 0.03	2.8	12.0	2.0	V	W3
SA93	14:02:47.90	+57:08:52.04	23.70	22.75	21.68	1.22 ± 0.04	3.2	18.6	2.0	A	W3
SA94	14:03:51.68	+57:23:50.41	24.08	22.48	21.72	0.51 ± 0.03	0.0	0.0	2.7	A	W3
SA95 ^G	14:04:54.46	+52:00:24.70	20.10	18.66	17.88	0.49 ± 0.03	2.2	9.3	2.7	A	W3
SA96 ^m	14:05:54.33	+54:45:48.68	19.50	18.18	17.49	0.41 ± 0.03	2.8	10.7	3.0	V	W3
SA97	14:08:13.82	+54:29:08.12	20.28	18.79	18.04	0.48 ± 0.02	8.0	33.4	4.0	A	W3
SA98	14:11:20.53	+52:12:09.91	20.16	18.75	17.93	0.52 ± 0.03	18.4	80.3	2.0	A	W3
SA99 ^m	14:13:55.43	+53:43:44.72	19.03	17.83	17.26	0.29 ± 0.03	2.4	7.3	2.0	A	W3
SA100	14:14:47.19	+54:47:03.59	21.19	19.67	18.45	0.63 ± 0.02	14.7	70.3	3.7	A	W3
SA101	14:16:44.52	+56:42:16.18	22.99	21.41	19.94	1.29 ± 0.16	3.5	20.5	2.0	A	W3
SA102 ^R	14:19:12.17	+53:26:11.44	21.83	20.30	19.11	0.69 ± 0.02	9.9	49.2	3.7	A	W3
SA103 ^{mG}	14:19:17.25	+51:17:28.63	20.78	19.50	18.72	0.47 ± 0.03	4.1	16.9	3.0	V	W3
SA104	14:21:02.56	+52:29:42.51	17.74	16.79	16.33	0.18 ± 0.01^z	11.7	24.9	2.0	A	D3
SA105	14:21:18.35	+52:50:22.37	21.40	19.89	19.14	0.47 ± 0.05	2.8	11.6	3.0	V	D3
SA106	14:22:58.34	+51:24:39.50	22.78	21.75	20.80	0.74 ± 0.04	1.9	9.7	2.5	A	W3
SA107	14:23:49.27	+57:26:33.90	23.20	22.15	21.21	0.69 ± 0.06	2.2	10.9	2.0	A	W3
SA108	14:25:44.27	+57:07:24.47	25.45	23.87	22.53	0.86 ± 0.04	4.5	24.2	2.7	A	W3
SA109	14:26:08.04	+57:45:23.90	20.56	19.49	18.99	0.39 ± 0.03	3.2	11.9	2.0	A	W3
SA110 ^m	14:28:10.54	+56:39:48.36	17.67	16.76	16.30	0.80 ± 0.28	4.1	21.5	2.3	A	W3
SA111	14:28:34.82	+52:13:06.44	22.28	20.75	19.94	0.52 ± 0.03	5.0	21.8	2.7	A	W3
SA112	14:30:00.65	+55:46:47.97	21.58	20.02	19.12	0.55 ± 0.02	4.3	19.3	4.0	A	W3
SA113	14:31:39.77	+55:33:22.81	21.83	20.57	19.42	0.71 ± 0.03	3.0	15.1	3.0	V	W3
SA114	14:31:52.67	+57:28:36.73	22.87	21.52	20.19	0.83 ± 0.03	3.5	18.6	2.3	A	W3
SA115	14:34:03.87	+51:21:36.07	19.98	18.66	18.06	0.39 ± 0.02	2.6	9.6	2.0	A	W3
SA116	14:34:34.69	+56:59:20.17	21.19	19.63	18.74	0.57 ± 0.02	4.1	18.7	2.7	A	W3
SA117 ^m	22:01:51.79	+04:10:08.42	18.53	17.73	17.19	0.43 ± 0.04	7.3	28.7	2.7	A	W4
SA118 ^m	22:02:01.66	+01:47:09.57	18.82	17.63	17.07	0.30 ± 0.02	5.0	15.6	3.0	A	W4
SA119 ^G	22:03:29.03	+02:05:18.89	21.24	19.99	19.37	0.38 ± 0.04	2.6	9.5	4.0	V	W4
SA120 ^G	22:05:06.92	+01:47:03.71	21.20	19.91	19.15	0.46 ± 0.06	2.1	8.6	2.0	A	W4
SA121	22:06:42.03	+04:11:30.85	21.20	19.81	18.88	0.62 ± 0.03	3.7	17.6	3.0	A	W4
SA122	22:13:06.93	-00:30:37.05	21.19	19.98	18.81	0.69 ± 0.02	2.8	13.9	3.0	A	W4
SA123	22:13:31.85	+00:48:36.14	23.37	21.87	20.56	1.00 ± 0.03	4.8	26.9	4.0	A	W4
SA124	22:14:09.57	-17:30:56.23	22.63	21.08	19.85	0.83 ± 0.05	7.4	39.4	4.0	V	D4
SA125	22:14:18.82	+01:10:33.85	20.31	19.24	18.84	0.74 ± 0.08	0.0	0.0	3.0	A	W4
SA126	22:17:29.38	-00:38:36.60	19.93	18.94	18.32	0.78 ± 0.02	1.9	9.9	2.0	A	W4
SA127	22:21:43.74	-00:53:02.89	19.36	17.98	17.35	0.39 ± 0.02	4.7	17.4	3.3	V	W4

Notes. **m**: this galaxy falls within the masked region as per the catalog from which the magnitudes and the redshift are extracted. **z**: the magnitudes and/or redshift are not from the Coupon et al. catalog instead are measured by the author using *sExtractor* and/or *ZEBRA* (Feldmann et al. 2006), respectively. **C**: this lens is identified in both D2 and COSMOS fields. Note that other lenses within D2 have not been reported in the COSMOS lens sample (Faure et al. 2008). **R**: this lens is also found in RCS (see G03). **G**: this lens is also a part of the SL2S-RINGS sample.

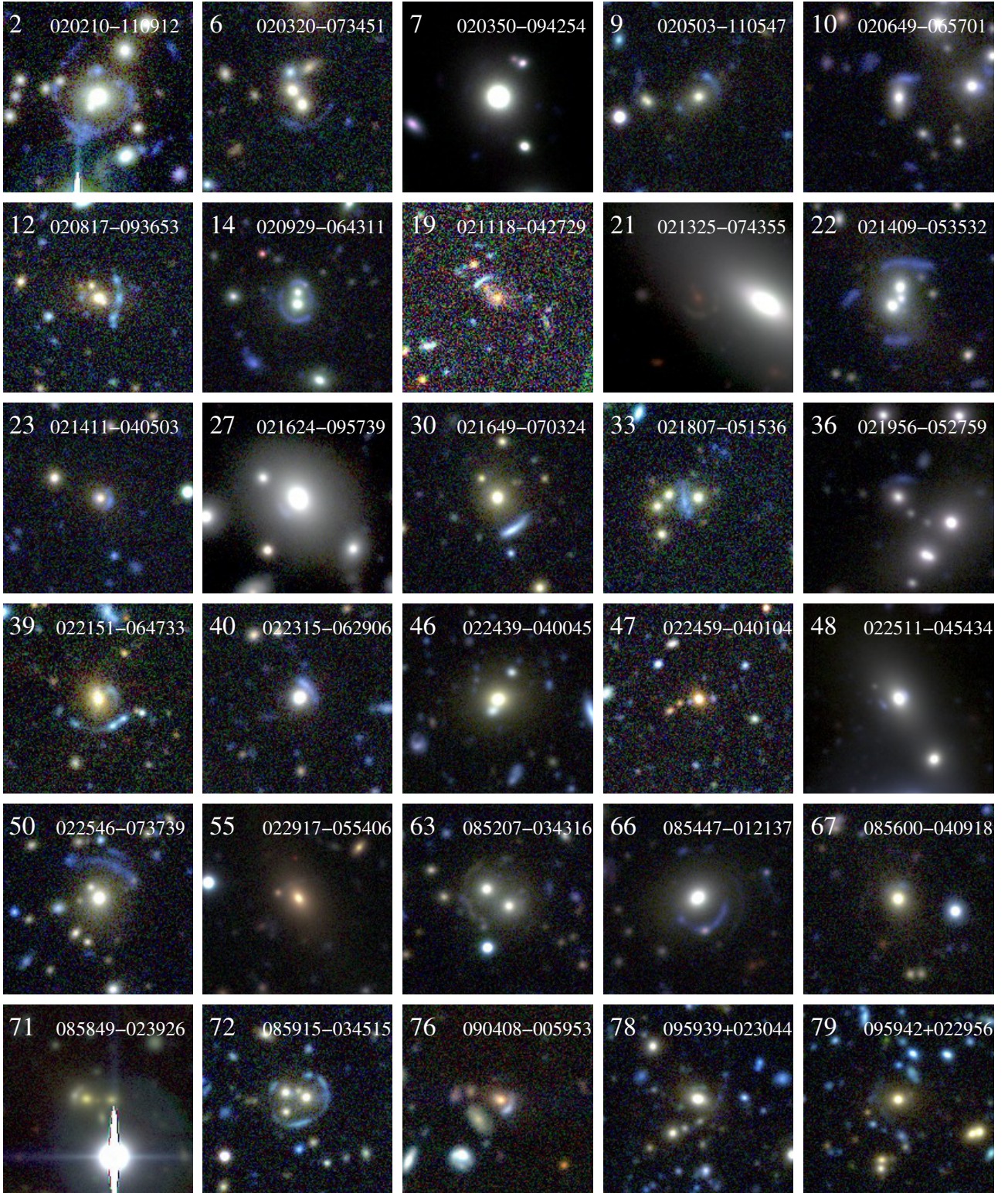


Figure 3. SARCS sample showing the 54 promising lens systems with a rank of 3 and above. All color cutouts are made from CFHT imaging in g , r , and i bands. The cutouts are $\sim 30''$ on a side. The candidate SA78 is known as COSMOS 5939+3044.

(A color version of this figure is available in the online journal.)

giant arcs and presence of radial arcs in the sample. Finally, we measure the azimuthal distribution and image separation distribution (ISD) of the arcs and argue their importance as diagnostics for understanding the matter distribution of the lenses, statistically.

3.1. Lens Redshift Distribution

The lenses producing giant arcs (e.g., length-to-width ratio ≥ 10) consist of clusters which lie at the high end of the halo mass function. The redshift distribution and abundance of such

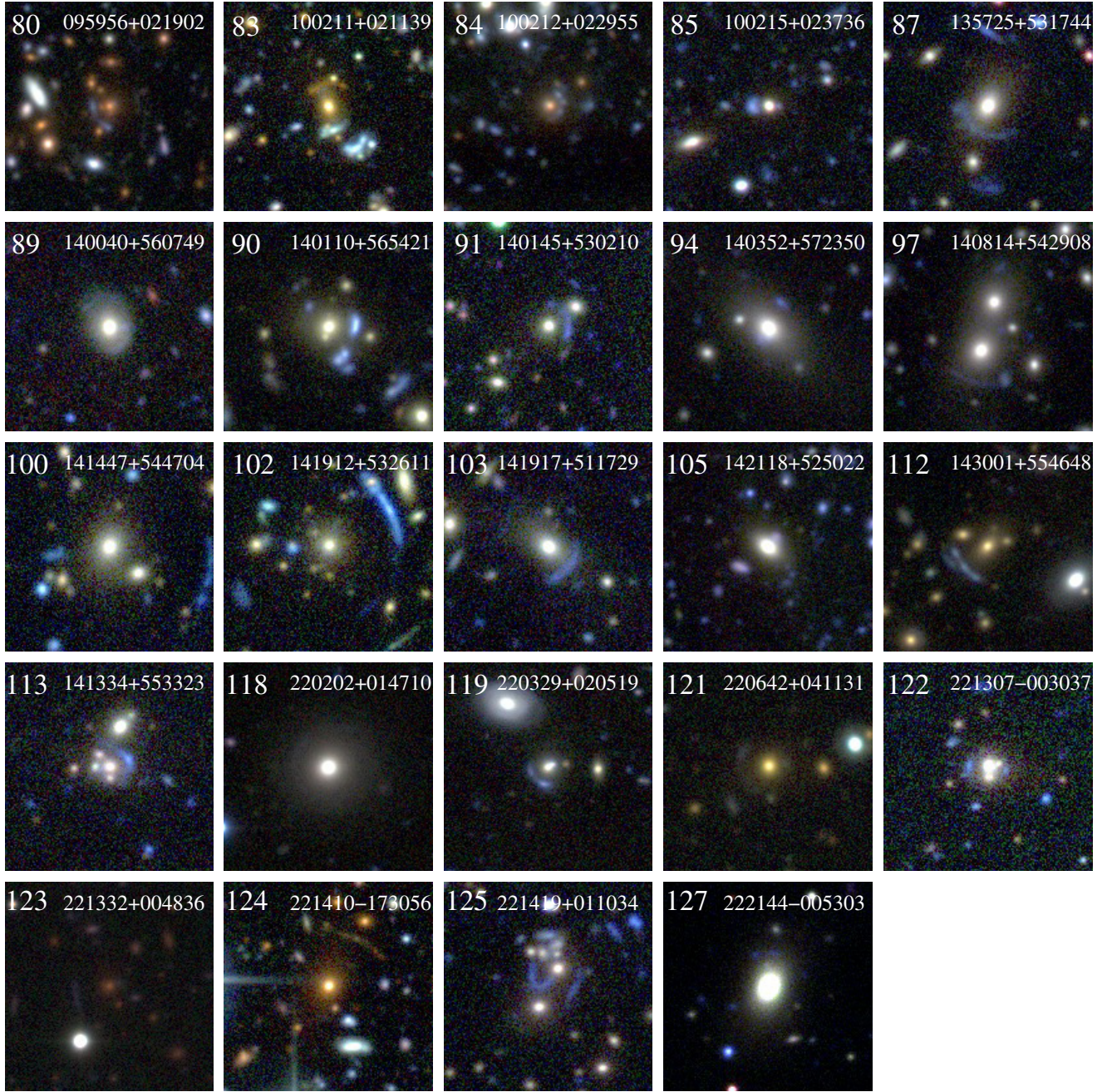


Figure 4. Continuation of Figure 3. The candidates SA83 and SA102 are known as COSMOS 0211+1139 and RCS 1419.2+5326, respectively. (A color version of this figure is available in the online journal.)

massive clusters depend on the parameters of a cosmological model. Bartelmann et al. (1998) estimated that most of the lensing clusters giving rise to giant arcs should peak at around $z \sim 0.3-0.4$ for the currently accepted standard cosmological model.

We use the CFHTLS photometric redshift catalogs (Coupon et al. 2009), which are generated from the code LE PHARE (Ilbert et al. 2006) to calculate the SARCS lens redshift distribution. The accuracy on the redshifts of galaxies in the WIDE with magnitudes $i < 21.5$ is $\sigma_{\Delta z/(1+z)} \sim 0.037$ and with magnitudes $22.5 < i < 23.5$ is $\sigma_{\Delta z/(1+z)} \sim 0.08$. In Figure 6, we show the redshift distribution for all the lenses in the SARCS sample (solid histogram) and for lenses consisting

of giant arcs only (dashed histogram). In Appendix B, we describe how we estimated the mean and 1σ uncertainty given the redshift measurement errors (see Table 2). We find that the mean of the lens redshift distribution for the SARCS sample is $z = 0.58 \pm 0.22$ and that for the sample of giant arcs is $z = 0.64 \pm 0.19$. We note that the mean of the giant arcs sample is at a higher redshift compared to the peak expected from Bartelmann et al. (1998) but certainly consistent within 2σ confidence interval. For comparison, the RCS sample G03 finds that most of the lenses with giant arcs have redshifts upward of ~ 0.6 .

We make a qualitative comparison of the redshift distributions of the lens populations from other surveys in the literature (not

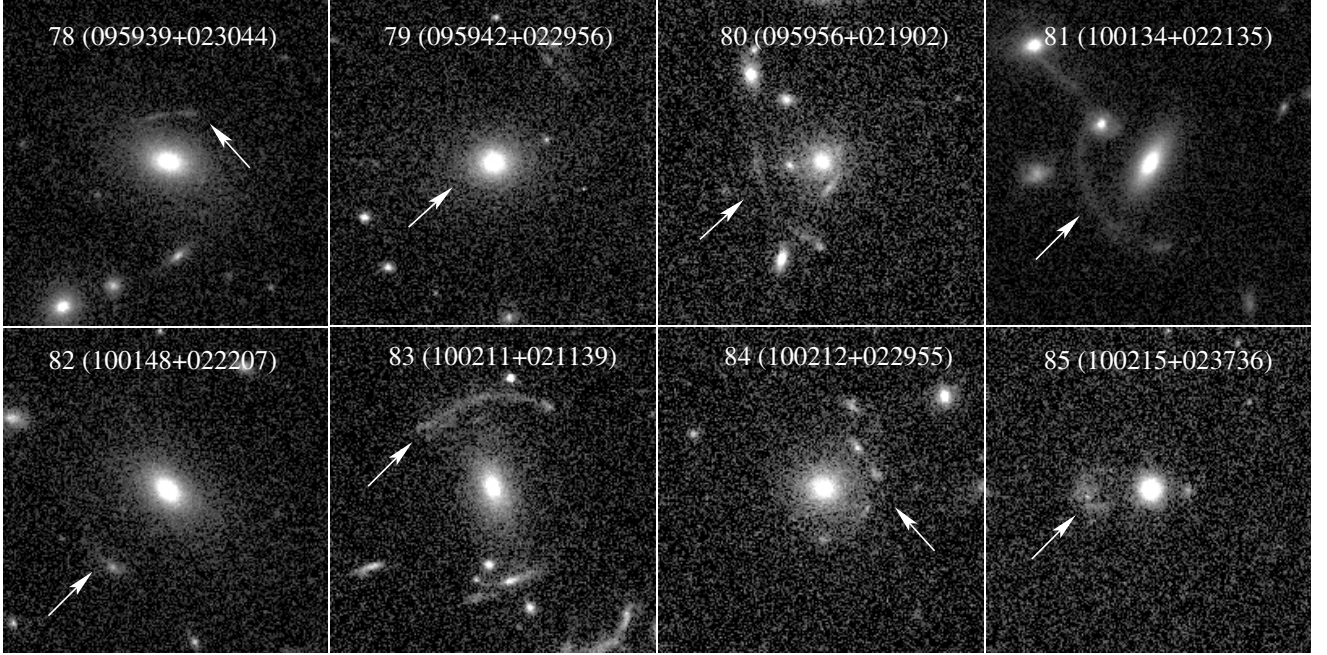


Figure 5. *HST* *I*-band (F814W) imaging of the SARCS lens candidates within the D2 field extracted from the COSMOS archive. The IDs and coordinates are labeled for each system. The arrows point toward the putative lensed arcs. The arc in SA79 is too faint to be visible in the *I*-band *HST* image shown here. All candidates are new detections except SA78 (COSMOS ID: 5939+3044) and SA83 (COSMOS ID: 0211+1139). The images are 6'' on a side. North is up and east is left.

Table 3
SARCS Candidates with Follow-up Information from the SL2S Collaboration

R.A.	Decl.	Reference	z_l, z_s	Comment
02:09:57.67	-03:54:57.08	VM	... , ...	V, H
02:13:24.52	-07:43:54.82	...	0.72, ...	K, V, H
02:14:08.07	-05:35:32.39	L09,V11	0.444,	V, H
		VM	$1.023 \pm 0.001/1.7 \pm 0.1$	
02:14:11.24	-04:05:02.71	M11,VM	0.609, ...	K, V, H
02:16:49.25	-07:03:23.80	VM	... , ...	V, H
02:18:07.29	-05:15:36.16	M11	0.647, ...	V, H
02:19:56.42	-05:27:59.21	VM	... , ...	V, H
02:21:51.18	-06:47:32.66	L09,VM	0.618,	V, H
02:25:11.04	-04:54:33.54	R11	0.238, 1.199	K, H
02:25:46.13	-07:37:38.52	L09	0.511,	G
08:52:07.18	-03:43:16.28	VM	... , ...	V, H
08:54:46.55	-01:21:37.08	L09,L10	$0.3530 \pm 0.0005, 1.2680 \pm 0.0003$	K, V, H
08:58:48.83	-02:39:25.79 , ...	H
08:59:14.55	-03:45:14.85	L09,VM	0.647, ...	V, H
09:04:07.97	-00:59:52.85 , ...	H
10:02:11.22	+02:11:39.46 , ...	H
14:08:13.82	+54:29:08.12	L09	0.416, ...	S, H
14:14:47.19	+54:47:03.59 , ...	H
14:19:12.17	+53:26:11.44 , ...	H
14:19:17.25	+51:17:28.63 , ...	H
14:30:00.65	+55:46:47.97	T10	$0.497 \pm 0.001, 1.435 \pm 0.001$	G, H
14:31:39.77	+55:33:22.81	T10	$0.669 \pm 0.001, ...$	G, H
22:03:29.03	+02:05:18.89 , ...	H
22:13:06.93	-00:30:37.05	L09	... , ...	H
22:13:31.85	+00:48:36.14	L09	... , ...	H
22:14:18.82	+01:10:33.85 , ...	H
22:21:43.74	-00:53:02.89	L09	0.334, ...	S, H

Notes. Col 3: L09—Limousin et al. (2009), L10—Limousin et al. (2010), T10—Thanjavur et al. (2010), R11—Ruff et al. (2011), V11—Verdugo et al. (2011) and M11—Muñoz et al. (2012, in prep, PI—V. Motta, ESO-080.A-0610). VM is assigned to those systems which are being followed up for spectroscopy with the VLT by V. Motta (PI, ESO-086.A-0412). Col 4: Spectroscopic redshifts for the lens galaxy and lensed source from the follow-up observations along with their error bars, if available. Col 5: V—VLT, K—Keck, and G—Gemini indicate telescopes used for follow-up spectroscopy and S-SDSS spectroscopy. H corresponds to *HST* imaging followed up by J-P. Kneib (PI, C15 and C16) and/or R. Gavazzi (PI, C17).

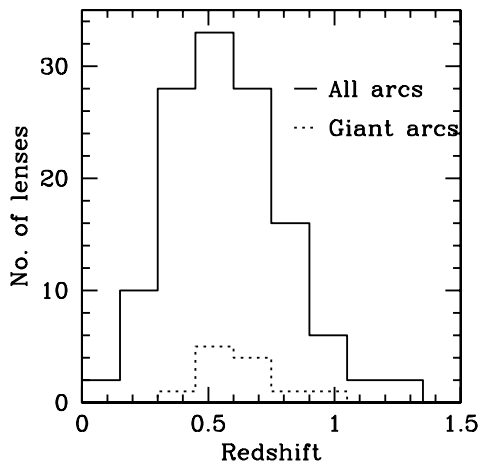


Figure 6. Redshift distributions of the lens galaxies from the SARCS sample. The solid histogram corresponds to lenses from the whole sample whereas the dashed histogram corresponds to lenses with giant arcs only. The respective means of their redshift distributions are $z = 0.58 \pm 0.22$ and $z = 0.64 \pm 0.19$ where the uncertainties indicate a 68% confidence level.

shown in the figure). However, we note that these surveys have significantly different selection functions and hence quantitative conclusions should not be drawn. The distribution of lens sample from CASTLES¹¹ peaks between 0.3 and 0.4, which is lower than the mean redshift of the SARCS sample. CASTLES has a large enough sample of lenses but is not homogeneously selected. Nevertheless, the peaks are consistent within 2σ (assuming an error of 0.05) in spite of the differences in the sample selection. The COSMOS lens sample (Faure et al. 2008), on the other hand, is fairly homogeneous but the sample size of confirmed lenses is relatively small. COSMOS has a bimodal lens redshift distribution with a minimum at ~ 0.5 – 0.6 . This is in stark contrast with the redshift distribution of SARCS (see Figure 6).

3.2. Giant and Radial Arcs

Here, we report detections of giant and radial arcs from our sample. The arcs, both radial and tangential, produced in massive clusters are conventionally referred to as giant arcs, if their length-to-width (l/w) ratio is larger than about 8 or 10. For a (non-singular) circularly symmetric projected density profile, the inverse magnification matrix of a lensed image has two eigenvectors, one in the radial and the other in the tangential direction. If the radial eigenvalue becomes 0, then the arcs are magnified and stretched radially with respect to the center of the lens and are called radial arcs. If the tangential eigenvalue becomes 0, then the arcs are magnified and stretched tangentially and are called tangential arcs.

3.2.1. Giant Arcs

The statistics of giant arcs allows the detection of clusters at the massive end of halo mass function that are rare. The statistics of such rare massive structures is sensitive to the cosmological model of the universe. Hence, several attempts have been made to predict the giant arcs statistics (e.g., Bartelmann et al. 1998; Wambsganss et al. 2004; Dalal et al. 2004, henceforth, D04) that suggested a large discrepancy compared to the observed abundance of arcs from a well-defined cluster population (e.g., Luppino et al. 1999; Gonzalez et al. 2001; Gladders et al.

2003; Li et al. 2005, 2006). However, the discrepancy has been substantially diminished due to more realistic assumptions such as using a realistic source redshift distribution and improved predictions which consider the contribution of central galaxy or substructure within the halos (e.g., Meneghetti et al. 2000, 2003; Horesh et al. 2005).

We present the abundance of giant arcs in our sample, which could be tested with predictions from realistic simulations by taking into account the observational limitations. Within a total unmasked area of $\sim 150 \text{ deg}^2$, eight of the arcs have l/w of ~ 10 or above. Additionally, four more arcs have $l/w \sim 8$, which are included in the sample of giant arcs because these appear to be broken either due to noise or due to a satellite galaxy. Since one of the giant arcs is from DEEP, we use the rest of the 11 giant arcs from the WIDE data for comparison with RCS. We use the primary sample of RCS, which has a roughly similar depth compared to WIDE data. The primary RCS lens sample has six arcs with $l/w \geq 8$ found within a total area of 90 deg^2 G03. Therefore, the RCS sample has $0.07 \pm 0.03 \text{ arcs deg}^{-2}$ which is consistent with the $0.07 \pm 0.02 \text{ arcs deg}^{-2}$ from the SARCS sample.

3.2.2. Radial Arcs

The radial arcs are formed when the source falls on the radial caustic (see Appendix A). The size of the radial caustic and hence, the cross section to form radial arcs depends on the slope of inner regions of the density profile of the lens (e.g., Hattori et al. 1999). The statistics of radial arcs can thus be used to constrain the slope of the central density profiles of clusters and thereby allow a better understanding of the nature of dark matter (Molikawa & Hattori 2001). More thorough investigations have been carried out to test the effects of realistic assumptions of properties such as lens ellipticity, source size, and ellipticity on the statistics of radial and tangential arcs (e.g., Keeton 2001; Oguri 2002). Sand et al. (2005) used archival *HST* (WFPC2) data on various lensing cluster samples to do a systematic study of the number ratio of radial-to-tangential arc statistics. They accounted for the effects due to the central galaxy in the expected number ratio and placed loose constraints on the slope of the average inner density profile of the dark matter. They underlined the need of larger observational data sets to further explore effects of substructure, mass of the central galaxy, and homogeneity of the sample.

We report detections of radial arc candidates in the SARCS sample during the visual inspection. We found one candidate which appears like a radial arc in the system SL2SJ141447+544704 (SA100 in Table 2). This lens system also has a giant tangential arc (T1) with the same color as the radial arc (R1; see the left panel of Figure 7). The subsequent *HST* observation in the F606W band shows another radial arc candidate (R2; see the right panel of Figure 7). The nature of the radial arc candidates needs to be verified with spectroscopy and mass modeling since these could be blue edge-on disk galaxies. Radial arcs are usually faint and are overshadowed by the bright central galaxies near which they are formed. Nevertheless, we argue that a follow-up imaging of the promising SARCS candidates at high resolution will help in creating a homogeneous sample of radial and tangential arcs which could provide crucial insights in understanding the density distributions in the inner regions of the lens systems.

3.3. Galaxy-arcs Orientation

In this section, we quantify the angular distribution of arcs with respect to the major axis of the ellipticity of the lensing

¹¹ <http://www.cfa.harvard.edu/castles/>

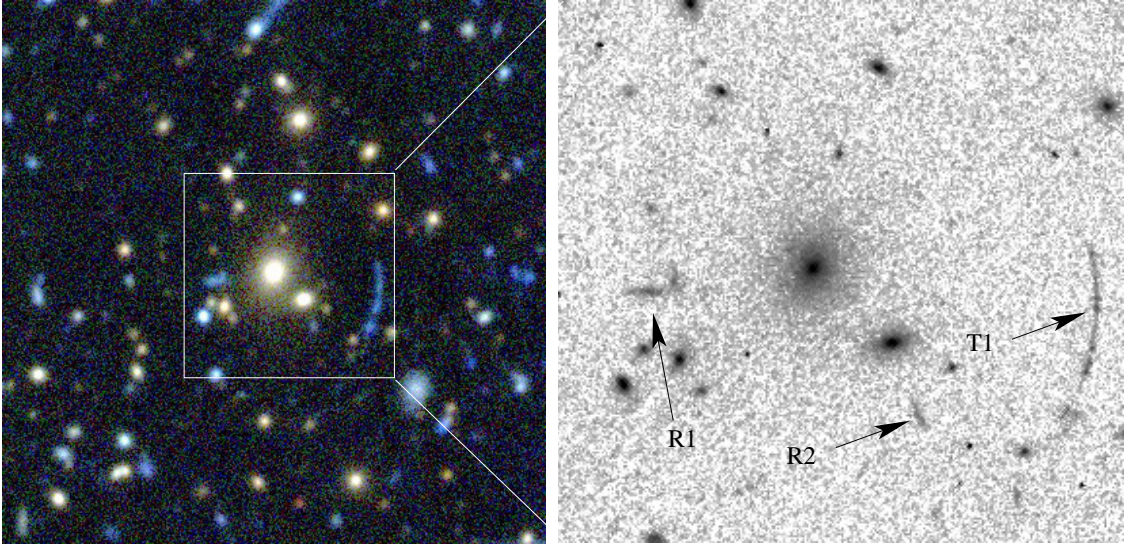


Figure 7. CFHTLS *gri* image of SL2SJ141447+544704 (SA100) on the left and *HST* F606W (*V* band) image on the right. The high resolution of *HST* suggests two radial arc candidates labeled as R1 and R2 whereas the tangential arc labeled as T1 is a confirmed lensed arc. The CFHTLS image is $74''.4$ on a side and the *HST* image is $\sim 28''.3$ on a side.

(A color version of this figure is available in the online journal.)

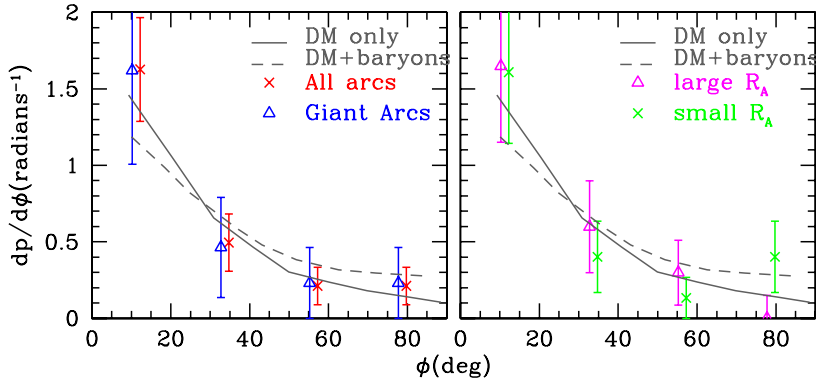


Figure 8. Angular distribution of arcs with respect to the lens galaxy. The data points in both the panels are from the SARCS sample. In the right panel, the “all arcs” sample is divided into small and large R_A . The expected curves for dark matter (DM) only (solid) and DM + $3 \times 10^{12} h^{-1} M_\odot$ (dashed) are taken from D04, which are calculated from the cluster sample of the GIF simulation (Kauffmann et al. 1999).

(A color version of this figure is available in the online journal.)

halo. D04 suggested that triaxial dark matter halos, when acting as lenses, usually form lip caustics (e.g., Hattori et al. 1999) and the formation of giant arcs tends to be at the ends of the lip caustics. Using numerical simulations, they showed that the giant arcs are oriented very close to the major axis of the dark matter halo. If a central galaxy is further added to the halo, it then appeared to isotropize the angular distribution of arcs to a small extent. In order to compare these predictions to the observations, D04 measured the angular distribution of giant arcs from the EMSS cluster sample under the assumption that the ellipticity of the lensing galaxy is a good representation of the ellipticity of the underlying DM halo. They found that most of the giant arcs had an orientation of <45 deg, consistent with their predictions.

We use the same definition as that used in D04 for the orientation of the arcs, that is, the angle between the major axis of the lens galaxy and the line connecting the center of the lens galaxy to the midpoint of the arc. The measurement of orientation of real arcs tends to be somewhat subjective since there exists an ambiguity in defining the extent of the arc, which

is required to find the midpoint of the arc. The midpoint of the arc and its orientation from the major axis of the lens is calculated manually. When there is a single dominant lensing galaxy we measure the position angle (P.A.) of the major axis of the lens galaxy with SExtractor (Bertin & Arnouts 1996); otherwise we adopt the following strategy. If there are two or three (nearly collinear) lens galaxies with similar colors and brightness, then the P.A. of the ellipticity is assumed to be along the line joining the lens galaxies. If a circle going through the arc encloses multiple lens galaxies with comparable brightness but no obvious elongation, then such a system is rejected. If one of the lens galaxies is predominantly brighter than the companion galaxies, then the ellipticity of the dominant galaxy is assumed to reflect the overall ellipticity of the gravitational potential and hence, of the caustics.

After applying the above selection cuts, we are left with 36 all-arc candidates and 11 giant arcs with an average ranking >2.5 . The angular distribution of the giant arcs from the SARCS sample is shown in the left panel of Figure 8. We compare the observed distribution to the expected distributions from D04

which correspond to two cases: (1) for dark-matter-only lensing halo (solid curve) and (2) a dark matter halo to which a galaxy of $3 \times 10^{12} h^{-1} M_{\odot}$ is added (dashed curve). The distribution of giant arcs from our sample appears to follow the expected trend although it is not possible to distinguish between the two cases. We also show the distribution of orientation of all-arc candidates (see the left panel of Figure 8) which seems to follow the expected anisotropy. This extends the result obtained by D04 to group-scale lens systems. Furthermore, we split the all-arcs sample into small R_A ($< 5''$) and large R_A ($\geq 5''$) samples to see the dependence of the angular distribution on the Einstein radius (or the arc radius). The choice of cut at $5''$ is arbitrary. The baryonic matter tends to make the matter distribution in halos more spherical at the center. Therefore, the angular distribution of arcs for the sample with smaller R_A is expected to be more isotropic compared to the sample with large R_A . However, we do not find any clear differences in the angular distribution of small and large R_A for the SARCS sample within the uncertainties (see the right panel of Figure 8). We note that these measurements may have some systematic errors due to the orientation dependence of the selection function. Ambiguities also exist in the definition of the orientation in few cases, especially when multiple candidate lens galaxies are involved. In addition, the current analysis consists of lens candidates as opposed to confirmed lens systems. Therefore, our conclusions should be treated more of a qualitative nature.

3.4. Image Separation Distribution

The ISD is sensitive to the halo mass, the abundance of the lens population, the mass distribution in the lens, and the source redshift. Therefore, the ISD measured from galaxy to cluster scales contains information about the cosmological parameters and various scaling relations between galaxy properties and halo mass. Hitherto, the ISD has been measured either at small image separations (θ) primarily, with lens samples such as CASTLES (e.g., Keeton et al. 2000; Khare 2001) and CLASS (e.g., Kochanek & White 2001; Oguri 2006) or at large θ with cluster-scale lenses, for example, the MACS sample (Zitrin et al. 2011). With the SARCS sample, we can probe the intermediate-mass regime corresponding to group-scale lenses. The SARCS sample is selected based on the presence of elongated arc-like features and is not directly biased toward selecting a specific lens population. The ISD measured from the lens samples is referred to as the observed ISD and the ISD calculated from various models is referred to as the expected/predicted ISD throughout this paper.

3.4.1. Model for the Expected Distribution

In the past, the expected ISD was computed with models consisting of either galaxy-dominated (e.g., Turner et al. 1984) or dark-matter-dominated lensing halos (e.g., Narayan & White 1988). However, since the density profile of dark matter is known to be affected due to the presence of baryons at the center, the need for a more complex model to explain the observed ISD was pointed out by Keeton et al. (1998) and demonstrated by subsequent studies (e.g., Porciani & Madau 2000; Kochanek & White 2001; Oguri 2006, henceforth O06). We follow the framework developed in O06 and Oguri et al. (2002) to calculate the expected ISD in order to compare it with the observed ISD from the SARCS sample. We also adopt the cosmology used in O06 which constitutes of the following cosmological parameters: $\Omega_m = 0.3$, $\Omega_{\Lambda} = 0.7$, and $\sigma_8 = 0.9$. We describe in

detail how each of the model parameters are calculated before proceeding to the comparison of various models.

The probability for a source at redshift, z_s , to get lensed with image separation greater than θ is given by

$$P(> \theta; z_s) = \int_0^{z_s} dz_l \frac{d\chi}{dz_l} \int_0^{\infty} dM n(M, z_l) \times \sigma_{\text{lens}} \Theta(M - \tilde{M}), \quad (4)$$

where χ is the comoving distance, z_l is the redshift of the lens, M corresponds to the halo mass, $n(M, z_l)$ is the halo mass function, \tilde{M} is the minimum halo mass that causes an image separation equal to θ , and Θ is the Heaviside step function. The biased lensing cross section, σ_{lens} is measured in comoving units and is given by

$$\sigma_{\text{lens}} = \pi y_r^2 \xi_0^2 B(z_s), \quad (5)$$

where $y_r \xi_0$ corresponds to the radius of the outermost caustic in the lens plane¹² and it depends on the matter density distribution around the lens. The quantity $B(z_s)$ denotes the magnification bias which causes sources, fainter than the limiting magnitude of the survey, to be detected in the sample. It is the ratio of the number of sources that can be potentially lensed into an image with luminosity L to the number of sources that have an intrinsic luminosity L . In general, the magnification bias depends upon the luminosity of the source and under the assumption of spherical symmetry, it is given by

$$B(z_s, L) = \frac{1}{\pi y_r^2 \Phi(z_s, L)} \int_0^{y_r} dy 2\pi y \Phi\left(z_s, \frac{L}{\mu(y)}\right) \frac{dL}{\mu(y)}, \quad (6)$$

where $\Phi(z_s, L)$ is the true source luminosity function and $\mu(y)$ is the lensing magnification at an angular position y inside the caustic. Under the assumption of a power-law luminosity function which does not evolve with redshift, the luminosity dependence of the magnification bias drops out.

Differentiating both sides of Equation (4), we obtain the differential probability

$$\left| \frac{dP}{d\theta} \right| = \int_0^{z_s} dz_l \frac{d\chi}{dz_l} \int_0^{\infty} \frac{dM}{d\theta} n(M, z_l) \sigma_{\text{lens}} \delta[M - \tilde{M}(\theta)] = \int_0^{z_s} dz_l \frac{d\chi}{dz_l} n(\tilde{M}[\theta], z_l) \sigma_{\text{lens}} \frac{d\tilde{M}}{d\theta}, \quad (7)$$

which can be directly related to the ISD of the observed lens sample.

In O06, the above equation is used to predict the ISD resulting from different components in a given halo. To use the above equation, we have to specify the distribution of mass inside a halo and the halo mass function. The former allows us to calculate $\tilde{M}(\theta)$ and the biased cross section for lensing. For the latter, O06 assumed the state-of-the-art calibration of the mass function given by Sheth & Tormen (1999). For the mass distribution inside a halo, O06 considered the following different components.

1. At the center of the dark matter halo, the matter density is dominated by the central galaxy and the total matter distribution is very close to that of a singular isothermal

¹² For lens models with spherical symmetry that are considered here, the radial caustic is the outermost caustic and a source lying within the outermost caustic gets strongly lensed, i.e., multiply imaged.

sphere (SIS). This distribution is given in terms of the one-dimensional velocity dispersion (σ_{vel}) such that $\rho(r) \propto \sigma_{\text{vel}}^2/r^2$. Following Section 2.3.1 of Oguri et al. (2002), we calculate the size of the radial caustic ($y_r \xi_0$) in comoving coordinates, the total magnification of the lensed images, and the relation between the velocity dispersion and the image separation for the SIS mass distribution. To relate the mass of the halo to the velocity dispersion of the central galaxy, O06 used galaxy scaling relations. They adopted the halo-mass–luminosity relation from Vale & Ostriker (2004) using the abundance matching technique and the Faber–Jackson relation obtained by Bernardi et al. (2003) using SDSS galaxies to relate the luminosity to the velocity dispersion of the galaxy. Following Cooray & Milosavljević (2005), they also included a lognormal scatter in the halo-mass–luminosity relation with a scatter of 0.25 dex (see also More et al. 2009b, 2011b).

- On large scales, the distribution of dark matter follows the Navarro–Frenk–White (NFW; Navarro et al. 1997) profile given by

$$\rho(r) = \frac{\rho_s}{(r/r_s)(1+r/r_s)^2}, \quad (8)$$

where the scale radius $r_s = R_{\text{vir}}/c$; the concentration parameter c is related to the mass M with a considerable scatter. O06 used the mean relation between concentration and mass of Bullock et al. (2001), given by

$$\bar{c} = \frac{10}{1+z} \left(\frac{M}{M_*} \right)^{-0.13}. \quad (9)$$

The distribution of concentrations at fixed halo mass is assumed to be lognormal with a scatter of 0.3 dex. For the NFW case, we calculate the caustic size, the magnification, and the relation between halo mass and the image separation numerically. We defer the details of our procedure to calculate these quantities to Appendix A.

- In addition to the above two simple profiles, O06 also considered a combined total profile which included the central galaxy, the dark matter halo, and the effect of adiabatic contraction (AC) of dark matter in response to the baryonic component of the galaxy at the center. In this case, O06 assumed the central galaxy to have a Hernquist profile (Hernquist 1990), given by

$$\rho(r) = \frac{M_b}{2\pi} \frac{1}{(r/r_b)(r_b+r)^3}, \quad (10)$$

where M_b is the stellar mass of the galaxy and r_b is a core radius. The stellar mass M_b was obtained using the halo-mass–luminosity relation found by Vale & Ostriker (2004) and adopting a constant mass-to-light ratio of $3.0h_{70} M_\odot/L_\odot$. The scaling relations of Bernardi et al. (2003) can be used to obtain the effective radius R_0 as a function of the luminosity of the galaxy, which is related to the core radius of the Hernquist profile such that $r_b = 0.551R_0$. The AC is carried out using the analytical formalism presented by Gnedin et al. (2004). Having specified the total dark matter distribution, the caustic size, the magnification, and the relation between halo mass and the image separation need to be calculated numerically. We describe the procedure we use in Appendix A.

O06 assumed the background source population to lie at a redshift of $z_s = 2$, and the source luminosity function,

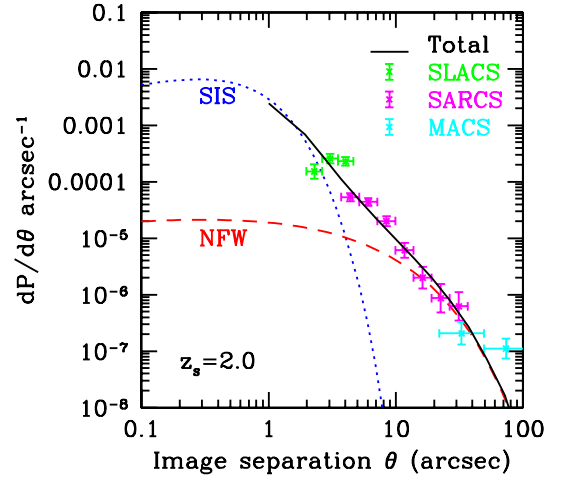


Figure 9. Image separation distribution. Theoretically calculated image separation distribution curves for the SIS profile (dotted), NFW profile (dashed), and total profile (solid) following the O06 model. The data points from SLACS (green), SARCS sample (magenta), and MACS (cyan) where the vertical bars indicate Poissonian errors and horizontal bars show the bin width. As discussed in Section 3.4.2, we multiply the ISDs of the lens samples by their respective $P(> \theta_{\text{cut}})$.

(A color version of this figure is available in the online journal.)

$\Phi(z_s, L) \propto L^{-2.1}$ appropriate for the radio survey CLASS (Myers et al. 2003; Rusin & Tegmark 2001).¹³ We are able to reproduce the expected ISDs from O06, given by Equation (7), for all the three density distributions mentioned above. The expected ISDs corresponding to these three density distributions are shown in Figure 9.

3.4.2. Observed Distribution

The observed ISD is calculated by logarithmically binning the image separations of 125 SARCS candidates¹⁴ with $\theta_{\text{cut}} \geq 20$ pixels (that is, $> 3''.7$) and an average ranking of 2 and above. The image separation for each lens candidate is taken as twice the Einstein radius or roughly the arc radius, which is the distance between the candidate lensed image and the center of respective lens galaxy. Let $\theta - d\theta = \theta_l$ and $\theta + d\theta = \theta_h$; then the observed ISD is given by

$$\left. \frac{dP_{\text{lens}}}{d\theta} \right|_{\text{obs}} = \frac{P(> \theta_h) - P(> \theta_l)}{2d\theta} = \frac{N(> \theta_h) - N(> \theta_l)}{N(> \theta_{\text{cut}})2d\theta}, \quad (11)$$

where the total number of observed lenses is $N(> \theta_{\text{cut}})$. While comparing their theoretical predictions ($dP/d\theta$) to the observed ISDs from the CLASS sample, O06 assumed an arbitrary normalization for their data points. Instead we note that,

$$\begin{aligned} P_{\text{lens}}(> \theta) &= \frac{N_{\text{lens}}(> \theta)}{N_{\text{lens}}(> \theta_{\text{cut}})} \\ &= \frac{N_{\text{lens}}(> \theta)}{N_{\text{src}}} \frac{N_{\text{src}}}{N_{\text{lens}}(> \theta_{\text{cut}})}, \\ &= \frac{P(> \theta)}{P(> \theta_{\text{cut}})}, \end{aligned} \quad (12)$$

¹³ The luminosity density for such a steep faint-end slope ($\alpha_{\text{LF}} < -2$) diverges as $L \rightarrow 0$ and necessarily requires a cutoff below some value of L_{min} .

¹⁴ Two of the candidates are excluded since their lensing configurations or the centers of their lens potential were ambiguous. These candidates have $R_A = 0''.0$ in Table 2.

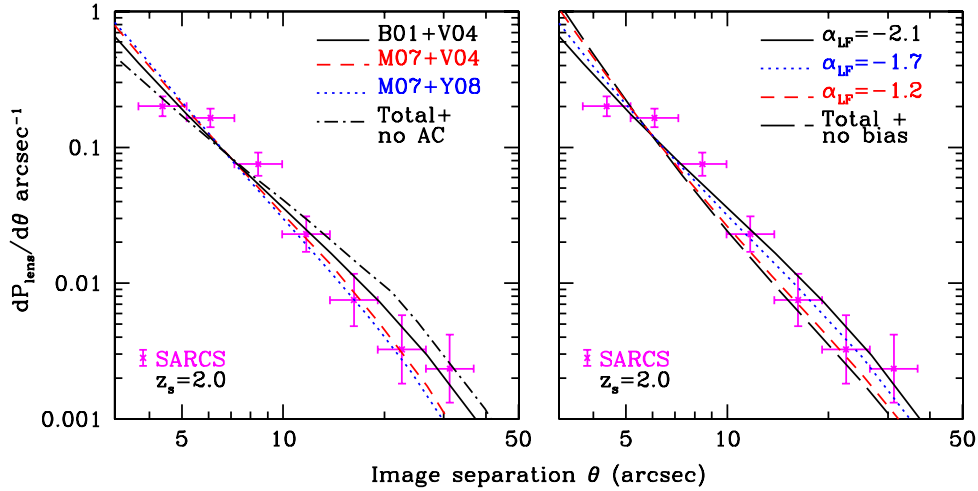


Figure 10. Image separation distribution. Theoretical curves for the total profile, shown with the solid black line, are the same as in Figure 9. Left: adopting the c - M relation of M07 (dashed) steepens the total profile. The dotted curve, with M - L relation of Y08 and c - M relation of M07, steepens further but negligibly. The total profile without the AC (dash-dotted) is also shown. Right: the effect of varying α_{LF} on the ISD is shown for the total profile. The total profile without any bias (dashed) is independent of α_{LF} . Changes in various model parameters have degenerate effects on the expected ISD. The current uncertainties on the data do not have further constraining power on the tested model parameters. All of the theoretical curves are multiplied by the $P(>\theta_{3''.7})$ since the SARCS sample consists of lenses with $\theta > 3''.7$.

(A color version of this figure is available in the online journal.)

$$\Rightarrow \left| \frac{dP}{d\theta} \right| = \left| \frac{dP_{\text{lens}}}{d\theta} \right| P(>\theta_{\text{cut}}). \quad (13)$$

To facilitate a direct comparison of the observed ISD to the theoretical expectation from O06 (see Equation (7)), we multiply Equation (11) by $P(>\theta_{\text{cut}})$. The quantity $P(>\theta_{\text{cut}})$ is obtained by integrating Equation (7) from θ_{cut} to ∞ . The SARCS data points are shown in magenta in Figure 9. The vertical error bars are calculated assuming Poisson number statistics and the horizontal bars show the bin width.

The SARCS data points demonstrate that the average density profile of the halos, giving rise to the intermediate θ values ($\sim 3''$ – $12''$), is best represented by a combined profile for the main galaxy and the dark matter halo as opposed to a pure SIS or pure NFW profile. It is clear from Figure 9 that the SARCS sample follows a steeper ISD at the intermediate scales compared to halos with NFW profile and shallower than halos with only SIS profile.

It is interesting to compare the SARCS sample with the SLACS and MACS samples which span the lower end and higher end of the ISD, respectively. These samples also have different selection functions compared to the SARCS sample. We apply the same procedure to calculate the observed ISD for SLACS and MACS data points shown in Figure 9. Intriguingly, the SLACS data points lie in the regime where the SIS density profile just ceases to be dominant. Although the SLACS sample appears to be incomplete by a factor of two to three in the lowest θ bin, the ISD of SLACS could be seen as an extrapolation of the ISD from the SARCS sample. As expected, the MACS sample is nearly consistent with either the NFW or total profile. Assuming that incompleteness is the only major factor in the ISD of SLACS, the expected ISD corresponding to the total profile best matches the SLACS, SARCS, and MACS samples combined.

We note that we have not accounted for any effects due to purity or incompleteness of the SARCS sample in this paper. We suspect that the completeness of the sample as a function of

the image separation is not severely affected due to the selection function. We are currently investigating this issue and the results will be presented in a forthcoming paper.

3.4.3. Tests with Varying Models

Here, we test the effects of varying the different components of the O06 model and compare them against the observed ISD. Since different models have different values of $P(>\theta_{\text{cut}})$, we predict $dP_{\text{lens}}/d\theta$ from each model and compare it with the observed ISD in Figure 10. We test only for image separations spanning the observed θ values. In Figure 9 and both panels of Figure 10, the solid line represents the same ISD corresponding to the total two-component profile, which accounts for the contraction of the dark matter. First, we test the influence of excluding the AC while computing the total profile. This has the effect of making the expected ISD shallower as shown by the dash-dotted curve in the left panel of Figure 10. Prima facie, the AC model fits the data better than the model without AC. However, as we show below, there are other degeneracies in the model which prevent us from ruling out the “no AC” model at high significance.

Next, we test the effect of using different c - M relations on the ISD. For example, we use the c - M relation by Macciò et al. (2007, henceforth M07) instead of that given by Bullock et al. (2001). The c - M relation of M07 is roughly 15%–20% lower than that of Bullock et al. (2001). The combined profile using the c - M relation of M07 is shown by the dashed curve in the left panel of Figure 10. Within the current statistical limits on the data, both of the c - M relations appear plausible, although the data appears to slightly favor the c - M relation of M07. Since the c - M relations differ significantly at small and large image separations, we will need additional samples of galaxy or cluster-scale lenses to test between the different c - M relations.

We also test the effect of using a more recent determination of the M - L relation obtained by Yang et al. (2008, henceforth Y08) from a sample of SDSS groups along with the c - M relation of M07 for the combined total profile. The M - L relation of Y08 differs by ~ 0.2 dex from that of Vale & Ostriker (2004) at the

intermediate-mass regime, which is the regime of interest. This appears to cause a very negligible change in the predicted ISD.

We try to quantify the effect of varying the slope of the source luminosity function at the faint end. We show the effect on the combined profile of O06 and vary the power-law index, α_{LF} , of the source luminosity function, $\Phi(z_s, L) \propto L^{\alpha_{LF}}$. This influences the lens cross section via the magnification bias. The solid curve in Figure 10 shows the expected ISD using the fiducial value of $\alpha_{LF} = -2.1$, while the dotted and short-dashed curves show the ISD in the right panel, corresponding to α_{LF} equal to -1.7 and -1.2 , respectively. It is evident from the figure that the observed ISD can be used to constrain the slope of the luminosity function, if the statistical error bars could be reduced.

We note that the magnification bias factor in the biased lens cross section is calculated assuming that the background sources are point sources such as quasars. However, the background sources corresponding to the lensed arcs are mostly galaxies with extended surface brightness and their magnification bias could be negligible (e.g., Narayan & Wallington 1993). Therefore, we calculate the ISD assuming no bias, that is, by substituting $B(z_s) = 1$ in Equation (5). The long-dashed curve in the right panel of Figure 10 shows the ISD without the bias.

The data are consistent with all of the above tested models within the uncertainties. The various scaling relations from our model that are tested here have degenerate effects on the expected ISD. For example, varying the c - M relation has the same effect as changing the slope of the luminosity function or excluding AC. However, constraints from independent observations such as dynamics and strong lensing could be used to determine the c - M relation. This will allow us to better constrain the slope of the luminosity function or make more robust statements about AC.

For all of the theoretical calculations, we have assumed $z = 2$ for the source redshift. We checked the effect of adopting different source redshifts, $z_s = 1.5$ and $z_s = 3.0$, on the predicted ISD. We found that using a higher (lower) source redshift causes the predicted $dP/d\theta$ to be larger (smaller) by roughly a constant factor at all values of θ . However, the predicted $dP_{lens}/d\theta$ is not affected because the corresponding increase (decrease) in $P(> \theta_{cut})$ almost perfectly cancels out the increase (decrease) in $dP/d\theta$. This implies that the expected ISD would not be drastically different had we accounted for the distribution of source redshifts instead of assuming a single value for the source redshift.

4. SUMMARY

We have presented the SARCS sample from the completed CFHTLS-WIDE and CFHTLS-DEEP covering a combined unmasked area of $\sim 150 \text{ deg}^2$ in the sky. The lens sample is compiled through a semi-automatic technique consisting of using the ARCFINDER algorithm, followed by visual inspection and ranking of the candidates. We briefly described how ARCFINDER works (Alard 2006) and the modifications implemented in the newer version of the algorithm. Although ARCFINDER V2.0 is faster, there is still scope for improving the algorithm in terms of increasing the purity without compromising the completeness of the arc detections.

We have compiled a total of 127 candidates in the SARCS sample, out of which 38 are found serendipitously. From the complete sample, 54 are promising lens systems (ranking of 3 and above). A total of 31 systems are almost certain or confirmed systems, out of which 27 systems have been followed up via techniques such as spectroscopy, high-resolution imaging,

and/or lens mass modeling. We found two radial arc candidates in the SARCS sample and both of them are located in the system SA100. The second radial arc is clearly identified from the high-resolution *HST* imaging only. Our sample may have more radial arcs, which could be discovered with high-resolution imaging. With statistics of radial and tangential arcs from a homogeneous and a larger sample of lenses, interesting constraints could be placed on the slope of inner density profiles of the dark matter distribution.

We have discovered a total of 12 giant arcs ($l/w \geq 8$) in our sample. Statistics with giant arcs is considered to be a good probe of cluster properties or cosmological parameters but not an easy one. We have presented the redshift distributions of the lens galaxies with giant arcs and all arcs in the SARCS sample using the photometric redshifts and found them to have mean values at $z \sim 0.6$. This is somewhat higher than the expected peak at redshift of 0.3–0.4 (Bartelmann et al. 1998) but is consistent within the uncertainties. Note that the predictions need to be revised with improved simulations and more realistic assumptions. We also calculated the angular distribution of giant arcs which are sensitive to the ellipticity of the halo. We found an anisotropy in the orientation of arcs in our sample consistent with that seen in simulated lens clusters (e.g., see D04). In addition, the angular distribution of all arcs from the SARCS sample exhibits similar anisotropy. This anisotropy appears to hold at all arc radii within the current uncertainties albeit needs to be verified with a sample of confirmed lenses. Thus, we have extended this result to group-scale halos, observationally. It would be interesting to check if lensed arcs in simulated group-scale halos also show a similar anisotropy in their azimuthal distribution and what constraints could be placed on the baryonic physics important in the inner few kiloparsecs, which is probed by these lensed arcs.

We followed the formalism of O06 to calculate the expected ISD in order to compare it with the observed ISD from SARCS sample. We first reproduced the results of O06 and then introduced variations in different scaling relations used in their model. The SARCS sample allowed us, for the first time, to probe the intermediate-mass regime corresponding to group-scale halos via the ISD. We showed that the density profile of the halos are reproduced well by a combined profile (NFW and Hernquist) at the group scales, which is consistent with the predictions. Given the uncertainties in the data and the degeneracies in the model, both of the models that account for or exclude the role of AC are consistent with the observed ISD. With the availability of larger statistics of confirmed lenses and understanding of the sample selection function, the distinction between models with and without AC would be possible.

Next, we varied the c - M relation, the halo-mass–luminosity relation, the slope of a power-law source luminosity function, and the source redshift. We found that given the current uncertainties in the observed ISD, the c - M relations of both Bullock et al. (2001) and the more recent, Macciò et al. (2007), are plausible. The expected ISD does not vary significantly and fits the data well, if the halo-mass–luminosity relations have an uncertainty of ~ 0.2 dex. Following O06, we adopted a power-law index of $\alpha_{LF} = -2.1$ for the background source luminosity function to account for the magnification bias. We further tested the effect of varying the α_{LF} on the expected ISD and found it to be consistent with the data. However, within the uncertainties, the data are also consistent, if no magnification bias is assumed. We did not test the effects of any evolution of the luminosity function or any other functional form such as a broken power law.

We found that varying the model parameters has degenerate effects on the ISD, for instance, changing the c - M relation and changing the slope of the luminosity function, α_{LF} . Therefore, using priors from independent methods on one of these relations could help in constraining the others via the observed ISD. Since the background sources are assumed to be at a redshift of 2, we tested the effect of varying the source redshift. The expected ISD ($dP_{\text{lens}}/d\theta$) is not affected by choosing different redshifts ($z_s = 1, 2, 3$) between the range we tested.

As described above, we have used arcs statistics to probe the average density profiles of group-scale lenses and we have shown the possibility to use arcs statistics in constraining some scaling relations. However, the models assumed in our work are simplistic and will need refinement as the lens samples become larger with upcoming surveys. On the observational side, understanding the selection effects will also become crucial, if the model parameters need to be constrained with high accuracy. We hope to address some of these important issues in future studies.

The authors acknowledge support from CNRS and ANR grant ANR-06-BLAN-0067. R.G. acknowledges support from the Centre National des Etudes Spatiales. V.M. gratefully acknowledges support from FONDECYT through grant 1090673. A.M. thanks Neal Dalal, Sherry Suyu, and Tomas Verdugo for useful suggestions. A.M. also appreciates comments from the referee which improved the structure and content of the paper. M.L. acknowledges the Centre National de la Recherche Scientifique (CNRS) for its support. The Dark Cosmology Centre is funded by the Danish National Research Foundation. The authors recognize and acknowledge the very significant cultural role and reverence that the summit of Mauna Kea has always had within the indigenous Hawaiian community. We are most fortunate to have the opportunity to conduct observations from this mountain. Tests with varying models of ISD used in this work have been performed on the Joint Fermilab–KICP Supercomputing Cluster, supported by grants from Fermilab, the Kavli Institute for Cosmological Physics, and the University of Chicago.

Facilities: CFHT, VLT:Antu

APPENDIX A

NUMERICAL DETERMINATION OF LENSING QUANTITIES

We describe how we numerically determined the relation between the halo mass and the image separation, the size of radial caustic, and the position-dependent magnification for general spherically symmetric mass distributions. These are used in the calculation of the expected ISD in the two models we tested, namely, the NFW and the total (NFW and Hernquist) profiles.

Let the position of the lens in the plane of the sky be the origin of the coordinate system. The lensing equation relates the true angular position, β , of the background source to the observed angular position of its image, θ , in the plane of the sky, such that

$$\beta = \theta - \alpha(\theta), \quad (\text{A1})$$

where α is the scaled deflection angle. In the case of a spherically symmetric density distribution for the lens, the deflection angle α lies along the same direction as θ , and the lens equation can

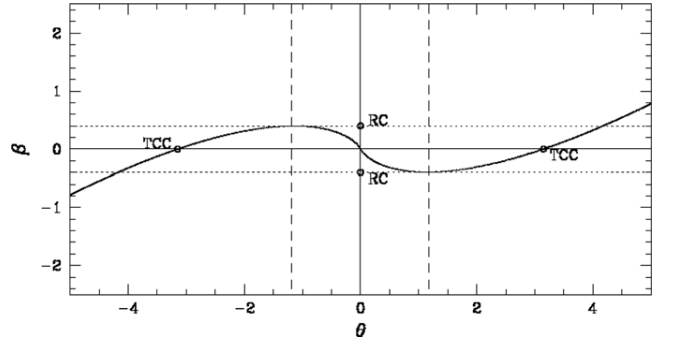


Figure 11. Source position as a function of image position for spherically symmetric lens density distribution. The center of the lens potential is at the origin. RC is the location of the radial caustic and TCC is the location of the tangential critical curve which corresponds to the Einstein radius.

be written as

$$\beta = \theta - \frac{\alpha(\theta)}{\theta}, \quad (\text{A2})$$

where the quantities not in bold are the magnitudes of the corresponding vectors in bold. The relation between the deflection angle α and the magnitude of the image position θ is given by

$$\alpha(\theta) = \frac{4GM(< D_l\theta)}{c^2 D_l\theta}, \quad (\text{A3})$$

where D_l is the angular diameter distance to the lens and $M(< D_l\theta)$ denotes the projected lens mass within a physical radius of size $\xi = D_l\theta$, which can be obtained using the following equation:

$$M(< \xi) = 2\pi \int_0^\xi R' dR' \int_0^{R_{\text{max}}} 2\rho(\sqrt{z^2 + R^2}) dz, \quad (\text{A4})$$

where $R_{\text{max}} = \sqrt{R_{\text{vir}}^2 - \xi^2}$ and R_{vir} is the virial radius.

In Figure 11, we show the generic shape of how β and θ are related to each other for a spherically symmetric mass distribution which has a finite density at the center (non-singular). For large values of β , $\theta \approx \beta$, corresponding to the weak-lensing regime. As the source approaches the lens in projection, i.e., as $\beta \rightarrow 0$, the source position β corresponds to multiple values of θ , referred to as the strong-lensing regime. The first instance of this is when the source is at the radial caustic (labeled as RC in Figure 11) and here, the numerical derivative of β with respect to θ is zero. When $\beta \approx 0$, θ corresponds to the Einstein radius (θ_E) which is the location of the tangential critical curve (see TCC in Figure 11). The image separation is approximately equal to $2\theta_E$.

The magnification of the lensed image at θ is given by the determinant of

$$\mu(\theta) = \left| \frac{\partial \boldsymbol{\beta}}{\partial \boldsymbol{\theta}} \right|^{-1}. \quad (\text{A5})$$

In component notation, the required derivative is given by

$$\frac{\partial \beta_i}{\partial \theta_j} = \delta_{ij} \left(1 - \frac{\alpha}{\theta}\right) - \frac{\partial}{\partial \theta} \left(\frac{\alpha}{\theta} - 1\right) \frac{\partial \theta}{\partial \theta_j} \theta_i \quad (\text{A6})$$

$$= \delta_{ij} \frac{\beta}{\theta} + \frac{\partial}{\partial \theta} \left(\frac{\beta}{\theta}\right) \frac{\theta_i \theta_j}{\theta} \quad (\text{A7})$$

$$= \delta_{ij} \frac{\beta}{\theta} + \left(\frac{\partial \beta}{\partial \theta} - \frac{\beta}{\theta} \right) \frac{\theta_i \theta_j}{\theta^2}. \quad (\text{A8})$$

The inverse of the determinant of the above equation simplifies to

$$\mu(\theta) = \frac{\theta}{\beta} \frac{\partial \theta}{\partial \beta}. \quad (\text{A9})$$

To summarize, given a spherically symmetric density distribution $\rho(r)$, we first obtain the value of β for different values of θ using Equations (A2)–(A4). We use cubic splines to approximate the function $\beta(\theta)$. The value of β which corresponds to the local extrema of this function gives the angular size of the radial caustic. The image separation is given by two times the value of θ when $\beta = 0$. The mass within this angular image separation can be calculated using Equation (A4). Finally, the magnification as a function of θ can be obtained using Equation (A9). The required derivative is calculated by using the cubic spline fit. The magnification bias can thus be calculated using Equation (6).

APPENDIX B

MEASUREMENT OF THE PEAK OF THE REDSHIFT DISTRIBUTION

Consider a lensing galaxy with true redshift z_t for which the photometric redshift estimate is $z_i \pm \sigma_i$. Let us assume that the true redshifts of the lens population follow a Gaussian distribution, $G(\bar{z}_t, \sigma_t^2)$, with the mean and variance given by \bar{z}_t and σ_t^2 , respectively. The probability that the estimated redshift of the lens galaxy is equal to z_i , is then given by

$$P(z_i|G) = \int P(z_i|z_t)P(z_t|G)dz_t, \quad (\text{B1})$$

$$= \frac{1}{2\pi} \int \frac{1}{\sigma_i \sigma_t} \exp \left[- \left(\frac{(z_i - z_t)^2}{2\sigma_i^2} + \frac{(z_t - \bar{z}_t)^2}{2\sigma_t^2} \right) \right] dz_t. \quad (\text{B2})$$

Rewriting the factor inside the exponential as a quadratic in z_t and completing the square yields

$$P(z_i|G) = \frac{1}{2\pi \sigma_i \sigma_t} \exp \left[\frac{-(z_i - \bar{z}_t)^2}{2(\sigma_i^2 + \sigma_t^2)} \right] \times \int \exp \left[\frac{-[z_t - \bar{z}]^2}{2} \left(\frac{1}{\sigma_i^2} + \frac{1}{\sigma_t^2} \right) \right] dz_t, \quad (\text{B3})$$

where $\bar{z} = (\sigma_i^2 + \sigma_t^2)^{-1} (z_i \sigma_i^{-2} + \bar{z}_t \sigma_t^{-2})$. Carrying out the integral gives

$$P(z_i|G) = \frac{1}{\sqrt{2\pi(\sigma_i^2 + \sigma_t^2)}} \exp \left[\frac{-(z_i - \bar{z}_t)^2}{2(\sigma_i^2 + \sigma_t^2)} \right]. \quad (\text{B4})$$

Since the determinations of the photometric redshifts of lens galaxies are independent of each other, the combined likelihood for the data, given our model, can be written as $\mathcal{L} = \prod_{i=1}^N P(z_i|G)$. The posterior distribution for our model parameters given the data is then given by Bayes' theorem

$$P(\bar{z}_t, \sigma_t^2 | z_i, \sigma_i) \propto \mathcal{L} P(\bar{z}_t, \sigma_t^2). \quad (\text{B5})$$

We assume uninformative priors on the parameters \bar{z}_t and σ_t^2 and sample from the above posterior distribution using a Monte Carlo Markov Chain. We quote the mean of the redshift distribution and the 68% confidence interval on it using the samples from the chain.

REFERENCES

- Alard, C. 2006, arXiv:astro-ph/0606757
Alard, C., & Lupton, R. H. 1998, *ApJ*, **503**, 325
Auger, M. W., Treu, T., Bolton, A. S., et al. 2010, *ApJ*, **724**, 511
Balogh, M. L., McGee, S. L., Wilman, D., et al. 2009, *MNRAS*, **398**, 754
Balogh, M. L., McGee, S. L., Wilman, D. J., et al. 2011, *MNRAS*, **412**, 2303
Barnabè, M., Czoske, O., Koopmans, L. V. E., et al. 2009, *MNRAS*, **399**, 21
Bartelmann, M., Huss, A., Colberg, J. M., Jenkins, A., & Pearce, F. R. 1998, *A&A*, **330**, 1
Bernardi, M., Sheth, R. K., Annis, J., et al. 2003, *AJ*, **125**, 1866
Bertin, E., & Arnouts, S. 1996, *A&AS*, **117**, 393
Blandford, R., & Narayan, R. 1986, *ApJ*, **310**, 568
Blandford, R. D., & Narayan, R. 1992, *ARA&A*, **30**, 311
Bolton, A. S., Burles, S., Koopmans, L. V. E., Treu, T., & Moustakas, L. A. 2006, *ApJ*, **638**, 703
Bolton, A. S., Burles, S., Schlegel, D. J., Eisenstein, D. J., & Brinkmann, J. 2004, *AJ*, **127**, 1860
Bullock, J. S., Kolatt, T. S., Sigad, Y., et al. 2001, *MNRAS*, **321**, 559
Cabanac, R. A., Alard, C., Dantel-Fort, M., et al. 2007, *A&A*, **461**, 813
Coles, J. 2008, *ApJ*, **679**, 17
Cooray, A., & Milosavljević, M. 2005, *ApJ*, **627**, L89
Coupon, J., Ilbert, O., Kilbinger, M., et al. 2009, *A&A*, **500**, 981
Dai, X., Bregman, J. N., Kochanek, C. S., & Rasia, E. 2010, *ApJ*, **719**, 119
Dalal, N., Holder, G., & Hennawi, J. F. 2004, *ApJ*, **609**, 50
Ebeling, H., Edge, A. C., & Henry, J. P. 2001, *ApJ*, **553**, 668
Falco, E. E., Impey, C. D., Kochanek, C. S., et al. 1999, *ApJ*, **523**, 617
Fassnacht, C. D., Moustakas, L. A., Casertano, S., et al. 2004, *ApJ*, **600**, L155
Faure, C., Anguita, T., Alloin, D., et al. 2011, *A&A*, **529**, A72
Faure, C., Kneib, J.-P., Covone, G., et al. 2008, *ApJS*, **176**, 19
Feldmann, R., Carollo, C. M., Porciani, C., et al. 2006, *MNRAS*, **372**, 565
Ferreras, I., Saha, P., Leier, D., Courbin, F., & Falco, E. E. 2010, *MNRAS*, **409**, L30
Gavazzi, R., Treu, T., Rhodes, J. D., et al. 2007, *ApJ*, **667**, 176
Gladders, M. D., Hoekstra, H., Yee, H. K. C., Hall, P. B., & Barrientos, L. F. 2003, *ApJ*, **593**, 48
Gnedin, O. Y., Kravtsov, A. V., Klypin, A. A., & Nagai, D. 2004, *ApJ*, **616**, 16
Gonzalez, A. H., Zaritsky, D., Dalcanton, J. J., & Nelson, A. 2001, *ApJS*, **137**, 117
Grillo, C., Eichner, T., Seitz, S., et al. 2010, *ApJ*, **710**, 372
Hattori, M., Kneib, J., & Makino, N. 1999, *Prog. Theor. Phys. Suppl.*, **133**, 1
Helsdon, S. F., & Ponman, T. J. 2000, *MNRAS*, **315**, 356
Hernquist, L. 1990, *ApJ*, **356**, 359
Horesh, A., Ofek, E. O., Maoz, D., et al. 2005, *ApJ*, **633**, 768
Ilbert, O., Arnouts, S., McCracken, H. J., et al. 2006, *A&A*, **457**, 841
Impellizzeri, C. M. V., McKean, J. P., Castangia, P., et al. 2008, *Nature*, **456**, 927
Jackson, N. 2008, *MNRAS*, **389**, 1311
Jiang, G., & Kochanek, C. S. 2007, *ApJ*, **671**, 1568
Kauffmann, G., Colberg, J. M., Diaferio, A., & White, S. D. M. 1999, *MNRAS*, **303**, 188
Keeton, C. R. 2001, *ApJ*, **562**, 160
Keeton, C. R., Christlein, D., & Zabludoff, A. I. 2000, *ApJ*, **545**, 129
Keeton, C. R., Kochanek, C. S., & Falco, E. E. 1998, *ApJ*, **509**, 561
Khare, P. 2001, *ApJ*, **550**, 153
Kochanek, C. S. 2006, in Saas-Fee Advanced Course 33: Gravitational Lensing: Strong, Weak and Micro, ed. G. Meylan, P. North, & P. Jetzer (Berlin: Springer), 91
Kochanek, C. S., Mochejska, B., Morgan, N. D., & Stanek, K. Z. 2006, *ApJ*, **637**, L73
Kochanek, C. S., & White, M. 2001, *ApJ*, **559**, 531
Koopmans, L. V. E., Bolton, A., Treu, T., et al. 2009, *ApJ*, **703**, L51
Koopmans, L. V. E., & Treu, T. 2003, *ApJ*, **583**, 606
Koopmans, L. V. E., Treu, T., Bolton, A. S., Burles, S., & Moustakas, L. A. 2006, *ApJ*, **649**, 599
Krusch, E., Rosenbaum, D., Dettmar, R.-J., et al. 2006, *A&A*, **459**, 759
Lenzen, F., Schindler, S., & Scherzer, O. 2004, *A&A*, **416**, 391
Li, G.-L., Mao, S., Jing, Y. P., et al. 2005, *ApJ*, **635**, 795
Li, G. L., Mao, S., Jing, Y. P., et al. 2006, *MNRAS*, **372**, L73
Limousin, M., Cabanac, R., Gavazzi, R., et al. 2009, *A&A*, **502**, 445

- Limousin, M., Jullo, E., Richard, J., et al. 2010, *A&A*, **524**, A95
- Lintott, C. J., Schawinski, K., Slosar, A., et al. 2008, *MNRAS*, **389**, 1179
- Luppino, G. A., Gioia, I. M., Hammer, F., Le Fèvre, O., & Annis, J. A. 1999, *A&AS*, **136**, 117
- Macciò, A. V., Dutton, A. A., van den Bosch, F. C., et al. 2007, *MNRAS*, **378**, 55
- Mandelbaum, R., Seljak, U., & Hirata, C. M. 2008, *J. Cosmol. Astropart. Phys.*, **JCAP08(2008)006**
- Marshall, P. J., Hogg, D. W., Moustakas, L. A., et al. 2009, *ApJ*, **694**, 924
- Mediavilla, E., Muñoz, J. A., Falco, E., et al. 2009, *ApJ*, **706**, 1451
- Meneghetti, M., Bartelmann, M., & Moscardini, L. 2003, *MNRAS*, **346**, 67
- Meneghetti, M., Bolzonella, M., Bartelmann, M., Moscardini, L., & Tormen, G. 2000, *MNRAS*, **314**, 338
- Meneghetti, M., Fedeli, C., Zitrin, A., et al. 2011, *A&A*, **530**, A17
- Molikawa, K., & Hattori, M. 2001, *ApJ*, **559**, 544
- More, A., Jahnke, K., More, S., et al. 2011a, *ApJ*, **734**, 69
- More, A., McKean, J. P., More, S., et al. 2009a, *MNRAS*, **394**, 174
- More, A., McKean, J. P., Muxlow, T. W. B., et al. 2008, *MNRAS*, **384**, 1701
- More, S., van den Bosch, F. C., Cacciato, M., et al. 2009b, *MNRAS*, **392**, 801
- More, S., van den Bosch, F. C., Cacciato, M., et al. 2011b, *MNRAS*, **410**, 210
- Muñoz, J. A., Falco, E. E., Kochanek, C. S., et al. 1998, *Ap&SS*, **263**, 51
- Myers, S. T., Jackson, N. J., Browne, I. W. A., et al. 2003, *MNRAS*, **341**, 1
- Narayan, R., & Wallington, S. 1993, *Liege International Astrophysical Colloquia*, **31**, 217
- Narayan, R., & White, S. D. M. 1988, *MNRAS*, **231**, 97P
- Navarro, J. F., Frenk, C. S., & White, S. D. M. 1997, *ApJ*, **490**, 493
- Oguri, M. 2002, *ApJ*, **573**, 51
- Oguri, M. 2006, *MNRAS*, **367**, 1241
- Oguri, M., Taruya, A., Suto, Y., & Turner, E. L. 2002, *ApJ*, **568**, 488
- Parker, L. C., Hudson, M. J., Carlberg, R. G., & Hoekstra, H. 2005, *ApJ*, **634**, 806
- Porciani, C., & Madau, P. 2000, *ApJ*, **532**, 679
- Ratnatunga, K. U., Griffiths, R. E., & Ostrander, E. J. 1999, *AJ*, **117**, 2010
- Richard, J., Kneib, J.-P., Ebeling, H., et al. 2011, *MNRAS*, **414**, L31
- Rines, K., & Diaferio, A. 2010, *AJ*, **139**, 580
- Ruff, A. J., Gavazzi, R., Marshall, P. J., et al. 2011, *ApJ*, **727**, 96
- Rusin, D., & Tegmark, M. 2001, *ApJ*, **553**, 709
- Sand, D. J., Treu, T., Ellis, R. S., & Smith, G. P. 2005, *ApJ*, **627**, 32
- Scoville, N., Aussel, H., Brusa, M., et al. 2007, *ApJS*, **172**, 1
- Seidel, G., & Bartelmann, M. 2007, *A&A*, **472**, 341
- Sheth, R. K., & Tormen, G. 1999, *MNRAS*, **308**, 119
- Sonnenfeld, A., Treu, T., Gavazzi, R., et al. 2011, arXiv:1111.4215
- Suyu, S. H., & Halkola, A. 2010, *A&A*, **524**, A94
- Suyu, S. H., Marshall, P. J., Auger, M. W., et al. 2010, *ApJ*, **711**, 201
- Swinbank, A. M., Webb, T. M., Richard, J., et al. 2009, *MNRAS*, **400**, 1121
- Sygné, J. F., Tu, H., Fort, B., & Gavazzi, R. 2010, *A&A*, **517**, A25
- Thanjavur, K., Crampton, D., & Willis, J. 2010, *ApJ*, **714**, 1355
- Treu, T., Auger, M. W., Koopmans, L. V. E., et al. 2010, *ApJ*, **709**, 1195
- Treu, T., & Koopmans, L. V. E. 2002a, *ApJ*, **575**, 87
- Treu, T., & Koopmans, L. V. E. 2002b, *MNRAS*, **337**, L6
- Turner, E. L., Ostriker, J. P., & Gott, J. R., III 1984, *ApJ*, **284**, 1
- Vale, A., & Ostriker, J. P. 2004, *MNRAS*, **353**, 189
- Vegetti, S., Czoske, O., & Koopmans, L. V. E. 2010a, *MNRAS*, **407**, 225
- Vegetti, S., Koopmans, L. V. E., Bolton, A., Treu, T., & Gavazzi, R. 2010b, *MNRAS*, **408**, 1969
- Verdugo, T., Motta, V., Muñoz, R. P., et al. 2011, *A&A*, **527**, A124
- Wambsgans, J., Bode, P., & Ostriker, J. P. 2004, *ApJ*, **606**, L93
- Warren, S. J., Hewett, P. C., Lewis, G. F., et al. 1996, *MNRAS*, **278**, 139
- Wyithe, J. S. B. 2004, *MNRAS*, **351**, 1266
- Yang, X., Mo, H. J., & van den Bosch, F. C. 2008, *ApJ*, **676**, 248
- Zaritsky, D., & Gonzalez, A. H. 2003, *ApJ*, **584**, 691
- Zitrin, A., & Broadhurst, T. 2009, *ApJ*, **703**, L132
- Zitrin, A., Broadhurst, T., Barkana, R., Rephaeli, Y., & Benítez, N. 2011, *MNRAS*, **410**, 1939

A new window of exploration in the mass spectrum: strong lensing by galaxy groups in the SL2S^{★,★★}

M. Limousin^{1,2,3}, R. Cabanac¹, R. Gavazzi^{4,5}, J.-P. Kneib², V. Motta⁶, J. Richard^{7,8}, K. Thanjavur⁹, G. Foex¹⁰,
R. Pello¹⁰, D. Crampton¹¹, C. Faure¹², B. Fort^{4,5}, E. Jullo², P. Marshall¹³, Y. Mellier^{4,5}, A. More², G. Soucail¹⁰,
S. Suyu¹⁴, M. Swinbank¹⁵, J.-F. Sygnet^{4,5}, H. Tu^{16,4,5}, D. Valls-Gabaud¹⁷, T. Verdugo⁶, and J. Willis⁹

(Affiliations can be found after the references)

Received 4 December 2008 / Accepted 25 May 2009

ABSTRACT

The existence of strong lensing systems with Einstein radii covering the full mass spectrum, from $\sim 1\text{--}2''$ (produced by galaxy scale dark matter haloes) to $>10''$ (produced by galaxy cluster scale haloes) have long been predicted. Many lenses with Einstein radii around $1\text{--}2''$ and above $10''$ have been reported but very few in between. In this article, we present a sample of 13 strong lensing systems with Einstein radii in the range $3''\text{--}8''$ (or image separations in the range $6''\text{--}16''$), i.e. systems produced by *galaxy group scale dark matter haloes*. This group sample spans a redshift range from 0.3 to 0.8. This opens a new window of exploration in the mass spectrum, around $10^{13}\text{--}10^{14} M_{\odot}$, a crucial range for understanding the transition between galaxies and galaxy clusters, and a range that have not been extensively probed with lensing techniques. These systems constitute a subsample of the Strong Lensing Legacy Survey (SL2S), which aims to discover strong lensing systems in the Canada France Hawaii Telescope Legacy Survey (CFHTLS). The sample is based on a search over 100 square degrees, implying a number density of ~ 0.13 groups per square degree. Our analysis is based on multi-colour CFHTLS images complemented with *Hubble Space Telescope* imaging and ground based spectroscopy. Large scale properties are derived from both the light distribution of elliptical galaxies group members and weak lensing of the faint background galaxy population. On small scales, the strong lensing analysis yields Einstein radii between $2.5''$ and $8''$. On larger scales, strong lens centres coincide with peaks of light distribution, suggesting that light traces mass. Most of the luminosity maps have complicated shapes, implying that these intermediate mass structures may be dynamically young. A weak lensing signal is detected for 6 groups and upper limits are provided for 6 others. Fitting the reduced shear with a Singular Isothermal Sphere, we find $\sigma_{\text{SIS}} \sim 500 \text{ km s}^{-1}$ with large error bars and an upper limit of $\sim 900 \text{ km s}^{-1}$ for the whole sample (except for the highest redshift structure whose velocity dispersion is consistent with that of a galaxy cluster). The mass-to-light ratio for the sample is found to be $M/L_i \sim 250$ (solar units, corrected for evolution), with an upper limit of 500. This compares with mass-to-light ratios of small groups (with $\sigma_{\text{SIS}} \sim 300 \text{ km s}^{-1}$) and galaxy clusters (with $\sigma_{\text{SIS}} > 1000 \text{ km s}^{-1}$), thus bridging the gap between these mass scales. The group sample released in this paper will be complemented with other observations, providing a unique sample to study this important intermediate mass range in further detail.

Key words. gravitational lensing; cosmology; large-scale structure of Universe

1. Introduction

1.1. Galaxy groups and cosmology

Galaxy groups are believed to play a key role in the formation and evolution of structures in the Universe. They contain the majority of the galaxies in the Universe, and within a hierarchical framework, they span the regime between individual galaxies and massive galaxy clusters, making them cosmologically significant. They are also more varied in their properties than

galaxy clusters, as demonstrated by comparisons between various scaling relations in galaxy groups to those in galaxy clusters. This indicates that galaxy groups are probably not a homogeneous class of objects, e.g. they cannot be considered simple scaled-down versions of galaxy clusters. Detailed studies of this intermediate regime of the mass spectrum ($\sim 10^{13}\text{--}10^{14} M_{\odot}$) are needed to understand better the physical processes behind formation of galaxy groups and how galaxy groups participate to structure formation and evolution.

Properties of low and intermediate redshift galaxy groups ($z < 0.5$) have been studied using X-ray and optical tracers (e.g. Helsdon & Ponman 2000, 2003; Osmond & Ponman 2004; Willis et al. 2005; Finoguenov et al. 2007; Rasmussen & Ponman 2007; Mamon 2007; Faltenbacher & Mathews 2007; Gastaldello et al. 2007; Yang et al. 2008; van den Bosch et al. 2008; Sun et al. 2009, and references therein). Galaxy groups have also been studied numerically (e.g. D'Onghia et al. 2005; Sommer-Larsen 2006, and references therein).

1.2. Strong lens statistics

Figure 1 shows the predicted contributions of different types of haloes in the image separation distributions (from Oguri 2006, Fig. 9) extracted from N-body simulations, where θ corresponds

* Appendix A is only available in electronic form via <http://www.aanda.org>

** Based on observations obtained with MegaPrime/MegaCam, a joint project of CFHT and CEA/DAPNIA, at the Canada-France-Hawaii Telescope (CFHT) which is operated by the National Research Council (NRC) of Canada, the Institut National des Sciences de l'Univers of the Centre National de la Recherche Scientifique (CNRS) of France, and the University of Hawaii. This work is based in part on data products produced at TERAPIX and the Canadian Astronomy Data Centre as part of the Canada-France-Hawaii Telescope Legacy Survey, a collaborative project of NRC and CNRS. Based on observations made with the NASA/ESA Hubble Space Telescope, obtained at the Space Telescope Science Institute, which is operated by the Association of Universities for Research in Astronomy, Inc., under NASA contract NAS 5-26555. These observations are associated with programs 10876 and 11289.

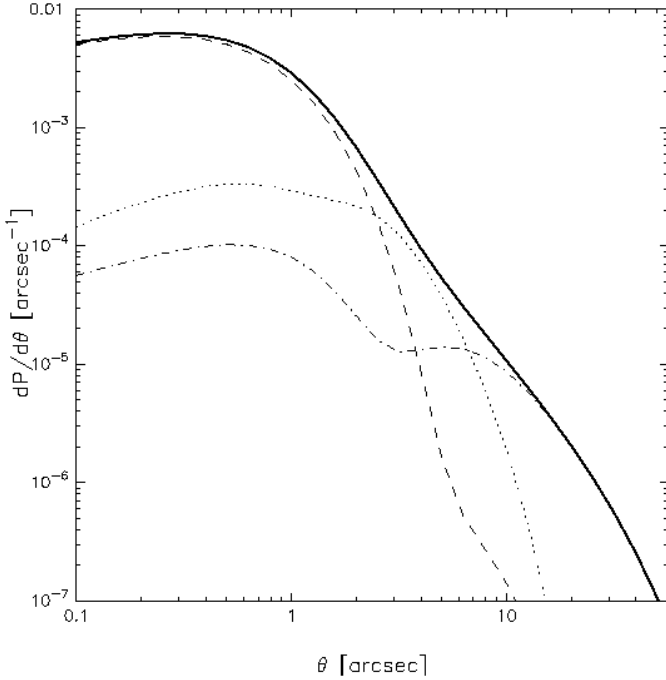


Fig. 1. The contributions of different types of haloes on the image separation distribution, from [Oguri \(2006\)](#): galaxy (dashed); groups (dot) and clusters (dot-dashed). The sum of distributions of three types is shown by thick solid line.

to about twice the Einstein radius of the lens¹. This plot shows that there are large overlaps among the halo types, but also that some scales are dominated by different regimes: on small scales, the distribution is dominated by galaxy-scale dark-matter haloes, with $R < 2''$, and on larger scales, by cluster-scale dark-matter haloes, with $R > 10''$. In between, the distribution is dominated by haloes generating strong lensing deflection of radii between $\sim 3''$ and $\sim 8''$, whose mass is in the range 10^{13} – $10^{14} M_{\odot}$, i.e. by *group-scale dark-matter haloes*.

Hence according to simulations, strong lenses from intermediate mass systems should exist in a Λ CDM Universe. Until now, only a few cases have been detected observationally in the SDSS, which we discuss in Sect. 7.6.

Strong lensing deflector: In this paper, we refer to a “deflector” as the foreground mass distribution giving rise to multiple images, and we focus on its central part. Specifically, a strong lensing deflector refers to the area of the foreground mass distribution enclosed by the multiple images. This region can be populated by more than a single galaxy on scales smaller than R , as it is the case for some of the galaxy groups reported in this work. In order to avoid confusion, we use the term deflector instead of lensing galaxy. This is particularly important for group scale deflectors since their mass may no longer be associated to a single galaxy. This definition is well adapted to most of the groups studied in this paper, where the multiple images identification is clear and therefore the region enclosed by these images is well defined. However, this is not the case for three of the groups presented in this paper.

¹ In this paper, we will use the Einstein radius R to characterise the lenses.

1.3. Strong lensing in and by a galaxy group

We shall emphasise the distinction between strong lensing *in* a galaxy group and *by* a galaxy group. Strong lensing *in* a galaxy group corresponds to the observation of a strong lensing feature, with a typical Einstein radius of $\sim 2''$, generated by a galaxy group member. Since the high-density environment is likely to enhance the strong galaxy-galaxy lensing cross section (see [Kovner 1987](#); [Möller et al. 2002](#); [Fassnacht et al. 2006](#); [Oguri et al. 2005](#); [King 2007](#); [Newton et al. 2008](#), but see [Faure et al. 2008](#), in the field), many strong lensing systems in groups (or clusters) have been reported (e.g. [Kundic et al. 1997](#); [Fassnacht & Lubin 2002](#); [Morgan et al. 2005](#); [Williams et al. 2006](#); [Momcheva et al. 2006](#); [Auger et al. 2007](#); [Tu et al. 2008](#); [Auger et al. 2008](#); [Grillo et al. 2008](#); [Treu et al. 2009](#); [Inada et al. 2009](#)). If the creation of multiple images is boosted by external shear and convergence from a smooth group component, these strong lensing systems are, to first order, generated by a galaxy-scale dark-matter halo populated by a single galaxy (most of the time an elliptical galaxy, but note that efforts are currently underway to find lenses generated by haloes populated by spiral galaxies, see [Feron et al. 2008](#); [Trott et al. 2008](#)).

On the other hand, strong lensing by a galaxy group corresponds to the observation of strongly lensed features with a typical Einstein radius between $\sim 3''$ and $\sim 8''$. This translates into a projected mass enclosed within this radius around $\sim 10^{12.5}$ – $10^{13} M_{\odot}$, i.e. characteristic of a *group-scale dark-matter halo*. Note that the highest limit of $8''$ adopted here is somewhat arbitrary and may be considered by others as a characteristic size of a poor cluster.

1.4. Galaxy groups in the strong lensing legacy survey

A straightforward method for finding lens systems is to identify them directly within existing multi-band wide-field imaging surveys. For this purpose, we have started to explore systematically the Canada France Hawaii Telescope Legacy Survey (CFHTLS), using a dedicated automatic search procedure optimised for the detection of arcs. This subsample of the CFHTLS forms the Strong Lensing Legacy Survey (SL2S, [Cabanac et al. 2007](#)). This sample is not biased towards high masses by any prior X-ray selection and because of the wide area covered, cosmic variance is neglected and the resulting sample of strong lenses is assumed to be representative of what can be found in the Universe. However, selection biases inherent to our detection technique do exist and will be addressed in a forthcoming publication using numerical simulations. The SL2S sample probes a wide range of masses and a wide range of redshifts for the lenses. Thanks to unsurpassed combined depth, area and image quality of the CFHTLS, we have uncovered a new population of lenses, with Einstein radii between $\sim 3''$ and $\sim 8''$, i.e. generated by *galaxy-group scale-dark matter haloes*. This new population effectively bridges the gap between single galaxies and massive clusters, opening a *new window of exploration in the mass spectrum*. The purpose of this paper is to present the first representative sample of such lenses. Note that this sample is not statistically complete since the survey is not complete yet and that we do not understand properly our selection function.

This paper is organised as follows: data used in this work are presented in Sect. 2. Sections 3–5 present the methodology of the systematic analysis we apply on each group. Results are presented in Sect. 6 and discussed in Sect. 7. In the Appendix, each group is described individually, with some images. All our results are scaled to a flat, Λ CDM cosmology

with $\Omega_M = 0.3$, $\Omega_\Lambda = 0.7$ and a Hubble constant $H_0 = 70 \text{ km s}^{-1} \text{ Mpc}^{-1}$. All images are aligned with WCS coordinates, i.e. north is up, east is left. Magnitudes are given in the AB system.

2. Data

In this section, we present the various data sets used in this work. Multicolour imaging from the CFHTLS constitutes the basis of our analysis and is complemented with ongoing HST imaging and ongoing ground-based spectroscopy.

2.1. The Canada-France-Hawaii telescope legacy survey

2.1.1. Description

The CFHTLS is a major photometric survey of more than 450 nights over 5 years (started on June 1st, 2003, ending 2008) using the wide field imager MIPOM which covers ~ 1 square degree on the sky, with a pixel size of $0.186''$. The project is comprehensively described in <http://www.cfht.hawaii.edu/Science/CFHLS/> and links therein. The CFHTLS has two components aimed at extragalactic studies: a very Deep component made of 4 pencil-beam fields of 1 deg^2 and a Wide component made of 3 mosaics covering 170 deg^2 in total, both in 5 broadband filters. The data are pre-reduced at CFHT with the Elixir pipeline² which removes the instrumental artifacts in individual exposures. The CFHTLS images are then evaluated, astrometrically calibrated, photometrically inter-calibrated, resampled and stacked by the Terapix group at the Institut d'Astrophysique de Paris (IAP) and finally archived at the Canadian Astronomy Data Centre (CADC). Terapix also provides weightmap images, quality assessments meta-data for each stack as well as mask files that mask straylight, saturated stars and defects on each image.

2.1.2. Terapix release T0004

The SL2S group sample presented here is based on the T0004 release (July 2007), corresponding to data obtained between the Spring 2003 and the spring 2007. A detailed description of this release is given at the Terapix web site³ and CADC site⁴. The T0004 release includes 120 deg^2 of stacked fields in the Wide survey observed in broadband g' , r' and i' filters, and a stack of the 35 Wide and 4 Deep fields in the 5 bands, for a total area of 124 deg^2 , or ca. 110 deg^2 of unmasked area, i.e. area not contaminated by instrumental artefacts from bright stars (internal reflections, bleeding). Table 1 summarises the main characteristics of the T0004 release. The 4 Deep fields are much deeper, with a seeing ranging from $0.9''$ in u^* to $0.7''$ in z' . Because of the observing strategy, the Wide survey image quality is prone to large variations from $1''$ to $0.6''$ seeing in all bands. Nevertheless, the Wide survey is more suited to our strong lensing selection processes, because of its wide angular coverage.

2.2. Space based imaging

The strong lensing features detected from ground-based images have been observed with the *Hubble Space Telescope* (HST)

² <http://www.cfht.hawaii.edu/Instruments/Elixir/>

³ <http://terapix.iap.fr>

⁴ <http://www2.cadc-ccda.hia-ihp.nrc-cnrc.gc.ca/cfht/T0004.html>

Table 1. CFHTLS: Terapix T0004 release (July 2007).

Deep fields	AB Magnitudes Limits				
	u^*	g'	r'	i'	z'
D1-25	26.7	27.5	27.5	27.3	26.0
D2-25	25.6	27.3	27.3	27.0	25.6
D3-25	26.6	27.5	27.4	27.2	26.1
D4-25	26.9	27.5	27.5	27.1	26.0
D1-25 seeing	0.93	0.93	0.75	0.74	0.71
D2-25 seeing	0.83	0.83	0.77	0.71	0.72
D3-25 seeing	0.89	0.89	0.77	0.73	0.64
D4-25 seeing	0.86	0.86	0.77	0.72	0.71
Wide fields	AB Average Magnitudes Limits				
W1	25.8	26.5	26.0	25.8	25
W2	25.8	26.5	26.0	25.8	25
W3	25.8	26.5	26.0	25.8	25
W4	25.8	26.5	26.0	25.8	25
W1 area (unmasked)	44 (39) deg^2				
W2 area (unmasked)	20 (16) deg^2				
W3 area (unmasked)	40 (34) deg^2				
W4 area (unmasked)	16 (13) deg^2				

For a point source $S/N = 5$ (AB to Vega $u^* - 0.35$, $g' + 0.09$, $r' - 0.17$, $i' - 0.40$, $z' - 0.55$)

for 11 of the 13 groups presented in this paper. Observations were done in snapshot mode (C 15 and C 16, P.I. Kneib, ID 10 876 and 11 289). 3 groups have been imaged in three bands with the ACS camera (F814, F606 and F475), and the remaining in the F606 band only with the WFPC2 camera. Space-based imaging generally allows one to better resolve the strong lensing systems we are interested in.

2.3. Spectroscopy

Various ongoing spectroscopic campaigns are targeting both the galaxy group members as well as the multiply imaged systems. We use the following facilities:

1. FORS 2 on VLT: resolution of 600 RI, exposure 2 800 s, with $\Delta\lambda$ from 5000 to 8000 Å;
2. LRIS on Keck: Dichroic 680 and 560 nm, exposure 600 s and 1200 s with a slit of $1.5''$;
3. Gemini (Program GN-2007A-Q-114): we observed SL2S J14300+5546 on June 2007 using GMOS LS+R400 grating at 7500 Å during 3750 s.

When available and relevant to this work, we will report some of the results of our spectroscopic campaigns. Details of the observing runs and spectra will be presented in forthcoming publications. For SL2S J14081+5429 and SL2S J22214-0053, we report the spectroscopic redshift measured by the Sloan Digital Sky Survey (SDSS).

2.4. Photometric redshifts

Photometric redshifts were estimated for all the groups, based on the magnitudes of the brightest galaxy populating the strong lensing deflector whose coordinates are given in Table 3. Aperture magnitudes were extracted with

2.5 (Bertin & Arnouts 1996) and photometric redshifts were estimated using the HyperZ software (Bolzonella et al. 2000). For all groups but two (SL2S J14300+5546 and SL2S J14314+5533), 5 photometric bands are available.

Photometric redshifts, with 3σ error bars are given in Table 3. They can be compared to the spectroscopic measurements available for 9 of the groups. We note that in the case of 4 groups over 9, the spectroscopic redshifts are not consistent with the 3σ confidence intervals of the photometric redshifts estimates. However, the difference between each estimate is smaller than 0.03. This has no influence on the lensing properties of the galaxy groups and therefore does not bias our analysis.

In addition, we have been looking systematically in the NED database at all known sources within $5'$ of each strong lensing event to gather any observational data relevant to this study.

3. Building luminosity maps

Luminosity maps were created from the i -band isophotal magnitudes of all the elliptical galaxies tagged as members of the group. This is the deepest band that best represents the old stellar population of elliptical galaxies. Catalogues of objects positions and magnitudes have been generated using [2.5](#).

3.1. Selecting group members

We build matched g, r, i bands catalogues of all objects with a radius of $5'$ of the lens centre. We compute the $r - i$ colour of the brightest galaxy populating the strong lensing deflector. We refer to this quantity in the following as $(r - i)_0$. We then consider all galaxies whose $r - i$ colour satisfy:

$$(r - i)_0 - 0.15 < r - i < (r - i)_0 + 0.15 \ \& \ i < \text{mag}_{\text{lim}}(z) \quad (1)$$

as possible galaxy group red-sequence members (e.g. [Gladders et al. 1998](#)). We miss the faintest group members but the most luminous ellipticals are correctly selected. When spectroscopy of group members is available, we verified that our procedure does select the spectroscopically confirmed group members. A more robust selection will require us to analyse multi-object spectroscopy of the fields.

In order to compare the group luminosity maps across the redshift range, we restrict our group member catalogue to galaxies brighter than a magnitude threshold $\text{mag}_{\text{lim}}(z)$. This magnitude threshold is set by the apparent magnitude of the faintest elliptical member of the highest redshift group (SL2S J22133+0048 at $z_{\text{phot}} = 0.83$). That apparent magnitude is converted into a rest-frame absolute luminosity, converted back into a redshift-dependent apparent magnitude $\text{mag}_{\text{lim}}(z)$ for each group.

3.2. Contamination

The red sequence technique is known to suffer from contamination. In our case, because the number count of objects per group that satisfy Eq. (1) is small (less than 100), we visually inspected each group member candidate and manually rejected galaxies that were unlikely to be physically connected to the group (e.g. higher redshift spiral galaxies). We also estimated contamination from background/foreground objects serendipitously falling in the same colour bin from random fields, i.e. fields large enough to ensure that they are, on average, empty. Using CFHTLS deep fields galaxy catalogues and applying Eq. (1) selection, we estimated the total background/foreground luminosity that adds up to the group catalogues. This estimation is consistent with what we have manually removed from our visual inspection. Therefore, we prefer removing the background contamination by eye since the method allows us to identify the contaminating

galaxies, whereas a statistical approach would lead to subtraction of constant luminosity sheets across groups and a loss of positional information.

3.3. Luminosity contours

We build luminosity maps to help us characterise the large-scale luminous properties of the group sample. The CFHTLS i -band image is divided into cells 20-pixels wide (corresponding to $3.7''$). Considering the centre of each cell, we compute the total rest-frame i -band luminosity L by summing individual luminosities of the five closest group members, deduced from their isophotal magnitude M :

$$L = 10^{(M_{\odot} - M + DM + k + \text{ev})/2.5} \quad (2)$$

where M_{\odot} is the Sun i -band absolute magnitude; DM is the distance modulus, k the k -correction factor and ev the passive evolution correction, estimated from an elliptical template ([Bruzual & Charlot 2003](#)). This total luminosity is divided by the circular area enclosing the fifth neighbour: this gives a density within the considered cell that we express in units $L_{\odot} \text{kpc}^{-2}$. The computed luminosity density map is then convolved with a Gaussian kernel of width 3 cells.

The choice for 5 neighbours is small compared to the number of catalogued group members (on average 46 members).

We found that the size of the cells does not influence the shape of the resulting luminosity contours. We checked that the distance to the fifth neighbour is always larger than $\text{cell}/\sqrt{2}$, which means we do not undersample any region of the field.

4. Weak gravitational lensing analysis

We perform a one dimensional weak lensing (WL) analysis on each group with the goal of probing the projected mass distribution on large scales. This technique is well established and is widely used on galaxy cluster scales (e.g. [Bardeau et al. 2007](#); [Hoekstra 2007](#)). The basic idea is the following: from the shape of the background lensed galaxy population, we can estimate the shear vector (or more precisely, the reduced shear, see e.g. [Mellier 1999](#)). Its tangential component (with respect to the centre of the deflector) is directly proportional to the mass distribution of the deflector, whereas its radial component is expected to be equal to zero in the case of perfect data. Given the relatively smaller mass of galaxy groups (compared to galaxy clusters), detecting weak lensing by groups of galaxies is challenging. Until now, weak lensing signals of such mass scales has been recovered only by stacking groups ([Hoekstra et al. 2001](#); [Parker et al. 2005](#); [Mandelbaum et al. 2006](#)). Moreover, the strength of the weak lensing signal is expected to decrease with the redshift of the deflector, thus we expect to detect a weak lensing signal only for the lower redshift groups. In any case, an upper limit on the velocity dispersion of the structures studied in this work is of interest. Because strongly lensed source redshifts are unknown, weak-lensing derived velocity dispersion upper limits constitute the only way to show that our sample contains only groups or poor clusters and no massive clusters. Indeed, an Einstein radius of $\sim 6''$ could be generated by a massive cluster lensing a low redshift background source.

4.1. Weak lensing methodology

We have been following the methodology developed by [Bardeau et al. \(2005, 2007\)](#), using the [package](#)

Table 2. Summary of the strong lensing modelling.

SL2S Group	Nb	X ["]	Y ["]	e	θ (degree)	R	rms	χ^2
J22214-0053	4	-0.2 ± 0.06	-2.0 ± 0.15	[0]	[0]	6.83 ± 0.15	0.08	0.0
J08544-0121	8	0.0 ± 0.1	0.0 ± 0.06	0.59 ± 0.0	20.8 ± 1.2	5.48 ± 0.12	0.28	17
J09413-1100	4	-1.3 ± 0.2	-1.9 ± 0.9	[0]	[0]	7.50 ± 0.81	0.07	1.5
J14300+5546	4	-0.2 ± 1.4	-1.1 ± 1.5	[0]	[0]	4.69 ± 1.43	0.02	0.1
J02140-0532	8	0.85 ± 0.3	$-2.6_{-0.03}^{+1.2}$	0.56 ± 0.11	111.2 ± 0.1	7.31 ± 0.49	0.1	1.1
J02254-0737	4	-1.9 ± 0.15	-2.6 ± 0.6	[0]	[0]	6.00 ± 0.31	0.04	0.4
J02215-0647	6	0.14 ± 0.15	-1.3 ± 0.2	0.57 ± 0.01	104 ± 3	2.56 ± 0.14	0.2	20
J 22133+0048	4	-1.7 ± 0.15	-0.8 ± 0.3	[0]	[0]	3.40 ± 0.2	0.01	0

Number of constraints Nb and optimised SIE parameters. Error bars represents 1σ confidence level on the parameters inferred from the optimisation. Values into brackets are not optimised. This corresponds to models where the number of observational constraints is smaller than the number of free parameters characterising the SIE profile. The goodness of the fit is quantified by the RMS in the image plane and the reduced χ^2 . e is the ellipticity of the mass distribution (in units $(a^2 - b^2)/(a^2 + b^2)$).

(Bardeau 2004). We refer the reader to these papers for a detailed description of the cataloguing. Here we give a brief outline of the different steps involved in the analysis of the reduced and calibrated images.

The first step is to construct a photometric catalogue for each individual image. Object positions and magnitudes were extracted with `2.5`. The second step of the analysis is to extract a star catalogue which will be used to estimate the local Point Spread Function (`PSF`). We select stars and clean the resulting catalogue as described in Bardeau et al. (2005). In order to measure the shapes of the stars, we used the `2` software developed by Bridle et al. (2002). At this stage, we have a map of the `PSF` distribution over the entire field. The third step is to compute the galaxy catalogues selected for the weak lensing analysis. Galaxies are selected from the photometric catalogues according to the criterion described in Bardeau et al. (2005). To measure the shapes of galaxies, we first linearly interpolate the local `PSF` at each galaxy position by averaging the shapes of the five closest stars. The number of 5 stars is found to be large enough to locally interpolate the `PSF`, whereas choosing a much larger number would over-smooth the `PSF` characteristics. `2` then computes intrinsic shapes of galaxies by convolving a galaxy model with the interpolated local `PSF`, and determines which one is the most likely by minimising residuals. In the end, `2`'s output gives a most likely model for the fitted galaxy characterised by its position, size, ellipticity and orientation, and errors on all of these quantities. For the purpose of the weak lensing analysis, we use the shape parameters derived from the CFHTLS i band: observations in this photometric band have been optimised for weak lensing purposes, thus data quality in terms of seeing and source density is superior to the other bands.

Note that the reliability of the `2` software has been validated through the simulated data of the STEP project (Heymans et al. 2006) and the results show that no significant bias is introduced by the deconvolution. It has been successfully applied in a number of weak lensing works (Kneib et al. 2003; Cypriano et al. 2004, 2005; Bardeau et al. 2005, 2007; Limousin et al. 2007a,b; Medezinski et al. 2007; Carrasco et al. 2007).

4.2. Background Galaxies: selection and redshift distribution

We select as background lensed sources the galaxies whose i -band magnitudes fall between 21.5 and 24, hence close to the completeness magnitude for all groups (Table 3). The mean density of background galaxies equals to ~ 12 per square arcminute.

Applying the same magnitude cuts to the four CFHTLS deep fields catalogues, we find a density of ~ 15 per square arcminute, slightly larger than the mean density of background galaxies used in our weak lensing analysis. This is expected since we have kept only objects whose shape parameters are reliably measured, as detailed in Bardeau et al. (2005, 2007).

In order to relate the strength of the weak lensing signal to a physical velocity dispersion characterising the group potential, one needs to estimate the mean geometrical factor D_{ls}/D_s , where D_{ls} is the angular diameter distance between the lens (here the group) and the source and D_s is the angular diameter distance between the observer and the source. For this estimation, we consider the photometric redshift catalogue from the T0004 release of the CFHTLS-Deep survey, which corresponds to the deep stacks of the repeated observations of four independent M C fields. These data are therefore collected with the same instrument in the same photometric bands as the data used in this work. The CFHTLS-Deep is much deeper (at least one magnitude deeper in r) and the multicolour observations in 5 bands allow the determination of photometric redshifts. We have used the publicly available photometric redshift catalogue provided by Roser Pello⁵ which has been calibrated and validated with spectroscopic samples (Ienna & Pelló 2006). We applied to this catalogue the same magnitude selection criteria that we applied to our background galaxy catalogue (i.e. i between 21.5 and 24). For each group, we compute the average geometrical factor D_{ls}/D_s by integrating this redshift probability distribution between 0 and 5. We also compute the effective source redshift z_{eff} that is defined by the redshift at which the geometrical factor becomes equals to the mean geometrical factor. Both quantities are given in Table 3.

Coupon et al. (2008) recently estimated photometric redshift for 35 deg² of the Wide survey. Since our group catalogue is based on a search of 100 deg², all groups do not fall in the study by Coupon et al. (2008). Moreover, they provide photometric redshifts for galaxies brighter than $i = 22.5$ whereas our background galaxy catalogues contains objects as faint as $i = 24$. Therefore, we cannot benefit from this work in assigning photometric redshifts individually to each background galaxy.

Coupon et al. (2008) also estimate photometric redshifts for the Deep fields down to $i = 24$. A thorough comparison of both catalogues is beyond the scope of this paper, but we can check if the presented results change significantly if we use this catalogue instead of ours. We apply the same magnitude selection to the Coupon et al. (2008) catalogue and recompute the

⁵ http://www.ast.obs-mip.fr/users/roser/CFHTLS_T0004/

Table 3. Summary of the main properties of SL2S groups.

SL2S Group	RA	Dec	z_{spec}	z_{phot}	R (")	R (")	R (")	D_{ls}/D_s	z_{eff}	σ_{SIS} (")	M (2Mpc)	N_{back}	L	Seeing	M_c
J09013-0158	135.41443	-1.9811666	-	$0.296^{+0.052}_{-0.017}$	~ 6.8	3.83 ± 2.97	0.487	0.641	521^{+174}_{-274}	4.0 ± 3.1 (3.9 \pm 3.0)	11.8	2.78 ± 0.38	0.80	24.13	
J22214-0053	335.43226	-0.88404303	0.334	$0.314^{+0.026}_{-0.017}$	6.83 ± 0.15	3.15 ± 3.10	0.448	0.660	494^{+261}_{-432}	3.6 ± 3.5 (3.5 \pm 3.4)	10.3	1.36 ± 0.27	0.72	24.60	
J08544-0121	133.69395	-1.3603506	0.351	$0.324^{+0.067}_{-0.017}$	5.48 ± 0.12	5.37 ± 2.12	0.430	0.671	658^{+119}_{-149}	6.3 ± 2.5 (6.2 \pm 2.4)	13.5	3.29 ± 0.40	0.51	23.91	
J09413-1100	145.39478	-11.015091	0.385	$0.418^{+0.003}_{-0.016}$	7.50 ± 0.81	2.98 ± 2.64	0.393	0.688	508^{+149}_{-337}	3.7 ± 3.4 (3.7 \pm 3.3)	10.4	1.27 ± 0.24	0.69	24.25	
J14081+5429	212.05808	54.484634	0.416	$0.436^{+0.016}_{-0.038}$	~ 4.5	< 4.83	0.362	0.705	< 680	< 6.8 (6.6)	10.8	2.46 ± 0.39	0.72	23.61	
J14300+5546	217.50275	55.779964	0.435	$0.486^{+0.038}_{-0.024}$	4.69 ± 1.43	< 4.64	0.344	0.715	< 684	< 6.8 (6.6)	14.7	2.15 ± 0.27	0.72	24.39	
J02140-0532	33.533465	-5.5923947	0.444	$0.440^{+0.026}_{-0.016}$	7.31 ± 0.49	3.62 ± 2.45	0.335	0.719	612^{+180}_{-264}	5.5 ± 3.7 (5.3 \pm 3.6)	13.0	2.90 ± 0.39	0.61	23.96	
J02254-0737	36.44216	-7.6273523	0.511	$0.480^{+0.016}_{-0.016}$	6.00 ± 0.31	< 2.56	0.274	0.751	< 569	< 4.7 (4.4)	11.9	1.93 ± 0.30	0.67	23.76	
J22130-0030	333.27883	-0.51030426	-	$0.606^{+0.011}_{-0.011}$	~ 3.6	< 3.06	0.201	0.805	< 726	< 6.1 (6.2)	11.8	3.19 ± 0.50	0.61	24.41	
J02215-0647	35.463263	-6.792443	0.618	$0.636^{+0.028}_{-0.044}$	2.56 ± 0.14	< 1.22	0.196	0.810	< 463	< 3.1 (2.8)	12.0	1.50 ± 0.27	0.51	24.24	
J14314+5533	217.9156	55.556308	-	$0.640^{+0.040}_{-0.040}$	~ 2.5	< 3.98	0.182	0.822	< 870	< 11.1 (9.9)	13.4	3.55 ± 0.48	0.72	24.14	
J08591-0345	134.81024	-3.7540217	0.647	$0.586^{+0.040}_{-0.032}$	~ 8	-	-	-	-	-	-	-	0.82	23.79	
J22133+0048	333.38274	0.81002713	-	$0.826^{+0.032}_{-0.032}$	3.40 ± 0.2	2.46 ± 1.91	0.095	0.946	947^{+315}_{-409}	13.1 ± 10.2 (10.8 \pm 8.5)	11.1	3.34 ± 0.54	0.54	24.08	

J2000.0 coordinates of the main galaxy populating the deflector; spectroscopic redshift z_{spec} ; photometric redshift z_{phot} ; Einstein radius derived from the strong lensing modelling, when possible. For the non cusp group, we report with a \sim the distance between the lensed feature and the brightest group member; Einstein radius derived from fitting a Singular Isothermal Sphere (SIS) to the weak lensing signal; mean geometrical factor D_{ls}/D_s and corresponding effective redshift z_{eff} ; velocity dispersion; projected mass derived from weak lensing computed within a circular aperture of radius equals to 2 Mpc, in units $10^{14} M_{\odot}$ (masses derived using the Coupon et al. (2008) photometric redshift catalogue are given within brackets); density of background galaxies, expressed in objects per square arcminute; total i band rest frame luminosity corrected for evolution, in units $10^{12} L_{\odot}$; seeing of the i band observations; i band completeness magnitude. Einstein radii and seeings are expressed in arcseconds.

quantities of interest. The main quantity we are interested in is the weak lensing inferred mass. Therefore, we present in Table 3 in brackets the masses derived using the Coupon et al. (2008) catalogue that can be compared to the masses derived using our catalogue. We find the difference between each estimate to be much smaller than the associated error bars. Therefore, we conclude that adopting one photometric catalogue or the other does not change significantly the presented results.

4.3. Fitting the shear profile

For each group, we look for a shear signal centred on the lens between 150 kpc and 1.2 Mpc from the lens. In the case of SL2S J08544-0121, a bimodal group, we use the barycentre of the light distribution instead since the lens does not dominate the light distribution. We fit an Singular Isothermal Sphere model (SIS) to the signal within this range. The choice of this model is motivated by the fact that we do not expect to get a weak lensing signal strong enough that could allow us to probe more complicated mass profiles. We use the average geometrical factor to convert the fitted Einstein radius into an SIS velocity dispersion σ_{SIS} .

5. Strong gravitational lensing analysis

The strong lensing features can be divided in two categories. Of the 13 groups, 8 exhibit a typical ‘‘cusp’’ configuration where a multiply imaged system forms a characteristic arc on one side of the deflector, sometimes with a counter image on the other side of the deflector. The other 5 groups have more complex strong lensing configurations for which identification of multiple images is challenging and for which no strong lensing modelling is possible at this stage. More details on each strong lensing configuration are discussed in the Appendix.

For the 8 cusp groups, we apply a simple mass modelling in order to estimate the Einstein radius, using the code (see Jullo et al. 2007, for a description of the method and how error bars are derived). The refinement of this modelling will depend on the number of available observational constraints. A realistic parametric mass modelling requires at least 5 parameters. For instance a Singular Isothermal Ellipsoid (SIE) has position (x, y) , ellipticity (e) , position angle (PA) and Einstein radius. For a multiply imaged system where a background source is imaged n times, and assuming its redshift is known, we have $2 \times (n-1)$ constraints. Only if $n \geq 4$ can we constrain an SIE profile. In the cusp sample, we have typically only one multiply imaged system, composed of 3 to 4 images which translates into 4 to 6 observational constraints. When the number of observational constraints does not allow to probe 5 free parameters, we set the ellipticity and position angle to 0, leading to a non-elliptical mass distribution. The main robust quantity we aim to derive is the Einstein radius. For the non-cusp group, we evaluate the Einstein radius simply by measuring the distance between the strong lensing feature and the brightest group galaxy.

Optimisations are performed in the image plane, assuming a positional uncertainty equals to $0.1''$. The ellipticity of the mass distribution was forced to be smaller than 0.6 (in units $(a^2 - b^2)/(a^2 + b^2)$) as motivated by numerical simulations (Jing & Suto 2002). Table 2 summarises information relevant to strong lensing modelling: number of constraints available; optimised parameters (position, ellipticity, position angle, Einstein radius); RMS in the image plane and reduced χ^2 , which quantifies the goodness of the fit. We note that for two systems, we are

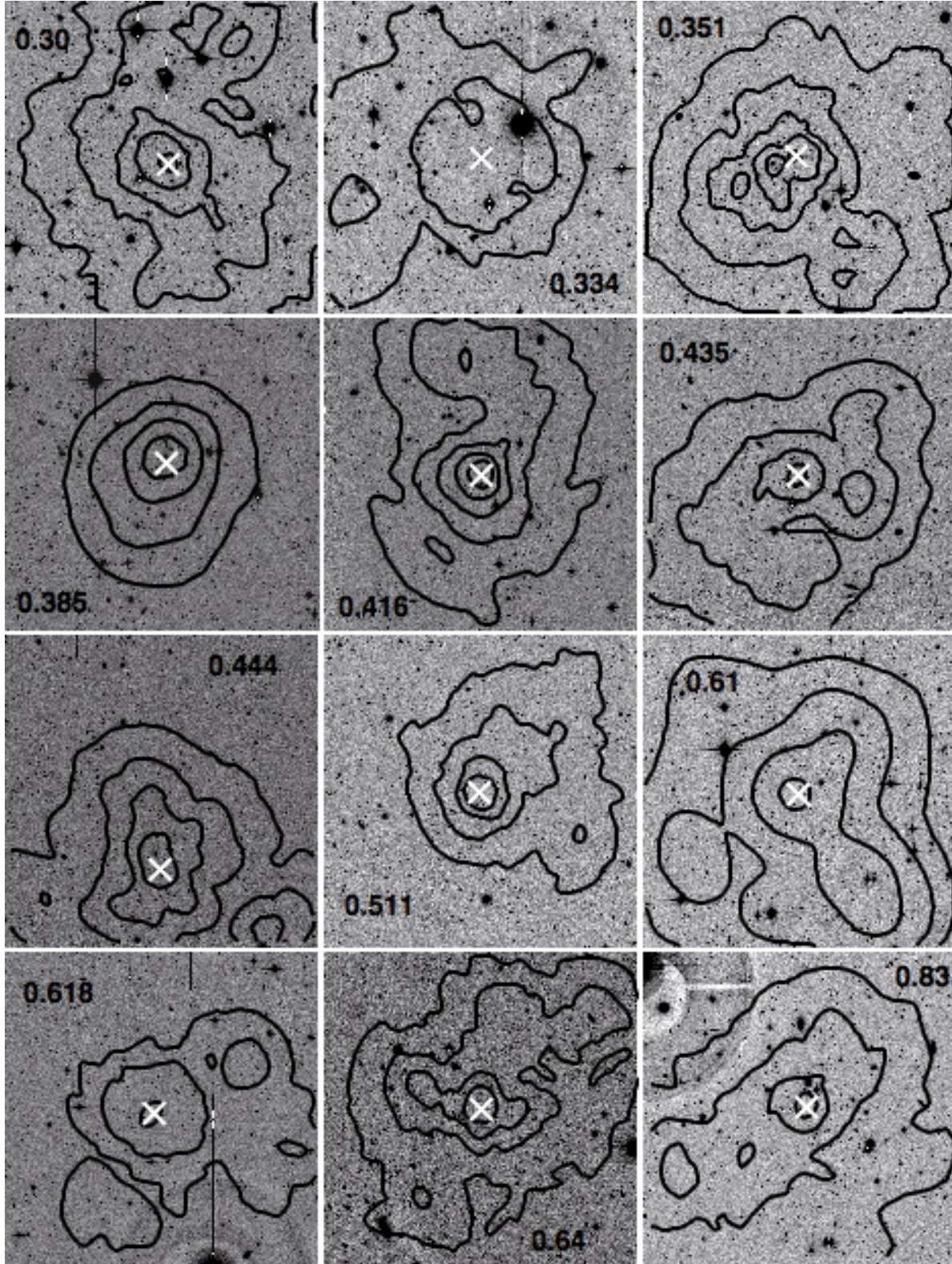


Fig. 2. Large scale $10' \times 10'$ CFHTLS *i* band image for all groups but one (SL2S J08591-0345 for which data are missing). Pictures are ranked by increasing redshifts as in Table 3. Redshift is reported on each picture, with three digits precision when spectroscopically measured. The white cross shows where the lens is located. Black contours correspond to luminosity contours (corrected for passive evolution) equal to 10^5 , 3×10^5 , 10^6 , 3×10^6 and $10^7 L_{\odot} \text{kpc}^{-2}$.

unable to correctly retrieve the observational constraints, with RMS larger than the positional uncertainty: SL2S J08544-0121, $\text{rms} = 0.28''$ and SL2S J02215-0647, $\text{rms} = 0.2''$.

6. Results

The main properties of the groups are summarised in Table 3 and illustrated in the following figures. The name of each group

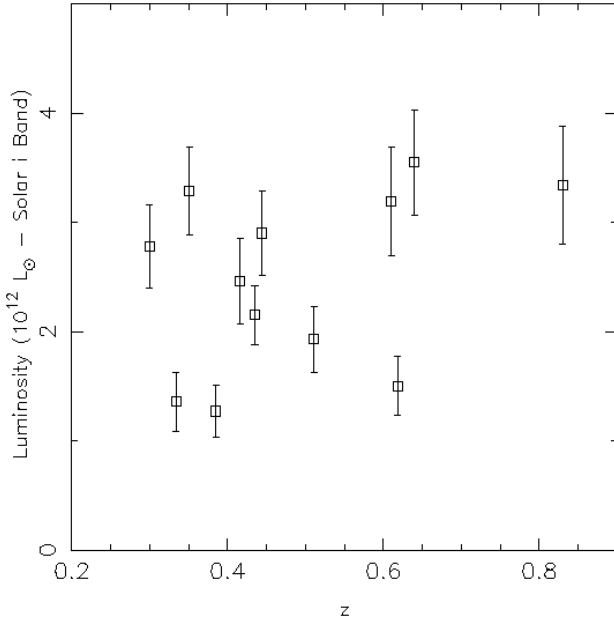


Fig. 3. Luminosities (corrected for passive evolution) versus group redshifts.

corresponds to the equatorial coordinates (J 2000) of the brightest member. In the Appendix, we dedicate a paragraph to detail the properties of each group together with the following images:

1. a large scale $10' \times 10'$ CFHTLS i band image. The white cross shows where the lens is located. We draw luminosity contours (corrected for passive evolution) equal to 10^5 , 3×10^5 , 10^6 , 3×10^6 and $10^7 L_{\odot} \text{ kpc}^{-2}$;
2. a 1-square-arcminute colour image from g, r, i CFHTLS imaging centred on the deflector;
3. the HST image (when available) centred on the deflector, with the image size given in the figure caption. The image is in colour when observations are available in three bands (F475, F606 and F814), and is in F606 otherwise.

Some of these visual information are summarised in Fig. 2, where we show the large scale CFHTLS images for the 12 groups (all except SL2S J08591-0345 for which data is incomplete, see Sect. 6.7).

6.1. Einstein radii and redshift distributions

The group sample presented here spans $z = 0.30$ to $z = 0.83$, with a mean redshift $\langle z \rangle = 0.50$. We report in Table 3 the fitted R for the 8 cusp groups, as well as the measured R for the remaining 5 non cusp groups. They span $2.5''$ to $8''$. We expect the distribution of R to decrease with increasing R (Fig. 1). This is not seen here, but we need to correct this distribution for selection biases. Clearly we will miss more $R \sim 2''$ than $R \sim 5''$ systems with our detection robot (simply because a small R is more likely to be embedded within the light distribution of the lensing galaxy and missed for that reason).

6.2. Luminosities

In all cases, we find that the brightest galaxy populating the strong lensing deflector is the brightest group member. Total luminosities, corrected for passive evolution, are reported in Table 3. Figure 3 shows the luminosity as a function of redshift.

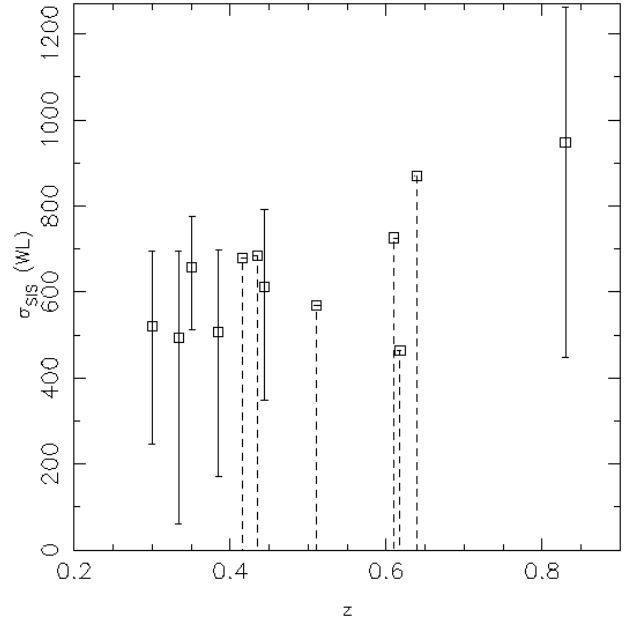


Fig. 4. Velocity dispersions inferred from fitting a Singular Isothermal Sphere to the reduced shear profile, as a function of group redshifts. Dashed lines corresponds to upper limits only.

We find that the group sample presented in this work is homogeneous in terms of total luminosities.

6.3. Weak lensing

We report the inferred SIS velocity dispersion for each group in Table 3. Figure 4 shows the fitted σ_{SIS} as a function of redshift. As expected, we see that the weak lensing constraints are tighter for the lowest redshift groups. Considering the whole sample, we see that $\sigma_{\text{SIS}} \sim 500 \text{ km s}^{-1}$ with large error bars and an upper limit of $\sim 900 \text{ km s}^{-1}$. Therefore, we verify that no massive cluster with $\sigma_{\text{SIS}} > 1000 \text{ km s}^{-1}$, which would lens a close background source, is included in our sample and that it consists of groups or poor clusters only. Note, however, that the highest redshift structure included in the present work has a velocity dispersion between 432 and 1218 km s^{-1} . The upper limit is therefore consistent with a galaxy cluster, see Sect. 6.8.

We are not able, given the data at hand, to pursue a more refined 2-D weak lensing study from which we could infer the shape of the mass distribution over the field and compare more precisely with the luminosity contours. Indeed, it is already challenging to infer an SIS velocity dispersion from our 1-D analysis and error bars are large. A 2 dimensional analysis would involve more free parameters and is not feasible here.

6.4. Mass-to-light ratios

From the above, we are able to compute mass-to-light ratios. From the weak lensing analysis, we compute the projected mass of the group within a circular aperture of 2 Mpc centred on the lens (except SL2S J08544-0121, a bimodal group that we centre on the barycentre of the light distribution). Then we consider the total luminosity, corrected for passive evolution. Values are given in Table 3 and illustrated in Fig. 5. The mean value is equal to ~ 250 (i band, solar units, corrected for passive evolution), with an upper limit of 500.

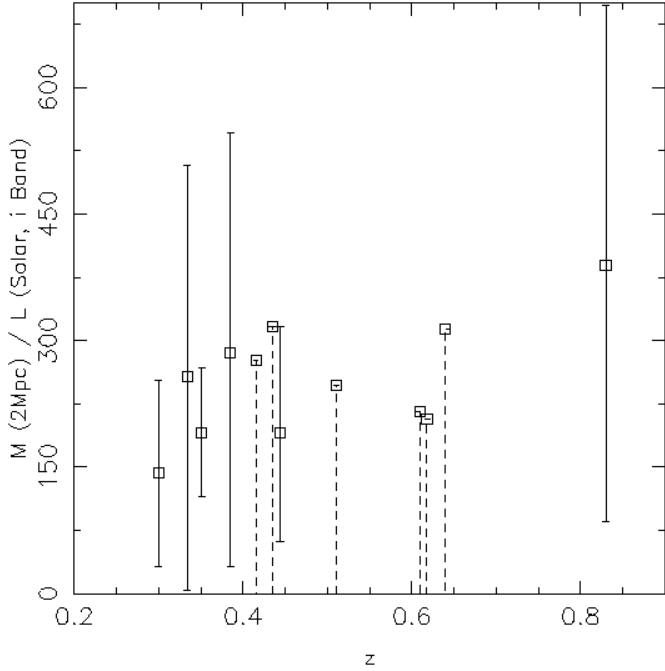


Fig. 5. Mass to Light ratio for the group sample, taking into account passive evolution correction. Dashed lines corresponds to upper limits only.

6.5. Trends with luminosity

If the mass is proportional to the luminosity of the systems, we expect the SIS velocity dispersion to correlate with the luminosity of the galaxy groups. We show in Fig. 6 velocity dispersions inferred from the weak lensing analysis as a function of luminosities (corrected for passive evolution). The expected trend is suggested but not statistically significant due to the large error bars.

6.6. Number density

We have found 13 group scale lenses within a field of ~ 100 square degrees (Table 1). This gives a rough estimate of the number density of ~ 0.13 groups per square arcminute. We note that some group candidates found on the CFHTLS images were not confirmed on the HST imaging and not included here. Moreover, at this stage of the project, we do not understand properly our selection function. Selection biases inherent to our detection technique exist and will be addressed in a forthcoming publication using numerical simulations. Once the SL2S will be completed and the selection function understood, we will be able to compare the distribution of observationally determined R to the predictions from Oguri (2006), which may provide an interesting test of the Λ CDM scenario.

6.7. The case of SL2S J08591-0345

This system at $z_{\text{spec}} = 0.647$ is presented in the Appendix in more detail. The observational setup makes this system special: the lens is located close ($75'' = 508$ kpc) to the edge of the field of view. Therefore, it is very likely that we are missing a significant part of this interesting structure (note the exotic strong lensing configuration). Therefore, we do not report a value of the luminosity for this group, neither do we pursue any weak lensing analysis.

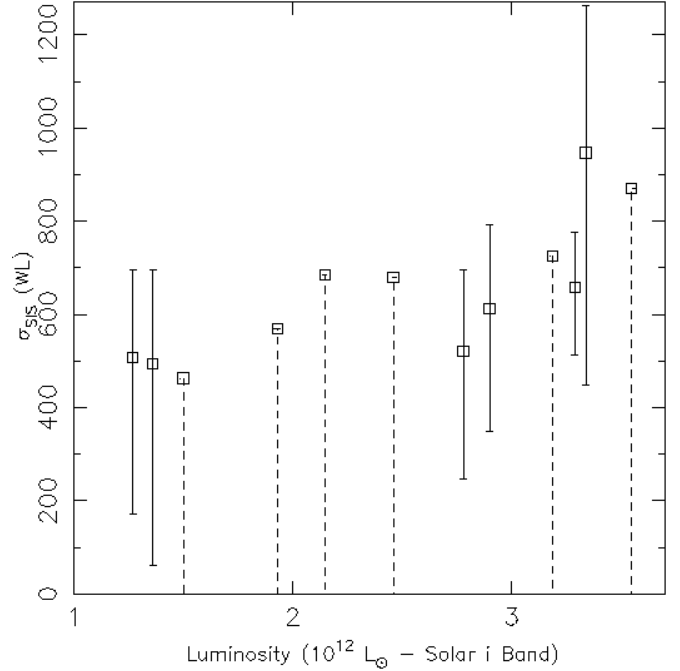


Fig. 6. SIS velocity dispersion inferred from the weak lensing analysis as a function of luminosity (corrected for passive evolution).

6.8. The case of SL2S J22133+0048

The weak lensing analysis of this system located at $z_{\text{phot}} = 0.83$ yields a velocity dispersion between 432 and 1218 km s^{-1} which makes it consistent with a galaxy cluster. We note that its Einstein radius is rather small for a galaxy cluster, about $3.4''$. It is possible that SL2S J22133+0048 is indeed a galaxy cluster with a velocity dispersion larger than 1000 km s^{-1} lensing a close background source. An estimate of the redshift of the strongly lensed background source would help to alleviate the doubt. We also note that the redshift of this structure has been estimated photometrically. If this estimation is biased such that this structure is located at lower redshift, then we are currently overestimating its velocity dispersion.

7. Discussion

In this section, we discuss the results obtained on the group sample. Our statements are clearly limited by the large error bars obtained on the quantities of interest, in particular on the weak-lensing mass estimates. Therefore, part of the following discussion is qualitative only.

7.1. Mass is traced by light

The strong lensing system is always found to coincide with the peak of the light distribution, as can be seen in Fig. 2 (see, however, the case of SL2S J08544-0121 discussed in the Appendix). Because a strong lensing system is always associated with a significant mass concentration (occurrence of strong lensing implies $\Sigma > \Sigma_{\text{critic}}$), this suggests that the light is a good tracer of the mass and this justifies the choice of the strong lensing system as the group centre when we perform a weak lensing analysis. We note that this statement is limited to the fact that the centres of the luminosity and mass distributions are located approximately at the same position. We cannot say much at this point because of the limitations of the weak lensing analysis (Sect. 6.3).

7.2. A homogeneous sample?

The sample is homogeneous in term of luminosities ranging between 1 and $4 \times 10^{12} L_{\odot}$ (Fig. 3). However, Fig. 2 shows that the luminosity contours have very different shapes from one group to another and that all but two (SL2S J09413-1100 at $z = 0.38$ and SL2S J02254-0737 at $z = 0.51$) have complicated shapes, suggesting that these intermediate mass structures may be dynamically young.

7.3. Evolution with redshift?

We looked at possible evolution of the mass-to-light ratio with redshift in Fig. 5. However, given the large error bars on this quantity, we cannot reliably infer any trend.

7.4. Comparison to other studies

There have been at least two different estimations of the mass-to-light ratio of galaxy groups from weak lensing. The first measurement of the average mass-to-light ratios was performed by Hoekstra et al. (2001) in the CNOC2 survey. They stacked the weak lensing signal obtained for 50 groups that have been selected on the basis of a dynamical analysis of group candidates. Their weak lensing detection points towards much less massive systems than the one presented in this paper: their best-fit singular isothermal sphere yields a velocity dispersion of $274^{+48}_{-59} \text{ km s}^{-1}$. However, they find a mass-to-light ratio of $254 \pm 110 h$ (solar units, B band rest frame corrected for evolution).

Subsequently, another similar study on a sample of 116 CNOC2 galaxy groups was performed by Parker et al. (2005). Given more statistics, they were able to split the group sample into subsets of poor and rich groups. Their poor galaxy groups were found to have an average velocity dispersion of $193 \pm 38 \text{ km s}^{-1}$ and a mass-to-light ratio of $134 \pm 26 h$ (solar units, B band rest frame), while their rich galaxy groups have a velocity dispersion of $270 \pm 39 \text{ km s}^{-1}$ and a mass-to-light ratio of $278 \pm 42 h$, thus finding evidence for a steep increase in the mass-to-light ratio as a function of mass.

The groups presented in the present work are more massive than the rich galaxy group sample from Parker et al. (2005). Given the error bars obtained on the mass-to-light ratios, it is difficult to reliably compare our findings to those from Parker et al. (2005). However, considering the 6 groups for which we achieved a weak lensing detection, we get a mean velocity dispersion of 623 km s^{-1} and a mean mass-to-light ratio of 242, consistent with the results of Parker et al. (2005). Note that these values are close to mass-to-light ratios of galaxy clusters (e.g. Carlberg et al. 1997; Bardeau et al. 2007).

Our results suggest that after the steep increase in mass-to-light ratio as a function of mass pointed out by Parker et al. (2005) which seems to occur at velocity dispersions around 200 km s^{-1} (or mass scale of order $\sim 10^{13} M_{\odot}$), mass-to-light ratios reach a plateau and do not evolve much from the mass scale of groups with velocity dispersions around 300 km s^{-1} up to rich galaxy clusters with velocity dispersion larger than 1000 km s^{-1} . The group sample studied in this article therefore helps to bridge the gap between estimates of the mass-to-light ratio of galaxy groups with velocity dispersions in the range $200\text{--}300 \text{ km s}^{-1}$ and for galaxy clusters.

7.5. The naked cusp sample

Eight galaxy groups reported in this article exhibit typical cusp configurations, with a clear tangential arc on one side of the deflector. For 5 of these groups, we have not been able to find the expected counter image which is usually located on the other side of the deflector, even when HST imaging was available. This incomplete cusp configuration is called “naked cusp” (see, e.g. Schneider et al. 1992; Oguri & Keeton 2004). In two cases, SL2S J02215-0647 and SL2S J08544-0121, the counter image of the cusp is clearly identified on the HST images. In SL2S J22133+0048, the detection of the counter image is tentative only. Moreover, note that the case of SL2S J08544-0121 is a bit special since this cusp configuration is not located at the centre of the total light distribution, whereas the other cusp groups are. To summarise, we find that most of the cusp groups are naked. It may be that the current observations did not allow us to find the counter images, but this naked state of a cusp can be linked with lens statistic issue. If CDM haloes have central density slopes < 1.5 , Oguri & Keeton (2004) predict that a significant fraction ($> 20\%$) of large separation lenses should have naked cusp image configurations. Therefore, our results could suggest that the groups studied in this work may have shallow central density slopes.

7.6. Other intermediate separation lenses

We claim this work to be the first representative sample of strong lensing systems generated by group scale dark matter haloes, with intermediate image separation (in the range $\sim 3''\text{--}8''$). However, at least five intermediate separation lenses have been reported so far, even though the authors did not always consider the group-scale haloes as being responsible for the image separation, and are interpreting the results in terms of massive galactic scale haloes. A remarkable example is the so called Cosmic Horseshoe (Belokurov et al. 2007; Dye et al. 2008), an almost complete Einstein ring of radius $5''$ from a luminous red galaxy at $z = 0.44$. The authors argued that this is the most massive galaxy lens discovered so far, with a mass enclosed within its Einstein radius of $5 \times 10^{12} M_{\odot}$, making this galaxy as massive as the entire Local Group. We rather suggest that this lensing system is simply produced by a *group-scale* dark-matter halo, whose centre is populated by the luminous red galaxy. Indeed, this galaxy is the brightest object in the group of ~ 26 members as revealed by the SDSS photometry. As suggested by the nearly perfect circle outlined by the ring, no external shear was required in the model of the system, which is not surprising because the deflector traces the centre of the group halo. This important discovery led to a more systematic data mining looking for large separation lenses in the Sloan Digital Sky Survey: the CAMbridge Sloan Survey Of Wide ARcs in the skY (CASSOWARY⁶). Recently, Belokurov et al. (2009) reported two new large separation lenses, with Einstein radius equal to $4''$ and $8''$. More recently, Lin et al. (2009), in a systematic search for bright arcs in the SDSS, reported a strongly lensed $z = 2$ galaxy by a deflector whose Einstein Radius equals $3.82''$. We also mention an intermediate separation lens ($R \sim 2.5''$) found in the CLASS survey, B2108+213 (McKean et al. 2005; More et al. 2008).

We expect to find new intermediate separation lenses on completion of the CFHTLS, which, in combination with group scale lenses from other promising dedicated searches in surveys

⁶ <http://www.ast.cam.ac.uk/research/cassowary/>

such as the SDSS⁷, will increase the statistics of intermediate separation lenses, thus allowing us to get insights on this intermediate mass range.

8. Conclusion

We have presented a sample of 13 strong lensing features with Einstein radii between 3'' and 8'', i.e. generated by *galaxy group-scale dark-matter haloes*. This is the first representative sample (not yet complete) of intermediate image separations lenses, bridging the gap between galaxy and cluster scales. Our conclusions are the following:

1. The strong lensing analysis yields Einstein radii between 2.5'' and 8''.
2. We have studied the luminosity distribution to infer properties on large scales: the strong lenses coincide with the peak of the light distribution; most of the luminosity maps have complicated shapes, suggesting dynamically young structures.
3. A weak lensing analysis yields $\sigma_{\text{SIS}} \sim 500 \text{ km s}^{-1}$ with large error bars and an upper limit of $\sim 900 \text{ km s}^{-1}$ for the whole sample. This confirms that our sample consists of rich groups.
4. σ_{SIS} seems to increase with luminosity but given the large error bars this is not statistically significant.
5. The mass-to-light ratio for the sample is found $M/L_i \sim 250$ (solar units, corrected for evolution), with an upper limit of 500.

We note again that our conclusions are limited by the large error bars obtained on the weak lensing inferred mass estimates.

Complementary observations are ongoing: we are currently analysing multi object spectroscopy of group members as well as near infrared WIRCAM imaging. This sample will be complemented in the near future with other observations in order to help address issues of structure formation and evolution.

Once the Strong Lensing Legacy Survey will be completed and the selection function well understood, we will compare the distribution of observed Einstein radii to the predictions from Oguri (2006), which may provide an interesting test of the Λ CDM scenario.

Acknowledgements. ML acknowledges the Agence Nationale de la Recherche (Project number 06-BLAN-0067) and the Centre National d' Etudes Spatiales (CNES) for their support. The Dark Cosmology Centre is funded by the Danish National Research Foundation. JR is grateful to Caltech for its support. J.P.K. acknowledges the Centre National de la Recherche Scientifique for its support. Part of this project is done under the support of National Natural Science Foundation of China No. 10878003, 10778752, 973Program No. 2007CB815402, Shanghai Foundation No. 08240514100, 07dz22020, and the Leading Academic Discipline Project of Shanghai Normal University DZL805. M.L. acknowledges Sébastien Bardeau for making its package available, and Masamune Oguri for providing the data used to generate Fig. 1. V.M. acknowledges partial support from FONDECYT through grant 1071008. We acknowledge the referee for a careful reading of the submitted paper and constructive suggestions. This research has made use of the NASA/IPAC Extragalactic Database (NED) which is operated by the Jet Propulsion Laboratory, California Institute of Technology, under contract with the National Aeronautics and Space Administration.

References

- Alard, C. 2009, ArXiv e-prints 0901.0344
 Auger, M. W., Fassnacht, C. D., Abrahamse, A. L., Lubin, L. M., & Squires, G. K. 2007, AJ, 134, 668
 Auger, M. W., Fassnacht, C. D., Wong, K. C., et al. 2008, ApJ, 673, 778

- Bardeau, S. 2004, Ph.D. Thesis, Université Paul Sabatier, Toulouse III, France
 Bardeau, S., Kneib, J.-P., Czoske, O., et al. 2005, A&A, 434, 433
 Bardeau, S., Soucaill, G., Kneib, J.-P., et al. 2007, A&A, 470, 449
 Belokurov, V., Evans, N. W., Moiseev, A., et al. 2007, ApJ, 671, L9
 Belokurov, V., Evans, N. W., Hewett, P. C., et al. 2009, MNRAS, 392, 104
 Bertin, E., & Arnouts, S. 1996, A&A, 117, 393
 Bolzonella, M., Miralles, J.-M., & Pelló, R. 2000, A&A, 363, 476
 Bridle, S., Kneib, J.-P., Bardeau, S., & Gull, S. 2002, in The shapes of galaxies and their dark halos, Proceedings of the Yale Cosmology Workshop, New Haven, Connecticut, USA, 28–30 May 2001, ed. P. Natarajan, 38
 Bruzual, G., & Charlot, S. 2003, MNRAS, 344, 1000
 Cabanac, R. A., Alard, C., Dantel-Fort, M., et al. 2007, A&A, 461, 813
 Carlberg, R. G., Yee, H. K. C., & Ellingson, E. 1997, ApJ, 478, 462
 Carrasco, E. R., Cypriano, E. S., Neto, G. B. L., et al. 2007, ApJ, 664, 777
 Condon, J. J., Cotton, W. D., Greisen, E. W., et al. 1998, AJ, 115, 1693
 Coupon, J., Ilbert, O., Kilbinger, M., et al. 2008, ArXiv e-prints 0811.3326
 Cypriano, E. S., Sodr , L. J., Kneib, J.-P., & Campusano, L. E. 2004, ApJ, 613, 95
 Cypriano, E. S., Lima Neto, G. B., Sodr , Jr., L., Kneib, J.-P., & Campusano, L. E. 2005, ApJ, 630, 38
 D'Onghia, E., Sommer-Larsen, J., Romeo, A. D., et al. 2005, ApJ, 630, L109
 Dye, S., Evans, N. W., Belokurov, V., Warren, S. J., & Hewett, P. 2008, MNRAS, 388, 384
 Faltenbacher, A., & Mathews, W. G. 2007, MNRAS, 375, 313
 Fassnacht, C. D., & Lubin, L. M. 2002, AJ, 123, 627
 Fassnacht, C. D., McKean, J. P., Koopmans, L. V. E., et al. 2006, ApJ, 651, 667
 Faure, C., Kneib, J., Hilbert, S., et al. 2008, ArXiv e-prints 0810.4838
 Feron, C., Hjorth, J., McKean, J. P., & Samsing, J. 2008, ArXiv e-prints 0810.0780
 Finoguenov, A., Ponman, T. J., Osmond, J. P. F., & Zimer, M. 2007, MNRAS, 374, 737
 Gastaldello, F., Buote, D. A., Humphrey, P. J., et al. 2007, ApJ, 669, 158
 Gladders, M. D., Lopez-Cruz, O., Yee, H. K. C., & Kodama, T. 1998, ApJ, 501, 571
 Grillo, C., Lombardi, M., Rosati, P., et al. 2008, A&A, 486, 45
 Helsdon, S. F., & Ponman, T. J. 2000, MNRAS, 315, 356
 Helsdon, S. F., & Ponman, T. J. 2003, MNRAS, 339, L29
 Heymans, C., Van Waerbeke, L., Bacon, D., et al. 2006, MNRAS, 368, 1323
 Hoekstra, H. 2007, MNRAS, 379, 317
 Hoekstra, H., Franx, M., Kuijken, K., et al. 2001, ApJ, 548, L5
 Ienna, F., & Pell , R. 2006, in SF2A-2006: Semaine de l'Astrophysique Francaise, ed. D. Barret, F. Casoli, G. Lagache, A. Lecavelier, & L. Pagan, 347
 Inada, N., Oguri, M., Shin, M.-S., et al. 2009, ApJ, 696, 1319
 Jing, Y. P., & Suto, Y. 2002, ApJ, 574, 538
 Jullo, E., Kneib, J.-P., Limousin, M., et al. 2007, New J. Phys., 9, 447
 Kassiola, A., Kovner, I., & Blandford, R. D. 1992, ApJ, 396, 10
 King, L. J. 2007, MNRAS, 956
 Kneib, J., Hudelot, P., Ellis, R. S., et al. 2003, ApJ, 598, 804
 Kovner, I. 1987, ApJ, 321, 686
 Kubo, J. M., Allam, S. S., Annis, J., et al. 2008, ArXiv e-prints 0812.3934
 Kundic, T., Hogg, D. W., Blandford, R. D., et al. 1997, AJ, 114, 2276
 Limousin, M., Kneib, J. P., Bardeau, S., et al. 2007a, A&A, 461, 881
 Limousin, M., Richard, J., Jullo, E., et al. 2007b, ApJ, 668, 643
 Lin, H., Buckley-Geer, E., Allam, S. S., et al. 2009, ApJ, 699, 1242
 Mamon, G. A. 2007, in Groups of Galaxies in the Nearby Universe, ed. I. Saviane, V. D. Ivanov, & J. Borissova, 203
 Mandelbaum, R., Seljak, U., Cool, R. J., et al. 2006, MNRAS, 372, 758
 McKean, J. P., Browne, I. W. A., Jackson, N. J., et al. 2005, MNRAS, 356, 1009
 Medezinski, E., Broadhurst, T., Umetsu, K., et al. 2007, ApJ, 663, 717
 Mellier, Y. 1999, ARA&A, 37, 127
 M ller, O., Natarajan, P., Kneib, J.-P., & Blain, A. W. 2002, ApJ, 573, 562
 Momcheva, I., Williams, K., Keeton, C., & Zabludoff, A. 2006, ApJ, 641, 169
 More, A., McKean, J. P., Muxlow, T. W. B., et al. 2008, MNRAS, 384, 1701
 Morgan, N. D., Kochanek, C. S., Pevunova, O., & Schechter, P. L. 2005, AJ, 129, 2531
 Newton, E. R., Marshall, P. J., & Treu, T. 2008, ArXiv e-prints 0810.3934
 Oguri, M. 2006, MNRAS, 367, 1241
 Oguri, M., & Keeton, C. R. 2004, ApJ, 610, 663
 Oguri, M., Keeton, C. R., & Dalal, N. 2005, MNRAS, 364, 1451
 Osmond, J. P. F., & Ponman, T. J. 2004, MNRAS, 350, 1511
 Parker, L. C., Hudson, M. J., Carlberg, R. G., & Hoekstra, H. 2005, ApJ, 634, 806
 Rasmussen, J., & Ponman, T. J. 2007, MNRAS, 380, 1554
 Schneider, P., Ehlers, J., & Falco, E. E. 1992, Gravitational Lenses (Berlin: Springer-Verlag)
 Sommer-Larsen, J. 2006, MNRAS, 369, 958
 Sun, M., Voit, G. M., Donahue, M., et al. 2009, ApJ, 693, 1142

⁷ one month after this work was submitted, Kubo et al. (2008) reported the finding of five new group scale lenses in the SDSS.

- Treu, T., Gavazzi, R., Gorecki, A., et al. 2009, *ApJ*, 690, 670
- Trott, C. M., Treu, T., Koopmans, L. V. E., & Webster, R. L. 2008, *ArXiv e-prints* 0812.0748
- Tu, H., Limousin, M., Fort, B., et al. 2008, *MNRAS*, 1169
- van den Bosch, F. C., Pasquali, A., Yang, X., et al. 2008, *ArXiv e-prints* 0805.002
- Williams, K. A., Momcheva, I., Keeton, C. R., Zabludoff, A. I., & Lehár, J. 2006, *ApJ*, 646, 85
- Willis, J. P., Pacaud, F., Valtchanov, I., et al. 2005, *MNRAS*, 363, 675
- Yang, X., Mo, H. J., & van den Bosch, F. C. 2008, *ApJ*, 676, 248
-
- ¹ Laboratoire d'Astrophysique de Toulouse-Tarbes, Université de Toulouse, CNRS, 57 avenue d'Azereix, 65000 Tarbes, France
e-mail: marceau.limousin@ast.obs-mip.fr
- ² Laboratoire d'Astrophysique de Marseille, UMR 6110, CNRS-Université de Provence, 38 rue Frédéric Joliot-Curie, 13388 Marseille Cedex 13, France
- ³ Dark Cosmology Centre, Niels Bohr Institute, University of Copenhagen, Juliane Maries Vej 30, 2100 Copenhagen, Denmark
- ⁴ CNRS, UMR 7095, Institut d'Astrophysique de Paris, 75014 Paris, France
- ⁵ UPMC Université Paris 06, UMR 7095, Institut d'Astrophysique de Paris, 75014 Paris, France
- ⁶ Universidad de Valparaíso, Departamento de Física y Astronomía, Avenida Gran Bretaña 1111, Valparaíso, Chile
- ⁷ Durham University, Physics and Astronomy Department, South Road, Durham DH3 1LE, UK
- ⁸ Department of Astronomy, California Institute of Technology, 105-24, Pasadena, CA91125, USA
- ⁹ Department of Physics and Astronomy, University of Victoria, Victoria, BC, V8W 3P6, Canada
- ¹⁰ Laboratoire d'Astrophysique de Toulouse-Tarbes, Université de Toulouse, CNRS, 14 avenue Édouard Belin, 31400 Toulouse, France
- ¹¹ Herzberg Institute of Astrophysics, National Research Council, 5071 West Saanich Road, Victoria, BC V9E 2E7, Canada
- ¹² Laboratoire d'Astrophysique, Ecole Polytechnique Fédérale de Lausanne (EPFL), Observatoire de Sauverny, 1290 Versoix, Switzerland
- ¹³ Department of Physics, University of California, Santa Barbara, CA 93106, USA
- ¹⁴ Argelander-Institut für Astronomie, Universität Bonn, Auf dem Hügel 71, 53121 Bonn, Germany
- ¹⁵ Institute for Computational Cosmology, Department of Physics, Durham University, South Road, Durham DH1 3LE, UK
- ¹⁶ Physics Department & Shanghai Key Lab for Astrophysics, Shanghai Normal University, 100 Guilin Road, Shanghai 200234, China
- ¹⁷ Observatoire de Paris, GEPI, CNRS-UMR 8111, 5 place Jules Janssen, 92195 Meudon Cedex, France

Appendix A: Presentation of each group

We dedicate below a paragraph to each group to describe its main properties. The information are summarised in Table 3 and illustrated in the Appendix images.

A.1. Group description

SL2S J09013-0158 at $z_{\text{phot}} = 0.30$ (Fig. A.1): The luminosity distribution is elongated in the north-south direction. We report a straight arc between the two main bright central galaxies: this is a typical beak-to-beak configuration (Kassiola et al. 1992). This arc is found closer to the northern galaxy ($\sim 7''$) than the southern one. No HST image is available for this group. A radio source has been reported by Condon et al. (1998) between the two bright central galaxies. Given the coordinates and associated errors of this radio source, it could be associated with one of the two smaller central galaxies.

SL2S J22214-0053 at $z_{\text{spec}} = 0.334$ (Fig. A.2): The SDSS provides a redshift measurement for the main galaxy populating the deflector of 0.334, and a velocity dispersion of $281 \pm 45 \text{ km s}^{-1}$. The strong lensing deflector is populated by a single bright galaxy.

SL2S J08544-0121 at $z_{\text{spec}} = 0.351$ (Fig. A.3): The strong lensing deflector is populated by a single bright galaxy whose ellipticity and position angle equals 0.3 and 25 ± 5 degrees, respectively. The luminosity contours are elongated in the east-west direction and define a position angle consistent with that of the bright galaxy. We also find the position angle of the SIE halo (~ 21 degrees, Sect. 5) to be consistent with that of the bright galaxy.

Note (Fig. A.3) that the innermost luminosity contour at $10^7 L_{\odot} \text{ kpc}^{-2}$ encompass the SL system but also two bright galaxies located $\sim 54''$ east from the SL system, making this light distribution bimodal. This is the only group for which the luminosity distribution is not clearly dominated by the lens, making this configuration rather exceptional: the large Einstein radius ($\sim 5''$) points toward a massive structure associated with this lens, but the luminosity distribution is found bimodal. This suggest a dynamically young structure in the process of formation. This bright galaxy has a spectroscopic redshift measured from Keck of 0.3514. We detect two multiply imaged systems: the brightest one is perturbed by a small satellite galaxy whose redshift is equal to 0.3517 (FORS 2); and the outer one is seen on the ACS colour image (Fig. A.3). Note how the northern counter image is found much further ($\sim 8''$) than the main arc ($\sim 5''$), suggesting a strong contribution from the external shear associated with the host galaxy group. The HST data brings significant additional information on this lensing feature.

SL2S J09413-1100 at $z_{\text{spec}} = 0.385$ (Fig. A.4): The luminosity contours look circular. The strong lensing deflector is populated by a bright galaxy whose stellar halo is extended and presents a large ellipticity ($b/a = 0.59$) with a position angle of 74 degrees. Interestingly, this position angle is found compatible with the orientation of the luminosity contours. Note that this is the only group for which the central galaxy presents an extended stellar halo. We measured a spectroscopic redshift for this galaxy using FORS 2 to be 0.385. We report a blue arc composed by two merging images north of the deflector, with its counter image.

We have not been able to find another counter image on the other side of the deflector, even after subtraction of the galaxy on the HST images.

SL2S J14081+5429 at $z_{\text{spec}} = 0.416$ (Fig. A.5): The luminosity distribution is elongated in the north-south direction. The centre of this group is dominated by three bright galaxies aligned in the north-south direction. The brightest one (A, $\text{mag}_i = 18.03$) is the central one, that is also closest to the arc feature. North of A is a galaxy B ($\text{mag}_i = 18.37$) and south of is a galaxy C ($\text{mag}_i = 18.46$). The SDSS provides a redshift measurement for A ($z = 0.415979$) and for B ($z = 0.411022$). A straight arc without any detected feature is located between bright central galaxies.

SL2S J14300+5546 at $z_{\text{spec}} = 0.435$ (Fig. A.6): The luminosity distribution is elongated in the east-west direction. The strong lensing deflector is populated by a single galaxy whose redshift equals 0.435 (Gemini). A tangential arc is found south-east of the deflector. The position angle of the galaxy populating the deflector (~ 45 degrees) is consistent with the position angle defined by the luminosity distribution.

SL2S J02140-0532 at $z_{\text{spec}} = 0.444$ (Fig. A.7): The luminosity distribution is elongated in the north-south direction. The strong lensing deflector is populated by three galaxies. The two brightest ones have redshift measured spectroscopically from Keck (0.4422 and 0.4439) and may be bound gravitationally. We report an arc north of the deflector composed by two merging images showing substructure. The counter image is easily identified east of the deflector. Note that on the ground based image, we see a possible counter image south of the deflector which seems to have colour compatible with the other images. However, on the ACS data, it is clear that this feature cannot be associated with the proposed multiply imaged system. This is also confirmed by the modelling: no acceptable fit was able to reproduce the multiple images as one could have inferred from the ground based data. We note, however, that a recent independent study by Alard (2009) considers the southern image as part of the multiply imaged system. Spectroscopy of each feature is needed in order to remove the uncertainty. The HST data brings significant additional information on this lensing feature: not only does it help to identify the different images belonging to the same system, but it also resolves substructures within each lensed image, increasing the number of constraints for the analysis. The halo of the deflector is oriented with a position angle well constrained at 111 ± 3 degrees. This is the same direction as the one defined by the luminosity contours.

SL2S J02254-0737 at $z_{\text{spec}} = 0.511$ (Fig. A.8): The luminosity contours look circular. The strong lensing deflector is populated by a single galaxy whose redshift equals 0.511 (Gemini). We observe a tangential arc north of the lens galaxy, likely to be composed by two merging images, with an additional counter image a bit further east. The location of the deflector coincide with a radio emission reported by Condon et al. (1998).

SL2S J22130-0030 at $z_{\text{phot}} = 0.61$ (Fig. A.9): The luminosity distribution is elongated in the north-south direction. The HST image reveals that the strong lensing deflector is populated by a very compact group of at least 6 galaxies. We report a blue

arc east of the deflector, and a likely counter image presenting the same colour as the arc on the other side of the deflector.

SL2S J02215-0647 at $z_{\text{spec}} = 0.618$ (Fig. A.10): We find a gap of 1.3 mag in the *R* band between the brightest and the second brightest galaxy, not enough to be considered as a fossil group. The strong lensing deflector is populated by a single galaxy whose redshift equals 0.618 (FORS 2). We report an arc south of the deflector, composed by two merging images. There is a counter image south-east of the deflector, as well as an additional counter image located on the other side of the deflector, resolved by HST data. We report a possible second multiply imaged system constituted by two images with same CFHTLS colours.

SL2S J14314+5533 at $z_{\text{phot}} = 0.64$ (Fig. A.11): The luminosity distribution is elongated in the south-east north-west direction. A small tangential arc is found around bright galaxies. We cannot conjugate any images that may merge to form the arc. It is possible that this blue lensed feature in fact is singly imaged.

SL2S J08591-0345 at $z_{\text{spec}} = 0.647$ (Fig. A.12): The lens is located close ($75'' = 508$ kpc) to the edge of the field of view. It is very likely that we are missing a significant part of this group. Therefore, we have not been reported any values of this group luminosity, neither did we pursue any weak lensing analysis for this group. We observe a rather exotic strong lensing configuration: the deflector is populated by three bright galaxies and two smaller ones. One of the bright one has a redshift of 0.647 (FORS 2). The multiple images draw an oval contour around the deflector. It is difficult at this point to know how many multiple images we observe and if they are coming from a single or multiple background sources. An advanced modelling of this exotic lens would be very interesting and will require deep multi colour space based data with dedicated ground based spectroscopy.

SL2S J22133+0048 at $z_{\text{phot}} = 0.83$ (Fig. A.13): The luminosity distribution is elongated in the south-east north-west direction. The strong lensing deflector is populated by a single galaxy. A tangential arc composed by two merging images is found east of the deflector. A possible counter image on the other side of the deflector is detected on the space based images. The location of the deflector coincides with a radio emission reported by [Condon et al. \(1998\)](#). Our weak lensing analysis yields a velocity dispersion between 432 and 1218 km s⁻¹. The upper limit is therefore consistent with a galaxy cluster. Since its Einstein radius is estimated to be about 3.4'', it is possible that SL2S J22133+0048 is indeed a galaxy cluster with a velocity dispersion larger than 1000 km s⁻¹ lensing a close background source. An estimate of the redshift of the strongly lensed background source would help to alleviate the doubt. We note also that the redshift of this structure has been estimated photometrically. If this estimation is biased and if this structure is located at lower redshift, then we are currently overestimating its velocity dispersion.

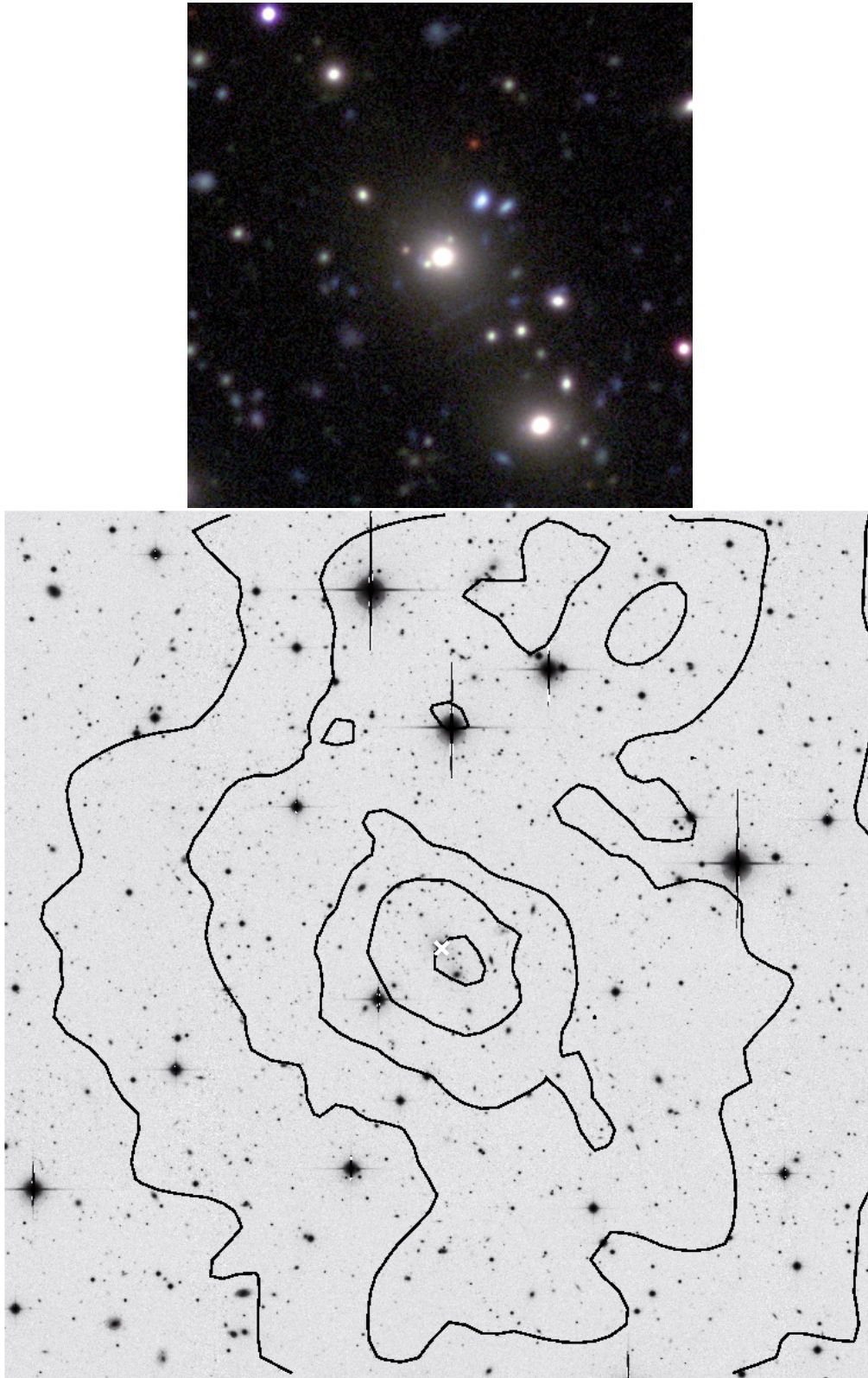


Fig. A.1. Group SL2S J09013-0158 at $z_{\text{phot}} = 0.30$. *Upper:* composite CFHTLS g, r, i colour image (1 square arcminute = $267 \times 267 \text{ kpc}^2$). A straight arc is detected between two elliptical group members. No HST imaging is available. *Lower:* CFHTLS i band ($10' \times 10' = 2672 \times 2672 \text{ kpc}^2$). We draw in black luminosity contours (corrected for passive evolution) equal to 10^5 , 3×10^5 , 10^6 , 3×10^6 and $10^7 L_{\odot} \text{ kpc}^{-2}$, and the white cross shows the location of the SL system.

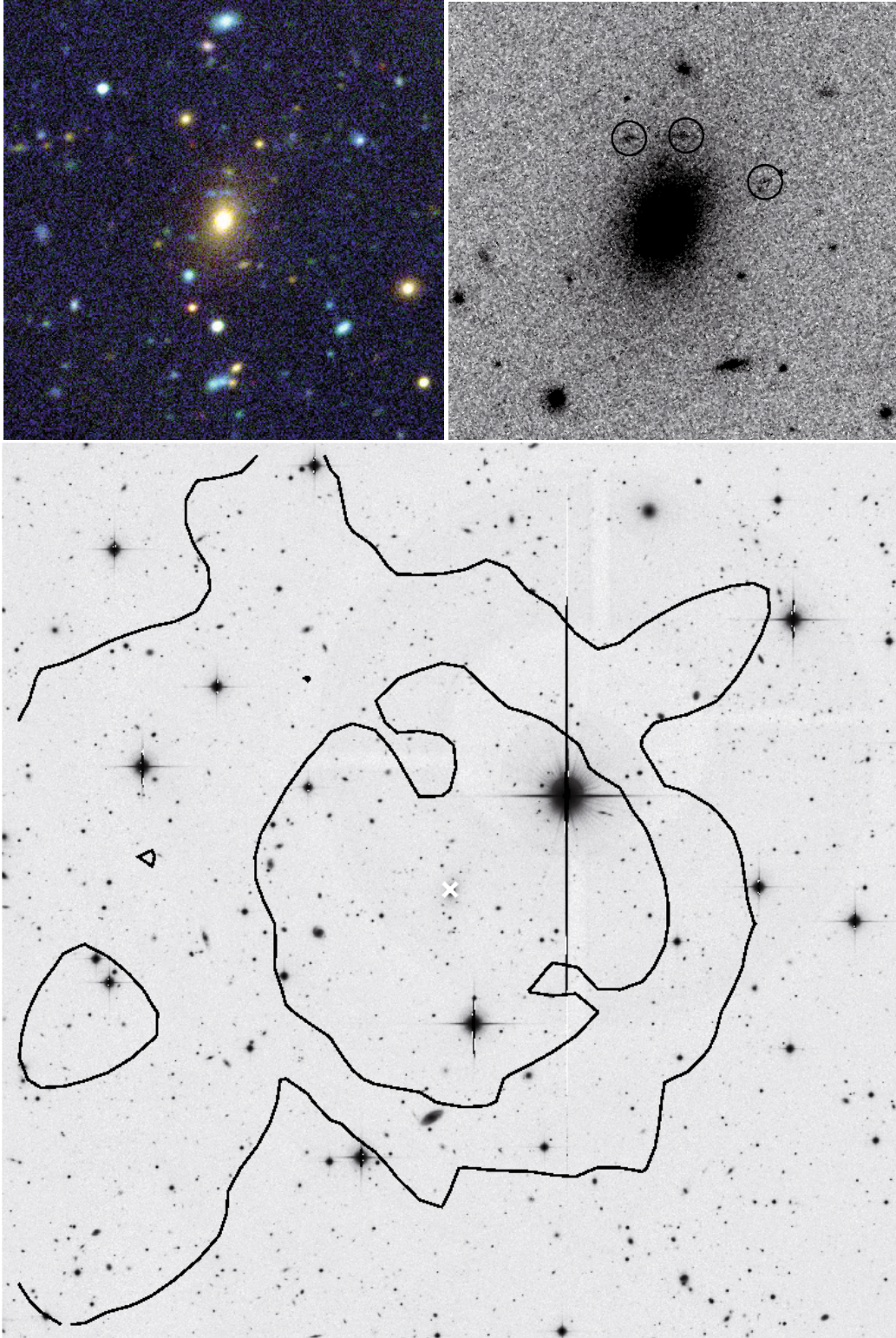


Fig. A.2. Group SL2S J22214-0053 at $z_{\text{spec}} = 0.334$. *Upper Left:* composite CFHTLS g, r, i colour image (1 square arcminute = 287×287 kpc²). *Upper Right:* HST F606 image ($29'' \times 29'' = 139 \times 139$ kpc²). *Lower:* CFHTLS i band ($10' \times 10' = 2874 \times 2874$ kpc²). White cross shows the location of the SL system, and contours are the same as in Fig. A.1.

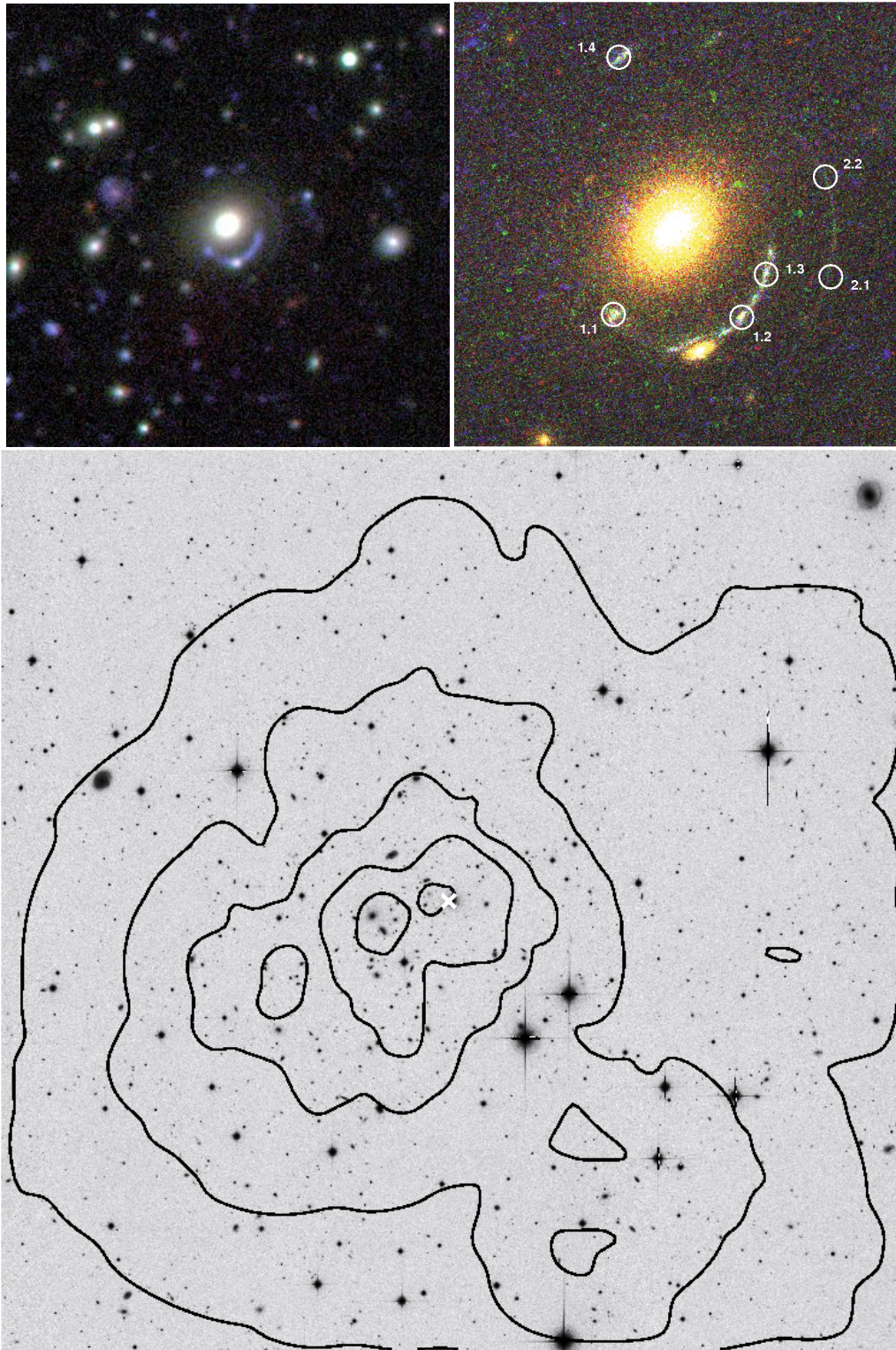


Fig. A.3. Group SL2S J08544-0121 at $z_{\text{spec}} = 0.351$. *Upper Left:* composite CFHTLS g, r, i colour image (1 square arcminute = $297 \times 297 \text{ kpc}^2$). *Upper Right:* composite HST/ACS F814, F606, F475 colour image ($15'' \times 15'' = 74 \times 74 \text{ kpc}^2$). *Lower:* CFHTLS i band ($10' \times 10' = 2969 \times 2969 \text{ kpc}^2$). White cross shows the location of the SL system, and contours are the same as in Fig. A.1.

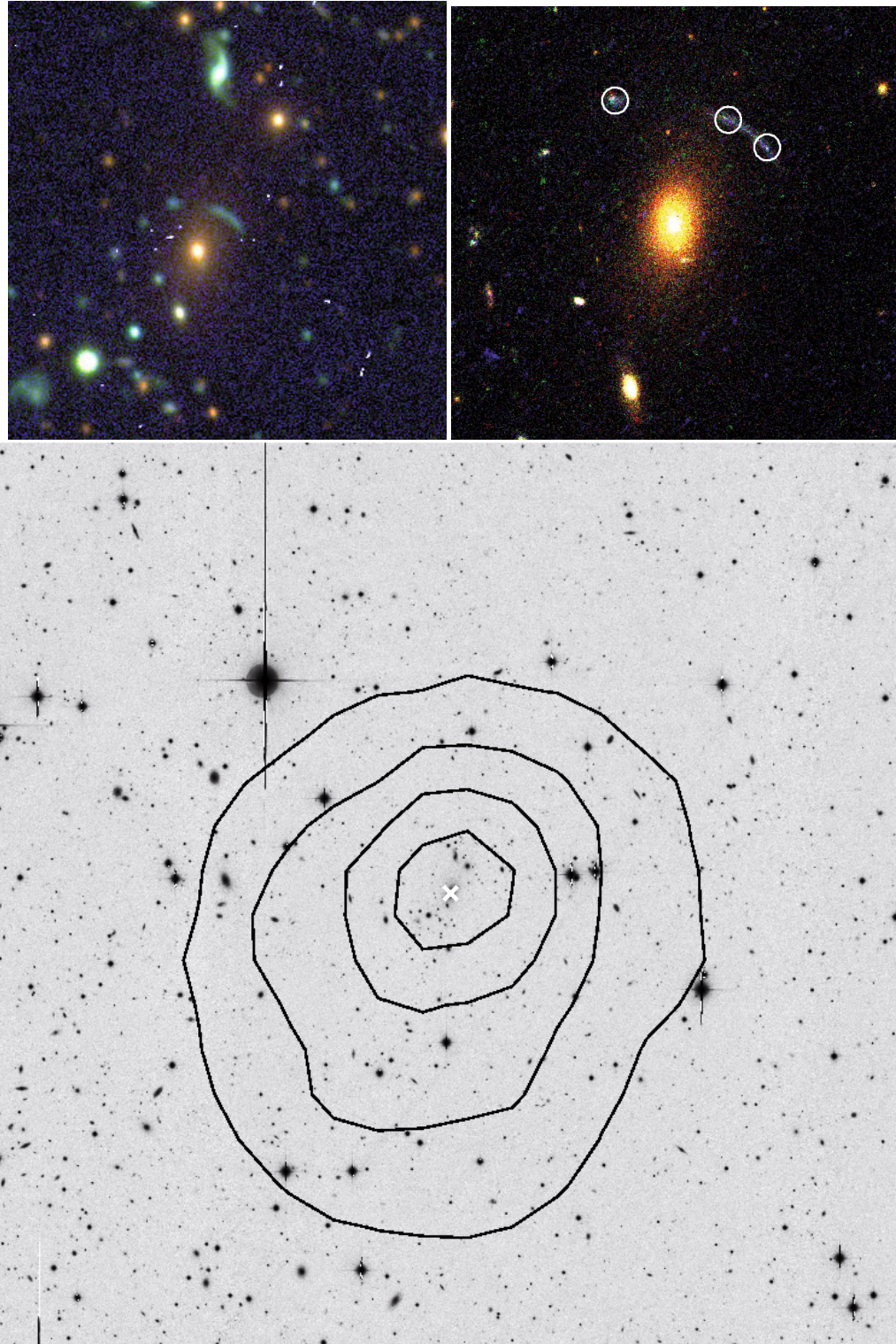


Fig. A.4. Group SL2SJ09413-1100, at $z_{\text{spec}} = 0.385$. *Upper Left:* composite CFHTLS g, r, i colour image (1 square arcminute = $315 \times 315 \text{ kpc}^2$). *Upper Right:* composite HST/ACS F814, F606, F475 colour image ($22'' \times 22'' = 115 \times 115 \text{ kpc}^2$). *Lower:* CFHTLS i band ($10' \times 10' = 3148 \times 3148 \text{ kpc}^2$). White cross shows the location of the SL system, and contours are the same as in Fig. A.1.

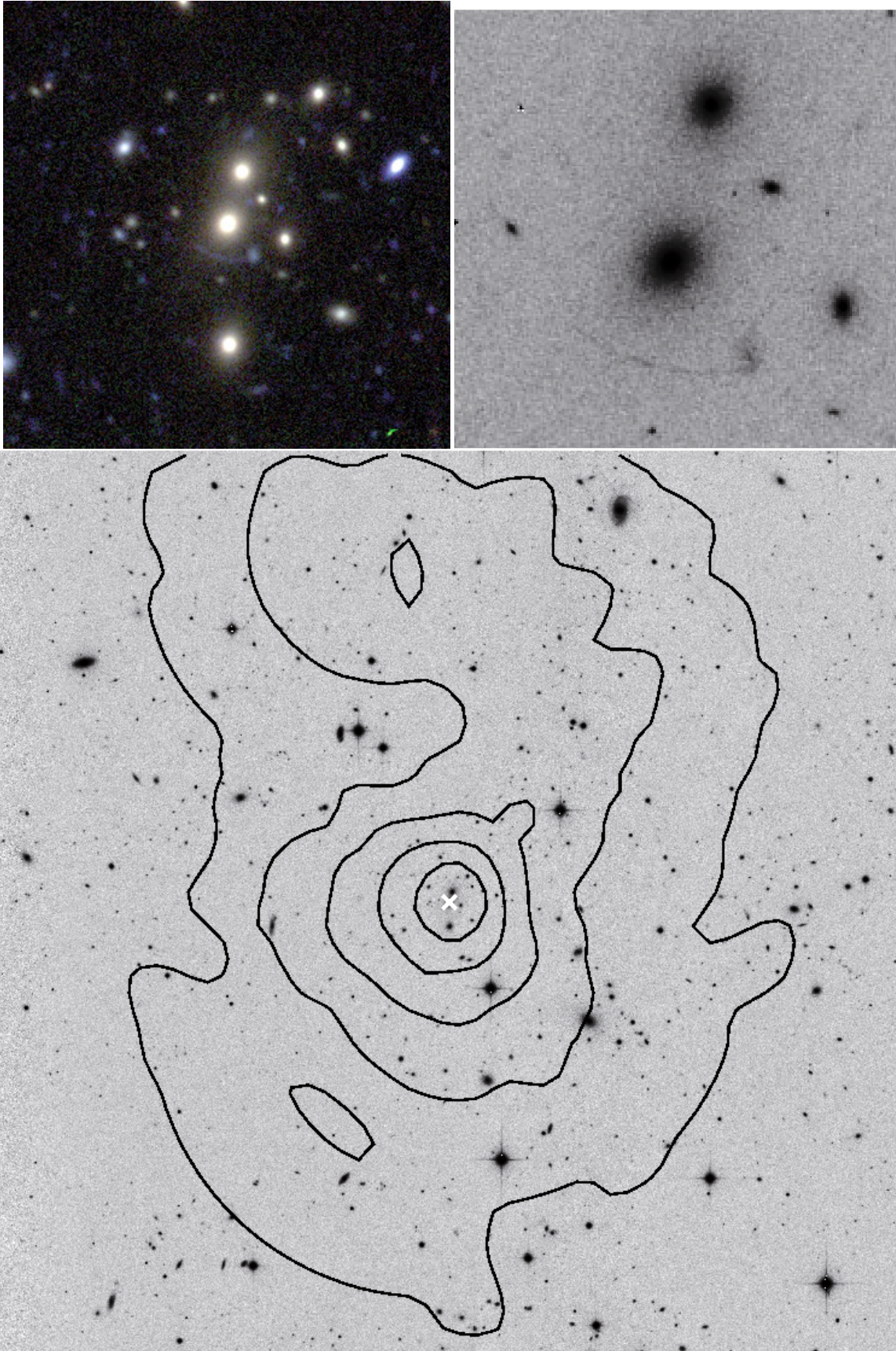


Fig. A.5. Group SL2S J14081+5429 at $z_{\text{spec}} = 0.416$. *Upper Left:* composite CFHTLS g, r, i colour image (1 square arcminute = $330 \times 330 \text{ kpc}^2$). *Upper Right:* HST F606 image ($20'' \times 20'' = 110 \times 110 \text{ kpc}^2$). *Lower:* CFHTLS i band ($10' \times 10' = 3300 \times 3300 \text{ kpc}^2$). White cross shows the location of the SL system, and contours are the same as in Fig. A.1.

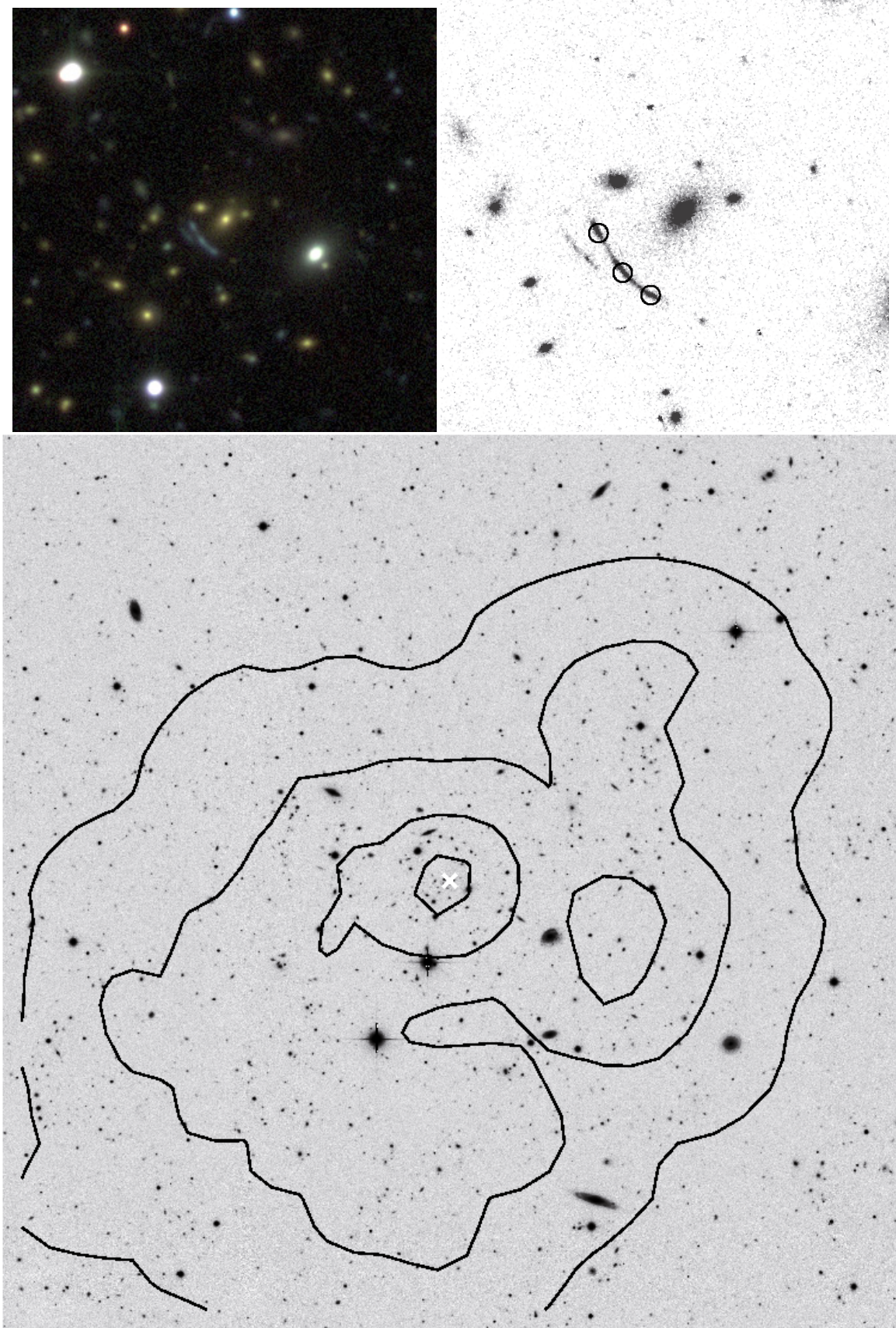


Fig. A.6. Group SL2S J14300+5546 at $z_{\text{spec}} = 0.435$. *Upper Left:* composite CFHTLS g, r, i colour image (1 square arcminute = $339 \times 339 \text{ kpc}^2$). *Upper Right:* HST F606 image ($15'' \times 15'' = 85 \times 85 \text{ kpc}^2$). *Lower:* CFHTLS i band ($10' \times 10' = 3388 \times 3388 \text{ kpc}^2$). White cross shows the location of the SL system, and contours are the same as in Fig. A.1.

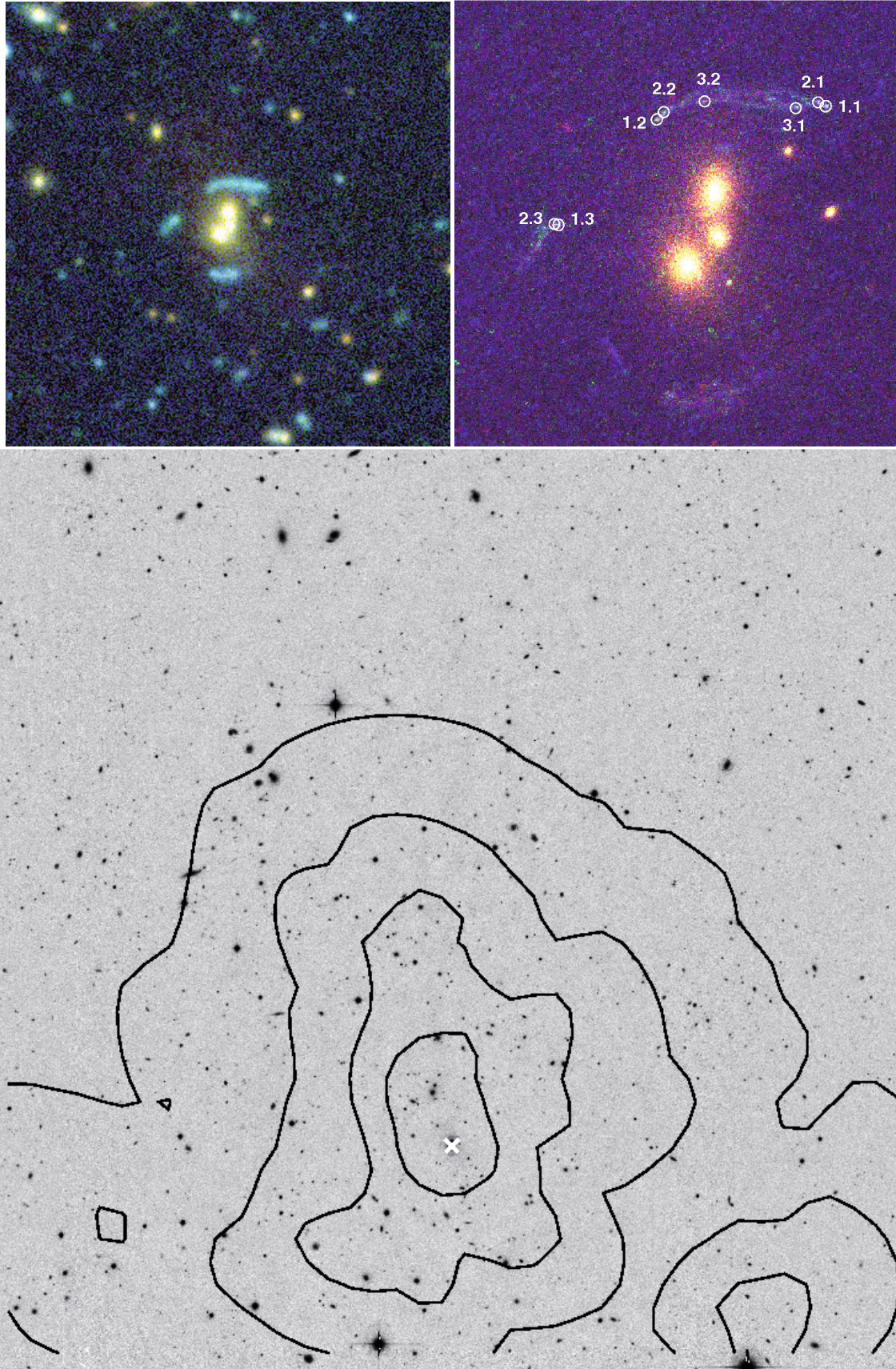


Fig. A.7. Group SL2SJ02140-0532 at $z_{\text{spec}} = 0.444$. *Upper Left:* composite CFHTLS g, r, i colour image (1 square arcminute = 343×343 kpc²). *Upper Right:* composite HST/ACS F814, F606, F475 colour image ($18'' \times 18'' = 103 \times 103$ kpc²). The multiply imaged system shows substructures: we conjugate three spots on the main arc and two spots on the counterimage. Note how the space based image significantly improves the identification of multiple images. *Lower:* CFHTLS i band ($10' \times 10' = 3429 \times 3429$ kpc²). White cross shows the location of the SL system, and contours are the same as in Fig. A.1.

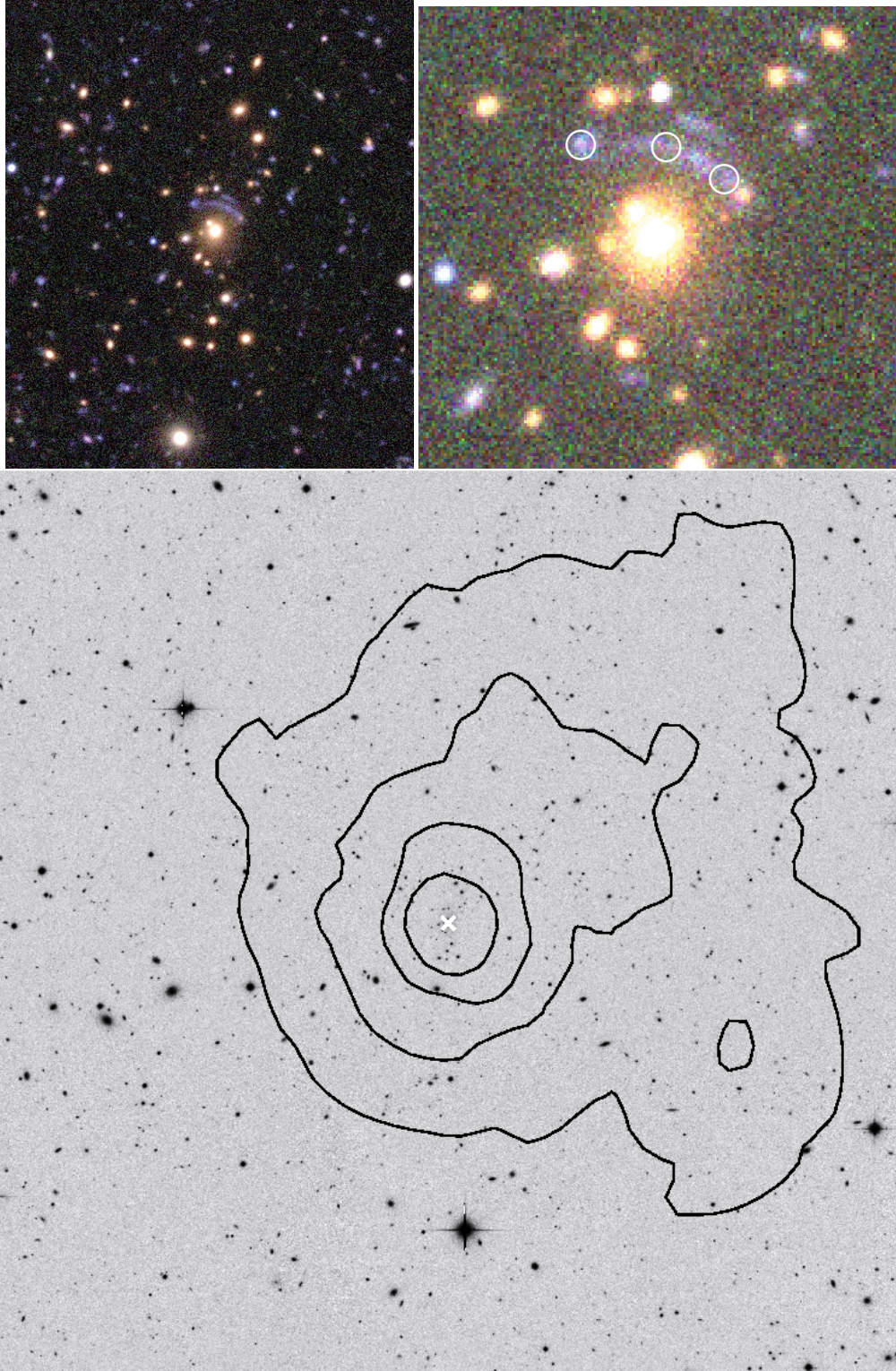


Fig. A.8. Group SL2SJ02254-0737 at $z_{\text{spec}} = 0.511$. *Upper Left:* composite CFHTLS g, r, i colour image (1 square arcminute = $370 \times 370 \text{ kpc}^2$). No HST imaging is available. *Upper Right:* composite CFHTLS g, r, i colour image ($30'' \times 30'' = 185 \times 185 \text{ kpc}^2$) with multiple images identified. *Lower:* CFHTLS i band ($10' \times 10' = 3705 \times 3705 \text{ kpc}^2$). White cross shows the location of the SL system, and contours are the same as in Fig. A.1.

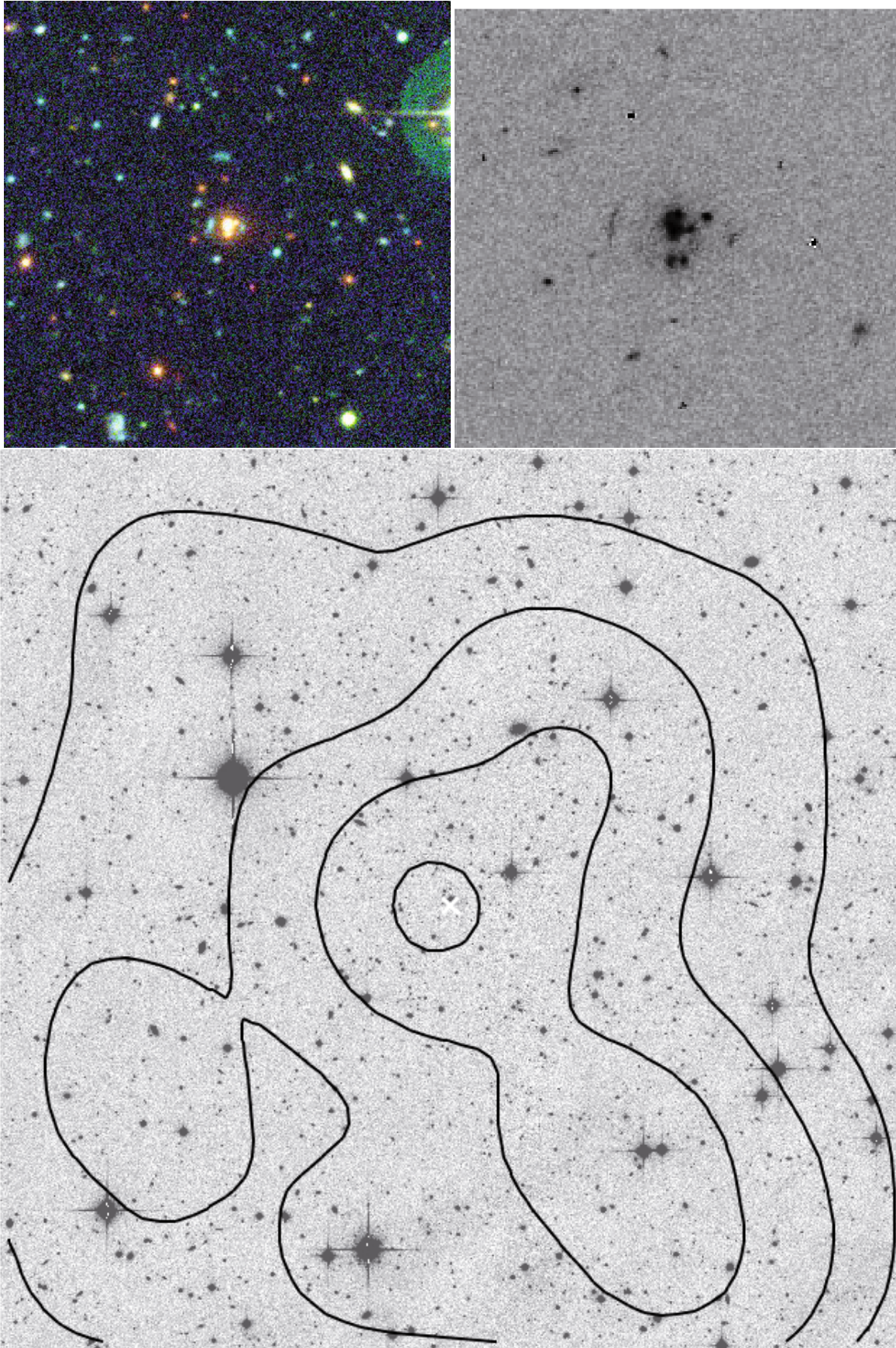


Fig. A.9. Group SL2S J22130-0030 at $z_{\text{phot}} = 0.61$. *Upper Left:* composite CFHTLS g, r, i colour image ($1 \text{ square arcminute} = 450 \times 450 \text{ kpc}^2$). *Upper Right:* HST F606 image ($19'' \times 19'' = 143 \times 143 \text{ kpc}^2$). *Lower:* CFHTLS i band ($10' \times 10' = 4042 \times 4042 \text{ kpc}^2$). White cross shows the location of the SL system, and contours are the same as in Fig. A.1.

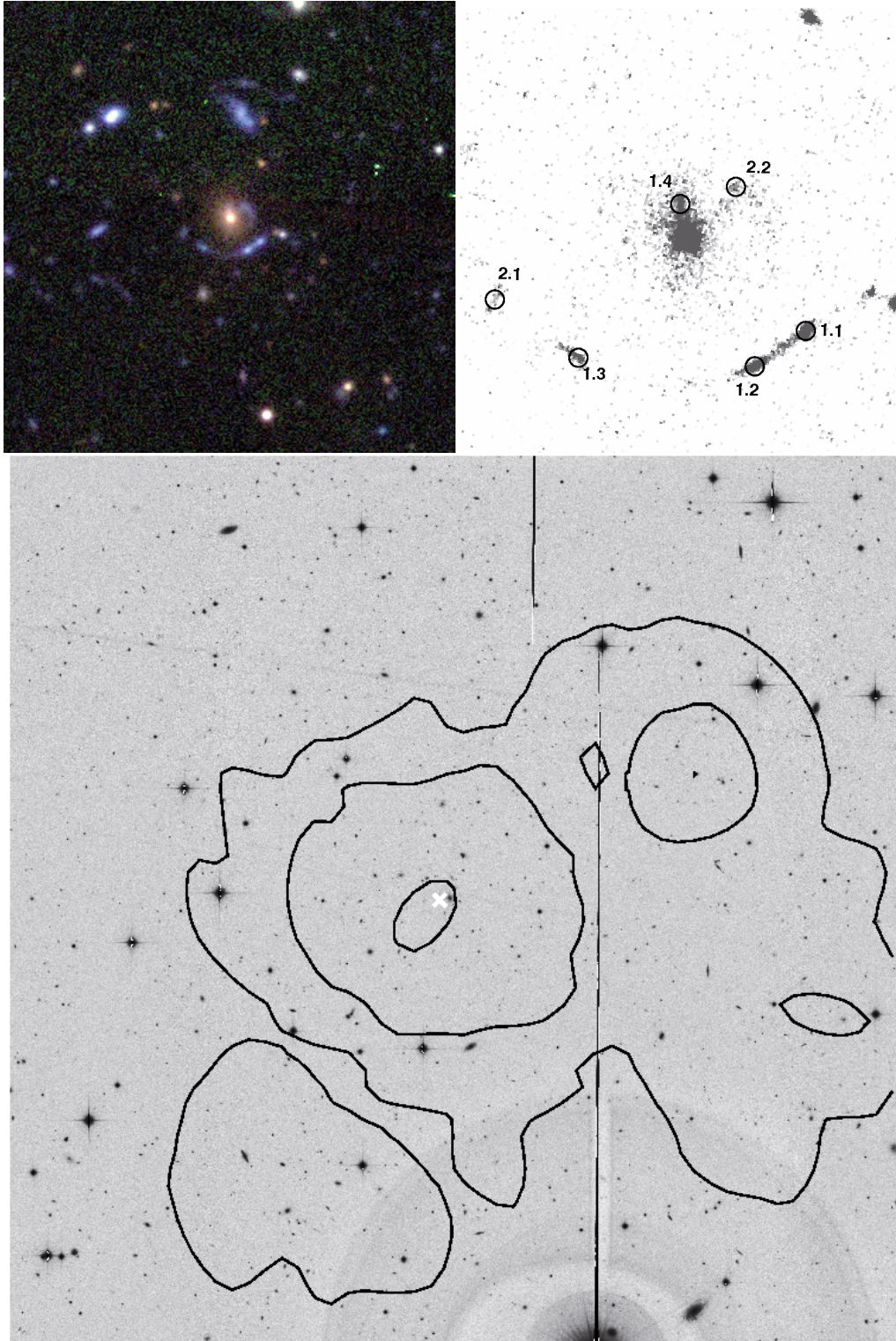


Fig. A.10. Group SL2S J02215-0647 at $z_{\text{spec}} = 0.618$. *Upper Left:* composite CFHTLS g, r, i colour image (1 square arcminute = 406×406 kpc²). *Upper Right:* HST F606 image ($29'' \times 29'' = 196 \times 196$ kpc²). We propose two multiply imaged system: system 1 is a typical cusp configuration and system 2 a radial system. *Lower:* CFHTLS i band ($10' \times 10' = 4606 \times 4606$ kpc²). White cross shows the location of the SL system, and contours are the same as in Fig. A.1.

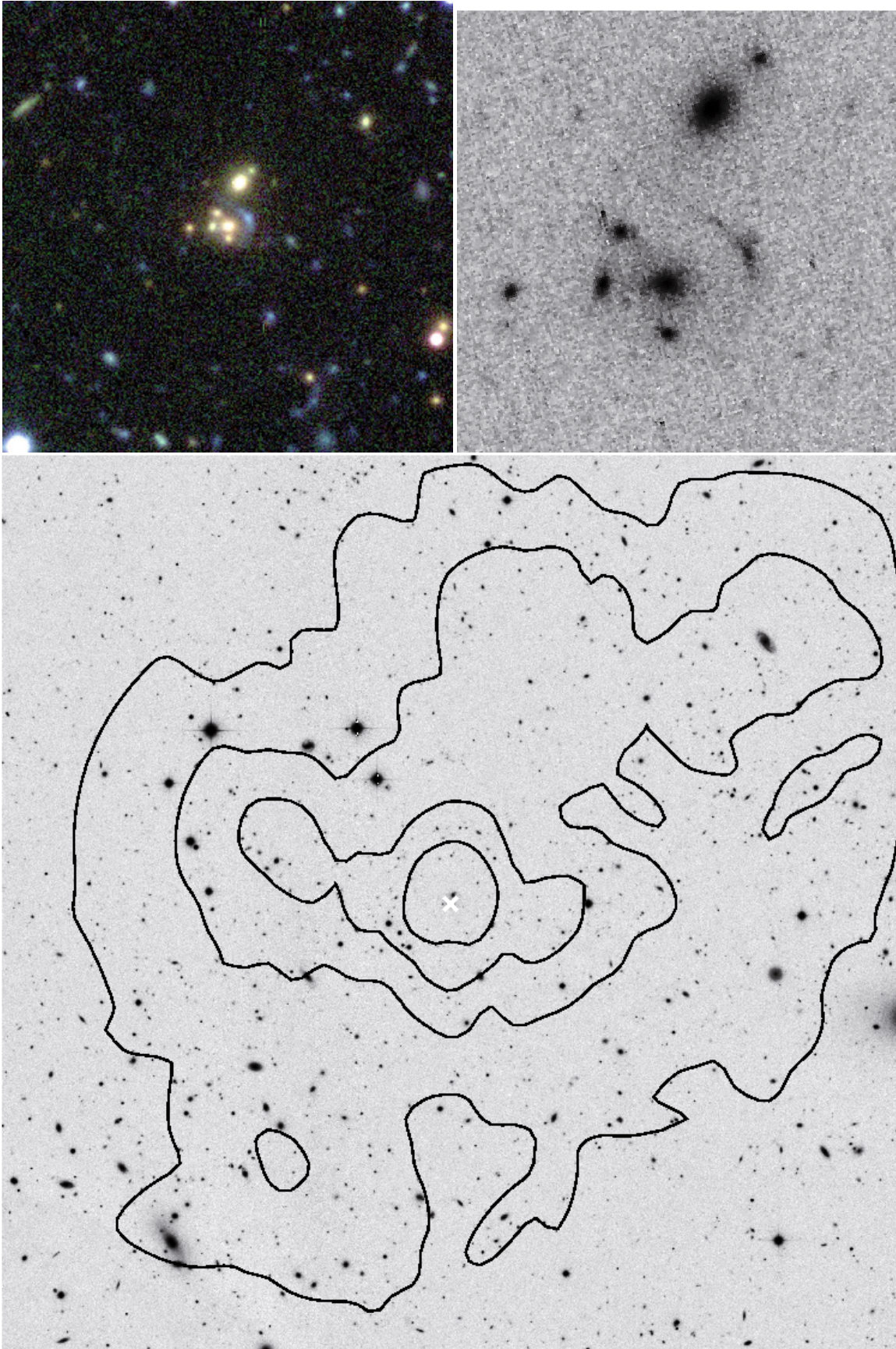


Fig. A.11. Group SL2S J14314+5533 at $z_{\text{phot}} = 0.64$. *Upper Left:* composite CFHTLS g, r, i colour image (1 square arcminute = $413 \times 413 \text{ kpc}^2$). *Upper Right:* HST F606 image ($14'' \times 14'' = 96 \times 96 \text{ kpc}^2$). *Lower:* CFHTLS i band ($10' \times 10' = 4129 \times 4129 \text{ kpc}^2$). White cross shows the location of the SL system, and contours are the same as in Fig. A.1.

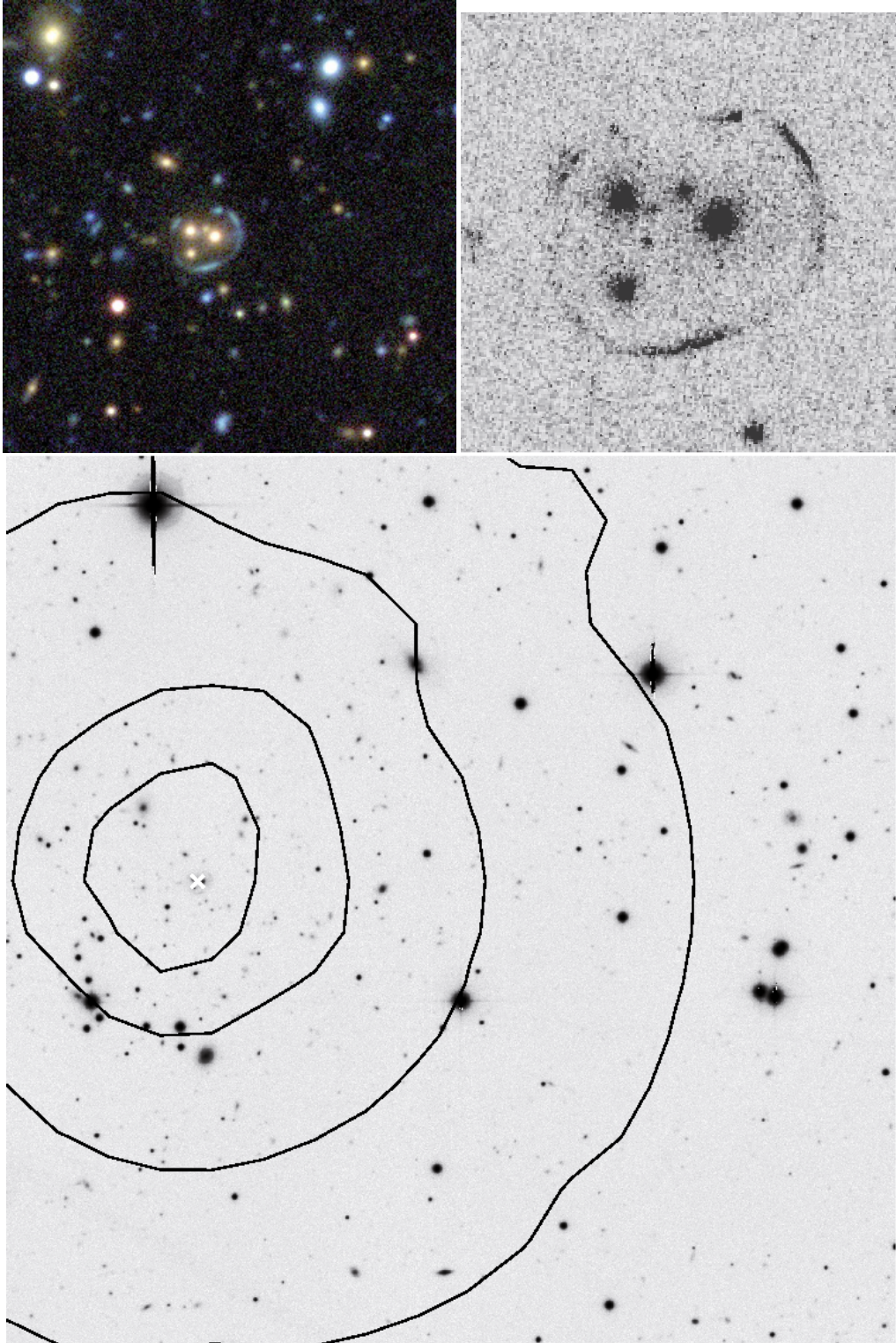


Fig. A.12. Group SL2S J08591-0345 at $z_{\text{spec}} = 0.647$. *Upper Left:* composite CFHTLS g, r, i colour image (1 square arcminute = $415 \times 415 \text{ kpc}^2$). *Upper Right:* HST F606 image ($15'' \times 15'' = 104 \times 104 \text{ kpc}^2$). *Lower:* CFHTLS i band ($5.3' \times 5.3' = 2199 \times 2199 \text{ kpc}^2$). Note that we miss data to probe the east part of the group. Given the observational setup, it is very likely that we miss a significant part of this galaxy group. White cross shows the location of the SL system, and contours are the same as in Fig. A.1.

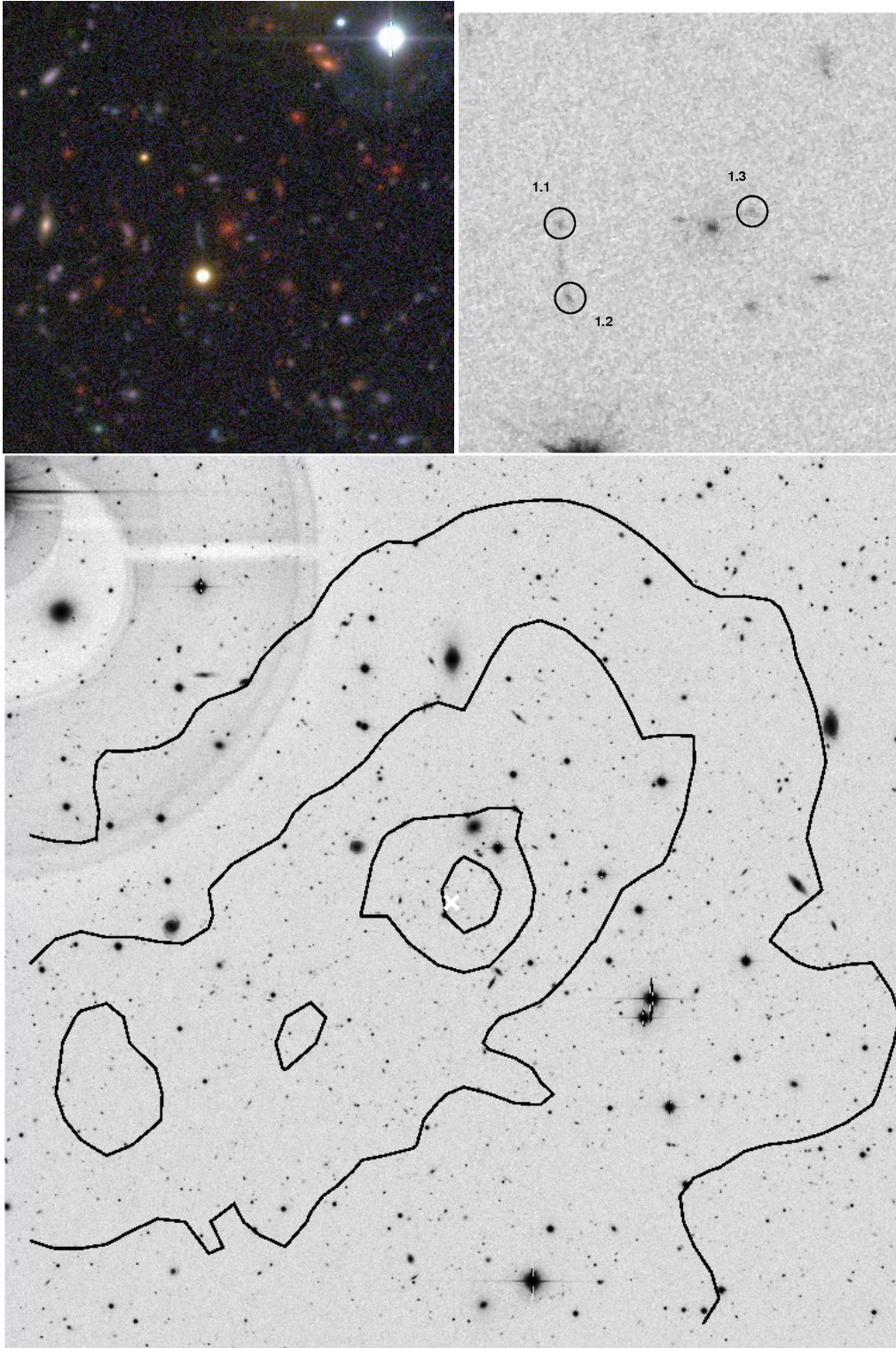


Fig. A.13. Group SL2S J22133+0048 at $z_{\text{phot}} = 0.83$. *Upper Left:* composite CFHTLS g, r, i colour image (1 square arcminute = 456×456 kpc²). *Upper Right:* HST F606 image ($28'' \times 28'' = 213 \times 213$ kpc²). *Lower:* CFHTLS i band ($10' \times 10' = 4560 \times 4560$ kpc²). White cross shows the location of the SL system, and contours are the same as in Fig. A.1.

Dynamical analysis of strong-lensing galaxy groups at intermediate redshift^{★,★★,★★★}

R. P. Muñoz^{1,2}, V. Motta¹, T. Verdugo^{1,3}, F. Garrido², M. Limousin^{4,5}, N. Padilla², G. Foëx¹, R. Cabanac⁶, R. Gavazzi⁷, L. F. Barrientos², and J. Richard⁸

¹ Departamento de Física y Astronomía, Universidad de Valparaíso, Avda. Gran Bretaña 1111, 2360102 Valparaíso, Chile
e-mail: rmunoz@astro.puc.cl

² Departamento de Astronomía y Astrofísica, Pontificia Universidad Católica de Chile, Avda. Vicuña Mackenna 4860, Casilla 306, Santiago 22, Chile

³ Centro de Investigaciones de Astronomía, AP 264, Mérida 5101-A, Venezuela

⁴ Aix Marseille Université, CNRS, LAM (Laboratoire d'Astrophysique de Marseille) UMR 7326, 13388 Marseille, France

⁵ Dark Cosmology Centre, Niels Bohr Institute, University of Copenhagen, Juliane Marie Vej 30, 2100 Copenhagen, Denmark

⁶ Laboratoire d'Astrophysique de Toulouse-Tarbes, Université de Toulouse, CNRS, 57 avenue d'Azereix, 65000 Tarbes, France

⁷ Institut d'Astrophysique de Paris, UMR 7095 CNRS & Université Pierre et Marie Curie, 98bis Bd Arago, 75014 Paris, France

⁸ CRAL, Université Lyon 1, Observatoire de Lyon, 9 avenue Charles André, 69561 Saint Genis Laval Cedex, France

Received 23 November 2011 / Accepted 7 January 2013

ABSTRACT

We present VLT spectroscopic observations of seven newly discovered galaxy groups between $0.3 < z < 0.7$. The groups were selected from the Strong Lensing Legacy Survey (SL2S), a survey that consists of a systematic search for strong lensing systems in the Canada-France-Hawaii Telescope Legacy Survey (CFHTLS). We give details about the target selection, spectroscopic observations, and data reduction for the first release of confirmed SL2S groups. The dynamical analysis of the systems reveals that they are gravitationally bound structures, with at least 4 confirmed members and velocity dispersions between 300 and 800 km s⁻¹. Their virial masses are between 10^{13} and $10^{14} M_{\odot}$, so they can be classified as groups or low mass clusters. Most of the systems are isolated groups, except two of them that show evidence of an ongoing merger of two substructures. We find that weak lensing estimates of the group velocity dispersions are 50% greater than estimates based upon the radial velocities of its members, and conclude that the dynamics of baryonic matter is a good tracer of the total mass content in galaxy groups.

Key words. galaxies: groups: general – galaxies: kinematics and dynamics – galaxies: evolution – galaxies: high-redshift

1. Introduction

Galaxy groups are the most common structures in the Universe, containing at least 50% of all galaxies at the present day (Eke et al. 2004), and they cover the intermediate mass range between large elliptical galaxies and galaxy clusters. A wide array of methods have been used to identify groups at intermediate and high- z : percolation algorithms based on optical photometric and spectroscopic data (Marinoni et al. 2002; Eke et al. 2004; Adami et al. 2005; Yang et al. 2007; Zapata et al. 2009), X-ray emission

from hot intragroup gas (Brough et al. 2006; Finoguenov et al. 2009), and bright arcs due to strong lensing (Cabanac et al. 2007; Limousin et al. 2009; More et al. 2012).

The first large sample of groups detected in redshift space was presented by Geller & Huchra (1983), who found 176 groups up to $z = 0.03$ by using the Center for Astrophysics (CfA) galaxy redshift survey. Nowadays, with the advent of large spectroscopic surveys such as the Two Degree Field Galaxy Redshift Survey (2dFGRS; Colless et al. 2001), the Sloan Digital Sky Survey (SDSS; York et al. 2000), and the Deep Extragalactic Probe 2 Redshift Survey (DEEP2; Davis et al. 2003), well over 5000 groups have been identified up to $z \sim 1$. Eke et al. (2004) identified about 7000 groups and clusters in the 2dFGRS with at least four members, and found that they cover a wide range in mass between 10^{12} and $10^{15} M_{\odot}$. At low redshift, Berlind et al. (2006) used a friends-of-friends (FOF) algorithm to identify groups in the SDSS Data Release 2 (DR2; Abazajian et al. 2004) and found about 8100 groups between $0.01 < z < 0.10$. At higher redshift, Gerke et al. (2005) found about 900 groups with two or more members between $0.7 < z < 1.4$ using the DEEP2 survey.

Recently, Knobel et al. (2012) have presented a sample of about 1500 galaxy groups between redshifts 0.1 and 1.0 that were identified in the zCOSMOS-bright survey (Lilly et al. 2007). They detected clear evidence of the growth of cosmic

* Based on observations collected at the European Southern Observatory, Paranal, Chile (Program P80.A-0610B); based on observations obtained with MegaPrime/MegaCam, a joint project of CFHT and CEA/DAPNIA, at the Canada-France-Hawaii Telescope (CFHT), which is operated by the National Research Council (NRC) of Canada, the Institut National des Sciences de l'Univers of the Centre National de la Recherche Scientifique (CNRS) of France, and the University of Hawaii. This work is based in part on data products produced at TERAPIX and the Canadian Astronomy Data Centre as part of the Canada-France-Hawaii Telescope Legacy Survey, a collaborative project of NRC and CNRS.

** Appendices are available in electronic form at <http://www.aanda.org>

*** Reduced spectra are only available at the CDS via anonymous ftp to cdsarc.u-strasbg.fr (130.79.128.5) or via <http://cdsarc.u-strasbg.fr/viz-bin/qcat?J/A+A/552/A80>

structure over the past seven billion years because the fraction of galaxies that are found in groups (in volume-limited samples) decreases significantly to higher redshifts.

The analysis of the galaxy content in groups and clusters is essential for understanding the effects of the local environment on galaxy formation and evolution processes. For instance, galaxy collisions are expected to be most effective in less massive groups, where the system velocity dispersions are comparable to the internal velocities of galaxies, leading to strong galaxy-galaxy interactions and therefore enhancing star formation (Mihos & Hernquist 1996). Furthermore, the feedback from supernovae and supermassive black holes on the hot intragroup gas is expected to be relevant in suppressing the onset of catastrophic cooling of the hot gas (e.g. Churazov et al. 2001), since the energy input associated with these sources is comparable to the binding energies of these systems (McCarthy et al. 2010).

The evolution of the stellar and gas content of galaxies strongly depends on the properties of their host galaxy cluster (Oemler 1974). For instance, Hansen et al. (2009) studied a large sample of groups and clusters in the Sloan Digital Sky Survey (SDSS; York et al. 2000), and found that the fraction of red-sequence galaxies increases with cluster mass, and it decreases with cluster-centric distance (see also Padilla et al. 2010).

To obtain reliable conclusions about the relative importance of different physical processes in driving galaxy evolution in groups, it is necessary to build composite samples of galaxy groups and then use the virial mass as the mass normalization. Biviano et al. (2006) studied the accuracy of the virial mass estimate from numerical simulations using both the dark-matter particles and simulated galaxies in 67 synthetic clusters. To analyze how the observational strategy and sample sizes affect the cluster mass estimates, they used these synthetic clusters to select a sample of galaxies and estimate the cluster dynamical mass by using two different estimators. They find that the total mass of clusters can be estimated with an accuracy of 10 to 15 percent when using 400 cluster members and that these figures become twice as large when the available number of members is 20. In this paper, we follow Biviano et al. (2006) to analyze our lens galaxy groups.

In this paper we introduce the first spectroscopically confirmed groups of the SL2S survey that were observed at the Very Large Telescope (VLT). The SL2S survey is a small and well defined sample of groups of galaxies selected by their strong lensing features (Cabanac et al. 2007; More et al. 2012). The description of the spectroscopic observations, their reduction and calibrations are presented in Sect. 2. In Sect. 3 we present the membership determination and velocity dispersion estimation for the confirmed groups. The numerical simulations used to study the accuracy of the velocity dispersion estimations are presented in Sect. 4. The discussion of the main results is presented in Sect. 5, and the conclusions are summarized in Sect. 6.

We assume a Λ CDM cosmology with $\Omega_M = 0.25$, $\Omega_\Lambda = 0.75$, and a Hubble constant of $H_0 = 73 \text{ km s}^{-1} \text{ Mpc}^{-1}$.

2. Observations and data reduction

The groups studied in this work were selected from the Strong Lensing Legacy Survey (SL2S; Cabanac et al. 2007), a large systematic search for strong-lensing systems in the Canada-France-Hawaii Telescope Legacy Survey (CFHTLS)¹. The detection and classification of group candidates is explained in Cabanac et al. (2007), but it basically consisted of running

the ARCFINDER algorithm by Alard (2006) on the stacked CFHTLS images and then doing a visual inspection to reject spurious candidates.

Recently, More et al. (2012) have published a catalog of 127 strong-lensing systems detected in the SL2S survey with photometric redshifts between 0.2 and 1.2. They find a systematic alignment of the giant arcs with the major axis of the baryonic component of the putative lens, and more important, they were able to probe the average density profiles of groups using the image separation distribution. Several SL2S systems presented in Cabanac et al. (2007) and More et al. (2012) have been followed up with optical observations at the Hubble Space Telescope (HST), near-infrared observations at the CFHT, and optical spectroscopy at the ESO Very Large Telescope (VLT).

In this work, we present medium-resolution spectroscopy of eight SL2S systems observed at the ESO VLT telescope. They were selected for showing extended arcs with Einstein radius (R_E) lower than $8''$ and having photometric redshifts (z_{phot}) between 0.3 and 0.7. The selection criteria are based on the predicted angular separations from N -body numerical simulations of dark matter halos by Oguri (2006), where they found that strong-lensing arcs with $3'' < R_E < 8''$ are likely generated by galaxy-group scale dark matter halos.

Several of the systems presented in this work have weak lensing mass estimates from Limousin et al. (2009). They measured the weak lensing signal for 13 SL2S systems between $0.3 < z_{\text{phot}} < 0.8$, and were able to estimate weak lensing masses for six of them. Furthermore, the gravitational potential of the system SL2S02140-0535 presented in this work was studied in detail by Verdugo et al. (see 2011) by combining strong-lensing, weak-lensing, and dynamic measurements.

2.1. Imaging

The groups have u , g , r , i , and z -band photometry as part of the CFHTLS survey, a major photometric survey in five bands that covers a total area of 159 deg^2 (T0006 release of the CFHTLS Deep and Wide surveys; see more details in Goranova et al. 2009²). The CFHTLS survey observations were obtained at the 3.6 m CFHT telescope with the MEGACAM camera, a wide-field imager that consists of $36 \text{ } 2048 \times 4612$ pixels CCDs of pixel size $0.186''$.

The images and photometric catalogs used in this work are based on the T0005 release of the CFHTLS survey (November, 2008) and were built at the TERAPIX data processing center at the Institut d'Astrophysique de Paris (IAP; see more details in Mellier et al. 2008³). The 50% completeness magnitude of point-like sources in these catalogs are $u = 25.34$, $g = 25.47$, $r = 24.82$, $i = 24.48$, and $z = 23.60$.

2.2. Spectroscopy

We obtained medium resolution spectra of group galaxies with the Focal Reducer and low dispersion Spectrograph 2 (FOR2; Appenzeller et al. 1998) at the VLT telescope. The FOR2/VLT observations were carried out during the ESO observing program P80.A-0610B (P.I. Motta) and consisted of multi-object spectroscopy (MOS) of 8 SL2S systems. We used a medium resolution grism (GRIS_600RI, $0.83 \text{ \AA}/\text{pix}$) since we wanted to measure the internal velocity dispersion of the brightest group

² <http://terapix.iap.fr/cplt/T0006-doc.pdf>

³ <http://terapix.iap.fr/cplt/oldSite/Descart/CFHTLS-T0005-Release.pdf>

¹ <http://www.cfht.hawaii.edu/Science/CFHTLS>

Table 1. VLT/FORS2 spectroscopic data.

Target	Date	Mask	Exposure
SL2SJ02132-0743	2008-08-11	M013	2 × 1400
SL2SJ02140-0535	2007-10-19	M012	2 × 1400
	2008-02-01	M010	2 × 1400
SL2SJ02141-0405	2007-10-19	M014_1	2 × 1400
SL2SJ02180-0515	2008-02-07	M014_2	2 × 1400
	2008-08-26	M014_3	2 × 1400
SL2SJ02215-0647	2008-08-24	M016_1	2 × 1400
	2008-09-10	M016_2	2 × 1400
SL2SJ08544-0121	2007-12-12	M005	1 × 1200
	2008-02-06	M005	2 × 1400
SL2SJ08591-0345	2007-12-12	M002_1	1 × 1400
	2007-12-18	M002_2	1 × 1400
SL2SJ09413-1100	2007-12-18	M001	2 × 1400

Notes. The columns show the name of the target; UT date of observations; name of the multi-object spectroscopy mask; number of individual exposures and their corresponding exposure time in seconds.

galaxies, and adopted a 2×2 binning in order to improve the signal-to-noise ratio (S/N) of the spectra.

Depending on the number of group member candidates, we used one or two FORS2 masks to do MOS of each group. One FORS2 mask allowed us to take spectra of ~ 40 targets simultaneously within a field of view of $4.25' \times 4.25'$. The criteria used to select the galaxies that entered in the MOS masks was based on the magnitudes and colors of galaxies. We defined as candidates those galaxies with magnitudes $i < 22.0$ and colors within $(g - i)_{\text{lens}} - 0.15 < g - i < (g - i)_{\text{lens}} + 0.15$, where $(g - i)_{\text{lens}}$ is the color of the brightest lens galaxy within the R_E . As the masks could not be filled only with group candidates, we randomly selected galaxies within the field of view with $i < 20.0$ and no color restrictions.

For all the masks we obtained two exposures of 1400 s each, except for the SL2SJ08591-0345 mask where we used only one exposure because of time constraints. We found that two exposures were enough to remove most of the cosmic rays from the 2D spectra, although a couple of them were not removed and had to be manually masked in the 1D spectra. The number of masks and total exposure time for each group is given in Table 1.

The MOS masks were reduced using the standard ESO data reduction procedures⁴ and the Optimal Spectrum Extraction Package (OSEP) for IDL⁵. The basic data reduction steps consisted of bias subtraction, flat-fielding, and wavelength calibration, which were done using the ESO Recipe Execution Tool (EsoRex; <http://www.eso.org/sci/software/cpl/esorex.html>) and the Common Pipeline Library (CPL; <http://www.eso.org/sci/software/cpl>). The advanced steps consisted of the removal of cosmic rays, the background subtraction from the 2D spectra, the 1D spectra extraction and the average of multiple spectra for each source, and they were done using the OSEP IDL procedures inspired in the optimal extraction algorithm by Home (1986).

⁴ Very Large Telescope Paranal Science Operations FORS data reduction cookbook, v1

⁵ <http://physics.ucf.edu/~jh/ast/software/optspecextr-0.3.1/doc>

3. Analysis and results

3.1. Redshift measurements

The spectroscopic redshifts were determined using the Radial Velocity SAO package (RVSAO; Kurtz & Mink 1998) within the IRAF software⁶. We first identified several emission and absorption lines by doing visual inspection of the galaxy spectra, and then we determined the redshifts by cross-correlating a spectrum against template spectra of known velocities.

The galaxy spectra cover the wavelength range $5200 \text{ \AA} < \lambda < 8400 \text{ \AA}$, and the S/N per resolution element varies from ~ 5 to ~ 30 . For most of the galaxy spectra, we were able to identify the Ca + , G-band and Mg absorption lines, and for a few of them we also identified the O , H β , O , and H α emission lines. The errors in the redshift measurements are affected by the instrumental resolution and the RVSAO template fit, and it is $\delta z = 0.001$.

The redshifts were classified into three types: secure, questionable, and unknown. Secure redshifts correspond to spectra having at least three identified lines, between absorption and emission lines; questionable redshifts to spectra having only one or two identified lines; and unknown redshifts to spectra having no identified lines. The success ratio of secure redshift determination is between 50% and 70%, which correspond to groups SL2SJ02140-0535 and SL2SJ08544-0121, respectively. We found that this ratio strongly depends on the total exposure time and magnitude of the targets.

For all the SL2S group candidates, we were able to measure the redshift of the brightest galaxy within the Einstein radius, hereafter called main lens galaxy. The spectra of the main lens galaxy of SL2S groups are shown in the top panel of the figures in Appendix A, and the main absorption and emission lines have been identified.

The galaxy redshift distributions in the direction of the SL2S group candidates are shown in Fig. 1. For five of the eight group candidates, we detected a strong peak in the redshift distribution around the redshift of the main lens galaxy.

3.2. Group membership and velocity dispersions

We adopted the formalism by Wilman et al. (2005) to determine the group membership of the SL2S systems. For the systems that showed a single peak in the redshift distribution around the redshift of the main lens galaxy, we identified the group members as follows: the group was initially assumed to be located at the redshift of the main lens galaxy, z_{lens} , with an initial observed-frame velocity dispersion of $\sigma(v)_{\text{obs}} = 500(1 + z_{\text{lens}}) \text{ km s}^{-1}$. Then, we computed the maximum redshift shell, δz_{max} , and the maximum spatial distance, $\delta\theta_{\text{max}}$, as

$$\delta z_{\text{max}} = \frac{2\sigma(v)_{\text{obs}}}{c}, \quad (1)$$

$$\delta\theta_{\text{max}} = 206,265'' \frac{c \delta z_{\text{max}}}{b(1 + z_{\text{lens}})H(z)D_{\theta}(z)}, \quad (2)$$

where c is the speed of light, $H(z)$ the Hubble constant at z , $D_{\theta}(z)$ the angular diameter distance at z , and b the axis ratio of the cylindrical linking volume. In N -body numerical simulations of dark matter halos, the cylindrical linking volume is a cylinder

⁶ IRAF is distributed by the National Optical Astronomy Observatories, which are operated by the Association of Universities for Research in Astronomy, Inc., under cooperative agreement with the National Science Foundation.

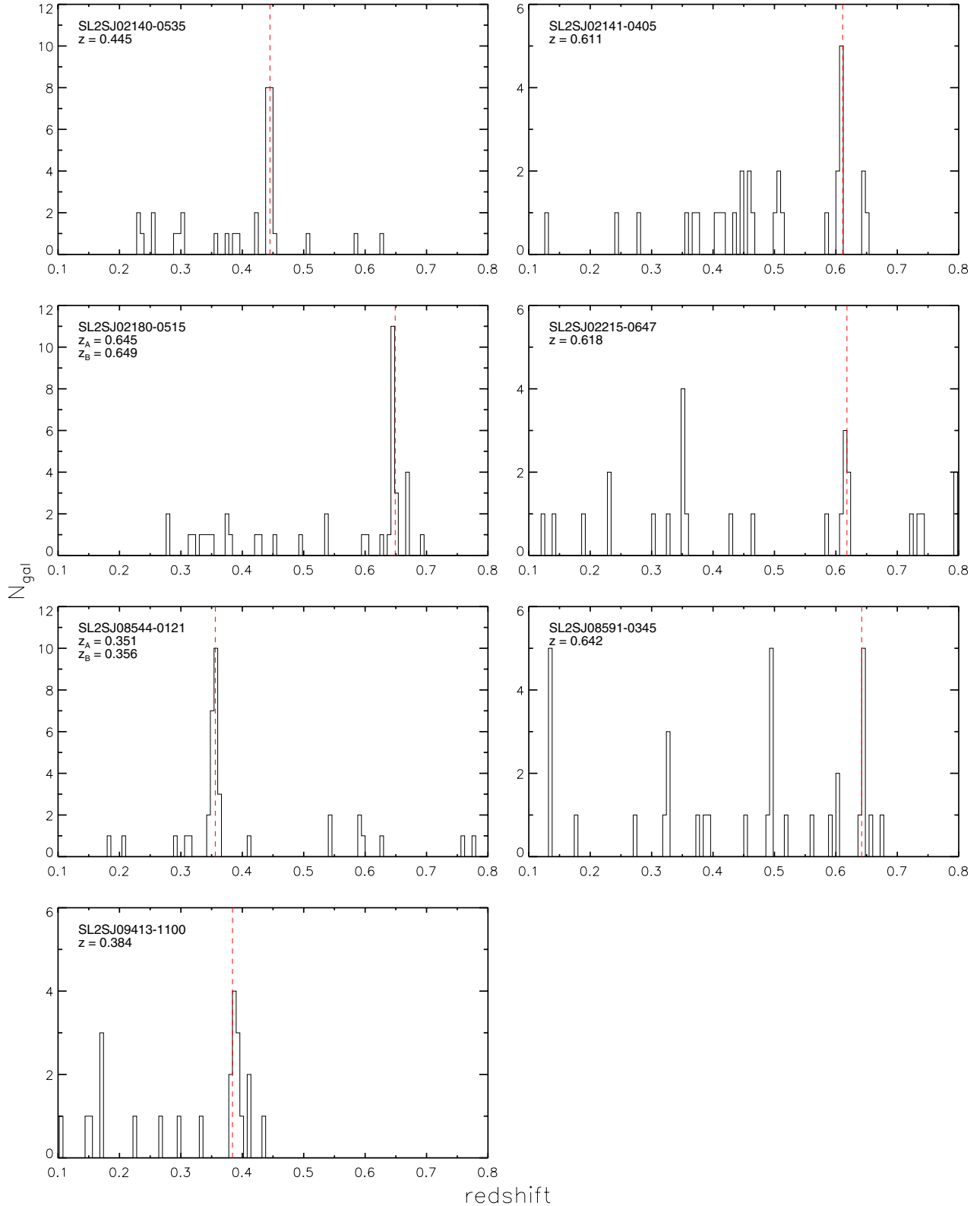


Fig. 1. Redshift distribution of galaxies in the group fields. The spectroscopic redshift of isolated groups is denoted by the quantity z , and for double components of bimodal groups, by z_A and z_B . The vertical dashed line corresponds to the redshift of the most massive component. The bin size of the histogram is $\delta z = 0.006$.

oriented along the line of sight with a radius equal to the projected linking length. We adopted a value of $b = 3.5$ in this work.

The initial guess for the velocity dispersion was based on the estimated velocity dispersion of the strong-lensing galaxy

group B2108+213 measured by [McKean et al. \(2010\)](#). They obtained a mean value of 555 km s^{-1} for the galaxy group using three different linking velocity kernels. The factor $(1 + z_{\text{lens}})$ is used to account for the cosmological expansion of the Universe.

Table 2. Summary of confirmed SL2S groups.

Group	RA	Dec	\bar{z}_{spec}	$\sigma(v)_{\text{los}}$	N_{spec}	$N_{\text{spec,RS}}$	N_{gal}
SL2SJ02140-0535	02:14:08.03	-05:35:32.3	0.445	364^{+60}_{-137}	16	11	40
SL2SJ02141-0405	02:14:11.21	-04:05:02.8	0.611	478^{+48}_{-178}	7	5	6
SL2SJ02180-0515	02:18:10.09	-05:15:33.5	0.645	131^{+29}_{-61}	6	8	8
	02:18:07.29	-05:15:36.2	0.649	148^{+37}_{-56}	5		
SL2SJ02215-0647	02:21:51.17	-06:47:33.7	0.618	234^{+76}_{-40}	4	2	2
SL2SJ08544-0121	08:54:46.55	-01:21:36.9	0.351	185^{+30}_{-62}	8	10	64
	08:54:47.10	-01:21:35.6	0.356	341^{+43}_{-109}	10		
SL2SJ08591-0345	08:59:14.46	-03:45:14.2	0.642	507^{+107}_{-336}	5	3	6
SL2SJ09413-1100	09:41:34.99	-11:00:55.0	0.384	350^{+57}_{-210}	5	–	–

Notes. The columns show the name of the identified SL2S groups; J2000.0 coordinates of the brightest group member with spectroscopic redshift; spectroscopic redshift of the group, \bar{z}_{spec} ; line-of-sight velocity dispersion of the group in units of km s^{-1} ; number of spectroscopically confirmed members, N_{spec} ; number of confirmed members within the E/S0 ridgeline (RS) and inside a group-centric distance of $1 \text{ h}^{-1} \text{ Mpc}$, $N_{\text{spec,RS}}$; estimated total number of group members within the E/S0 ridgeline and inside $1 \text{ h}^{-1} \text{ Mpc}$, N_{gal} (see Sect. 5).

Upon identifying potential members as those galaxies located inside the maximum redshift shell and the maximum projected distance, we computed the observed velocity dispersion of the group $\sigma(v)_{\text{obs}}$. For those groups with more than ten members we used the biweight estimator (Beers et al. 1990) to compute the velocity dispersion, and for those with less than ten members we used the gapper algorithm (Beers et al. 1990). The new computed value of $\sigma(v)_{\text{obs}}$ was then used to compute new values of δz_{max} and $\delta\theta_{\text{max}}$. Finally, we defined the galaxies located within these limits as confirmed group members.

For the groups that showed a bimodal redshift distribution, we identified the group members of each component as follows. The first component was initially assumed to be located at the higher redshift peak, $z_{\text{peak,high}}$, with an initial observed-frame velocity dispersion of $\sigma(v)_{\text{obs}} = 250(1 + z_{\text{peak,high}}) \text{ km s}^{-1}$. Then, we applied the same procedure we detailed before for groups with a single component, and finally determined the group members of the higher redshift component.

To determine the membership of the lower redshift component, we first excluded the galaxies linked to the first component. Then, we repeated the same procedure used for the first component, but this time using the lower redshift peak as a first guess.

We classified as groups those structures having at least four confirmed members in order to reduce the contamination by spurious structures in the catalogs. The final list of SL2S groups is shown in Table 2, and consists of five structures with a single component in redshift space, and two structures with a double component. The system SL2SJ02132-0743 was excluded from the group list since only two galaxies have a redshift consistent with the redshift of the main lens galaxy and also no overdensity in redshift space was found.

The group redshifts, \bar{z}_{spec} , and the number of spectroscopically confirmed members, N_{spec} , are shown in Cols. 4 and 6 of Table 2. The group redshift was computed by taking the mean of the redshift of the spectroscopically confirmed members (presented in Table B.1 of Appendix B), and then removing the peculiar motion of the Sun with respect to the CMB. To study the accuracy of the velocity dispersions and mass estimates presented in this work (see Sect. 3.3), we also computed the number of confirmed members with colors consistent with the observed E/S0 ridgeline of galaxy groups and clusters (Dressler 1984) and located inside a group-centric distance of $1 \text{ h}^{-1} \text{ Mpc}$, and denoted it by $N_{\text{spec,RS}}$ in Table 2.

The group velocity dispersions were estimated using the recessional velocity of their members. The measured redshift of a galaxy member, z , can be related to its peculiar velocity with respect to the group center of mass by

$$1 + z = (1 + z_{\text{O}})(1 + z_{\text{R}})(1 + z_{\text{G}}),$$

where z_{O} is the local observer O comoving with the expanding Universe, z_{R} the cosmological redshift of the structure as measured by O relative to a comoving observer R in the vicinity of the structure, and z_{G} the peculiar velocity of the galaxy with respect to the center of mass of the structure. The z_{O} contribution is negligible for groups at $z > 0.02$.

Substituting z_{R} by the spectroscopic redshift of the group, we obtain the following equation for the line-of-sight velocity of a galaxy with respect to the group center of mass,

$$v_{\text{los}} = \frac{c(z - \bar{z}_{\text{spec}})}{1 + \bar{z}_{\text{spec}}}, \quad (3)$$

where \bar{z}_{spec} is the group redshift as shown in Table 2.

The group velocity dispersion is related to the sum in quadrature of the v_{los} of all group members, and this value is affected by the recessional velocity errors. We computed the rest-frame velocity dispersion of each group by applying the biweight estimator of scale (Beers et al. 1990) to the v_{los} of its members. To remove the recessional velocity errors from the velocity dispersion measurements, we followed the prescription by Danese et al. (1980); i.e., we subtracted in quadrature the mean v_{los} errors from the velocity dispersion. The corrected line-of-sight velocity dispersions, $\sigma(v)_{\text{los}}$, of the SL2S groups are shown in Table 2. The upper and lower errors in $\sigma(v)_{\text{los}}$ were estimated by using a bootstrap technique of 10 000 repetitions (see Beers et al. 1990, for details on the methodology).

3.3. Mass estimates

The total mass of the SL2S groups was estimated by using the virial theorem. We assumed that the groups are in hydrostatic equilibrium, have spherical symmetry, and have isotropic velocity distributions. It is important to note that the first assumption could be wrong for the youngest and least massive groups, at which the internal velocity dispersions of the galaxies are comparable to that of the group and, therefore, galaxy mergers are favored (Hickson 1997).

Table 3. Virial radii and masses of SL2S groups.

Group	\bar{z}_{spec}	R_{PV}	M_{V}	$M_{\text{WL}}(2\text{Mpc})^a$
SL2SJ02140-0535	0.445	0.78	$1.14^{+0.41}_{-0.69}$	5.5 ± 3.7
SL2SJ02141-0405	0.611	0.43	$1.08^{+0.23}_{-0.66}$	
SL2SJ02180-0515	0.645	0.69	$0.13^{+0.02}_{-0.09}$	– <i>b</i>
	0.649	0.23	$0.05^{+0.01}_{-0.03}$	– <i>b</i>
SL2SJ02215-0647	0.618	0.72	$0.43^{+0.33}_{-0.04}$	$< 3.1^c$
SL2SJ08544-0121	0.351	0.45	$0.17^{+0.03}_{-0.09}$	6.3 ± 2.5
	0.356	1.07	$1.37^{+0.37}_{-0.73}$	
SL2SJ08591-0345	0.642	0.53	$1.51^{+0.71}_{-1.34}$	– <i>d</i>
SL2SJ09413-1100	0.384	1.11	$1.49^{+0.52}_{-1.26}$	3.7 ± 3.4

Notes. The columns show the name of the SL2S group; spectroscopic redshift of the group, \bar{z}_{spec} ; projected virial radius of the group, R_{PV} , in units of Mpc; virial mass of the group in units of $10^{14} M_{\odot}$; projected mass derived from weak lensing as computed within a circular aperture of radius 2 Mpc, in units of $10^{14} M_{\odot}$. ^(a) M_{WL} inside a projected radius of 2 Mpc taken from Limousin et al. (2009). ^(b) R_{E} is below 3 arcsec and is within galaxy lensing regime. ^(c) The weak lensing signal is low, and only an upper limit could be established. ^(d) The system is located at the edge of the field of view.

For distant galaxy clusters and groups, it is only possible to measure their projected velocity dispersions and galaxy separations. We computed the projected virial radius for each group using the sky angular distances between all its members, following the formalism by Girardi et al. (1998). The projected virial radius and mass were computed as

$$R_{\text{PV}} = D_{\theta}(\bar{z})N(N-1) \frac{1}{\sum_{i=1}^N \sum_{j=i+1}^N \frac{1}{\theta_{ij}}}, \quad (4)$$

$$M_{\text{V}} = \frac{3\pi \sigma(v)_{\text{los}}^2 R_{\text{PV}}}{2G}, \quad (5)$$

where R_{PV} is the projected virial radius, M_{V} the virial mass, $D_{\theta}(\bar{z})$ the angular diameter distance at redshift z , N the number of confirmed members, θ_{ij} the sky angular distance between galaxies i and j , and G the gravitational constant.

The projected virial radii and virial masses of SL2S groups are shown in Table 3, in units of Mpc and $10^{14} M_{\odot}$, respectively.

4. Accuracy of velocity dispersion and mass estimates

The dynamical masses estimated for the lensed clusters can be subject to statistical and systematic biases. In this section we use GALFORM semi-analytic galaxies from the Bower et al. (2006) version of the model, which populate the Millennium simulation (Springel et al. 2005).

This simulation adopts a flat Λ CDM cosmology with $z = 0$ dark-matter and baryon density parameters $\Omega_{\text{dm}} = 0.205$, $\Omega_b = 0.045$, a dimensionless Hubble constant of $h = 0.73$, rms linear mass fluctuations in spheres of $8 h^{-1} \text{Mpc}$ of $\sigma_8 = 0.9$, and a $n = 1$ slope for the primordial power spectrum. The simulation followed 2160³ particles from $z = 127$ to $z = 0$ in a comoving periodic volume of $500 h^{-1} \text{Mpc}$ a side. The resulting galaxy population after applying the Bower et al. (2006) model can be considered complete down to an absolute magnitude in the r-band of $M_r = -15$.

To check the presence of biases in the method that was used to compute the SL2S group masses (Sect. 3.3), it is necessary

to first determine the observational selection and completeness effects. The dominant selection effect is the fraction of group members that were observed and classified as secure members of each SL2S group. Coupon et al. (2009) computed the photometric redshifts for galaxies in the CFHTLS survey, and obtained a mean photometric redshift error of $\sigma_{z/(1+z)} \sim 0.038$ and an outlier rate of $\eta \sim 3\%$ using a sample of 1532 galaxies (from W1 field) with secure spectroscopic redshifts. We estimated the total number of red-sequence galaxies for each group, N_{gal} , using a method similar to the one used by Koester et al. (2007) for building the MaxBCG cluster catalog, but we added photometric redshift information to reduce the contamination by background and foreground galaxies. We estimated N_{gal} for each group by counting the number of galaxies within a radius of 1 Mpc that have magnitudes brighter than $R = 22.5$ and colors within $|g - R| < 0.24$ (equivalent to $2\sigma_{\delta(g-R)}$) with respect to the E/S0 ridgeline, and have $|z_{\text{phot}} - \bar{z}_{\text{spec}}| \leq 0.038 * (1 + \bar{z}_{\text{spec}})$, i.e. $1\sigma_z$. We found that the number of red-sequence galaxies in the SL2S groups goes between 2 and 64 galaxies (see Table 2). The fraction of group members with measured recessional velocities was estimated as the ratio between $N_{\text{spec,RS}}$ and N_{gal} , and it ranges from 0.25 to 0.85 (not considering the bimodal groups).

We selected halos from the $z = 0.509$ simulation output and repeated the observational procedure as closely as possible to measure cluster dynamical masses. The simulation cube consists of (X, Y, Z) spatial coordinates and (v_X, v_Y, v_Z) velocities. A first step consists of choosing the Z coordinate axis in the simulation cube as the line of sight and of defining the recessional velocity by $Z \times 100 h \text{ km s}^{-1} \text{ Mpc}^{-1} + v_Z$. Since all the groups studied in this work are bona fide gravitational lensing systems, we assume the sample to be free of spurious groups and clusters, so used the full sample of halos to do these tests.

For each individual dark-matter halo we selected galaxies in the red sequence (defined using empirical color cuts) in a cylinder with depth $\Delta v = 500 \text{ km s}^{-1}$ and width $\Delta\theta = 220''$, transformed into comoving coordinates at the redshift corresponding to the selected output ($z = 0.509$). These values of Δv and $\Delta\theta$ are iteratively corrected once the velocity dispersion and harmonic projected radius of the halo are obtained from the possible members of the halo. Their final values are used to calculate the gapper mass of the halo. Figure 2 shows a comparison between the recovered and simulated masses of group-size dark matter halos (the latter being simply the number of dark-matter particles per halo multiplied by the particle mass), where it can be seen that when the member galaxies are those brighter than $M_r = -18$ (which corresponds to the observed $i = 22$ mag for a group at $z \sim 0.4$), the gapper method introduces important uncertainties in the recovered masses of about of 20% and 50% for masses of $\sim 10^{14} h^{-1} M_{\odot}$ and $\sim 10^{15} h^{-1} M_{\odot}$, respectively. We notice the significantly higher values than in the results of Biviano et al. (2006), mainly due to how few members are available in our observational samples.

A more detailed interpretation of the simulation tests is shown in Fig. 3. The top left-hand panel shows the ratio between the gapper and simulated mass of the dark matter halos as a function of the number of group members that were selected to estimate their respective group virial masses. We use the entire sample of galaxy groups from the simulation, and on average the number of members is 60. As can be seen, the statistical errors shown by the error bars (enclosing 68 percent of the individual results) is significantly larger than the systematic bias. In the case of the larger sample of galaxies (selected with $M_r < -18$), the bias is almost zero, with a slight tendency to recover a lower value for the estimated mass as the fraction increases. The same

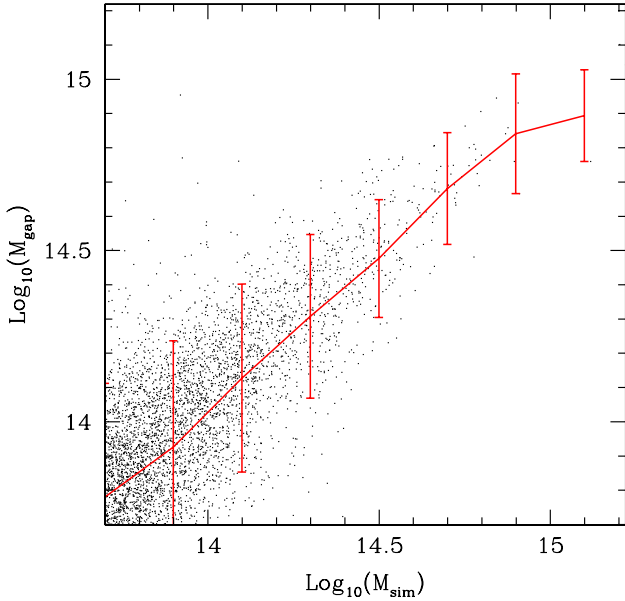


Fig. 2. Comparison between estimated gapper mass and underlying halo mass in the simulation. This shows the results when using a 30% of the group members brighter than $M_r = -18$, randomly selected. Dots represent individual measurements; the solid lines correspond to the median in bins of halo mass, and the errorbars enclose 68 percent of the individual measurements.

conclusion applies for the analysis using the brighter sample of members, with the difference that, regardless of the fraction of members used in the analysis, the estimated group masses are always lower than their simulated counterparts. It is interesting to note that biases in the mass estimates are lower than 20 percent for all the cases, and that their error bars decrease as the fraction of group members used in the calculation of the mass approaches 20%. We emphasize that the average number of true members is constant across the x -axis; i.e., we only change the number of spectroscopic members used to estimate the group mass. The top right-hand panel shows the mass ratio as a function of the total number of members, which spans between 20 and 300 members on average. As discussed in Sect. 2, the mean fraction of group members with spectroscopic measurements for the SL2S groups is about 30%; as can be seen, using a larger fraction would not have resulted in much of an improvement (and would require significantly more telescope time).

To account for the sources of uncertainty in the estimation of the virial mass, in the bottom left-hand panel of Fig. 3, we show the ratio between the group velocity dispersions estimated by using the gapper method and the ones obtained from the full numerical simulation. In the bottom right-hand panel, we show the ratio between the estimated harmonic radii, r_{gap} , and the average 3D radii of simulated dark matter halos, $r_{3\text{D}}$. Our results suggest that the velocity dispersion is always underestimated and that it gets closer to the underlying value as the fraction of observed group members increases (with little change above a fraction of 0.3). Furthermore, we found that the virial radius is also underestimated, and it departs from the actual value as the fraction of members increases. We note that the ratio $r_{\text{gap}}/r_{3\text{D}}$ cannot be compared with the ratios in columns 9 and 10 of Table 1 from Biviano et al. (2006), since we use a different method to estimate the virial radius.

The previous tests were applied to bound systems with masses higher than $10^{14} M_{\odot}$, but could also be applied to a subset of simulated groups of masses similar to any of the observed

SL2S groups. We chose the group SL2SJ02140-0535 as a particular case for applying the test, since this group has the largest number of confirmed members and a virial mass properly covered by the numerical simulation (Verdugo et al. 2011). We selected halos from the numerical simulation with velocity dispersions within a narrow range around the measured value for SL2SJ02140-0535 ($264 < \sigma(v)_{\text{los}} < 464 \text{ km s}^{-1}$), and restricted to halos having a total number of $M_r < -21$ galaxies between 20 and 40, which brackets the estimated number of members for this group. The main aim of studying this restricted sample of groups was to obtain the systematic and statistical uncertainties in the estimated mass of SL2SJ02140-0535. The ratio between the estimated and actual masses for this subsample of halos is shown in Fig. 4, where as can be seen, when using galaxies brighter than $M_r = -18$ the resulting biases are comparable to those found for the full sample of halos in the numerical simulation.

The main conclusions are that the expected biases in the virial mass estimation are lower than the statistical uncertainties of group properties in a narrow range of mass and that the virial mass is underestimated by about 15% when using 30% of the group members. According to Fig. 4, the bias appears to worsen for higher fractions of members, but this effect is likely due to the small sample of halos resulting from the cuts applied to mimic SL2SJ02140-0535.

5. Discussion

The formation and evolution history of galaxies has been shown to strongly depend on the properties of the environment they inhabit. The existence of this environmental dependence has been confirmed both in the local (Goto et al. 2003; Helsdon & Ponman 2003; Bamford et al. 2009) and intermediate redshift Universe (Dressler et al. 1997; Treu et al. 2003; Pannella et al. 2009), and the observational results suggest that star formation and galaxy merging processes are accelerated in high density environments, such as galaxy groups and clusters.

Therefore, galaxy groups represent natural laboratories for studying the relative importance of the different astrophysical processes occurring in dense regions of the Universe. For instance, galaxy collisions are expected to be most effective in groups because the dynamical friction timescale is similar to the orbital timescale of galaxies within the group. Since galaxy groups contain a low number of members (less than one hundred within 1 Mpc) and cover a wide range in mass, velocity dispersion and hot gas content, it is necessary to characterize their properties in detail in order to build representative samples of groups and to properly study the relative importance of the different mechanisms.

The virial mass estimation relies on the following assumptions: sphericity, kinematic isotropy and virialization. In our virial mass estimation we use the velocity dispersion, which we assume constant through the group, and the harmonic radius as an estimate of the virial radius (see Sect. 3.1). These assumptions depart slightly from observational results. For instance, i) groups and clusters usually show substructure (Riemer-Sørensen et al. 2009); ii) it is known that nearby clusters show a small gradient in the velocity dispersion (Kent & Gunn 1982); and iii) some groups at high redshift show evidence of having merging events, and therefore are not in a virialized state (McKean et al. 2010). Furthermore, it is well known that the harmonic radius depends strongly on the area covered by the spectroscopic observations and the number of confirmed members (Biviano et al. 2006; Girardi et al. 1998), biasing the measurement of the virial radius.

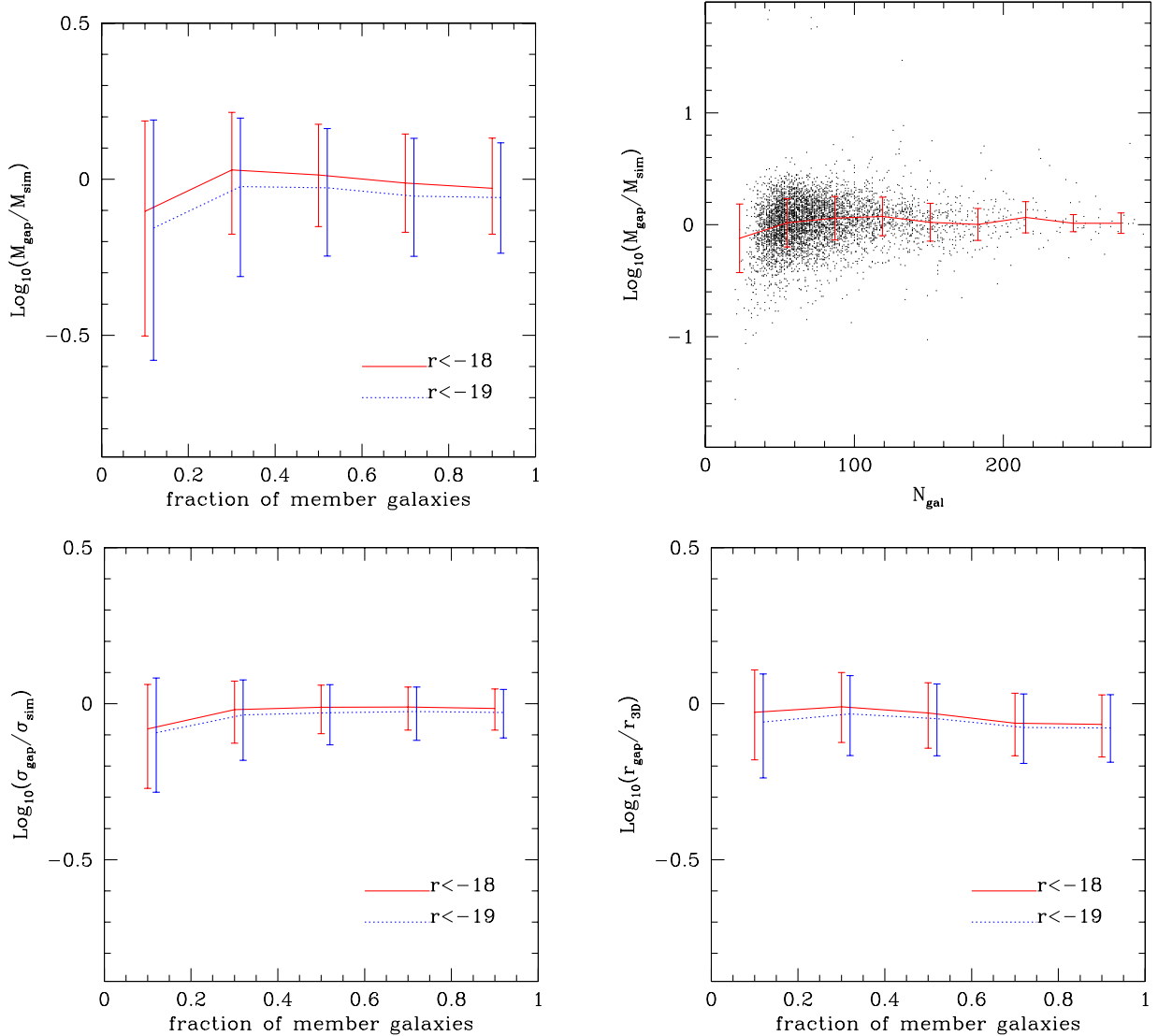


Fig. 3. *Top left:* ratio between the estimated and actual masses of group-size dark matter haloes as a function of the fraction of group members with recession velocity measurements, as obtained from the numerical simulations presented in this work. *Top right:* ratio between the estimated and actual masses of group-size dark matter haloes as a function of the number of member galaxies. *Bottom left:* ratio between the velocity dispersion as estimated with the gapper method and as obtained from the actual group members in the simulation. *Bottom right:* ratio between the deprojected virial radius and the mean 3D radius of actual groups members in the simulation, as a function of the fraction of members. The solid red lines show the results when using only members with absolute magnitudes brighter than $M_r = -18$, and the dotted blue lines for members brighter than $M_r = -19$. Errorbars enclose 68% of the measurements in each bin of fraction.

From our simulations, it seems that the virial radius is underestimated when the number of members increases, contrary to the results obtained by Biviano et al. (2006). The difference between our results and those from Biviano et al. (2006) could be explained by the differences in the simulations, since the latter uses an N -body hydrodynamical simulation.

We ran numerical simulations to assess the bias introduced in the virial mass estimation (see Sect. 4). The results show that the method adopted in this work allows to recovering the mass of the simulated groups within the error bars, showing no systematic deviations (see top panel of Fig. 3). It is also important to note that i) the mass estimation of a group with 40% of their members observed is as good as when using 90% of the members; ii) the mass estimation improves with the number of groups used and justifies the stacking of groups of similar properties in order to obtain better estimations. However, for the particular case in which we applied a cut in velocity dispersion, the case of

SL2SJ02140-0535, the simulation shows that the method underestimates the group mass by about 20% (see Fig. 4). The analysis of simulated groups selected from the numerical simulations (see Sect. 4 and Fig. 3) reveals that the virial mass of the SL2S groups is underestimated by 15%.

Limousin et al. (2009) computed the weak lensing velocity dispersions and masses for several of the SL2S systems studied in this work. The mass estimate obtained from weak lensing measurements makes no assumption regarding the dynamic state of the systems, as opposed to the kinematical measurements presented in this work. Although weak lensing requires less assumptions, it has been shown that the estimated mass of galaxy clusters can be strongly affected by intervening large-scale structure along its line of sight (Hoekstra et al. 2011).

Figure 5 shows the line-of-sight velocity dispersions as estimated from dynamics and weak lensing measurements for the groups SL2SJ02140-0535, SL2SJ02215-0647,

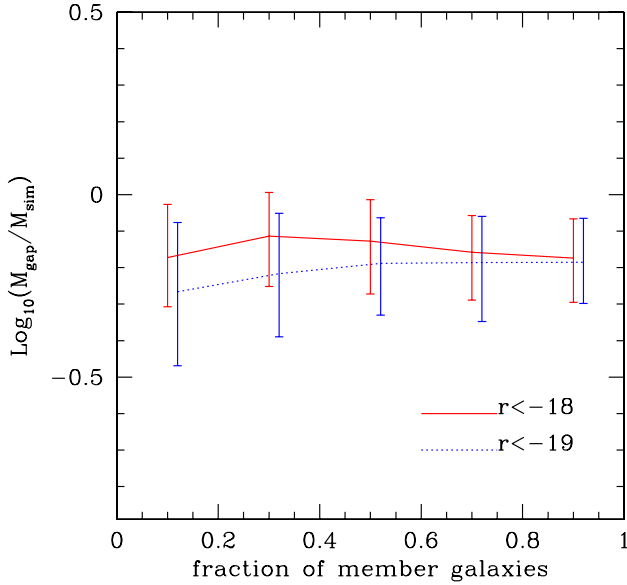


Fig. 4. Ratio between the estimated and actual masses of simulated groups with total number of members and velocity dispersions similar to the ones measured for SL2SJ02140-0535, i.e. number of members between 20 and 40, and velocity dispersion between 260 and 460 km s⁻¹. The number of groups in each bin of the plot remains constant. The x -axis corresponds to the fraction of members used for calculating the group mass.

SL2SJ08544-0121, and SL2SJ09413-1100. We found that weak lensing estimates are systematically larger by 50% than dynamical estimates. This is in stark contrast to measurements from galaxy-galaxy lensing by SLACS (Treu et al. 2006a,b), where the ratio between the central stellar velocity dispersion and the velocity dispersion that best fit the lensing model is 1.01 ± 0.02 . Although numerical simulations (see Sect. 4) suggest that the virial mass is underestimated by 20%, this is not enough to explain the inferred discrepancy. Thus, our results may indicate that the isothermal sphere model is not a good assumption for galaxy groups.

6. Conclusions

This paper presents the spectroscopic follow-up and dynamical analysis of eight group candidates identified in the SL2S survey. Our analysis reveals that seven of the systems correspond to gravitationally bound structures, where five have a single component in redshift-space and two have a double component (bimodal galaxy distribution). They span a wide range in redshift between 0.35 and 0.65, and a wide range in mass between $5 \times 10^{13} M_{\odot}$ and $1.5 \times 10^{14} M_{\odot}$.

The main results of this paper are given as follows:

1. The success rate of the spectroscopic confirmation of groups identified in the SL2S survey is about 88%. It is similar to the success rate of clusters followed-up in the Red-Sequence Cluster Survey (RCS-1; Gladders & Yee 2005).
2. We find that weak lensing estimates of the group velocity dispersions are 50% greater than dynamical estimates. This discrepancy has been never reported before by other studies of groups and clusters, and is in stark contrast to measurements from galaxy-galaxy lensing.
3. From numerical simulations, we concluded that measuring redshifts for only 30% of the total galaxy population in

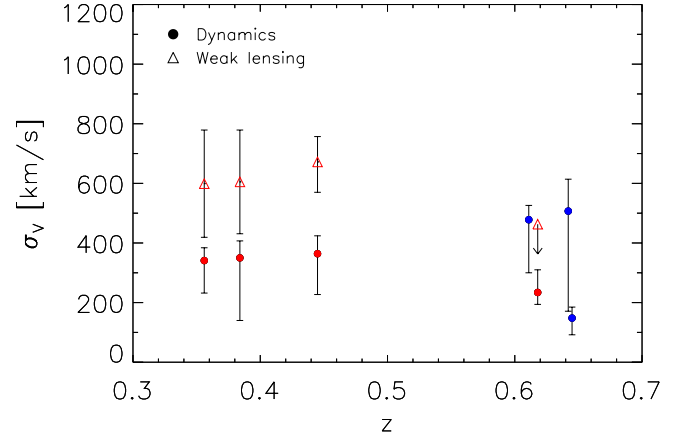


Fig. 5. Velocity dispersion of SL2S groups as estimated from galaxy dynamics (solid circles) and weak lensing measurements (open triangles). The red symbols show the groups with dynamical and weak lensing estimates, while blue symbols those groups with only dynamical estimates. Only one group at $z > 0.6$ has enough weak lensing signal to estimate an upper limit to its velocity dispersion.

groups is enough to recover the group velocity dispersion with less than 5% systematic error.

Acknowledgements. We thank Ricardo Salinas and Anupreet More for enlightening conversations. We thank the referee for the useful and constructive comments to improve this paper. The authors acknowledge support from Fondo ALMA-CONICYT N° 31090019, Comité Mixto ESO-Gobierno de Chile, FONDECYT through grant 1090637 and Programme National de Cosmologie (PNCG). R.P. Muñoz acknowledges support from CONICYT CATA-BASAL and FONDECYT through grant 3130750. V. Motta gratefully acknowledges support from FONDECYT through grant 1090673 and 1120741. T. Verdugo acknowledges support from FONDECYT through grant 3090025 and CONACYT through grant 165365. M. Limousin acknowledges the Centre National de la Recherche Scientifique for its support and the Dark Cosmology Centre is funded by the Danish National Research Foundation. N. Padilla acknowledges support from FONDAP “Center for Astrophysics”, CONICYT CATA-BASAL and FONDECYT through grant 1110328. G. Foëx acknowledges support from FONDECYT through grant 3120160. R. Gavazzi acknowledges support from the Centre National des Études Spatiales. This work made use of the Geryon cluster at the Centro de Astro-Ingeniería UC.

References

- Abazajian, K., Adelman-McCarthy, J. K., Agüeros, M. A., et al. 2004, *AJ*, 128, 502
- Adami, C., Mazure, A., Ilbert, O., et al. 2005, *A&A*, 443, 805
- Alard, C. 2006 [[arXiv:astro-ph/0606757](https://arxiv.org/abs/astro-ph/0606757)]
- Appenzeller, I., Fricke, K., Fürtig, W., et al. 1998, *The Messenger*, 94, 1
- Bamford, S. P., Nichol, R. C., Baldry, I. K., et al. 2009, *MNRAS*, 393, 1324
- Beers, T. C., Flynn, K., & Gebhardt, K. 1990, *AJ*, 100, 32
- Berlind, A. A., Frieman, J., Weinberg, D. H., et al. 2006, *ApJS*, 167, 1
- Biviano, A., Murante, G., Borgani, S., et al. 2006, *A&A*, 456, 23
- Bower, R. G., Benson, A. J., Malbon, R., et al. 2006, *MNRAS*, 370, 645
- Brough, S., Forbes, D. A., Kilborn, V. A., & Couch, W. 2006, *MNRAS*, 370, 1223
- Cabanac, R. A., Alard, C., Dantel-Fort, M., et al. 2007, *A&A*, 461, 813
- Churazov, E., Brüggén, M., Kaiser, C. R., Böhringer, H., & Forman, W. 2001, *ApJ*, 554, 261
- Colless, M., Dalton, G., Maddox, S., et al. 2001, *MNRAS*, 328, 1039
- Coupon, J., Ilbert, O., Kilbinger, M., et al. 2009, *A&A*, 500, 981
- Danese, L., de Zotti, G., & di Tullio, G. 1980, *A&A*, 82, 322
- Davis, M., Faber, S. M., Newman, J., et al. 2003, in *SPIE Conf.* 4834, ed. P. Guhathakurta, 161
- Dressler, A. 1984, *ARA&A*, 22, 185
- Dressler, A., Oemler, Jr., A., Couch, W. J., et al. 1997, *ApJ*, 490, 577
- Eke, V. R., Baugh, C. M., Cole, S., et al. 2004, *MNRAS*, 348, 866
- Finoguenov, A., Connelly, J. L., Parker, L. C., et al. 2009, *ApJ*, 704, 564

- Geller, M. J., & Huchra, J. P. 1983, *ApJS*, 52, 61
Gerke, B. F., Newman, J. A., Davis, M., et al. 2005, *ApJ*, 625, 6
Girardi, M., Giuricin, G., Mardirossian, F., Mezzetti, M., & Boschini, W. 1998, *ApJ*, 505, 74
Gladders, M. D., & Yee, H. K. C. 2005, *ApJS*, 157, 1
Goto, T., Yamauchi, C., Fujita, Y., et al. 2003, *MNRAS*, 346, 601
Hansen, S. M., Sheldon, E. S., Wechsler, R. H., & Koester, B. P. 2009, *ApJ*, 699, 1333
Helsdon, S. F., & Ponman, T. J. 2003, *MNRAS*, 339, L29
Hickson, P. 1997, *ARA&A*, 35, 357
Hoekstra, H., Hartlap, J., Hilbert, S., & van Uitert, E. 2011, *MNRAS*, 412, 2095
Horne, K. 1986, *PASP*, 98, 609
Kent, S. M., & Gunn, J. E. 1982, *AJ*, 87, 945
Knobel, C., Lilly, S. J., Iovino, A., et al. 2012, *ApJ*, 753, 121
Koester, B. P., McKay, T. A., Annis, J., et al. 2007, *ApJ*, 660, 221
Kurtz, M. J., & Mink, D. J. 1998, *PASP*, 110, 934
Lilly, S. J., Le Fèvre, O., Renzini, A., et al. 2007, *ApJS*, 172, 70
Limousin, M., Cabanac, R., Gavazzi, R., et al. 2009, *A&A*, 502, 445
Marinoni, C., Davis, M., Newman, J. A., & Coil, A. L. 2002, *ApJ*, 580, 122
McCarthy, I. G., Schaye, J., Ponman, T. J., et al. 2010, *MNRAS*, 406, 822
McKean, J. P., Auger, M. W., Koopmans, L. V. E., et al. 2010, *MNRAS*, 404, 749
Mihos, J. C., & Hernquist, L. 1996, *ApJ*, 464, 641
More, A., Cabanac, R., More, S., et al. 2012, *ApJ*, 749, 38
Oemler, Jr., A. 1974, *ApJ*, 194, 1
Oguri, M. 2006, *MNRAS*, 367, 1241
Padilla, N., Lambas, D. G., & González, R. 2010, *MNRAS*, 409, 936
Pannella, M., Gabasch, A., Goranova, Y., et al. 2009, *ApJ*, 701, 787
Riemer-Sørensen, S., Paraficz, D., Ferreira, D. D. M., et al. 2009, *ApJ*, 693, 1570
Springel, V., White, S. D. M., Jenkins, A., et al. 2005, *Nature*, 435, 629
Treu, T., Ellis, R. S., Kneib, J.-P., et al. 2003, *ApJ*, 591, 53
Treu, T., Koopmans, L. V., Bolton, A. S., Burles, S., & Moustakas, L. A. 2006a, *ApJ*, 640, 662
Treu, T., Koopmans, L. V. E., Bolton, A. S., Burles, S., & Moustakas, L. A. 2006b, *ApJ*, 650, 1219
Verdugo, T., Motta, V., Muñoz, R. P., et al. 2011, *A&A*, 527, A124
Wilman, D. J., Balogh, M. L., Bower, R. G., et al. 2005, *MNRAS*, 358, 71
Yang, X., Mo, H. J., van den Bosch, F. C., et al. 2007, *ApJ*, 671, 153
York, D. G., Adelman, J., Anderson, Jr., J. E., et al. 2000, *AJ*, 120, 1579
Zapata, T., Perez, J., Padilla, N., & Tissera, P. 2009, *MNRAS*, 394, 2229

Appendix A: Presentation of each group

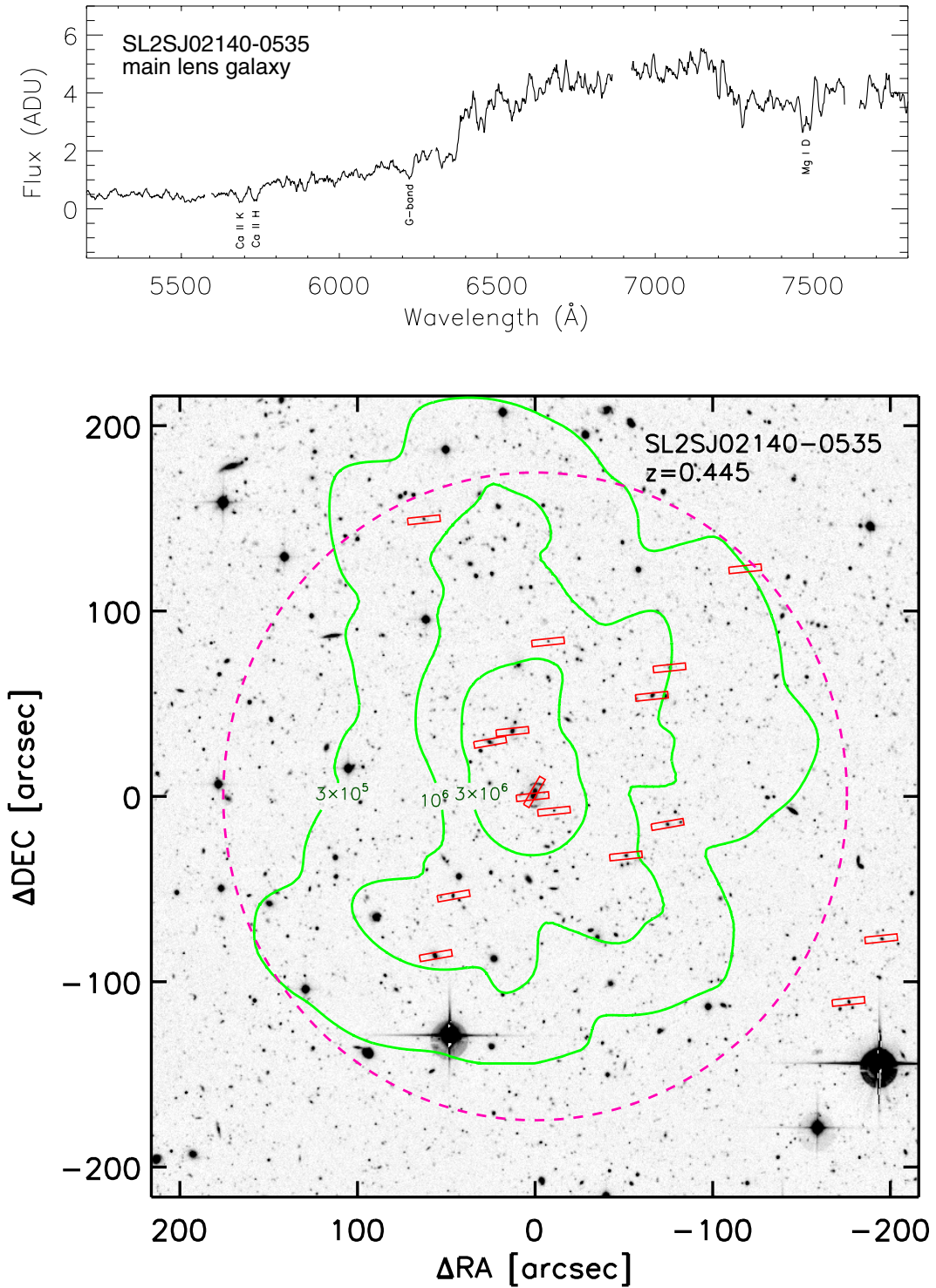


Fig. A.1. *Top panel:* optical spectra of the brightest confirmed member of SL2SJ02140-0535. The main absorption lines used to determine the redshift of the main lens galaxy have been identified. *Bottom panel:* spatial distribution of galaxies in the group field of SL2SJ02140-0535. Red rectangles show the position of the spectroscopically confirmed members. The dashed magenta circle shows a circular aperture of radius 1 Mpc at $z = 0.44$. The contours in green show the luminosity contours equal to 3×10^5 , 10^6 , 3×10^6 and $10^7 L_{\odot} \text{ kpc}^{-2}$ from outermost to innermost, as computed by Limousin et al. (2009).

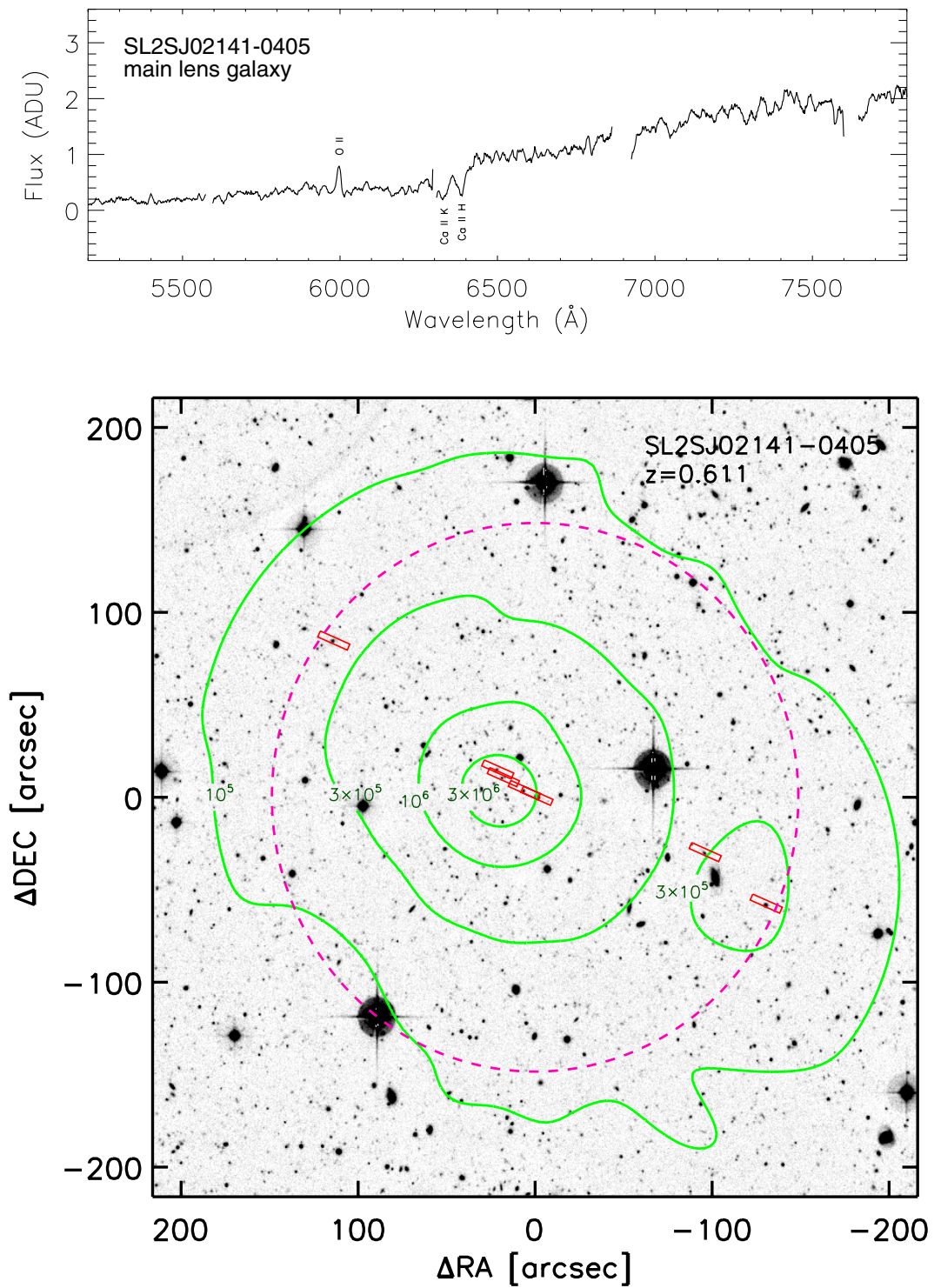


Fig. A.2. *Top panel:* optical spectra of the brightest confirmed member of SL2SJ02141-0405. The main absorption and emission lines used to determine the redshift of the main lens galaxy have been identified. *Bottom panel:* spatial distribution of galaxies in the group field of SL2SJ02141-0405. Red rectangles show the position of the spectroscopically confirmed members. The dashed magenta circle shows a circular aperture of radius 1 Mpc at $z = 0.61$. The contours are the same as in Fig. A.1.

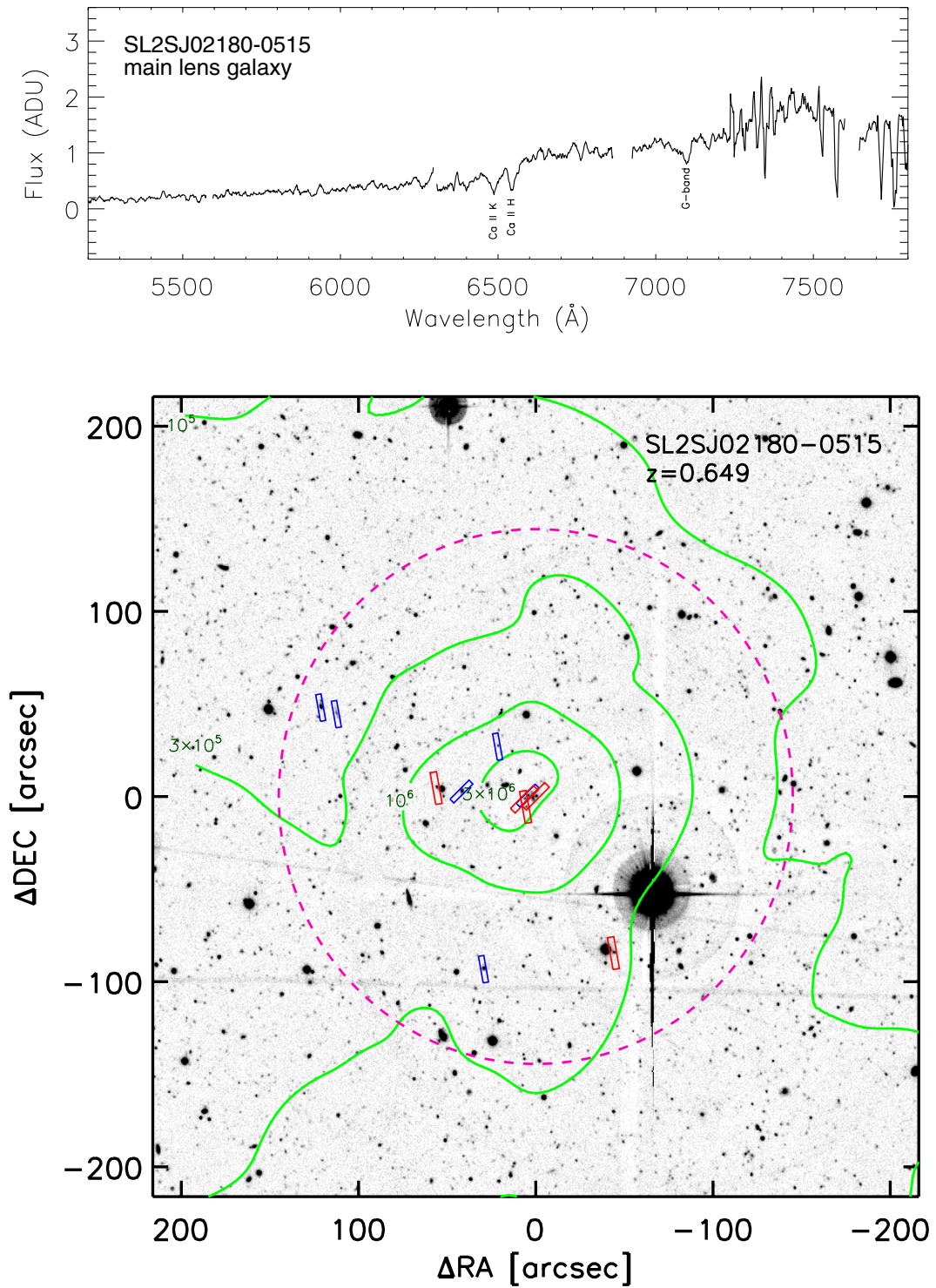


Fig. A.3. *Top panel:* optical spectra of the brightest confirmed member of SL2SJ02180-0515. The main absorption lines used to determine the redshift of the main lens galaxy have been identified. *Bottom panel:* spatial distribution of galaxies in the group field of SL2SJ02180-0515. Red rectangles show the position of the spectroscopically confirmed members. The dashed magenta circle shows a circular aperture of radius 1 Mpc at $z = 0.64$. The contours are the same as in Fig. A.1.

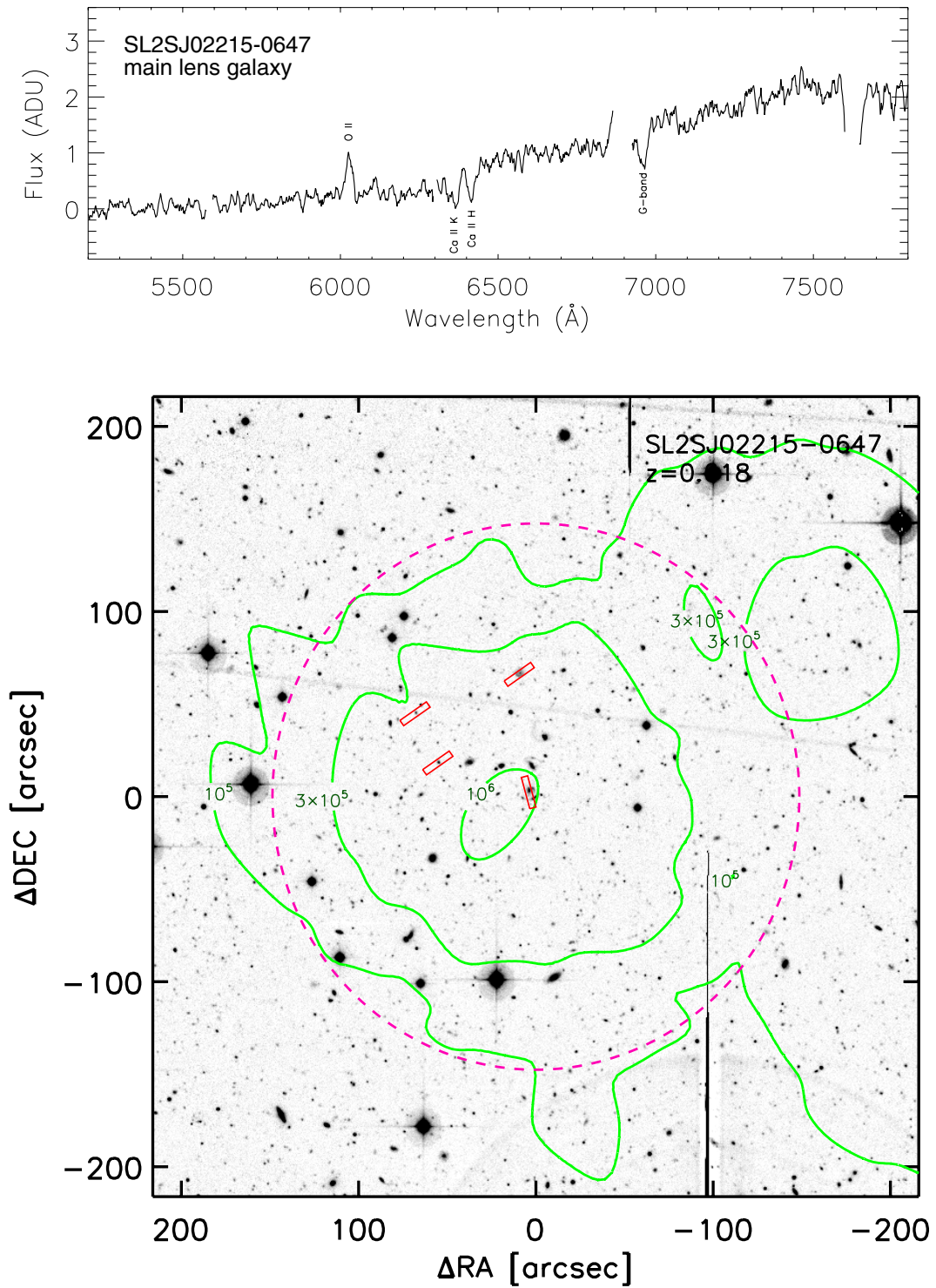


Fig. A.4. *Top panel:* optical spectra of the brightest confirmed member of SL2SJ02215-0647. The main absorption and emission lines used to determine the redshift of the main lens galaxy have been identified. *Bottom panel:* spatial distribution of galaxies in the group field of SL2SJ02215-0647. Red rectangles show the position of the spectroscopically confirmed members. The dashed magenta circle shows a circular aperture of radius 1 Mpc at $z = 0.62$. The contours are the same as in Fig. A.1.

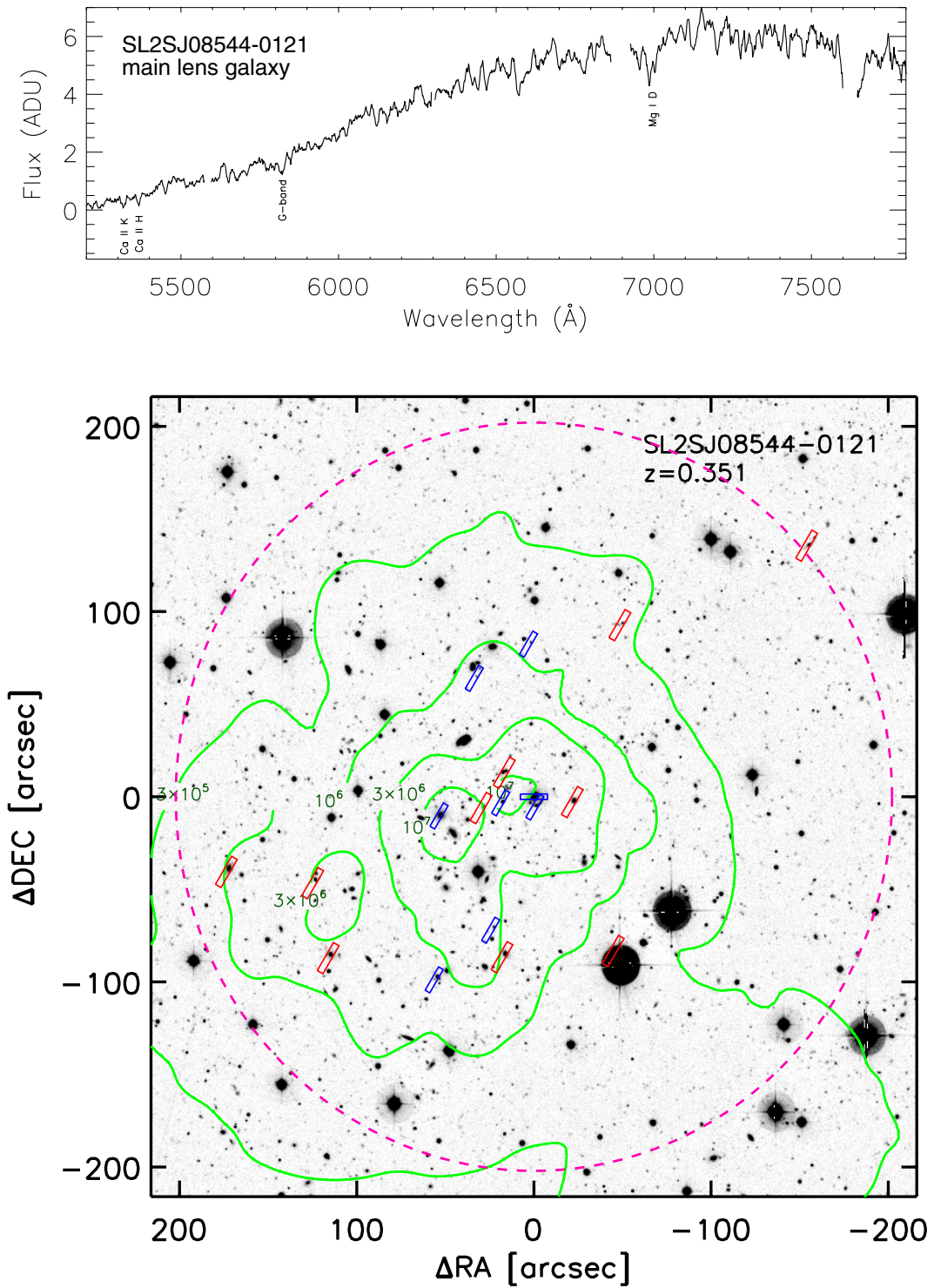


Fig. A.5. *Top panel:* optical spectra of the brightest confirmed member of SL2SJ08544-0121. The main absorption lines used to determine the redshift of the main lens galaxy have been identified. *Bottom panel:* spatial distribution of galaxies in the group field of SL2SJ08544-0121. Red rectangles show the position of the spectroscopically confirmed members. The dashed magenta circle shows a circular aperture of radius 1 Mpc at $z = 0.35$. The contours are the same as in Fig. A.1.

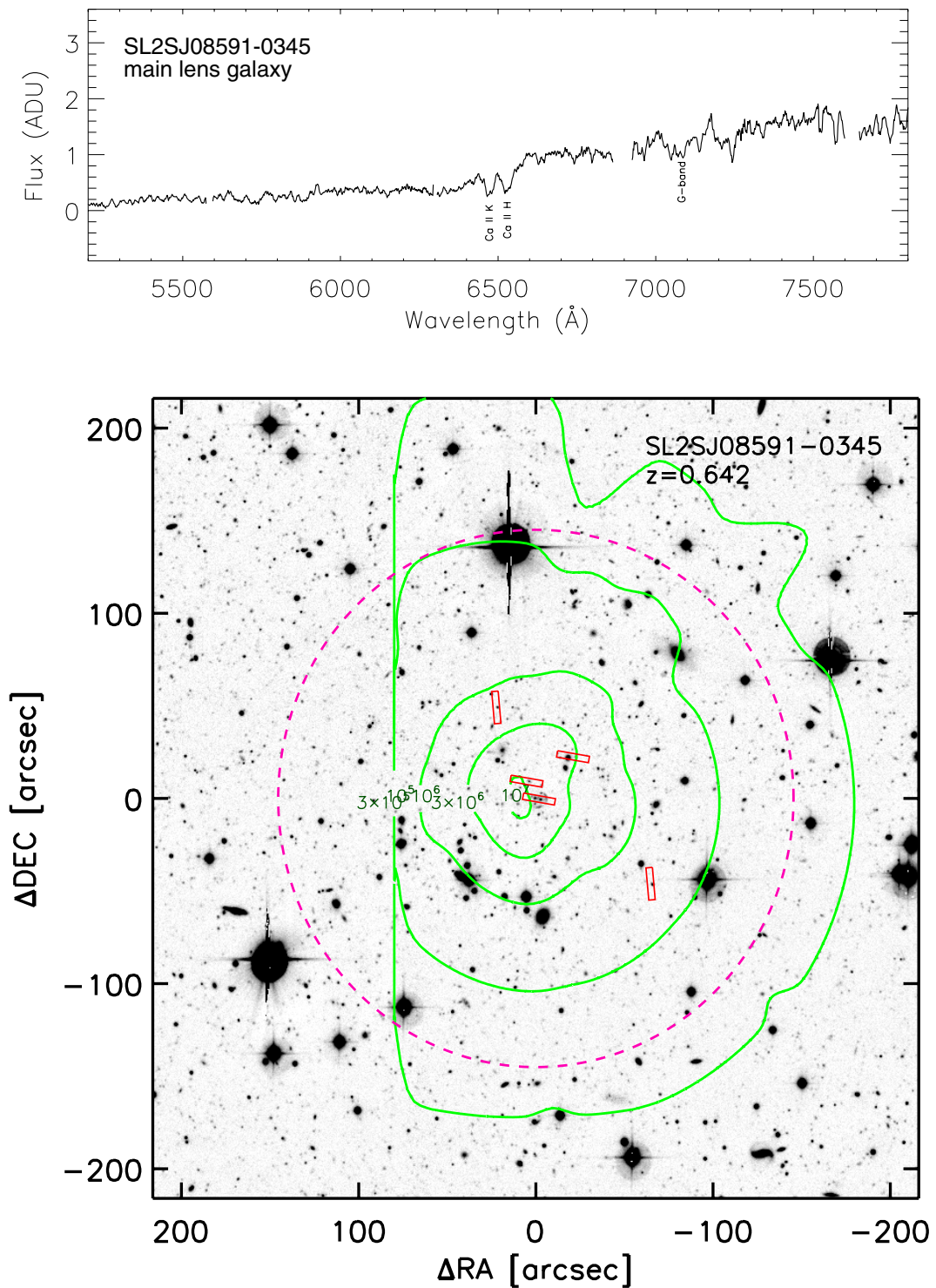


Fig. A.6. *Top panel:* optical spectra of the brightest confirmed member of SL2SJ08591-0345. The main absorption lines used to determine the redshift of the main lens galaxy have been identified. *Bottom panel:* spatial distribution of galaxies in the group field of SL2SJ08591-0345. Red rectangles show the position of the spectroscopically confirmed members. The dashed magenta circle shows a circular aperture of radius 1 Mpc at $z = 0.64$. The contours are the same as in Fig. A.1.

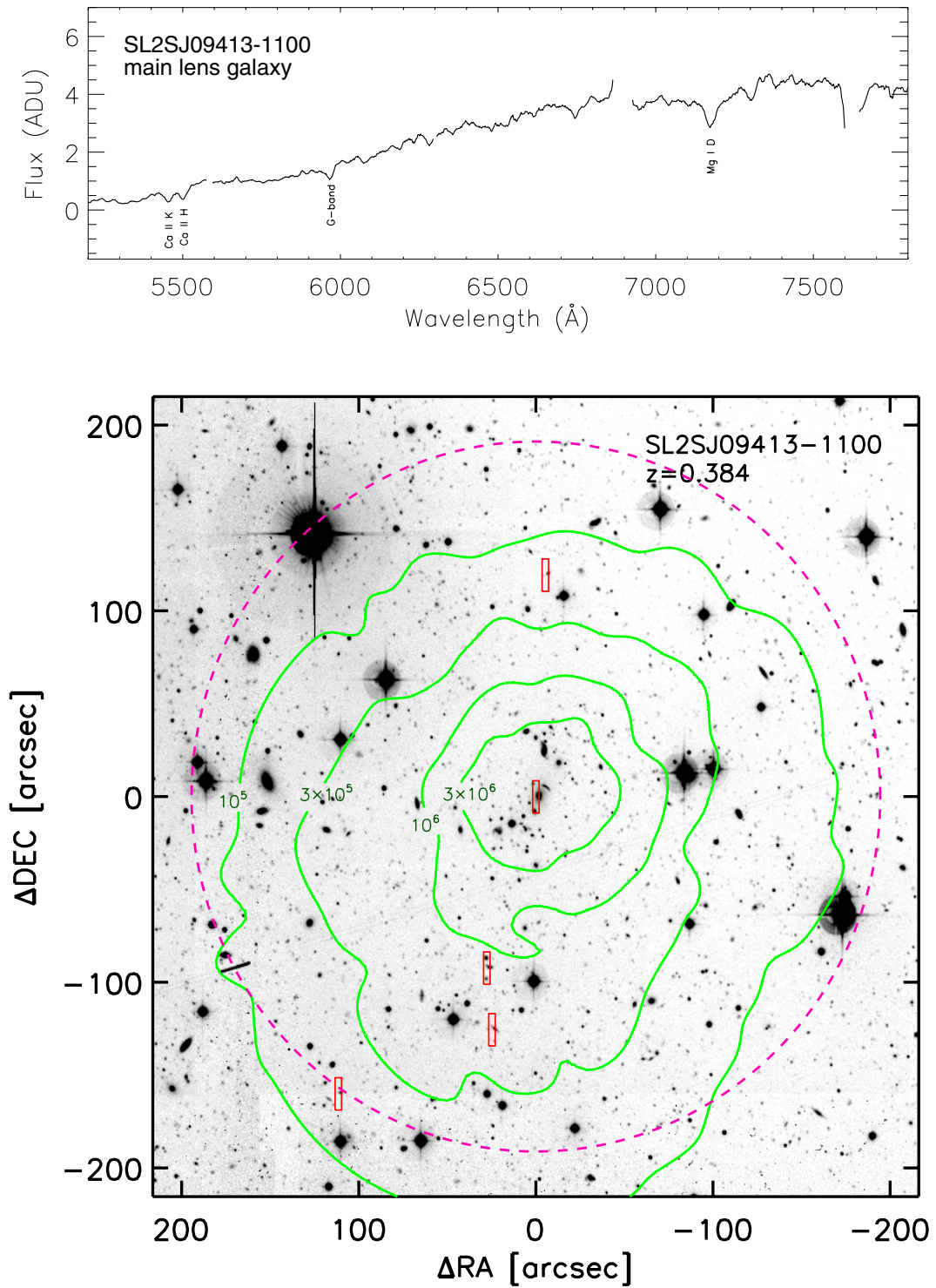


Fig. A.7. *Top panel:* optical spectra of the brightest confirmed member of SL2SJ09413-1100. The main absorption lines used to determine the redshift of the main lens galaxy have been identified. *Bottom panel:* spatial distribution of galaxies in the group field of SL2SJ09413-1100. Red rectangles show the position of the spectroscopically confirmed members. The dashed magenta circle shows a circular aperture of radius 1 Mpc at $z = 0.39$. The contours are the same as in Fig. A.1.

Appendix B: Summary of FORS2 masks and spectroscopic confirmed members for each group**Table B.1.** Summary of group members.

Group	Mask	Chip	Slit	RA	Dec	z_{spec}
	M012	CHIP1	2	33.550777	-5.551144	0.444
	M012	CHIP1	5	33.536942	-5.582868	0.443
	M012	CHIP1	7	33.533779	-5.592632	0.445
	M012	CHIP1	9	33.530430	-5.594814	0.447
	M012	CHIP1	10	33.531372	-5.569443	0.449
	M012	CHIP1	15	33.519188	-5.601521	0.446
	M012	CHIP1	19	33.515137	-5.577593	0.444
SL2SJ02140-0535	M012	CHIP1	21	33.512367	-5.573329	0.444
	M012	CHIP1	25	33.500538	-5.558484	0.446
	M012	CHIP1	29	33.484375	-5.623324	0.444
	M012	CHIP1	33	33.479259	-5.613928	0.444
	M010	CHIP1	1	33.546135	-5.607511	0.444
	M010	CHIP1	2	33.540424	-5.584474	0.443
	M010	CHIP1	9	33.512676	-5.596797	0.447
	M010	CHIP2	5	33.548912	-5.616460	0.443
	LRIS	-	-	33.533501	-5.591930	0.445
	M014_1	CHIP1	3	33.552521	-4.079994	0.605
	M014_1	CHIP1	4	33.551716	-4.081113	0.610
SL2SJ02141-0405	M014_1	CHIP1	6	33.548416	-4.083041	0.605
	M014_1	CHIP1	7	33.547485	-4.083448	0.608
	M014_1	CHIP1	22	33.522072	-4.091465	0.611
	M014_1	CHIP1	27	33.512501	-4.099202	0.610
	M014_1	CHIP2	10	33.578384	-4.060563	0.610
	M014_2	CHIP1	9	34.536358	-5.252573	0.644
SL2SJ02180-0515A	M014_2	CHIP1	13	34.561638	-5.247695	0.643
	M014_2	CHIP1	14	34.564087	-5.246713	0.643
	M014_2	CHIP2	10	34.538578	-5.285957	0.642
	M014_3	CHIP1	3	34.542030	-5.259311	0.643
	M014_3	CHIP1	6	34.531658	-5.259928	0.644
	M014_2	CHIP1	5	34.531971	-5.261622	0.646
SL2SJ02180-0515B	M014_2	CHIP1	8	34.546001	-5.258788	0.648
	M014_2	CHIP2	9	34.518215	-5.283539	0.648
	M014_3	CHIP1	5	34.532192	-5.260464	0.646
	M014_3	CHIP1	7	34.530411	-5.260028	0.648
	M016_1	CHIP1	4	35.477470	-6.788154	0.617
SL2SJ02215-0647	M016_1	CHIP1	5	35.481045	-6.780771	0.617
	M016_1	CHIP1	12	35.464710	-6.774853	0.619
	M016_2	CHIP1	3	35.463230	-6.792549	0.617
	M005	CHIP1	4	133.708832	-1.363143	0.353
	M005	CHIP1	7	133.699173	-1.361177	0.351
	M005	CHIP1	8	133.693802	-1.361807	0.352
SL2SJ08544-0121A	M005	CHIP1	16	133.703308	-1.342510	0.353
	M005	CHIP1	21	133.694809	-1.337374	0.353
	M005	CHIP2	12	133.709595	-1.387739	0.352
	M005	CHIP2	17	133.700745	-1.380287	0.353
	LRIS	-	-	133.693954	-1.360260	0.352
	M005	CHIP1	2	133.681519	-1.383398	0.357
	M005	CHIP1	6	133.702240	-1.361963	0.357
	M005	CHIP1	10	133.698608	-1.356661	0.359
	M005	CHIP1	11	133.687943	-1.361066	0.358
SL2SJ08544-0121B	M005	CHIP1	25	133.680481	-1.334525	0.360
	M005	CHIP1	33	133.651199	-1.322610	0.356
	M005	CHIP2	9	133.726212	-1.384477	0.356
	M005	CHIP2	11	133.742172	-1.371531	0.355
	M005	CHIP2	13	133.728638	-1.373227	0.354
	M005	CHIP2	16	133.698975	-1.384341	0.358
	M002_1	CHIP1	5	134.812363	-3.751204	0.644
	M002_1	CHIP1	6	134.810410	-3.753887	0.645
SL2SJ08591-0345	M002_1	CHIP1	9	134.805069	-3.747538	0.642
	M002_2	CHIP1	1	134.817093	-3.740146	0.644
	M002_2	CHIP1	19	134.792923	-3.766603	0.639
	M001	CHIP1	5	145.394897	-11.015464	0.386
	M001	CHIP1	16	145.393402	-10.982292	0.386
SL2SJ09413-1100	M001	CHIP2	5	145.425903	-11.059779	0.383
	M001	CHIP2	8	145.401794	-11.050273	0.385
	M001	CHIP2	10	145.402603	-11.041045	0.386

SARCS strong-lensing galaxy groups

I. Optical, weak lensing, and scaling laws^{★,★★}

G. Foëx¹, V. Motta¹, M. Limousin^{2,3}, T. Verdugo⁴, A. More^{5,6}, R. Cabanac⁷, R. Gavazzi⁸, and R. P. Muñoz⁹

¹ Departamento de Física y Astronomía, Universidad de Valparaíso, 1111 Avda. Gran Bretaña, Valparaíso, Chile
e-mail: gael.foex@uv.cl

² Aix Marseille Universit, CNRS, LAM (Laboratoire d'Astrophysique de Marseille) UMR 7326, 13388 Marseille, France

³ Dark Cosmology Centre, Niels Bohr Institute, University of Copenhagen, Juliane Maries Vej 30, 2100 Copenhagen, Denmark

⁴ Centro de Investigaciones de Astronomía, AP 264, 5101-A Mérida, Venezuela

⁵ Kavli Institute for Cosmological Physics, U. of Chicago, 5640 S. Ellis Ave., IL-60637 Chicago, USA

⁶ Kavli IPMU, University of Tokyo, 5-1-5 Kashiwanoha, 277-8583 Kashiwa, Japan

⁷ CNRS, Institut de Recherche en Astrophysique et Planétologie, 57 avenue d'Azereix, 65000 Tarbes, France

⁸ Institut d'Astrophysique de Paris, UMR 7095 CNRS & Université Pierre et Marie Curie, 98bis Bd Arago, 75014 Paris, France

⁹ Departamento de Astronomía y Astrofísica, Pontificia Universidad Católica de Chile, V. Mackenna 4860, 782-0436 Macul, Santiago, Chile

Received 15 January 2013 / Accepted 21 August 2013

ABSTRACT

We present the weak-lensing and optical analysis of the SL2S-ARCS (SARCS) sample of strong-lensing candidates. The sample is based on the Strong Lensing Legacy Survey (SL2S), a systematic search of strong-lensing systems in the photometric Canada-France-Hawaii Telescope Legacy Survey (CFHTLS). The SARCS sample focusses on arc-like features and is designed to contain mostly galaxy groups. We briefly present the weak-lensing methodology that we used to estimate the mass of the SARCS objects. Among 126 candidates, we obtained a weak-lensing detection (at the 1σ level) for 89 objects with velocity dispersions of the singular isothermal sphere mass model (SIS) ranging from $\sigma_{\text{SIS}} \sim 350 \text{ km s}^{-1}$ to $\sim 1000 \text{ km s}^{-1}$ with an average value of $\sigma_{\text{SIS}} \sim 600 \text{ km s}^{-1}$, corresponding to a rich galaxy group (or poor cluster). From the galaxies belonging to the bright end of the group's red sequence ($M_i < -21$), we derived the optical properties of the SARCS candidates. We obtained typical richnesses of $N \sim 5-15$ galaxies and optical luminosities of $L \sim 0.5-1.5 \times 10^{12} L_{\odot}$ (within a radius of 0.5 Mpc). We used these galaxies to compute luminosity density maps, from which a morphological classification reveals that a large fraction of the sample ($\sim 45\%$) are groups with a complex light distribution, either elliptical or multi-modal, suggesting that these objects are dynamically young structures. We finally combined the lensing and optical analyses to define a sample of the 80 most secure group candidates, i.e. weak-lensing detection and over-density at the lens position in the luminosity map, to remove false detections and galaxy-scale systems from the initial sample. We use this reduced sample to probe the optical scaling relations in combination with a sample of massive galaxy clusters. We detect the expected correlations over the probed range in mass with a typical scatter of $\sim 25\%$ in σ_{SIS} at a given richness or luminosity, making these scaling laws interesting mass proxies.

Key words. gravitational lensing: weak – cosmology: observations – dark matter – galaxies: groups: general

1. Introduction

From a nearly homogenous and uniform matter-density field, the Universe has evolved through cosmic time to a complex distribution of filamentary and clumpy structures. The Universe's main matter (dark matter) follows a hierarchical model of structure formation and evolution (Kaiser 1986; White & Frenk 1991) depicted in great detail with numerical simulations, which trace the gravitational growth of dark matter haloes (Evrard et al. 2002; Springel et al. 2005; Dolag et al. 2006). The so-called cosmic web filling the present Universe has been observationally confirmed by several large spectroscopic surveys (Colless et al. 2001; Pimblet et al. 2004; Pandey & Bharadwaj 2006), revealing the presence of large-scale filaments that feed nodes of massive and rich galaxy clusters (e.g. Jauzac et al. 2012). In the picture of this evolving matter density field, the intermediate-mass range of the galaxy groups play a key role in structure formation as they contain the majority of all galaxies (at least at

low redshifts, Eke et al. 2004) and bridge the gap between large massive galaxy clusters and single galaxies.

A precise characterization of the total mass contained in groups and clusters of galaxies and its connection to the visible baryonic tracers is one of the most important and yet challenging goals for cosmological and astrophysical purposes. For instance, the group and cluster mass function (number density of object as function of total mass), and its redshift evolution is one of the most powerful cosmological constraints since it is sensitive to both the Universe's expansion and the growth rate of structures (e.g. White et al. 1993; Haiman et al. 2001; Wang et al. 2004; Rozo et al. 2009). To be fully effective, this cosmological probe requires large samples of groups and clusters with precise mass estimates. Several methodologies can provide direct measurements of their mass, such as the analysis of the X-ray emission of the hot intra-cluster medium (ICM), the galaxies' velocity dispersion, or the gravitational lensing signal produced on background galaxies. However, all these techniques require high-quality data sets and non-trivial analyses. It is therefore more convenient to make use of baryonic tracers as mass proxies to quickly derive masses for large numbers of groups and

* Strong Lensing Legacy Survey SL2S-ARCS.

** Table 2 and Appendix A are available in electronic form at <http://www.aanda.org>

clusters. In the simplest model of structure formation involving a purely gravitational collapse of dark matter haloes, groups and clusters form a population of self-similar objects with simple relations between their total mass and other physical quantities (Kaiser 1986). Numerous works have explored and tried to fully characterize these links between mass and baryonic observables such as the ICM X-ray luminosity, temperature, pressure, or entropy from X-ray observations (Finoguenov et al. 2001; Vikhlinin et al. 2002; Ettori et al. 2004; Arnaud 2005; Kotov & Vikhlinin 2005; Vikhlinin et al. 2006; Hoekstra 2007; Rykoff et al. 2008; Pratt et al. 2009; Leauthaud et al. 2010; Okabe et al. 2010; Mahdavi et al. 2013), the Compton parameters derived from Sunyaev-Zel'dovich (SZ) observations (McCarthy et al. 2003; Morandi et al. 2007; Bonamente et al. 2008; Marrone et al. 2009; Lancaster et al. 2011; Planck Collaboration et al. 2011c,b), or the galaxy velocity dispersions, richness and optical luminosity from optical observations (Lin et al. 2003, 2004; Popesso et al. 2005, 2007; Becker et al. 2007; Johnston et al. 2007; Reyes et al. 2008; Mandelbaum et al. 2008; Rozo et al. 2009; Andreon & Hurn 2010; Foëx et al. 2012). However, many observational results have found discrepancies between the theoretical predictions derived from the gravitationally driven model of structure formation (different slope and normalization, break of self-similarity at low mass, large intrinsic scatter, non-standard redshift evolution), thus revealing the combined influence of various non-gravitational physical processes that affect the properties of groups and clusters (e.g. Voit 2005 for a review). A precise calibration of these scaling relations over the full range in mass and redshift is mandatory for high-precision cosmology through the group and cluster mass function. The use of large numbers of objects would indeed lose its interest in the presence of any remaining and uncorrected bias in the final relations. On the cluster scale, numerous works have converged towards well defined scaling laws up to relatively high redshifts. On the group scale, such precise calibrations are more difficult to achieve because groups present a much wider range of properties at any given mass, i.e. large intrinsic scatters (e.g. Osmond & Ponman 2004; Giodini et al. 2009; Rykoff et al. 2008; Balogh et al. 2011a). Moreover, precise mass measurements on this scale are much more difficult to perform regardless of the methodology employed, thus increasing the uncertainties on the scaling relation fits.

From the astronomical point of view, these scaling laws are also of great interest since they can be used to put constraints on the underlying physical processes. Observational results can indeed be compared to hydrodynamical simulations of cluster formation to study the relative influence of several mechanisms that modify the ICM properties, such as radiative cooling, supernovae and active galactic nucleus feedback, or pre-heating of the gas (e.g. Voit 2005). On the other hand, a precise characterization of group and cluster masses provides a unique way to probe relevant mechanisms, such as galaxy harassment, ram pressure stripping, or galaxy starvation/strangulation, which drive the evolution of the galaxy properties (stellar mass, size, star formation rate, spectral/morphological type, etc.) as a function of their local environment, from field galaxies to the core of massive clusters (Smail et al. 1998; Balogh et al. 1999; Tran et al. 2003; Treu et al. 2003; Dressler et al. 2004; Poggianti 2004; Boselli & Gavazzi 2006; Poggianti et al. 2006; Balogh et al. 2007; De Lucia et al. 2007; Jeltema et al. 2007; Popesso et al. 2007; Huertas-Company et al. 2009; Lubin et al. 2009; Stott et al. 2009; Wilman et al. 2009; Balogh et al. 2011b; Carollo et al. 2013). It is, therefore, very important to use representative group and cluster samples that cover a wide range in mass and

redshift to study and constrain the galaxy and ICM properties along with robust and direct mass estimates of the parent halo. The main goal of our study is to analyse a sample of galaxy groups in order to constrain different optical scaling relations, which can be used for cosmological purposes. This study also provides a secure sample of intermediate-mass-range objects to investigate the galaxy properties in more detail and to compare them to field and cluster galaxies.

To construct large samples of groups and clusters of galaxies, one can use several methods: spectroscopic identification of galaxy over-densities (e.g. Miller et al. 2005; Knobel et al. 2009; Cucciati et al. 2010), optical detection based on the red-sequence galaxies (e.g. Gladders & Yee 2005; Koester et al. 2007a), detection of variations in the cosmic microwave radiation due to the SZ effect (e.g. Carlstrom et al. 2002; Staniszewski et al. 2009; Planck Collaboration et al. 2011a), detection of the ICM diffuse X-ray emission (e.g. Mulchaey & Zabludoff 1998; Böhringer et al. 2000; Finoguenov et al. 2007a; Vikhlinin et al. 2009), observation of weak-lensing distortions of background galaxies (e.g. Marian & Bernstein 2006; Gavazzi & Soucail 2007; Massey et al. 2007; Bergé et al. 2008).

Each of these techniques has its own advantages and limitations. For instance, SZ detections are less redshift dependent than X-ray observations that are limited to the high-mass end of the mass function when going to high redshifts. Weak lensing loses its efficiency to low-mass objects and high-redshift ones, but it is also insensitive to the dynamical state of the target. Optical detections can probe a wide range in mass and redshift but suffers from contamination from projection effects. Spectroscopic redshifts are potentially powerful for constructing large samples of groups and clusters, but this method requires large quantities of observing time. For anyone who wants to target low-mass objects up to high redshift, the strong-lensing signal produced in the core of some dark matter halo is an interesting alternative. Although such strong-lensing events remain rare, their theoretical distribution in terms of angular separation (e.g. Oguri 2006) has been probed over a wide range of halo mass, from galaxy-scale (e.g. Muñoz et al. 1998; Myers et al. 2003; Bolton et al. 2006; More et al. 2011) to cluster-scale objects (e.g. Luppino et al. 1999; Ebeling et al. 2001; Zaritsky & Gonzalez 2003; Gladders et al. 2003; Wen et al. 2011). With an automatic search of a large sky area, the observed number of such strong-lensing systems will increase, making this detection method interesting (e.g. with the Large Synoptic Survey Telescope, Ivezić et al. 2008).

On intermediate scales in mass, galaxy groups have been largely investigated with optical (including strong lensing) and X-ray tracers (e.g. Mulchaey & Zabludoff 1998; Helsdon & Ponman 2000; Zabludoff & Mulchaey 2000; Helsdon & Ponman 2003a,b; Osmond & Ponman 2004; Willis et al. 2005; Jeltema et al. 2006; Finoguenov et al. 2007b; Rasmussen & Ponman 2007; Mamon 2007; Faltenbacher et al. 2007; Gastaldello et al. 2007; Fassnacht et al. 2008; Yang et al. 2008; Giodini et al. 2009; Sun et al. 2009; Cucciati et al. 2010; Leauthaud et al. 2010; Balogh et al. 2011b; Connelly et al. 2012). More et al. (2012) present the most up-to-date sample of objects detected by their strong-lensing signal. Its main specificity resides in a selection designed to focus on strong lenses on the galaxy group scale. The study we present here is, therefore, the first analysis of a large sample of strong-lensing galaxy groups up to high redshift, in combination with the previous work of Limousin et al. (2009).

This Paper is organized as follows. In Sect. 2 we present the SARCS sample of lens candidates. We briefly recall our weak-lensing methodology in Sect. 3, along with the results of the

shear profile fitting. Section 4 is dedicated to the optical analysis of the sample: selection of the bright red galaxies, estimates of richnesses and optical luminosities, luminosity maps, and the morphological classification. In Sect. 5, we combine results from the weak-lensing and optical analyses to draw up a sample of 80 most secure candidates and study the optical scaling relations. We finally draw some conclusions in Sect. 6. Paper II (Foëx et al., in prep.) will focus more on the properties of the galaxy population and correlations with their environment.

Throughout this paper, we use a standard Λ -CDM cosmology defined by $\Omega_M = 0.3$, $\Omega_\Lambda = 0.7$ and a Hubble constant $H_0 = 70 \text{ km s}^{-1}/\text{Mpc}$.

2. The SARCS sample

2.1. The CFHTLS survey

The Canada-France-Hawaii Telescope Legacy Survey (CFHTLS¹) is a photometric survey made in five bands u' , g' , r' , i' , z' close to the bands of the Sloan Digital Sky Survey (Fukugita et al. 1996). Observations were taken with the CFHT prime focus instrument MEGAPRIME covering a field-of-view of 1 deg^2 on the sky with a pixel size of $0.186''$. The survey includes two components; the WIDE component made of four regions of the sky at high galactic latitudes and low extinction, covering in total 170 deg^2 , and the DEEP component, made up of four pencil-beam fields of 1 deg^2 . One of the DEEP fields (D1) is located within its WIDE counterpart (W1). After masking unusable areas (bright stars and other defects), the CFHTLS survey covers an effective area of 150.4 deg^2 .

The raw images were pre-reduced at CFHT with the elixir pipeline² and then astrometrically calibrated, photometrically inter-calibrated, resampled, stacked, and released by the Terapix group at the Institut d'Astrophysique de Paris (IAP). We used the CFHTLS T0006 release, in which the DEEP fields are offered in two stacks, D-25, which combines the 25% best-seeing individual pointings, and D-85 using the 85%. Both the detection of the lens candidates and the weak-lensing analysis were done on the D-25 images as they provide a smaller seeing. i' -band images that we used for the weak-lensing analysis have a seeing $\leq 0.65''$ for the DEEP fields, going up to $0.9''$ for the WIDE fields. Typical completeness magnitudes are $m_{i'} = 25 \text{ mag}$ (D) and $m_{i'} = 24 \text{ mag}$ (W). More details on the T0006 release can be found on the Terapix website³.

2.2. The SL2S-ARCS sample

The Strong Lensing Legacy Survey (SL2S, Cabanac et al. 2007) is an semi-automated search of strong-lensing systems on CFHTLS DEEP and WIDE fields. The SL2S lens sample was compiled using two detection algorithms optimized for different classes of strong-lensing systems. The `sl2s` is an object-oriented colour-based algorithm searching for galaxy-scale lenses around ellipticals. The `sl2s` produced the SL2S RING sample (Gavazzi et al., in prep.). The `sl2s` (Alard 2006; More et al. 2012) is a generic algorithm aimed at detecting elongated and curved features anywhere in the CFHTLS images, thus more efficient at finding group and cluster-scale lenses. The scan of the complete CFHTLS survey

resulted in the SL2S-ARCS sample (SARCS) fully described in More et al. (2012).

Basically, `sl2s` search FITS images for elongated and contiguous features of pixels above a given intensity threshold and tag the most promising features as arc candidates according to their width, length, area, and curvature (see Table 1 of More et al. 2012). In the CFHTLS fields, `sl2s` thresholds were kept low to favour completeness over purity. This led to roughly $1000 \text{ candidates/deg}^2$. Then, the candidates were inspected visually, reducing the sample to 413 candidates ($\sim 2.75 \text{ candidates/deg}^2$). These potential lenses were then ranked separately by three people, from 1 to 4, where 4 is most likely a strong-lensing system. The final SARCS sample was extracted from this ranked sample by selecting candidates reaching rank 2 or higher with an arc radius $R_A \geq 2''$ in order to filter out galaxy-scale systems (the arc radius, defined as the distance between the candidate lensed image and the centre of the respective lens galaxy, is a reasonable proxy for the mass of strong-lensing systems). In total, 127 systems were selected, and their general properties are given in Table 2 of More et al. (2012). The redshift distribution of the sample, derived from the photometric redshifts of Coupon et al. 2009, spans a range $z \in [0.2-1.2]$ and peaks at $z \sim 0.5$ (Fig. 7 of More et al. 2012). As seen in Fig. 10 of More et al. (2012), the distribution of the image separation of the SARCS systems is located between the galaxy-scale SLACS sample (Bolton et al. 2006) and the massive cluster MACS sample (Ebeling et al. 2001), thus corresponding mostly to groups and poor clusters of galaxies.

To the SARCS sample, we added an extra group-scale lens discovered in a different M C observation from the CFHTLS fields. This group was part of the previous sample analysed in Limousin et al. (2009; SL2S J09413-1100) and is referred to in the following as SA0. We also removed two candidates from the initial SARCS sample, SA21 and SA56, because of the presence of a large foreground galaxy close enough to the central galaxy to make its colour determination unreliable, which is problematic for optical analyses (richness, luminosity, and morphology). In total, we then have a sample of 126 lens candidates. We use both the weak-lensing and optical analyses of this initial sample to provide a subsample of the most secure SARCS group candidates (see Sect. 5.1).

3. Individual weak-lensing measurements

3.1. Methodology

The weak-lensing pipeline we used is fully described in Foëx et al. (2012). A similar methodology has been already employed by Limousin et al. (2009) on the first SL2S sample of groups and by Bardeau et al. (2007) and Soucail (2012) on several galaxy clusters. We outline in the following the main steps in extracting weak-lensing masses from the CFHT observations.

3.1.1. Galaxy selection

First, we detect the objects on the images with SE⁴ (Bertin & Arnouts 1996). We then use the i -band photometric properties to construct a catalogue of stars and a catalogue of galaxies. The distinction is made through a combination of the size of the objects with respect to the point spread function (PSF), their position in the magnitude/central-flux diagram (i.e. with respect to the *star branch*) and their stellarity given by

¹ <http://www.cfht.hawaii.edu/Science/CFHTLS/>

² <http://www.cfht.hawaii.edu/Instruments/Elixir/>

³ <http://terapix.iap.fr/cpl/T0006-doc.pdf>

⁴ <http://www.astromatic.net/software/sextractor>

SE . After this first step, we obtain typical number densities of 3 arcmin^{-2} for stars and $65/25 \text{ arcmin}^{-2}$ for galaxies in the DEEP/WIDE fields.

From the galaxy catalogs, we select the lensing sources as follows. We remove all galaxies within the red sequence (see Sect. 4.1 for its definition) down to $m_i < 23$ mag, a limit that is low enough to reject most of the faint galaxies of the groups without rejecting too many faint field galaxies with similar colours as the group members. Then, we keep only the remaining galaxies with $21 < m_i < m_{\text{comp}} + 0.5$, where m_{comp} is the 50% completeness limit of the galaxy catalogues in the i' -band. The lower limit close to the completeness magnitude ensures that a control is kept on the redshift distribution of the selected galaxies (required to estimate the lensing strength, see below), while the upper limit $m_i > 21$ offers a good compromise between removing the foreground galaxies without rejecting too many lensed galaxies. In doing so, we get final densities of roughly $40/15 \text{ arcmin}^{-2}$ galaxies in the DEEP/WIDE fields.

3.1.2. Shape measurements

Next, we estimate the shape of the galaxies using the software IM2SHAPE⁵ (Bridle et al. 2002) as done in many other studies (Cypriano et al. 2004; Bardeau et al. 2005, 2007; Limousin et al. 2007a,b). Our implementation of IM2SHAPE follows exactly the one presented in Foëx et al. (2012). We use one elliptical Gaussian to model the light distribution of the stars and galaxies to derive their shape parameters. The estimation of the PSF field is made by taking the average shape of the five nearest stars at each galaxy position. The MCMC sampler returns the most likely ellipticity components for each galaxy, along with robust statistical errors. With the STEP1 simulations reproducing ground-based observations (Heymans et al. 2006), this implementation of IM2SHAPE was found to present a lensing bias of $\sim -10\%$ (Foëx et al. 2012), a value that is balanced out in this work by having increased the measured shear by 10%.

3.1.3. Shear profiles

Once the shape parameters of the galaxies had been estimated with the above method, we used them to construct shear profiles. After we assumed circular symmetry of the lens mass distribution and a random orientation of field galaxies, the average shape of background galaxies in a region of constant potential gives an estimate of the reduced shear $\langle e \rangle = g$. Thus, the average tangential ellipticity of galaxies in concentric annuli around the lens provides a shear profile $g(r)$ that can be fitted by analytical models to estimate the mass. To reduce the impact of galaxies with a noisy shape estimation, we weighted the ellipticity of each galaxy by the inverse of its variance added in quadrature to the intrinsic shape noise, i.e. the width of the galaxies intrinsic ellipticity distribution ($\sigma_{\text{int}} = 0.25$, e.g. Brainerd et al. 1996). The lensed galaxies were binned in logarithmic annuli, starting at 50 kpc from the centre (see below for its definition) and with a ratio of 1.25 between the outer and inner limits of the bin. These logarithmic profiles ensure a roughly constant signal-to-noise ratio of the shear in each bin, along with a good spatial resolution in the central parts. All the profiles were fitted within $r \in [100 \text{ kpc} - 2 \text{ Mpc}]$. We chose to use a fixed range for all the SARCS groups, to avoid over-estimations of the mass by only selecting the region where the signal is significantly positive. We could have used a fixed range of angular radius, but

SA66

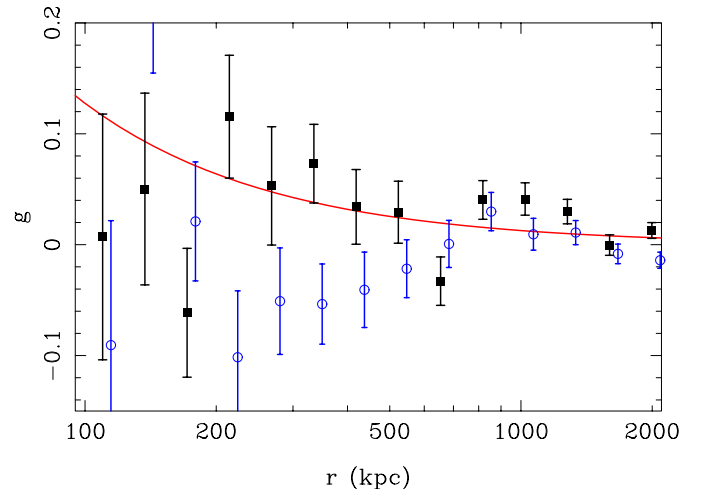


Fig. 1. Shear profile for the candidate SA66 ($\sigma_{\text{SIS}} = 644 \text{ km s}^{-1}$, $z_{\text{spec}} = 0.35$). The black filled squares shows the tangential component of the shear, the blue open circles the B-mode of one of the shifted profiles (for clarity). The red curve is the SIS best fit to the tangential shear.

given the large coverage in redshift of the SARCS sample, it would have led to very different regions according to the redshift of the object. As we are mainly studying galaxy groups, the outer limit of 2 Mpc was high enough to probe the shear signal beyond the virial radius.

As described in Foëx et al. (2012), we constructed several *shifted* shear profiles to reduce sampling effects in the central bins where there were few galaxies. In practice, we moved the inner part of the first bin by a fraction of its width (e.g. 1/50, so 50 shifted profiles), giving a new estimation of the shear at the corresponding position. Each of these shifted profiles are correlated, but not fitted together, so a classical χ^2 minimization still holds. For each of these profiles, we drew 1000 new Monte Carlo profiles (assuming a Gaussian distribution for the shear estimates in each bin). This led to a large number of estimates for the best fit parameters of the model (50 times 1000). We used the final distribution to derive the best model, i.e. the mode of the distribution, along with robust statistical errors. An example of the measured shear profile is given in Fig. 1.

3.1.4. Normalization of the profiles

Before we ran the fitting procedure of the shear profiles, we had to adjust their normalization. Here we had to deal with two effects. The first one was the contamination of the sources catalogues by unlensed galaxies. Despite our selection criteria, we expected to have a significant fraction of foreground galaxies in our catalogs, thus implying a dilution of the shear signal. We also had some contamination by group members. However, because of their small number in galaxy groups and thanks to the removal of the red sequence, they did not have a significant effect on the shear measurements. We checked that, in most cases, the number density profile of the lensing sources was roughly flat in the central parts, meaning that the number of remaining group members (compared to field galaxies) in the lens catalogues was negligible. In our case, this possible contamination did not require any correction as, for instance, for rich galaxy clusters (e.g. Hoekstra 2007; Foëx et al. 2012).

⁵ <http://www.sarahbridle.net/im2shape/>

The second effect was to determine the strength of the shear signal to turn the observed distortions into physical quantities. Both were treated simultaneously via the determination of the geometrical factor D_{ls}/D_s , ratio of the angular diameter distances between the lens and the source D_{ls} to the distance of the source D_s . We followed the same methodology as used in Limousin et al. (2009) and Foëx et al. (2012), which is based on the photometric redshifts catalogue from the T0004 release of the CFHTLS-DEEP survey. The main advantage of this catalogue is that the data were taken with the same instrument in the same photometric system as our observations. The photometric redshifts we used are in the publicly available catalogue provided by Roser Pello⁶, which are redshifts derived with H Z (Bolzonella et al. 2000) and carefully calibrated with spectroscopic samples (Ienna & Pelló 2006). Following previous works (e.g. Cypriano et al. 2004; Hoekstra 2007; Limousin et al. 2009; Oguri et al. 2009; Foëx et al. 2012), we therefore applied directly the same colour and magnitude criteria to this catalogue as were used to select the lensed galaxies in order to get a similar redshift distribution. This point required neglecting the cosmic variance, which is not always valid on the scale of 1 deg² fields of view. We indeed checked that the redshift distribution of the D2 field (part of the COSMOS field, known to be overly dense) gives slightly different results on the average D_{ls}/D_s than the D1, D3, and D4 distributions. In the following, we have only used the distribution of photometric redshifts from the D1 field.

Setting $D_{ls}/D_s = 0$ for the galaxies with $z_{\text{phot}} < z_{\text{lens}}$, we then computed the geometrical factor (i.e. the shear strength) averaged over the full redshift distribution. In doing so, we account at the same time for the contamination by foreground galaxies in the source catalogs. We therefore simply translated the dilution of the observed shear signal by unlensed galaxies into the estimate of its strength through the distances ratio. This average geometrical factor can be inverted into an effective redshift z_{eff} such as $\langle D_{ls}/D_s \rangle = D_{l,z_{\text{eff}}}/D_{z_{\text{eff}}}$. These effective redshifts are given in Table 2, and because of the contamination by field galaxies, they are much lower than the typical values used elsewhere to derive the strength of the shear signal of low- z clusters, i.e. $z_s \sim 1$ (e.g. Okabe & Umetsu 2008; Radovich et al. 2008). As verified in Limousin et al. (2009), the photometric redshifts from R. Pello give consistent results compared to those obtained with the catalogue of Coupon et al. (2009).

Instead of assuming a typical source redshift, using a geometrical factor averaged over the whole redshift distribution is a better way to convert the observed shear into physical quantities. But it remains an approximation since the reduced shear is not linear in D_{ls}/D_s (e.g. Seitz & Schneider 1997; Hoekstra et al. 2000). However, we start to fit the shear profiles at 100 kpc from the centre, which is a distance where the convergence κ is subcritical and low enough for group-scale haloes to reduce the influence of this approximation.

A last point that needed to be verified was the accuracy of the redshifts we used to estimate D_{ls} , along with the impact on the derived lensing masses. Although we have a spectroscopic redshift for some of the SARCS objects (see Table 2), we used the photometric redshift of the central galaxy derived by Coupon et al. (2009) in most cases. First, we simply compared the spectroscopic and photometric redshifts of the 14 SARCS candidates having both values. As seen in Fig. 2, we obtained overall good agreement, with only two objects presenting a difference larger than 0.2. The first one, SA33, has its central galaxy falling in a masked region. However, the distribution of photometric

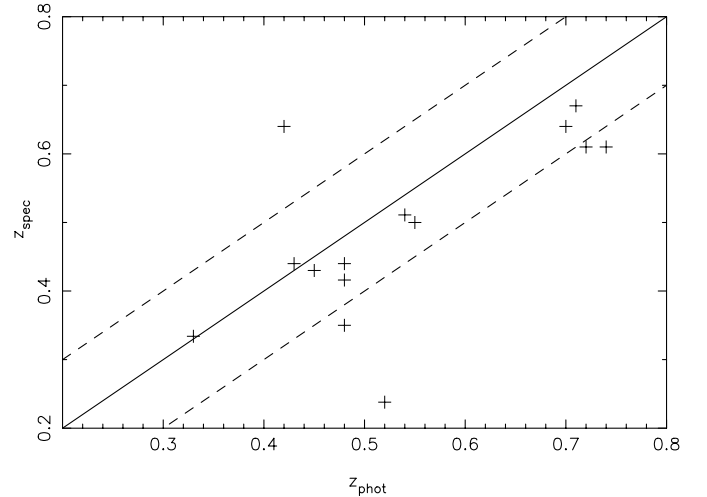


Fig. 2. Spectroscopic redshifts versus photometric redshifts for the SARCS objects (see Table 2). The solid line shows the equality, the two dashed lines are at ± 0.1 , i.e. a typical uncertainty on photometric redshifts.

redshifts (estimated with HyperZ) in the central part of the lens and corrected for the field distribution peaks at $z \sim 0.65$, which is a value in perfect with the spectroscopic redshift $z_{\text{spec}} = 0.64$. For the second catastrophic error, SA48, a large and bright foreground galaxy $\sim 15''$ away from the lens galaxy might contaminate its photometric redshift estimation. Given how few galaxy members there are for this lens, we could not apply the same procedure as for SA33 with a field-subtracted photometric redshift distribution. In such cases, be they a lens in a masked region, a nearby contaminating galaxy, or a close arc, estimating the redshift of the lens with only the central galaxy can be problematic.

The shear signal is fitted by $\gamma = \langle D_{ls}/D_s \rangle \times f(M)$, where $f(M)$ is a function of the lens mass M . Therefore, an (over-) underestimation of the lens redshift will increase (decrease) D_{ls} and translate into an (over-) underestimation of its mass. According to our methodology for deriving $\langle D_{ls}/D_s \rangle$, two effects are added here when changing the redshift of the lens: the variation in the distance D_{ls} , and the value of the contamination level, i.e. the number of galaxies in the D1 catalogue matching the selection criteria of lensed galaxies and having $z_{\text{phot}} < z_{\text{lens}}$. Since both effects have a strength that depends on the lens redshift, we tested the procedure described above in three different cases, for a low-redshift group (SA48, $z_{\text{spec}} = 0.24$), one at the peak of the SARCS sample $n(z)$ (SA50, $z_{\text{spec}} = 0.51$), and one at high redshift (SA123, $z_{\text{phot}} = 1.00$). For each group, we derived the average geometrical factor corresponding to different shifts in the lens redshift around its original value, and the results are presented in Fig. 3. As we can see in this plot, for a given variation Δz_s , the change in $\langle D_{ls}/D_s \rangle$ is greater for a lens with a higher redshift. However, the main variation occurs from low to medium redshifts, because the variations observed for SA50 ($z = 0.51$) and SA123 ($z = 1.00$) are very similar. For a typical z_{phot} uncertainty of $\Delta z_s = \pm 0.1$, we would get an error of 20%–30% on the geometrical factor, hence a mass over-/under-estimation of the same amount. Assuming that the z_{phot} for most of the SARCS lenses is accurate up to this 0.1 precision, the precise knowledge of z_s introduces a lower error than the statistical one (quoted in Table 2) owing to the dispersion of the galaxy intrinsic ellipticities. As detailed below, we used for the weak-lensing analysis the singular isothermal sphere mass model, which has a shear function $\gamma \propto (D_{ls}/D_s) \times \sigma_v^2$. In that case, a variation less

⁶ http://www.ast.obs-mip.fr/users/rosfer/CFHTLS_T0004/

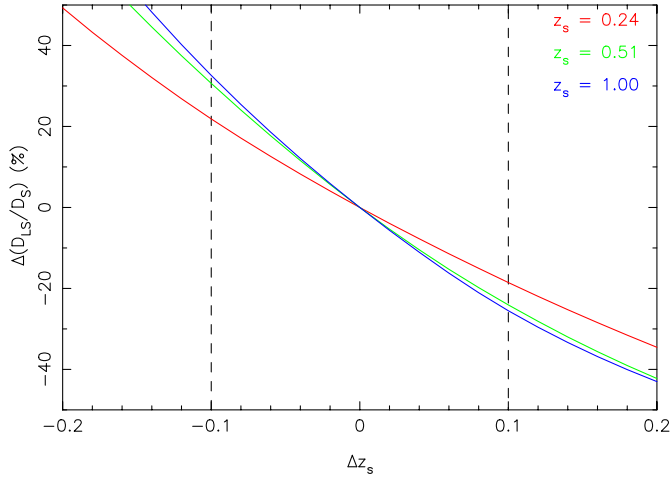


Fig. 3. Variation in the average geometrical factor $\langle D_{ls}/D_s \rangle$ as a function of the shift around the true lens redshift for three groups, SA48 (red curve), SA50 (green curve), and SA123 (blue curve). The two vertical dashed lines mark the typical ± 0.1 uncertainty of photometric redshifts.

than 30% in D_{ls}/D_s induces a change less than 20% in the velocity dispersion σ_v . Therefore, the intrinsic ellipticity dispersion remains the principal limitation in our weak-lensing analysis. However, in specific cases with larger Δz_s , we obtain a significant bias. For instance, SA48 has $z_{\text{phot}} = 0.52$, and $z_{\text{spec}} = 0.24$, so a geometrical factor underestimated by $\sim 40\%$. Using the photometric value to fit the shear profile would have led in that case to a velocity dispersion $\sigma_v^{\text{phot}} = \sqrt{1/0.6} \times \sigma_v^{\text{spec}}$, i.e. $\sim 30\%$ more than the value derived with the spectroscopic redshift.

3.2. Choice of the centre

To construct a shear profile, one needs to specify its centre, which should correspond to the centre of the mass distribution. With enough constraints, its position can be considered as a free parameter of the mass model that is fitted during the weak-lensing analysis. It is also possible to use 2D pixelized mass reconstructions and to associate the highest projected density peak to the mass centre. However, since we are dealing mainly with group-scale dark matter haloes here, the shear signal is not strong enough to do that. A few attempts to fit both the mass profile and the centre (using the LENSTOOL code, Kneib et al. 1996; Jullo et al. 2007) have shown in some cases that no robust constraint can be obtained from the weak-lensing signal we have. We also tried to reconstruct 2D mass maps, but in most cases they were too noisy to derive the location of the mass centre. Moreover, Dietrich et al. (2012) have shown from a set of ground-based simulated data that, on 2D mass distributions derived from weak lensing, shifts between the real centre and the reconstructed one have a median value of $1'$, therefore seriously limiting the use of this method to derive a reliable position of the mass centre.

By its definition, the SARCS sample has the advantage of giving an idea where the highest density regions are located. The SARCS lens candidates are indeed detected by a strong-lensing feature with an arc radius that corresponds to a strong-lensing event by a group-scale halo. The selection threshold of $RA \gtrsim 2''$ limits the presence in the sample of strong-lensing events by a galaxy-scale halo enhanced by a group-scale halo, see e.g. Limousin et al. (2009). Thus we can assume that the strong-lensing system is a good indicator of the position of the

actual mass centre as a high enough mass density is required, i.e. $\kappa \gtrsim 1$. However, we expect that this assumption might be wrong in some cases where the lens is not a regular and isolated dark matter halo but rather presents a complex morphology. For instance, Limousin et al. (2010b) showed that the SARCS lens SA66 (SL2S J08544-0121 in their paper) is a clear bimodal object spectroscopically confirmed by Muñoz et al. (2013), for which the mass centre is not associated to the centre of the strong-lensing system. As shown in Sect. 4.2, there is a non-negligible number ($\sim 15\%$) of such complex and multi-modal systems in the SARCS sample.

The other option usually taken when no gravitational arcs unambiguously identify the centre of the halo consists of assuming that the brightest galaxy in the dark matter halo lies in the centre of its mass distribution. The models of formation of large cD galaxies, such as infall and merging of galaxies on the central one (Ostriker & Tremaine 1975; Hausman & Ostriker 1978) or accretion of the intra cluster gas due to the cooling flow in the centre of the gravitational potential well (Cowie & Binney 1977), predict that such objects are indeed found in the centre of their host halo. This hypothesis is also supported by observational results where the cD galaxy is found in the kinematical centre (e.g. Quintana & Lawrie 1982). However, the brightest galaxy is not always at rest in the gravitational potential well, but rather a large elliptical galaxy that is not necessarily located at the centre of the mass distribution. For instance, Jeltema et al. 2007 have studied a sample of seven X-ray-loud galaxy groups at intermediate redshifts ($0.2 < z < 0.6$), and for two of them, the brightest galaxy presents an offset $\sim 100 h_{70}^{-1}$ kpc with the X-ray emission peak. They also found two groups where no dominant elliptical galaxy is present, but rather several ones with comparable luminosities (see also the more recent work by George et al. 2012, of the COSMOS X-ray-selected groups). In such cases, the assumption of tracing the mass centre by the position of the most luminous galaxy might be wrong as well. This problem, sometimes referred to the central galaxy paradigm (e.g. Skibba et al. 2011, for a review), is clearly a limitation to building an accurate shear profile from the position of the brightest member in a halo. In our case, it seems wiser to use the strong-lensing system to trace the position of the mass centre, and we use it for all objects in the sample, even if the lens galaxy is not the brightest one in the halo. In some cases, the strong lensing-system is indeed associated to a satellite galaxy; we discuss the impact of using the strong lensing-system as centre instead of the brightest galaxy for such groups in the Appendix.

Finally, it is worth mentioning that the mass underestimation due to small miscenterings can be limited simply by not using the central parts of the shear profiles in the fitting process (Mandelbaum et al. 2010). Because we start to fit the profiles at 100 kpc, we therefore avoid any possible underestimations in most cases.

3.3. Results

Observed shear profiles are fitted using the singular isothermal sphere model (SIS hereafter), which describes the mass density of a relaxed massive sphere characterized by a constant velocity dispersion σ_v . The lensing functions are written as $\gamma(r) = \kappa(r) = R_E/2r$, where $\gamma(r)$ is the shear, $\kappa(r)$ the dimensionless projected mass density, and r the projected distance to the lens centre. The Einstein radius scales as $R_E \propto (D_{ls}/D_s)\sigma_v^2$. The (one-dimensional) velocity dispersion σ_v is used as the free parameter to fit the SIS model and not the Einstein radius, since it requires an estimate of the source redshift. As mentioned previously, the

signal-to-noise ratios that we measure are in most cases too low to get reliable information on the properties of the mass distribution, so we did not try to fit, for instance, the widely used NFW model (Navarro et al. 1997, 2004), thus avoiding poorly constrained results. We emphasize that the SIS model is only employed to derive a raw mass estimate and not to probe the shape of the mass profiles. As shown by Oguri (2006) (see also More et al. 2012), the range of image separations probed by the SARCS sample corresponds to lensing events produced by a mix of SIS (low-mass end) and NFW (high-mass end) haloes. Most of the SARCS candidates are supposed to be galaxy groups, and they present an arc radius compatible with a SIS lens. We therefore introduce a bias due to the SIS modelling in our weak-lensing analysis only for the few massive galaxy clusters in the sample. But even in these cases, given the large statistical noise we have on the lensing measurements, the SIS approximation does not result in significant variations in the total mass. An alternative would have been to stack the objects and increase the quality of the signal, as done for instance in Mandelbaum et al. (2006), Johnston et al. (2007), Leauthaud et al. (2010), Okabe et al. (2010), and Oguri et al. (2012). However, we are more interested here in the weak-lensing detection of each SARCS objects rather than a precise analysis of the mass distribution on the group scale, which could also be achieved with a combination of the weak-lensing signal on a large scale with a strong-lensing modelling of the central mass distribution and a dynamical analysis of the group members (e.g. Verdugo et al. 2011). The stacking analysis of this sample and the characterization of the mass profile will be presented in Paper II.

On the other hand, the SIS model gives results that can easily be compared to other methods to estimate the mass such as dynamical analysis (e.g. Muñoz et al. 2013). Moreover, in the case of the SARCS sample, it is straightforward to compare the weak lensing Einstein radius to the observed arc radius R_A , which is equivalent to the actual Einstein radius for axisymmetric lenses. Values are given in Table 2, where the weak lensing σ_{SIS} are converted in $R_E(z_s, \sigma_{\text{SIS}})$ with a source redshift z_s derived from the redshift distribution of More et al. (2011) with the CFHTLS T0006 release i -band limiting magnitude $m_{\text{lim}} = 24.48$. For some objects, the difference between R_A and R_E is significant, suggesting either an inaccurate weak lensing estimation or a complicated mass distribution of the lens that affects the $R_A - R_E$ relation (strong lensing associated to a satellite galaxy, large ellipticity/asymmetry of the lens, substructures, etc). A deeper study of some of these cases using strong-lensing modelling will be presented in Verdugo et al. (in prep.).

From this systematic analysis of the whole SARCS sample, we obtained constraints at the 1σ level on the SIS velocity dispersion for 89 candidates ($\sim 71\%$ of the sample). In the rest of the paper, we call these objects *weak-lensing detections*. For the remaining objects, the fit of the shear profile only returns an upper limit on σ_v , and we will not use them in the rest of the analysis (objects labelled further as *non-detected*). Using a 3σ level cut to select the weak-lensing detections leads to a sample of 75 objects. However, the goal here is not to select the most secure lenses but rather to remove the most likely false detections. We checked, for instance, that some of the objects having a detection level between 1σ and 3σ present an obvious optical luminosity over-density on the luminosity map (Sect. 4.2), along with a clear strong-lensing system. That is why we chose here a rather loose selection criterion to be combined in Sect. 5.1 with the optical selection criterion. To calibrate the scaling relations in Sect. 5.3 we do, however, use only objects with a 3σ weak-lensing detection level.

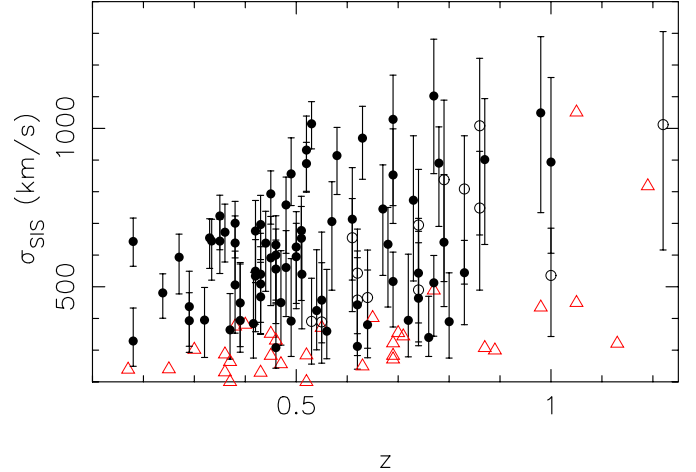


Fig. 4. Velocity dispersion derived from the fit of the shear profile using the SIS model. Red open triangles show the upper limit on σ_v for those objects not having a 1σ weak-lensing detection. Open circles are candidates with a weak-lensing detection less than 3σ , filled circles are those having a reliable detection (above 3σ).

The distribution of the SARCS candidates in the $z - \sigma_v$ plane is shown in Fig. 4. The average velocity dispersion of the 89 weak-lensing detections is $\langle \sigma_v \rangle = 618 \pm 197 \text{ km s}^{-1}$, corresponding to a rich group or a poor cluster, depending on where the boundary between the two regimes is drawn. From Fig. 4, we see that the distribution $\sigma_v(z)$ is fairly homogeneous over the redshift range. We detect, however, more massive objects above $z = 0.5$. From a weak-lensing analysis it is expected because for a source at a given redshift, the lensing strength decreases for lenses at higher redshifts. Therefore it is normal to observe a higher fraction of more massive systems at higher redshifts. We also see in Fig. 4 that these high-redshift objects present larger error bars on the velocity dispersion, owing to the lower density of available background galaxies to measure the shear signal. It is interesting to notice that we do not observe a strong trend between the non-detected objects and their redshift. This lack of correlation suggests that the intrinsic quality of the ground-based optical images (seeing, pixel size) that we used is the main limitation to detecting low-mass objects, rather than the noise induced by lower densities of background galaxies.

Finally, it is worth mentioning that at the low-mass end of the sample, the shear signal is weak enough to be close to the noise level. As a result, our weak-lensing measurements for such objects have to be taken with caution. We emphasize here that we are more interested in detecting of the objects rather than in getting accurate mass estimates. On the group scale, we probably lose some real lenses and also have some false detections or galaxy-scale systems among our 89 objects. The cross-checking with the optical properties (Sect. 5.1) shows, for instance, that some of the weak-lensing detections have no optical counterpart, corresponding to those cases where our lensing procedure fits noise.

Looking in more detail at the properties of these non-detections, it appears first of all that they mainly correspond to SARCS candidates with a small arc radius. We indeed have 29 objects with $R_A < 4''$, i.e. $\sim 78\%$ of the non-detections. The whole SARCS sample contains 88 objects with $R_A < 4''$ ($\sim 70\%$ of the sample), a slightly lower value that simply reflects that less massive objects (i.e. with smaller arc radius) are more difficult to detect via weak lensing. We only have two candidates not detected in weak lensing with $R_A > 5''$, one of them having

a large arc radius, SA104 with $R_A = 11.7''$ ($z_{\text{phot}} = 0.15$). This object (rank 2 in [More et al. 2012](#)) shows a single very large elliptical galaxy without any obvious companion around. Given the arc radius of $\sim 12''$, this object should have much more members because it would correspond to a poor cluster. We then can safely consider this object as a false detection in the SARCS sample. The other object is SA41 ($R_A = 6.1''$, $z_{\text{phot}} = 0.52$). This object presents a bimodal light distribution. A wrong choice of the centre to compute the shear profile could be the reason for the weak-lensing non-detection. However, using a different centre does not improve the constraints (see Appendix).

Among the 37 non-detections, we have 25 candidates with a rank less than 3, i.e. $\sim 68\%$. This value is slightly higher than the ratio obtained for the entire sample, which contains $\sim 57\%$ of such low-ranked candidates. It suggests that the threshold rank ≥ 2 used to build the initial SARCS sample is not strong enough to prevent keeping false detections. In Sect. 5.1, we discuss the properties of the most secure candidates in terms of the initial selection parameters (rank and arc radius).

Besides those systems falsely identified as strong lenses, one can think of several hypotheses to explain why objects with a small arc radius are not detected with the weak lensing method. First, these strong lensing features are most likely produced by less massive systems (or even galaxy-scale haloes), which do not produce a weak-lensing signal strong enough to be detected with ground-based data. Second, a star field that is too sparse to properly sample the PSF across the field-of-view can reduce the quality of the galaxy shape estimation, hence introducing more noise into the signal. On the other hand, a field with too many large diffracted stars has a smaller effective area to measure the shear signal, which can bias the weak-lensing analysis. Third, the intrinsic mass distribution of the lens might as well be a strong factor of noise in the measured shear signal. We indeed use the simplest weak-lensing analysis that assumes circular symmetry. In the case of highly elliptical mass distributions, such an approximation can result in a significant underestimation of the shear. It can also generate apparent small arc radius, which are not representative of the total mass of the halo, thus explaining why we have weak-lensing detections for some candidates with small R_A . For multi-modal systems, the question of the centre and the fit to a single halo might also bias the mass determination. In the Appendix, we present some results for such complex systems, along with some cases where the strong-lensing system is not associated to the brightest galaxy in the halo but to a satellite galaxy. We emphasize here all these possible reasons just to recall that a weak-lensing detection is sufficient but not necessary to conclude that we are observing a massive halo.

3.4. Comparison with previous mass measurements

Several SARCS groups have been already analysed using different data sets and methodologies:

- Weak lensing: with the CFHTLS T0004 release, [Limousin et al. \(2009\)](#) derived weak lensing constraints on σ_{SIS} only for five groups of their sample of 12 objects. With these five objects, we find an average ratio $\langle \sigma_{\text{WL}} / \sigma_{\text{SIS}} \rangle = 0.93 \pm 0.10$ (where σ_{SIS} are the velocity dispersions derived in this work and σ_{WL} those from [Limousin et al. 2009](#)). There is only one group in the sample of [Limousin et al. \(2009\)](#) for which we did not get a weak-lensing detection, SA122 ($z_{\text{phot}} = 0.69$, $R_A = 2.8$, rank = 3.0) and for which [Limousin et al. \(2009\)](#) only obtained an upper limit on σ_{SIS} .

- Strong lensing: eight objects were analysed by [Limousin et al. \(2009\)](#) using the CFHTLS ground-based images, and four new groups have been studied with HST data ([Verdugo et al.](#), in prep.). To compare the results of [Limousin et al. \(2009\)](#) to ours, we have converted their Einstein radius into σ_{SL} assuming the source redshift given in Table 2. With these 8 + 4 groups, we obtain an average ratio $\langle \sigma_{\text{SL}} / \sigma_{\text{SIS}} \rangle = 0.92 \pm 0.25$.
- Dynamical analysis: seven objects have been studied by [Muñoz et al. \(2013\)](#) using VLT/FORS2 spectra. Here we obtain an average ratio of $\langle \sigma_{\text{dyn.}} / \sigma_{\text{SIS}} \rangle = 0.61 \pm 0.25$.

Even though our weak lensing methodology follows that of [Limousin et al. \(2009\)](#) closely (same procedure for selecting the lensed galaxies and estimating their shape parameters, same normalization of the shear profiles), we managed to measure σ_{SIS} for 11 of their sample of 12 groups, while they obtained constraints only for five of them. We attribute this increased number of detection to our statistical analysis of the shear signal. On the other hand, the results we have are very similar with a ratio of ~ 0.9 and a small scatter of 10%. Our velocity dispersions are also compatible on average with the values derived from the strong-lensing analysis of [Limousin et al. \(2009\)](#) and [Verdugo et al. \(in prep.\)](#), again with a ratio of ~ 0.9 , but with a larger scatter of $\sim 25\%$. This seems to indicate that these groups do not present very high ellipticity with a major axis aligned along the line-of-sight or, equivalently, a high concentration that could artificially enhance the measured mass when extrapolating the strong-lensing constraints to the larger scales probed with weak-lensing signal.

The comparison of our measurement with the dynamical velocity dispersions derived by [Muñoz et al. \(2013\)](#) is more puzzling. We obtain indeed a ratio of ~ 0.6 with a scatter of $\sim 25\%$. Among the seven groups, six have a dynamical velocity dispersion that is smaller than the weak lensing one. Only one group, SA72, has $\sigma_{\text{dyn}} > \sigma_{\text{WL}}$, with compatible values at the 1σ level given the high uncertainty on σ_{dyn} . [Muñoz et al. \(2013\)](#) argue that one reason of such a discrepancy could arise from the choice of the SIS model to characterize the actual mass distribution of the groups. With numerical simulations, they also show that mass estimates derived from the velocity dispersion of galaxies in a halo can be underestimated up to 20%. This is, however, not enough to explain the discrepancies observed here. Another possibility to account for the differences between the lensing and dynamical results would be the presence of massive structures along the line of sight. Because the weak-lensing signal is produced by all the projected matter between the lensed galaxies and the observer, groups and clusters of galaxies or even large-scale structures can affect the shear signal and induce an overestimation of the mass. Using the Millennium simulation, [Hoekstra et al. \(2011\)](#) find that randomly positioned massive structures do not statistically bias the weak-lensing mass estimate of a galaxy cluster but instead increase its uncertainty, with values comparable to those owing to the intrinsic dispersion of the galaxies ellipticity. Most of the overestimated masses they obtained have an excess less than 20%, but going up to a factor ~ 2 for some objects. Such projection effects could therefore explain the higher weak-lensing masses we have. We can also invoke a poor lensing signal-to-noise ratio from which the weak-lensing analysis can return biased masses. Because the objects analysed by [Muñoz et al. \(2013\)](#) are mostly low-mass groups with $\sigma_{\text{dyn}} < 500 \text{ km s}^{-1}$, they indeed do not produce a strong shear signal, possibly leading to wrong estimates. However, we observe a similar discrepancy for all objects, which suggests that

this systematic difference in the velocity dispersions is due to the methodologies employed, rather than to the groups properties or poor constraints. In fact, the estimation of galaxy groups and clusters' velocity dispersion is known to be biased low by several effects (see e.g. [Biviano et al. 2006](#), and references therein), such as the inclusion of interlopers (i.e. infalling galaxies along filaments), the rejection of high-velocity galaxy members, presence of substructures, or the so-called velocity-bias (i.e. different velocity dispersions between galaxies and the dark matter). We are currently increasing the number of groups analysed via the dynamical methodology, and we will explore the discrepancy between the lensing and dynamical estimate of the groups velocity dispersion in more detail ([Motta et al.](#), in prep.).

4. Optical properties

Although the weak-lensing results suggest that some of the SARCS candidates are galaxy-scale lenses or false detections, we did the optical analysis for all objects in the sample. We therefore intend to make a cross-correlation of the two analyses to derive a sample of the most bona fide SARCS groups candidates used to constrain the optical scaling relations.

4.1. Richness and optical luminosity

We derived the optical properties of the SARCS lens candidates from the bright galaxies that belong to the red sequence. Because most of the SARCS objects are groups with few galaxies, we did not attempt to fit this red sequence as usually done when dealing with rich galaxy clusters. We used the same criteria for all the candidates and defined the red sequence as the region in the colour-magnitude diagram where galaxies have a $r' - i'$ colour close to that of the lens galaxy, i.e. the one at the centre of the strong-lensing system. In the cases where this lens galaxy is not the brightest one but rather a satellite galaxy, we used the colour of the former to define the red sequence. To account for the expected slope of the red sequence (e.g. [Stott et al. 2009](#)), we chose asymmetric limits and selected galaxies with $(r' - i')_{\text{lens}} - 0.2 < r' - i' < (r' - i')_{\text{lens}} + 0.15$. As said previously, the galaxy at the centre of the strong-lensing system is not necessarily the brightest one, so its colour $(r' - i')_{\text{lens}}$ can be slightly different from that of the brightest member, which is usually taken as reference; however, it gives a robust estimator of the group members colour, since by definition, it belongs to the group. Because the colours are derived from magnitudes estimated in a fixed aperture of $3''$, this $(r' - i')_{\text{lens}}$ colour tends to be underestimated for systems presenting an arc radius $R_A \leq 3''$ where the lens galaxy is close to the strong lensing feature (a blue arc in most cases). For these objects, we used the average colour of the surrounding bright galaxies that are most likely part of the system.

We restricted the red sequence to an absolute magnitude $M_r = -21$. In doing so, we roughly probed a constant fraction of the luminosity function, which allows direct comparison from group to group regardless of their redshift. Focussing on the brightest galaxies also avoids the fall out of the completeness magnitude of the CFHTLS observations for groups at high redshifts.

In [Limousin et al. \(2009\)](#), the group members were visually selected and no background correction was applied. Here, since we adopt an automated approach for all objects, we also have to account for the contamination by field galaxies. We determined the density of galaxies falling in the definition of the

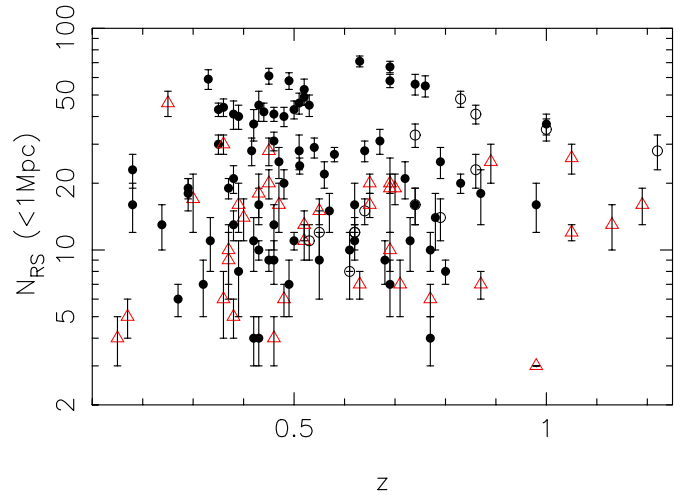


Fig. 5. Richnesses estimated within 1 Mpc using the bright red galaxies of the 126 SARCS candidates. Open red triangles are objects without a 1σ weak-lensing detection, open circles have a detection between 1 and 3σ , filled circles are those with a detection above 3σ .

red sequence of each group in a reference field. To keep it simple, we used the 1 deg^2 image of the field where the group was found (for systems in the WIDE part of the CFHTLS survey, we only used the central pointing as reference). To get a rough estimate of the fluctuations due to local over-/under-densities in the distribution of field galaxies, we computed the background density in 1000 circular patches randomly positioned in the reference field. The size of these patches is chosen to match the area where group members are counted, i.e. within a projected radius of 0.5 and 1 Mpc from the central galaxy. We chose to compute the optical properties within two different radius in order to test its influence on the calibration of the scaling relations.

To reduce the impact of overestimating the local density of field galaxies, which can lead to a negative number of galaxies for poor groups (as well as for systems falsely identified as a group), we divided the area where galaxies are counted into concentric annuli. The background subtraction was done in each of these annuli, and we finally took the sum of only the positive counts excesses. The richnesses we derived (i.e. the number of galaxies within our selection criteria) are the average of these sums over the 1000 values of the background densities. The scatter around this average gives a rough estimate of the corresponding statistical error. We did the same to compute the optical luminosities accounting for both the k -correction and the passive evolution of an elliptical galaxy (values derived from the synthetic SED model of [Bruzual & Charlot 2003](#)). For consistency, we applied this method to all the SARCS candidates, regardless of whether they are false detections, poor groups, or poor clusters for which a usual background subtraction works fine. The distribution of richnesses and optical luminosities for the SARCS objects are given in Figs. 5 and 6. Within an aperture of 1 Mpc around the centre of the strong-lensing system and cutting the luminosity function at $M_r = -21$, the sample covers richnesses up to 70 galaxies and luminosities up to $\sim 6 \times 10^{12} L_\odot$. Both distributions are roughly homogeneous in redshift, and are dominated by group-scale objects with $N \sim 5\text{--}20$ and $L \sim 0.5\text{--}1.5 \times 10^{12} L_\odot$.

We chose to derive the optical properties of the SARCS candidates from the galaxies within their red sequence. These galaxies are indeed easier to detect and select (stronger contrast with the population of field galaxies), and most of studies about the

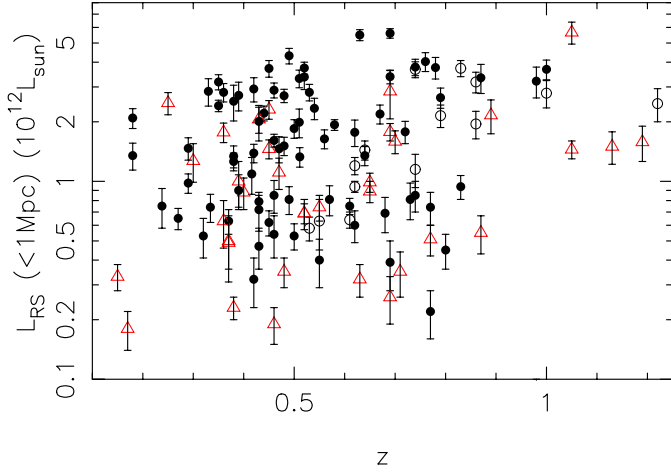


Fig. 6. Same as Fig. 5 for the optical i' -band luminosities estimated within 1 Mpc using the bright red galaxies of the 126 SARCS candidates.

optical scaling relations make use of this specific population of early-type galaxies. However, we would like to emphasize here that such a selection can introduce some systematics into the analysis. It has indeed been observed that at higher redshifts, groups and clusters contain a greater portion of blue star-forming late-type galaxies (Butcher & Oemler 1984; Ellingson et al. 2001; Lubin et al. 2002), with, on the other hand, a smaller fraction of red passive early-type galaxies (Smail et al. 1998; Kodama et al. 2004; De Lucia et al. 2007). This evolution of the red sequence, where the blue spirals evolve into red elliptical galaxies with a transient state of green galaxies (Balogh et al. 2011b), naturally introduces a bias into our galaxy selection as a function redshift since we used a fixed broad red sequence for all objects. Another possible source of systematics in the estimation of richnesses and optical luminosities is the actual fraction of the galaxy population that inhabit the red sequence. For instance, Zabludoff & Mulchaey (1998) have studied a sample of 12 nearby poor galaxy groups and found significant variations (up to a factor 2) in the fraction of early-type galaxies. Similar variations in the galaxy population from group to group have been obtained by Jeltema et al. (2007) at intermediate redshifts. Therefore, we do not probe the same fraction of group members for each object in our sample. However, given the relatively large size of the SARCS sample and its broad redshift range, we expect to average such effects (intrinsic variations and redshift evolution), so we did not attempt to correct them or to include the green and blue galaxies in the analysis.

4.2. Morphological classification

From the catalogues of galaxies falling in the red sequence (to get more galaxies and less statistical noise when drawing the luminosity contours, we pushed the limiting magnitude to $M_{i'} = -20$ instead of -21), we computed luminosity maps following Limousin et al. (2009). The $15' \times 15'$ field-of-view around the lens is divided into cells of 20×20 pixels. From the centre of each of these cells (the pixels of the luminosity maps), we looked for the five nearest galaxies belonging to the red sequence, a low enough value to avoid oversampling. The luminosity density of the corresponding pixel is simply the sum of the luminosity of these five galaxies divided by the circular surface covered by the farthest one. The maps of the luminosity density are then

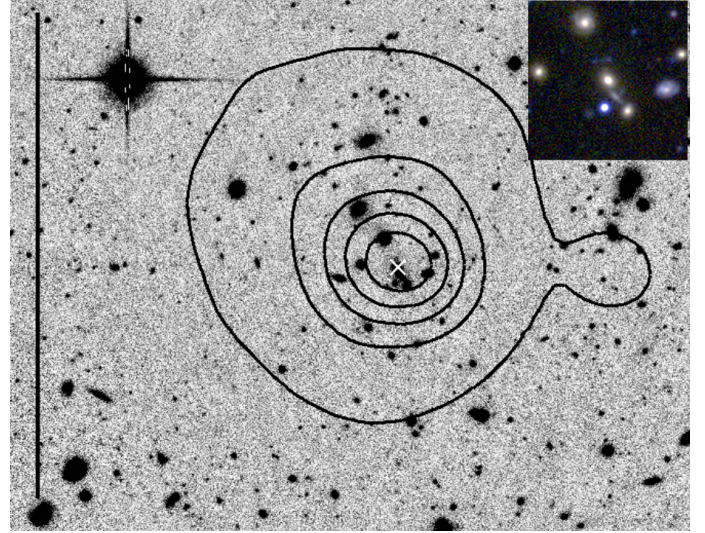


Fig. 7. Luminosity density contours (in black) for SA15 equal to 10^6 , 4×10^6 , 7×10^6 , 10^7 , and $1.3 \times 10^7 L_{\odot} \text{ kpc}^{-2}$. The white cross marks the galaxy at the centre of the strong-lensing system. The black vertical line on the left is 1 Mpc long. SA15 is at $z = 0.44$. The stamp in the top-right corner shows a $30'' \times 30''$ colour image of the system.

smoothed by a Gaussian kernel with an FWHM of seven pixels ($\sim 25''$). We checked that the shape of the resulting maps are weakly dependent on the pixel size or the smoothing width.

As stated previously, we did not clean the catalogues of the red galaxy members from field galaxies. The maps therefore suffer from the background contamination, but we can assume it to be roughly homogenous across the field, thus not leading to strong shape distortions of the group/cluster itself. However, this can be wrong for groups with low numbers of galaxies in the red sequence. Despite our adaptive smoothing, the classification between a regular or elongated object can indeed be affected by statistical noise due to local variations in the density of field galaxies. On the other hand, because of the large width of the red sequence we used, we expect to pick up over-densities of galaxies that are not necessarily linked to the initial target (i.e. not a multi-modal object). In fact, this can be used as a tool to trace the cosmic web and reveal large-scale structures around galaxy groups (Cabanac et al., in prep.).

Once the maps were built, we visually inspected them to assess the luminous morphology of the SARCS objects according to the shape of the luminosity contours, whose levels were adapted for each object. However, we checked that the value chosen for the innermost luminosity contour does not influence the occurrence of high-luminosity peaks, i.e. the multi-modal groups definition. We sorted the groups according to their morphology in four classes:

- false detection or galaxy-scale strong lensing feature (i.e. no clear over-density in the map) \rightarrow 30 objects;
- regular (i.e. roughly circular isophotes around the strong-lensing system) \rightarrow 39 objects;
- elongated (i.e. elliptical isophotes with a roughly constant position angle from inner to outer parts) \rightarrow 40 objects;
- multi-modal (i.e. 2 or more peaks in the central part of the map) \rightarrow 17 objects.

Figures 7–9 present the luminosity map for a regular group (SA15), an elongated group (SA2), and a bimodal group (SA90). Multimodal class refers here only to two or more peaks in the

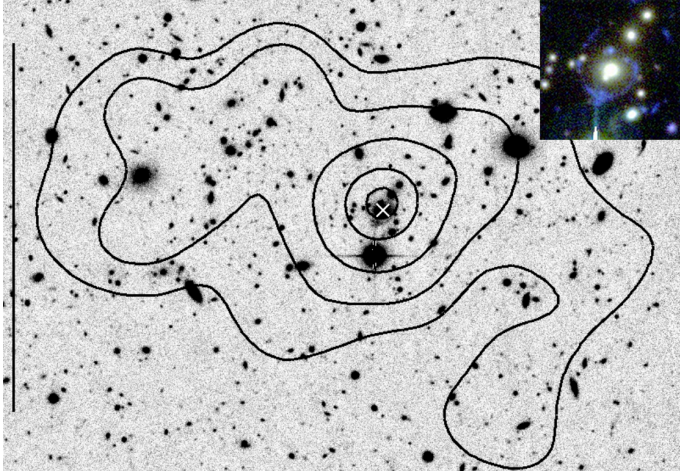


Fig. 8. Luminosity density contours (in black) for SA2 equal to 2×10^6 , 4×10^6 , 7×10^6 , 1.5×10^7 , and $2 \times 10^7 L_{\odot} \text{ kpc}^{-2}$. The white cross marks the galaxy at the centre of the strong-lensing system. The black vertical line on the left is 1 Mpc long. SA2 is at $z = 0.48$. The stamp in the top-right corner shows a $30'' \times 30''$ colour image of the system.

luminosity map found within a 0.5 Mpc radius of the strong-lensing system. Extending this limit to a larger radius would increase the number of objects in this class, e.g. 23 members if we look up to 1 Mpc from the centre. However, in these cases we are most likely observing two distinct objects (or an ongoing merging event) rather than a single halo since, given the mass range of these groups, the virial radius is expected to be $\lesssim 1$ Mpc (see e.g. Muñoz et al. 2013). We look for a trend between the morphological class and the redshift or mass of the objects in Sect. 5.1, after defining the final sample of the best candidates.

From this qualitative morphological classification, it appears that the main part of the SARCS candidates are groups or poor clusters with irregular shapes, either elongated or more complex, i.e. $(40 + 17)/96 \sim 60\%$ of the optically detected lenses. This suggests that groups of galaxies are mostly in a young dynamical state. In the context of the large-scale structure formation and evolution, this is somehow expected since groups are continuously forming and merging into more massive clusters (e.g. Evrard 1990; Bekki 1999). Paper II will present a more quantitative analysis of the groups morphology, along with studying correlations to the groups' environment.

5. Combining the weak lensing and optical analyses

5.1. Selection of the most secure candidates

As mentioned in Sect. 2.2, the thresholds applied to the algorithm were chosen to favour completeness over purity. Despite the visual ranking performed by three different persons, the final SARCS sample still contains galaxy-scale lenses and even some false detections. Both the weak-lensing and the optical analyses have indeed shown that some objects do not reach our criteria for selection as a group-scale lens.

From the weak-lensing analysis, we end up with a reduced sample of 89 objects with a weak-lensing detection. The rejected objects are either false detections, not massive enough haloes (very poor groups or galaxy-scale lenses) or objects with shear signal that is too noisy to derive a secure SIS velocity dispersion (sparse data, morphology too complex for a simple spherical mass model, etc.). As said in Sect. 3.3, they present more

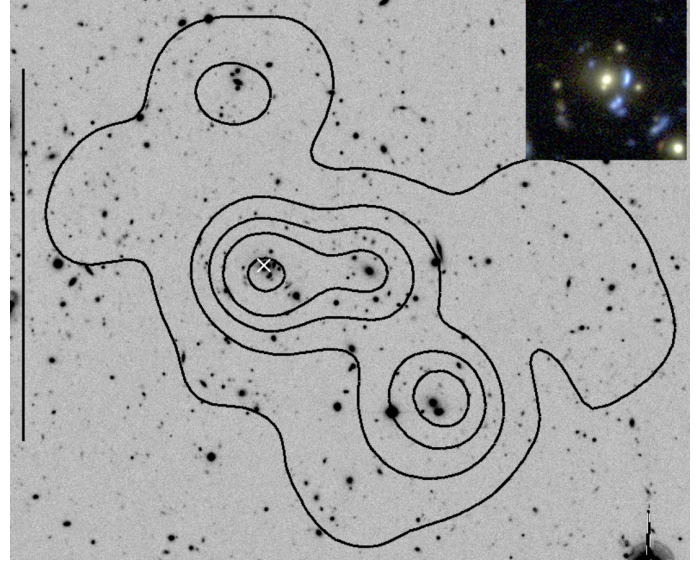


Fig. 9. Luminosity density contours (in black) for SA90 equal to 1.5×10^6 , 4×10^6 , 7×10^6 , 10^7 , and $1.5 \times 10^7 L_{\odot} \text{ kpc}^{-2}$. The white cross marks the galaxy at the centre of the strong-lensing system. The black vertical line on the left is 1 Mpc long. SA90 is at $z = 0.53$. The stamp in the top-right corner shows a $30'' \times 30''$ colour image of the system.

low-ranked objects with smaller arc radius R_A than in the total sample.

From visual inspection of the colour images and the luminosity maps, the initial SARCS sample got reduced to 96 objects among which 39 present regular isophotes, 40 elongated ones, and 17 have a multi-modal configuration. Here, we rejected all the candidates for which we do not observe a clear over-density of light associated to the strong-lensing system, i.e. objects where the lensing feature is in a poor environment without evidence of a population of galaxies with similar colours. As for the weak lensing selection, this optical selection mainly rejects SARCS candidates with a small arc radius, i.e. probably galaxy-scale objects or very poor group lenses. Only four rejections are associated to arc radius $R_A > 3''$ and most likely correspond to false detections, e.g. edge-on spiral galaxies.

While the optical selection removes 30 objects, the weak lensing selection rejects 37 candidates, so a similar number of possible lenses. Interestingly, the two methods have 21 rejected candidates in common, which are most certainly not group-scale lenses and can be securely removed from the final sample. On the other hand, we have 16 candidates not detected in weak lensing but flagged as probable groups from their luminosity maps. Among them, only four objects have regular isophotes, which suggests that we do not measure a good enough shear signal because of the complex morphology of the mass distribution (multi-modal or highly elliptical). We also have nine objects for which we managed to put constraints on σ_{SIS} , but which do not have an obvious optical counterpart (our richness estimator gives for all of them a null or negative value). We visually inspected these *dark lenses*, and for four of them we found a significant galaxy concentration less than $5'$ away from the supposed strong-lensing system. In these cases, the shear signal that we measured is most likely due to a close (in projection) massive structure not associated to the SARCS candidate. In two other cases, the PSF map derived from the field of stars shown an irregular pattern that might generate a false shear signal. For the three remaining objects, we could not find any obvious explanation for the measured shear signal given that the optical images

clearly show the absence of a galaxy concentrations around the SARCS candidate.

Finally, the combination of our selection criteria leads to a sample of 80 lenses ranging from group- to cluster-scale haloes. Their weak-lensing and optical properties are given in Table 2. In terms of the morphological distribution of this sample of most secure lenses, we have 34 objects with regular isophotes ($\sim 42\%$), 33 with elongated/elliptical ones ($\sim 42\%$), and 13 multi-modal groups ($\sim 16\%$) with a second luminosity peak closer than 0.5 Mpc to the strong-lensing system. The different ratios are roughly similar to those obtained for the 96 candidates having a clear optical detection, and our final sample still contains a large proportion of objects with an irregular light distribution ($\sim 57\%$). The average velocity dispersions in each morphological class are all compatible within their 1σ statistical scatter since we obtain $592 \pm 175 \text{ km s}^{-1}$ for the regular groups, $589 \pm 201 \text{ km s}^{-1}$ for the elongated ones, and $716 \pm 147 \text{ km s}^{-1}$ for the multi-modal, i.e. a slightly higher value. We also looked for any redshift trend, but the three classes have a very similar average redshift.

The initial sample has $\sim 70\%$ of objects with $R_A < 4''$ (observed R_A , not derived from σ_{SIS}) and $\sim 57\%$ objects ranked less than 3, which is the threshold used in More et al. (2012) to define the most promising candidates. In our final sample we obtain percentages of $\sim 63\%$ and $\sim 49\%$: our optical and lensing criteria result in a sample with a higher proportion of promising candidates (based only on the visual inspection of the strong lensing features) and with larger arc radius. If we assume that the best group- and cluster-scale lens candidates can be defined a priori as those having both a rank ≥ 3 and $R_A \geq 4''$, then our final sample contains 18/20 of the best candidates in the initial SARCS sample, which suggests that these two criteria are fairly robust to be able selecting such real lenses on the group scale.

To reduce the impact of unreliable measurements, we only keep the objects with a 3σ weak-lensing detection to fit the scaling relation. This subsample of the most secure candidates according to our combined weak-lensing and optical analysis contains 67 objects. In doing so, we lose some objects at high redshifts, without improving the dispersion in richness or optical luminosity (see Figs. 4–6). Because we have 14 objects (13 with an optical confirmation, among which 2 have a spectroscopic confirmation and a strong lensing model) with a weak-lensing detection level between 1 and 3σ , we lose $\sim 16\%$ of the 80 lenses' subsample defined here. Therefore, this sample with a larger statistic, especially at high redshift, will be used in other works to study the population of galaxy groups (e.g. Verdugo et al., in prep.).

5.2. Scaling relations on the group scale

We used the sample of the 80 most secure candidates as defined previously to look for correlations between the mass derived from weak lensing and the optical properties. Such scaling relations, characterized by power laws, have been observed on different mass scales and redshifts (e.g. Lin et al. 2003, 2004; Popesso et al. 2005; Brough et al. 2006; Becker et al. 2007; Johnston et al. 2007; Popesso et al. 2007; Reyes et al. 2008; Mandelbaum et al. 2008; Rozo et al. 2009; Andreon & Hurn 2010; Foëx et al. 2012). Usually, scaling relations are investigated using spherical NFW mass at a given density contrast, e.g. M_{200} , since they are related to the total virial mass. Because the SARCS sample is mainly made up of galaxy groups, we kept our weak-lensing analysis to its simplest version with only estimates

of the SIS velocity dispersion. As the SIS model is already a significant approximation of the actual mass distribution, we did not use SIS masses in a given aperture because it would increase the scatter of the correlations, but simply used the SIS velocity dispersions. Moreover, the lack of information on the actual mass profile of the lenses means we do not have estimates of their virial radius, although Muñoz et al. (2013) give a raw estimation for some of the groups. Therefore, we used richnesses and luminosities derived in fixed physical apertures (0.5 and 1 Mpc) regardless of the mass and the redshift of the objects.

Our results are presented in Fig. 10. In all cases, we observe quite a large dispersion in σ_{SIS} with scatters ranging from 15% to 35%, without any obvious trend as a function of richness or luminosity. However, when the objects are binned according to their richness or luminosity, we detect the expected correlations, where the more massive objects are more luminous and have more galaxies populating their red sequence.

It is interesting to note in both right-hand panels of Fig. 10 the presence of a clear outlier in the bottom right-hand corner. This object is embedded in a large-scale structure that extends over several Mpc. It is located close to the node of this filamentary structure, so when counting galaxies up to 1 Mpc, we face contamination by the surrounding clumps of galaxies. We also observe three outliers for the $N - \sigma_v$ relations with an apparently over-estimated velocity dispersion given the richness ($\sigma_v > 800 \text{ km s}^{-1}$, $N_{0.5 \text{ Mpc}} < 10$). However, these objects do not appear as outliers in the $L - \sigma_v$ relations. In two cases, the presence of two bright galaxies of similar magnitude in the centre can explain this behaviour (for the third one, another bright galaxy with similar colours falls into the 0.5 Mpc region from the lens). However, owing to the large size of the red sequence, we cannot securely distinguish between group members and field galaxies from which projections effects could explain the observed high luminosity given the richness of these three objects. Projection effects could also be responsible here for over-estimated lensing masses.

A more accurate calibration of these relations will be presented in Paper II, where groups will be stacked and outliers removed, such as objects in large-scale structures or with a very disturbed light morphology.

5.3. From poor groups to rich clusters

To get a wider range in mass, we combined this sample of the best SARCS candidates with the sample of rich and massive galaxy clusters presented in Foëx et al. (2012). These 11 clusters are part of the EXCPRES sample (*Evolution of X-ray galaxy Cluster Properties in a REpresentative Sample*, Arnaud et al. in prep.), which was designed as the REXCESS sample (Böhringer et al. 2007) in order to study the evolution of the X-ray properties of clusters. The full EXCPRES sample contains 20 clusters in the redshift range $0.4 < z < 0.6$, observed with XMM-Newton. Only clusters with an X-ray luminosity $L_X > 5 \times 10^{44} \text{ erg/s}$ in the [0.5–2.0] keV band within the detection radius were selected for an optical follow-up at the CFHT. The X-ray properties and the results of the weak-lensing analysis of this subsample of 11 clusters are presented in Foëx et al. (2012).

To be consistent with the work on the SARCS sample, we analysed the optical images (M data) of the EXCPRES clusters with the exact same procedure as used here to get the richnesses and luminosities. In total, we have 67+11 objects to adjust four scaling relations, $\sigma_{\text{SIS}} - N_{0.5 \text{ Mpc}}$, $\sigma_{\text{SIS}} - N_{1 \text{ Mpc}}$, $\sigma_{\text{SIS}} - L_{0.5 \text{ Mpc}}$, and $\sigma_{\text{SIS}} - L_{1 \text{ Mpc}}$. We used single measurements to fit

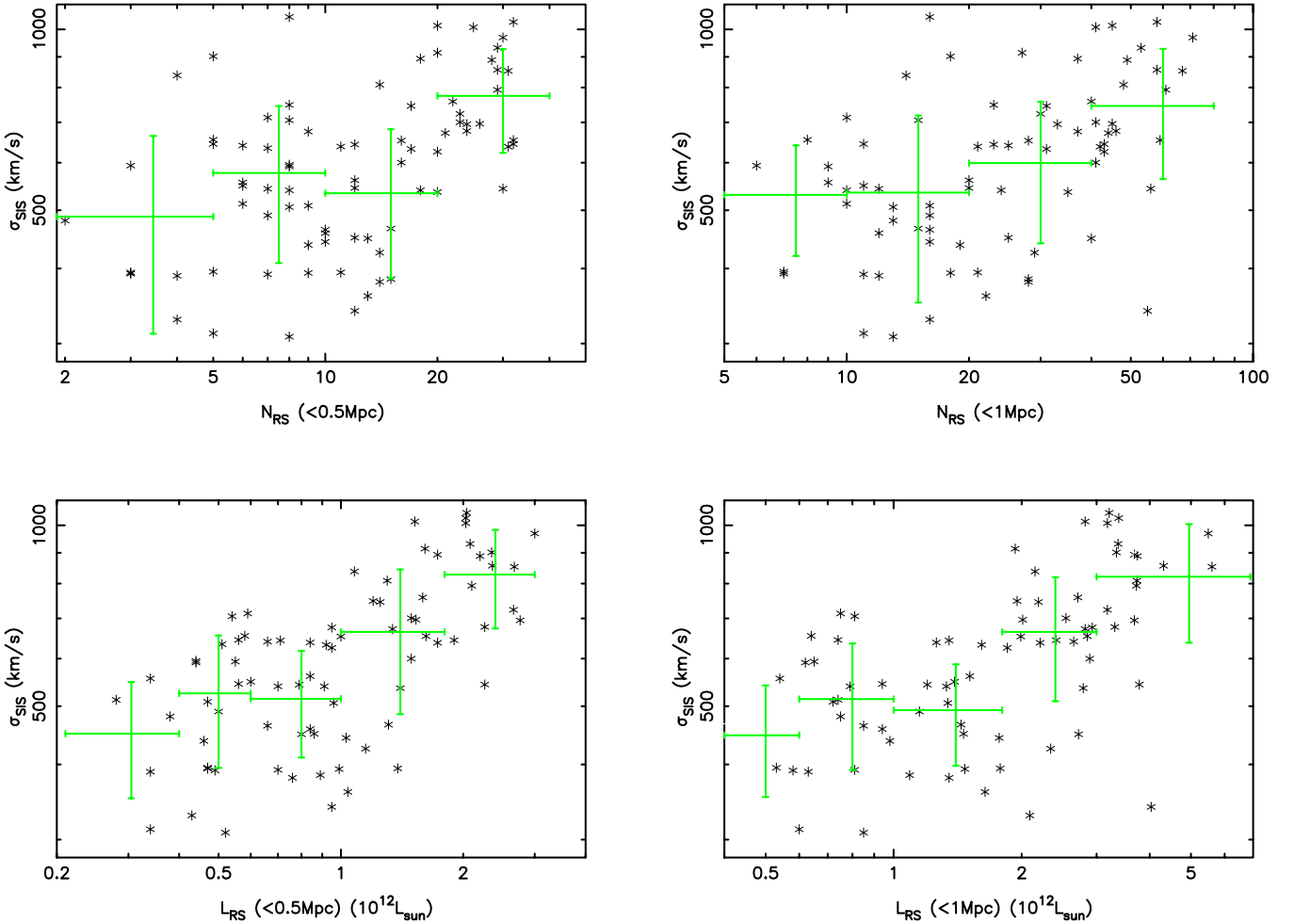


Fig. 10. Velocity dispersion derived from weak lensing as a function of optical richness (*first row*) and luminosity (*second row*) estimated with the bright red galaxies in 2 apertures, 0.5 Mpc (*left column*) and 1 Mpc (*right column*). We used only the sample of the 80 candidates defined in Sect. 5.1 (error bars on each individual measurement are omitted for clarity, see Table 2). Green points with error bars highlight the increase in σ_v with richness and luminosity after binning the SARCS lenses according to their observed richness or luminosity.

the correlations, not binned values as in other works, such as Reyes et al. (2008) and Leauthaud et al. (2010). Some of the SARCS candidates are located close to the edge of the MegaCam field-of-view, at a projected distance smaller than the size of the aperture used to derive the optical properties. We removed these objects from the fit of the scaling laws, one for the correlation at 0.5 Mpc and four for those at 1 Mpc (objects notified by an asterisk in Table 2).

To get more quantitative results, we fitted the correlations using the bootstrapping orthogonal BCES estimator (*Bivariate Correlated Errors and intrinsic Scatter*, Akritas & Bershady 1996) as done in some previous works, e.g. Morandi et al. (2007), Pratt et al. (2009), Foëx et al. (2012). The main advantage of this approach over simple linear regression is that it accounts for the intrinsic dispersion of the objects around the best fit. This dispersion needs to be included and evaluated in the fit. It indeed gives a crude idea of the impact of some physical processes that cause a departure from the theoretical predictions. For instance, the large intrinsic dispersion observed in the mass-X-ray luminosity scaling relation is a good tracer of the physics that take place in clusters of galaxies such as radiative cooling, pre-heating, or feedback from supernovae (e.g. Voit 2005 for a review).

To optimize the fit of the scaling relation and reduce the correlation between its logarithmic slope and normalization, we

normalized both variables by a pivot representative of the sample: 10 and 20 for richnesses in 0.5 Mpc and 1 Mpc, $10^{12} L_{\odot}$ and $2 \times 10^{12} L_{\odot}$ for luminosities. The velocity dispersions are normalized by 600 km s^{-1} . The results of the BCES estimator are given in Table 1 and Fig. 11 shows the best BCES fit for the $\sigma_{\text{SIS}} - N_{1\text{Mpc}}$ scaling law. As in Lin et al. (2004) and Foëx et al. (2012), we also give the value of the Spearman correlation coefficient ρ , which shows the degree of monotony of a given correlation.

First of all, the correlations appear to be roughly the same when working at 0.5 or 1 Mpc from the centre. This basically means that the choice of the aperture in which richnesses and luminosities are estimated is not a dominant parameter. This has already been observed in similar studies (e.g. Andreon & Hurn 2010; Foëx et al. 2012) with consistent results using either a fixed aperture or scaling it with mass. Thanks to the large number of objects, we obtain small statistical dispersions, the intrinsic scatter around the best fit being the main source of noise (see Fig. 11) and 12, with $\sigma_{\text{int}} \sim 0.11$ (dex). The correlations are fairly strong with Spearman coefficients of $\rho \sim 0.6$ – 0.7 : both the richness and the optical luminosity of the bright red galaxies in a halo are good tracers of mass. We can assess the quality of our best fits as mass proxies simply by converting richnesses and luminosities into $\sigma_{v,\text{proxy}}$ and looking at that average relative error over the sample $R = \langle |(\sigma_{v,\text{WL}} - \sigma_{v,\text{proxy}}) / \sigma_{v,\text{WL}}| \rangle$ (see

Table 1. Summary of the fitting results for the scaling relations $(\sigma/\sigma_0) = A \times (Obs./P_{Obs.})^\alpha$.

Scaling law	α	A	σ_{raw}	σ_{stat}	σ_{int}	ρ	R	$P_{\text{Obs.}}$
$\sigma_{\text{SIS}} - N_{0.5 \text{ Mpc}}$	0.36 ± 0.05	0.96 ± 0.04	0.13 ± 0.02	0.06 ± 0.01	0.11 ± 0.02	0.65	24%	10
$\sigma_{\text{SIS}} - N_{0.5 \text{ Mpc}}$ (SARCS only)	0.24 ± 0.05	0.93 ± 0.03	0.11 ± 0.01	0.08 ± 0.01	0.03 ± 0.18	0.68	24%	10
$\sigma_{\text{SIS}} - L_{0.5 \text{ Mpc}}$	0.45 ± 0.05	1.04 ± 0.03	0.13 ± 0.01	0.07 ± 0.01	0.11 ± 0.02	0.70	24%	$10^{12} L_\odot$
$\sigma_{\text{SIS}} - L_{0.5 \text{ Mpc}}$ (SARCS only)	0.32 ± 0.05	0.98 ± 0.03	0.10 ± 0.01	0.08 ± 0.01	0.01 ± 0.40	0.76	24%	$10^{12} L_\odot$
$\sigma_{\text{SIS}} - N_{1 \text{ Mpc}}$	0.38 ± 0.05	0.94 ± 0.04	0.12 ± 0.02	0.06 ± 0.01	0.10 ± 0.02	0.65	24%	20
$\sigma_{\text{SIS}} - N_{1 \text{ Mpc}}$ (SARCS only)	0.25 ± 0.06	0.93 ± 0.04	0.11 ± 0.01	0.08 ± 0.01	0.06 ± 0.12	0.68	25%	20
$\sigma_{\text{SIS}} - L_{1 \text{ Mpc}}$	0.42 ± 0.06	1.10 ± 0.04	0.13 ± 0.01	0.07 ± 0.01	0.11 ± 0.02	0.67	25%	$2 \times 10^{12} L_\odot$
$\sigma_{\text{SIS}} - L_{1 \text{ Mpc}}$ (SARCS only)	0.28 ± 0.06	1.02 ± 0.03	0.11 ± 0.01	0.08 ± 0.01	0.01 ± 0.23	0.73	24%	$2 \times 10^{12} L_\odot$

Notes. Columns are (1) scaling relation; (2) best fit logarithmic slope; (3) best fit normalization; (4–5–6) total, statistic, and intrinsic logarithmic dispersions; (7) Spearman coefficient; (8) relative error on σ_v using the scaling relation as mass proxy; (9) pivot chosen to normalize the observable (velocity dispersions are normalized by $\sigma_0 = 600 \text{ km s}^{-1}$).

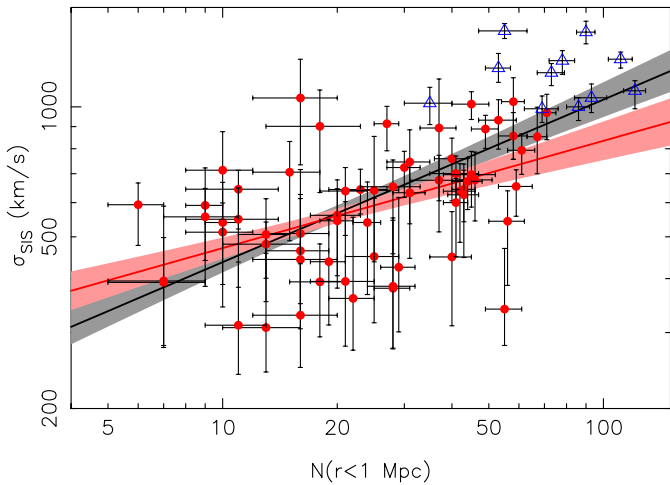


Fig. 11. Richness-velocity dispersion scaling relation. The black solid line shows the best BCES orthogonal fit of the $N_{1 \text{ Mpc}} - \sigma_{\text{SIS}}$ relation using the SARCS most secure candidates (red points) and adding the EXCPRES galaxy clusters of Foëx et al. (2012) (blue open triangles). The grey shaded area gives the statistical 1σ uncertainty given by the best fit parameters (statistical dispersion σ_{stat}). The red line (and corresponding shaded area) is the best fit using only the SARCS most secure candidates.

Table 1). According to this criterion, our scaling relations are efficient for recovering velocity dispersions with an accuracy of better than $\sim 25\%$.

While the hierarchical model of structure formation predicts a number of subhaloes proportional to the mass of the parent halo, i.e. $N \propto M$ (e.g. De Lucia et al. 2004; Gao et al. 2004), including baryons in numerical simulations results in a decrease in the number of galaxies for a halo of higher masses, i.e. $N \propto M^\alpha$ with $\alpha < 1$ (see e.g. White et al. 2001; Berlind et al. 2003). Several mechanisms can be responsible of this reduced slope, such as a decrease in gas cooling and star formation efficiency (Springel & Hernquist 2003; Borgani et al. 2004; Kravtsov et al. 2004) or an increased merger/destruction rate of galaxies in higher mass objects (White et al. 2001; Lin et al. 2003). Our results for the $\sigma_v - N$ relations are in good agreement with theoretical predictions from numerical simulations with a slope of 0.33 (e.g. Evrard et al. 2008; Lau et al. 2010), as well as similar work (Andreon & Hurn 2010). However, we do not observe any significant evidence of the influence of physical processes that might affect the galaxy population. For the $\sigma_{\text{SIS}} - L$ relations, we obtain slightly steeper slopes than the $\sigma_{\text{SIS}} - N$ correlation with values that are not consistent with a constant mass-to-light ratio. This result suggests that the physical mechanisms inside a

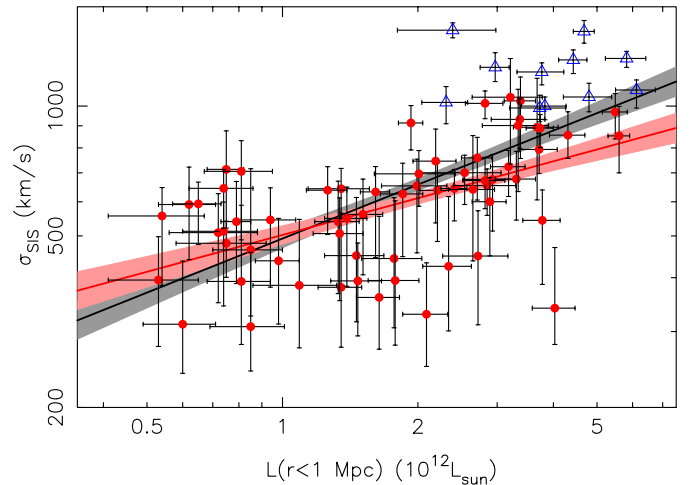


Fig. 12. Same as Fig. 11 but for the luminosity-velocity dispersion scaling relation.

dark matter halo are more efficient to affect the luminosity rather than the number of red-sequence galaxies, including for instance ram pressure stripping or galaxy harassment (see e.g. Treu et al. 2003; Poggianti 2004; Boselli & Gavazzi 2006). The presence of a higher fraction of galaxies with evolved stellar populations in higher mass objects has also been invoked to explain the increase in the mass-to-light ratio with mass (e.g. Bahcall & Comerford 2002). However, this assumption has been ruled out by Popesso et al. (2007) and their study of the fundamental plane of the cluster ellipticals, showing that they have a constant mass-to-light ratio that cannot explain the variations in the total mass-to-light ratio of clusters. We intend to use our spectroscopic surveys of the SARCS groups to investigate this hypothesis in more detail and down to lower-mass objects in Paper II.

We also fit these scaling relations using only the sample of galaxy groups. We obtained slopes that are slightly lower but consistent within 2σ uncertainties with the groups+clusters combined fits (see Table 1; also see Figs. 11 and 12). This result is not surprising since we use bootstrapping to derive the best fit parameters, which gives more weight to the SARCS groups as they are more numerous than the EXCPRES clusters. With the relations calibrated with the SARCS objects alone, we derived the associated R value. The $\sigma_{\text{SIS}} - L_{1 \text{ Mpc}}$ scaling gives $R = 24\%$ (22% when applied on the SARCS sample only, 37% for the EXCPRES clusters alone), and the $\sigma_{\text{SIS}} - N_{1 \text{ Mpc}}$ relation gives $R = 25\%$ (23% and 34%). These relations give similar accuracies despite lower slopes. This is mainly the result of the different sizes of the two samples, the SARCS one dominating

the statistic. We find higher R values for only the EXCPRES sample, suggesting a break in the scalings between the low- and high-mass ends of the combined sample. However, since we do not obtain statistically significant differences in the slopes of the scaling relations between groups and groups+clusters (discrepancies lower than 3σ), we cannot reliably distinguish between a single population of similar objects over the whole mass range and the presence of two distinct subpopulations.

5.4. Comparison with previous works

Although this work is the first one based on such a large sample of strong lensing groups, we are not the first to investigate the group properties through some scaling relations. As stated previously, groups have already been extensively studied with different baryonic tracers, from X-ray or optical observations. Despite some difficulty making proper comparisons (e.g. different ways of defining the optical richness, measure the X-ray luminosity, etc), we review here some of these works.

From the X-ray point of view, Jeltema et al. (2006, 2007) present the analysis of a sample of nine X-ray emitting galaxy groups at intermediate redshifts (Mulchaey et al. 2006). In particular they find that these intermediate-redshift groups present similar properties as local groups, thus excluding strong non-standard redshift evolution. The X-ray properties of these objects (temperature, luminosity, entropy) follow the scaling relations obtained with galaxy clusters and/or nearby galaxy groups (see also Mulchaey & Zabludoff 1998). In Sect. 5.1, we showed that we obtained large scatters in the velocity dispersion at a given richness or optical luminosity, which was also observed by Jeltema et al. (2006) for a given temperature or X-ray luminosity of the gas.

More recently, a large sample of 200 X-ray galaxy groups up to a redshift of 1 has been drawn from the COSMOS field (Scoville et al. 2007) and studied with a weak-lensing analysis to put constraints on the mass-X-ray luminosity scaling relation by Leauthaud et al. (2010). They find very good agreement with other studies, i.e. that this correlation can be characterized by a single power law over a very wide range in mass (see also Foëx et al. 2012). Despite some hints of a possible break of similarity on the cluster scale, we have shown in the previous section that a single power law also gives an acceptable fit of the scaling with richness and luminosity from poor groups to rich clusters. They claim to observe little evidence for a non-standard redshift evolution of the relation, but without a strong statistical significance. Their work therefore also confirms that galaxy groups are following the same scalings as galaxy clusters rather than presenting special properties. Giodini et al. (2009) studied some galaxy groups and poor clusters observed in the COSMOS field. Their analysis of the stellar mass fraction associated to the galaxy members again showed no evidence of a non-standard redshift evolution since their scaling relation agrees with the one obtained for local clusters (see also the work by Connelly et al. 2012). Their results on galaxy groups are also in good agreement with those for only galaxy clusters, again supporting the idea that galaxy groups are not a particular population of haloes but just a scaled-down version of clusters, as expected in the simple model of hierarchical structure formation and evolution.

As stated in Sect. 3.2, using the same COSMOS data, George et al. (2012) confirmed the findings of Jeltema et al. (2007) about the BGG/BCG in groups and clusters: an early-type galaxy, but not necessarily a dominant one, and with observed shifts up to 100 kpc with respect to the X-ray peak (see also Hoekstra et al. 2012, and their sample of 50 massive galaxy clusters). In our

study of the SARCS sample, we observed the same behaviour in some specific cases such as the multi-modal groups where there is not a single early-type galaxy dominating the light distribution, and/or where the strong-lensing system is not associated to the brightest member. A more quantitative analysis of this problematic will be presented in Paper II.

Numerous works have explored galaxy groups based on optical observations, both from the side of the properties of individual galaxies and as a global population correlated to the host dark matter halo. In this paper, we focussed on the second point of view through some optical scaling relations. Our results obtained in Sect. 5.3 on the calibration of the $\sigma_v - N$ and $\sigma_v - L$ scaling relations do not give strong evidence of departing from the purely gravitationally driven model of structure formation, although the mass-to-light ratio we observed is not constant across the range in mass. As mentioned previously, galaxy-galaxy and galaxy-halo interactions are taking place in groups and clusters, and they can modify the global properties of the galaxies populating the halo (see e.g. Lin et al. 2004). Several studies have been looking for observational evidence of these mechanisms associated to the baryonic content of dark matter haloes. For instance, the maxBCG sample of optically selected groups and clusters observed in the SDSS survey (Koester et al. 2007a,b) has been widely analysed to derive the optical $M - N$ and $M - L$ scaling laws. Reyes et al. (2008) used $\sim 13\,000$ objects in the maxBCG catalog, cutting towards low richnesses at $N_{200} \geq 10$ (according to their definition of the red sequence), and covering a range in redshift from 0.1 to 0.3. They binned the objects in several ways, according either to richness, luminosity, or luminosity of the BCG. They derived the corresponding stacked weak lensing mass and fitted the optical scaling laws. They obtained consistent behaviours over the entire mass range, with a little evidence of non-gravitational processes (they derived slopes larger than 1 at the 2σ level). Similar results were obtained by Johnston et al. (2007) using a slightly different sample, i.e. one that includes objects at lower richnesses (see also Mandelbaum et al. 2008; Rozo et al. 2009). However, as noticed in Andreon & Hurn (2010), the sample used by Johnston et al. (2007) suffers from the Malmquist bias, resulting in smaller slopes. We expect here to face the same problem because of our weak-lensing selection criterion at the low-mass end of the SARCS sample, where the shear signal gets too low and noisy. In Sect. 3.3 we indeed showed that 76% of the weak-lensing non-detections are associated to strong-lensing systems with an observed arc radius smaller than $4''$. Therefore, we most likely miss a significant number of the low-mass objects in the sample, translating in smaller fitted slopes, hence higher discrepancy with the theoretical predictions.

Despite a large number of works with different methodologies, the precise characterization of the optical scaling relations (slopes and scatters) remains an open problem. There is a trend in the different studies with evidence of the role of the baryonic physics through slopes steeper than 1, such as the works on the maxBCG catalog or Muzzin et al. (2007) with $M \propto N^{1.4 \pm 0.2}$ from 15 clusters, Lin et al. (2004) with $N \propto M^{0.82 \pm 0.04}$ and $L \propto M^{0.72 \pm 0.04}$ from 93 groups and clusters, and Bardeau et al. (2007) with $M \propto L^{1.8 \pm 0.24}$ with ten galaxy clusters (see also Marinoni & Hudson 2002; Popesso et al. 2005; Parker et al. 2005; Popesso et al. 2007). However some authors still obtain slopes consistent with one, hence no evidence of the processes affecting the galaxy properties (see e.g. Andreon & Hurn 2010; Foëx et al. 2012). With the present work, we did not rule out the simplest model of structure formation, although our mass-to-light ratio seems to indicate some differences between the

population of the most massive haloes and that of small galaxy groups. A more extensive analysis of the galaxy properties in the SARCS groups will be presented in Paper II. We will make use of this sample to investigate where and when are galaxies the most affected, such as interaction with the parent halo during the infall, galaxy-galaxy interactions, environment effects (see e.g. Cibinel et al. 2013 and references therein).

6. Conclusions

In this first paper we presented the weak-lensing analysis of the SARCS sample of lens candidates, a work that follows the previous one by Limousin et al. (2009) on a first sample of group candidates. These potential groups and clusters of galaxies were detected on the CFHTLS survey by the presence of a possible strong-lensing feature. Taking advantage of the high quality of the CFHT images, in particular deep observations and good seeing, we studied each object one by one, which was done for the first time on the group scale (previous weak lensing studies of galaxy groups were stacking objects). We were able to measure a shear signal for a large part of the sample since we derived a SIS velocity dispersion greater than 0 at least at the 1σ level for 89 candidates. As most of the SARCS objects are galaxy groups up to high redshifts ($z = 1.2$) with a faint and noisy shear signal, we only focussed on estimates of the total mass via the SIS mass distribution instead of trying to assess the radial or 2D mass distribution. The SIS velocity dispersion we obtained for the SARCS sample is dominated by galaxy-group objects with an average value of $\sigma_v \sim 600 \text{ km s}^{-1}$. We also found some galaxy clusters in the sample with velocity dispersions up to 1000 km s^{-1} . We did not find strong evidence of a correlation between the measured SIS velocity dispersion and redshift, indicating that the SARCS sample is fairly homogenous up to $z \sim 0.8$.

We also performed the optical analysis of SARCS objects. Using the galaxies belonging to the red sequence down to an absolute magnitude of $M_r = -21$, we estimated for each object its optical richness and luminosity in different fixed apertures, i.e. not scaled with mass or redshift. We obtained typical values of $N(R < 1 \text{ Mpc}) \sim 5-20$ (up to ~ 70) and $L(R < 1 \text{ Mpc}) \sim 0.5-1.5 \times 10^{12} L_\odot$ (up to $\sim 6 \times 10^{12} L_\odot$). We also use the catalogues of red galaxies to construct 2D luminosity maps and explore the morphology of the SARCS candidates. Our classification resulted in two main conclusions:

- (i) A significant number of the confirmed groups and poor clusters present complex morphologies, such as very disturbed luminosity contours or several luminosity peaks in the central parts. This suggests that groups of galaxies are mostly dynamically young structures.
- (ii) As for the weak-lensing analysis, some of the objects were not clearly detected, possibly corresponding to galaxy-scale lenses or false detections. The combination of the optical and weak-lensing results led us to a final sample of 80 galaxy groups, removing some clearly false detections, such as SA104, thus improving the purity of the sample. Compared to the initial SARCS sample, we obtained a similar morphological distribution. On the other hand, we obtained a larger fraction of highly ranked objects with larger arc radius. The selection criteria used in More et al. (2012) were indeed selected to favour completeness over purity, which is most likely much higher in our final sample.

Finally, we quickly explored the relation between mass and the main optical properties. Despite significant scatters up to 35% in σ_v at a given richness or luminosity, we found good

correlations since more massive systems are richer and more luminous. We combined the SARCS sample with a sample of rich clusters of galaxies and obtained consistent results over the entire range in mass with obvious scaling relations between the SIS velocity dispersion and the overall properties of the galaxies population. With this work, we confirm the possibility of using the optical scaling relations as reasonable mass proxies to analyse large samples of groups and clusters of galaxies and derive cosmological constraints via their mass function. However, our results have to be considered with caution as we performed a lensing analysis on single objects, which can lead to biased results for the low-mass objects and, in most cases, to large uncertainties in the mass measurement, which are the current limitation of the statistical significance of the results presented here. In Paper II (Foex et al., in prep.), we will stack the objects to get a more robust weak-lensing signal, and thus put tighter constraints on these scaling relations. In doing so, we hope to significantly reduce the systematic uncertainties until the point where the lack of a good understanding of the SARCS selection function will have to be accounted for. We are attempting to assess the problem of the SARCS selection function by conducting a lens search of the complete CFHTLS imaging via a citizen science project (More et al., in prep.).

This Paper is only one step in the study of the SARCS sample. Ongoing and complementary observations will provide new results to be compared to this preliminary weak-lensing and optical analyses. In particular, multi-object spectroscopy will increase the number of groups presented in Muñoz et al. (2013) for which the mass inferred by a dynamical methodology can be used to test the reliability of the weak-lensing results presented here. With a combination of these dynamical results with our weak-lensing study and some strong lensing modelling (Verdugo et al., in prep, see also Verdugo et al. 2011), we intend to investigate the mass profile from the central parts of the group up to large radius in more detail, thus testing some predictions from numerical simulations. We will also explore the properties of the galaxies more closely inside the groups such as the evolution of the red sequence with redshift, the size of galactic dark matter haloes inside groups with a galaxy-galaxy weak-lensing analysis, or the halo occupation distribution and the central galaxy paradigm (Foex et al., in prep., Paper II). Thanks to the large field of view of M and the large area covered by the CFHTLS survey, a search for large-scale structures linked to the SARCS objects is being explored (Cabanac et al., in prep.). We also intend to correlate all these observational results with large N -body dark matter numerical simulations to put constraints on the formation and the evolution of galaxy groups and their link with the large-scale structures of the Universe.

Acknowledgements. G.F. acknowledges support from FONDECYT through grant 3120160. V.M. acknowledges support from FONDECYT through grant 112074. M.L. acknowledges the Centre National de la Recherche Scientifique (CNRS) for its support. The Dark Cosmology Centre is funded by the Danish National Research Foundation. T.V. acknowledges support from CONACYT grant 165365 through the programme ÓEstancias posdoctorales y sabbáticas al extranjero para la consolidación de grupos de investigación. R.G. acknowledges support from the Centre National des Etudes Spatiales. R.M. acknowledges support from CONICYT CATA-BASAL and FONDECYT through grant 3130750. G.F., V.M., M.L. and R.C. acknowledge support from ECOS-CONICYT C12U02. We acknowledge support from Programme National de Cosmologie (PNCG). Based on observations obtained with MEGAPRIME/MegaCam, a joint project of CFHT and CEA/DAPNIA, at the Canada-France-Hawaii Telescope (CFHT), which is operated by the National Research Council (NRC) of Canada, the Institut National des Science de l'Univers of the Centre National de la Recherche Scientifique (CNRS) of France, and the University of Hawaii. This work is based in part on data products produced at TERAPIX and the Canadian Astronomy Data Centre as part of the Canada-France-Hawaii Telescope Legacy Survey, a collaborative project of the NRC and CNRS.

References

- Akritas, M. G., & Bershad, M. A. 1996, *ApJ*, 470, 706
- Alard, C. 2006 [[arXiv:astro-ph/0606757](https://arxiv.org/abs/astro-ph/0606757)]
- Andreon, S., & Hum, M. A. 2010, *MNRAS*, 404, 1922
- Arnaud, M. 2005, in *Background Microwave Radiation and Intracluster Cosmology*, eds. F. Melchiorri, & Y. Rephaeli, 77 (The Netherlands: JOBS press and Bologna: Società Italiana di Fisica)
- Bahcall, N. A. 2000, *Phys. Rep.*, 333, 233
- Bahcall, N. A., & Comerford, J. M. 2002, *ApJ*, 565, L5
- Balogh, M. L., Morris, S. L., Yee, H. K. C., Carlberg, R. G., & Ellingson, E. 1999, *ApJ*, 527, 54
- Balogh, M. L., Wilman, D., Henderson, R. D. E., et al. 2007, *MNRAS*, 374, 1169
- Balogh, M. L., Mazzotta, P., Bower, R. G., et al. 2011a, *MNRAS*, 412, 947
- Balogh, M. L., McGee, S. L., Wilman, D. J., et al. 2011b, *MNRAS*, 412, 2303
- Bardeau, S., Kneib, J.-P., Czoske, O., et al. 2005, *A&A*, 434, 433
- Bardeau, S., Soucail, G., Kneib, J.-P., et al. 2007, *A&A*, 470, 449
- Becker, M. R., McKay, T. A., Koester, B., et al. 2007, *ApJ*, 669, 905
- Bekki, K. 1999, *ApJ*, 510, L15
- Bergé, J., Pacaud, F., Réfrégier, A., et al. 2008, *MNRAS*, 385, 695
- Berlind, A. A., Weinberg, D. H., Benson, A. J., et al. 2003, *ApJ*, 593, 1
- Bertin, E., & Arnouts, S. 1996, *A&A*, 117, 393
- Biviano, A., Murante, G., Borgani, S., et al. 2006, *A&A*, 456, 23
- Böhringer, H., Voges, W., Huchra, J. P., et al. 2000, *ApJS*, 129, 435
- Böhringer, H., Schuecker, P., Pratt, G. W., et al. 2007, *A&A*, 469, 363
- Bolton, A. S., Burles, S., Koopmans, L. V. E., Treu, T., & Moustakas, L. A. 2006, *ApJ*, 638, 703
- Bolzonella, M., Miralles, J.-M., & Pelló, R. 2000, *A&A*, 363, 476
- Bonamente, M., Joy, M., LaRoque, S. J., et al. 2008, *ApJ*, 675, 106
- Borgani, S., Murante, G., Springel, V., et al. 2004, *MNRAS*, 348, 1078
- Boselli, A., & Gavazzi, G. 2006, *PASP*, 118, 517
- Brainerd, T. G., Blandford, R. D., & Smail, I. 1996, *ApJ*, 466, 623
- Bridle, S., Gull, S., Bardeau, S., & Kneib, J.-P. 2002, in *Proc. of the Yale Cosmology Workshop: The Shapes of Galaxies and their Dark Halos*, 38 (World Scientific)
- Brough, S., Forbes, D. A., Kilborn, V. A., & Couch, W. 2006, *MNRAS*, 370, 1223
- Bruzual, G., & Charlot, S. 2003, *MNRAS*, 344, 1000
- Butcher, H., & Oemler, Jr., A. 1984, *ApJ*, 285, 426
- Cabanac, R. A., Alard, C., Dantel-Fort, M., et al. 2007, *A&A*, 461, 813
- Carlstrom, J. E., Holder, G. P., & Reese, E. D. 2002, *ARA&A*, 40, 643
- Carollo, C. M., Cibinel, A., Lilly, S. J., et al. 2013, *ApJ*, 776, 71
- Cibinel, A., Carollo, C. M., Lilly, S. J., et al. 2013, *ApJ*, 777, 116
- Colless, M., Dalton, G., Maddox, S., et al. 2001, *MNRAS*, 328, 1039
- Connelly, J. L., Wilman, D. J., Finoguenov, A., et al. 2012, *ApJ*, 756, 139
- Coupon, J., Ilbert, O., Kilbinger, M., et al. 2009, *A&A*, 500, 981
- Cowie, L. L., & Binney, J. 1977, *ApJ*, 215, 723
- Cucciati, O., Marinoni, C., Iovino, S., et al. 2010, *A&A*, 520, A42
- Cypriano, E. S., Sodré, Jr., L., Kneib, J., & Campusano, L. E. 2004, *ApJ*, 613, 95
- De Lucia, G., Kauffmann, G., Springel, V., et al. 2004, *MNRAS*, 348, 333
- De Lucia, G., Poggianti, B. M., Aragón-Salamanca, A., et al. 2007, *MNRAS*, 374, 809
- Dietrich, J. P., Böhnert, A., Lombardi, M., Hilbert, S., & Hartlap, J. 2012, *MNRAS*, 419, 3547
- Dolag, K., Meneghetti, M., Moscardini, L., Rasia, E., & Bonaldi, A. 2006, *MNRAS*, 370, 656
- Dressler, A., Oemler, Jr., A., Poggianti, B. M., et al. 2004, *ApJ*, 617, 867
- Ebeling, H., Edge, A. C., & Henry, J. P. 2001, *ApJ*, 553, 668
- Eke, V. R., Baugh, C. M., Cole, S., et al. 2004, *MNRAS*, 348, 866
- Ellingson, E., Lin, H., Yee, H. K. C., & Carlberg, R. G. 2001, *ApJ*, 547, 609
- Ettori, S., Borgani, S., Moscardini, L., et al. 2004, *MNRAS*, 354, 111
- Evrard, A. E. 1990, *ApJ*, 363, 349
- Evrard, A. E., MacFarland, T. J., Couchman, H. M. P., et al. 2002, *ApJ*, 573, 7
- Evrard, A. E., Bialek, J., Busha, M., et al. 2008, *ApJ*, 672, 122
- Faltenbacher, A., Hoffman, Y., Gottlöber, S., & Yepes, G. 2007, *MNRAS*, 376, 1327
- Fassnacht, C. D., Kocevski, D. D., Auger, M. W., et al. 2008, *ApJ*, 681, 1017
- Finoguenov, A., Reiprich, T. H., & Böhringer, H. 2001, *A&A*, 368, 749
- Finoguenov, A., Guzzo, L., Hasinger, G., et al. 2007a, *ApJ*, 172, 182
- Finoguenov, A., Ponman, T. J., Osmond, J. P. F., & Zimer, M. 2007b, *MNRAS*, 374, 737
- Foëx, G., Soucail, G., Pointecouteau, E., et al. 2012, *A&A*, 546, A106
- Fukugita, M., Ichikawa, T., Gunn, J. E., et al. 1996, *AJ*, 111, 1748
- Gao, L., White, S. D. M., Jenkins, A., Stoehr, F., & Springel, V. 2004, *MNRAS*, 355, 819
- Gastaldello, F., Buote, D. A., Humphrey, P. J., et al. 2007, *ApJ*, 669, 158
- Gavazzi, R., & Soucail, G. 2007, *A&A*, 462, 459
- George, M. R., Leauthaud, A., Bundy, K., et al. 2012, *ApJ*, 757, 2
- Giodini, S., Pierini, D., Finoguenov, A., et al. 2009, *ApJ*, 703, 982
- Gladders, M. D., Hoekstra, H., Yee, H. K. C., Hall, P. B., & Barrientos, L. F. 2003, *ApJ*, 593, 48
- Gladders, M. D., & Yee, H. K. C. 2005, *ApJS*, 157, 1
- Haiman, Z., Mohr, J. J., & Holder, G. P. 2001, *ApJ*, 553, 545
- Hausman, M. A., & Ostriker, J. P. 1978, *ApJ*, 224, 320
- Helsdon, S. F., & Ponman, T. J. 2000, *MNRAS*, 315, 356
- Helsdon, S. F., & Ponman, T. J. 2003a, *MNRAS*, 339, L29
- Helsdon, S. F., & Ponman, T. J. 2003b, *MNRAS*, 340, 485
- Heymans, C., Van Waerbeke, L., Bacon, D., et al. 2006, *MNRAS*, 368, 1323
- Hoekstra, H. 2007, *MNRAS*, 379, 317
- Hoekstra, H., Franx, M., & Kuijken, K. 2000, *ApJ*, 532, 88
- Hoekstra, H., Hartlap, J., Hilbert, S., & van Uitert, E. 2011, *MNRAS*, 412, 2095
- Hoekstra, H., Mahdavi, A., Babul, A., & Bildfell, C. 2012, *MNRAS*, 427, 1298
- Huertans-Company, M., Foëx, G., Soucail, G., & Pelló, R. 2009, *A&A*, 505, 83
- Ienna, F., & Pelló, R. 2006, in *SF2A-2006: Semaine de l'Astrophysique Française*, eds. D. Barret, F. Casoli, G. Lagache, A. Lecavelier, & L. Pagani, 347
- Ivezic, Z., Tyson, J. A., Acosta, E., et al. 2008 [[arXiv:0805.2366](https://arxiv.org/abs/0805.2366)]
- Jauzac, M., Jullo, E., Kneib, J.-P., et al. 2012, *MNRAS*, 426, 3369
- Jeltema, T. E., Mulchaey, J. S., Lubin, L. M., Rosati, P., & Böhringer, H. 2006, *ApJ*, 649, 649
- Jeltema, T. E., Mulchaey, J. S., Lubin, L. M., & Fassnacht, C. D. 2007, *ApJ*, 658, 865
- Johnston, D. E., Sheldon, E. S., Wechsler, R. H., et al. 2007 [[arXiv:0709.1159](https://arxiv.org/abs/0709.1159)]
- Jullo, E., Kneib, J., Limousin, M., et al. 2007, *New J. Phys.*, 9, 447
- Kaiser, N. 1986, *MNRAS*, 222, 323
- Kneib, J., Ellis, R. S., Smail, I., Couch, W. J., & Sharples, R. M. 1996, *ApJ*, 471, 643
- Knobel, C., Lilly, S. J., Iovino, A., et al. 2009, *ApJ*, 697, 1842
- Kodama, T., Yamada, T., Akiyama, M., et al. 2004, *MNRAS*, 350, 1005
- Koester, B. P., McKay, T. A., Annis, J., et al. 2007a, *ApJ*, 660, 239
- Koester, B. P., McKay, T. A., Annis, J., et al. 2007b, *ApJ*, 660, 221
- Kotov, O., & Vikhlinin, A. 2005, *ApJ*, 633, 781
- Kravtsov, A. V., Berlind, A. A., Wechsler, R. H., et al. 2004, *ApJ*, 609, 35
- Lancaster, K., Birkinshaw, M., Gawroński, M. P., et al. 2011, *MNRAS*, 418, 1441
- Lau, E. T., Nagai, D., & Kravtsov, A. V. 2010, *ApJ*, 708, 1419
- Leauthaud, A., Finoguenov, A., Kneib, J., et al. 2010, *ApJ*, 709, 97
- Limousin, M., Kneib, J. P., Bardeau, S., et al. 2007a, *A&A*, 461, 881
- Limousin, M., Richard, J., Jullo, E., et al. 2007b, *ApJ*, 668, 643
- Limousin, M., Cabanac, R., Gavazzi, R., et al. 2009, *A&A*, 502, 445
- Limousin, M., Ebeling, H., Ma, C., et al. 2010a, *MNRAS*, 405, 777
- Limousin, M., Jullo, E., Richard, J., et al. 2010b, *A&A*, 524, A95
- Lin, Y., Mohr, J. J., & Stanford, S. A. 2003, *ApJ*, 591, 749
- Lin, Y., Mohr, J. J., & Stanford, S. A. 2004, *ApJ*, 610, 745
- Lubin, L. M., Oke, J. B., & Postman, M. 2002, *AJ*, 124, 1905
- Lubin, L. M., Gal, R. R., Lemaux, B. C., Kocevski, D. D., & Squires, G. K. 2009, *AJ*, 137, 4867
- Luppino, G. A., Gioia, I. M., Hammer, F., Le Fèvre, O., & Annis, J. A. 1999, *A&AS*, 136, 117
- Mahdavi, A., Hoekstra, H., Babul, A., et al. 2013, *ApJ*, 767, 116
- Mamon, G. A. 2007, in *Groups of Galaxies in the Nearby Universe*, eds. I. Saviane, V. D. Ivanov, & J. Borissova, 203 (Springer Verlag)
- Mandelbaum, R., Seljak, U., Cool, R. J., et al. 2006, *MNRAS*, 372, 758
- Mandelbaum, R., Seljak, U., Hirata, C. M., et al. 2008, *MNRAS*, 386, 781
- Mandelbaum, R., Seljak, U., Baldauf, T., & Smith, R. E. 2010, *MNRAS*, 405, 2078
- Marian, L., & Bernstein, G. M. 2006, *Phys. Rev. D*, 73, 123525
- Marinoni, C., & Hudson, M. J. 2002, *ApJ*, 569, 101
- Marrone, D. P., Smith, G. P., Richard, J., et al. 2009, *ApJ*, 701, L114
- Massey, R., Rhodes, J., Ellis, R., et al. 2007, *Nature*, 445, 286
- McCarthy, I. G., Babul, A., Holder, G. P., & Balogh, M. L. 2003, *ApJ*, 591, 515
- Miller, C. J., Nichol, R. C., Reichart, D., et al. 2005, *AJ*, 130, 968
- Morandi, A., Ettori, S., & Moscardini, L. 2007, *MNRAS*, 379, 518
- More, A., Jahnke, K., More, S., et al. 2011, *ApJ*, 734, 69
- More, A., Cabanac, R., More, S., et al. 2012, *ApJ*, 749, 38
- Muñoz, J. A., Falco, E. E., Kochanek, C. S., et al. 1998, *Ap&SS*, 263, 51
- Muñoz, R. P., Motta, V., Verdugo, T., et al. 2013, *A&A*, 552, A80
- Mulchaey, J. S., & Zabludoff, A. I. 1998, *ApJ*, 496, 73
- Mulchaey, J. S., Lubin, L. M., Fassnacht, C., Rosati, P., & Jeltema, T. E. 2006, *ApJ*, 646, 133
- Muzzin, A., Yee, H. K. C., Hall, P. B., & Lin, H. 2007, *ApJ*, 663, 150
- Myers, S. T., Jackson, N. J., Browne, I. W. A., et al. 2003, *MNRAS*, 341, 1
- Navarro, J. F., Frenk, C. S., & White, S. D. M. 1997, *ApJ*, 490, 493
- Navarro, J. F., Hayashi, E., Power, C., et al. 2004, *MNRAS*, 349, 1039
- Oguri, M. 2006, *MNRAS*, 367, 1241

- Oguri, M., Hennawi, J. F., Gladders, M. D., et al. 2009, *ApJ*, 699, 1038
- Oguri, M., Bayliss, M. B., Dahle, H., et al. 2012, *MNRAS*, 420, 3213
- Okabe, N., & Umetsu, K. 2008, *PASJ*, 60, 345
- Okabe, N., Takada, M., Umetsu, K., Futamase, T., & Smith, G. P. 2010, *PASJ*, 62, 811
- Osmond, J. P. F., & Ponman, T. J. 2004, *MNRAS*, 350, 1511
- Ostriker, J. P., & Tremaine, S. D. 1975, *ApJ*, 202, L113
- Pandey, B., & Bharadwaj, S. 2006, *MNRAS*, 372, 827
- Parker, L. C., Hudson, M. J., Carlberg, R. G., & Hoekstra, H. 2005, *ApJ*, 634, 806
- Pimbblet, K. A., Drinkwater, M. J., & Hawkrigg, M. C. 2004, *MNRAS*, 354, L61
- Planck Collaboration 2011a, *A&A*, 536, A8
- Planck Collaboration 2011b, *A&A*, 536, A11
- Planck Collaboration 2011c, *A&A*, 536, A10
- Poggianti, B. 2004, in *Baryons in Dark Matter Halos*, eds. R. Dettmar, U. Klein, & P. Salucci, *Proc. Sci.*, 104
- Poggianti, B. M., von der Linden, A., De Lucia, G., et al. 2006, *ApJ*, 642, 188
- Popesso, P., Biviano, A., Böhringer, H., Romaniello, M., & Voges, W. 2005, *A&A*, 433, 431
- Popesso, P., Biviano, A., Böhringer, H., & Romaniello, M. 2007, *A&A*, 464, 451
- Pratt, G. W., Croston, J. H., Arnaud, M., & Böhringer, H. 2009, *A&A*, 498, 361
- Quintana, H., & Lawrie, D. G. 1982, *AJ*, 87, 1
- Radovich, M., Puddu, E., Romano, A., Grado, A., & Getman, F. 2008, *A&A*, 487, 55
- Rasmussen, J., & Ponman, T. J. 2007, *MNRAS*, 380, 1554
- Reyes, R., Mandelbaum, R., Hirata, C., Bahcall, N., & Seljak, U. 2008, *MNRAS*, 390, 1157
- Rozo, E., Rykoff, E. S., Evrard, A., et al. 2009, *ApJ*, 699, 768
- Ruff, A. J., Gavazzi, R., Marshall, P. J., et al. 2011, *ApJ*, 727, 96
- Rykoff, E. S., Evrard, A. E., McKay, T. A., et al. 2008, *MNRAS*, 387, L28
- Scoville, N., Aussel, H., Brusa, M., et al. 2007, *ApJS*, 172, 1
- Seitz, C., & Schneider, P. 1997, *A&A*, 318, 687
- Skibba, R. A., van den Bosch, F. C., Yang, X., et al. 2011, *MNRAS*, 410, 417
- Smail, I., Edge, A. C., Ellis, R. S., & Blandford, R. D. 1998, *MNRAS*, 293, 124
- Soucail, G. 2012, *A&A*, 540, A61
- Springel, V., & Hernquist, L. 2003, *MNRAS*, 339, 312
- Springel, V., White, S. D. M., Jenkins, A., et al. 2005, *Nature*, 435, 629
- Staniszewski, Z., Ade, P. A. R., Aird, K. A., et al. 2009, *ApJ*, 701, 32
- Stott, J. P., Pimbblet, K. A., Edge, A. C., Smith, G. P., & Wardlow, J. L. 2009, *MNRAS*, 394, 2098
- Sun, M., Voit, G. M., Donahue, M., et al. 2009, *ApJ*, 693, 1142
- Thanjavur, K., Crampton, D., & Willis, J. 2010, *ApJ*, 714, 1355
- Tran, K.-V. H., Franx, M., Illingworth, G., Kelson, D. D., & van Dokkum, P. 2003, *ApJ*, 599, 865
- Treu, T., Ellis, R. S., Kneib, J., et al. 2003, *ApJ*, 591, 53
- Verdugo, T., Motta, V., Muñoz, R. P., et al. 2011, *A&A*, 527, A124
- Vikhlinin, A., van Speybroeck, L., Markevitch, M., Forman, W. R., & Grego, L. 2002, *ApJ*, 578, L107
- Vikhlinin, A., Kravtsov, A., Forman, W., et al. 2006, *ApJ*, 640, 691
- Vikhlinin, A., Kravtsov, A. V., Burenin, R. A., et al. 2009, *ApJ*, 692, 1060
- Voit, G. M. 2005, *Rev. Mod. Phys.*, 77, 207
- Wang, S., Houry, J., Haiman, Z., & May, M. 2004, *Phys. Rev. D*, 70, 123008
- Wen, Z.-L., Han, J.-L., & Jiang, Y.-Y. 2011, *Res. Astron. Astrophys.*, 11, 1185
- White, S. D. M., & Frenk, C. S. 1991, *ApJ*, 379, 52
- White, S. D. M., Navarro, J. F., Evrard, A. E., & Frenk, C. S. 1993, *Nature*, 366, 429
- White, M., Hernquist, L., & Springel, V. 2001, *ApJ*, 550, L129
- Willis, J. P., Pacaud, F., Valtchanov, I., et al. 2005, *MNRAS*, 363, 675
- Wilman, D. J., Oemler, Jr., A., Mulchaey, J. S., et al. 2009, *ApJ*, 692, 298
- Yang, X., Mo, H. J., & van den Bosch, F. C. 2008, *ApJ*, 676, 248
- Zabludoff, A. I., & Mulchaey, J. S. 1998, *ApJ*, 496, 39
- Zabludoff, A. I., & Mulchaey, J. S. 2000, *ApJ*, 539, 136
- Zaritsky, D., & Gonzalez, A. H. 2003, *ApJ*, 584, 691

Table 2. Results of the weak-lensing and optical analysis of the best SARCS candidates.

Name	z_{spec}	z_{phot}	D_{ls}/D_s	z_{eff}	σ_{SIS} (km s^{-1})	R_A (arcsec)	$R_E(z_s)$ (arcsec) (–)	$N_{0.5 \text{ Mpc}}$	$L_{0.5 \text{ Mpc}}$ ($10^{12} L_{\odot}$)	$N_{1 \text{ Mpc}}$	$L_{1 \text{ Mpc}}$ ($10^{12} L_{\odot}$)
SA1	–	0.46	0.35	0.77	308^{+150}_{-65}	2.2	$1.6^{+2.5}_{-0.9} (1.42^{+0.77}_{-0.57})$	8 ± 1	0.52 ± 0.07	13 ± 3	0.85 ± 0.16
SA2	–	0.48	0.31	0.75	758^{+88}_{-153}	5.0	$9.4^{+4.3}_{-5.4} (1.43^{+0.77}_{-0.56})$	22 ± 2	1.58 ± 0.13	40 ± 4	2.72 ± 0.21
SA6	–	0.58	0.23	0.80	914^{+89}_{-123}	5.0	$12.0^{+5.6}_{-6.5} (1.45^{+0.76}_{-0.54})$	20 ± 1	1.61 ± 0.08	26 ± 2	1.92 ± 0.12
SA8	–	0.33	0.47	0.69	654^{+61}_{-96}	10.8	$8.5^{+2.7}_{-3.7} (1.40^{+0.78}_{-0.59})$	32 ± 2	1.63 ± 0.16	60 ± 6	2.85 ± 0.44
SA9	–	0.62	0.21	0.83	543^{+139}_{-191}	3.3	$4.0^{+3.8}_{-3.0} (1.47^{+0.76}_{-0.53})$	6 ± 1	0.78 ± 0.06	12 ± 2	1.20 ± 0.12
SA10	–	0.49	0.30	0.75	856^{+114}_{-100}	3.2	$11.9^{+6.0}_{-5.7} (1.43^{+0.77}_{-0.56})$	29 ± 2	2.37 ± 0.17	56 ± 5	3.65 ± 0.36
SA11	–	0.62	0.20	0.81	458^{+134}_{-175}	4.3	$2.9^{+3.1}_{-2.2} (1.47^{+0.76}_{-0.53})$	10 ± 1	0.84 ± 0.06	12 ± 1	0.94 ± 0.06
SA12	–	0.74	0.15	0.91	464^{+252}_{-138}	3.4	$2.5^{+5.3}_{-1.9} (1.51^{+0.74}_{-0.50})$	10 ± 1	0.66 ± 0.10	16 ± 3	0.85 ± 0.15
SA13	–	0.29	0.52	0.67	393^{+88}_{-100}	3.5	$3.2^{+2.0}_{-1.8} (1.39^{+0.78}_{-0.59})$	19 ± 2	1.09 ± 0.13	45 ± 5	1.67 ± 0.22
SA15	0.44 ^e	0.43	0.35	0.71	534^{+129}_{-152}	3.9	$5.0^{+3.9}_{-3.2} (1.42^{+0.77}_{-0.57})$	8 ± 0	0.69 ± 0.03	10 ± 1	0.78 ± 0.06
SA18	–	0.38	0.41	0.70	506^{+106}_{-152}	2.0	$4.8^{+3.1}_{-3.0} (1.41^{+0.78}_{-0.58})$	8 ± 1	0.96 ± 0.09	13 ± 2	1.33 ± 0.17
SA22	0.44 ^d	0.48	0.36	0.74	638^{+101}_{-152}	7.1	$7.0^{+3.8}_{-4.2} (1.42^{+0.77}_{-0.57})$	31 ± 2	1.73 ± 0.10	42 ± 4	2.21 ± 0.19
SA23	0.61 ^d	0.74	0.21	0.81	713^{+163}_{-192}	1.9	$7.0^{+6.1}_{-4.8} (1.46^{+0.76}_{-0.54})$	7 ± 1	0.59 ± 0.05	10 ± 2	0.75 ± 0.07
SA26	–	0.69	0.17	0.88	853^{+145}_{-153}	16.4	$9.0^{+6.8}_{-5.7} (1.49^{+0.75}_{-0.52})$	31 ± 2	2.67 ± 0.15	67 ± 4	5.60 ± 0.31
SA27	–	0.18	0.66	0.59	643^{+74}_{-78}	2.8	$9.8^{+3.0}_{-3.1} (1.39^{+0.78}_{-0.60})$	12 ± 1	0.71 ± 0.07	24 ± 4	1.36 ± 0.20
SA28	–	0.86	0.13	1.04	748^{+179}_{-259}	2.4	$5.5^{+6.1}_{-4.4} (1.57^{+0.72}_{-0.47})$	8 ± 1	1.19 ± 0.13	23 ± 4	1.95 ± 0.32
SA29	–	0.72	0.17	0.92	394^{+209}_{-115}	2.4	$1.9^{+3.8}_{-1.4} (1.51^{+0.74}_{-0.51})$	11 ± 1	1.38 ± 0.10	21 ± 4	1.78 ± 0.23
SA30	0.43 ^e	0.45	0.37	0.74	509^{+118}_{-159}	5.6	$4.5^{+3.4}_{-3.0} (1.42^{+0.77}_{-0.57})$	9 ± 1	0.47 ± 0.05	16 ± 3	0.71 ± 0.16
SA31	–	0.27	0.55	0.66	593^{+73}_{-116}	3.2	$7.5^{+2.7}_{-3.5} (1.39^{+0.78}_{-0.59})$	3 ± 1	0.55 ± 0.04	6 ± 1	0.65 ± 0.08
SA33	0.64 ^d	0.42	0.22	0.87	380^{+173}_{-104}	2.4	$1.9^{+3.2}_{-1.3} (1.47^{+0.75}_{-0.53})$	14 ± 1	0.76 ± 0.05	28 ± 3	1.33 ± 0.15
SA36	–	0.35	0.45	0.70	724^{+65}_{-107}	3.0	$10.1^{+3.3}_{-4.5} (1.40^{+0.78}_{-0.58})$	23 ± 2	2.6 ± 0.18	30 ± 3	3.18 ± 0.28
SA37	–	0.79	0.14	0.96	641^{+214}_{-203}	2.2	$4.5^{+6.1}_{-3.4} (1.54^{+0.73}_{-0.49})$	6 ± 1	0.66 ± 0.08	25 ± 4	2.66 ± 0.31
SA39	0.61 ^d	0.72	0.20	0.80	655^{+124}_{-233}	5.2	$5.9^{+4.4}_{-4.5} (1.46^{+0.76}_{-0.54})$	5 ± 0	0.58 ± 0.05	8 ± 2	0.64 ± 0.07
SA42	–	0.98	0.08	1.09	1049^{+241}_{-315}	2.6	$9.3^{+11.0}_{-7.3} (1.64^{+0.71}_{-0.45})$	8 ± 1	2.04 ± 0.26	16 ± 4	3.26 ± 0.57
SA45	–	0.68	0.23	0.95	634^{+116}_{-198}	3.5	$5.1^{+4.0}_{-3.7} (1.49^{+0.75}_{-0.52})$	7 ± 1	0.51 ± 0.08	$9 \pm 2^*$	$0.69 \pm 0.14^*$
SA47	–	0.80	0.19	1.06	390^{+154}_{-115}	1.9	$1.6^{+2.6}_{-1.2} (1.54^{+0.73}_{-0.49})$	$4 \pm 1^*$	$0.33 \pm 0.06^*$	$8 \pm 1^*$	$0.45 \pm 0.09^*$
SA48	0.24 ^b	0.52	0.62	0.70	481^{+60}_{-80}	2.8	$5.1^{+1.8}_{-2.1} (1.39^{+0.78}_{-0.60})$	2 ± 0	0.38 ± 0.03	13 ± 3	0.74 ± 0.18
SA49	–	0.62	0.28	0.94	312^{+125}_{-72}	4.3	$1.3^{+1.9}_{-0.9} (1.47^{+0.76}_{-0.53})$	5 ± 1	0.34 ± 0.05	11 ± 2	0.60 ± 0.11
SA50	0.51 ^c	0.54	0.29	0.77	540^{+130}_{-172}	5.8	$4.6^{+3.8}_{-3.2} (1.43^{+0.77}_{-0.56})$	18 ± 1	0.90 ± 0.09	24 ± 2	1.32 ± 0.15
SA52	–	0.53	0.26	0.77	391^{+136}_{-135}	2.1	$2.3^{+2.7}_{-1.7} (1.44^{+0.76}_{-0.55})$	7 ± 1	0.49 ± 0.04	11 ± 2	0.58 ± 0.08
SA53	–	0.55	0.27	0.81	389^{+187}_{-130}	3.9	$2.3^{+3.7}_{-1.6} (1.45^{+0.76}_{-0.55})$	4 ± 1	0.34 ± 0.04	12 ± 3	0.63 ± 0.18
SA54	–	0.45	0.35	0.76	793^{+72}_{-96}	6.3	$10.7^{+4.0}_{-5.0} (1.42^{+0.77}_{-0.57})$	29 ± 2	2.10 ± 0.18	61 ± 5	3.73 ± 0.38
SA55	–	0.38	0.42	0.72	701^{+69}_{-109}	2.6	$9.1^{+3.3}_{-4.3} (1.41^{+0.78}_{-0.58})$	23 ± 2	1.49 ± 0.20	41 ± 5	2.58 ± 0.47
SA58	–	0.46	0.34	0.75	632^{+92}_{-187}	2.6	$6.7^{+3.5}_{-4.4} (1.42^{+0.77}_{-0.57})$	17 ± 1	0.92 ± 0.06	31 ± 3	1.61 ± 0.12
SA59	–	0.79	0.11	0.92	838^{+251}_{-322}	1.9	$7.6^{+9.6}_{-6.2} (1.54^{+0.73}_{-0.49})$	4 ± 1	1.08 ± 0.05	14 ± 3	2.15 ± 0.28
SA61	–	0.51	0.29	0.77	677^{+108}_{-133}	7.4	$7.2^{+4.3}_{-4.2} (1.43^{+0.77}_{-0.56})$	24 ± 2	2.27 ± 0.16	46 ± 5	3.30 ± 0.35
SA63	–	0.48	0.34	0.79	561^{+116}_{-155}	5.0	$5.2^{+3.6}_{-3.3} (1.43^{+0.77}_{-0.56})$	12 ± 1	0.84 ± 0.08	20 ± 3	1.51 ± 0.16
SA66	0.35 ^d	0.48	0.43	0.67	644^{+69}_{-102}	4.8	$8.0^{+2.9}_{-3.7} (1.40^{+0.78}_{-0.58})$	32 ± 2	1.90 ± 0.09	44 ± 3	2.42 ± 0.17
SA67	–	0.45	0.34	0.73	591^{+131}_{-150}	2.1	$6.0^{+4.3}_{-3.7} (1.42^{+0.77}_{-0.57})$	8 ± 1	0.44 ± 0.05	9 ± 1	0.62 ± 0.09
SA68	–	0.42	0.38	0.74	549^{+100}_{-167}	2.8	$5.3^{+3.2}_{-3.5} (1.41^{+0.77}_{-0.57})$	6 ± 1	0.59 ± 0.10	11 ± 3	1.41 ± 0.15
SA70	–	0.29	0.51	0.66	438^{+111}_{-125}	3.9	$4.0^{+2.8}_{-2.3} (1.39^{+0.78}_{-0.59})$	9 ± 1	0.47 ± 0.07	19 ± 2	0.97 ± 0.11
SA72	0.64 ^d	0.70	0.19	0.83	466^{+150}_{-160}	4.5	$2.9^{+3.4}_{-2.2} (1.47^{+0.75}_{-0.53})$	15 ± 2	1.31 ± 0.15	15 ± 2	1.44 ± 0.16

Notes. ^(*) Groups that are closer to the edge of the field of view than the aperture in which richness and luminosity are estimated. ^(a) Muñoz et al. (2013). ^(b) Ruff et al. (2011). ^(c) Limousin et al. (2009). ^(d) Thanjavur et al. (2010). ^(e) Motta et al. (in prep.). Columns are (1) SARCS name; (2) spectroscopic redshift; (3) photometric redshift from Coupon et al. (2009); (4) average geometrical factor; (5) effective redshift derived from the average geometrical factor; (6) SIS velocity dispersion derived from the shear profile (quoted errors are the statistical uncertainties from the shear profile fitting); (7) arc radius (from More et al. 2012); (8) Einstein radius from σ_{SIS} and the source redshift in parenthesis (error bars account both for errors on σ_{SIS} and the PDF of z_s); (9–10) optical richness and luminosity derived from the bright red galaxies; (11–12) same as (9–10) but using an aperture of 1 Mpc.

Table 2. continued.

Name	z_{spec}	z_{phot}	D_{ls}/D_s	z_{eff}	σ_{SIS} (km s^{-1})	R_A (arcsec)	$R_E(z_s)$ (arcsec)	$N_{0.5 \text{ Mpc}}$	$L_{0.5 \text{ Mpc}}$ ($10^{12} L_{\odot}$)	$N_{1 \text{ Mpc}}$	$L_{1 \text{ Mpc}}$ ($10^{12} L_{\odot}$)
SA74	–	0.36	0.45	0.72	672^{+89}_{-94}	3.2	$8.6^{+3.7}_{-3.8} (1.40^{+0.78}_{-0.58})$	21 ± 2	1.34 ± 0.13	44 ± 4	2.83 ± 0.31
SA78	–	0.74	0.21	1.00	543^{+96}_{-157}	3.2	$3.4^{+2.8}_{-2.5} (1.51^{+0.74}_{-0.50})$	30 ± 3	2.26 ± 0.18	56 ± 6	3.78 ± 0.35
SA79	–	0.76	0.21	1.03	340^{+130}_{-60}	3.5	$1.3^{+2.0}_{-0.8} (1.52^{+0.74}_{-0.50})$	12 ± 2	0.95 ± 0.13	55 ± 7	4.03 ± 0.44
SA80	–	1.00	0.11	1.17	536^{+149}_{-193}	2.4	$2.4^{+3.2}_{-1.9} (1.65^{+0.70}_{-0.44})$	20 ± 1	1.39 ± 0.14	35 ± 5	2.78 ± 0.44
SA84	–	0.77	0.21	1.05	513^{+86}_{-169}	1.9	$2.9^{+2.4}_{-2.3} (1.53^{+0.74}_{-0.50})$	6 ± 1	0.28 ± 0.08	11 ± 2	0.74 ± 0.14
SA86	–	0.46	0.35	0.77	600^{+82}_{-151}	3.7	$6.1^{+3.0}_{-3.7} (1.42^{+0.77}_{-0.57})$	16 ± 1	1.49 ± 0.11	41 ± 3	2.88 ± 0.25
SA87	–	0.54	0.25	0.77	425^{+192}_{-124}	3.5	$2.7^{+4.2}_{-1.9} (1.44^{+0.76}_{-0.55})$	14 ± 1	1.16 ± 0.12	29 ± 3	2.35 ± 0.28
SA89	–	0.42	0.34	0.68	676^{+96}_{-163}	3.7	$8.1^{+4.0}_{-4.8} (1.41^{+0.77}_{-0.57})$	9 ± 1	0.95 ± 0.13	37 ± 5	2.93 ± 0.40
SA90	–	0.53	0.26	0.77	1015^{+70}_{-79}	3.7	$15.8^{+5.8}_{-7.2} (1.44^{+0.76}_{-0.55})$	20 ± 2	1.52 ± 0.12	45 ± 5	2.82 ± 0.27
SA91	–	0.56	0.24	0.78	360^{+195}_{-87}	3.0	$1.9^{+3.6}_{-1.2} (1.45^{+0.76}_{-0.55})$	13 ± 1	1.03 ± 0.09	22 ± 3	1.64 ± 0.19
SA92	–	0.50	0.31	0.78	595^{+105}_{-164}	2.8	$5.7^{+3.6}_{-3.7} (1.43^{+0.77}_{-0.56})$	8 ± 1	0.44 ± 0.06	$11 \pm 1^*$	$0.53 \pm 0.08^*$
SA94	–	0.51	0.29	0.76	653^{+100}_{-196}	0.0	$6.7^{+3.9}_{-4.6} (1.43^{+0.77}_{-0.56})$	16 ± 1	1.01 ± 0.12	27 ± 5	1.99 ± 0.32
SA95	–	0.49	0.28	0.73	392^{+197}_{-112}	2.2	$2.5^{+4.1}_{-1.6} (1.43^{+0.77}_{-0.56})$	3 ± 1	0.70 ± 0.07	7 ± 2	0.81 ± 0.13
SA96	–	0.39	0.37	0.67	449^{+123}_{-138}	2.8	$3.7^{+3.1}_{-2.4} (1.41^{+0.78}_{-0.58})$	13 ± 2	0.80 ± 0.13	40 ± 5	2.74 ± 0.42
SA97	0.42 ^c	0.48	0.34	0.67	384^{+162}_{-109}	8.0	$2.6^{+3.4}_{-1.7} (1.41^{+0.77}_{-0.57})$	15 ± 1	0.89 ± 0.09	28 ± 4	1.09 ± 0.23
SA98	–	0.52	0.28	0.77	932^{+107}_{-133}	18.4	$13.5^{+6.5}_{-7.1} (1.44^{+0.77}_{-0.56})$	29 ± 2	2.08 ± 0.21	56 ± 3	3.37 ± 0.46
SA99	–	0.32	0.48	0.67	395^{+103}_{-118}	2.4	$3.1^{+2.3}_{-1.9} (1.40^{+0.78}_{-0.59})$	4 ± 1	0.46 ± 0.10	7 ± 2	0.54 ± 0.12
SA100	–	0.63	0.19	0.82	969^{+100}_{-130}	14.7	$12.6^{+6.5}_{-7.1} (1.47^{+0.75}_{-0.53})$	30 ± 2	3.00 ± 0.16	71 ± 4	5.49 ± 0.35
SA101	–	0.87	0.10	0.99	902^{+192}_{-268}	3.5	$7.9^{+8.2}_{-6.1} (1.58^{+0.72}_{-0.47})$	5 ± 1	2.36 ± 0.24	18 ± 5	3.36 ± 0.54
SA102	–	0.69	0.16	0.86	1028^{+140}_{-272}	9.9	$13.1^{+8.5}_{-9.2} (1.49^{+0.75}_{-0.52})$	32 ± 2	2.03 ± 0.13	58 ± 4	3.40 ± 0.27
SA103	–	0.47	0.28	0.70	450^{+164}_{-134}	4.1	$3.4^{+3.9}_{-2.2} (1.42^{+0.77}_{-0.57})$	12 ± 1	0.86 ± 0.08	25 ± 4	1.46 ± 0.22
SA106	–	0.74	0.15	0.91	490^{+185}_{-176}	1.9	$2.8^{+4.1}_{-2.2} (1.51^{+0.74}_{-0.50})$	7 ± 1	0.50 ± 0.11	16 ± 3	1.14 ± 0.21
SA108	–	0.86	0.10	0.99	1008^{+213}_{-345}	4.5	$10.1^{+10.2}_{-8.0} (1.57^{+0.72}_{-0.47})$	25 ± 1	2.01 ± 0.20	41 ± 4	3.18 ± 0.39
SA109	–	0.39	0.41	0.72	394^{+183}_{-100}	3.2	$2.9^{+4.1}_{-1.7} (1.41^{+0.78}_{-0.58})$	3 ± 1	0.47 ± 0.11	$8 \pm 3^*$	$0.90 \pm 0.18^*$
SA110	–	0.18	0.66	0.58	329^{+104}_{-80}	4.1	$2.6^{+2.1}_{-1.3} (1.39^{+0.78}_{-0.60})$	4 ± 1	0.42 ± 0.07	16 ± 4	2.09 ± 0.24
SA111	–	0.52	0.29	0.79	889^{+67}_{-88}	5.0	$12.3^{+4.6}_{-5.8} (1.44^{+0.77}_{-0.56})$	28 ± 2	2.21 ± 0.13	49 ± 4	3.73 ± 0.26
SA112	0.50 ^d	0.55	0.29	0.75	626^{+112}_{-178}	4.3	$6.3^{+4.0}_{-4.1} (1.43^{+0.77}_{-0.56})$	20 ± 1	0.95 ± 0.08	43 ± 4	1.85 ± 0.19
SA113	0.67 ^d	0.71	0.17	0.85	745^{+139}_{-210}	3.0	$7.1^{+5.6}_{-5.0} (1.49^{+0.75}_{-0.52})$	16 ± 2	1.25 ± 0.12	32 ± 3	2.21 ± 0.23
SA114	–	0.83	0.11	0.97	809^{+168}_{-300}	3.5	$6.7^{+6.6}_{-5.4} (1.56^{+0.73}_{-0.48})$	14 ± 1	1.30 ± 0.14	48 ± 4	3.72 ± 0.37
SA116	–	0.57	0.24	0.80	706^{+126}_{-216}	4.1	$7.3^{+5.0}_{-5.1} (1.45^{+0.76}_{-0.54})$	8 ± 1	0.54 ± 0.05	15 ± 3	0.81 ± 0.14
SA117	–	0.43	0.37	0.74	697^{+92}_{-111}	7.3	$8.5^{+4.0}_{-4.2} (1.42^{+0.77}_{-0.57})$	26 ± 3	1.51 ± 0.24	45 ± 7	1.98 ± 0.41
SA120	–	0.46	0.24	0.76	556^{+91}_{-172}	2.1	$5.2^{+3.0}_{-3.5} (1.42^{+0.77}_{-0.57})$	6 ± 1	0.34 ± 0.04	9 ± 2	0.54 ± 0.13
SA121	–	0.62	0.12	0.84	443^{+170}_{-137}	3.7	$2.7^{+3.7}_{-1.9} (1.47^{+0.76}_{-0.53})$	10 ± 2	1.03 ± 0.13	16 ± 4	1.76 ± 0.26
SA123	–	1.00	0.07	1.11	894^{+267}_{-288}	4.8	$6.6^{+9.5}_{-5.3} (1.65^{+0.70}_{-0.44})$	18 ± 2	1.73 ± 0.16	37 ± 4	3.70 ± 0.42
SA124	–	0.83	0.20	1.11	545^{+102}_{-164}	7.4	$3.1^{+2.8}_{-2.3} (1.56^{+0.73}_{-0.48})$	12 ± 1	0.56 ± 0.07	20 ± 2	0.93 ± 0.14
SA125	–	0.74	0.15	0.91	695^{+176}_{-235}	0.0	$5.6^{+5.9}_{-4.3} (1.51^{+0.74}_{-0.50})$	24 ± 2	2.75 ± 0.22	33 ± 4	3.66 ± 0.34
SA127	0.33 ^c	0.33	0.47	0.70	645^{+68}_{-123}	4.7	$8.2^{+2.9}_{-4.0} (1.40^{+0.78}_{-0.59})$	5 ± 1	0.56 ± 0.05	11 ± 3	0.74 ± 0.12
SA0	0.38 ^d	–	0.41	0.71	638^{+85}_{-135}	6.1	$7.6^{+3.4}_{-4.1} (1.41^{+0.78}_{-0.58})$	11 ± 1	0.84 ± 0.04	21 ± 3	1.26 ± 0.12

Appendix A

In Sect. 3.2 we briefly discuss the question of choosing the most likely centre of the halo mass distribution. From the optical luminosity maps, we have shown that several SARCS objects present complex morphology. Assuming that light traces mass on the group and cluster scale (e.g. Bahcall 2000), these substructures in the distribution of galaxies might be associated to massive subhaloes. As the weak-lensing estimator is sensitive to all the mass components where the signal is measured, a fit using a single halo will be affected by all the present substructures. However, the question of the centre remains as a source of uncertainties: substantial miscentering can lead to weak-lensing masses underestimated up to 30% (e.g. George et al. 2012).

Here we explore the effect of changing the position of the centre used to construct the shear profile. We limit the analysis to the SARCS groups with a multi-modal structure in their luminosity maps within a 0.5 Mpc radius from the centre of the strong-lensing system. For group-scale haloes, typical values of the virial radius are ~ 1 Mpc, so within a 0.5 Mpc radius we expect to instead observe substructures than two distinct haloes. Fitting shear profiles with a single component thus remains valid, so we changed the position of the centre of the shear profile for these groups by simply positioning it either between the two optical over-densities or on the second observed peak, i.e. not associated to the strong-lensing system.

The results we obtained are presented Fig. A.1. For two groups, SA35 and SA83, we managed to obtain better constraints than in the initial configuration. It suggests that the strong-lensing system is not exactly at the mass centre but rather associated to a satellite galaxy. For SA90, we observe a strong change according to the centre's position, with a σ_{SIS} much higher when using the strong-lensing system as the centre of the shear profile. For this group, the brightest galaxy is also at the centre of the strong-lensing system, which seems to indicate that the mass associated to the second luminosity peak is negligible compared to the main halo. SA91 presents the opposite behaviour, with a velocity dispersion higher when the centre of the shear profile is moved towards the second luminosity peak. As for SA35 and SA83, we suppose that the strong-lensing system is associated with a satellite galaxy.

In the remaining cases, we only observe slight variations with compatible velocity dispersions within their 1σ error bar, which makes interpreting the results speculative. For groups that have the highest σ_{SIS} when the centre of the shear profile is taken between the two luminosity over-densities as SA89, one can explain such a variation by the presence of two clumps of galaxies evolving in a single dark matter halo whose mass centre is located in the middle of the galaxy distribution. For instance, SA66 was studied in more detail by Limousin et al. (2010a) with a strong-lensing modelling that requires a substantial external shear, and by Muñoz et al. (2013), with a dynamical analysis that revealed two distinct populations of galaxies. In that case, the results suggest a merging event of two subhaloes. Such a configuration is consistent with the weak-lensing results since moving the centre of the shear profile in both directions from the total mass centre induces a lower SIS velocity dispersion, with a larger decrease when going towards the second luminosity peak (not associated with the strong-lensing system). It is therefore tempting to infer the same for the groups showing the same variation in σ_{SIS} . One can also think of two distinct dark matter haloes with similar masses that generate their own shear signal, and thus we observe the opposite variation with lower values of σ_{SIS} when taking the centre of the profiles between the two luminosity over-densities (SA26, SA55). Another possible configuration would be a mass distribution dominated by a halo located on the strong-lensing system, and in that case, the measured velocity dispersion decreases when moving away, such as for SA61.

Even though we observe statistically significant changes for some groups, given the weakness of the signal we measure on single objects, it remains difficult to probe the position of the actual mass centre via weak lensing and draw reliable conclusions from the small observed variations in the shear profile. Our first assumption of positioning the mass centre on the strong-lensing system then remains on average a valid approximation. In specific cases, a deeper analysis combining a strong-lensing modelling (external shear) and dynamical information (two distinct populations of galaxies) might, however, help to increase the precision of the mass determination for such complex configurations.

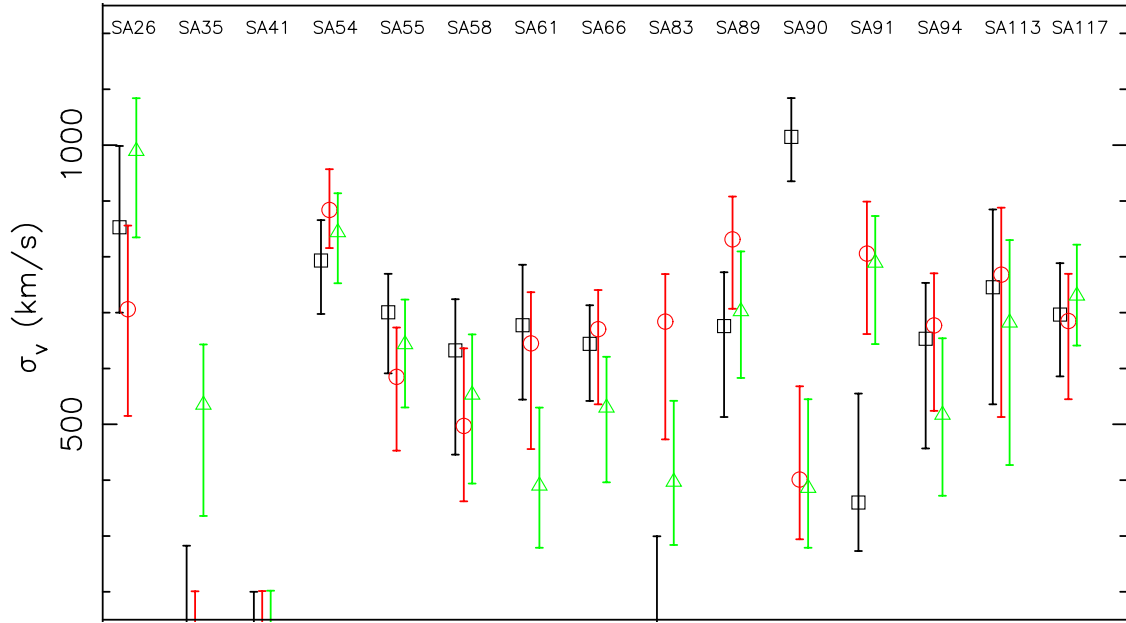


Fig. A.1. SIS model on the multi-modal SARCS candidates. The centre chosen for the shear profile is located either on the strong-lensing system (black open squares), at the middle of the 2 luminosity over-densities (red open circles) or on the luminosity peak not associated to the strong lensing features (green open triangles). The measured dispersion at the three different positionings can be used as an indicator of the dominance of the strong lens within its group.

Strong lensing as a probe of the mass distribution *beyond* the Einstein radius

Mass and light in SL2S J08544-0121, a galaxy group at $z = 0.35$

M. Limousin^{1,2,3}, E. Jullo^{4,1}, J. Richard^{5,6}, R. Cabanac²,
S. H. Suyu⁷, A. Halkola⁸, J.-P. Kneib¹, R. Gavazzi^{9,10}, and G. Soucail^{11,*}

¹ Laboratoire d'Astrophysique de Marseille, UMR 6610, CNRS-Université de Provence, 38 rue Frédéric Joliot-Curie, 13388 Marseille Cedex 13, France

e-mail: marceau.limousin@oamp.fr

² Laboratoire d'Astrophysique de Toulouse-Tarbes, Université de Toulouse, CNRS, 57 avenue d'Azereix, 65000 Tarbes, France

³ Dark Cosmology Centre, Niels Bohr Institute, University of Copenhagen, Juliane Maries Vej 30, 2100 Copenhagen, Denmark

⁴ Jet Propulsion Laboratory, California Institute of Technology, Pasadena, CA 91109, USA

⁵ Durham University, Physics and Astronomy Department, South Road, Durham DH3 1LE, UK

⁶ Department of Astronomy, California Institute of Technology, 105-24 Pasadena, CA 91125, USA

⁷ Argelander-Institut für Astronomie, Universität Bonn, Auf dem Hügel 71, 53121 Bonn, Germany

⁸ Excellence Cluster Universe, Technische Universität München, Boltzmannstr. 2, 85748 Garching, Germany

⁹ CNRS, UMR 7095, Institut d'Astrophysique de Paris, 75014 Paris, France

¹⁰ UPMC Université Paris 06, UMR 7095, Institut d'Astrophysique de Paris, 75014 Paris, France

¹¹ Laboratoire d'Astrophysique de Toulouse-Tarbes, Université de Toulouse, CNRS, 14 avenue Edouard Belin, 31400 Toulouse, France

Received 22 June 2010 / Accepted 9 September 2010

ABSTRACT

Strong lensing has been employed extensively to obtain accurate mass measurements *within* the Einstein radius. We here use strong lensing to probe mass distributions *beyond* the Einstein radius. We consider SL2S J08544-0121, a galaxy group at redshift $z = 0.35$ with a bimodal light distribution and with a strong lensing system located at one of the two luminosity peaks separated by $\sim 54''$. The main arc and the counter-image of the strong lensing system are located at $\sim 5''$ and $\sim 8''$ from the lens galaxy centre. We find that a simple elliptical isothermal potential cannot satisfactorily reproduce the strong lensing observations. However, with a mass model for the group built from its light-distribution with a smoothing factor s and a mass-to-light ratio M/L , we obtain an accurate reproduction of the observations. We find $M/L = 98 \pm 27$ (i band, solar units, not corrected for evolution) and $s = 20'' \pm 9$ (2σ confidence level). Moreover, we use weak lensing to independently estimate the mass of the group, and find a consistent M/L in the range 66-146 ($1-\sigma$ confidence level). This suggests that light is a good tracer of mass. Interestingly, this also shows that a strong lensing-*only* analysis (on scales of $\sim 10''$) can constrain the properties of nearby objects (on scales of $\sim 100''$). We characterise the type of perturbed strong lensing system that allows such an analysis: *a non dominant strong lensing system used as a test particle to probe the main potential*. This kind of analysis needs to be validated with other systems because it could provide a quick way of probing the mass distribution of clusters and groups. This is particularly relevant in the context of forthcoming wide-field surveys, which will yield thousands of strong lenses, some of which perturbed enough to pursue the analysis proposed in this paper.

Key words. gravitational lensing: strong – dark matter

1. Introduction

Gravitational lensing probes the mass distribution projected along the line of sight. When the surface mass density of a lens is higher than a critical threshold, i.e. in the strong lensing (SL) regime, the light from a background source galaxy is lensed into

* Based on observations obtained with MegaPrime/MegaCam, a joint project of CFHT and CEA/DAPNIA, at the Canada-France-Hawaii Telescope (CFHT) which is operated by the National Research Council (NRC) of Canada, the Institut National des Sciences de l'Univers of the Centre National de la Recherche Scientifique (CNRS) of France, and the University of Hawaii. This work is based in part on data products produced at TERAPIX and the Canadian Astronomy Data Centre as part of the Canada-France-Hawaii Telescope Legacy Survey, a collaborative project of NRC and CNRS. Also based on HST data, program 10876 and Keck telescope data.

multiple images. These multiple images provide strong observational constraints on the projected mass distribution of the lens within the Einstein radius. Since the discovery of the first gravitational arc in the galaxy cluster Abell 370 twenty years ago (Lynds & Petrosian 1986; Soucail et al. 1987; Richard et al. 2010), strong lensing has been widely used to probe the mass distribution of structures at different scales: galaxies (see, e.g. the SLACS survey, Koopmans et al. 2006), galaxy clusters (see, e.g. Halkola et al. 2006) and recently galaxy groups (Cabanac et al. 2007; Limousin et al. 2009; Belokurov et al. 2009).

1.1. Perturbing a strong lensing system

Because most of the galaxies in the Universe are part of larger structures, either groups or clusters, so are many SL systems

(see, e.g. Kundic et al. 1997; Fassnacht & Lubin 2002; Faure et al. 2004; Morgan et al. 2005; Williams et al. 2006; Momcheva et al. 2006; Auger et al. 2007; Tu et al. 2008; Auger et al. 2008; Grillo et al. 2008; Treu et al. 2009; Inada et al. 2009). A mass distribution located at a small angular distance from a strong lens may induce measurable perturbations in the lensing signal. Not taking this external perturbation into account can seriously bias the results inferred from the SL modelling as shown by Keeton & Zabludoff (2004): they found that if the environment is neglected, SL modelling of double-image lenses largely overestimate both the ellipticity of the lens galaxy ($\Delta e/e \sim 0.5$) and the Hubble constant ($\Delta h/h \sim 0.22$). In contrast, models of four-image lenses in which perturbations by the environment are incorporated as a tidal shear, recover the ellipticity reasonably well, while still overestimating the Hubble constant ($\Delta h/h \sim 0.15$). They argue that most of the biases are owing to the neglected convergence from nearby massive groups or clusters of galaxies. More generally, the topic of modelling a lens with an external mass perturbation has been addressed by different authors (see, e.g. Keeton et al. 1997; Kochanek et al. 2001; Keeton & Zabludoff 2004; Oguri et al. 2005, 2008; Dye et al. 2007, and references therein).

To summarise, a precise SL modelling can be *affected* by external mass distributions, and scientists have tried to take this bias into account in order to improve the SL modelling. As observations become more and more accurate, we can expect to be more and more sensitive to external mass distributions near strong lenses. We propose to *exploit this external effect* by using the perturbations measured in SL modelling as *probes of the external mass distribution*.

1.2. The “ring” test in Abell 1689

We first remind the reader of a previous attempt we made to locally probe the potential of the galaxy cluster Abell 1689 with a perturbed SL system. In the core of galaxy cluster Abell 1689, Limousin et al. (2007) reported SL systems (“rings”) formed around three elliptical galaxies located 100’’ away from the cluster centre, i.e. the transitional region between the strong and weak lensing regimes. These SL systems should be sensitive to the external shear and convergence produced by their parent cluster (Kochanek & Blandford 1991). Based on simulations, Tu et al. (2008) showed that these strong lenses could be used to locally probe the cluster potential. They applied this method to the three rings discovered in Abell 1689, and found that solely modelling these three rings (i.e. without including any other multiply-imaged systems that are also produced by the cluster) provides strong evidence for bimodality of the cluster core; it is impossible to simultaneously model the three rings assuming a unimodal mass distribution for the cluster. This bimodality confirms previous parametric SL studies of Abell 1689 (Miralda-Escude & Babul 1995; Halkola et al. 2006; Limousin et al. 2007; Leonard et al. 2007; Saha et al. 2007; Okura et al. 2008). More importantly, this result shows that SL features of 1–2’’-wide Einstein rings actually contain information on the mass distribution of the parent cluster, i.e. on a much larger scale than their Einstein radii. In other words, this study suggests that strong lenses can be used to probe mass distributions *beyond* their Einstein radius. We further develop this idea on another perturbed SL system located in a galaxy group, SL2S J08544-0121.

All results are scaled to a flat, Λ CDM cosmology with $\Omega_M = 0.3$, $\Omega_\Lambda = 0.7$ and a Hubble constant $H_0 = 70 \text{ km s}^{-1} \text{ Mpc}^{-1}$. In this cosmology, 1’’ corresponds to a physical transverse distance

of 4.94 kpc at $z = 0.35$. All images are aligned with the WCS coordinates, i.e. north is up and east is left. Magnitudes are given in the AB system. Luminosities are given for the i band, in solar units, not corrected for passive evolution. Ellipticities are expressed as $(a^2 - b^2)/(a^2 + b^2)$, and position angles are given counterclockwise with respect to the west. Shear and convergence are computed for a source redshift of $z_s = 1.268$.

2. SL2S J08544-0121: presentation and data

SL2S J08544-0121 is part of the Strong Lensing Legacy Survey (SL2S, Cabanac et al. 2007), which collects SL systems in the Canada France Hawaii Telescope Legacy Survey (CFHTLS). SL2S J08544-0121 is a galaxy group at $z = 0.35$ presented by Limousin et al. (2009), which contains a SL system (Fig. 1).

2.1. Ground-based imaging

SL2S J08544-0121 has been observed in five bands as part of the CFHTLS. The i -band data are used to build luminosity maps from isophotal magnitudes of elliptical group members and to perform a weak-lensing analysis.

The bottom panel of Fig. 1 shows a $10' \times 10'$ CFHTLS i -band image. The white cross gives the location of the strong lens. We draw luminosity isodensity contours of 10^5 , 3×10^5 , 10^6 , 3×10^6 and $10^7 L_\odot \text{ kpc}^{-2}$. The top-right panel also shows a CFHTLS 1-arcmin² gri colour image centred on the lens.

2.2. Space-based imaging

The strong lensing features detected from ground-based images have been observed with the *Hubble Space Telescope* (HST). Observations were done in snapshot mode (C15, P.I. Kneib, ID 10876) in three bands with the ACS camera (F475, F606, and F814). Figure 1 shows a colour image of the strong lens based on these observations. We report two multiply-imaged systems: the first system is bright and forms a typical cusp configuration perturbed by a satellite galaxy (labelled Dwarf in Fig. 1). The second system is a very faint arc located west of the lens at a larger radius. It is not possible to reliably identify individual images on the faint arc. Moreover, given its faintness, spectroscopy is hopeless with current facilities, as the surface brightness is ca. 31 mag arcsec⁻², and therefore it is not used in the following analysis. As can be appreciated from Fig. 1, the HST data brings significant amounts of additional information on the lensed features.

2.3. Spectroscopy

We have used the Low Resolution Imager and Spectrograph (LRIS, Oke et al. 1995) on the Keck telescope to measure the spectroscopic redshift of both the lens and the brightest arc of the SL2S J08544-0121 system. On 2007 January 14, we obtained 300 seconds on the lensing galaxy and four exposures of 900 seconds each on the arc, using a 1.0’’ wide slit. A 600 lines mm⁻¹ grism blazed at 4000 Å and a 400 lines mm⁻¹ grating blazed at 8500 Å were used in the blue and red channels of the instrument, both light paths being separated by a dichroic at 5600 Å. The corresponding dispersions are 0.6/1.85 Å and resolutions are 4.0/6.5 Å in the blue/red channel. The resulting extracted spectra are shown in Fig. 2. The lens presents a typical elliptical spectrum at $z = 0.3530 \pm 0.0005$ with prominent H and K CaII lines, 4000 Å break, and G band. The spectrum of the arc shows

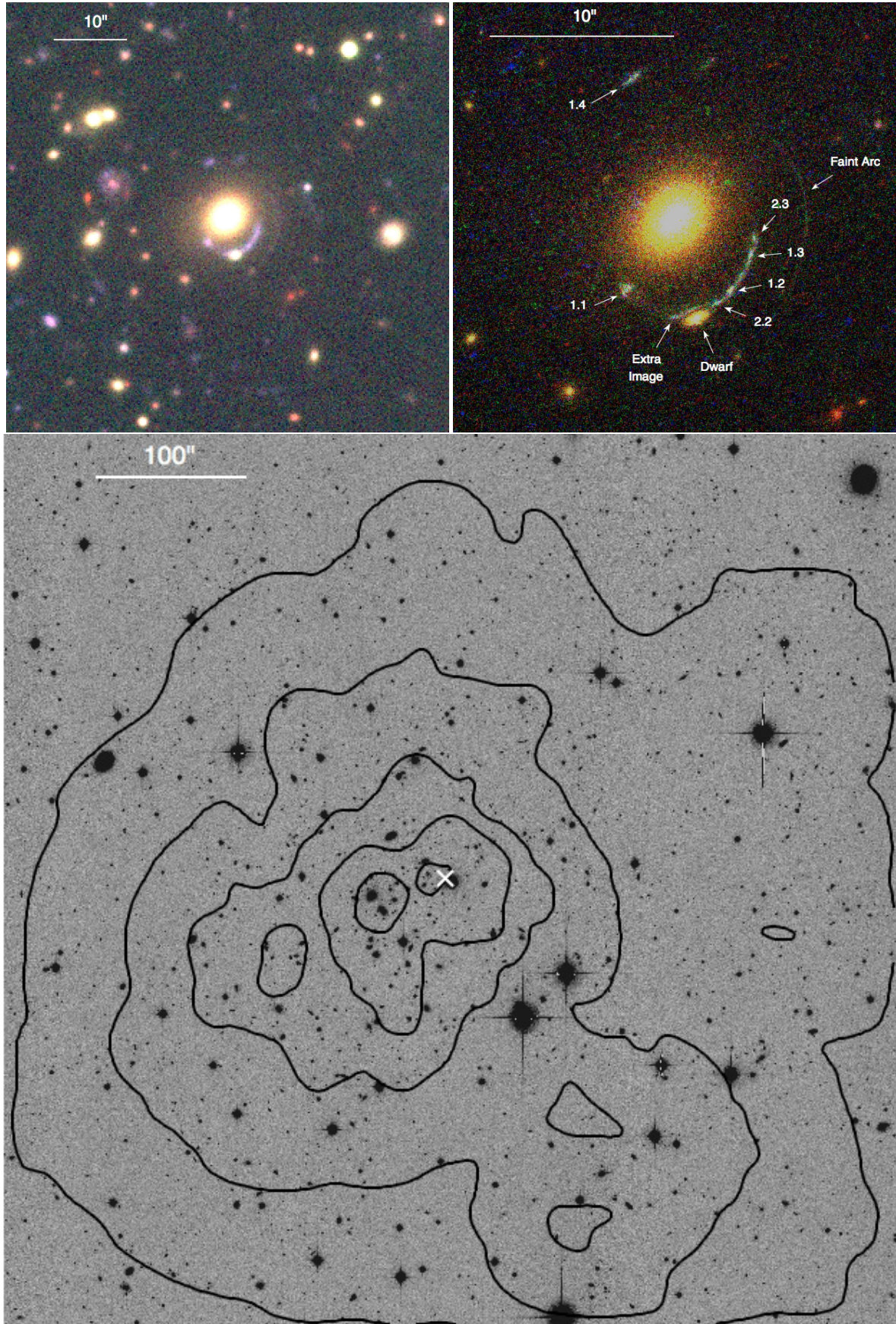


Fig. 1. Group SL2S J08544-0121 at $z_{\text{spec}} = 0.353$. *Upper Left:* composite CFHTLS *gri* colour image ($1 \text{ arcmin}^2 = 297 \times 297 \text{ kpc}^2$). *Upper Right:* composite HST/ACS F814W-F606W-F475W colour image ($24'' \times 24'' = 118 \times 118 \text{ kpc}^2$). We show the proposed multiple-image identification. The dwarf galaxy and the main extra image it produces is labelled. *Lower:* CFHTLS *i* band ($10' \times 10' = 2969 \times 2969 \text{ kpc}^2$). Luminosity isodensity contours of 10^5 , 3×10^5 , 10^6 , 3×10^6 and $10^7 L_{\odot} \text{ kpc}^{-2}$ are drawn (continuous black line), and the white cross shows the location of the SL system.

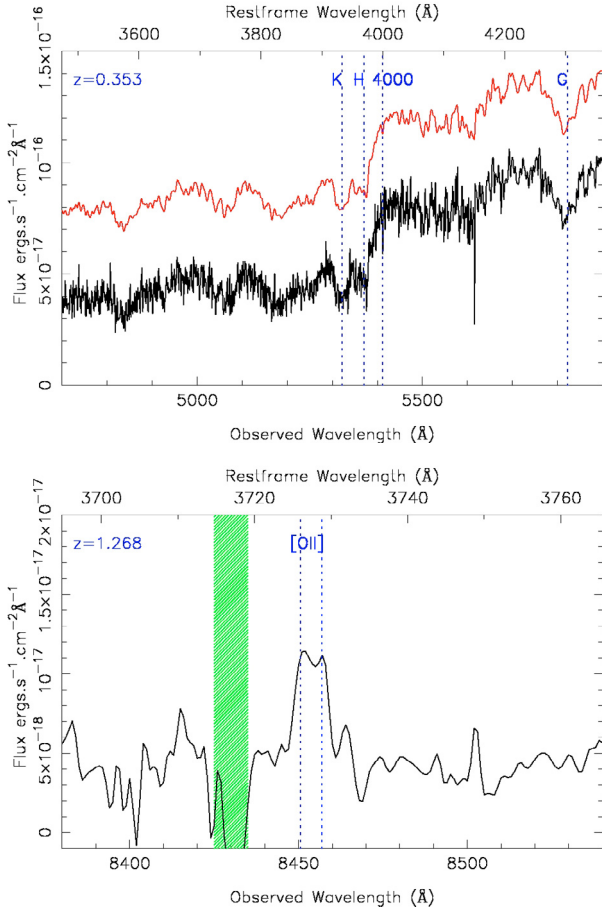


Fig. 2. 1-D spectra of the lens (*up*) and of the bright arc (*low*). The green shaded region masks the residuals of a strong OH atmospheric emission.

a strong emission line at 8454 Å, resolved in a doublet separated by ~ 5 Å. This gives us an unambiguous redshift determination of $z = 1.2680 \pm 0.0003$ with [OII] emission.

2.4. Global properties

The luminosity contours of SL2S J08544-0121 are elongated in the east-west direction. The SL deflector is populated by a single bright galaxy. Note (Fig. 1) that the innermost luminosity isodensity contour at $10^7 L_{\odot} \text{ kpc}^{-2}$ encompasses the SL system, but also two bright galaxies located $\sim 54''$ east from the SL system, making this light distribution bimodal. This is the only group of the sample presented by Limousin et al. (2009) for which the luminosity isodensity distribution is not clearly dominated by the lens, making this configuration rather exceptional: the large Einstein radius ($\sim 5''$) indicates a significant mass concentration associated with this lens, but the luminosity isodensity distribution is actually bimodal.

3. Modelling the lens

In this section, we attempt to reproduce the SL multiple images using a single elliptical isothermal potential centred on the bright galaxy. All optimisations are performed in the *image plane* with the **L** software (Jullo et al. 2007). We quantify the goodness of the fit by using the image plane RMS and the corresponding χ^2 . When necessary, we compare the fits using the Bayesian Evidence.

3.1. Observational constraints

As explained in Sect. 2.2, we do not use the faint arc in the analysis and focus on the bright multiply-imaged system. This system is composed of four main images: 1.1, 1.2, 1.3 and 1.4. Additional images are produced by the satellite (dwarf) galaxy. These are not considered in the analysis because we do not want to complicate the modelling by adding a sub-halo for the satellite galaxy. We also *make the assumption* that, given its small size, the satellite galaxy does not influence images 1.1 to 1.4. This assumption will be discussed in Sect. 8 and addressed further in a forthcoming publication. Because the merging arc composed of images 1.2 and 1.3 is well resolved, we can safely associate two other images on this arc, namely 2.2 and 2.3 (Fig. 1). Their counter-images that are expected near images 1.1 and 1.4 are not safely identified, therefore we do not use them in the analysis. Indeed, parametric strong lensing analyses are highly sensitive to misidentifications of images, and we prefer to use only the images we are confident in. This gives us a total of eight observational constraints.

3.2. Shape of the bright galaxy

In this subsection, we describe the properties of the light distribution of the bright galaxy that populates the strong lensing deflector. We use the IRAF task *ellipse* to measure the shape of its isophotes. We find an ellipticity of $e = 0.206$ and a position angle of 39 ± 5 degrees at $2''$ from the centre. A closer inspection of the galaxy centre clearly reveals a double core even though the outer isophotes are elliptical. The above measurements therefore correspond to the superposition of the light from each component. The spectrum of the galaxy presented in Fig. 2 does not show features of another galaxy at a different lens redshift along the line of sight. Given the similar colours of these two components, the bright galaxy may be the result of a recent merger.

3.3. Positional uncertainty

The sizes of the multiple images have been estimated with the IRAF task *imexamine*. They range from $0.11''$ to $0.15''$, with a mean of $0.13''$. Therefore, the positional uncertainty is set to $0.13''$. We note that this positional uncertainty may seem large for HST data but we stress that we are not dealing with point-like objects (quasar lensing) where the astrometric precision can reach $0.01''$. In our case, the images are extended and the depth of the snapshot observations does not allow us to better resolve the conjugated points with *imexamine*. We note that large positional uncertainties are often used for extended images (see, e.g. Oguri 2010).

3.4. Mass model

The lens potential is parameterised by a dual Pseudo Isothermal Elliptical Mass Distribution (dPIE, see Elíasdóttir et al. 2007). The 3D density distribution of the dPIE is

$$\rho(r) = \frac{\rho_0}{(1 + r^2/r_{\text{core}}^2)(1 + r^2/r_{\text{cut}}^2)}; \quad r_{\text{cut}} > r_{\text{core}}. \quad (1)$$

This distribution represents a spherical system with scale radius r_{cut} , core radius r_{core} and central density ρ_0 .

This profile is formally the same as the Pseudo Isothermal Mass Distribution (PIEMD) described in Limousin et al. (2005). Its scale radius is set to 250 kpc, i.e. larger than the range where the observational constraints are found. Allowing r_{core} to vary

Table 1. Parameters of the lens inferred from two optimisations.

Model	$\delta(x)$	$\delta(y)$	e	θ	σ_0 (km s ⁻¹)	RMS	χ^2	log(Evidence)	Prior
1 Lens	-0.24 ± 0.12	-0.02 ± 0.10	$0.597^{+0.002}_{-0.038}$	17.9 ± 1.6	476 ± 7	$0.38''$	86/3	-62	$e < 0.6$
Ext. Perturb.	0.01 ± 0.05	-0.26 ± 0.08	0.499 ± 0.04	21.5 ± 0.9	447 ± 3	$0.05''$	0.96	-20	$e < 0.6$

Notes. *First line:* a single halo models the lens potential. *Second line:* we add an external mass perturbation on top of the halo lens potential. Coordinates are given in arcseconds with respect to the centre of the galaxy deflector. e is the central halo ellipticity. Error bars correspond to 1 σ confidence levels.

produces models with core radii much smaller than the range of radii for which we have observational constraints. Therefore, we can set $r_{\text{core}} = 0$, and the dPIE profile are close to isothermal in the range of interest. The remaining free parameters of the dPIE profile are:

- the halo centre position (X, Y) , which is allowed to vary within $3''$ of the light distribution centre;
- the halo ellipticity e , which is forced to be smaller than 0.6, as suggested by numerical simulations (Jing & Suto 2002);
- its position angle θ , which is allowed to vary between 0 and 180 degrees;
- the fiducial velocity dispersion¹ which is allowed to vary between 200 and 900 km s⁻¹.

We emphasise that this fiducial velocity dispersion is not the Spherical Isothermal Sphere velocity dispersion. It is usually lower, and we refer the reader to Elíasdóttir et al. (2007) for a self-contained description of the dPIE profile.

3.5. Results: bad optimisation

Results of the optimisation are given in Table 1. This first optimisation results in a poor fit to the data, with the RMS error of image positions $\sim 0.38''$ in the image plane (i.e. significantly larger than the assumed positional uncertainty of $0.13''$) and a reduced χ^2 of 29. The halo position is found to coincide with the light distribution centre within error bars. The halo ellipticity is at the upper bound of the input prior, and the position angle is equal to ~ 18 deg. Only when we allow the halo ellipticity to reach values as high as 0.9 are we able to reproduce the observational constraints (RMS equals to $0.06''$ for $e = 0.9$, $\theta \sim 19.5$ degrees, and the halo centre is offset from the light distribution centre by one arcsecond.

We conclude that a single potential does not satisfactorily reproduce the observational constraints. We have used the lens modelling method based on Halkola et al. (2006, 2008) parallel to our method, and found that the observational constraints used in this work require an external shear component in order to be properly reproduced. In the rest of the paper, we include the contribution of the external mass distribution in the lens modelling.

4. An external mass perturbation based on the light distribution: does light traces mass?

The large-scale properties of SL2S J08544-0121 shown in Fig. 1 together with the failed modelling attempted in the previous section suggest the need to take into account an external mass perturbation. In order to test the hypothesis that light traces mass, this external perturbation will be mapped from the known light distribution properties.

¹ linked to the central density by: $\sigma_0^2 = \frac{4}{3} G \pi \rho_0 \frac{r_{\text{core}}^2 r_{\text{cut}}^2}{(r_{\text{cut}} - r_{\text{core}})(r_{\text{cut}} + r_{\text{core}})}$.

4.1. Luminosity maps

The first step is to build luminosity maps of SL2S J08544-0121 from which we will derive the external mass perturbation properties. To identify group members, we select all galaxies with an $r - i$ colour difference smaller than 0.15 mag from the bright galaxy deflector (Limousin et al. 2009). Because we want to describe the perturbation of the galaxy group on the SL system, this luminosity map should not take into account the light coming from the galaxies populating the SL deflector. Therefore, we select all group members *except for the bright galaxy populating the deflector and the associated satellite galaxy*. This partial group luminosity is referred to as L_{ext} hereafter. From this catalogue, we generate smoothed luminosity maps, and hence the mass maps, assuming that mass follows light. An important ingredient of this procedure is the smoothing scale of the luminosity maps. Because this influences the properties of the derived mass maps, we adopt the smoothing scale as a free parameter for describing the external mass perturbation.

We use the following smoothing scheme: the $10' \times 10'$ CFHTLS i -band image is divided into cells of size c pixels, which translates into $c \times 0.186''$ (since the pixel size equals $0.186''$). We compute the rest-frame i -band luminosity L of each galaxy located in a given cell with

$$L = 10^{(M_{\odot} - M + DM + k)/2.5}, \quad (2)$$

where M is the i -band isophotal magnitude of the galaxy, M_{\odot} is the solar absolute magnitude in the i band, DM is the distance modulus, and k the k -correction factor that is estimated from elliptical templates by Bruzual & Charlot (2003) using single-burst stellar formation models. Then we sum up the luminosities of all galaxies in each cell to get the total luminosity for the cell. The resulting luminosity isodensity map is then convolved with a Gaussian kernel of width w . This gives an angular smoothing scale s that equals $c \times 0.186 \times w''$. Figure 3 shows three luminosity maps, where we distribute the same total luminosity L_{ext} for three smoothing scales. We draw luminosity isodensity contours of 10^7 and $10^8 L_{\odot} \text{arcsec}^{-2}$. One can appreciate how the smoothing scale s influences the shape of the luminosity isodensity contours.

4.2. From light map to mass map

Once a luminosity map with a given smoothing scale s is obtained, we assume a constant mass-to-light ratio $M_{\text{ext}}/L_{\text{ext}}$ to convert it into a mass map. This $M_{\text{ext}}/L_{\text{ext}}$ is the second free parameter describing the perturbation produced by the galaxy group. Because we have excluded the bright galaxy populating the deflector when building the luminosity map, this mass map can be considered as the external mass perturbation. Therefore we refer to the mass contained in this map as M_{ext} . Then, we use the algorithm developed by Jullo & Kneib (2009) to transform this mass map into a grid of analytic circular dPIE potentials, supported by L

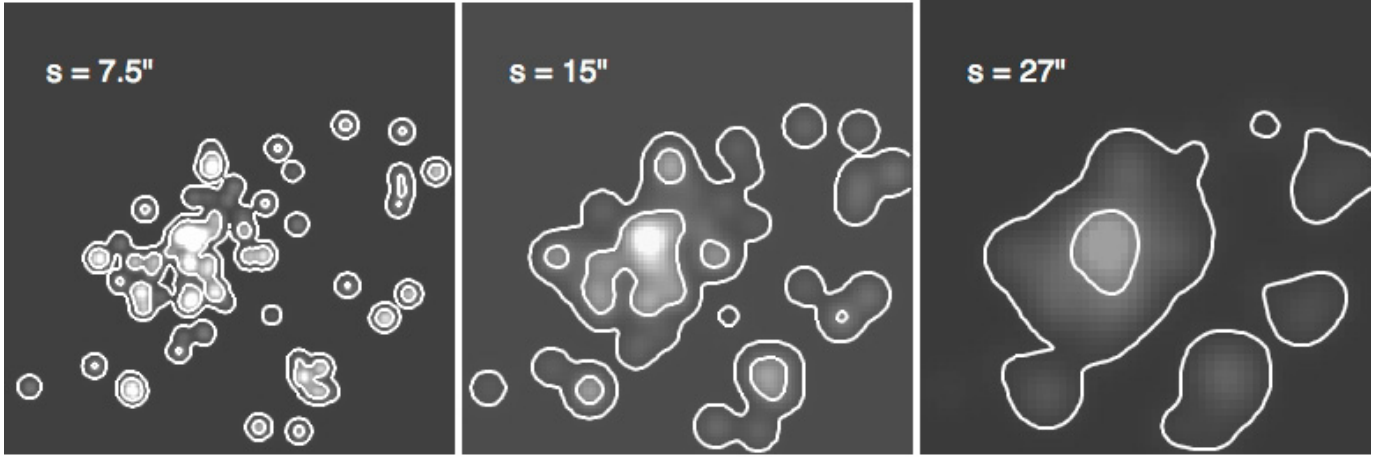


Fig. 3. Three luminosity maps of the same luminosity L_{ext} for different smoothing scales as indicated in each panel. We draw in white the luminosity isodensity contours of 10^7 and $10^8 L_{\odot} \text{arcsec}^{-2}$. The smoothing scale s influences the shape of the luminosity isodensity contours, and by construction the shape of the resulting mass distribution, hence its lensing properties.

We model the mass distribution of SL2S J08544-0121 with a $5'$ hexagonal grid of dPIE potentials. In order to build an adaptive grid where the resolution follows the 2-D mass density, we recursively split the input mass map into equilateral triangles until the mean surface mass density per triangle is lower than $10^7 M_{\odot} \text{arcsec}^{-2}$. Then we place a dPIE potential at each node of the grid with the following parameters: core radii r_{core} are set to the local grid resolution and cut-off radii $r_{\text{cut}} = 3 \times r_{\text{core}}$. In Jullo & Kneib (2009), we found that these values of r_{cut} ensured a smooth and extended density profile. We estimate the dPIE central velocity dispersions σ_i by inverting the equation

$$\sigma_i^2 = M_{i,j} \Sigma_j, \quad (3)$$

where Σ_j is the surface mass density at the grid nodes location, and $M_{i,j}$ is a mapping matrix whose coefficients depend of the dPIE core and cut-off radii (see Jullo & Kneib 2009). In order to prevent negative σ_i^2 , we invert Eq. (3) by a mean-square minimisation technique. The density threshold (for splitting the cells into triangles) controls the grid resolution, and might thus be considered as an important parameter. However, we have tried to use smaller thresholds, down to $10^5 M_{\odot} \text{arcsec}^{-2}$, and the results were unchanged. Therefore, we keep the $10^7 M_{\odot} \text{arcsec}^{-2}$ threshold because the corresponding mass maps require fewer mass clumps. We also force the algorithm to stop after four levels of splitting. On average, a grid cell contains about 200 dPIE potentials.

4.3. Modelling the lens including the external perturbation

We now model the SL system, taking into account the external mass perturbation parameterised by a smoothing scale s and a mass-to-light ratio $M_{\text{ext}}/L_{\text{ext}}$. We generated mass maps with smoothing scales s ranging from 1 to $40''$ in steps of $2.5''$ and mass-to-light ratios from 10 to 190 in steps of 20. Each mass map is then included in the modelling of the SL system. This modelling is performed in the image plane. We note that these two extra parameters describing the external mass perturbation are not treated the same way as the five parameters of the deflecting halo. For each set of parameters ($s, M_{\text{ext}}/L_{\text{ext}}$), we optimise the five parameters of the halo. Parameters for the strong lens deflector are the same as in Sect. 3.4. For each set of parameters ($s, M_{\text{ext}}/L_{\text{ext}}$), we quantify the goodness of the SL modelling using the image plane RMS, the corresponding χ^2 and the Bayesian Evidence.

Since our goal is to constrain the galaxy group as a whole, we use M/L below corresponding to the *total* mass-to-light ratio of the group; i.e. $M(L)$ is the sum of the external mass (luminosity) perturbation *and* the mass (luminosity) of the lens. We checked that degeneracies of each mass component near the lens are small. For the range of parameters ($s, M_{\text{ext}}/L_{\text{ext}}$) investigated in this work, we compute $M_{\text{ext}}/M_{\text{lens}}$ in a circle of radius $10''$ centred on the lens. This ratio falls between 10^{-7} and 10^{-5} .

Total masses and luminosities are computed within a region of $10' \times 10'$ centred on the lens. At the redshift of the group, it corresponds to $\sim 3 \times 3 \text{ Mpc}^2$ (Fig. 1).

5. Results: properties of SL2S J08544-0121

For a certain range of parameters characterising the external mass perturbation we obtain excellent fits to the observed constraints. We present first the best-fit model, and then the derived constraints on the galaxy group properties. We emphasise that what we achieve here is to constrain the properties of the galaxy group as a *whole* (on scales of $100''$) based on a local SL analysis *only* (on scales of $10''$).

5.1. Best-fit model for the lens

The modelling results are given in Table 1. The best-fit model has a total mass-to-light ratio of ≈ 75 (i band, solar units, not corrected for evolution) and a smoothing scale of $\approx 20''$ (Fig. 4). The RMS error between observed and modelled image positions in the image plane is $0.05''$, yielding a reduced χ^2 of 0.96. This is a significant improvement compared to the modelling without external mass perturbation, which had $\text{RMS} = 0.38''$. To quantitatively compare the two models (i.e. mass models with and without the inclusion of external perturbations), we compute the Bayesian evidence values of the two models. The evidence takes into account the additional complexity of the new model with the extra parameters for the external perturbations. The difference in the evidence of the two models, which is the relative probability of the models given the data (assuming the two models are equally probable a priori), is 2×10^{18} . The data therefore rank the perturbed model much higher than the simple model.

We find the position of the halo to coincide with the centre of the light distribution. The modelled position angle of the halo is 21.5 deg . Comparing this value to the position angle of the light

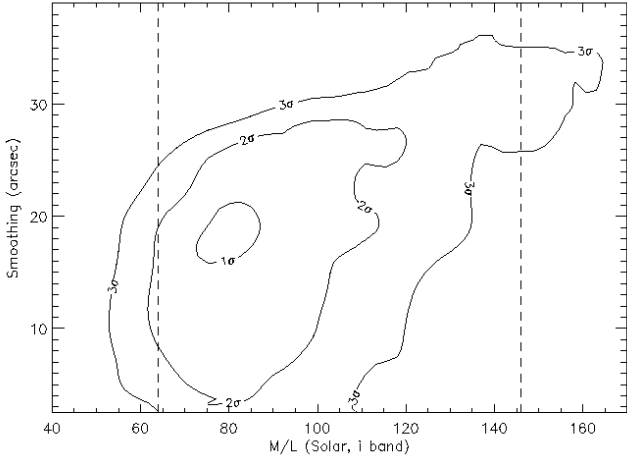


Fig. 4. Results: constraints on the galaxy group mass-to-light ratio M/L and smoothing scale s that characterises the size of dark matter clumps. Vertical dashed lines mark the lower and upper bounds of the constraint (1σ error bars) on the group mass-to-light ratio from an independent weak-lensing analysis (Sect. 7).

distribution is complicated because of the bimodal light distribution of the bright galaxy (Sect. 3.2). In particular, a merger will affect the light and mass distributions so that agreement may not necessarily be expected.

5.2. Constraints on the group as a whole

χ^2 differences between models with different s and M/L values are translated into confidence levels, which are drawn on Fig. 4. Considering the 2σ contour, we find $M/L = 98 \pm 27$ (i band, solar units, not corrected for evolution) and $s = 20'' \pm 9$.

5.3. Is mass traced by light?

We are able to accurately reproduce the observational constraints when considering an external mass perturbation drawn from the light distribution. Because our SL analysis is sensitive to the mass, this finding is consistent with the hypothesis that light is a good tracer of mass. We note, however, that we have not demonstrated the uniqueness of the smoothed light model.

6. Local effect of large-scale perturbation

In this section, we propose to explain why a *local* SL analysis is able to constrain *global* properties of the galaxy group hosting the lens. First, we investigate the impact of the external perturbation on the local SL modelling (i.e. on the local image positions).

6.1. Lensing properties of the external perturbation

The lensing properties of a mass distribution are commonly parameterised by a shear γ and a convergence κ (see, e.g. Schneider et al. 1992, for the definition of these quantities). Here we estimate the mean shear and convergence experienced locally by the lens for each set of parameters (s , $M_{\text{ext}}/L_{\text{ext}}$) by averaging γ and κ generated by the perturbation within a $7''$ square encompassing all multiple images.

Figure 5 shows κ and γ maps generated by an external perturbation of fixed mass ($5.7 \times 10^{14} M_{\odot}$) for different values of s (reported on each panel). These maps have been generated for a

source redshift of 1.268. Red crosses indicate the lens position. One can appreciate how the experienced shear and convergence are correlated with the smoothing scale.

6.2. Shape of the constraints

Figure 6 shows contours of κ and γ overlaid on the results from Fig. 4. We see that the constraints inferred from the SL analysis do not follow κ contours, but do follow γ contours. In particular, the best model generates a shear of ~ 0.075 . We interpret the shape of the constraints as follows: one needs to generate a shear value of ~ 0.075 with a mass distribution parameterised by a smoothing scale and a total mass. For a given total mass, the smoother this mass distribution (the higher s), the smaller the generated shear. Therefore, the smoother the mass distribution, the higher the total mass in order to generate a given shear level.

6.3. Why closed contours ?

Shear, convergence, and beyond

Figure 6 suggests that the observational constraints require locally an external shear component of ~ 0.075 . However, our analysis rejects some external mass perturbations characterised by this shear (Fig. 4). This suggests, as found by Keeton & Zabludoff (2004), that *the shear approximation fails to capture all of the environmental effects*. In other words, the shape of the contours for the constraints follows the curves of constant shear. However, the contours do close, which means that the constraints are sensitive to more than the shear, most probably to *higher order terms beyond the shear* that are naturally provided by the modelling proposed here.

In addition, we estimate the shear experienced by images 1.1, 1.2, 1.3 and 1.4. To do so, we consider all models falling in the 1σ contour. For each model, we compute the shear experienced by the images, and from these numbers, we estimate the mean shear and the associated standard deviation. The corresponding shear values for the images listed above are 0.075, 0.074, 0.073 and 0.073 respectively, with a typical uncertainty of 0.01. Therefore, each image does experience the same shear value within the error bars. We further investigate the differences between our approach and a constant external shear approach in the Appendix.

7. Mass-to-light ratio from weak lensing

We have presented constraints on the mass-to-light ratio of the galaxy group SL2SJ08544-0121 based on a local SL analysis. In this section, we aim to constrain the mass-to-light ratio of SL2SJ08544-0121 from an independent weak lensing (WL) analysis, which is intrinsically more sensitive to the projected mass distribution on large scales. The goal is to check whether the M/L ratios inferred from the two techniques are consistent.

For a detailed description of our WL methodology see Limousin et al. (2009). Here we give a brief reminder. We select as background sources all galaxies with i -band magnitudes in the range 21.5–24. The resulting galaxy number density is 13.5 arcmin^{-2} . The completeness magnitude in this band is 23.91 and the seeing is $\sim 0.51''$. A Bayesian method, implemented in the `I 2` software (Bridle et al. 2002), is used to fit the shape parameters of the faint background galaxies and to correct for the PSF smearing. From the catalogue of background galaxies, Limousin et al. (2009) performed a one-dimensional WL analysis. They fit a singular isothermal sphere (SIS) model to the reduced shear signal between 150 kpc and 1.2 Mpc from

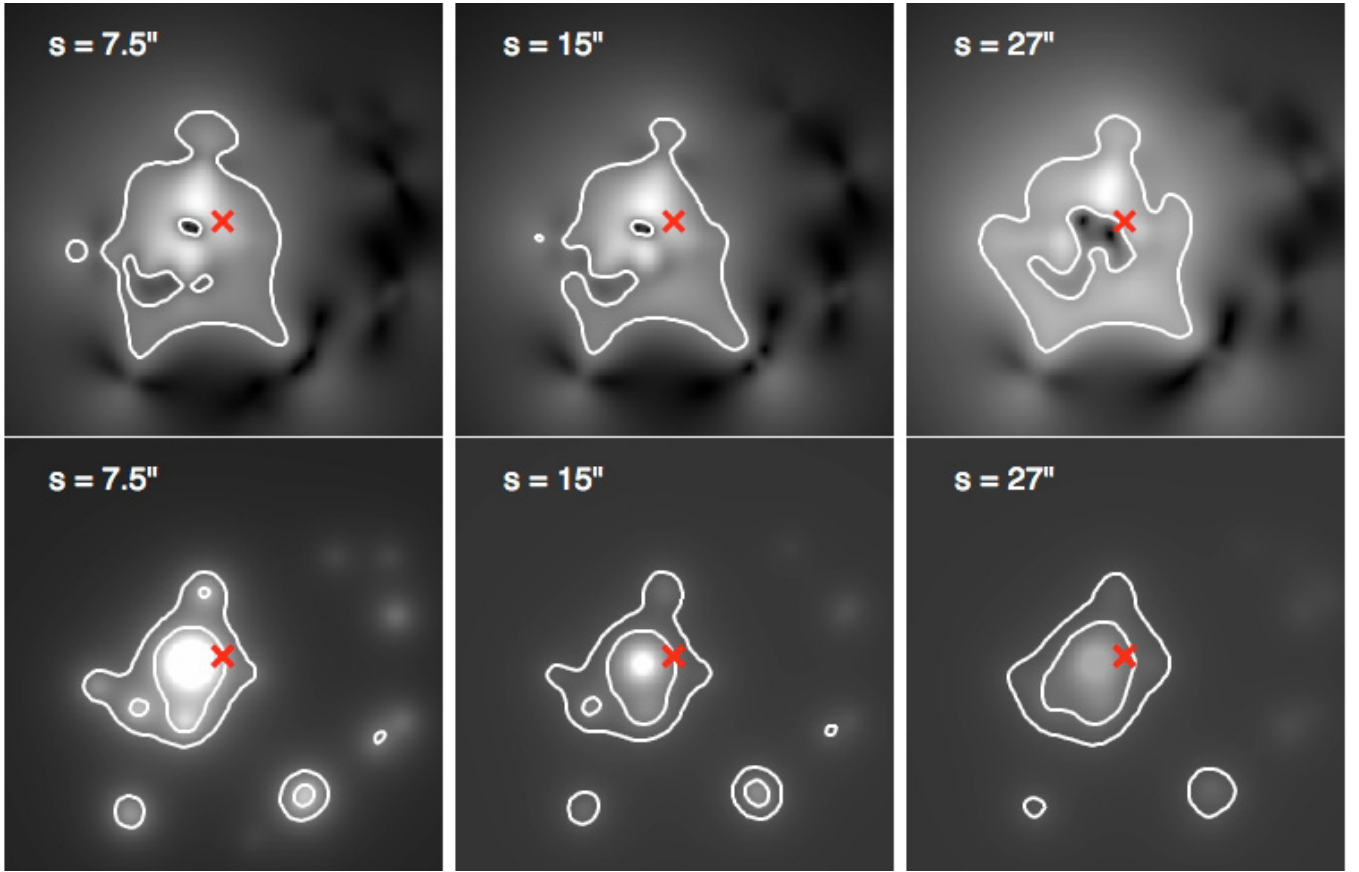


Fig. 5. Shear (*upper panels*) and convergence (*lower panels*) maps generated by the external perturbation and experienced by the SL system whose centre is given by the red cross. The total mass is fixed to the same value ($5.7 \times 10^{14} M_{\odot}$) in all panels. Panel sizes are 600×600 square arcseconds, and the smoothing scales s vary as indicated on each panel. White contours correspond to shear levels of 0.1 and convergence levels of 0.1 and 0.2. One can appreciate how the shear and convergence generated by the group are correlated with the smoothing scale.

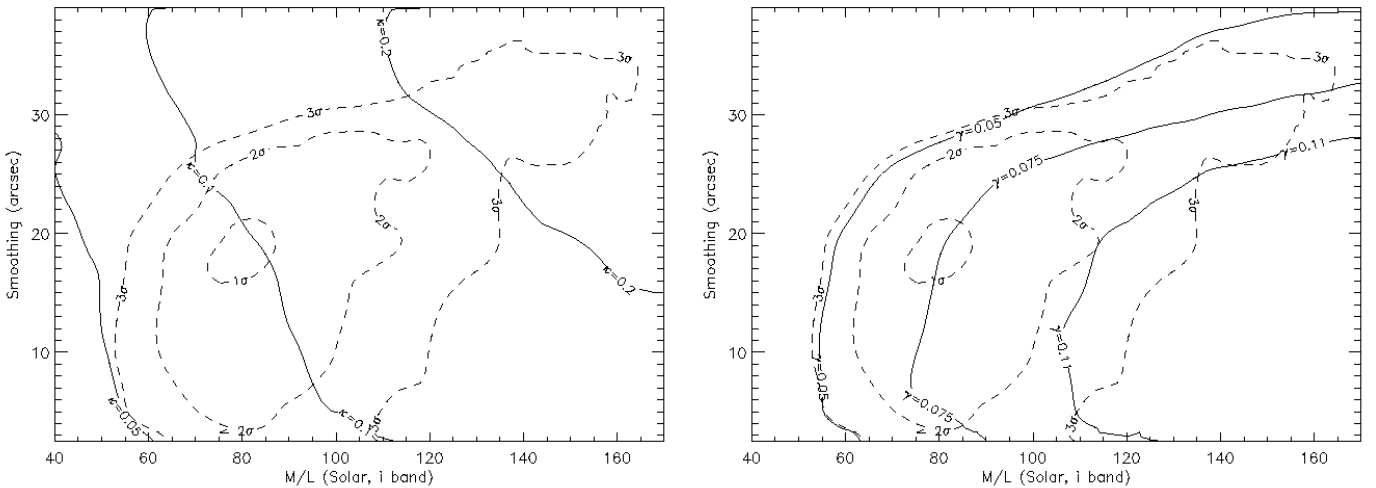


Fig. 6. As in Fig. 4, constraints obtained on the galaxy group as a whole derived from the *local* SL analysis are shown as dashed contours. Solid lines corresponds to lines of constant κ (*left*) and γ (*right*) generated by the external mass perturbation and experienced locally by the lens, their values are labelled on each line.

the group centre, finding an Einstein radius of $5.4 \pm 2.1''$. In order to relate the strength of the WL signal to a physical velocity dispersion characterising the group potential, Limousin et al. (2009) estimate the mean geometrical factor using the photometric redshift catalogue from the T0004 release of the CFHTLS-Deep survey² (Ienna & Pelló 2006). They find $\sigma_{\text{SIS}} = 658_{-146}^{+119} \text{ km s}^{-1}$.

² http://www.ast.obs-mip.fr/users/rosier/CFHTLS_T0004/

This translates into a total mass within the considered square of $5.3 \pm 2.0 \times 10^{14} M_{\odot}$. Because the total luminosity is $5 \times 10^{12} L_{\odot}$, we find a mass-to-light ratio of 106 ± 40 (*i* band, solar units, not corrected for passive evolution).

This is comparable to the M/L constrained by SL *only*. The good agreement (Fig. 4) between the two methods gives support to the analysis based on SL only.

8. Discussion

8.1. Mass is traced by light

An external mass perturbation derived from the light of the group members allows us to accurately fit the observed constraints. Because the observed constraints are sensitive to mass rather than light, this suggests that light is a good tracer of mass. We note that this result shows an efficient way of taking into account an external mass perturbation in SL modelling. Indeed, this perturbation is fully described with only two parameters, the mass-to-light ratio and the smoothing scale. In contrast, describing this perturbation parametrically with a mass clump would require at least three parameters (position and velocity dispersion), unless independent data constrain one or more of these parameters (see, e.g. Tu et al. 2009, where X-ray observations allow one to constrain the group centre).

8.2. What is the source of the constraints ?

Why does our SL analysis allow us to infer properties on the whole galaxy group? We claim that this is because of the perturbed state of the SL system of SL2S J08544-0121. Most of the perturbed signal of the multiply imaged system comes from image 1.4, because it is located farther away from the lens centre ($\sim 8''$) than images 1.1, 1.2 and 1.3 ($\sim 5''$). If we remove image 1.4 from the set of observational constraints, we are able to fit the remaining images very well without considering any external mass perturbation (the lens being modelled as in Sect. 3.4). In that case, we get $\text{RMS} = 0.03''$ and a reduced χ^2 equals to 0.03. Therefore, ignoring image 1.4 prevents us from putting any constraints on the external mass perturbation, i.e. the host galaxy group. This shows that image 1.4 yields the constraints presented here. This finding will help us diagnose the type of the SL systems to which our new analysis technique can be applied (see Sect. 8.5).

We note that the SL analysis presented here is very simple because we just conjugate a couple of images with each other. In particular, we do not use the constraints coming from the whole Einstein ring. More sophisticated methods fully take into account arc surface brightness constraints (see, e.g. Warren & Dye 2003; Suyu et al. 2006; Barnabè & Koopmans 2007). We are aware that we ignore some information that could allow us to put stronger constraints on the galaxy group. On the other hand, the basic level of the SL analysis done here emphasises even more the prospects of this method.

8.3. The satellite galaxy

We have assumed that the satellite galaxy does not produce significant shear on the images used as constraints. However, one could argue that neglecting this satellite galaxy effectively produces the claimed constraints from the SL analysis. This is not likely – because of the location of the satellite galaxy with respect to the multiple images (Fig. 1), the satellite galaxy may produce a marginal shear on images 1.1, 1.2 and 1.3, but is unlikely to have any significant influence on image 1.4, the image that yields most of the constraints. Indeed, the distance between the satellite galaxy and image 1.4 is $\sim 13''$. We note that we do not quantify the bias that could result from our working assumption.

Besides, a paper focusing on the properties of the satellite galaxy (Suyu & Halkola, submitted) shows that even with the satellite galaxy included in the lens model, an external shear

of about the same magnitude is needed to fit the observed constraints.

8.4. Choice of the lens' scale radius

The dPIE scale radius is where the logarithmic slope of the 3D density profile smoothly decreases from -2 to -4 . The scale radius of the lens is set to 250 kpc in the present analysis. We have also done a complete analysis for a scale radius of 400 kpc as a sanity check and found that the results inferred for the group do not change significantly. To understand why, we superimposed critical lines of the best-fit parameters of Table 1, for a source redshift of 1.268 (without external perturbation), and the critical lines of the best-fit parameters of Sect. 5.1 (with external mass perturbation). We find that the external mass perturbation generates a critical line shift of $1.3''$. In parallel, we investigated the critical lines shifts between various scale radii; increasing from 250 kpc to 400 kpc and decreasing from 250 kpc to 100 kpc. The shifts are $0.12''$, one order of magnitude smaller than the shift owing to the external mass perturbation.

8.5. Looking for perturbed SL systems

We propose to characterise the kind of perturbed SL systems one should target in order to perform analyses similar to the one presented in this work. From the ring test done in Abell 1689 (Tu et al. 2008, see Sect. 1.3) and the analysis presented here, we hint at the need for *a non-dominant SL system to be used as a test particle for probing the main potential*.

This is linked to the global geometry of the structure hosting the SL system: to be affected by a perturbation, the SL system should not be at the centre of the structure. Indeed, if the lens studied here would have dominated the whole group potential, image 1.4 would have been located at a similar distance from the lens centre as images 1.1, 1.2 and 1.3.

The Cosmic Horseshoe (Belokurov et al. 2007; Dye et al. 2008) illustrates this point: it is an almost complete Einstein ring of radius $5''$ containing a luminous red galaxy in its centre. As revealed by the SDSS photometry, this galaxy is the brightest object in the group of ~ 26 members and it dominates the group light distribution. No external shear is required in the model of the Cosmic Horseshoe SL system, which is already suggested by the nearly perfect circle outlined by the ring.

To summarise, we should look for multiply-imaged systems where one of the images is found at a larger radial distance than the other images of the SL system.

8.6. SL2S J08544-0121: more evidences for a bimodal mass distribution from spectroscopy of group members

We have shown that the modelling based on strong lensing *only* provides strong hints for a bimodal mass distribution: the first mass component is clearly associated with the strong lensing deflector, and the second one that perturbs the strong lensing configuration seems, to first order, to be associated with the second light peak of the bimodal light map. This suggests a dynamically young structure in the process of formation. A spectroscopic survey of the group further supports this hypothesis: we measured redshifts for 36 galaxies along the direction of SL2S J08544-0121 by using spectroscopic data acquired with FORS2 at the ESO Very Large Telescope (VLT), and confirmed the presence of a high concentration of galaxies at $z \sim 0.35$ (Muñoz et al., in prep.). A careful analysis of the redshift distribution of galaxies

around this peak reveals two close structures with a radial velocity difference of $V_r = 1180 \text{ km s}^{-1}$. This result agrees with the interpretation of our strong lensing *only* analysis.

9. Conclusion

We propose a method to constrain the dark matter distribution of galaxy groups and clusters. Exploiting information contained in perturbed SL systems, we use the SL geometry to probe the main potential of the host structure responsible for that perturbed state.

We show that the SL *only* constraints on the mass-to-light ratio of SL2S J08544-0121 agree well with WL constraints obtained independently, supporting the reliability of the proposed method. Moreover, the SL *only* analysis provides strong hints for a bimodal mass distribution, which is confirmed by the spectroscopic survey of galaxy group members.

We advocate the need for a dedicated search of perturbed SL systems in the HST archive in order to test and further validate this method, which is particularly promising in the light of future large surveys that will yield thousands of SL systems, some of which are perturbed enough to perform the test presented in this paper.

Acknowledgements. M.L. acknowledges Bernard Fort, Masamune Oguri & Phil Marshall for related discussions. M.L. acknowledges the anonymous referee for a detailed report, and Christopher Kochanek for insightful comments on the submitted version of this paper. M.L. acknowledges the Centre National d'Etudes Spatiales (CNES) and the Centre National de la Recherche Scientifique (CNRS) for their support. M.L. est bénéficiaire d'une bourse d'accueil de la Ville de Marseille. The Dark Cosmology Centre is funded by the Danish National Research Foundation. We thank the Danish Centre for Scientific Computing at the University of Copenhagen for providing a generous amount of time on its supercomputing facility. E.J. is supported by the NPP, administered by Oak Ridge Associated Universities through a contract with NASA. Part of this work was carried out at Jet Propulsion Laboratories, California Institute of Technology under a contract with NASA. J.R. acknowledges support from an EU Marie-Curie fellowship. S.H.S. is supported in part through the Deutsche Forschungsgemeinschaft (DFG) under project SCHN 342/7-1, and A.H. by the DFG cluster of excellence "Origin and Structure of the Universe". J.P.K. acknowledges CNRS for its support.

Appendix A: Taking an external mass perturbation into account: comparison with other approaches

We have proposed a way of taking into account an external mass perturbation in a strong lensing (SL) modelling. Here we try other possible and more conventional approaches: i) a constant external shear profile and ii) a singular isothermal sphere centred on the second high luminosity peak, which, by construction, is the main mass concentration perturbing the SL in the method proposed in this work.

A.1. A constant external shear

Although unphysical (any mass distribution will not generate shear only but also convergence), the external shear model is widely used and is often a good approximation. Here we address the modelling of the SL system with a constant external shear component parameterised by a position angle and a strength (γ_{Kst}). This modelling is performed in the image plane. Parameters of the potential describing the lens are set as in Sect. 3.4. The external shear strength is allowed to vary between 0 and 0.3. The upper limit corresponds to a very strong shear value: for comparison, the massive galaxy cluster Abell 1689

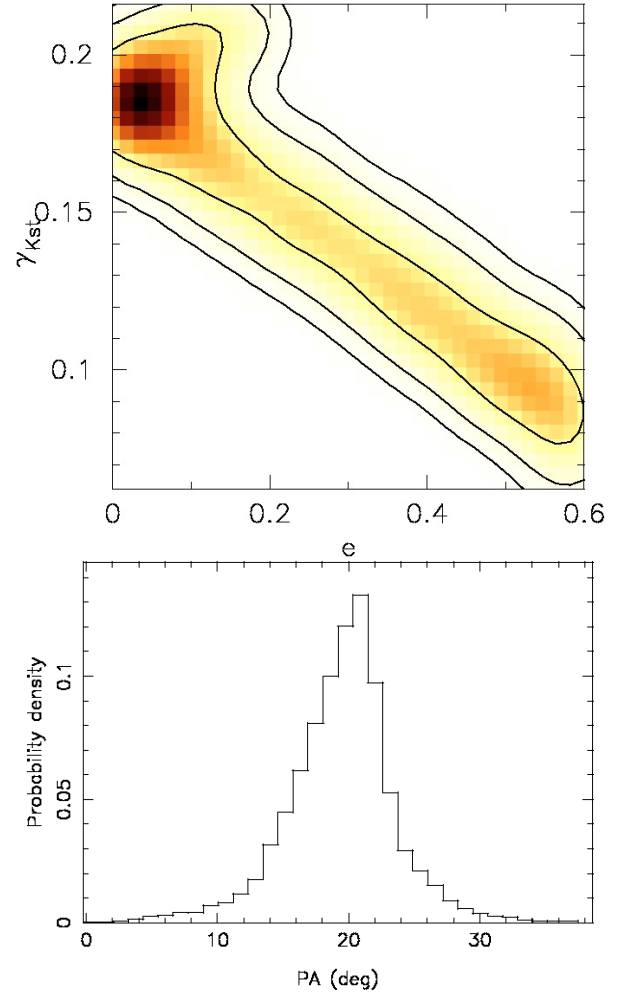


Fig. A.1. Results of a constant external shear model. *Top*: degeneracy between the halo ellipticity e and the strength of the external shear γ_{Kst} . *Bottom*: posterior probability distribution for the position angle of the external shear.

produces an average shear value of 0.23 at $50''$ away from its centre.

We are able to get a very good fit, with $\chi^2 < 1$. The best model corresponds to a circular halo for the lens ($e = 0.036$) centred on the bright galaxy ($X = -0.36'', Y = 0.07''$), making its position angle (95 degrees) irrelevant. The lens fiducial velocity dispersion equals $450 \pm 8 \text{ km s}^{-1}$ (1σ). The external shear is described by $\gamma_{\text{Kst}} = 0.19$, more than twice the one derived in Sect. 6.2 (~ 0.075), and a position angle equal to 19.8 degrees.

The `L` software does explore the parameter space using a MCMC sampler (Jullo et al. 2007). Therefore, we can use these MCMC realisations in order to investigate the degeneracies between the different parameters. The figures below have been generated this way.

Figure A.1 shows that there is a strong degeneracy between e and γ_{Kst} . We see that the solution derived in Sect. 5.1 (i.e. an external shear of ~ 0.075 and an ellipticity of ~ 0.5) is included in the $1\text{-}\sigma$ contour. On the other hand, the position angle of the external shear is very well constrained to be ~ 20 degrees. This position angle points towards the second high luminosity light clump. This suggests that, to first order, the external mass perturbation is dominated by this component. We note that the best-fit model needs an external shear of order 0.18, which is a pretty unlikely value in our case because it is comparable to what would be experienced at $\sim 100''$ from the centre of Abell 1689.

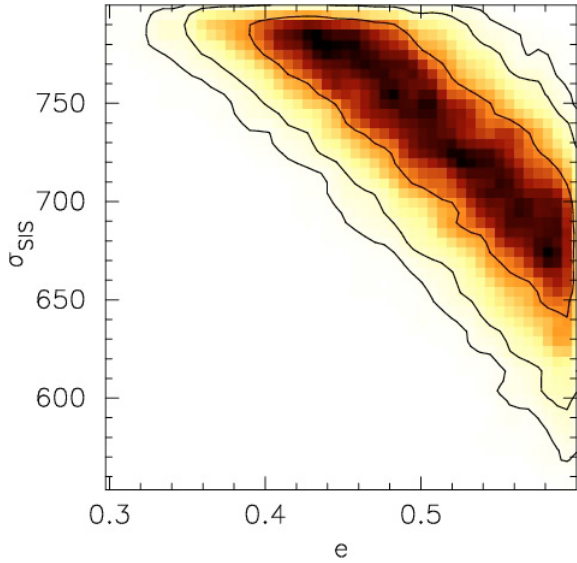


Fig. A.2. Degeneracies between the lens halo ellipticity and the SIS profile velocity dispersion, related to the strength of the external shear experienced by the multiple images.

A.2. An SIS profile

The first order mass perturbation is associated to a second peak of high luminosity. We put an SIS mass distribution at the location of this second luminosity peak ($X, Y = -53, 10''$ wrt the lens). We allow its velocity dispersion to vary up to 800 km s^{-1} , an upper limit motivated by the WL analysis of the full group (Sect. 7), and do the SL modelling with parameters set as in Sect. 3.4. We are able to get a very good fit, with $\chi^2 < 1$. The lens halo is centred on the bright galaxy. Its ellipticity equals $0.43^{+0.01}_{-0.12}$ and its position angle $27 \pm 2 \text{ deg}$. The lens fiducial velocity dispersion equals $441 \pm 7 \text{ km s}^{-1}$ (1σ). The external shear and convergence generated by the SIS profile at the location of the multiple images are equal by definition, between 0.07 and 0.10.

We show in Fig. A.2 the degeneracies between the lens halo ellipticity and the SIS profile velocity dispersion, related to the strength of the external shear experienced by the multiple images. We see that the solution derived in Sect. 5.1 (i.e. an external shear of ~ 0.075 , corresponding to $\sigma_{\text{SIS}} \sim 700 \text{ km s}^{-1}$ and an ellipticity of ~ 0.5) is included in the $1\text{-}\sigma$ contour.

A.3. Discussion

In each case investigated in this Appendix, we find that the solution we have derived in Sect. 5.1 using our original method is consistent with solutions derived with more conventional methods.

We note that conventional methods exhibit strong degeneracies between the lens halo ellipticity and the strength of the external shear. These degeneracies are lower for the SIS profile (lens ellipticity is constrained between 0.3 and 0.6) compared to the case of a constant shear profile (ellipticity unconstrained between the allowed priors: 0 and 0.6). The main difference between the SIS profile and the constant shear profile is that the SIS profile generates both shear and convergence.

With respect to the lens itself, we note that all fitted fiducial velocity dispersions are consistent, whatever the method used to take into account the external mass perturbation. They

fall between 433 km s^{-1} and 458 km s^{-1} . This translates into a projected mass computed in a radius of $10''$ between 0.93 and $1.04 \times 10^{13} M_{\odot}$. This is expected because the mass of the lens within this radius is set by the location of the SL constraints and therefore does not depend much on the external mass perturbation (see also Sect. 4.3).

References

- Auger, M. W., Fassnacht, C. D., Abrahamse, A. L., Lubin, L. M., & Squires, G. K. 2007, *AJ*, 134, 668
- Auger, M. W., Fassnacht, C. D., Wong, K. C., et al. 2008, *ApJ*, 673, 778
- Barnabè, M., & Koopmans, L. V. E. 2007, *ApJ*, 666, 726
- Belokurov, V., Evans, N. W., Moiseev, A., et al. 2007, *ApJ*, 671, L9
- Belokurov, V., Evans, N. W., Hewett, P. C., et al. 2009, *MNRAS*, 392, 104
- Bridle, S., Kneib, J.-P., Bardeau, S., & Gull, S. 2002, in *The shapes of galaxies and their dark halos*, Proceedings of the Yale Cosmology Workshop, New Haven, Connecticut, USA, 28–30 May 2001, ed. P. Natarajan, 38
- Bruzual, G., & Charlot, S. 2003, *MNRAS*, 344, 1000
- Cabanac, R. A., Alard, C., Dantel-Fort, M., et al. 2007, *A&A*, 461, 813
- Dye, S., Evans, N. W., Belokurov, V., Warren, S. J., & Hewett, P. 2008, *MNRAS*, 388, 384
- Dye, S., Smail, I., Swinbank, A. M., Ebeling, H., & Edge, A. C. 2007, *MNRAS*, 379, 308
- Elíasdóttir, Á., Limousin, M., Richard, J., et al. 2007, unpublished [arXiv:0710.5636]
- Fassnacht, C. D., & Lubin, L. M. 2002, *AJ*, 123, 627
- Faure, C., Alloin, D., Kneib, J. P., & Courbin, F. 2004, *A&A*, 428, 741
- Grillo, C., Lombardi, M., Rosati, P., et al. 2008, *A&A*, 486, 45
- Halkola, A., Seitz, S., & Pannella, M. 2006, *MNRAS*, 372, 1425
- Halkola, A., Hildebrandt, H., Schrabback, T., et al. 2008, *A&A*, 481, 65
- Ienna, F., & Pelló, R. 2006, in *SF2A-2006: Semaine de l'Astrophysique Française*, ed. D. Barret, F. Casoli, G. Lagache, A. Lecavelier, & L. Pagani, 347
- Inada, N., Oguri, M., Shin, M., et al. 2009, *AJ*, 137, 4118
- Jing, Y. P., & Suto, Y. 2002, *ApJ*, 574, 538
- Jullo, E., & Kneib, J. 2009, *MNRAS*, 395, 1319
- Jullo, E., Kneib, J.-P., Limousin, M., et al. 2007, *New J. Phys.*, 9, 447
- Keeton, C. R., & Zabludoff, A. I. 2004, *ApJ*, 612, 660
- Keeton, C. R., Kochanek, C. S., & Seljak, U. 1997, *ApJ*, 482, 604
- Kochanek, C. S., & Blandford, R. D. 1991, *ApJ*, 375, 492
- Kochanek, C. S., Keeton, C. R., & McLeod, B. A. 2001, *ApJ*, 547, 50
- Koopmans, L. V. E., Treu, T., Bolton, A. S., Burles, S., & Moustakas, L. A. 2006, *ApJ*, 649, 599
- Kundic, T., Hogg, D. W., Blandford, R. D., et al. 1997, *AJ*, 114, 2276
- Leonard, A., Goldberg, D. M., Haaga, J. L., & Massey, R. 2007, *ApJ*, 666, 51
- Limousin, M., Kneib, J.-P., & Natarajan, P. 2005, *MNRAS*, 356, 309
- Limousin, M., Richard, J., Jullo, E., et al. 2007, *ApJ*, 668, 643
- Limousin, M., Cabanac, R., Gavazzi, R., et al. 2009, *A&A*, 502, 445
- Lynds, R., & Petrosian, V. 1986, *BAAS*, 1014
- Miralda-Escude, J., & Babul, A. 1995, *ApJ*, 449, 18
- Momcheva, I., Williams, K., Keeton, C., & Zabludoff, A. 2006, *ApJ*, 641, 169
- Morgan, N. D., Kochanek, C. S., Pevunova, O., & Schechter, P. L. 2005, *AJ*, 129, 2531
- Oguri, M. 2010, *PASJ*, 62, 1017
- Oguri, M., Keeton, C. R., & Dalal, N. 2005, *MNRAS*, 364, 1451
- Oguri, M., Inada, N., Blackburne, J. A., et al. 2008, *MNRAS*, 391, 1973
- Oke, J. B., Cohen, J. G., Carr, M., et al. 1995, *PASP*, 107, 375
- Okura, Y., Umetsu, K., & Futamase, T. 2008, *ApJ*, 680, 1
- Richard, J., Kneib, J., Limousin, M., Edge, A., & Jullo, E. 2010, *MNRAS*, 402, L44
- Saha, P., Williams, L. L. R., & Ferreras, I. 2007, *ApJ*, 663, 29
- Schneider, P., Ehlers, J., & Falco, E. E. 1992, *Gravitational Lenses* (Berlin: Springer-Verlag)
- Soucail, G., Fort, B., Mellier, Y., & Picat, J. P. 1987, *A&A*, 172, L14
- Suyu, S. H., Marshall, P. J., Hobson, M. P., & Blandford, R. D. 2006, *MNRAS*, 371, 983
- Treu, T., Gavazzi, R., Gorecki, A., et al. 2009, *ApJ*, 690, 670
- Tu, H., Limousin, M., Fort, B., et al. 2008, *MNRAS*, 386, 1169
- Tu, H., Gavazzi, R., Limousin, M., et al. 2009, *A&A*, 501, 475
- Warren, S. J., & Dye, S. 2003, *ApJ*, 590, 673
- Williams, K. A., Momcheva, I., Keeton, C. R., Zabludoff, A. I., & Lehár, J. 2006, *ApJ*, 646, 85

Gravitational lensing and dynamics in SL2S J02140-0535: probing the mass out to large radius

T. Verdugo¹, V. Motta¹, R. P. Muñoz¹, M. Limousin^{2,3}, R. Cabanac⁴, and J. Richard^{5,*}

¹ Universidad de Valparaíso, Departamento de Física y Astronomía, Avenida Gran Bretaña 1111, Valparaíso, Chile
e-mail: tverdugo@dfa.uv.cl

² Laboratoire d'Astrophysique de Marseille, Université de Provence, CNRS, 38 rue Frédéric Joliot-Curie, 13388 Marseille Cedex 13, France

³ Dark Cosmology center, Niels Bohr Institute, University of Copenhagen, Juliane Marie Vej 30, 2100 Copenhagen, Denmark

⁴ Laboratoire d'Astrophysique de Toulouse-Tarbes, Université de Toulouse, CNRS, 57 Avenue d'Azereix, 65 000 Tarbes, France

⁵ Durham University, Physics and Astronomy Department, South Road, Durham DH3 1LE, UK

Received 10 May 2010 / Accepted 5 January 2011

ABSTRACT

Context. Studying the density profiles of galaxy groups offers an important insight into the formation and evolution of the structures in the universe, since galaxy groups bridge the gap between single galaxies and massive clusters.

Aims. We aim to probe the mass of SL2S J02140-0535, a galaxy group at $z = 0.44$ from the Strong Lensing Legacy Survey (SL2S), which has uncovered this new population of group-scale strong lenses.

Methods. We combine strong lensing modeling and dynamical constraints. The strong lensing analysis is based on multi-band HST/ACS observations exhibiting strong lensing features that we have followed-up spectroscopically with VLT/FORS2. To constrain the scale radius of an NFW mass profile that cannot be constrained by strong lensing, we propose a new method by taking advantage of the large-scale dynamical information provided by VLT/FORS2 and KECK/LRIS spectroscopy of group members.

Results. In contrast to other authors, we show that the observed lensing features in SL2S J02140-0535 belong to different background sources: one at $z = 1.7 \pm 0.1$ (photometric redshift) produces three images, while the other at $z = 1.023 \pm 0.001$ (spectroscopic redshift) has only a single image. Our unimodal NFW mass model reproduces these images very well. It is characterized by a concentration parameter $c_{200} = 6.0 \pm 0.6$, which is slightly greater than the value expected from Λ CDM simulations for a mass of $M_{200} \approx 1 \times 10^{14} M_{\odot}$. The spectroscopic analysis of group members also reveals a unimodal structure that exhibits no evidence of merging. The position angle of the halo is $\theta = 111.6 \pm 0.2$, which agrees with the direction defined by the luminosity contours. We compare our dynamic mass estimate with an independent weak-lensing based mass estimate finding that both are consistent.

Conclusions. Our combined lensing and dynamical analysis of SL2S J02140-0535 demonstrates the importance of spectroscopic information in reliably identifying the lensing features. Our findings argue that the system is a relaxed, massive galaxy group where mass is traced by light. This work shows a potentially useful method for constraining large-scale properties inaccessible to strong lensing, such as the scale radius of the NFW profile.

Key words. gravitational lensing: strong – galaxies: groups: general – galaxies: groups: individual: SL2S J02140-0535

1. Introduction

In the context of structure formation and evolution, galaxy groups play a key role, spanning the regime between individual galaxies and galaxy clusters. Therefore, detailed studies of this intermediate regime of the mass spectrum are relevant. Galaxy groups have been mostly studied using X-ray and optical tracers, as well as numerical simulations (e.g. Helsdon & Ponman 2000, 2003; Osmond & Ponman 2004; Willis et al. 2005; Finoguenov et al. 2007; Rasmussen & Ponman 2007;

Mamon 2007; Faltenbacher & Mathews 2007; Yang et al. 2008; van den Bosch et al. 2008; Gastaldello et al. 2007; D'Onghia et al. 2005; Sommer-Larsen 2006, and references therein). Only recently, thanks to the unsurpassed combined depth, area, and image quality of the Canada France Hawaii Telescope Legacy Survey (CFHTLS)¹, a new population of lenses has been uncovered, with Einstein radii between $\sim 3''$ and $\sim 8''$, generated by galaxy-group-scale dark-matter haloes (this subsample of the CFHTLS forms the Strong Lensing Legacy Survey² (SL2S), Cabanac et al. 2007). This new population effectively bridges the gap between single galaxies and massive clusters, opening a new window of exploration in the mass spectrum. The first representative sample of these lenses was presented by Limousin et al. (2009). Since then, a detailed investigation of some groups has been carried out: SL2S J02176-0513 (Tu et al. 2009) and SL2S J08544-0121 (Limousin et al. 2010). In this paper, we present a detailed analysis of SL2S J02140-0535 at $z = 0.44$,

* Based on observations obtained with MegaPrime/MegaCam, a joint project of CFHT and CEA/DAPNIA, at the Canada-France-Hawaii Telescope (CFHT) which is operated by the National Research Council (NRC) of Canada, the Institut National des Sciences de l'Univers of the center National de la Recherche Scientifique (CNRS) of France, and the University of Hawaii. This work is based in part on data products produced at TERAPIX and the Canadian Astronomy Data center as part of the Canada-France-Hawaii Telescope Legacy Survey, a collaborative project of NRC and CNRS. Also based on HST data as well as Keck (LRIS) and VLT (FORS 2) data.

¹ <http://www.cfht.hawaii.edu/Science/CFHTLS/>

² <http://www-sl2s.iap.fr/>

combining the dynamics of the group members, and both the strong and weak gravitational lensing.

Some researchers have demonstrated the advantages of combining the different lensing regimes with the constraints that come from the stellar kinematics of the central brightest cluster galaxy (BCG). For example, Sand et al. (2002, 2004) combined strong gravitational lensing with the velocity dispersion profile of the BCG and found that the models favored a shallower slopes in the NFW profiles. Newman et al. (2009) following the above works and adding weak-lensing analysis, sampled the dark matter profile over three decades in radius in the lensing cluster Abell 611. Despite all these works, on group scales the efforts in that direction are just beginning. First, because strong lensing in groups is a relatively new field of research, and second, owing to observational limitations, i.e., there are fewer lensing arcs in groups and detecting weak lensing by groups of galaxies is challenging. McKean et al. (2010) probed the inner part of a group-scale halo using strong gravitational lensing and stellar kinematics, and Thanjavur et al. (2010) showed that is possible to combine strong lensing and galaxy dynamics to characterize the mass distribution and the mass-to-light ratios of galaxy groups.

SL2S J02140-0535 was previously studied by Alard (2009) using a perturbative reconstruction of the gravitational lens. He found that the local shape of the potential and density of the lens, inferred from the perturbative solution, reveals the existence of an independent dark component that does not follow light. He argued that this particular shape of the dark halo is due to the merging of cold dark matter halos. Given these findings, the group properties represent a challenge, and to describe its mass distribution and perform a detailed study of the object is of significant worth and deserves attention. Our first aim in this work is to build a strong lensing mass model for SL2S J02140-0535 using lensed features observed in HST/ACS data combined with ground-based spectroscopy. The second is to combine the strong lensing constraints with the dynamics of the groups members to study the mass profile out to the scale radius. Finally, we wish to compare the masses obtained with the three methods, namely, strong lensing, weak lensing, and group dynamics, to shed some light on SL2S J02140-0535.

The paper is organized as follows. In Sect. 2, we describe the observational data images and spectroscopy and present the multiple image identification. In Sect. 3, we define how the dynamical constraints (on galaxy and group scales) enter into our strong lensing model. We also depict the profiles for both, the group and the galaxy-scale mass components. In Sect. 4, we present the strong lensing as well as the weak lensing analysis of SL2S J02140-0535 and the main results of the work. In Sect. 5, we summarize and discuss our results. Finally in Sect. 6, we present the conclusions. All our results are scaled to a flat, Λ CDM cosmology with $\Omega_M = 0.3$, $\Omega_\Lambda = 0.7$ and a Hubble constant $H_0 = 70 \text{ km s}^{-1} \text{ Mpc}^{-1}$. All images are aligned with WCS coordinates, i.e. north is up, east is left. Magnitudes are given in the AB system.

2. Observations and multiple images identification

SL2S J02140-0535 has been imaged by both ground and space based telescopes. From the ground, this group was observed in five filters (u^* , g' , r' , i' , z') as part of the CFHTLS using the wide field imager M₃₁P₁, which covers ~ 1 square degree on the sky, and a pixel size of $0.186''$. From space, the lens was followed-up with the *Hubble Space Telescope* (HST). Observations were performed in snapshot mode (C 15,

P.I. Kneib) in three bands with the ACS camera (F814, F606, and F475). Moreover, a spectroscopic follow-up of the arcs and the group members have been carried out from VLT and Keck.

2.1. Imaging

The strong lensing deflector in this group is populated by three galaxies (see Fig. 1, top left). The lensed images consist of three arcs surrounding the deflectors: one arc (labeled A) situated north of the deflector composed by two merging images, a second arc in the east (labeled B), and a third one (labeled C) in the south. In this ground-based image, we see a possible system consisting of ABC images that seem to have compatible colors. In Fig. 1 (top right), we show a color composition from the HST-ACS camera for the central part of the group. Since in the HST image, arc C exhibits different color from both A and B, is it possible that this arc is not associated with the proposed multiple-image system? This scenario is supported by the substructure in arcs A and B that are not present in arc C (see top right of Fig. 1). Given that Alard (2009) published an analysis based on this southern image being part of the multiply imaged system, special care will be used to properly assess the multiple image identification, which is crucial for the analysis.

The photometry for the central galaxies labeled G1, G2, and G3 (see top right of Fig. 1), and for the arcs was performed in all CFHT bands with the IRAF package *apphot*. For the galaxies, the magnitudes were derived by measuring fluxes inside a fixed circular aperture of 12 pixels ($\sim 2.22''$) for galaxies G1 and G2, and 6 pixels ($\sim 1.12''$) in galaxy G3. For the arcs, we employed polygonal apertures to obtain more accurate measurements. The vertices of the polygons for each arc were determined using the IRAF task *polymark*, and the magnitudes inside these apertures were calculated using the IRAF task *polyphot*.

The general properties of the central galaxies as well as the arcs are presented in Table 1. Column 1 lists the identification for each object. Columns 2 and 3 list the relative positions measured with respect to the brightest group galaxy (BGG) with coordinates $\alpha = 02:14:08:097$ and $\delta = -05:35:33.77$. Columns 4–7 list the colors $u^* - g'$, $g' - r'$, $r' - i'$ and $i' - z'$. Columns 8 and 9 show the geometric parameters derived from SExtractor (Bertin & Arnouts 1996), i.e., ellipticity ϵ and position angle θ_0 , which imply the orientation of the semi-major axis from the horizontal line in the image, measured counter-clockwise. Finally, Col. 10 lists the redshifts (see the next subsections). We note in Table 1 that the colors $u^* - g'$ and $g' - r'$ for arc C differ significantly from the colors in A and B, which have almost similar values (within the errors).

2.2. Spectroscopy

Two spectroscopic runs have been performed in the field of SL2S J02140-0535. Using LRIS (Oke et al. 1995) on Keck (dichroic 680 and 560 nm, exposure 600 s and 1200 s with a slit of $1.5''$), we measured the redshifts of one of the brightest galaxies populating the strong lensing deflector (G2) and we found $z = 0.4449 \pm 0.0003$.

We also used FORS 2 on VLT (P.I. V. Motta) with a medium resolution grism (GRIS 600RI) to target both group members and the strongly lensed features. Two masks were used and two exposures of 1400s were made with each mask. We selected the targets (other than strongly lensed features) as a two step process. First we choose galaxies whose $g - i$ color is within 0.15 of the $g - i$ color of the two brightest galaxies populating the strong

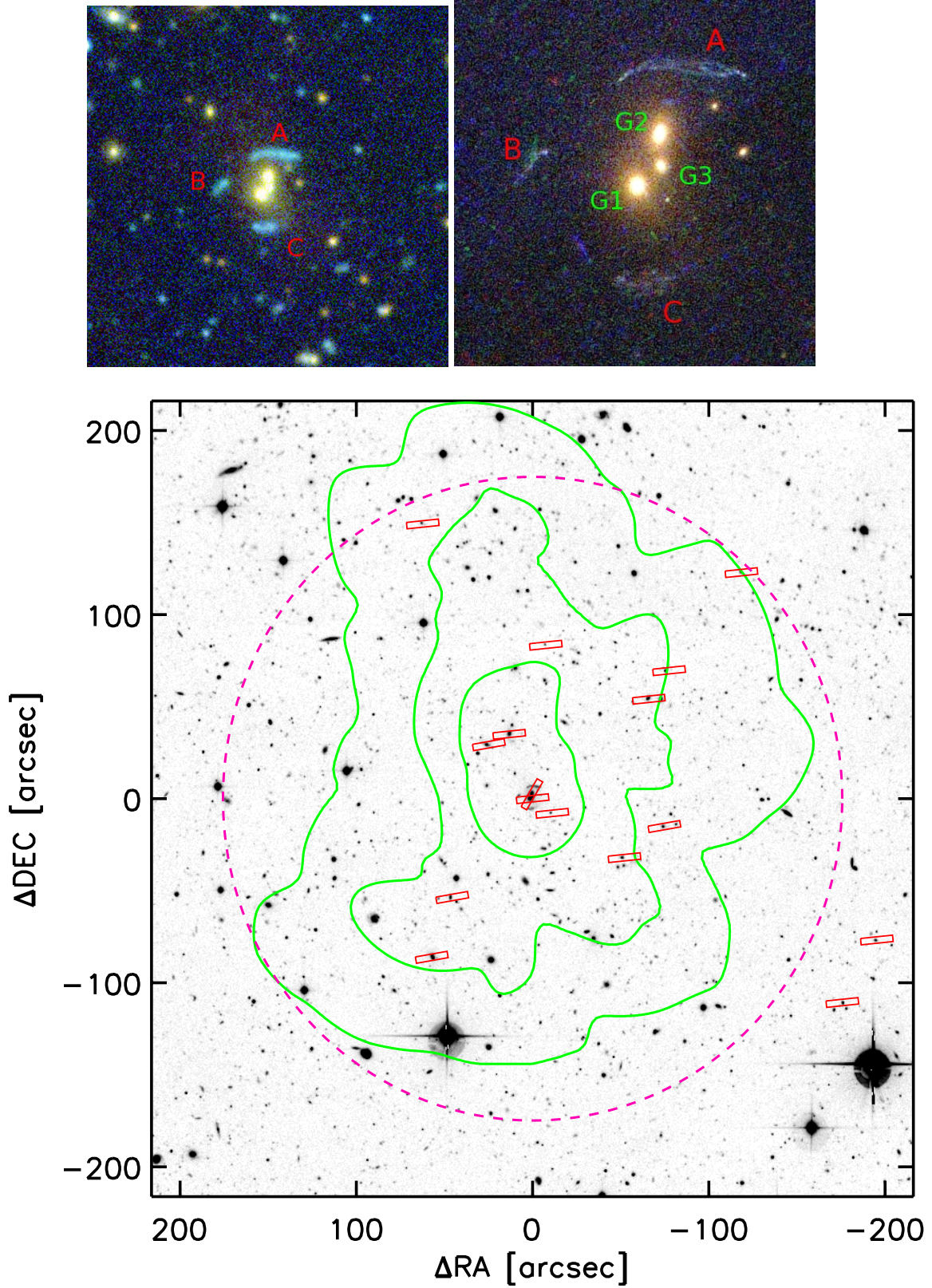


Fig. 1. The group SL2S J02140-0535 at $z_{\text{spec}} = 0.44$. *Upper left:* composite CFHTLS g, r, i color image ($1 \text{ square arcmin} = 341 \times 341 \text{ kpc}^2$). *Upper right:* composite HST/ACS F814, F606, F475 color image ($22'' \times 22'' = 125 \times 125 \text{ kpc}^2$). Note how the space-based image significantly improves the identification of multiple images and heightens the resolution allowing us to detect the substructure. *Lower:* CFHTLS i band ($7.2' \times 7.2' = 2.46 \times 2.46 \text{ Mpc}^2$) centered on the strong lensing system. We draw in green the luminosity contours (corrected for passive evolution) corresponding to 10^6 , 3×10^6 , and $10^7 L_{\odot} \text{ kpc}^{-2}$, respectively. Red rectangles show the location of the slits used for spectroscopy for the 16 confirmed members of the group and the magenta circle denotes a 1 Mpc distance from the center of the group.

Table 1. Photometric and spectroscopic data of the galaxies and the arcs.

ID Name	X [$''$]	Y [$''$]	$u^* - g'$	$g' - r'$	$r' - i'$	$i' - z'$	ϵ	θ_0 [$^\circ$]	z
<i>G1</i>	0.00	0.00	2.35 ± 0.11	1.61 ± 0.02	0.86 ± 0.01	0.36 ± 0.01	0.158	-41.0	0.4446 ± 0.0002
<i>G2</i>	1.16	3.09	2.99 ± 0.23	1.64 ± 0.03	0.87 ± 0.01	0.37 ± 0.01	0.424	64.2	0.4449 ± 0.0003
<i>G3</i>	1.37	1.25	1.81 ± 0.15	1.47 ± 0.06	0.88 ± 0.04	0.33 ± 0.03	0.177	18.26	—
<i>A</i>	—	—	0.73 ± 0.09	0.30 ± 0.09	0.47 ± 0.10	0.31 ± 0.11	—	—	[1.7 ± 0.1]
<i>B</i>	—	—	0.60 ± 0.11	0.07 ± 0.11	0.39 ± 0.14	0.36 ± 0.14	—	—	[1.7 ± 0.1]
<i>C</i>	—	—	0.18 ± 0.09	0.58 ± 0.09	0.60 ± 0.09	0.41 ± 0.09	—	—	1.023 ± 0.001

Notes. Column 1 lists the identification for each object as in Fig. 1. Columns 2 and 3 list the relative positions measured with respect to the brightest group galaxy (BGG) with coordinates $\alpha = 02:14:08.097$ and $\delta = -05 : 35 : 33.77$. Columns 4–7 list the CFHTLS colors. Columns 8 and 9 show the geometric parameters: ellipticity ϵ and position angle θ_0 , which gives the orientation of the semi-major axis from the horizontal line in the image, measured counterclockwise. In the last column we list the redshift; values in square brackets are photometric redshifts.

lensing deflector (see, Limousin et al. 2009). Since the field was too crowded in the center but not fully sampled at larger distances, we also selected all bright galaxies in the outer field regardless of their color. Figure 1 shows the slit configuration for all confirmed group members. Full details of the spectroscopy of the group members will be presented in a forthcoming publication (Muñoz et al., in prep.). Here we concentrate only on the spectroscopy of the lensed features.

No spectroscopic features were found in arcs A and B. On the other hand, the spectra of feature C reveals a strong emission line at 7538.4 \AA . As we can appreciate in Fig. 2, the emission line has a spatial extension that covers the whole arc (although the slits do not completely cover arcs A and B, they cover the brightest parts, and in arc B only a small fraction is outside). From this analysis, two possible scenarios emerge: system AB and arc C come from two different sources, or belong to the same source but the fluxes in system AB are not strong enough to detect the line. From the magnitudes in u^* band, it is possible to measure the flux ratios for the arcs, $f_B/f_C \sim 0.5$ and $f_A/f_C \sim 2.5$ (we used half of the flux in arc A to make the calculations). Assuming that the magnification is not very different in the arcs and they come from one single source, if the emission line is detected in arc C then it should be detected in arc A. It should even be detected in arc B, since the flux is only half of the flux in C and the feature is strong enough (see top and bottom panel of Fig. 2). That this is not detected, excludes the second scenario and supports the conclusion that system AB and arc C are produced by different sources.

The line detected in C may correspond to either [OII] $\lambda 3727$ at $z \sim 1$ or Ly α at $z \sim 5$. However, the low redshift solution is much more likely, and as we discuss below, the photometric redshift estimate supports this conclusion. Thus, assuming emission from [OII] $\lambda 3727$ and applying a Gaussian fitting, we obtain $z_{\text{spec}} = 1.023 \pm 0.001$. This line coming from the whole arc C is inconsistent with the model of SL2S J02140-0535 presented in Alard (2009). He assumed that arcs A, B, and C belong to the same source and he argued that the differences in colors observed in the HST-ACS images were related to the crossing of the caustic line by part of the source. His model predicts that one half of image C comes from the same part of the source as images A and B, but the other half corresponds to an area of the source that has no counterpart in the large arcs (A and B). The lack of spectroscopic features in arcs A and B does not support this scenario.

As a matter of fact, it is known that arcs produced by one single source could have different colors if the source is located over a caustic line. For example, in the case of a spiral galaxy for

which the disk (but not the bulge) is located over a caustic line, part of the disk can be mapped onto an arc with colors that do not agree with that of the counter-image. In some extreme cases, a tangential arc can indeed show no evidence of having been formed by two mirror images (e.g. Smith et al. 2005). Thus a model based only on the analysis of arc colors and their possible associations can lead to results that are not robust. A more detailed study of the color in the arcs, divided into components, is not the solution and may be wrong because the errors obtained from this kind of measurements become greater as we divide the arc into small fractions. For instance, Alard (2009) separated the individual elements in the arcs into two kinds: areas with bright sharp details and areas with smoother images. He found that bright regions have the same colors in the three arcs (as well as the smoother areas), and that the differences in colors between both areas (i.e. comparing the brightest ones with the smoother ones) were statistically significant. Thus, he argued that one single source produces the arc configuration in SL2S J02140-0532. However, the magnitudes obtained by performing photometry in regions of 5 pixels in radius could have errors of ~ 0.1 mag in bright details, and reach ~ 0.3 mag in the smoother areas where the signal is very low. Even with the ACS SnapShots, the errors are substantial, the images are not deep enough for this kind of analysis, and we need to be very cautious about his conclusions. As we discussed above, a model based only on colors would not be robust. This system clearly shows the need for a spectroscopic redshift to obtain an accurate lens model.

2.3. Photometric redshifts

Using the magnitudes reported in Table 1, we estimated the photometric redshifts for the features labeled A, B, and C with the HyperZ software (Bolzonella et al. 2000). We present the output probability distribution function (PDF) from HyperZ in Fig. 3. Arc C is constrained to be at $z_{\text{phot}} = 1.0 \pm 0.06$, which is in very good agreement with the identification of the emission line as [OII] $\lambda 3727$ at $z_{\text{spec}} = 1.023 \pm 0.001$. The multiply imaged system represented by arcs A and B has $z_{\text{phot}} = 1.7 \pm 0.1$ and $z_{\text{phot}} = 1.7 \pm 0.1$, for the arcs respectively. Although the probability distributions in the three cases are very broad (which is common in photometric redshift estimations using only five filters), there is no overlap in the solutions between system AB and arc C below a 3σ value. Along with the similarity between the distributions of arcs A and B, and the spectroscopic data, the possibility that A, B, and C belong to the same source is again ruled out.

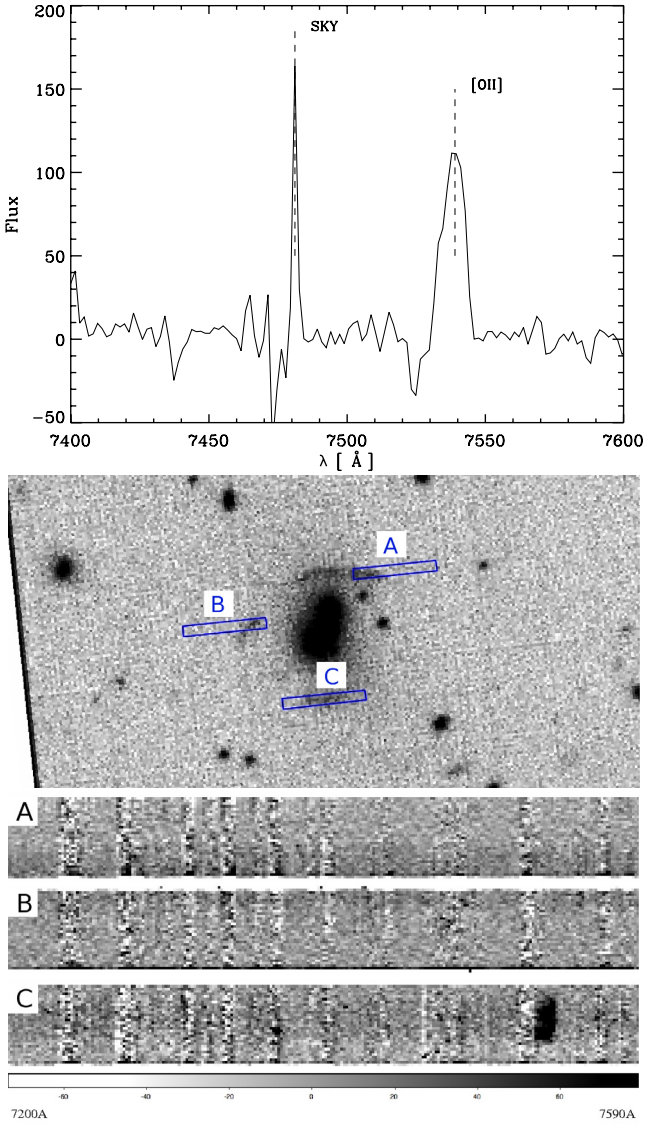


Fig. 2. *Top panel.* Spectrum of arc C. It shows a strong feature probably associated with [OII] λ 3727. *Middle panel.* VLT pre-image of the central part of SL2S J02140-0535 with the slits positions. *Bottom panel.* The 2D spectra of arcs A, B, and C in the same wavelength region. Note the extended emission line in C spectrum.

2.4. Pixelizing the arcs: increasing the number of constraints

When a source is mapped onto a system that shows multiple sub-components (surface brightness peaks), similar to the one displayed by SL2S J02140-0535 (system AB), the number of constraints can be increased as well as the degrees of freedom (for a fixed number of free parameters), since the peaks can be conjugated as different multiple image systems. To highlight the substructures appearing in system AB, we subtracted the six central galaxies of the group (G1, G2, G3, and the three small ones near those, see Fig. 1 top left). Following McLeod et al. (1998), we analyzed the F475W image and fitted a model convolved with a PSF. We used six de Vaucouleurs profiles to fit the galaxies and a synthetic PSF because there was no suitable non-saturated star in the field of view. To account for possible differences, we also convolved the PSF with a Gaussian profile. In Fig. 4, we show the central region of the group after the galaxy subtraction.

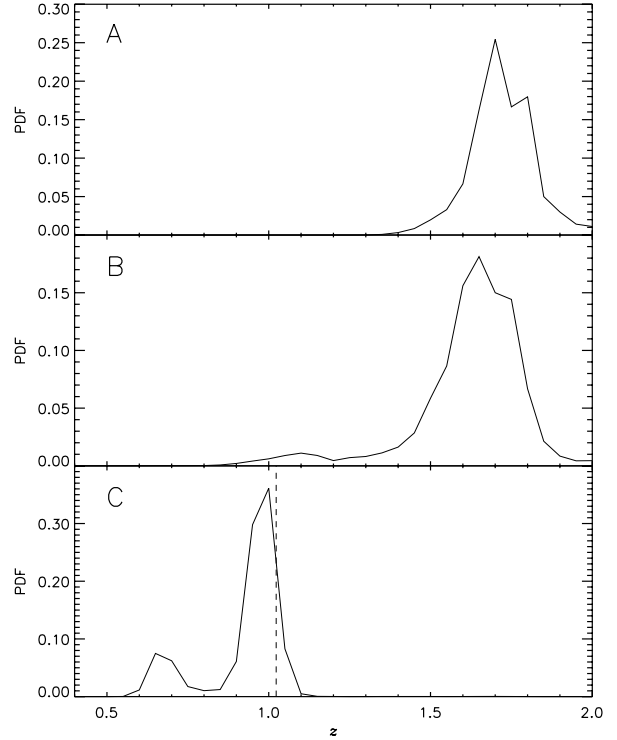


Fig. 3. Output photometric redshift PDF (see text) for arcs labeled A, B, and C (top to bottom). The dashed vertical line corresponds to the spectroscopic redshift inferred assuming the emission line comes from [OII] λ 3727.

To avoid introducing any bias into the modelling, we conjugated any bright peaks for which we were high confidence. This procedure transforms our simple AB system into four different systems, 1.*i*, 2.*i*, 3.*i*, and 4.*i*, where *i* goes from 1 to 3. In Fig. 4, we show the image identification of the peaks, and in Table 2 we report the positions (we assume that the typical uncertainties in the positions of identified conjugated images are 1 pixel $\sim 0.05''$). To keep the same notation and avoid confusion, we renamed arc C as 5.1. Therefore, our model have five different arc systems in the optimization procedure.

In summary, we have shown that features presented in system AB originate from the same background source, which is multiply imaged. This background source at $z_{\text{phot}} = 1.7 \pm 0.1$ yields three images in the image plane: arc A composed of two merging images and arc B. For each image, we have been able to conjugate substructures (systems 1.*i*, 2.*i*, 3.*i*, and 4.*i*). In addition, we have convincingly shown that arc C (now system 5.1) is a different object that is not multiple imaged.

3. Dynamical constraints

We describe the profiles used in our strong lensing model and also present how the dynamical constraints enter into the model on both the galaxy and group scales. In short, we propose that the dark matter component of the group consists of a single large-scale clump and we add smaller-scale clumps as galaxy-scale perturbations that are associated with the three individual galaxies at the center of SL2S J02140-0535. For these smaller clumps, we use the internal velocity dispersion of galaxy G1 as well as common scaling laws that links the parameters of the galaxies to their luminosity. In the large scale-clump, the dynamical information obtained from spectroscopic data is used to set the

Table 2. Multiple image identification.

Systems	α (J2000)	δ (J2000)
1.1	02:14:07.684	-05:35:27.37
1.2	02:14:08.184	-05:35:27.54
1.3	02:14:08.477	-05:35:31.68
2.1	02:14:07.708	-05:35:27.19
2.2	02:14:08.165	-05:35:27.32
2.3	02:14:08.493	-05:35:31.69
3.1	02:14:07.739	-05:35:27.26
3.2	02:14:08.110	-05:35:26.95
3.3	02:14:08.517	-05:35:32.00
4.1	02:14:07.770	-05:35:27.35
4.2	02:14:08.048	-05:35:26.93
4.3	02:14:08.538	-05:35:32.48
5.1	02:14:08.015	-05:35:38.54

possible range of values in the parameters that characterize the profile.

3.1. Galaxy scale

We assume that the density profile of the stellar mass distribution in the central galaxies of SL2S J02140-0535 follows a pseudo isothermal elliptical mass distribution (PIEMD). This profile was derived by [Kassiola & Kovner \(1993\)](#) and is parameterized by a central density ρ_0 , linked to the central velocity dispersion, σ_0 , which in turn is related to the depth of the potential well (see [Limousin et al. 2005](#); [Elíasdóttir et al. 2007](#), for a detailed discussion of the properties of this mass profile). It is described using two characteristic radii that relate to changes in the slope of the density profile. In the inner region, the profile behaves like a non-singular isothermal profile with central density ρ_0 and core radius r_{core} . In the outer parts ($r_{\text{cut}} < r$), the density progressively falls from $\rho \propto r^{-2}$ to $\rho \propto r^{-4}$, introducing a natural cut-off. A clump modeled using PIEMD can be characterized using seven parameters: the center position, (X, Y) , the ellipticity ϵ , the position angle θ , and the parameters of the density profile, σ_0 , r_{core} , and r_{cut} . Below, we discuss the parameters associated with the dynamics of the central galaxies, namely, σ_0 and r_{cut} and we return to those remaining in the next section.

Our spectroscopic data include the two brightest central galaxies in the group, G1 and G2. However, given the poor quality of the G2 galaxy spectra (low S/N ratio), we only measured the line-of-sight internal velocity dispersion of galaxy G1. Using the penalized pixel-fitting method developed by [Cappellari & Emsellem \(2004\)](#), we found that $\sigma_{\text{los}}^* = 215 \pm 34 \text{ km s}^{-1}$ for the G-band absorption line profile. Hereafter we denote with an asterisk quantities associated with galaxy G1. This velocity corresponds to $\sigma_0^* = 253 \text{ km s}^{-1}$, according to the relation reported by [Elíasdóttir et al. \(2007\)](#) who studied the internal velocity dispersion of some galaxies in the Abell 2218 cluster. Assuming that the galaxy profiles can be described by spherically symmetric PIEMD profiles, [Elíasdóttir et al. \(2007\)](#) found that the ratio of the measured velocity dispersion (which is derived using spectroscopic data) to the fiducial velocity dispersion of the PIEMD profiles, (i.e., the ratio of the stellar to dynamical mass) has an almost constant value ($\sigma_0^* \approx \sigma_{\text{los}}^*/0.85$) across the region where the spectra were obtained.

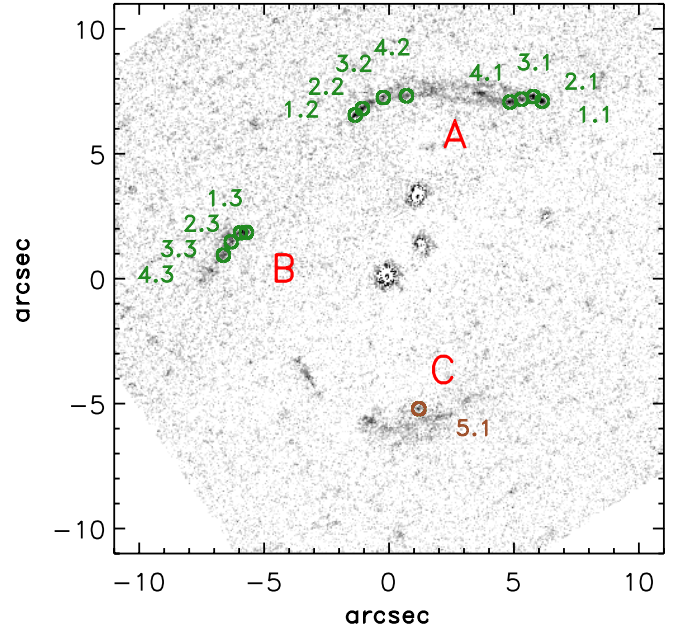


Fig. 4. F475W image ($22'' \times 22''$) after subtraction of the six central galaxies of the group. The green circles show the positions of the conjugated images that constitutes the AB arc system. The brown circle, mark the location of arc C.

Since the total stellar mass of the galaxy is related to σ_0^* and r_{cut}^* by the expression ([Elíasdóttir et al. 2007](#))

$$M_* = \frac{1.5\pi}{G} r_{\text{cut}}^* \sigma_0^{*2}, \quad (1)$$

the parameter r_{cut}^* can be constrained if we determine M_* in an independent way. To measure the stellar mass of galaxy G1, we followed two different methods. First, we converted the g -band magnitude into an absolute rest frame V-band luminosity and found that $L_V = 3.0 \times 10^{10} L_{\odot}$. We then used the mass-to-light ratio reported in SLACS lenses ([Gavazzi et al. 2007](#)) to estimate the stellar mass and found that $M_* \approx 1.0 \times 10^{11} M_{\odot}$. For the second method, we employed the HyperZ software ([Bolzonella et al. 2000](#)) with the five magnitudes of galaxy G1 reported in Table 1. We found a slightly greater value of $M_* \approx 4.0 \times 10^{11} M_{\odot}$. Once we apply Eq. (1), these range of masses produce a range of possible values for r_{cut}^* of 1–6 kpc.

The parameters of the two remaining galaxies are obtained using the scaling relations

$$r_{\text{cut}} = r_{\text{cut}}^* \left(\frac{L}{L^*} \right)^{1/2}, \quad (2)$$

$$\sigma_0 = \sigma_0^* \left(\frac{L}{L^*} \right)^{1/4}, \quad (3)$$

where σ_0^* , r_{cut}^* and L^* are set by those values of galaxy G1 discussed above. For a discussion of these scaling relations, we refer to [Limousin et al. \(2007\)](#).

3.2. Group scale

3.2.1. Velocity dispersion and virial mass

In Fig. 5, we show the redshift distribution of the galaxies in the field of SL2S J02140-0535; as we can note, the spectroscopy reveals a well defined group without any evidence of bimodality.

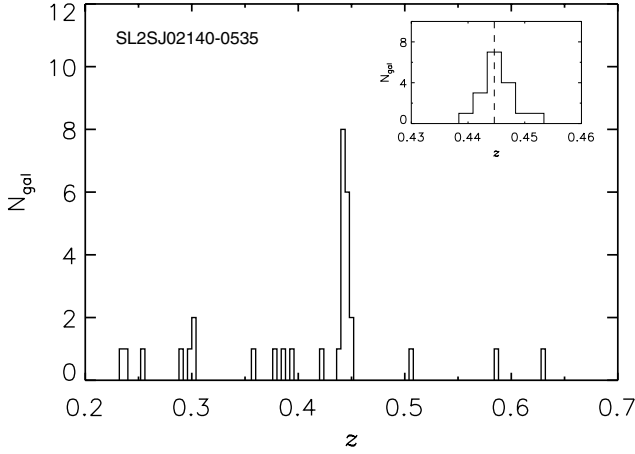


Fig. 5. The histogram (bin size $\Delta = 0.004$) shows the redshift distribution along the direction of SL2S J02140-0535. The spectroscopic data reveals a well-defined group at $z = 0.444$. The inset highlights the central part rebinned to $\Delta = 0.0025$. There are 17 galaxies in the histogram, but after the iterative algorithm (see text) one outlier was removed.

The dynamical study of this group will be presented in a forthcoming publication (Muñoz et al., in prep.) as part of a detailed study of seven strong-lensing galaxy groups in the SL2S. Here we briefly describe the method used. We adopted the formalism by Wilman et al. (2005) in order to determine the group membership. We identified the group members as follows: the group was initially assumed to be located at the redshift of the main bright lens galaxy, z_{lens} , with an initial observed-frame velocity dispersion of $\sigma_{\text{obs}} = 500(1 + z_{\text{lens}})$ km s⁻¹. After computing the required redshift range for group membership and applying a biweight estimator (Beers et al. 1990) the iterative process was found to have reached a stable membership solution with 16 secure members and $\sigma = 630 \pm 107$ km s⁻¹. These galaxies are shown with red rectangles at the bottom of Fig. 1.

Assuming that the group has an isotropic velocity dispersion and is no longer undergoing net expansion or contraction, we apply the virial theorem to estimate the mass of SL2S J02140-0535. Since in our lensing models we probe the two-dimensional (2D) mass of the groups, we define $M_{\text{v}} = 3\pi\widetilde{R}_{\text{v}}\sigma_{\text{los}}^2/2G$ as the virial mass inside the projected radius \widetilde{R}_{v} . Using the measured $\sigma_{\text{los}} = \sigma/\sqrt{3} = 364$ km s⁻¹ and a virial radius $\widetilde{R}_{\text{v}} = R_{\text{H}} = 0.8 \pm 0.3$ Mpc, where R_{H} is the projected harmonic mean radius (e.g. Irgens et al. 2002), we obtain a mass of $(1.1 \pm 0.8) \times 10^{14} M_{\odot}$. We stress that this is not the true 2D mass at \widetilde{R}_{v} , but only an estimate of the mass inside \widetilde{R}_{v} , and that this mass is probably underestimated (e.g. Biviano et al. 2006).

3.2.2. Dynamical constraints in the NFW profile

We describe our galaxy-group density profile as an NFW profile (Navarro et al. 1997)

$$\rho(r) = \frac{\rho_{\text{s}}}{(r/r_{\text{s}})(1 + r/r_{\text{s}})^2}, \quad (4)$$

where ρ_{s} is a characteristic density, and r_{s} is a scale radius that corresponds to the region where the logarithmic slope of the density equals the isothermal value. To link the velocity dispersion calculated in the last subsection with the velocity associated with the potential of the NFW halo, we follow two different and independent methods. First we define the velocity in terms of the

scale radius and the characteristic density to be

$$\sigma^2 \equiv 4 \left(1 + \ln \frac{1}{2}\right) G r_{\text{s}}^2 \rho_{\text{s}}. \quad (5)$$

It is defined in such a way that it represents a realistic velocity dispersion and not only a scaling parameter, which is useful when comparing the velocity predicted by strong lensing models with the velocity dispersion measured in dynamical studies (see the discussion in Verdugo et al. 2007). In a second way, following Elíasdóttir et al. (2007) we calculate the projected average line-of-sight velocity dispersion inside the radius \widetilde{R}_{v} as

$$\langle \sigma_{\text{los}}^2 \rangle(\widetilde{R}_{\text{v}}) = \frac{2\pi \int_0^{\widetilde{R}_{\text{v}}} \sigma_{\text{p}}^2(R) \Sigma(R) R dR}{M_{2\text{D}}(\widetilde{R}_{\text{v}})}, \quad (6)$$

where R is a 2D radius and $\sigma_{\text{p}}^2(R)$ is the projected line-of-sight velocity dispersion given by

$$\sigma_{\text{p}}^2(R) = \frac{2G}{\Sigma(R)} \int_R^{\infty} \frac{M_{3\text{D}}(r)\rho(r)}{r^2} \sqrt{r^2 - R^2} dr, \quad (7)$$

and $\Sigma(R)$ the surface mass density. We note that Eq. (6) depends not only on the virial radius, \widetilde{R}_{v} , but also in the parameters that characterize the profile. Integrating Eq. (4), we obtain

$$M_{3\text{D}}(r) = 4\pi r_{\text{s}}^3 \rho_{\text{s}} \left[\ln(1 + r/r_{\text{s}}) - \frac{r/r_{\text{s}}}{1 + r/r_{\text{s}}} \right]. \quad (8)$$

Integrating the surface mass density (see Appendix), we then obtain the expression for $M_{2\text{D}}(\widetilde{R}_{\text{v}})$, and substituting Eqs. (8) and (4) into Eq. (7), it is possible to rewrite Eq. (6) as

$$\langle \sigma_{\text{los}}^2 \rangle(\widetilde{R}_{\text{v}}) = 2\pi G \rho_{\text{s}} \frac{G(\widetilde{R}_{\text{v}}, r_{\text{s}})}{F(\widetilde{R}_{\text{v}}, r_{\text{s}})}, \quad (9)$$

where

$$G(\widetilde{R}_{\text{v}}, r_{\text{s}}) = \int_0^{\widetilde{R}_{\text{v}}} \int_R^{\infty} \left[\ln(1 + r/r_{\text{s}}) - \frac{r}{r_{\text{s}} + r} \right] \times \frac{1}{(r/r_{\text{s}})(1 + r/r_{\text{s}})^2} \frac{\sqrt{r^2 - R^2}}{r^2} R dr dR \quad (10)$$

and $F(\widetilde{R}_{\text{v}}, r_{\text{s}})$ is given by Eq. (A.4). We emphasize that the dependence of the projected average line-of-sight velocity dispersion (Eq. (9)) on the virial radius, the scale radius, and the characteristic density. If we assume that Eqs. (5) and (9) are related by the expression $\langle \sigma_{\text{los}}^2 \rangle(\widetilde{R}_{\text{v}}) = \sigma^2/3$ (which is qualitatively correct in the sense that σ represents a 3D velocity dispersion and $\langle \sigma_{\text{los}}^2 \rangle(\widetilde{R}_{\text{v}})$ represents the projected average line-of-sight velocity dispersion assuming no anisotropy and a spherically symmetric NFW profile), then

$$1 = \frac{3\pi}{2(1 + \ln 1/2)r_{\text{s}}^2} \frac{G(\widetilde{R}_{\text{v}}, r_{\text{s}})}{F(\widetilde{R}_{\text{v}}, r_{\text{s}})}. \quad (11)$$

Thus, given \widetilde{R}_{v} , we can use the above equation to obtain the possible range of values for the scale radius. It is noteworthy that although the velocity dispersion does not appear explicitly in the equation, the equation is not independent of this value since our virial radius is computed from the relative positions of the confirmed members, which in turn depends on the velocity dispersion of the group. In other words, the velocity dispersion is

implicit in the equation, and therefore, in our calculations of the scale radius. For $\widetilde{R}_v = 0.8 \pm 0.3$ Mpc we obtain $r_s = 150 \pm 50$ kpc. It then follows that $c_{\text{NFW}} = \widetilde{R}_v/r_s = 5 \pm 3$. After the scale radius is estimated, the 2D mass of the halo expressed in terms of the velocity dispersion of the group and the virial radius can be determined in a simple fashion using Eqs. (5) and (A.3), and expressed as

$$M_{2\text{D}}(\widetilde{R}_v, r_s, \sigma) = \frac{2\pi\sigma^2 r_s}{(1 + \ln 1/2)G} F(\widetilde{R}_v, r_s). \quad (12)$$

Using our previously computed values, this yields $M_{2\text{D}} = (4 \pm 2) \times 10^{14} M_\odot$. This estimate is, within the errors, slightly greater than the value M_v computed from dynamics, although we show in Sect. 5 that it is in good agreement with the strong and weak lensing mass estimates. For the strong lensing analysis (see Sect. 4), we use these dynamical results to put some priors in the range in which the parameters are allowed to vary: we set the velocity dispersion range to be $523 \text{ km s}^{-1} \leq \sigma \leq 737 \text{ km s}^{-1}$, and the scale radius to be $100 \text{ kpc} \leq r_s \leq 200 \text{ kpc}$, i.e. to vary within $1\text{-}\sigma$ of their values.

4. Gravitational lensing analysis

4.1. Strong lensing

To study the lensing group SL2S J02140-0535, we used the parametric method implemented in the LENSTOOL³ ray-tracing code (Kneib 1993). This software use a Bayesian Monte Carlo Markov chain (MCMC) method to search for the most likely parameters in the lens modeling (Jullo et al. 2007).

The identification of the multiply imaged system presented in Sect. 2 leads to 16 observational constraints. With these constraints, we computed a model (optimized in the image plane) with the following set of free parameters $\{X, Y, \epsilon, \theta, r_s, \sigma, z_1, z_2, z_3, z_4, r_{\text{cut}}^*\}$, where the first six parameters characterize the NFW profile and z_i represents the redshifts for the systems 1.*i*, 2.*i*, 3.*i*, and 4.*i*, respectively. All the parameters are allowed to vary with uniform priors except r_s and σ for which we used Gaussian priors with the $1\text{-}\sigma$ errors computed in the last section. System 5.1, at $z_{\text{spec}} = 1.023 \pm 0.001$ is used in the analysis as a singly imaged object. Multiple image systems were allowed to vary between 1.5 and 2.0 (approximately $2\text{-}\sigma$ from the value inferred from the photometric redshift analysis) to take into account the broad PDF common to these measurements; and for the same reason we do not choose a Gaussian prior in this case. The remaining parameters, those that describe the central galaxies, were set as follows: the center of the profiles and the ellipticity and position angle are assumed to be the same as for the luminous components. We use the values reported in Table 1. The velocities dispersions are given by Eq. (3) for a $\sigma_0^* = 253 \text{ km s}^{-1}$.

Figure 6 shows the PDF for the arc systems, and the best-fit model solutions for z_i obtained after the optimization. The mean optimal value is $\bar{z} = 1.7 \pm 0.2$. It is clear from the figure that the model PDFs are slightly far to be Gaussians and z values greater than two are still favored. This reflects the lack of arc systems (only one system with a fixed redshift) available to constrain the model and shows the importance of using the photometric redshift as a prior. The results of our best fits are summarized in Table 3. In Fig. 7, we show the predicted positions of our best

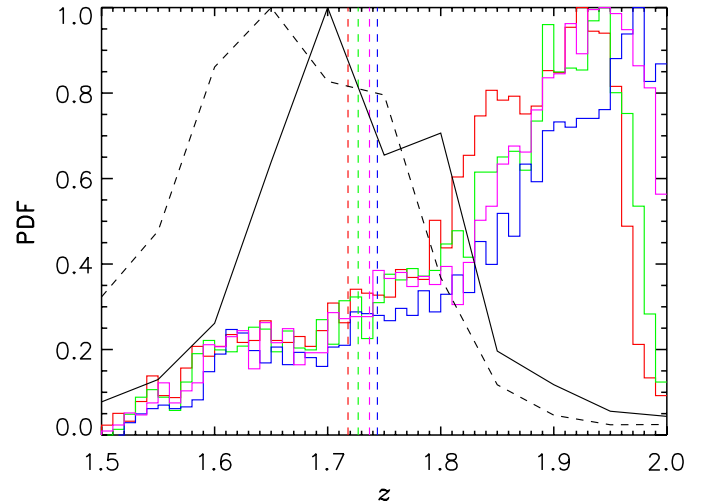


Fig. 6. Normalized PDFs. The red, blue, green and magenta histograms shows the distributions obtained with our model, for z_1 , z_2 , z_3 and z_4 respectively. The vertical lines corresponds to the best-fit model solutions given by the optimization procedure. Black continuous and black dashed lines are the distributions shown in Fig. 3 for arcs A and B, respectively.

model (orange and cyan squares), as well as the observed positions (green and brown circles). The remarkable agreement between both positions is quantified by a mean scatter in the image plane smaller than $0.04''$. We obtained $\chi_{\text{DOF}}^2 = 1.2$, showing that the extent of the match between the observed positions and those predicted by the model is in accord with the error variance. This χ_{DOF}^2 is defined in the image plane (see Jullo et al. 2007) assuming the same uncertainties in the positions for all the images (see Sect. 2.4). We note that our model do not predict extra images, which supports the reliability of our strong lensing model.

4.2. Weak lensing

The weak lensing analysis of this galaxy group was performed in Limousin et al. (2009). We refer the interested reader to that paper for a detailed description of the methodology, and present below a brief summary. They selected as background sources the galaxies whose *i* band magnitude falls between 21.5 and 24. Their density equals to 13 arcmin^{-2} . The completeness magnitude in this band is 23.96 and the seeing equals $0.61''$. A Bayesian method, implemented in the I² software (Bridle et al. 2002), is used to fit the shape parameters of the faint background galaxies and correct for PSF smearing. From the catalogue of background galaxies, Limousin et al. (2009) pursued a one-dimensional weak lensing analysis. They fitted a singular isothermal sphere model (SIS) to the reduced shear signal between 150 kpc and 1.2 Mpc from the group center, finding an Einstein radius equals to $3.6 \pm 2.4''$. To relate the strength of the weak lensing signal to a physical velocity dispersion characterising the group potential, Limousin et al. (2009) estimated the mean geometrical factor using the photometric redshift catalogue from the T0004 release of the CFHTLS-Deep survey⁴ (Ienna & Pelló 2006). They found that $\sigma_{\text{SIS}} = 612^{+180}_{-264} \text{ km s}^{-1}$. This translates into a projected mass computed within a circular aperture of radius equals to 1 Mpc of $(2.8 \pm 1.5) \times 10^{14} M_\odot$.

³ This software is publicly available at: <http://www.oamp.fr/cosmology/lenstool/>

⁴ http://www.ast.obs-mip.fr/users/rosier/CFHTLS_T0004/

Table 3. Best-fit model parameters.

Comp.	X ["]	Y ["]	ϵ	θ [$^\circ$]	r_{core} [kpc]	r_s [kpc]	r_{cut} [kpc]	c_{200}	σ_0 [km s $^{-1}$]	σ [km s $^{-1}$]	χ^2_{DOF}
Group	1.3 ± 0.1	0.5 ± 0.3	0.28 ± 0.02	111.6 ± 0.2	–	170 ± 18	–	6.0 ± 0.6	–	664 ± 18	1.2
L^*	–	–	–	–	[0.15]	–	5.6 ± 1.3	–	[253]	–	–

Notes. The first column identifies the different scale components. The L^* denotes the galaxy-scale mass component. Columns 2 and 3 list the position in arcseconds relative to the BGG. In Cols. 4 and 5 we provide the geometric parameters. From Cols. 6 to 11, we present the different profiles parameters, and in the last column the χ^2_{DOF} . Values in square brackets are not optimized.

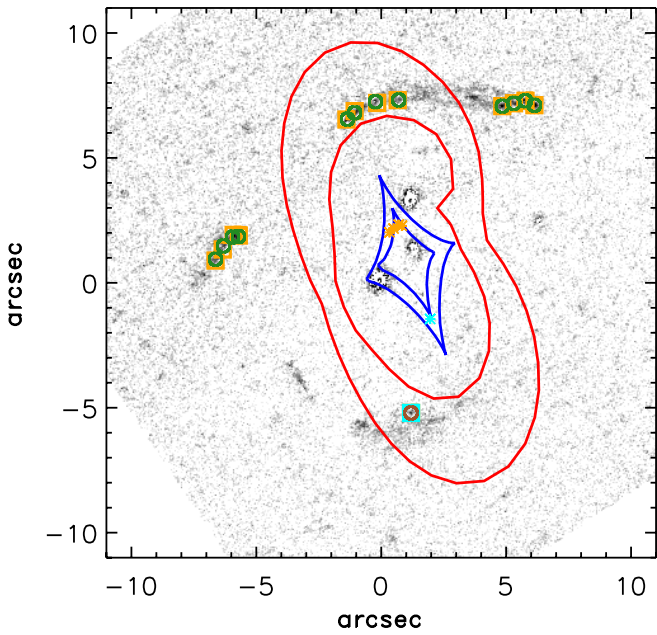


Fig. 7. Tangential critical lines (red) and caustic lines (blue) for two different sources located at $z = 1.0$ and $z = 1.7$. As in Fig. 4, the circles show the measured positions of the images (input data for the model). The squares (orange and cyan) are the model-predicted image positions after optimization, and the asterisks (orange and cyan) the positions in the source plane. Although the cyan asterisk appears to over lay the caustic line, this is only an artifact, a product of the thick lines, and the size of the asterisks that we used to highlight the figure. The source is *not* over the caustic line.

5. Discussion

Our best-fit model demonstrates that it is possible to recover the observational features presented in the galaxy group SL2S J02140-0535 using a single halo for the group component plus three galaxy scale components associated with the central galaxies. We do not need extra assumptions about the mass distribution in the group. In addition, the position angle of the halo is oriented with a well-constrained position angle at $\theta = 111.6 \pm 0.2$, which is the same direction as the one defined by the luminosity contours (Limousin et al. 2009) and is consistent with the spatial distribution of the confirmed members of the group (see Fig. 1 bottom). This supports a scenario where the mass is traced by light.

The degeneracies in the σ - r_s space are very common in strong lensing modeling (e.g. Jullo et al. 2007) since the region where the arcs appear is limited to the central region of the clusters and the scale radius is generally three or four times the

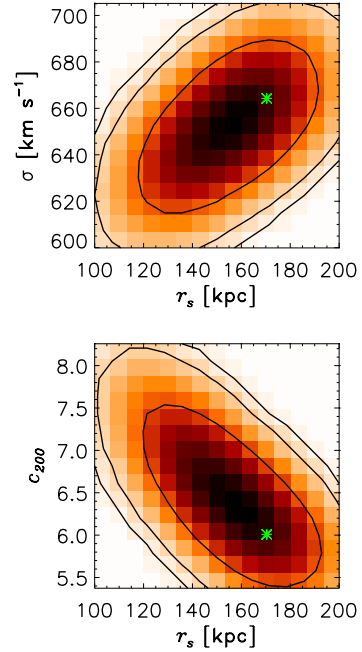


Fig. 8. PDFs of the parameters σ , c_{200} and r_s . The three contours stand for the 68%, 95%, and 99% confidence levels. The values obtained for our best-fit model are marked by a green asterisk.

distance to that region. In galaxy groups, this region is indeed, even smaller than in clusters. Thus, it is impossible to constrain the scale radius of a group using only its observed strong lensing features. To highlight this behavior, we depicted in the top panel of Fig. 8 the PDFs for the σ and r_s parameters. We note how models with a scale radius greater than 200 kpc are still possible (in addition to those smaller than 100 kpc), but we placed a limit on this value using information from the group dynamics. Thus, this give us a method that would be useful in breaking the degeneracies in the σ - r_s space using the dynamics of the group obtained from spectroscopic data. This is important because it provides a technique to fill the gap between strong lensing and weak lensing constraints in galaxy groups.

To analyze the dark matter profile of SL2S J02140-0535 in greater detail, we calculated the concentration c_{200} from the values of r_s and σ (see the discussion in Verdugo et al. 2007). Here we assumed that $c_{200} = r_{200}/r_s$, where we defined r_{200} as the radius of a spherical volume within which the mean density is 200 times the critical density of the universe at the given redshift z of the group. The bottom panel of Fig. 8 shows the 2D histogram for the parameters c_{200} and r_s , where we can note the same tendency with r_s as in the top panel. Our best-fit model infers that $c_{200} = 6.0 \pm 0.6$, which is in good agreement with the value c_{NFW}

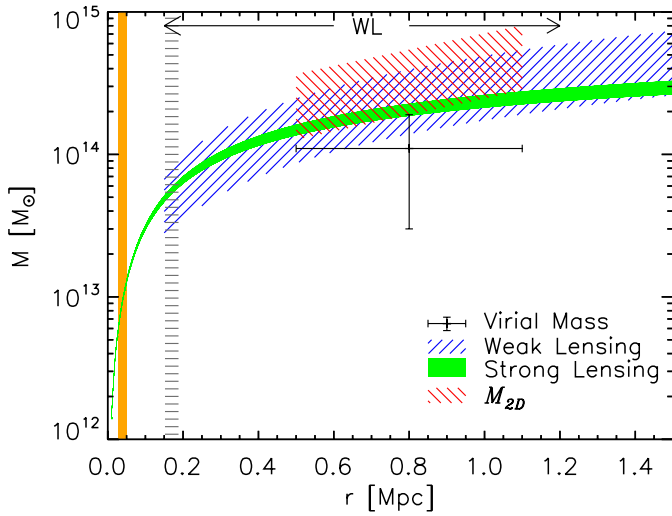


Fig. 9. The 2D projected mass as a function of the aperture radius measured from the BGG. The green and blue shaded areas corresponds to the mass profile within 1σ errors for the strong lensing and the weak lensing models, respectively. The red region illustrates the 2D mass derived from Eq. (12) as a function of \tilde{R}_v . The point with error bars is the mass estimate from dynamics. The orange-shaded region shows the area where the arc systems lie and the gray region shows the model-predicted scale radius. We also depict with an arrow the zone in which the weak lensing signal was measured.

presented in Sect. 4. On the other hand, if we compare it with the values expected from Λ CDM numerical simulations, we found that our concentration is slightly higher. From the work of Duffy et al. (2008), a DM halo at $z = 0.44$ with $M_{200} \approx 1 \times 10^{14} M_\odot$ has $c_{200} \approx 4.0$.

Given the relatively low mass of galaxy groups (compared with clusters), we do not expect to derive a weak lensing signal strong enough to allow us to fully probe an NFW profile. Until the work of Limousin et al. (2009), weak lensing signals on these mass scales had indeed been recovered only by stacking group images (e.g. Mandelbaum et al. 2006). However, the strength of the signal in SL2S J02140-0535 is sufficient to fit a SIS and obtain the projected mass as a function of the radius. In Fig. 9, we compare the masses obtained with the different methods adopted in the present work: strong lensing (green), weak lensing (blue), M_{2D} derived from Eq. (12) (red), and the virial mass (point with error bars). As we place limits on the possible values of the scale radius, the strong lensing mass is still reliable up to the scale radius ($r_s = 170 \pm 18$ kpc), but beyond this value the extrapolation of the mass becomes less secure. However, from Fig. 9 we can note that the first three masses are in agreement within the errors in the range $0.5 \text{ Mpc} \leq r \leq 1.1 \text{ Mpc}$, i.e. the interval defined by \tilde{R}_v . The virial mass, despite being lower than all masses, differs more from M_{2D} . However, we stress again that it is not the true 2D mass at \tilde{R}_v but only an estimate of the mass inside \tilde{R}_v . This mismatch between virial mass and lensing mass is also found in other groups, but the analysis of this subject is beyond the scope of the present work and will be discussed in detail in a forthcoming paper (Muñoz et al., in prep.).

Using a perturbative method, Alard (2009) reconstructed the structure and potential of the gravitational lens SL2S J02140-0535. In his work, he assumed that the A, B, and C arcs belong to the same source. He argued that the differences in colors observed in the HST-ACS images were related to the crossing of

the caustic line by part of the source. His model predicts that one half of image C comes from the same part of the source as images A and B, but the other half corresponds to an area of the source that has no counterpart in the large arcs (A and B). The perturbative method is capable of reproducing this arc configuration, but the model predicts the existence of an independent dark component that does not follow light. In the present work, we have demonstrated that AB system and C system belong to different sources, one at $z = 1.7 \pm 0.1$ and the other one at $z_{\text{spec}} = 1.023 \pm 0.001$. Our model, with a single NFW profile (which is consistent with the analysis of the luminosity contours, Fig. 1 bottom, and the redshift distribution of the galaxies in the field of SL2S J02140-0535, see Fig. 5), provide a good fit of the arc features observed in the group and our results point out that the projected light of the group traces the dark matter distribution.

6. Conclusions

We have probed the gravitational potential of SL2S J02140-0535 on a large radial range using complementary techniques: strong lensing, weak lensing, and dynamics. In the strong lensing regime, we performed a fit using an NFW profile and three galaxy-scale mass components as perturbations to the group potential. We used PIEMDs for the individual galaxies and set constraints on their geometrical and dynamical parameters using observational data (image and spectroscopy). We measured the velocity dispersion of the group using Keck (LRIS) and VLT (FOR2) spectra, and we applied this information to constrain and build a reliable strong lensing model based on one multiply imaged system and one single image system. In the weak lensing regime, we used the analysis reported in Limousin et al. (2009). Our main results can be summarized as follows:

1. We have shown that the AB and C systems belong to different sources, one at $z = 1.7 \pm 0.1$ (photometric redshift) and the other one at $z = 1.023 \pm 0.001$ (spectroscopic), respectively.
2. Our best-fit lens model reproduce quite well the image systems observed in the field of SL2S J02140-0535, with no extra assumptions about the underlying mass distribution (e.g. bimodal distribution). This agrees with the spectroscopic analysis that shows a well-defined group. Furthermore, we obtained a position angle of the halo of $\theta = 111.6 \pm 0.2$, that is consistent with the orientation of the luminosity contours and the spatial distribution of confirmed members.
3. The spectroscopic information provide constraints on the scale radius of the NFW profile. In the present work, we showed that is possible to use the dynamics at group scale to discriminate between a great range of possible r_s values and σ (in particular $100 \text{ kpc} \leq r_s \leq 200 \text{ kpc}$ and $523 \text{ km s}^{-1} \leq \sigma \leq 737 \text{ km s}^{-1}$, respectively).
4. The scale radius and the velocity dispersion found in our best-fit models, $r_s = 170 \pm 18 \text{ kpc}$ and $\sigma = 664 \pm 18 \text{ km s}^{-1}$, respectively, yields a concentration value $c_{200} = 6.0 \pm 0.6$, which is consistent with $c_{\text{NFW}} = 5 \pm 3$, but slightly greater than the one predicted by Λ CDM simulations.
5. The masses obtained with the strong lensing, weak lensing, and M_{2D} methods agree within the errors, but the virial mass is slightly below these values. Thus, we demonstrated that it is possible to combine these different methodologies to get a complete insight into the mass of a galaxy group.

The lensing and dynamical analysis of SL2S J02140-0535 presented in this paper, has had two principal points. First, it has

investigated the impact of including spectroscopic information of arcs (i.e. secure arc identifications) in strong lensing models to avoid complex mass distribution models that do not follow the light. Secondly, we studied the possibility of constraining large scale properties that could not be measured by strong lensing, such as the scale radius in the NFW profile. Future spectroscopic follow-up of the arcs A and B will provide confirmation of our model. In addition, the deepest HST images of the group will allow us to construct more accurate weak lensing models capable of probing an NFW profile on large scales, as well as improving our strong lensing model.

Acknowledgements. We thank the anonymous referee for thoughtful comments and suggestions. T. Verdugo acknowledge support from FONDECYT through grant 3090025. T. Verdugo thank the Laboratoire d’Astrophysique de Marseille and the Institut d’Astrophysique de Paris for the two kindly invitations to work in their facilities. V.M. acknowledges partial support from FONDECYT 1090673 and DIPUV 09/2007. R.P.M. acknowledges partial support from CONICYT CATA-BASAL and Comité Mixto ESO-Gobierno de Chile. M.L. thanks the center National d’Etudes Spatiales (CNES) and CNRS for their support. M.L. est bénéficiaire d’une bourse d’accueil de la Ville de Marseille. The Dark Cosmology center is funded by the Danish National Research Foundation. J.R. acknowledges support from a EU Marie-Curie fellowship. We also thank R. Pelló for helping with HyperZ.

Appendix A: M_{2D} inside the virial radius \widetilde{R}_v in the NFW profile

The surface mass density in the NFW profile is given by (Golse & Kneib 2002)

$$\Sigma(\xi) = 2\rho_s r_s F(\xi), \quad (\text{A.1})$$

where

$$F(\xi) = \begin{cases} \frac{1}{\xi^2-1} \left(1 - \frac{1}{\sqrt{1-\xi^2}} \operatorname{arccosh} \frac{1}{\xi} \right) & \text{if } \xi < 1 \\ \frac{1}{3} & \text{if } \xi = 1 \\ \frac{1}{\xi^2-1} \left(1 - \frac{1}{\sqrt{\xi^2-1}} \arccos \frac{1}{\xi} \right) & \text{if } \xi > 1 \end{cases} \quad (\text{A.2})$$

and the dimensionless coordinate ξ , is the radius in the XY plane in units of the scale radius, $\xi = (x/r_s, y/r_s)$. It then follows that the 2D mass inside the virial radius can be expressed as:

$$M_{2D}(\rho_s, \widetilde{R}_v, r_s) = 8\pi\rho_s r_s^3 F(\widetilde{R}_v, r_s), \quad (\text{A.3})$$

where

$$F(\widetilde{R}_v, r_s) = \int_0^1 \frac{1}{\sqrt{\xi^2-1}} \left[1 - \frac{1}{\sqrt{1-\xi^2}} \operatorname{arccosh} \frac{1}{\xi} \right] d\xi + \int_1^{\widetilde{R}_v} \frac{1}{\sqrt{\xi^2-1}} \left[1 - \frac{1}{\sqrt{\xi^2-1}} \arccos \frac{1}{\xi} \right] d\xi \quad (\text{A.4})$$

and $\widetilde{\xi} = \widetilde{R}_v/r_s$. We note that the mass depends on both the characteristic density and the scale radius of the NFW profile.

References

- Alard, C. 2009, A&A, 506, 609
Beers, T. C., Flynn, K., & Gebhardt, K. 1990, AJ, 100, 32
Bertin, E., & Arnouts, S. 1996, A&A, 117, 393
Biviano, A., Murante, G., Borgani, S., et al. 2006, A&A, 456, 23
Bolzonella, M., Miralles, J.-M., & Pelló, R. 2000, A&A, 363, 476
Bridle, S., Kneib, J.-P., Bardeau, S., & Gull, S. 2002, in The shapes of galaxies and their dark halos, Proceedings of the Yale Cosmology Workshop, New Haven, Connecticut, USA, 28–30 May 2001, ed. P. Natarajan, 38
Cabanac, R. A., Alard, C., Dantel-Fort, M., et al. 2007, A&A, 461, 813
Cappellari, M., & Emsellem, E. 2004, PASP, 116, 138
D’Onghia, E., Sommer-Larsen, J., Romeo, A. D., et al. 2005, ApJ, 630, L109
Duffy, A. R., Schaye, J., Kay, S. T., & Dalla Vecchia, C. 2008, MNRAS, 390, L64
Elíasdóttir, Á., Limousin, M., Richard, J., et al. 2007, unpublished [arXiv:0710.5636]
Faltenbacher, A., & Mathews, W. G. 2007, MNRAS, 375, 313
Finoguenov, A., Ponman, T. J., Osmond, J. P. F., & Zimer, M. 2007, MNRAS, 374, 737
Gastaldello, F., Buote, D. A., Humphrey, P. J., et al. 2007, ApJ, 669, 158
Gavazzi, R., Treu, T., Rhodes, J. D., et al. 2007, ApJ, 667, 176
Golse, G., & Kneib, J. 2002, A&A, 390, 821
Helsdon, S. F., & Ponman, T. J. 2000, MNRAS, 315, 356
Helsdon, S. F., & Ponman, T. J. 2003, MNRAS, 339, L29
Ienna, F., & Pelló, R. 2006, in SF2A-2006: Semaine de l’Astrophysique Française, ed. D. Barret, F. Casoli, G. Lagache, A. Lecavelier, & L. Pagani, 347
Irgens, R. J., Lilje, P. B., Dahle, H., & Maddox, S. J. 2002, ApJ, 579, 227
Jullo, E., Kneib, J.-P., Limousin, M., et al. 2007, New J. Phys., 9, 447
Kassiola, A., & Kovner, I. 1993, ApJ, 417, 450
Kneib, J.-P. 1993, Ph.D. Thesis, Université Paul Sabatier, Toulouse III, France
Limousin, M., Kneib, J.-P., & Natarajan, P. 2005, MNRAS, 356, 309
Limousin, M., Richard, J., Jullo, E., et al. 2007, ApJ, 668, 643
Limousin, M., Cabanac, R., Gavazzi, R., et al. 2009, A&A, 502, 445
Limousin, M., Jullo, E., Richard, J., et al. 2010, A&A, 524, A95
Mamon, G. A. 2007, in Groups of Galaxies in the Nearby Universe, ed. I. Saviane, V. D. Ivanov, & J. Borissova, 203
Mandelbaum, R., Seljak, U., Cool, R. J., et al. 2006, MNRAS, 372, 758
McKean, J. P., Auger, M. W., Koopmans, L. V. E., et al. 2010, MNRAS, 317
McLeod, B. A., Bernstein, G. M., Rieke, M. J., & Weedman, D. W. 1998, AJ, 115, 1377
Navarro, J. F., Frenk, C. S., & White, S. D. M. 1997, ApJ, 490, 493
Newman, A. B., Treu, T., Ellis, R. S., et al. 2009, ApJ, 706, 1078
Oke, J. B., Cohen, J. G., Carr, M., et al. 1995, PASP, 107, 375
Osmond, J. P. F., & Ponman, T. J. 2004, MNRAS, 350, 1511
Rasmussen, J., & Ponman, T. J. 2007, MNRAS, 380, 1554
Sand, D. J., Treu, T., & Ellis, R. S. 2002, ApJ, 574, L129
Sand, D. J., Treu, T., Smith, G. P., & Ellis, R. S. 2004, ApJ, 604, 88
Sommer-Larsen, J. 2006, MNRAS, 369, 958
Thanjavur, K., Crampton, D., & Willis, J. 2010, ApJ, 714, 1355
Tu, H., Gavazzi, R., Limousin, M., et al. 2009, A&A, 501, 475
van den Bosch, F. C., Pasquali, A., Yang, X., et al. 2008, [arXiv:0805.0002]
Verdugo, T., de Diego, J. A., & Limousin, M. 2007, ApJ, 664, 702
Willis, J. P., Pacaud, F., Valtchanov, I., et al. 2005, MNRAS, 363, 675
Wilman, D. J., Balogh, M. L., Bower, R. G., et al. 2005, MNRAS, 358, 71
Yang, X., Mo, H. J., & van den Bosch, F. C. 2008, ApJ, 676, 248

Characterizing SL2S galaxy groups using the Einstein radius^{★,★★,★★★}

T. Verdugo^{1,2}, V. Motta², G. Foëx², J. E. Forero-Romero³, R. P. Muñoz⁴, R. Pello⁵, M. Limousin^{6,7}, A. More⁸,
R. Cabanac⁵, G. Soucail⁹, J. P. Blakeslee¹⁰, A. J. Mejía-Narváez^{1,11}, G. Magris¹, and J. G. Fernández-Trincado^{1,11,12}

¹ Centro de Investigaciones de Astronomía, Apartado Postal 264, 5101-A Mérida, Venezuela
e-mail: verdugo@cida.ve

² Universidad de Valparaíso, Departamento de Física y Astronomía, Avenida Gran Bretaña 1111, Casilla 5030 Valparaíso, Chile

³ Departamento de Física, Universidad de los Andes, Cra. 1 No. 18A-10, Edificio Ip, A. A. 4976 Bogotá, Colombia

⁴ Instituto de Astrofísica, Facultad de Física, Pontificia Universidad Católica de Chile, Av. Vicuña Mackenna 4860, 7820436 Macul, Santiago, Chile

⁵ Laboratoire d'Astrophysique de Toulouse-Tarbes, Université de Toulouse, CNRS, 57 avenue d'Azereix, 65000 Tarbes, France

⁶ Laboratoire d'Astrophysique de Marseille, Université de Provence, CNRS, 38 rue Frédéric Joliot-Curie, 13388 Marseille Cedex 13, France

⁷ Dark Cosmology Center, Niels Bohr Institute, University of Copenhagen, Juliane Marie Vej 30, 2100 Copenhagen, Denmark

⁸ Kavli Institute for the Physics and Mathematics of the Universe (Kavli IPMU), The University of Tokyo, 5-1-5 Kashiwanoha, 277-8583 Kashiwa-shi, Chiba, Japan

⁹ Université de Toulouse, UPS-Observatoire Midi-Pyrénées, IRAP, 31400 Toulouse, France

¹⁰ Herzberg Institute of Astrophysics, National Research Council of Canada, Victoria, BC V9E 2E7, Canada

¹¹ Universidad de Los Andes, Posgrado de Física Fundamental, La Hechicera, 5101 Mérida, Venezuela

¹² Institute Utinam, CNRS UMR6213, Université de Franche-Comté, OSU THETA de Franche-Comté-Bourgogne, 25010 Besançon, France

Received 22 February 2014 / Accepted 9 September 2014

ABSTRACT

Aims. We aim to study the reliability of R_A (the distance from the arcs to the center of the lens) as a measure of the Einstein radius in galaxy groups. In addition, we want to analyze the possibility of using R_A as a proxy to characterize some properties of galaxy groups, such as luminosity (L) and richness (N).

Methods. We analyzed the Einstein radius, θ_E , in our sample of Strong Lensing Legacy Survey (SL2S) galaxy groups, and compared it with R_A , using three different approaches: 1) the velocity dispersion obtained from weak lensing assuming a singular isothermal sphere profile ($\theta_{E,I}$); 2) a strong lensing analytical method ($\theta_{E,II}$) combined with a velocity dispersion-concentration relation derived from numerical simulations designed to mimic our group sample; and 3) strong lensing modeling ($\theta_{E,III}$) of eleven groups (with four new models presented in this work) using *Hubble* Space Telescope (HST) and Canada-France-Hawaii Telescope (CFHT) images. Finally, R_A was analyzed as a function of redshift z to investigate possible correlations with L , N , and the richness-to-luminosity ratio (N/L).

Results. We found a correlation between θ_E and R_A , but with large scatter. We estimate $\theta_{E,I} = (2.2 \pm 0.9) + (0.7 \pm 0.2)R_A$, $\theta_{E,II} = (0.4 \pm 1.5) + (1.1 \pm 0.4)R_A$, and $\theta_{E,III} = (0.4 \pm 1.5) + (0.9 \pm 0.3)R_A$ for each method respectively. We found weak evidence of anti-correlation between R_A and z , with $\text{Log } R_A = (0.58 \pm 0.06) - (0.04 \pm 0.1)z$, suggesting a possible evolution of the Einstein radius with z , as reported previously by other authors. Our results also show that R_A is correlated with L and N (more luminous and richer groups have greater R_A), and a possible correlation between R_A and the N/L ratio.

Conclusions. Our analysis indicates that R_A is correlated with θ_E in our sample, making R_A useful for characterizing properties like L and N (and possibly N/L) in galaxy groups. Additionally, we present evidence suggesting that the Einstein radius evolves with z .

Key words. gravitational lensing: strong – galaxies: groups: general

* SL2S: Strong Lensing Legacy Survey.

** Based on observations obtained with MegaPrime/MegaCam, a joint project of CFHT and CEA/DAPNIA, at the Canada-France-Hawaii Telescope (CFHT) which is operated by the National Research Council (NRC) of Canada, the Institut National des Sciences de l'Univers of the center National de la Recherche Scientifique (CNRS) of France, and the University of Hawaii. This work is based in part on data products produced at TERAPIX and the Canadian Astronomy Data center as part of the Canada-France-Hawaii Telescope Legacy Survey, a collaborative project of NRC and CNRS. Also based on *Hubble* Space Telescope (HST) data as well as *Magellan* (IMACS) and VLT (FOR S 2) data.

*** Appendix A is available in electronic form at <http://www.aanda.org>

1. Introduction

Since most of the galaxies in the Universe belong to galaxy groups (Eke et al. 2004), the systematic examination of this intermediate regime of the mass-spectrum (between large elliptical galaxies and clusters) will shed light on the formation and evolution of structures in the hierarchical framework. Although galaxy groups have been the subject of study from different approaches, such as optical (e.g., Wilman et al. 2005a,b; Yang et al. 2008; Knobel et al. 2009; Cucciati et al. 2010; Balogh et al. 2011; Li et al. 2012), X-ray (e.g., Helsdon & Ponman 2000a,b; Osmond & Ponman 2004; Willis et al. 2005; Finoguenov et al. 2007; Rasmussen & Ponman 2007; Sun 2012), and numerical

simulations (e.g., Sommer-Larsen 2006; Romeo et al. 2008; Cui et al. 2011); the systematic investigation of such a mass regime from a lensing perspective has recently started (e.g., Mandelbaum et al. 2006; Limousin et al. 2009; More et al. 2012).

The Strong Lensing Legacy Survey (SL2S¹, Cabanac et al. 2007) selects its sample from the Canada-France-Hawaii Telescope Legacy Survey (CFHTLS)². The SL2S has allowed us to find and study a large sample of group-scale lenses (More et al. 2012), as well as galaxy-scale gravitational lenses (Gavazzi et al. 2012). Some galaxy groups discovered in the SL2S have been studied in detail using different techniques (e.g., Tu et al. 2009; Limousin et al. 2009, 2010; Thanjavur et al. 2010; Verdugo et al. 2011), further highlighting the importance of SL2S. More et al. (2012) showed the first compilation of lens candidates, the SL2S-ARCS (SARCS) sample, consisting of 127 objects, with 54 systems labeled as promising lenses. The authors also present the first constraints on the average mass density profile of groups using strong lensing. One of the main goals of the SL2S is to accurately determine the characteristics of the lensing groups through various methods, for example with dynamics using spectroscopy (Muñoz et al. 2013) as well as weak lensing analysis and luminosity density maps (Foëx et al. 2013). In particular, the latter work combines lensing and optical analysis to further constrain the sample, and presents a list of the 80 most secure lens candidates. Even though most of the objects in the sample must be confirmed, these objects present a weak-lensing signal (detection at the 1σ level), and show an over-density in their luminosity density maps (see Foëx et al. 2013, for a detailed discussion). Thus, these candidates give us the opportunity to test a wide range of astrophysical problems and to probe diverse phenomena.

For instance, Zitrin et al. (2012) analyzed the universal distribution of the Einstein radius on 10 000 clusters in the SDSS, discussing the possibility of an Einstein radius evolution with redshift. These authors reported that the mean effective Einstein radius decreases between $z = 0.1$ to $z = 0.45$, and argue that such a decrease is possibly related to cluster evolution, since clusters at lower z are expected to have more concentrated mass distributions, thus they are stronger lenses. Considering only geometrical effects, they demonstrated that a profile steeper than the singular isothermal sphere (SIS) is necessary to explain the decline of $\sim 40\%$. Zitrin et al. (2012) explain the tentative increase in the Einstein radius towards $z = 0.5$ invoking an increase in the size of the critical curves, as a result of merging subclumps in clusters (e.g., Torri et al. 2004; Dalal et al. 2004; Redlich et al. 2012).

Our sample of secure lens candidates (Foëx et al. 2013) can be useful to test such an assertion, namely the θ_E evolution with redshift. Although it is clearly in a distinct mass range, our sample has a larger range in redshift and the benefit of being selected by their strong lensing features. In our analysis we assume that R_A (the distance between the more extended lensed image and the brightest lens galaxy in the group) is roughly the Einstein radius (obtained by More et al. 2012). This is justified since the Einstein radius provides a natural angular scale to describe the lensing geometry (Narayan & Bartelmann 1996); the typical angular separation of images is on the order of $2\theta_E$. However, we need to be cautious because there are some factors that could bias the comparison. For example, the sample selected by More et al. (2012) is made up of groups that display small arcs and giant arcs

(see Sect. 4.1). For giant arcs, comparing R_A and θ_E is a rough estimation (e.g., Miralda-Escude & Babul 1995), since this kind of arc tends to appear close to the critical curve in a spherically symmetric mass distribution model (although in general lenses are elongated). On the other hand, comparing R_A and θ_E could be inaccurate for those images (which are not giant arcs) that appear, for example, along the major-axis critical curve. In this sense, it is important to note that arc radial positions could extend beyond the Einstein radius (depending on the Einstein radius definition, e.g., Puchwein & Hilbert 2009; Richard et al. 2009). Furthermore, comparison between the expected θ_E in the Lambda cold dark matter (Λ CDM) paradigm and observations may lead to different conclusions depending on the assumption of spherical or triaxial dark matter halos (e.g., Broadhurst & Barkana 2008; Oguri & Blandford 2009), and on which θ_E geometrical definition is used (see the discussion in the review of Meneghetti et al. 2013). Although from a lensing perspective galaxy groups are not as complex as galaxy clusters, some natural questions arise: is R_A a reliable estimation for θ_E ? What effect does asphericity or substructure have on such an assumption? The aim of the present work is to answer these questions and test the viability of using R_A as a proxy to characterize or even quantify some properties such as luminosity or richness in galaxy groups. As scaling relations are naturally expected (and have been observed at different redshifts) between the mass and optical properties in groups and clusters (e.g., Lin et al. 2003; Popesso et al. 2005; Becker et al. 2007; Reyes et al. 2008; Rozo et al. 2009; Andreon & Hurn 2010; Foëx et al. 2012, 2013), a correlation between R_A and these properties follows clearly because R_A scales with the mass of the halos.

Nowadays we have an extraordinary amount of data available in the search for and study of lensing galaxy groups from the Sloan Digital Sky Survey (Abazajian et al. 2003) or the CFHTLS, for example. There will be even more data with the upcoming long-term big survey projects such as LSST (LSST Dark Energy Science Collaboration 2012), the Dark Energy Survey (DES³), and EUCLID (Boldrin et al. 2012). Even though automated software is used to look for strong lensing candidate detection (e.g., Alard 2006; Seidel & Bartelmann 2007; Marshall et al. 2009; Sygnet et al. 2010; Maturi et al. 2014; Joseph et al. 2014; Gavazzi et al. 2014), we still lack crucial information for accurate lens modeling. For instance, the impossibility (in most cases) of spectroscopically confirming the lensing nature of arcs in groups, or even dynamically confirming that the members of the group-lensing candidates are gravitationally-bound structures (e.g., Thanjavur et al. 2010; Muñoz et al. 2013). The study presented by Foëx et al. (2013), and the present work, try to tackle this lack of spectroscopic information, by analyzing the strong-lensing group candidates using complementary approaches.

To this end, we present the Einstein radius analysis of the secure sample of galaxy groups in the SARCS sample. We consider three methods that use 1) the velocity dispersion from a weak lensing analysis, following Foëx et al. (2013); 2) strong lensing models following Broadhurst & Barkana (2008), together with numerical simulations that mimic the properties of our group sample; and 3) strong lensing modeling using a ray-tracing code (coupled with new spectroscopic data for one of the groups). Finally, we analyze the correlations between R_A and the optical properties of the groups. Our paper is arranged as follows: in Sect. 2 we present the observational data images and spectroscopy. We describe the numerical simulations

¹ <http://www-sl2s.iap.fr/>

² <http://www.cfht.hawaii.edu/Science/CFHTLS/>

³ <http://www.darkenergysurvey.org/>

Table 1. Photometric data for galaxies and arcs used in the four new gravitational lensing models.

ID	Galaxy/Arc	u^*	g'	r'	i'	z'	k_s
SL2S J08591–0345 (SA72)	G	25.4 ± 0.1	23.51 ± 0.02	21.96 ± 0.01	20.681 ± 0.004	20.245 ± 0.005	–
	A	25.0 ± 0.1	24.1 ± 0.1	23.4 ± 0.1	22.7 ± 0.1	22.4 ± 0.1	20.7 ± 0.1
SL2S J08520–0343 (SA63)	G1	23.62 ± 0.06	21.437 ± 0.009	19.808 ± 0.004	18.971 ± 0.003	18.577 ± 0.005	–
	A	27.2 ± 0.9	24.42 ± 0.07	23.39 ± 0.04	22.56 ± 0.03	22.52 ± 0.08	–
SL2S J09595+0218 (SA80)	G	25.59 ± 0.05	24.69 ± 0.02	23.098 ± 0.007	21.753 ± 0.003	20.987 ± 0.004	–
	A	25.23 ± 0.04	24.97 ± 0.03	25.20 ± 0.05	24.94 ± 0.05	24.14 ± 0.07	–
SL2S J10021+0211 (SA83)	G	25.59 ± 0.05	24.69 ± 0.02	23.098 ± 0.007	21.753 ± 0.003	20.987 ± 0.004	–
	B	25.83 ± 0.07	24.04 ± 0.01	23.42 ± 0.01	23.04 ± 0.01	22.68 ± 0.01	–

Notes. Column 1 is the identification for each object (see text); Col. 2 is the object type; Cols. 3–7 are the CFHTLS magnitudes; Col. 8 is the magnitude in the k_s band from WIRCam.

in Sect. 3. In Sect. 4 we explain the methodology used to calculate the Einstein radius with the three different methods. We summarize and discuss our results in Sect. 5. Finally in Sect. 6, we present the conclusions. All our results are scaled to a flat, Λ CDM cosmology with $\Omega_M = 0.3$, $\Omega_\Lambda = 0.7$ and a Hubble constant $H_0 = 70 \text{ km s}^{-1} \text{ Mpc}^{-1}$. All images are aligned with WCS coordinates, i.e., north is up, east is left. Magnitudes are given in the AB system.

2. Data

The objects presented in this work have been imaged by ground-based telescopes and in some cases by the *Hubble* Space Telescope (HST). From the ground, the groups were observed in five filters (u^* , g' , r' , i' , z') as part of the CFHTLS (see Gwyn 2011) using the wide-field imager MIPOM, which covers ~ 1 square degree on the sky, with a pixel size of $0.186''$. The galaxy group SL2S J08591–0345 (SA72) was observed by WIRCam (near infrared mosaic imager at CFHT) as part of the proposal 08BF08 (P.I. G. Soucail). From space, the lens was followed up with the HST in snapshot mode (C15, P.I. Kneib) in three Advanced Camera For Surveys (ACS) filters (*F814*, *F606*, and *F475*). In addition, spectroscopic follow-up of the arcs in SL2S J08591–0345 (SA72) and SL2S J08520–0343 (SA63) were carried out with IMACS at Las Campanas Observatory. Throughout the present paper we will keep both names for some of the discussed lensing groups, the long name, e.g. SL2S (see Cabanac et al. 2007) because it gives us the object’s coordinates, and the compact SARCS name, e.g. SA, to be consistent with More et al. (2012).

2.1. Imaging

Photometric redshifts for the group sample were reported in More et al. (2012). However, for the groups discussed in Sect. 4.3 the photometric redshifts (z_{phot}) were estimated for both the lens and the lensed galaxy. For these four lens groups we estimated their z_{phot} using the magnitudes of the brightest galaxy populating the strong lensing deflector. The photometry for these galaxies was performed in all CFHT bands with the IRAF⁴ package *apphot*. Considering that the magnitudes of the lens galaxy could be contaminated by the close and bright arcs (biasing

⁴ IRAF is distributed by the National Optical Astronomy Observatory, which is operated by the Association of Universities for Research in Astronomy (AURA) under cooperative agreement with the National Science Foundation.

Table 2. Results from simulations.

Center redshift bin	Simulation snapshot	Total number of Halos
0.05	82	781 764
0.16	76	816 422
0.28	70	854 495
0.40	66	869 768
0.52	62	901 588
0.64	60	909 205
0.75	56	920 882
0.87	54	923 512
0.99	52	904 938
1.10	50	898 774

Notes. Column 1 lists the center redshift bins used to query the MultiDark data base; Col. 2 the corresponding snapshot number in the simulation; Col. 3 the number of halos in the whole volume box with rms velocities in the range 300 km s^{-1} – 1000 km s^{-1} .

Table 3. Fitting results for θ_E vs. R_A .

Correlation	$a \pm \delta a$	$b \pm \delta b$	R	P
$\theta_{E,I} - R_A$	2.2 ± 0.9	0.7 ± 0.2	0.33	6×10^{-3}
$\theta_{E,II} - R_A$	0.4 ± 1.5	1.1 ± 0.4	0.40	1×10^{-3}
$\theta_{E,II} - R_A^\dagger$	0.4 ± 1.5	1.1 ± 0.4	0.40	1×10^{-3}
$\theta_{E,III} - R_A$	0.4 ± 1.5	0.9 ± 0.3	0.60	6×10^{-2}

Notes. ^(†) Second catalog. Column 1 lists the correlation; Cols. 2 and 3 list the coefficient values in the relation $Y = a + bX$; Cols. 4 and 5 list the Spearman’s rank correlation coefficient and the statistical significance, respectively.

the photometric redshift), we carefully measured the magnitudes using different apertures (5, 8, 11, 13, 15, and 18 pixels). Then each aperture measurement was used to estimate redshifts using the HyperZ software (Bolzonella et al. 2000). The best redshifts were selected, i.e. those with the highest probability; using selected apertures with no contamination due to arcs or other galaxies. The photometric data and redshifts estimations are presented in Tables 1 and 4.

The method is tested estimating photometric redshifts for some groups with reported spectroscopy (Limousin et al. 2009; Muñoz et al. 2013). These groups are SL2S J02215–0647 (SA39), SL2S J0854–0121 (SA66), SL2S J02140–0532 (SA22), SL2S J02141–0405 (SA23), SL2S J02180–0515

Table 4. Summary of the strong lensing modeling.

ID	N_c	z_l	z_s	X ["]	Y ["]	ϵ	θ [°]	$\theta_{E,IR}$ ["]	R_A^a ["]	rms	$\chi^2_{d.o.f.}$
SL2S J08591–0345 (SA72)	12	$0.642 \pm 0.001^*$	0.883 ± 0.001	1.342 ± 0.002	-0.233 ± 0.001	0.0158 ± 0.0004	138.6 ± 0.4	4.9 ± 0.2	4.5	0.57	19
SL2S J08520–0343 (SA63)	6	$0.457^{+0.016}_{-0.016}$	2.70 ± 0.08	2.0 ± 0.1	-0.98 ± 0.04	0.30 ± 0.03	157.0 ± 0.6	5.2 ± 0.1	5.0	0.03	0.3
SL2S J09595+0218 (SA80)	4	$0.816^{+0.019}_{-0.013}$	$1.2^{+0.1}_{-0.04}$	-0.48 ± 0.04	-0.77 ± 0.05	[0.30]	[30]	2.1 ± 0.1	2.4	0.05	0.89
SL2S J10021+0211 (SA83)	2	$0.801^{+0.022}_{-0.015}$	$2.26^{+0.01}_{-0.03}$	[0]	[0]	[0.25]	[105]	3.19 ± 0.04	2.6	0.00	0.00

Notes. ^(*) Spectroscopic redshifts from Muñoz et al. (2013). ^(o) More et al. (2012). Columns: number of constraints N_c and optimized SIE parameters. Error bars represents 1σ confidence level on the parameters inferred from the MCMC optimization. Values in brackets are not optimized. These values correspond to models where the number of observational constraints is smaller than the number of free parameters characterizing the SIE profile. The goodness of the fit is quantified by the RMS in the image plane and the reduced $\chi^2_{d.o.f.}$.

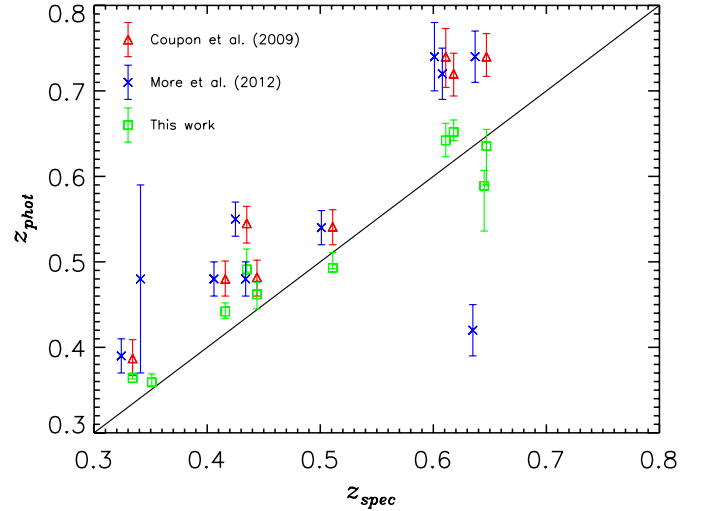


Fig. 1. Comparison between spectroscopic (from Limousin et al. 2009; Muñoz et al. 2013) and photometric redshifts. Red triangles depict the z_{phot} from Coupon et al. (2009), blue crosses the values reported in More et al. (2012), and green squares those from this work. Blue crosses were shifted in z_{spec} for clarity.

(SA33), SL2S J08591–0345 (SA72), SL2S J22214–0053 (SA127), SL2S J14081+5429 (SA97), SL2S J14300+5546 (SA112), and SL2S J02254–0737 (SA50). In Fig. 1 we compare our z_{phot} (as well as previously reported values) with the spectroscopic redshift. We note that the z_{phot} values from More et al. (2012) and Coupon et al. (2009) are slightly overestimated, probably because of the automatic extraction of the magnitudes used in those works.

Another effect to take into account in z_{phot} calculations is that the point-spread functions (PSF) are different for each filter band, which makes it difficult to match physical apertures. This is especially important when estimating the magnitudes of the arcs (Table 1) because the different degree of blurring in each filter band could produce an important bias in the redshift estimations (Hildebrandt et al. 2012). Thus, for the arcs, we proceed in another way.

Although photometric redshifts have been used extensively in clusters of galaxies to compute arc redshifts (e.g. Sand et al. 2005), in galaxy groups the process can be very challenging (see Verdugo et al. 2011) since the arcs are usually near the central galaxy (or galaxies) and skew the results by light contamination. In order to minimize this effect, we subtract the central galaxies in each group. Following McLeod et al. (1998), we analyzed the u , g , r , i , z , and k_s images and fitted a model convolved with a PSF (de Vaucouleurs profiles were fitted to the galaxies with synthetic PSFs). After the galaxy subtraction, we employed polygonal apertures to obtain more accurate flux measurements of the selected arcs. The vertices of the polygons for each arc were determined using the IRAF task *polymark*, and the magnitudes inside these apertures were calculated using the IRAF task *polyphot*. It is important to stress that the computed redshifts (see Table 4) for the arcs have a substantial uncertainty; the worst case is SL2S J08520–0343 (SA63) at 2σ , $\delta z_s \sim 0.16$. In spite of this deterrent, these values are used in our strong lensing models, since these errors do not have a strong influence on the Einstein radius estimations. As we will see in Sect. 4.3, the δz_s has more weight when the lensing source is located close (in redshift) to the lens. We present the output probability distribution function (PDF) for the selected arcs in the left column of Fig. 2.

In the right column we depict the best fit spectral energy distribution obtained from HyperZ where we superimposed the observed data as points with error bars. For SL2S J08591–0345 (SA72), the PDF is rather wide, which likely reflects the complexity of accurately removing the light contamination from the four galaxies that lie in the center of the lensing group (see top panel of Fig. 3). Nonetheless, the spectroscopic value lies within 2σ of the photometric redshift value.

2.2. Spectroscopy

Low resolution spectra for SL2S J08520–0343 (SA63) and SL2S J08591–0345 (SA72) were obtained with the Inamori-Magellan Areal Camera and Spectrograph (IMACS Short-Camera) at the *Magellan* telescope. Observations were carried out on February 19, 2012, and consisted of long-slit spectroscopy of the two systems (two exposures of 23 min for each target). The *grism* 200GR was used (2.037 Å/pix, 5000–9000 Å wavelength range) since we were interested in the lensed source redshifts. Spectra were reduced using standard IRAF procedures consisting of dark correction, flat-fielding, and wavelength calibration (RMS = 0.23). Advanced steps in the data reduction consisted of a two-exposure combination to remove cosmic ray, two-dimensional sky-subtraction, and one-dimensional spectra extraction also using IRAF tasks.

The spectrum obtained for SL2S J08520–0343 (SA63) did not show any clear features (emission or absorption lines) making it impossible to obtain a redshift estimation. On the other hand, the analysis of the spectrum in one of the arcs on SL2S J08591–0345 (SA72) shows some features. We show the long slit configuration for this object, as well as the obtained spectrum in Fig. 3. Some emission lines are clearly visible in the spectrum, like OII λ 3727, OIII, and H β . Considering a starburst galaxy (Kinney et al. 1996) as comparison, we found that the spectrum is consistent with an object at $z = 0.883 \pm 0.001$. Two-dimensional spectra clearly shows OII λ 3727 and H β (see bottom panel of Fig. 3). After applying a Gaussian fitting to those emission lines we obtain a redshift estimation of $z = 0.883 \pm 0.001$.

3. Simulations

In this section we present the characteristics of the simulation used in this work. We explain how the observational properties of our groups (More et al. 2012; Foëx et al. 2013) are used to select the dark matter halo sample that will be used in the next sections to infer the expected Einstein radii in our galaxy groups.

3.1. Simulation characteristics

We used a large N -body simulation called *Multidark* to extract statistics of halo parameters on cosmological scales. The data we use for this paper are publicly available through a database interface first presented by Riebe et al. (2013). Here we summarize the main characteristics of the *Multidark* volume. More details can be found in Prada et al. (2012).

The simulation was run using an adaptive-mesh refinement code called ART. Details about the technical aspects and comparisons with other N -body codes are given in Klypin et al. (2009). The simulations follow the non-linear evolution of a dark matter density field sampled with 2048^3 particles in a volume of $1000 h^{-1} \text{Mpc}^3$. The physical resolution of the simulation is almost constant in time $\sim 7 h^{-1} \text{kpc}$ between redshifts $z = 0-8$. The cosmological parameters in the

simulation are $\Omega_m = 0.27$, $\Omega_\Lambda = 0.73$, $n_s = 0.95$, $h = 0.70$, and $\sigma_8 = 0.82$ for the matter density, dark energy density, slope of the matter fluctuations, the Hubble constant at $z = 0$ in units of $100 \text{ km s}^{-1} \text{Mpc}^{-1}$, and the normalization of the power spectrum, respectively. These cosmological parameters are consistent with the results from WMAP5 and WMAP7 (Komatsu et al. 2009; Jarosik et al. 2011). With these characteristics the mass per simulation particle is $m_p = 8.63 \times 10^9 h^{-1} M_\odot$, which means that group-like halos of masses $\sim 10^{13} h^{-1} M_\odot$ are sampled with at least 1100 particles.

Dark matter halos are identified using a bound-density-maxima algorithm (BDM). The code starts by finding the density maxima at the particles' positions in the simulation volume. For each maxima it finds the radius R_{200} of a sphere containing a mass over-density given by

$$M_{200} = \frac{4\pi}{3} \Delta \rho_{\text{cr}}(z) R_{200}^3, \quad (1)$$

where ρ_{cr} is the critical density of the Universe and $\Delta = 200$ is the desired over-density. This procedure allows for the detection of both halos and subhalos. In our analysis we kept only the halos.

3.2. Concentration estimates

The estimation for the concentration values is done using an analytical property of the NFW profile (see Sect. 4.2) that relates the circular velocity at the virial radius,

$$V_{200} = \left(\frac{GM_{200}}{R_{200}} \right)^{1/2}, \quad (2)$$

with the maximum circular velocity,

$$V_{\text{max}}^2 = \max \left[\frac{GM(<r)}{r} \right]. \quad (3)$$

The V_{max}/V_{200} velocity ratio is used to determine the halo concentration c (the ratio between R_{200} and the scale radii of the NFW profile), using the following relation (Klypin et al. 2001, 2011),

$$\frac{V_{\text{max}}}{V_{200}} = \left(\frac{0.216c}{f(c)} \right)^{1/2}, \quad (4)$$

where $f(c)$ is

$$f(c) = \ln(1+c) - \frac{c}{(1+c)}. \quad (5)$$

For each BDM overdensity the V_{max}/V_{200} ratio is calculated in order to find the concentration c by solving numerically the previous two equations. This method provides a robust estimate of the concentration compared to a radial fitting to the NFW profile, which is strongly dependent on the radial range used for the fit (Klypin et al. 2011; Meneghetti & Rasia 2013). In particular, the NFW functional fit yields a small systematic offset of (5–15)%, and a lower concentration value when compared with the velocity ratio method (Prada et al. 2012).

3.3. Halo sample selection

We used the observational data to define ten redshift bins as given in Table 2 in order to construct a first catalog. We query the *Multidark* database to obtain all the information for halos with

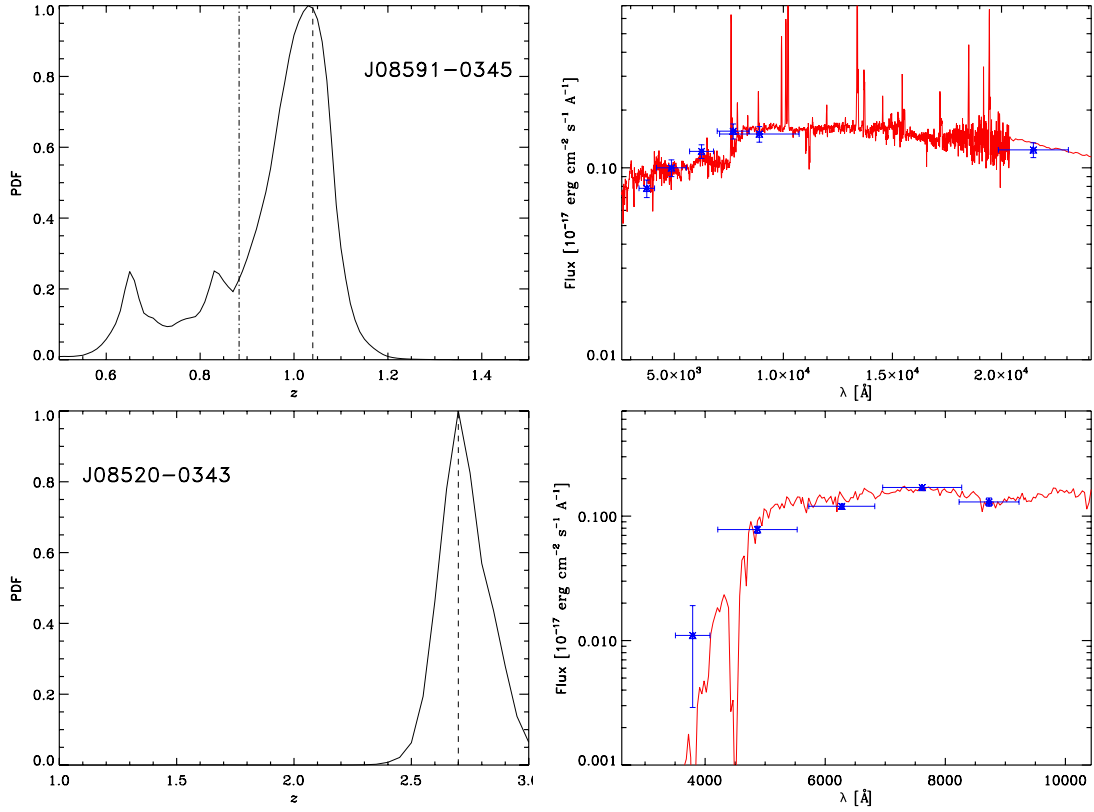


Fig. 2. *Left column:* output photometric redshift PDF for the selected arcs (see text). The dashed vertical lines corresponds to the best redshift estimation. In SL2S J08591-0345 the dash-dotted line corresponds to the spectroscopic value. *Right column:* best fit spectral energy distribution. Points with error bars are the observed CFHTLS broadband magnitudes and k_s from WIRCAM (vertical error bars correspond to photometric errors, horizontal error bars represent the range covered by the filter).

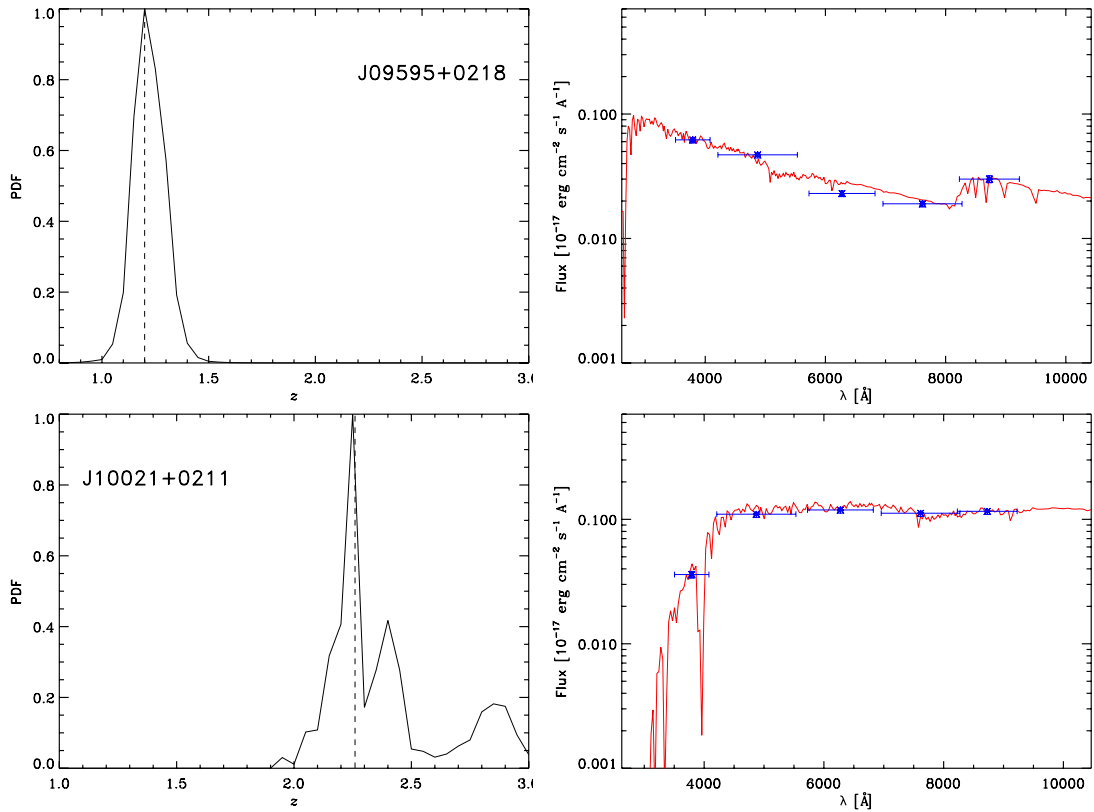


Fig. 2. continued. *Left column:* output photometric redshift PDF for the selected arcs (see text). The dashed vertical lines correspond to the best redshift estimation. *Right column:* best fit spectral energy distribution. Points with error bars are the observed CFHTLS broadband magnitudes (vertical error bars correspond to photometric errors, horizontal error bars represent the range covered by the filter).

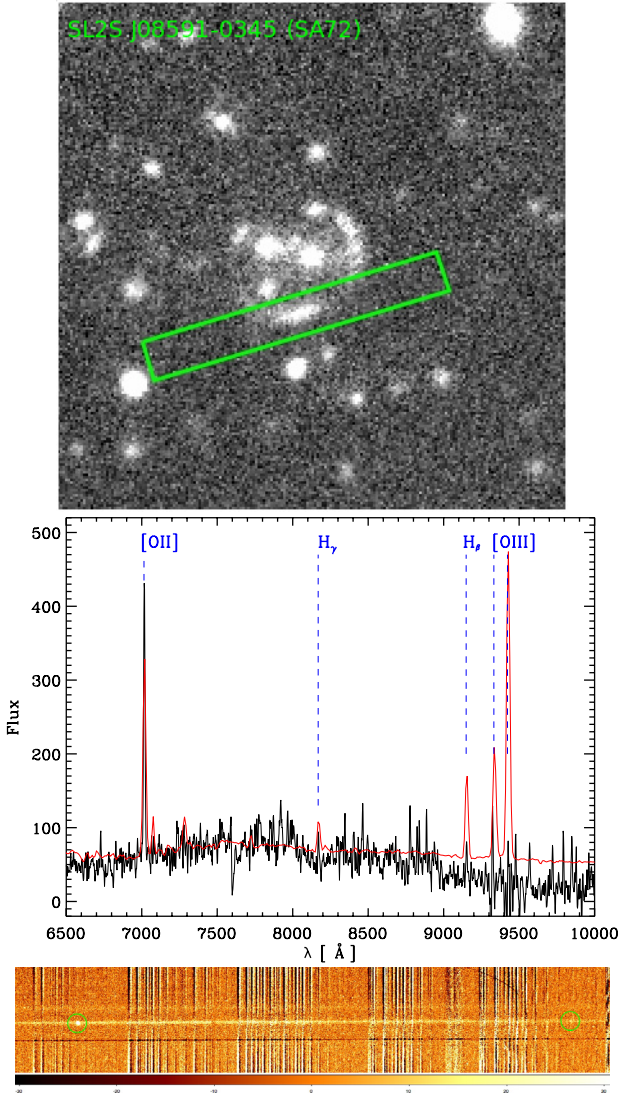


Fig. 3. *Top panel:* CFHTLS g -band image of SL2S J08591–0345 showing the slit position over arc A (see also second row, left panel in Fig. 8). *Middle panel:* observed spectrum of arc A (black continuous line). In red we depict a starburst template from Kinney et al. (1996) shifted at $z = 0.883$. Some emission lines are identified, e.g., [OII] λ 3727, H_γ , and H_β . *Bottom panel:* two-dimensional spectra of the same arc. We note the [OII] λ 3727 and H_β emission lines.

root mean square velocities (V_{rms}) in the range $300 \text{ km s}^{-1} < V_{\text{rms}} < 1000 \text{ km s}^{-1}$. We use the values of V_{rms} as a proxy for the velocity dispersion inferred in the observed lenses (velocities were reported in Foëx et al. 2013). For each redshift we construct a relationship $c - V_{\text{rms}}$ by binning the halos in the catalog in bins of 50 km s^{-1} width. For each velocity bin the average and standard deviation of the concentration is calculated (see top panel of Fig. 4). We note that the concentration falls approximately in the range of $5 \leq c \leq 6$, for such intervals of redshift and velocity.

Since this range in concentration is not considerably large, we decided to test the effect of assuming a fixed value of concentration for a given velocity bin. Thus, we constructed a second halo catalog using all the halos, matching the shape of the observational redshift distribution of the lenses (More et al. 2012; Foëx et al. 2013, see middle panel of Fig. 4). One of the main reasons for constructing this catalog is to have robust statistics from a single Λ CDM simulation volume, covering the mass

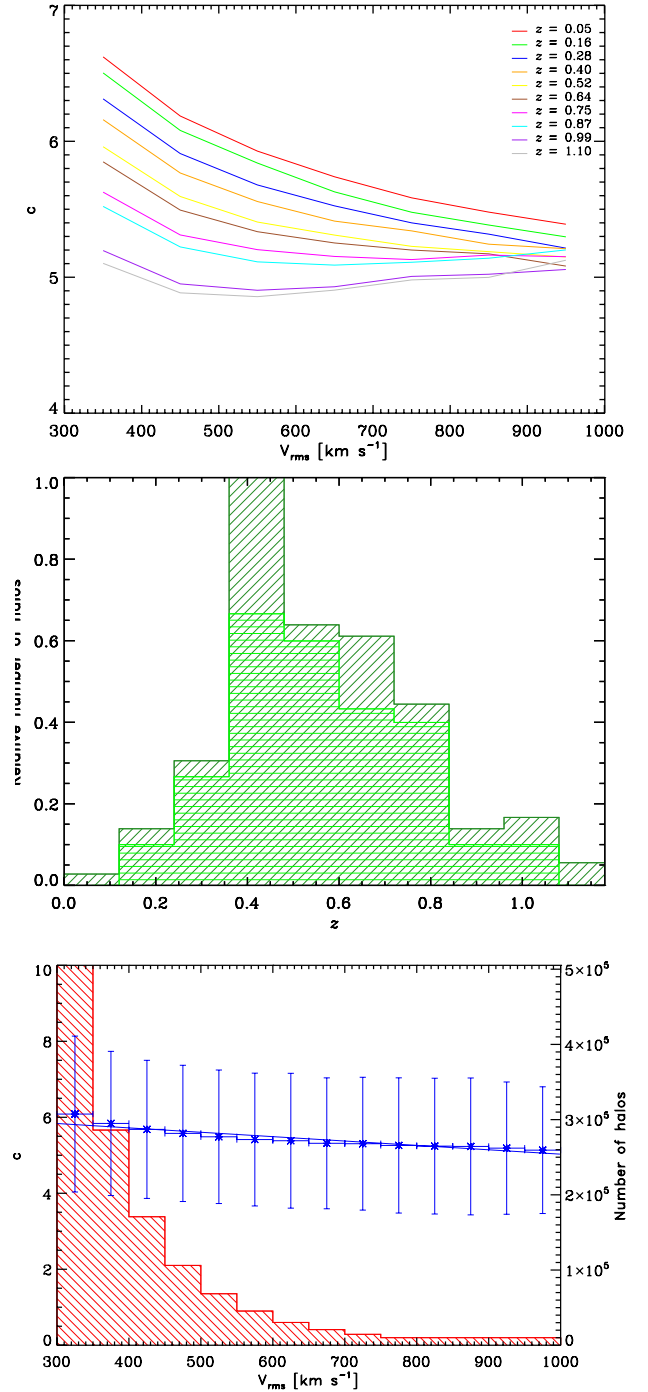


Fig. 4. *Top panel:* $c - V_{\text{rms}}$ relationship for different redshifts calculated from our simulations (see discussion in the text). *Middle panel:* relative number of halos calculated from the number of strong lensing groups observed in each redshift bin (according to Foëx et al. 2013). Dark green histogram with tilted lines shows the results from the whole sample, light green histogram with horizontal lines those for the secure candidates. *Bottom panel:* $c - V_{\text{rms}}$ obtained mixing, in each velocity bin, halos at different redshifts, where the relative number of halos at each redshift are equal to the observed ones, i.e., given by the fraction depicted in the middle panel. The histogram in red show the total number of halos in each velocity bin.

range from groups up to clusters. Another motivation is that we will stack these objects using their velocity dispersion (Foëx et al., in prep.), thus we need to know if there is any systemic

difference in the estimates of θ_E when using different catalogs. We proceed as follows: for each redshift bin we count the number of observed lenses and multiply it by 10^5 , then we randomly select the same number of halos from the simulation. This allows us to have a simulated sample 10^5 times larger than the observed one, with the same redshift distribution. From this new catalog we construct a new $c - V_{\text{rms}}$ relationship in the same way as described above. In the bottom panel of Fig. 4 we show the $c - V_{\text{rms}}$ relation, using halos at different redshifts for each velocity bin, and using the same relative number of halos for each redshift as the ones that were observed. Taking into account the errors in concentration, our mimic sample has $5 \lesssim c \lesssim 6$ in the range $300 \text{ km s}^{-1} < V_{\text{rms}} < 1000 \text{ km s}^{-1}$. This is consistent with the results depicted in the top panel of Fig. 4. Our values are in agreement with those reported by Faltenbacher & Mathews (2007), who investigate the concentration-velocity dispersion relation in galaxy groups using cold dark matter N -body simulations.

4. Einstein radius

We calculated the Einstein radius in three different ways using 1) weak lensing, following Foëx et al. (2013) and assuming a SIS model; 2) strong lensing, considering a modified version of the method in Broadhurst & Barkana (2008) together with the $c - V_{\text{rms}}$ relation obtained in the previous section; and 3) strong lensing modeling of eleven SL2S groups with HST images. The fitting is done with the LENSTOOL⁵ ray-tracing code (Kneib 1993), which uses a Bayesian Markov chain Monte Carlo (MCMC) method to search for the most likely parameters in the lens modeling (Jullo et al. 2007).

4.1. Weak lensing method

The methodology used in this work follows Bardeau et al. (2007), also applied by Limousin et al. (2009) on the first SL2S group sample. A full description of the procedure can be found in Foëx et al. (2012), and of its applications in the last SL2S sample in Foëx et al. (2013). Here we outline the method briefly.

To detect and select the lensed background galaxies, we used SExtractor (Bertin & Arnouts 1996) on the i -band images, which computes the best seeing among all the available filters. Considering object size, its magnitude, and central flux, we perform a first selection to build separate catalogs for stars and galaxies. The shape parameters of each object are estimated using the Im2shape software (Bridle et al. 2002) in i -band images. Stars are used to derive the PSF field at each galaxy position, simply by taking the average shape of the five nearest stars (the catalog of stars being first cleaned to keep only objects with similar shapes). This PSF field is convolved by Im2shape to a given model of the galaxy shapes, in our case a simple elliptical Gaussian (see Foëx et al. 2012, 2013). Exploring the space of free parameters with a MCMC sampler, the code finds the best model that minimizes the residuals between the PSF-distorted model of the galaxy (including noise and background level, treated as well as free parameters in the modeling) to its observed shape. For each galaxy, Im2shape returns an estimate of its shape parameters along with robust statistical uncertainties.

The next step of the analysis consists in selecting the lensed galaxies to estimate the shear signal. Here we used two selections. First, we kept galaxies with $21 < m_r < m_{\text{comp}} + 0.5$, i.e.,

we removed the brightest objects, which are most likely foreground field galaxies. We also removed the faintest ones as they are too faint to derive reliable shape parameters. By staying close to the completeness magnitude, m_{comp} , of the observed galaxy distribution, we also keep a certain control over the redshift distribution, which is required to derive the lensing strength. To remove most of the group and cluster members, we also used the classical red sequence selection: starting from the color of the central galaxy, we defined a region within the color-magnitude space where the red elliptical galaxies of the groups and clusters are located. Only galaxies outside this region were included in the catalog of the lensed galaxies.

To estimate masses from the weak-lensing signal, we computed shear profiles using the shape of the lensed galaxies. They were built with logarithmic bins centered around the lens galaxy. We fitted them with the SIS mass model within a fixed physical aperture, from 100 kpc to 2 Mpc with a classical χ^2 -minimization. To propagate the uncertainties on the shear profiles $\sigma_\gamma(r)$ (intrinsic ellipticity of lensed galaxies and measurement errors on their shape parameters), we generated 1000 Monte Carlo profiles, drawn assuming that each point of the observed shear profile $\gamma(r)$ follows a normal distribution $\mathcal{N}(\gamma(r), \sigma_\gamma(r))$. The distribution of the best-fit parameters is chosen to characterize the model that best describes our observations and the associated errors (68% confidence interval around the mode of the distribution). The shear signal was translated into physical units through the lensing strength $D_{\text{LS}}/D_{\text{OS}}$, which was derived from the photometric redshift distributions of the CFHTLS Deep fields provided by Pello. The same selection criteria (magnitude limits and color-magnitude) were applied to these catalogs in order to match the redshift distribution of our lensed galaxies. In doing so, we also accounted for the dilution of the shear signal by the residual foreground galaxies (see Foëx et al. 2013, for more details).

Given the SIS velocity dispersion obtained from weak lensing, we calculate the Einstein radius through the expression

$$\theta_{E,I} = 4\pi \frac{\sigma_{\text{WL}}^2}{c^2} \frac{D_{\text{LS}}}{D_{\text{OS}}}, \quad (6)$$

where σ_{WL} is the line-of-sight velocity dispersion calculated from weak lensing data, and D_{LS} and D_{OS} are the angular diameter distances between the lens and the source and the observer and the source, respectively. These distances are estimated using the most likely redshift of the source (Turner et al. 1984), with an upper limit given by Eq. (2) in More et al. (2011). In the top-left panel of Fig. 5 we show the ratio of $\theta_{E,I}$ calculated through Eq. (6) and their respective R_A values. The points are uniformly distributed on both sides of $R_A/\theta_{E,I} = 1$, with a mean of 1.02 and a standard deviation of 0.56 (indicating a large scatter). We also note that groups with multi-components or with a high degree of elongation (see Sect. 5) are also uniformly distributed in the plot. Groups with small values of $\theta_{E,I}$ with respect to R_A are always irregular. And likewise, those with extremely high $\theta_{E,I}$ values are also not regular groups. In the figure we highlight with different symbols those groups with strong lensing models (see Sect. 4.3) and those with giant arcs (with a length-to-width ratio larger than 10, according to More et al. 2012). We want to point out that the errors in R_A (measured directly from the images) are small compared to the errors in $\theta_{E,I}$. The former are around two pixels, which is roughly $0.4''$, thus, unless otherwise specified, we will omit the error bars of R_A in the plots.

To further investigate quantitatively this effect, we use the task *ellipse* in IRAF to fit ellipses to the luminosity maps of the

⁵ This software is publicly available at: <http://projets.lam.fr/projects/lenstool/wiki>

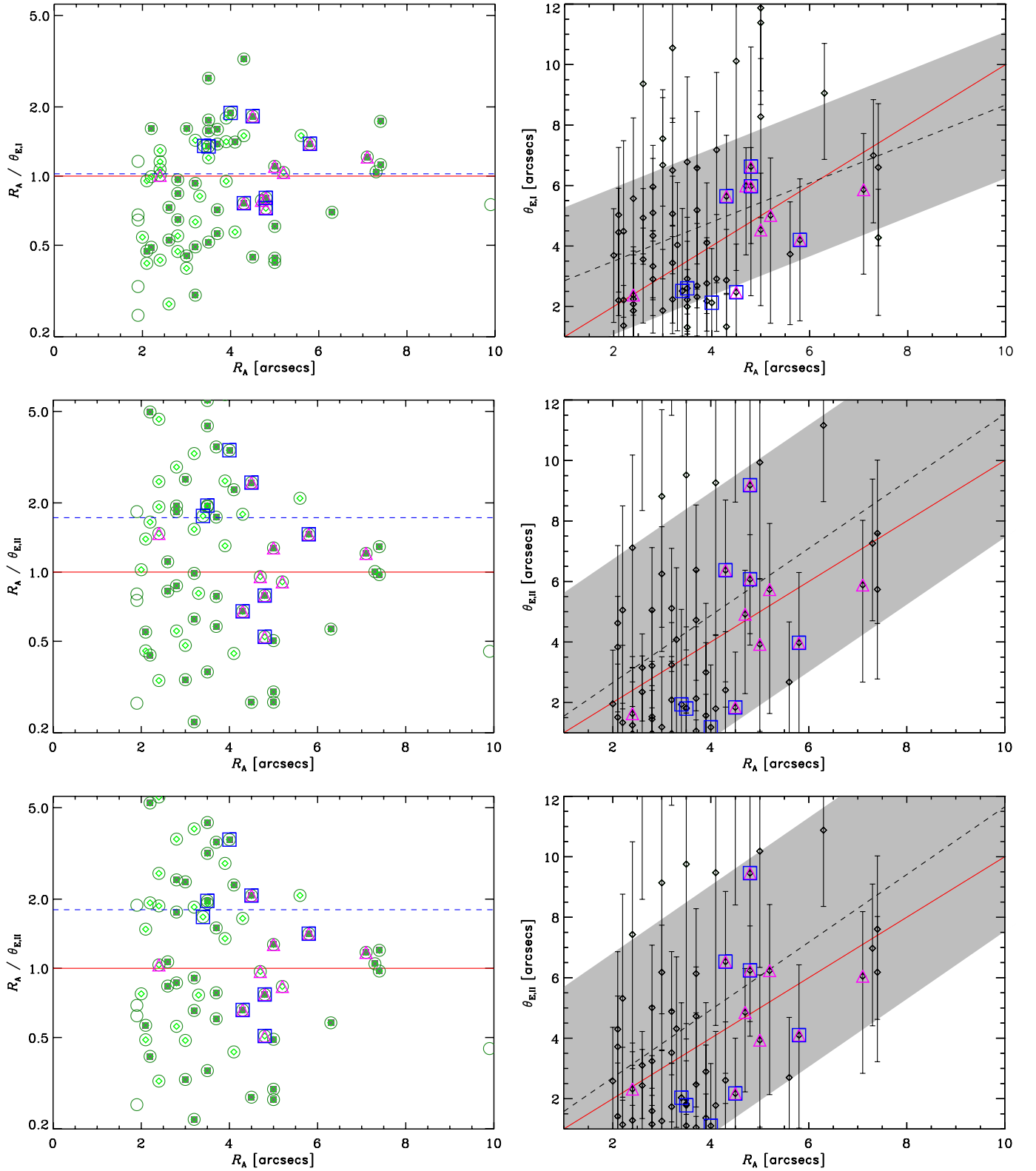


Fig. 5. *Left column:* R_A/θ_E vs. R_A for the two first methods discussed in this work. *Top panel:* $R_A/\theta_{E,I}$ vs. R_A . Green circles depict the secure group candidates (Foëx et al. 2013), green diamonds those with $2.0'' \leq R_A \leq 8.0''$. Green filled squares are groups with multi-component features or very elongated light contours (see Sect. 5). The blue dashed line depicts the mean $R_A/\theta_{E,I}$, the red continuous line shows the one-to-one relation, blue squares are groups with giant arcs (see Sect. 4.1), and magenta triangles represent those groups with strong lensing models (see Sect. 4.3). The error bars were omitted for clarity. *Middle panel:* $R_A/\theta_{E,II}$ vs. R_A using the catalog constructed using the V_{rms} as proxy for the velocity dispersion measured in the observed lenses. *Bottom panel:* $R_A/\theta_{E,III}$ vs. R_A using the catalog built to match the shape of the observational redshift distribution of the lenses. *Right column:* θ_E vs. R_A . Black triangles show all the groups (regular or irregular) that satisfy $2.0'' \leq R_A \leq 8.0''$. The black dashed line shows the fit to the data, with the 1σ -error depicted as a gray shaded region. As before, the red continuous line shows the one-to-one relation.

groups (see Foëx et al. 2013) and to obtain the ellipticity. For 14 groups it was not possible to obtain a fit because they present either multi-components or a high degree of elongation. In Fig. 6 we plot the ellipticity as a function of the ratio $R_A/\theta_{E,I}$. This result is consistent with Fig. 5 (top-left panel), i.e. elongated groups ($\epsilon > 0.3$) are evenly distributed in the $R_A/\theta_{E,I}$ axis. We note that two groups with giant arcs have $\epsilon > 0.3$, and three more do not appear in the plot (because they belong to the groups for which it was not possible to obtain a fit).

In the top-right panel of Fig. 5 we depicted $\theta_{E,I}$ vs. R_A for those groups with $2.0'' \leq R_A \leq 8.0''$. In Table 3 we show the results for our fit. We found a low correlation between both variables. It is possible to show that, if we eliminate extreme values (probably outliers) in the ratio $R_A/\theta_{E,I}$, the correlation coefficient and the significance improve. For example, with a $0.5 \leq R_A/\theta_{E,I} \leq 2.0$ cutoff (following Puchwein & Hilbert 2009, who showed that around these values in the radial distribution of tangential arcs is where, approximately, the minimum and maximum in the cross-sections occurs), we found $R = 0.6$, and $P = 1 \times 10^{-5}$. However the outliers were not eliminated, keeping the sample as it is. In Sect. 5 we will explain the reason for such low correlation. We note that some groups with giant arcs and strong lensing models are far from the one-to-one correlation.

4.2. Analytically from a NFW profile

The NFW universal density profile, predicted in cosmological N -body simulations, has a two-parameter functional form (Navarro et al. 1997),

$$\rho(r) = \frac{\rho_{cr}(z)\delta_c(z)}{(r/r_s)(1+r/r_s)^2}, \quad (7)$$

where δ_c is a characteristic density contrast, and r_s is a characteristic inner radius.

Integrating Eq. (7) and using Eq. (1), it is straightforward to show that the concentration c is related to δ_c by

$$\delta_c = \frac{200}{3} \frac{c^3}{[\ln(1+c) - c/(1+c)]}. \quad (8)$$

Then, for a given halo redshift, mass M_{200} , and concentration c , we can specify the parameters of the NFW model.

We now consider a spherical NFW density profile acting like a lens. The analytical solutions for this lens were given by Bartelmann (1996), and have been studied by different authors (Wright & Brainerd 2000; Golse & Kneib 2002; Meneghetti et al. 2003). The positions of the source and the image are related through the equation

$$\boldsymbol{\beta} = \boldsymbol{\theta} - \nabla\varphi(\boldsymbol{\theta}) = \boldsymbol{\theta} - \boldsymbol{\alpha}(\boldsymbol{\theta}), \quad (9)$$

where $\boldsymbol{\theta}$ and $\boldsymbol{\beta}$ are the angular position in the image and in the source planes, respectively; $\boldsymbol{\alpha}$ is the reduced deflection angle between the image and the source; and φ is the two-dimensional lens potential. We introduce the dimensionless radial coordinate $x = \theta/\theta_s$, where $\theta_s = r_s/D_{OL}$, and D_{OL} is the angular diameter distance between the observer and the lens. In the case of an axially symmetric lens, the relation becomes simpler, as the position vector can be replaced by its norm.

The reduced deflection angle then becomes (Golse & Kneib 2002)

$$\alpha(x) = \left(\frac{4\rho_{cr}\delta_c r_s}{\Sigma_{cr}} \right) \frac{\theta}{x^2} g(x) \hat{e}_x, \quad (10)$$

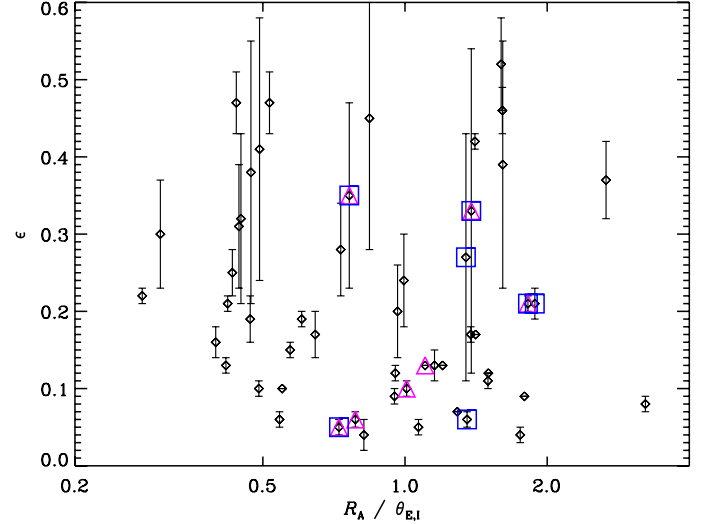


Fig. 6. Ellipticity as a function of the $R_A/\theta_{E,I}$ ratio. Blue squares are groups with giant arcs (see Sect. 4.1), and magenta triangles are those groups with strong lensing models (see Sect. 4.3).

where $g(x)$ is a function related to the surface density inside the dimensionless radius x , and is given by (Bartelmann 1996):

$$g(x) = \begin{cases} \ln \frac{x}{2} + \frac{2}{\sqrt{1-x^2}} \operatorname{arctanh} \sqrt{\frac{1-x}{1+x}} & \text{if } x < 1, \\ 1 + \ln \frac{1}{2} & \text{if } x = 1, \\ \ln \frac{x}{2} + \frac{2}{\sqrt{x^2-1}} \operatorname{arctan} \sqrt{\frac{x-1}{x+1}} & \text{if } x > 1. \end{cases} \quad (11)$$

The quantity $\Sigma_{crit} = (c^2/4\pi G)(D_{OS}/D_{OL}D_{LS})$ is the critical surface mass density for lensing.

If we express the deflection angle in terms of $\bar{\kappa} = (4\Sigma_{cr}\rho_{cr}\delta_c r_s g(x)/x^2)$, that is, the projected surface density Σ measured in units of the critical surface mass density, or, in other words, the mean enclosed surface density, then Eq. (10) can be expressed as:

$$\alpha(x) = \bar{\kappa}\theta \hat{e}_x. \quad (12)$$

Hence, the lens Eq. (9) can be written as:

$$\boldsymbol{\beta} = \boldsymbol{\theta}(1 - \bar{\kappa}). \quad (13)$$

Following Broadhurst & Barkana (2008), we define the Einstein radius as the projected radius where the mean enclosed surface density is equal to 1. Then, for a given halo concentration parameter c , mass, halo redshift z_l , and source redshift z_s , the Einstein radius is calculated by solving the equation

$$\theta_{E,II} = \left[\frac{4\rho_{cr}\delta_c r_s}{\Sigma_{cr}} \theta_s^2 g(\theta_{E,I}/\theta_s) \right]^{1/2}. \quad (14)$$

Thus, $\theta_{E,II}$ can be derived numerically using the $c - V_{rms}$ relationship obtained in Sect. 3. Since we can relate V_{rms} to the σ_{WL} value obtained previously for each group (Sect. 4.1). Inasmuch as M_{200} is an unknown variable, we assume it is given by the mass of the isothermal profile at the projected radius R_{200} , then

$$M_{200} = \frac{\pi r_{200} \sigma_{WL}^2}{G}. \quad (15)$$

This normalization is arbitrary, but R_{200} is usually taken as a measure of the cluster's virial radius. Although there is evidence from numerical simulations that the hydrostatic assumption is

valid probably within r_{500} , the kinetic pressure to thermal gas pressure ratio changes less than $\approx 15\%$ between both radii (see Fig. 3 in [Evrard et al. 1996](#)). Thus, we will keep the former radius. Therefore, using Eqs. (1) and (15), the scale radius in Eq. (14) is given by

$$r_s = \left[\frac{3}{4G\rho_{\text{cr}}\Delta} \right]^{1/2} \frac{\sigma_{\text{WL}}}{c}. \quad (16)$$

No doubt this is an oversimplification of the problem, since we are taking the same M_{200} for both profiles, the NFW and the isothermal. This is not a good assumption, and as we will see (Sect. 5) it could skew the results, but it is useful to shed some light as a first-order approximation. In Fig. 5 (left column, middle and bottom panels) we show the ratio between $\theta_{\text{E,II}}$, calculated through Eq. (14), and the respective R_A for both catalogs discussed in Sect. 3 (the first one constructed from the V_{rms} as proxy for the velocity dispersion inferred in the observed lenses and the second one built to match the shape of the observational redshift distribution of the lenses). For the first case, we obtained a mean of 1.7 and a standard deviation equal to 1.6, and for the second one we obtained a mean of 1.8 with a standard deviation of 1.8, indicating a slightly larger scatter compared with the first method.

The middle- and bottom-right panels of Fig. 5 show $\theta_{\text{E,II}}$ vs. R_A for the groups with $2.0'' \leq R_A \leq 8.0''$. As in the first method, we found a low correlation between both variables (see Table 3). As before, if we eliminate the outliers using a $0.5 \leq R_A/\theta_{\text{E,I}} \leq 2.0$ cutoff, the results improve, and we obtain $R = 0.7$ ($P = 2 \times 10^{-7}$) and $R = 0.7$ ($P = 1 \times 10^{-6}$) for the first and second catalog, respectively. We note again that some groups with giant arcs and strong lensing models are not close to the one-to-one correlation.

Finally, in Fig. 7 we plotted $\theta_{\text{E,II}}$ vs. $\theta_{\text{E,I}}$ to look for systematic differences between both estimates. It is clear that for larger values of $\theta_{\text{E,I}}$ there is a slight overestimation of $\theta_{\text{E,II}}$. This can be explained by the large velocity dispersion calculated for the groups: the halo associated with the NFW profile needs to be more massive in order to enclose the same mass at R_{200} as the one calculated from weak lensing (WL). Similarly, the opposite is true for small values of $\theta_{\text{E,I}}$. This trend explains the change in the slopes in the correlations obtained for $\theta_{\text{E,I}} - R_A$ and $\theta_{\text{E,II}} - R_A$, which is also clear in the three right panels of Fig. 5.

4.3. The ray-tracing code method

In this section, the comparison between R_A and θ_E is done using strong lensing models for 11 groups in the SARCS sample. The subsample consist of: SA22 (SL2SJ02140–0532), SA39 (SL2SJ02215–0647), SA50 (SL2SJ02254–0737), SA66 (SL2SJ08544–0121), SA112 (SL2SJ14300+5546), SA123 (SL2SJ22133+0048), SA127 (SL2SJ22214–0053), SA72 (SL2SJ08591–0345), SA63 (SL2SJ08520–0343), SA80 (SL2SJ09595+0218), and SA83 (SL2SJ10021+0211). The first seven groups were previously modeled and the results were presented in [Limousin et al. \(2009\)](#). The four remaining groups were selected because they have HST images, an important asset in lensing modeling. This kind of data allows us to resolve the features in the lensed images and to improve the constraints in the models. Other reasons for their selection are that they have different characteristics (luminosity contours, as well as number of galaxies in the center of the lens), different redshifts, and different lensing configurations (two of them, SA63 and SA80, without previously reported models). Figure 8 (first row)

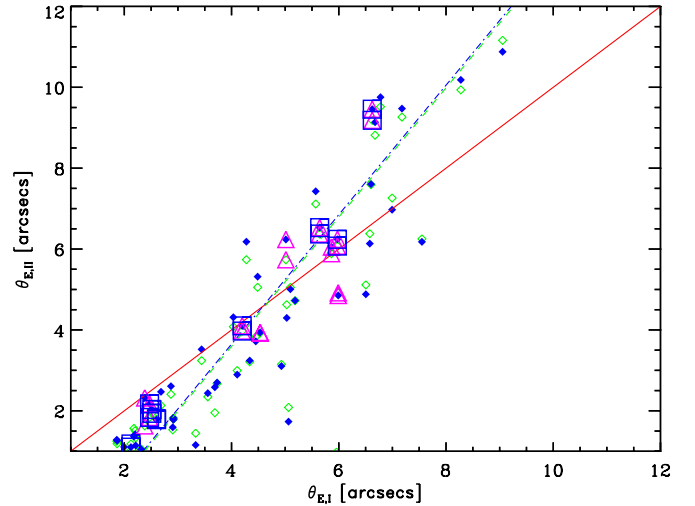


Fig. 7. $\theta_{\text{E,II}}$ vs. $\theta_{\text{E,I}}$. Green diamonds depict the objects used to construct the plots shown in the right column (*top and middle panels*) of Fig. 5. Green dashed line shows the fit to the data. Similarly, the blue filled diamonds are the objects associated with the correlations shown in the right column (*top and bottom panels*) of the same figure. Blue dash-dotted line shows the fit to the data. Blue squares are groups with giant arcs (see Sect. 4.1), magenta triangles are those groups with strong lensing model (see Sect. 4.3), and the red continuous line shows the one-to-one relation. The error bars are omitted for clarity.

shows the color composite CFHT images for these four lensing groups, SL2SJ08591–0345 (SA72) is the most complex, but it has the most constraints on the lens.

For the four groups quoted above, we apply a simple strong lensing mass modeling in order to estimate the Einstein radius using the LENSTOOL code ([Kneib 1993](#); [Jullo et al. 2007](#)). Since galaxy groups are generally not well suited to performing accurate lensing models because of the lack of observational constraints (see the discussion in [Limousin et al. 2009](#)), we use a singular isothermal ellipsoid (SIE), which has only five free parameters: the position (x and y), ellipticity (e), position angle (PA), and Einstein radius. All the optimizations were done in the image plane. We want to stress that constructing detailed models for the lens is far from the scope of the present work, and the current data do not allow us to undertake such an analysis. To test more complex models more spectroscopic data is required (we are currently in a campaign to obtain this data for the arcs and galaxies in some of the SL2S groups).

SL2SJ08591–0345 (SA72) at $z_1 = 0.642 \pm 0.001$ is a confirmed galaxy group (see [Muñoz et al. 2013](#)) with three bright galaxies and two smaller ones in the center of the lens. The multiple images of this exotic lens draw an oval contour around the deflector (see top-left panel of Fig. 8). The object was modeled by [Orban de Xivry & Marshall \(2009\)](#) as a four-component lens, showing the complexity of this compact group. In addition, the object was presented in the first sample of groups by [Limousin et al. \(2009\)](#), and later cataloged in the SARCS sample ([More et al. 2012](#)). Assuming that all the lensing features come from one single source at $z_s = 0.883 \pm 0.001$ ($z_{\text{phot}} = 1.04^{+0.04}_{-0.08}$), we constructed our model leaving all parameters free. Although our best model shows a large χ^2 (see Table 4), it is important to note that the complexity of a five-galaxy lens in the center of the group would require us to assume a more elaborate model than a simple SIE for its mass distribution.

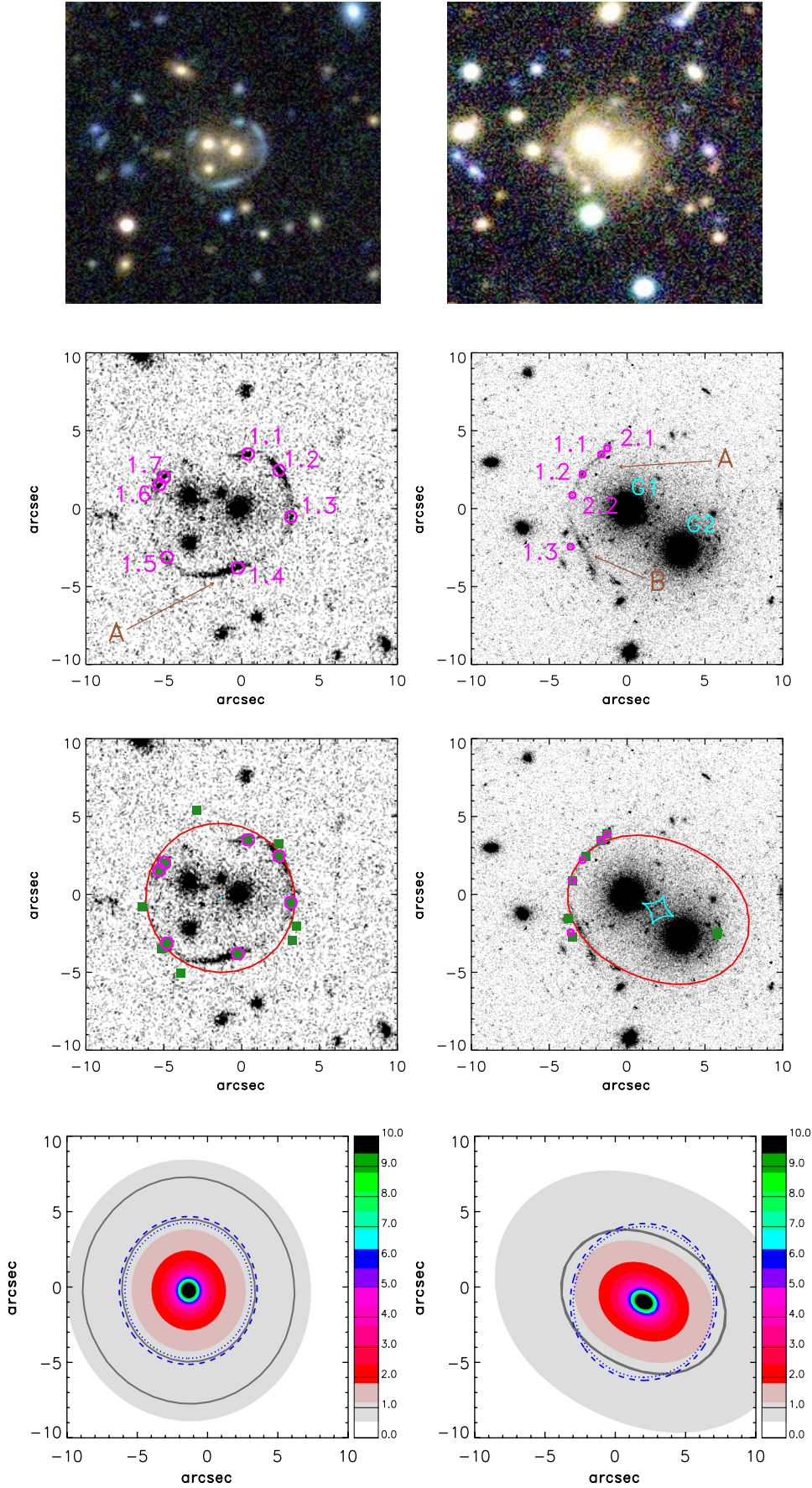


Fig. 8. SL2S J08591–0345 (SA72) and SL2S J08520–0343 (SA63), *left and right columns*, respectively. *First row*: composite CFHTLS *g*, *r*, *i* color images ($30'' \times 30''$). *Second row*: identification of the arcs and their substructure in each lens (see Sect. 4.3). *Third row*: critical (red) and caustic lines (cyan) for the strong lensing models. The magenta circles show the measured positions of the image (input data for the model) and the green filled squares are the model-predicted image positions. *Fourth row*: convergence maps. For a source located at the respective redshifts, z_s , given in Table 4. Dark gray lines show $\kappa = 1$ for sources located in $(z_{\text{phot}} - \delta z_{\text{phot}}, z_{\text{phot}} + \delta z_{\text{phot}})$. Dotted blue lines and dashed blue lines depict the values for R_A , and $\theta_{E,III}$, respectively.

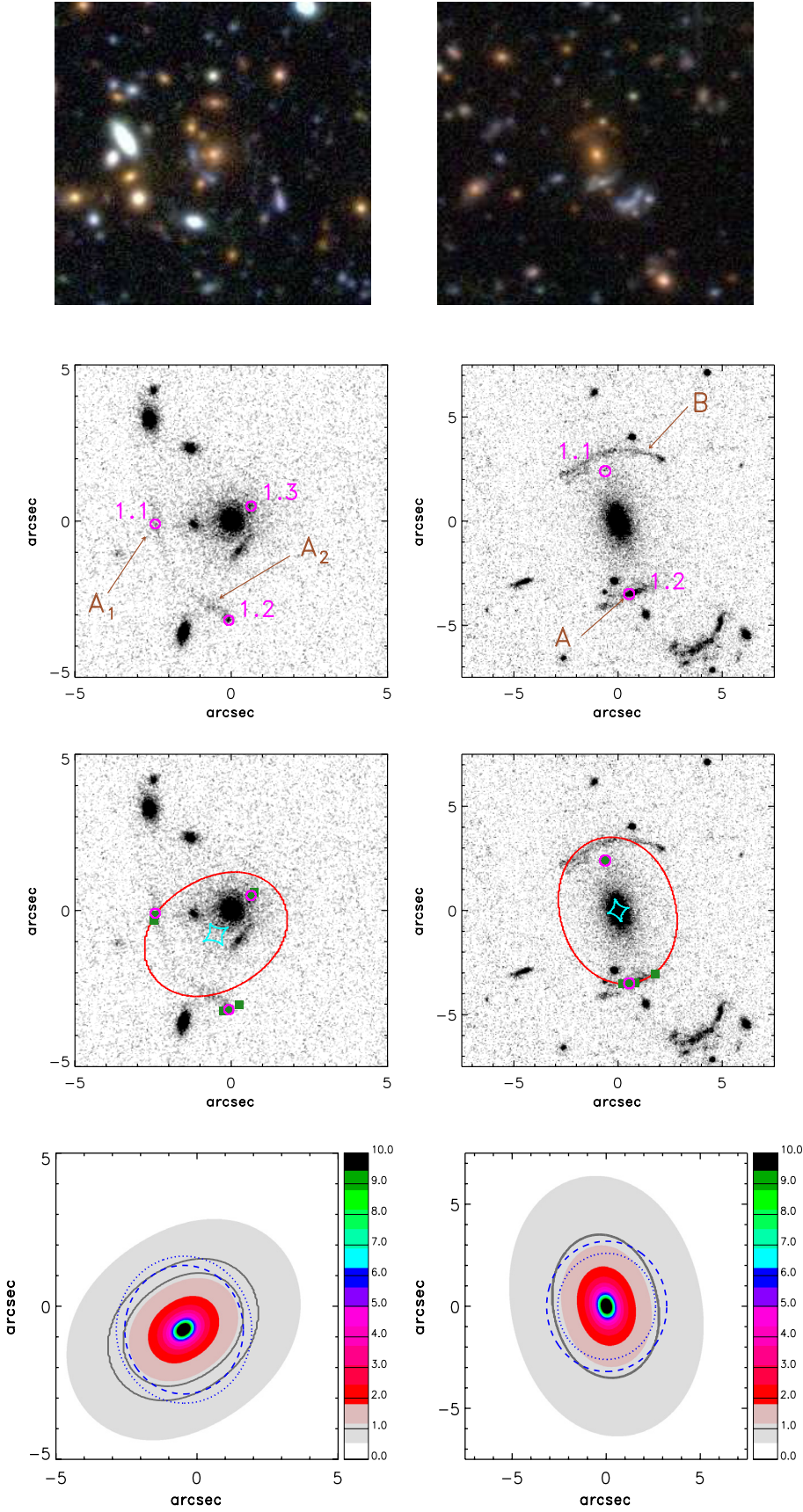


Fig. 8. continued. SL2SJ09595+0218 (SA80) and SL2SJ10021+0211 (SA83), *left and right columns*, respectively. *First row*: composite CFHTLS *g*, *r*, *i* color images ($30'' \times 30''$). *Second row*: identification of the arcs and their substructure in each lens (see Sect. 4.3). *Third row*: critical (red) and caustic lines (cyan) for the strong lensing models. The magenta circles show the measured positions of the image (input data for the model) and the green filled squares the model-predicted image positions. *Fourth row*: convergence maps. For a source located at the respective redshifts, z_s , given in Table 4. Dark gray lines shows $\kappa = 1$ for sources located in $(z_{\text{phot}} - \delta z_{\text{phot}}, z_{\text{phot}} + \delta z_{\text{phot}})$. Dotted blue lines and dashed blue lines depict the values for R_A , and $\theta_{\text{E,III}}$, respectively.

SL2SJ08520–0343 (SA63) is populated by two galaxies in the center (G1 and G2) and displays several arc features, with those labeled arc A and B being the most prominent (see

second row, right panel of Fig. 8). In the ground-based image, these arcs seem to belong to the same source, i.e., forming a system. However on the HST-ACS image this association is not

so clear since arc B is brighter and straighter than arc A. Thus, to construct our model we assume arcs A and B are different systems and we used only arc A to perform the optimization. Given the resolution of the HST-ACS image, we can conjugate two points on arc A, increasing the number of constraints to six (e.g., [Limousin et al. 2009](#); [Verdugo et al. 2011](#)). Our model predicts a demagnified counter-image for arc A (see third row, right panel of Fig. 8) near galaxy G2 that can be associated with some arc-like features close to this galaxy. The results of our best fits are summarized in Table 4.

SL2S J09595+0218 (SA80) shows a configuration with two bright arcs on one side of the deflector and a very demagnified image on the other side of the deflector (see second row, left panel of the continuation of Fig. 8). The photometric redshift sets the arc at $z \sim 1.2$. With only three multiple images forming the system, we have only four observational constraints. First, we set $x = 0$ and $y = 0$, leading to an elliptical mass distribution model with only three free parameters, namely, the ellipticity e , the position angle PA, and the Einstein radius. Given the impossibility of obtaining a good fit in these conditions, we proceeded in an alternative way. We set the ellipticity and the position angle with fixed values $e = 0.30$, and $PA = 30^\circ$, leaving x and y free. In the third row and left panel of the continuation of Fig. 8 we show the predicted positions of our best model, as well as the observed positions.

SL2S J10021+0211 (SA83) was discovered in the COSMOS survey ([Faure et al. 2008, 2011](#)). It has two arcs surrounding the central galaxy of the group, one long red arc (showing substructure) situated at the north (arc B) and another blue and more compact one (arc A) at the south (see second row, right panel of the continuation of Fig. 8). We were able to obtain the photometric redshift only for the blue arc, $z \sim 1$. Since arc A does not show surface brightness peaks that can be conjugated as different multiple image systems, there are not enough constraints to try even a simple model. However, using the position of a possible counter-image located below arc B (see second row, right panel of the continuation of Fig. 8), we have two constraints, which are enough to probe the Einstein radius. Thus, following [Faure et al. \(2008\)](#) we perform the optimization fixing the center of the lens as the center of the bright galaxy, $e = 0.25$, and $PA = 105^\circ$ (see Table 1). Our model (see third row, right panel of the continuation of Fig. 8) predicts that the counter-image of arc A will be very demagnified, which explains why it is not observed in the CFHT images. Our value of $\theta_{E,III}$ shown in Table 4 agrees with the value $\theta_E = 3.14''$ found by [Faure et al. \(2008\)](#), although our z_l and z_s values (obtained using a different methodology) are slightly different to those reported in that work.

The bottom panels of Fig. 8 presents the convergence map for each strong lensing model, considering a source located at the respective redshift, z_s , given in Table 4. Dark gray lines depict the convergence locus, $\kappa = 1$, considering two different sources situated at $z_{\text{phot}} \pm \delta z_{\text{phot}}$. We note that such values are consistent with R_A (dotted blue line) and $\theta_{E,III}$ obtained from the strong lensing model (dashed blue line). In the case of *SL2S J08591-0345 (SA72)*, the large difference between the extreme values of z_{phot} arises from the source and lens proximity in redshift.

Finally, in Fig. 9 we show $\theta_{E,III}$ vs. R_A for the eleven groups presented in this section. We found a good agreement between both values, with $\theta_{E,III} = (0.4 \pm 1.5) + (0.9 \pm 0.3)R_A$, a Spearman's rank correlation coefficient $R = 0.6$, and a significance $P = 6 \times 10^{-2}$. The two groups with slightly extreme values below the correlation are SA123 (*SL2S J22133+0048*) and SA39 (*SL2S J02215-0647*). This might be related to the multiple

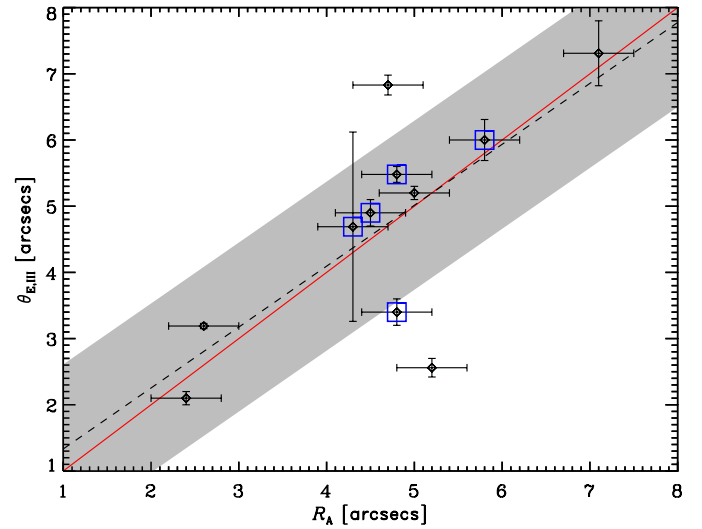


Fig. 9. $\theta_{E,III}$ vs. R_A for those groups with strong lensing models. The black dashed line shows the fit to the data, with the 1σ -error depicted as a gray shaded region. Blue squares are groups with giant arcs (see Sect. 4.1), and the red continuous line shows the one-to-one relation.

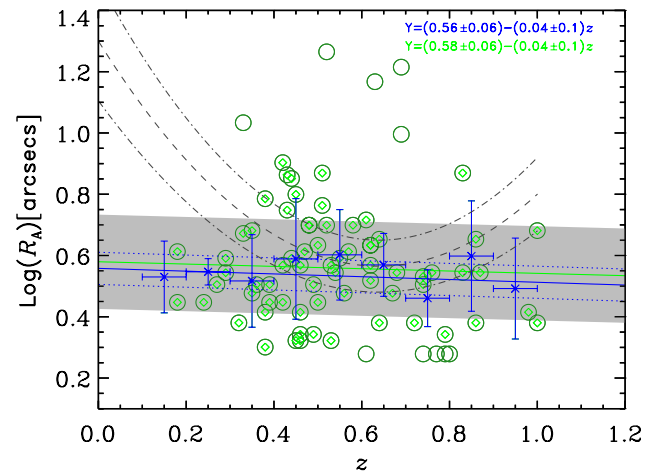


Fig. 10. R_A as a function of the redshift. Green circles depict the secure lens candidates ([Foëx et al. 2013](#)), and green diamonds those with $2.0'' \leq R_A \leq 8.0''$. Blue asterisks with error bars highlight the correlation between R_A and z after binning the data (green diamonds). The blue continuous line shows the fit to the binned data, with 1σ -error depicted as a dotted blue line. The green continuous line shows the fit to the green diamonds, with the 1σ -error depicted as a gray shaded region. The dashed line is a second-order polynomial function from [Zitrin et al. \(2012\)](#), assuming an error of 15% (dot-dashed line).

components present in their luminosity maps (see Sect. 5). On the other hand, the group with the value over the correlation, SA127 (*SL2S J22214-0053*), is a group with a high degree of elongation. We also note that the groups with giant arcs, except SA123 (*SL2S J22133+0048*), nearly follow the one-to-one relation.

5. Discussion

5.1. R_A vs. θ_E

In Sect. 4 we found a low correlation between $\theta_{E,I}$ and R_A , with a large scatter. We found $\theta_{E,I} = (2.2 \pm 0.9) + (0.7 \pm 0.2)R_A$ with a

correlation coefficient $R = 0.33$, and a significance $P = 6 \times 10^{-3}$. It is important to note that the analysis was done in the whole sample (with $2.0'' \leq R_A \leq 8.0''$), without distinction between regular and irregular groups. We also note that our sample, as we commented in the introduction, does not only include giant arcs. This introduces scatter in the correlation, but even in a sample with only giant arcs, there are some groups far from the one-to-one correlation (see right column of Fig. 5). This is related to another factor that we need to consider in this comparison between $\theta_{E,I}$ and R_A , namely that we are using information at large scale (weak lensing velocity) in a lower-scale regime (strong lensing).

Gavazzi (2005) shows that departures between lensing and true mass tend to vanish at large scale. Moreover, the asphericity has a lower effect on weak lensing and X-ray-based mass estimates (see Fig. 6 in Gavazzi 2005) than in the case of strong lensing. In this context, as we have measured σ_{WL} from weak lensing data (i.e. large scale), it is possible that, in some cases, we might not be able to recover the observed Einstein radius obtained when using the velocity dispersion directly in Eq. (6). Thus, at radii $\sim \theta_E$ we are probing a different mass. As we can see in the top-left panel of Fig. 5, the scatter is present in both directions, confirming this assertion. On the other hand, even if some galaxy groups look like simple lensing objects (but see Orban de Xivry & Marshall 2009; Limousin et al. 2010), they could be dynamical complex objects with multimodal components and substructures (e.g., Hou et al. 2009, 2012; Ribeiro et al. 2013). Some of our groups have luminous morphologies (Foëx et al. 2013) that cannot be associated with regular groups (roughly circular isophotes around the strong lensing system) and have elongated (elliptical isophotes with a roughly constant position angle from inner to outer parts) or multimodal morphologies (two or more peaks in the central part of the map). Since an irregular luminous morphology it is not a robust confirmation of the dynamical irregularity of a group (although the spectroscopic analysis of the seven objects in Muñoz et al. 2013 is consistent with the luminous morphology presented in Foëx et al. 2013), we carry out our analysis using groups with both irregular and regular luminous morphology. Moreover, as mentioned in Sect. 4.1, if we discard objects with extreme $R_A/\theta_{E,I}$ (for example with a cut off $0.5 \leq R_A/\theta_{E,I} \leq 2.0$), the correlation coefficient and the significance improve ($R = 0.6$, and $P = 1 \times 10^{-5}$). This is consistent with the idea presented above about the comparison between strong lensing mass and weak lensing mass, and is also consistent with the results found when we used the eleven strong lensing models (Sect. 4.3). For such groups with extreme ratios it is more inaccurate to associate the mass at large scale with the mass inside the Einstein radius.

The velocity dispersion σ_{WL} is transformed into the corresponding mass and used to compute $\theta_{E,II}$ through Eq. (14). As before, this mass comes from a large-scale measurement, and is probably overestimated (Muñoz et al. 2013) or underestimated (Gavazzi 2005), and so it could be inappropriate to link R_A and $\theta_{E,II}$ for some groups. We note that the behavior of the points on the top-left panel of Fig. 5 are inherited by the middle-left and bottom-left panels of the same figure, with an increase in the scatter and a shift to lower values of the Einstein radius. The trend is almost the same, independently of whether we use the catalog constructed using V_{rms} as proxy for the velocity dispersion inferred in the observed lenses, or the one built to match the observational shape of the redshift distribution of the lenses. This is an expected result because both quantities ($\theta_{E,I}$ and $\theta_{E,II}$) are correlated through Eq. (16). Both the shift and the scatter are related to the assumed mass, M_{200} , derived

Table 5. Least-squares fitting results for the scaling relations.

Scaling law	$a \pm \delta a$	$b \pm \delta b$	χ^2/ν	$Q\left(\frac{N-2}{2}, \chi^2/2\right)$
$\text{Log}[R_A] - N$	0.45 ± 0.04	0.007 ± 0.002	0.85	0.82
$\text{Log}[R_A] - L$	0.49 ± 0.04	$0.06 \pm 0.03^\dagger$	0.96	0.60
$\text{Log}[R_A] - (N/L)_N$	0.44 ± 0.06	0.2 ± 0.1	0.94	0.62

Notes. $^{(\dagger)} \times 10^{12}$. Column 1 lists the scaling law; Cols. 2 and 3 list the coefficient values in the relation $Y = a + bX$; Cols. 4 and 5 list the reduced χ^2 and the statistical significance, respectively.

from the velocity dispersion of the isothermal profile; as the mass grows without a boundary at large radii, this produces less concentrated halos, product of the $c - V_{rms}$ relation. The small values of $\theta_{E,II}$ can be interpreted as a failure of Λ CDM to reproduce the observed Einstein radius (e.g., Broadhurst & Barkana 2008), but this implication is ruled out in our case considering that our analysis has oversimplifications, the most important being the assumption of spherical symmetry. Thus, consistent with the first result discussed above, we found a low correlation between $\theta_{E,II}$ and R_A . We obtained $\theta_{E,II} = (0.4 \pm 1.5) + (1.1 \pm 0.4)R_A$ with a correlation coefficient $R = 0.4$ ($P = 1 \times 10^{-3}$), and $\theta_{E,II} = (0.4 \pm 1.5) + (1.1 \pm 0.4)R_A$ with $R = 0.4$ ($P = 1 \times 10^{-3}$) for the first and second catalog, respectively.

Furthermore, the two bottom plots in the right panel of Fig. 5 show the same behavior in the correlation: statistically $\theta_{E,II}$ is slightly larger than R_A . The same behavior occurs for small values of R_A for $\theta_{E,I}$ (see top-left panel of Fig. 5). This trend is probably related to the fact that our sample does not only contain giant arcs. For instance, it is possible that some images do not form at the tips of the critical lines, which biases the comparison. However, this factor probably has less influence than the one discussed before, namely, the fact that we are using the information at large scale to infer the Einstein radius. This assertion will be clear below, when we discuss the third method.

The analysis of our strong lensing models for SL2SJ0859–0345 (SA63), SL2SJ08520–0343 (SA72), SL2SJ09595+0218 (SA80), and SL2SJ10021+0211 (SA83), and the models previously reported by Limousin et al. (2009) show that R_A can be used as a proxy of θ_E , which is quantitatively supported by the fit: $\theta_{E,III} = (0.4 \pm 1.5) + (0.9 \pm 0.3)R_A$ with a correlation coefficient $R = 0.6$. In Fig. 9 we can see that the one-to-one relation is not only followed by those groups strictly defined as having giant arcs. If we compare this figure with the right column of Fig. 5, we see that groups with giant arcs are only near the one-to-one relation if we take into account the big error bars in $\theta_{E,I}$ and $\theta_{E,II}$. The fact that in our third method we found a better correlation (with less scatter) between $\theta_{E,III}$ and R_A is explained because we are using the arc positions in the models, i.e. even using simple SIE models we are directly constraining the mass inside the Einstein radius. Unfortunately, we cannot improve our statistics because we do not have enough data to perform such strong lensing models for more groups in our sample. Thus, we can regard the first and second method as a complementary study despite their lower robustness.

In Appendix A we present the luminosity density contours for the four new groups modeled in the present work. These contours were obtained using luminosity maps constructed following Limousin et al. (2009) and Foëx et al. (2013). From Figs. A.1–A.3 it is clear that SL2SJ08591–0345 (SA63), SL2SJ08520–0343 (SA72), and SL2SJ09595+0218 (SA80) are regular groups with circular isophotes around the strong

lensing deflector. The fourth group, SL2S J10021+0211 (SA83), has a weak-lensing detection less than 3σ , thus it is not part of the final sample of Foëx et al. (2013) and it does not appear in Fig. 5. However, this object is a good candidate to be a strong lensing group in More et al. (2012). This group also shows very elongated and elliptical isophotes, with multimodal peaks (see Fig. A.4). It is probably part of a large-scale structure, since a group or cluster is clearly present at a distance of less than 1 Mpc. There are some other examples of potentially large-scale structures (Foëx et al. in prep.) in the sample of galaxy groups, which is not surprising since such structures have been reported in local large galaxy surveys (Colless et al. 2001; Pimblet et al. 2004) or detected around massive clusters at higher redshifts (e.g., Limousin et al. 2012). Despite the complex morphology, R_A agrees with the value of θ_E computed from the strong lensing model, but as we noted in Fig. 5, and discussed before, irregular groups can have $R_A \approx \theta_E$.

Puchwein & Hilbert (2009) studied the cross-sections for giant arcs, using the Millennium simulation, and showed that the radial distribution of tangential arcs is broad and could extend out to several Einstein radii. Their results (see their Fig. 10) are in agreement with the work presented here in the sense that the ratio R_A/θ_E could be in some cases greater than 4 (see Fig. 5). On the other hand, if we analyze our sample of eleven groups discussed in Sect. 4.3, we found $R_A/\theta_{E,III} = 1$ with a standard deviation of $\approx 35\%$. It is interesting that an analogous result is found for $R_A/\theta_{E,I}$ and $R_A/\theta_{E,II}$ when the outliers are eliminated (i.e., with a $0.5 \leq R_A/\theta_{E,I} \leq 2.0$ cutoff). It is beyond the scope of the present paper to analyze the impact on the Einstein radii of other effects such as the orientation (e.g., Hennawi et al. 2007), the substructures, or structures along the line of sight (Meneghetti et al. 2007; Puchwein & Hilbert 2009), the bias in concentration (Oguri & Blandford 2009) and the effect of galaxies in the lensing properties of the groups (Puchwein & Hilbert 2009). That investigation could be done in the future if more space-based images become available (optical and X-ray) to construct accurate lensing models, and more spectroscopic data is obtained to confirm the group candidates and add additional constraints to the models (see Limousin et al. 2013, and the discussion about multi-wavelength approaches). However, we want to point out that the inclusion of galaxy-scale halos in our models can boost the lensing efficiency, between 40% and 10% given the redshift of our groups and sources (see Puchwein & Hilbert 2009). Thus we will use the 35% of scatter calculated in our analysis as an estimate of all the aforementioned possible sources of error in the use of R_A as a proxy of θ_E and its relationship with the luminosity and richness.

5.2. R_A as a proxy

In the light of the above discussion, we assume that statistically R_A can be used as a proxy of the Einstein radius, especially if the Einstein radius is estimated through lens modeling and not indirectly, as in the first two methods discussed in this paper. Thus we can employ it to study some properties in galaxy groups.

5.2.1. R_A and z

As we mentioned in Sect. 1, Zitrin et al. (2012) found a possible Einstein radius evolution with redshift. In Fig. 10 we depicted $\text{Log}(R_A)$ as a function of the redshift. It is evident that, if we restrict the analysis to lenses with $2.0'' \leq R_A \leq 8.0''$,

it is difficult to conclude the existence of an evolution of R_A with redshift, since our sample has few groups below $z = 0.2$. However, there is a trend showing a weak anti-correlation between R_A and z , which partially supports the preliminary results of Zitrin et al. (2012), i.e. galaxy groups (as clusters) are expected to be more concentrated at lower redshifts (see Sect. 3). We note that we cannot extend our conclusions to the cluster regime because of the low number of massive groups in our sample. However, if we consider as massive groups those with $R_A > 8''$, a slight increment is present in R_A for $z > 0.4$, agreeing again with Zitrin et al. (2012). For the binned data, we obtained a weak anti-correlation between R_A and z ; with $\text{Log} R_A = (0.56 \pm 0.06) - (0.04 \pm 0.1)z$. Similarly, for the un-binned data we found $\text{Log} R_A = (0.58 \pm 0.06) - (0.04 \pm 0.1)z$. In both cases, the Spearman's rank correlation coefficient was ~ 0.1 , but such weak statistical dependence between the two variables is probably a result of assuming R_A as a linear function of z . As our sample is poor below $z = 0.3$, we do not attempt to perform a second-order polynomial fitting like the one in Zitrin et al. (2012). In spite of this, it is important to point out the good agreement between their second-order polynomial fitting and the present work around redshift 0.5.

Considering that the background sources have a wide range of redshifts (within each bin on redshift of the groups), we can quantify the contribution of this geometrical effect in the scatter in Fig. 10. Let's consider a fixed mass for the lens in Eq. (6), $R_A \propto D_{LS}/D_{OS}$. Taking a bin centered at $z = 0.45$ (i.e., setting $z_1 = 0.45$) we found $\Delta \text{Log} R_A = 0.07$, using the maximum and minimum z_s values for the arcs included in that bin. Therefore, the geometrical effect, estimated through $\Delta \text{Log} R_A$, is considerably less than the dispersion observed in $\text{Log} R_A$ (less than the 1σ -error on the correlation). Similar or even smaller values for $\Delta \text{Log} R_A$ are found if we use the other bins, indicating that this effect is negligible.

5.2.2. R_A , luminosity and richness

The top and bottom panels in Fig. 11 show R_A as a function of luminosity and optical richness, respectively. Both parameters were measured at 0.5 Mpc from the center (see the discussion in Foëx et al. 2013). The correlations depicted in Fig. 11 are consistent with the results presented in Foëx et al. (2013). The same trends in richness and luminosity were discussed in Zitrin et al. (2012). Nevertheless, we want to stress the main differences between both works. First, we are presenting the analysis in a sample of galaxy groups. Although the mass regime is included in Zitrin et al. (2012), we have a smaller limit than their lower limit of eight members (this limit set by Hao et al. 2010, since their catalog includes clusters with at least this number of members within 0.5 Mpc). Second, our groups are a bona fide sample of strong lensing groups (in some cases confirmed through spectroscopy, Thanjavur et al. 2010; Muñoz et al. 2013). In Fig. 11 we also depicted the correlations reported by Zitrin et al. (2012, see their Fig. 13), taking into account the 1σ width in the distribution. Our results are in good agreement with their work in particular for $\text{Log}[R_A] - N$. In the case of $\text{Log}[R_A] - L$ our correlation is slightly shallower, possibly reflecting the different mass regime being analyzed; i.e. our sample has a cutoff at $R_A = 8.0''$. This cutoff is more noticeable in luminosity because for massive groups we probably miss some luminous members when using a 0.5 Mpc radius.

Estimating the error in using R_A as a proxy of θ_E is complicated because R_A is measured directly from the images (see More et al. 2012), in contrast to θ_E which is estimated through

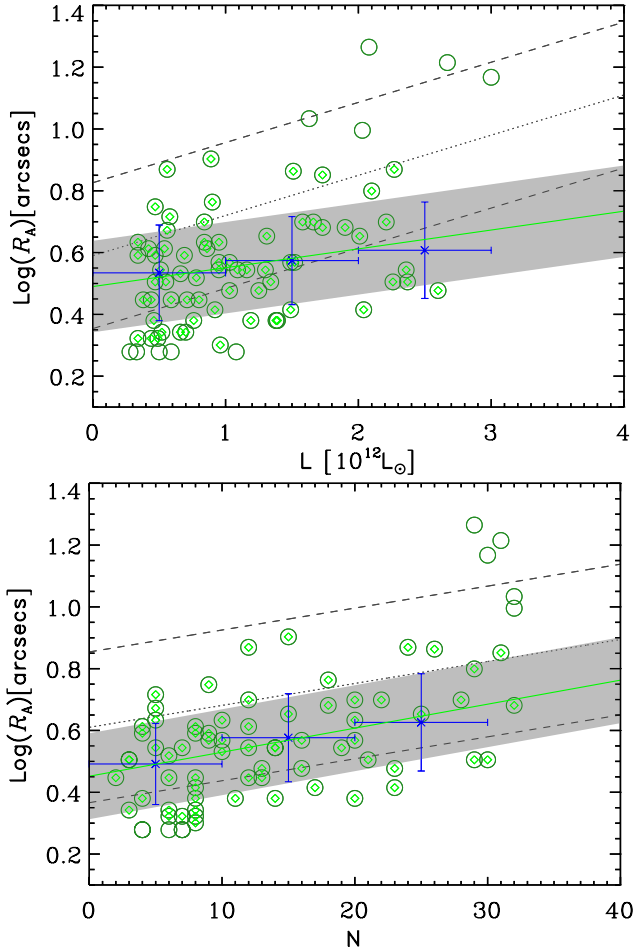


Fig. 11. *Top panel:* R_A as a function of the luminosity. Green circles depict the secure group candidates in Foëx et al. (2013), green diamonds those with $2.0'' \leq R_A \leq 8.0''$. *Bottom panel:* R_A as a function of optical richness. The quantities were measured within an aperture of 0.5 Mpc. The green continuous line shows the fit to the green diamonds, with the 1σ -error depicted as a gray shaded region. Blue asterisks with error bars are plotted to highlight the correlation between R_A and luminosity or optical richness after binning the data. The dotted line shows the relations reported by Zitrin et al. (2012) with a dispersion depicted by the two dashed lines (see Sect. 5.2).

modeling. Additionally, we need to consider the wide distance between the positions of the tangential arcs, i.e. R_A , and the Einstein radius, produced by substructures or structures along the line of sight, the bias in concentration, or orientation effects (Hennawi et al. 2007; Meneghetti et al. 2007; Puchwein & Hilbert 2009; Oguri & Blandford 2009). Thus, we choose a 35% error (see Sect. 5.1) in order to encompass the influence of such factors. This uncertainty on the Einstein radii is less conservative than the 25% imposed by Auger et al. (2013) in their analysis of strong gravitational lens candidates. The errors are omitted in Fig. 11 for clarity. In Table 5 we present the least-squares fitting results for both scaling relations, $\text{Log}[R_A] - N$ and $\text{Log}[R_A] - L$. We also calculate the statistical significance of the fit through the $Q[(N-2)/2, \chi^2/2]$ value. Although the probability is high, indicating a strong correlation, it is important to stress the potential overestimation of errors.

As R_A correlates with N and L , it is natural to infer some dependence between R_A and the ratio N/L . Figure 12 shows $\text{Log}[R_A]$ as a function of $(N/L)_N$, i.e. the optical richness-to-light ratio, normalized to the largest value. Table 5 show

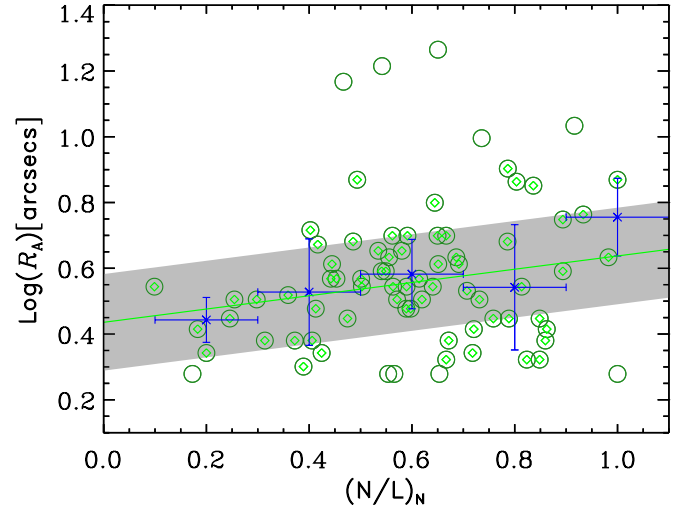


Fig. 12. R_A as a function of the $(N/L)_N$ ratio (see Sect. 5.2). Green circles depict the secure group candidates in Foëx et al. (2013), green diamonds those with $2.0'' \leq R_A \leq 8.0''$. The green continuous line shows the fit to the green diamonds, with the 1σ -error depicted as a gray shaded region. Blue asterisks with error bars represent the binned data.

the results for our fit. Because a mass-richness relationship is found in galaxy clusters (e.g., Gladders et al. 2007; Rozo et al. 2009; Gioldini et al. 2013, and references therein), we expect a correlation between N/L and the mass-to-light ratio (M/L), and thus a dependence between R_A and N/L , since the Einstein radius correlates with its enclosed mass. In particular, our group sample show R_A scale with the mass-to-light ratio (Foëx et al., in prep.). However, going beyond such connections, we want to understand the physical meaning of this correlation. Big groups, i.e. those with larger R_A , have a higher N/L ratio probably because they are less dynamically evolved (without enough time to build big galaxies), they are not relaxed, and they exhibit substructure. Thus, these groups are strong lenses, which means a large R_A . At the other end of the correlation, in small groups (small R_A) the luminosity is dominated by the brightest galaxy in the group, thus the luminosity of the group is well represented by only a few galaxy members. Given the scatter, we cannot go any further in the analysis of this correlation, and we only establish our results as tentative. Nevertheless, we are able to discuss two selection effects that would bias the correlation. First, we could have groups nearer in redshift or larger with a large R_A , thus, going down to much lower luminosities in the luminosity function (LF) would increase N and decrease L . This scenario is ruled out because both N and L are estimated within a given range in absolute magnitude (the bright part of the LF) for every redshift/velocity (see Foëx et al. 2013). Second, both N and L could have significant uncertainties due to contamination by interlopers. However, L suffers more contamination than N because, for instance, a couple of bright-foreground interlopers have a large effect on L but only change N by a comparatively small amount. We cannot completely rule out this second bias effect, and it could be associated with the discrepancies between Zitrin et al. (2012) and the correlation obtained for top panel in Fig. 11.

Foëx et al. (2013) showed that it was possible to use the optical-scaling relations as reasonable mass proxies to analyze large samples of lensing galaxy groups, and to obtain cosmological constraints. They explored the relation between σ_v and the main optical properties of the SARCS sample and found

good correlations, i.e. the more massive systems are richer and more luminous (despite a 35% scatter). The analysis presented here is one more step in the analysis of strong lensing galaxy groups. The correlations discussed in the preceding paragraphs demonstrate the potential of using R_A as a complementary proxy to study a sample of lensing groups. Being galaxy groups less complex than galaxy clusters from a lensing viewpoint, the R_A and the σ_v obtained from weak lensing will be important tools to characterize galaxy groups. These are valuable assets in the forthcoming era of big surveys (LSST, DES, EUCLID) since spectroscopic data for all the objects would be not always available.

6. Conclusions

We analyzed for the first time, using different approaches, the Einstein radii in a sample of objects that belongs to the SL2S (Cabanac et al. 2007; More et al. 2012) and where selected as secure group candidates in Foëx et al. (2013). The task was done using observational data, image and spectroscopy (CFHT, HST, IMACS), and numerical simulations (MultiDark). Our main results can be divided in two parts and summarized as follows:

- Despite the scatter, we found a correlation between R_A and the Einstein radius in galaxy groups.
 1. Using weak lensing data (Foëx et al. 2013) we show $\theta_{E,I}$ correlates with R_A with a large scatter; $\theta_{E,I} = (2.2 \pm 0.9) + (0.7 \pm 0.2)R_A$ with $R = 0.33$. However, when we eliminate extreme values (outliers) in the ratio $R_A/\theta_{E,I}$, both the correlation coefficient and the significance improve ($R = 0.6$, and $P = 1 \times 10^{-5}$). Since the distribution of tangential arcs extends beyond the Einstein radius (e.g., Puchwein & Hilbert 2009), some scatter is expected. In our sample the scatter comes mainly because we are using the information at large scale (weak lensing velocity) in a lower-scale regime (strong lensing).
 2. Using numerical simulations, we constructed two different catalogs to mimic our sample of galaxy groups. One with V_{rms} as proxy for the velocity dispersion measured in the observed lenses and the second one built to match the shape of the observational redshift distribution of the lenses. We found $\theta_{E,II} = (0.4 \pm 1.5) + (1.1 \pm 0.4)R_A$ with a correlation coefficient $R = 0.4$ ($P = 1 \times 10^{-3}$), and $\theta_{E,II} = (0.4 \pm 1.5) + (1.1 \pm 0.4)R_A$ with $R = 0.4$ ($P = 1 \times 10^{-3}$) for the first and second catalog, respectively. Thus, for the second method we also found a correlation between $\theta_{E,II}$ and R_A .
 3. We presented strong lensing models obtained using the LENSTOOL code for SL2SJ08591–0345 (SA63), SL2SJ08520–0343 (SA72), SL2SJ09595+0218 (SA80), and SL2SJ10021+0211 (SA83), showing that for these groups $R_A \sim \theta_{E,III}$. The first three groups have regular morphologies, while the last one exhibits a complex morphology, probably because it is part of a large-scale structure. With the information obtained from these new models, as well as the one obtained from Limousin et al. (2009), we found $\theta_{E,III} = (0.4 \pm 1.5) + (0.9 \pm 0.3)R_A$ with a correlation coefficient $R = 0.6$. This method shows more clearly that there is a correlation between θ_E and R_A . This better agreement can be explained because these models make use of arc positions, which directly constrain the mass inside the Einstein radius.

- We found that the proxy R_A is useful to characterize some properties such as luminosity and richness in galaxy groups.
 1. Analyzing $\text{Log } R_A$ as a function of z we found $\text{Log } R_A = (0.56 \pm 0.06) - (0.04 \pm 0.1)z$, and $\text{Log } R_A = (0.58 \pm 0.06) - (0.04 \pm 0.1)z$ for the binned and un-binned data, respectively. Since our sample has few groups below $z = 0.2$, we are unable to confirm the existence of an anti-correlation between R_A and z . However, using groups with $R_A > 8''$, we found a slight increment in R_A for $z > 0.4$, suggesting a possible evolution of the Einstein radius with redshift in agreement with Zitrin et al. (2012).
 2. It is shown that R_A is correlated with luminosity, and richness. The more luminous and richer the group is, the larger the R_A . We found, $\text{Log } R_A = (0.45 \pm 0.04) + (0.007 \pm 0.002)N$ and $\text{Log } R_A = (0.49 \pm 0.04) + (0.06 \pm 0.03)L$. This is consistent with the weak lensing analysis of our sample presented in Foëx et al. (2013), and it is an expected result given that the Einstein radius is related to the mass of those systems.
 3. We also found a possible correlation between R_A and the N/L ratio. Groups with higher N/L ratio have greater R_A . However, considering our sample might suffer from contamination effects, we emphasize these results are only tentative and require further analysis (Foëx et al., in prep.).

SL2S offers a unique sample for the study of a strong lensing effect in the galaxy-group range (Cabanac et al. 2007; Tu et al. 2009; Limousin et al. 2009, 2010; Thanjavur et al. 2010; Verdugo et al. 2011; More et al. 2012; Muñoz et al. 2013; Foëx et al. 2013). The present paper is an additional contribution to these efforts. Currently, our research team is working on different lines, such as photometric analysis of the groups members, dynamical analysis through spectroscopy, X-ray gas distribution (Gastaldello et al. 2014), large scale structure, and numerical simulations (Fernández-Trincado et al. 2014). New results will come, incrementing our understanding of lensing galaxy groups.

Acknowledgements. We thank the anonymous referee for thoughtful suggestions. The authors also acknowledge A. Jordan for giving us part of his time in *Magellan* to observe our targets. We thank R. Gavazzi for allowing us to use his HST reduced images. We also thank K. Vieira for helping with proofreading. T. Verdugo acknowledges support from CONACYT through grant 165365 and 203489 through the program Estancias posdoctorales y sabáticas al extranjero para la consolidación de grupos de investigación. V. Motta gratefully acknowledges support from FONDECYT through grant 1120741. G. Foëx acknowledges support from FONDECYT through grant 3120160. R.P. Muñoz acknowledges support from CONICYT CATA-BASAL and FONDECYT through grant 3130750. M. Limousin acknowledges the Centre National de la Recherche Scientifique for its support, and the Dark Cosmology Centre, funded by the Danish National Research Foundation. G.F., M.L., and V.M. also acknowledge support from ECOS-CONICYT C12U02.

References

- Abazajian, K., Adelman-McCarthy, J. K., Agüeros, M. A., et al. 2003, *AJ*, 126, 2081
- Alard, C. 2006 [[arXiv:astro-ph/0606757](https://arxiv.org/abs/astro-ph/0606757)]
- Andreon, S., & Hurn, M. A. 2010, *MNRAS*, 404, 1922
- Auger, M. W., Budzynski, J. M., Belokurov, V., Koposov, S. E., & McCarthy, I. G. 2013, *MNRAS*, 436, 503
- Balogh, M. L., McGee, S. L., Wilman, D. J., et al. 2011, *MNRAS*, 412, 2303
- Bardeau, S., Soucail, G., Kneib, J.-P., et al. 2007, *A&A*, 470, 449
- Bartelmann, M. 1996, *A&A*, 313, 697
- Becker, M. R., McKay, T. A., Koester, B., et al. 2007, *ApJ*, 669, 905
- Bertin, E., & Arnouts, S. 1996, *A&AS*, 117, 393
- Boldrin, M., Giocoli, C., Meneghetti, M., & Moscardini, L. 2012, *MNRAS*, 427, 3134

- Bolzonella, M., Miralles, J.-M., & Pelló, R. 2000, *A&A*, 363, 476
- Bridle, S. L., Kneib, J.-P., Bardeau, S., & Gull, S. F. 2002, in *The Shapes of Galaxies and their Dark Halos*, ed. P. Natarajan (World Scientific Publishing Co), 38
- Broadhurst, T., & Barkana, R. 2008, *MNRAS*, 390, 1647
- Cabanac, R. A., Alard, C., Dantel-Fort, M., et al. 2007, *A&A*, 461, 813
- Colless, M., Dalton, G., Maddox, S., et al. 2001, *MNRAS*, 328, 1039
- Coupon, J., Ilbert, O., Kilbinger, M., et al. 2009, *A&A*, 500, 981
- Cucciati, O., Marinoni, C., Iovino, A., et al. 2010, *A&A*, 520, A42
- Cui, W., Springel, V., Yang, X., De Lucia, G., & Borgani, S. 2011, *MNRAS*, 416, 2997
- Dalal, N., Holder, G., & Hennawi, J. F. 2004, *ApJ*, 609, 50
- Eke, V. R., Baugh, C. M., Cole, S., et al. 2004, *MNRAS*, 348, 866
- Evrard, A. E., Metzler, C. A., & Navarro, J. F. 1996, *ApJ*, 469, 494
- Faltenbacher, A., & Mathews, W. G. 2007, *MNRAS*, 375, 313
- Faure, C., Kneib, J.-P., Covone, G., et al. 2008, *ApJS*, 176, 19
- Faure, C., Anguita, T., Alloin, D., et al. 2011, *A&A*, 529, A72
- Fernández-Trincado, J. G., Forero-Romero, J. E., Foëx, G., Verdugo, T., & Motta, V. 2014, *ApJ*, 787, L34
- Finoguenov, A., Ponman, T. J., Osmond, J. P. F., & Zimer, M. 2007, *MNRAS*, 374, 737
- Foëx, G., Soucail, G., Pointecouteau, E., et al. 2012, *A&A*, 546, A106
- Foëx, G., Motta, V., Limousin, M., et al. 2013, *A&A*, 559, A105
- Gastaldello, F., Limousin, M., Foëx, G., et al. 2014, *MNRAS*, 442, L76
- Gavazzi, R. 2005, *A&A*, 443, 793
- Gavazzi, R., Treu, T., Marshall, P. J., Brault, F., & Ruff, A. 2012, *ApJ*, 761, 170
- Gavazzi, R., Marshall, P. J., Treu, T., & Sonnenfeld, A. 2014, *ApJ*, 785, 144
- Giodini, S., Lovisari, L., Pointecouteau, E., et al. 2013, *Space Sci. Rev.*, 177, 247
- Gladders, M. D., Yee, H. K. C., Majumdar, S., et al. 2007, *ApJ*, 655, 128
- Golse, G., & Kneib, J.-P. 2002, *A&A*, 390, 821
- Gwyn, S. D. J. 2011 [[arXiv:1101.1084](https://arxiv.org/abs/1101.1084)]
- Hao, J., McKay, T. A., Koester, B. P., et al. 2010, *ApJS*, 191, 254
- Helsdon, S. F., & Ponman, T. J. 2000a, *MNRAS*, 319, 933
- Helsdon, S. F., & Ponman, T. J. 2000b, *MNRAS*, 315, 356
- Hennawi, J. F., Dalal, N., Bode, P., & Ostriker, J. P. 2007, *ApJ*, 654, 714
- Hildebrandt, H., Erben, T., Kuijken, K., et al. 2012, *MNRAS*, 421, 2355
- Hou, A., Parker, L. C., Harris, W. E., & Wilman, D. J. 2009, *ApJ*, 702, 1199
- Hou, A., Parker, L. C., Wilman, D. J., et al. 2012, *MNRAS*, 421, 3594
- Jarosik, N., Bennett, C. L., Dunkley, J., et al. 2011, *ApJS*, 192, 14
- Joseph, R., Courbin, F., Metcalf, R. B., et al. 2014, *A&A*, 566, A63
- Jullo, E., Kneib, J.-P., Limousin, M., et al. 2007, *New J. Phys.*, 9, 447
- Kinney, A. L., Calzetti, D., Bohlin, R. C., et al. 1996, *ApJ*, 467, 38
- Klypin, A., Kravtsov, A. V., Bullock, J. S., & Primack, J. R. 2001, *ApJ*, 554, 903
- Klypin, A., Valenzuela, O., Colín, P., & Quinn, T. 2009, *MNRAS*, 398, 1027
- Klypin, A. A., Trujillo-Gomez, S., & Primack, J. 2011, *ApJ*, 740, 102
- Kneib, J.-P. 1993, Ph.D. Thesis, Université Paul Sabatier, Toulouse III, France
- Knobel, C., Lilly, S. J., Iovino, A., et al. 2009, *ApJ*, 697, 1842
- Komatsu, E., Dunkley, J., Nolta, M. R., et al. 2009, *ApJS*, 180, 330
- Li, I. H., Yee, H. K. C., Hsieh, B. C., & Gladders, M. 2012, *ApJ*, 749, 150
- Limousin, M., Cabanac, R., Gavazzi, R., et al. 2009, *A&A*, 502, 445
- Limousin, M., Jullo, E., Richard, J., et al. 2010, *A&A*, 524, A95
- Limousin, M., Ebeling, H., Richard, J., et al. 2012, *A&A*, 544, A71
- Limousin, M., Morandi, A., Sereno, M., et al. 2013, *Space Sci. Rev.*, 177, 155
- Lin, Y.-T., Mohr, J. J., & Stanford, S. A. 2003, *ApJ*, 591, 749
- LSST Dark Energy Science Collaboration 2012 [[arXiv:1211.0310](https://arxiv.org/abs/1211.0310)]
- Mandelbaum, R., Seljak, U., Cool, R. J., et al. 2006, *MNRAS*, 372, 758
- Marshall, P. J., Hogg, D. W., Moustakas, L. A., et al. 2009, *ApJ*, 694, 924
- Maturi, M., Mizera, S., & Seidel, G. 2014, *A&A*, 567, A111
- McLeod, B. A., Bernstein, G. M., Rieke, M. J., & Weedman, D. W. 1998, *AJ*, 115, 1377
- Meneghetti, M., & Rasia, E. 2013, *MNRAS*, submitted [[arXiv:1303.6158](https://arxiv.org/abs/1303.6158)]
- Meneghetti, M., Bartelmann, M., & Moscardini, L. 2003, *MNRAS*, 340, 105
- Meneghetti, M., Argazzi, R., Pace, F., et al. 2007, *A&A*, 461, 25
- Meneghetti, M., Bartelmann, M., Dahle, H., & Limousin, M. 2013, *Space Sci. Rev.*, 177, 31
- Miralda-Escude, J., & Babul, A. 1995, *ApJ*, 449, 18
- More, A., Jahnke, K., More, S., et al. 2011, *ApJ*, 734, 69
- More, A., Cabanac, R., More, S., et al. 2012, *ApJ*, 749, 38
- Muñoz, R. P., Motta, V., Verdugo, T., et al. 2013, *A&A*, 552, A80
- Narayan, R., & Bartelmann, M. 1996 [[arXiv:astro-ph/9606001](https://arxiv.org/abs/astro-ph/9606001)]
- Navarro, J. F., Frenk, C. S., & White, S. D. M. 1997, *ApJ*, 490, 493
- Oguri, M., & Blandford, R. D. 2009, *MNRAS*, 392, 930
- Orban de Xivry, G., & Marshall, P. 2009, *MNRAS*, 399, 2
- Osmond, J. P. F., & Ponman, T. J. 2004, *MNRAS*, 350, 1511
- Pimblett, K. A., Drinkwater, M. J., & Hawkrigg, M. C. 2004, *MNRAS*, 354, L61
- Popesso, P., Biviano, A., Böhringer, H., Romaniello, M., & Voges, W. 2005, *A&A*, 433, 431
- Prada, F., Klypin, A. A., Cuesta, A. J., Betancort-Rijo, J. E., & Primack, J. 2012, *MNRAS*, 423, 3018
- Puchwein, E., & Hilbert, S. 2009, *MNRAS*, 398, 1298
- Rasmussen, J., & Ponman, T. J. 2007, *MNRAS*, 380, 1554
- Redlich, M., Bartelmann, M., Waizmann, J.-C., & Fedeli, C. 2012, *A&A*, 547, A66
- Reyes, R., Mandelbaum, R., Hirata, C., Bahcall, N., & Seljak, U. 2008, *MNRAS*, 390, 1157
- Ribeiro, A. L. B., Schilling, A. C., de Carvalho, R. R., et al. 2013, *MNRAS*, 434, 784
- Richard, J., Pei, L., Limousin, M., Jullo, E., & Kneib, J. P. 2009, *A&A*, 498, 37
- Riebe, K., Partl, A. M., Enke, H., et al. 2013, *Astron. Nachr.*, 334, 691
- Romeo, A. D., Napolitano, N. R., Covone, G., et al. 2008, *MNRAS*, 389, 13
- Rozo, E., Rykoff, E. S., Evrard, A., et al. 2009, *ApJ*, 699, 768
- Sand, D. J., Treu, T., Ellis, R. S., & Smith, G. P. 2005, *ApJ*, 627, 32
- Seidel, G., & Bartelmann, M. 2007, *A&A*, 472, 341
- Sommer-Larsen, J. 2006, *MNRAS*, 369, 958
- Sun, M. 2012, *New J. Phys.*, 14, 5004
- Syget, J. F., Tu, H., Fort, B., & Gavazzi, R. 2010, *A&A*, 517, A25
- Thanjavur, K., Crampton, D., & Willis, J. 2010, *ApJ*, 714, 1355
- Torri, E., Meneghetti, M., Bartelmann, M., et al. 2004, *MNRAS*, 349, 476
- Tu, H., Gavazzi, R., Limousin, M., et al. 2009, *A&A*, 501, 475
- Turner, E. L., Ostriker, J. P., & Gott, III, J. R. 1984, *ApJ*, 284, 1
- Verdugo, T., Motta, V., Muñoz, R. P., et al. 2011, *A&A*, 527, A124
- Willis, J. P., Pacaud, F., Valtchanov, I., et al. 2005, *MNRAS*, 363, 675
- Wilman, D. J., Balogh, M. L., Bower, R. G., et al. 2005a, *MNRAS*, 358, 88
- Wilman, D. J., Balogh, M. L., Bower, R. G., et al. 2005b, *MNRAS*, 358, 71
- Wright, C. O., & Brainerd, T. G. 2000, *ApJ*, 534, 34
- Yang, X., Mo, H. J., & van den Bosch, F. C. 2008, *ApJ*, 676, 248
- Zitrin, A., Broadhurst, T., Bartelmann, M., et al. 2012, *MNRAS*, 423, 2308

Appendix A: Luminosity density contours

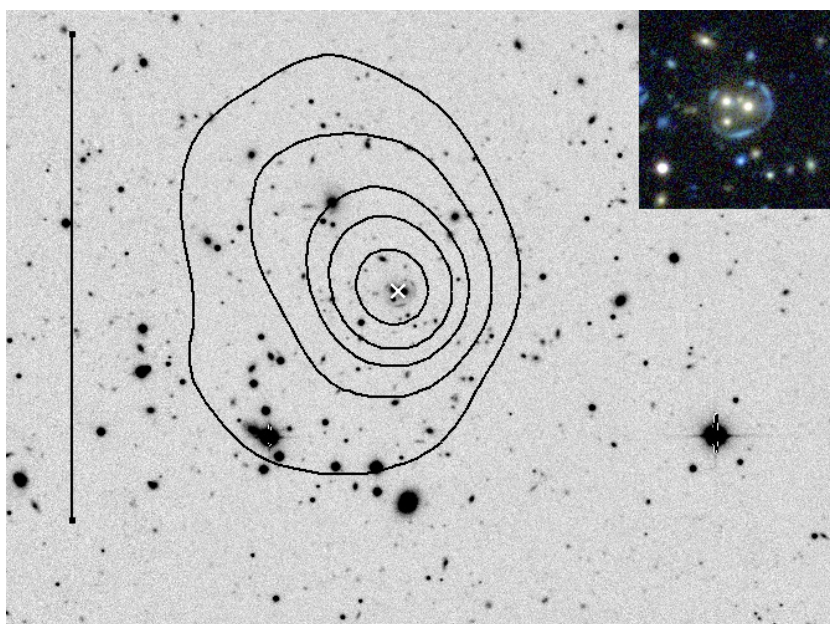


Fig. A.1. Luminosity density contours for SL2S J08591–0345 (SA63). They represent 2×10^6 , 4×10^6 , 7×10^6 and 10^7 , and $1.5 \times 10^7 L_{\odot} \text{ kpc}^{-2}$ from outermost to innermost. The white cross marks the galaxy at the center of the strong lensing system. The black vertical line on the left is 1 Mpc long. The stamp in the top-right corner shows a $30'' \times 30''$ CFHTLS false color image of the system.

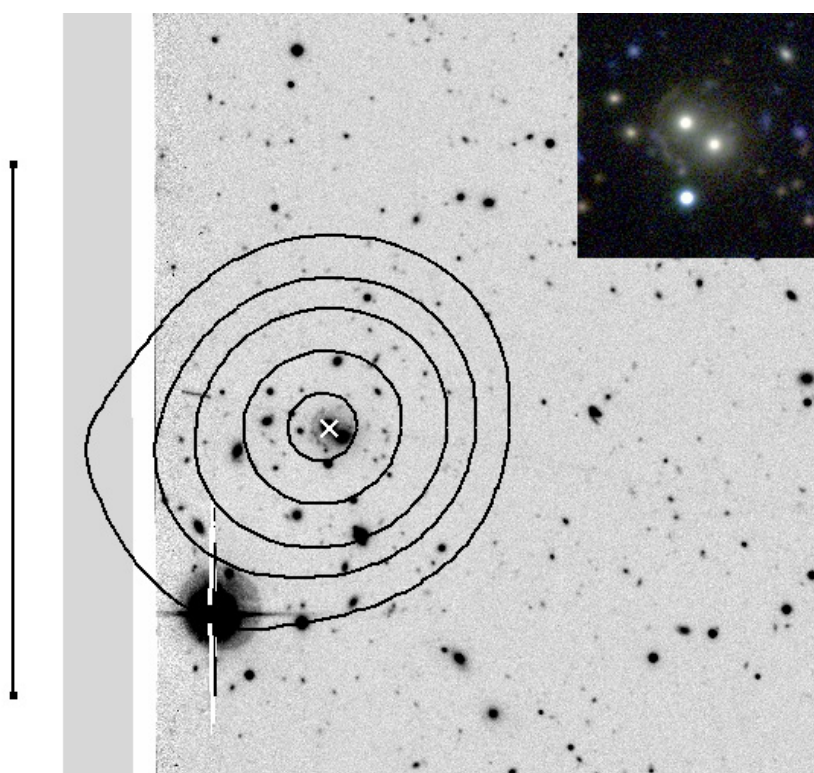


Fig. A.2. Same as Fig. A.1 for SL2S J08520–0343 (SA72).

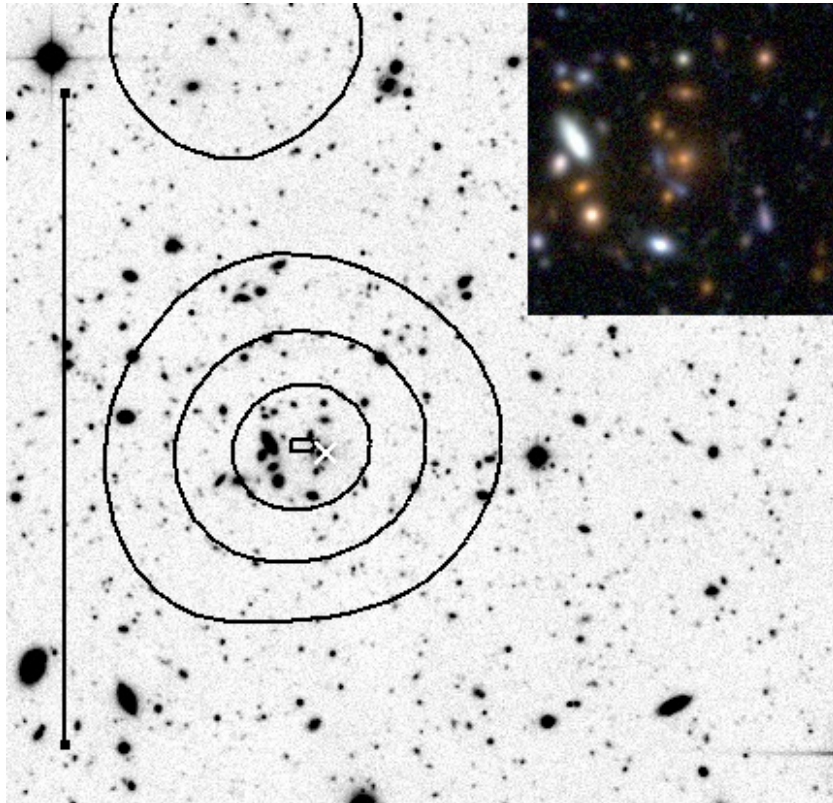


Fig. A.3. Same as Fig. A.1 for SL2S J09595+0218 (SA80).

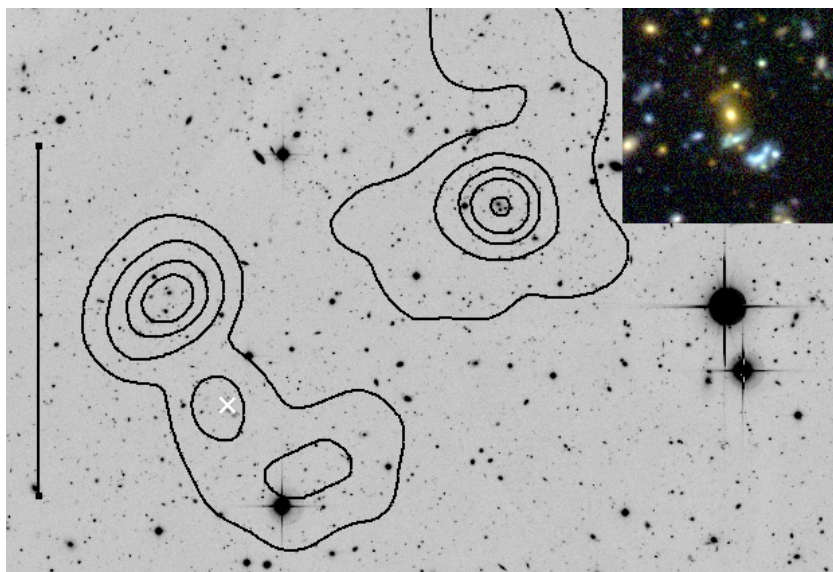


Fig. A.4. Same as Fig. A.1 for SL2S J10021+0211 (SA83).

Dark matter–baryons separation at the lowest mass scale: the Bullet Group[★]

F. Gastaldello,^{1,2,†} M. Limousin,^{3,4} G. Foëx,⁵ R. P. Muñoz,⁶ T. Verdugo,⁷ V. Motta,⁵ A. More,^{8,9} R. Cabanac,¹⁰ D. A. Buote,² D. Eckert,^{1,11} S. Ettori,^{12,13} A. Fritz,¹ S. Ghizzardi,¹ P. J. Humphrey,² M. Meneghetti^{12,13,14} and M. Rossetti^{1,15}

¹INAF – IASF Milano, via E. Bassini 15, I-20133 Milano, Italy

²Department of Physics and Astronomy, University of California at Irvine, 4129 Frederick Reines Hall, Irvine, CA 92697-4575, USA

³Aix Marseille Universit, CNRS, LAM (Laboratoire d'Astrophysique de Marseille), UMR 7326, F-13388 Marseille, France

⁴Dark Cosmology Centre, Niels Bohr Institute, University of Copenhagen, Juliane Maries Vej 30, DK-2100 Copenhagen, Denmark

⁵Instituto de Física y Astronomía, Universidad de Valparaíso, Avda. Gran Bretaña 1111, Playa Ancha, Valparaíso 2360102, Chile

⁶Instituto de Astrofísica, Facultad de Física, Pontificia Universidad Católica de Chile, Av. Mackenna 4860, 7820436 Macul, Santiago, Chile

⁷Centro de Investigaciones de Astronomía, AP 264, Mérida 5101-A, Venezuela

⁸Kavli Institute for Cosmological Physics, University of Chicago, 5640 S. Ellis Ave., Chicago, IL 60637, USA

⁹Kavli IPMU, University of Tokyo, 5-1-5 Kashiwanoha, Kashiwa 277-8583, Japan

¹⁰Universite de Toulouse-UPS, CNRS; Institut de Recherche en Astrophysique et Planetologie; 57 avenue d'Azereix, F-65000 Tarbes, France

¹¹Astronomical Observatory of the University of Geneva, ch. d'Ecogia 16, CH-1290 Versoix, Switzerland

¹²INAF, Osservatorio Astronomico di Bologna, via Ranzani 1, I-40127 Bologna, Italy

¹³INFN, Sezione di Bologna, viale Berti Pichat 6/2, I-40127 Bologna, Italy

¹⁴JPL, 4800 Oak Grove Dr., Pasadena, CA 91109, USA

¹⁵Dip. di Fisica, Università degli studi di Milano, via Celoria 16, I-20133 Milano, Italy

Accepted 2014 April 17. Received 2014 April 17; in original form 2014 February 12

ABSTRACT

We report on the X-ray observation of a strong lensing selected group, SL2S J08544-0121, with a total mass of $2.4 \pm 0.6 \times 10^{14} M_{\odot}$ which revealed a separation of 124 ± 20 kpc between the X-ray emitting collisional gas and the collisionless galaxies and dark matter (DM), traced by strong lensing. This source allows to put an order of magnitude estimate to the upper limit to the interaction cross-section of DM of $10 \text{ cm}^2 \text{ g}^{-1}$. It is the lowest mass object found to date showing a DM–baryons separation, and it reveals that the detection of bullet-like objects is not rare and confined to mergers of massive objects opening the possibility of a statistical detection of DM–baryons separation with future surveys.

Key words: gravitational lensing: strong – galaxies: groups: individual: SL2S J08544-0121 – dark matter – X-rays: galaxies: clusters.

1 INTRODUCTION

Merging galaxy clusters are unique astrophysical probes of the properties of dark matter (DM), which accounts for the majority of the mass in the Universe. During a cluster merger, the cluster galaxies are collisionless particles, affected only by gravitational interactions, while the X-ray emitting plasma clouds, the dominant baryonic components in mass, are slowed down by ram pressure. Collisionless DM behaves as the galaxies, so as the merging progresses the DM component is separated from the X-ray gas

(Furlanetto & Loeb 2002). The presence of DM and constraints on its self-interaction cross-section can therefore be inferred by measuring a spatial offset between the X-ray emission of the plasma and its total mass distribution as revealed by gravitational lensing, which is independent of the type of matter present.

An offset between the X-ray gas distribution and the mass inferred from gravitational lensing was detected for the first time in the Bullet cluster (Markevitch et al. 2004, M04 hereafter). A few other examples of ‘bullet-like clusters’ have been found following that discovery (e.g. Bradač et al. 2008; Merten et al. 2011; Dawson et al. 2012; Dahle et al. 2013). Since the collisions between two massive progenitors are rare (Shan et al. 2010), the number of detected massive clusters undergoing mergers with the proper configuration is not expected to increase significantly. The utility of a small number of individual systems is limited by observational uncertainties in their collision velocity, impact parameter and angle

† E-mail: gasta@lamberte.inaf.it

[★] Based on observations obtained with XMM-Newton, an ESA science mission with instruments and contributions directly funded by ESA member states and NASA.

with respect to the plane of the sky (e.g. Dawson 2013). Here, we show that these studies can be extended to less massive systems which are much more numerous than massive clusters.

All distance-dependent quantities have been computed assuming a cosmological model with $\Omega_m = 0.3$, $\Omega_\Lambda = 0.7$ and $H_0 = 70 \text{ km s}^{-1} \text{ Mpc}^{-1}$.

2 THE OBJECT SL2S J08544-0121

The object SL2S J08544-0121 is a gravitational lens found in the Strong Lensing Legacy Survey (SL2S), a semi-automated search for strong lensing (SL) systems on the Canada–France–Hawaii Telescope Legacy Survey (CFHTLS) Deep and Wide fields (Cabanac et al. 2007). SL2S uses an algorithm aimed at detecting efficiently group scale lenses, with image separations of the order of 3–12 arcsec, intermediate between the ones found in galaxies (1–2 arcsec) and massive clusters ($\gtrsim 20$ arcsec) (More et al. 2012). We will therefore define SL2S J08544-0121 as a group based on this criterion. SL2S J08544 is located at redshift 0.35, and it displays a bimodal light distribution with a SL system located at one of the two luminosity peaks separated by 54 arcsec (267 kpc transverse physical distance). The SL features detected from ground-based images have been followed up with ACS camera on the *Hubble Space Telescope* (*HST*), revealing a very perturbed lensing configuration. Indeed, the main arc and the counter-image of the SL system are located at ~ 5 and ~ 8 arcsec from the lens galaxy centre, respectively. It was found (Limousin et al. 2010) that a simple elliptical isothermal potential centred on the lensing galaxy could not satisfactorily reproduce the SL observations. One straightforward way to measure the lensing model quality is to quote the rms error which quantifies the distance between the observed position of the lensed images and the position derived from the lensing mass model. The smaller this distance, the better the mass model. For this model, the rms error in the image position is 0.38 arcsec. It was found that one needs to take into account in the modelling the mass distribution of the galaxy group within which the lens is embedded. In addition to the mass associated with the SL deflector, mass associated with the second luminosity peak is required in order to accurately reproduce the SL observations (rms of 0.05 arcsec), demonstrating that SL2S J08544 displays a bimodal mass distribution following the light distribution. If on the contrary we construct a mass model where we add a mass clump consistent with the X-ray gas distribution (see Section 3), we are not able to improve the fit (rms of 0.36 arcsec) with respect to the unsuccessful model where a single mass clump is associated with the SL deflector. The total mass of the group inferred from the SL analysis is found to be in good agreement with an independent weak lensing analysis (Foëx et al. 2013). Spectroscopic follow-up of 18 ellipticals with FOCAL Reducer and low dispersion Spectrograph (FORS) 2 at the Very Large Telescope (VLT) confirms the presence of a galaxy group at $z = 0.35$ (Muñoz et al. 2013). In particular, the two brightest galaxies populating the two luminosity peaks are found at the same redshift. We do not confirm the bimodal distribution of velocities suggested in Muñoz et al. (2013): the redshift histogram has indeed a broad high-velocity tail but a series of tests looking for departure from Gaussianity returned a null result. We applied an Anderson–Darling test (e.g. Hou et al. 2009) which returned a p value of 0.1553, therefore consistent with a Gaussian distribution. We also applied to the data Kaye’s Mixture Model test (Ashman, Bird, & Zepf 1994) which returned a p value of 0.06 for a two-group partition over a single group. The number of spectroscopic members does not allow a more detailed view of the

merger dynamics and in particular the component of the velocity along the line of sight.

3 THE XMM OBSERVATION OF SL2S J08544-0121

We observed SL2S J08544-0121 with *XMM* as part of an X-ray follow-up programme of the SL2S groups to obtain an X-ray detection of these SL-selected systems and a measurement of the X-ray luminosity and temperature. SL2S J08544-0121 was observed by *XMM* for 9.5 ks for the MOS detector and 5 ks for the pn detector. The data were reduced with *SAS* v12.0.0 using the tasks *emchain* and *epchain*. We considered only event patterns 0–12 for MOS and 0 for pn and the data were cleaned using the standard procedures for bright pixels and hot columns removal and pn out-of-time correction. Periods of high backgrounds due to soft protons were filtered out but their impact was negligible for this observation. We checked the observation for contamination by solar wind charge exchange: ACE (Advanced Composition Explorer) SWICS O+7/O+6 ratio was less than 0.3, a value which is typical of the quiescent Sun (Snowden et al. 2008). No variation in the light curve in the soft (0.5–2 keV) energy band was detected as a further check of negligible contamination by this background component.

For each detector, we created images in the 0.5–2 keV band with point sources, detected using the task *edetect_chain*, masked using circular regions of 25 arcsec radius centred at the source position. Point-source-free, cleaned images have been generated with the *CIAO* tool *dmfilth* which replaces photons within the source with a locally estimated Poisson-deviated noise. The images have been exposure corrected and background subtracted using the *XMM*-Extended Source Analysis Software (*ESAS*). The *XMM* image in the 0.5–2 keV band of the field of SL2S J08544-0121 is shown in Fig. 1. The X-ray emission of SL2S J08544-0121 is clearly extended: the best-fitting β -model to the surface brightness profile has a core radius of $r_c = 128^{+64}_{-49}$ kpc ($26 \text{ arcsec}^{+13}_{-10}$) and $\beta = 0.52^{+0.09}_{-0.06}$. The

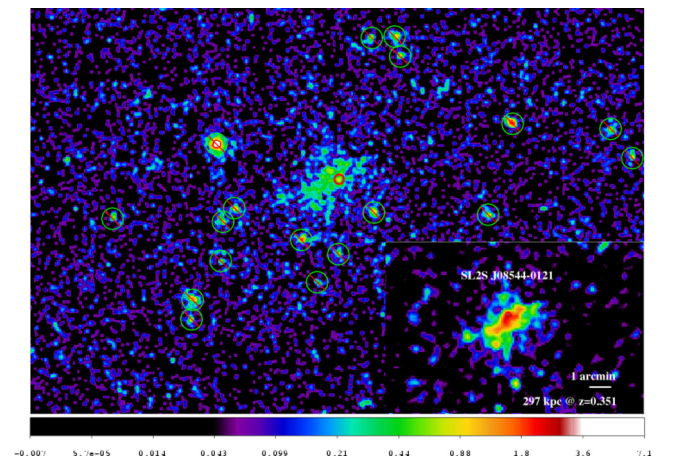


Figure 1. The EPIC 0.5–2 keV exposure-corrected and particle-background-subtracted image of SL2S J08544. The detected point sources are highlighted by the green circles; with the red circle of radius 11 arcsec the point source within the group diffuse emission is also indicated. Point sources have been removed with the *CIAO* tool *dmfilth* which replaces photons within the source with a locally estimated background. This processed image of the diffuse emission is shown in the inset in the bottom-right corner and it has been used to produce the X-ray contours shown in Fig. 3. The image has been smoothed with a 7.5 arcsec Gaussian (15 arcsec for the inset). The colour bar is in units of counts per pixel.

faint point source (a 3σ detection) in the SW embedded within the extended emission of the group has been replaced within a circle of 11 arcsec radius with a locally estimated Poisson noise with the same procedure adopted for the other point sources in the image. This is the largest region not overlapping with the peak of the emission itself (and corresponding roughly to 60 per cent of the encircled energy fraction, EEf, for a point source on-axis). We estimate that the possible contamination by the emission in the wings of the point spread function (PSF) corresponds to 1 per cent of the extended emission. The *XMM* astrometry is known to be accurate to within 1 arcsec (Guainazzi 2013), and we quantified the error in the determination of the peak by calculating the error in the position of the centre of a two-dimensional beta model fitted in a region of 30 arcsec radius (80 per cent of the EEf) with the CIAO software *SHERPA* (Freeman et al. 2001) which is of the order of 3 arcsec. We therefore estimate the error in the position of the X-ray peak to be 4 arcsec. If instead of replacing the weak point source we model it with an appropriate PSF model we obtain the same position for the X-ray peak within the errors.

To assess if the possible systematic error due to undetected source might be larger than the above estimate, we tested our analysis on simulations of 10^3 *XMM* images with a source list with flux distribution and source density computed using the $\log(N)$ – $\log(S)$ from Moretti et al. (2003) down to a level of 1×10^{-17} erg cm $^{-2}$ s $^{-1}$ and we then added the extended emission of the source; the main instrumental characteristics (PSF, vignetting, background) were taken into account. The standard deviation of the distribution of position of peaks was 3 arcsec, consistent with the estimated error.

For spectral fitting, we extracted spectra for each detector from a 1.5 arcmin aperture centred on the peak of the emission, with radius chosen to maximize the S/N over the background. Redistribution matrix files (RMFs) and ancillary response files (ARFs) were generated using the *SAS* tasks *rmfgen* and *arfgen* in extended source mode. The spectra from the three detectors were jointly fitted with an *APEC* thermal plasma (Smith et al. 2001) modified by Galactic absorption (Kalberla et al. 2005). The spectral fitting was performed with *XSPEC* (Arnaud 1996) in the 0.5–12 keV band (0.5–13 keV for the pn) using the C-statistic and quoted metallicities are relative to the abundances of Grevesse & Sauval (1998). To account for the background, we included additional spectral components in the fits: we included two *APEC* components ($kT = 0.07$ and 0.2 keV, the former unabsorbed) to account for the Galactic foreground and a power-law component ($\Gamma = 1.41$) for the cosmic X-ray background due to unresolved AGNs. To account for the instrumental background, we included a number of Gaussian lines and a broken power-law model, which were not folded through the ARF. The background parameters were constrained by fitting spectra extracted from an annular region close to the source extraction region and in a larger annulus of 10–12 arcmin and then the fitted normalizations were rescaled accordingly to the source extraction area. The estimated 0.5–2 keV background is in good agreement with the *ROSAT* All-sky Survey spectrum obtained using the X-ray Background Tool (Snowden et al. 1997). We obtained a fit with a C-stat/dof value of 31/36 and the best-fitting parameters are $kT = 3.5_{-0.5}^{+0.6}$ keV and $Z = 0.6_{-0.5}^{+0.7} Z_{\odot}$. We show in Fig. 2 the pn spectrum and the best-fitting model, highlighting the source component. As a further check to the maximum likelihood fitting, we use Markov chain Monte Carlo techniques and Bayesian inference in *XSPEC* to constrain the confidence level of the temperature determination. We allowed for a 10 per cent systematic in our background modelling setting Gaussian priors on the rescaled normalizations of the cosmic and particle background with a width of 10 per cent of their best-fitting values and we set constant priors on

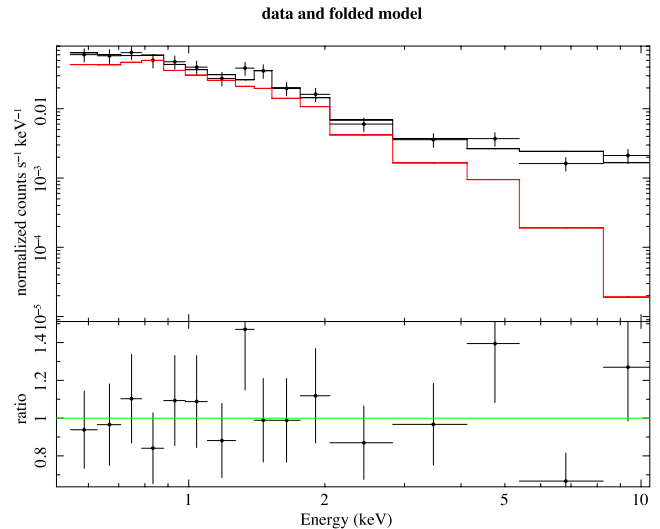


Figure 2. pn spectrum extracted from a 1.5 arcmin aperture: all the background components, instrumental and cosmic have been modelled and the source component is shown by the solid red line. The ratio of data over the model are also shown.

the source parameters. We produced a chain of length 10^4 steps, after an initial ‘burn-in’ of 5000 steps, with the Metropolis–Hastings sampler. We then marginalized over the all other parameters to generate a posterior probability for the temperature. The 68 per cent confidence interval is (3.0, 4.5) keV.

For the total mass determination of the system, we used the chain outputs for the temperature parameter as inputs in the M – T scaling relation of Arnaud, Pointecouteau, & Pratt (2005) obtained for the full sample investigated in that paper and within an overdensity of 200: we find an estimate for the mass of the system of $M_{200} = 2.4 \pm 0.6 \times 10^{14} M_{\odot}$ which is in good agreement with the lensing determination of $M_{200} = 2.2_{-0.6}^{+0.4} \times 10^{14} M_{\odot}$, derived adopting the value of dispersion velocity, 644_{-102}^{+69} km s $^{-1}$, of the Single Isothermal Sphere model used in the modelling of the weak lensing data (Foëx et al. 2013). Simulations indicate that clusters even in the middle of a major merger follow the M – T relation with a scatter of about 20–25 per cent along the mass axis (e.g. Rasia et al. 2011).

4 DM–BARYONS SEPARATION

The X-ray data reveal a single peak located between the two light/mass clumps with a clearly extended and disturbed morphology and an elongation of the emission along the south-east direction. These features are typical of an advanced merger event with the two clumps having already experienced their first passage following a south-east–north-west direction. The geometry of an elongated single X-ray feature between the two DM clumps revealed by lensing is analogous to the configuration seen in the cluster MACS J0025.4–1222 (Bradač et al. 2008). The peak of the baryonic mass distribution derived from the X-ray emission is offset by 25 arcsec ± 4 arcsec from the SL system in the north-west, corresponding to a transverse physical separation of 124 ± 20 kpc at the redshift of the object and given our adopted cosmology (see Fig. 3.)

The mass estimate of $M_{200} = 2.4 \pm 0.6 \times 10^{14} M_{\odot}$ makes SL2S J08544–0121 the smallest mass system found to date for which a significant DM–baryons separation has been detected, ~ 7 times less massive than the Bullet cluster and ~ 2 times less massive than the ‘Burst’ cluster, ZWCl 1234.0+02916 (Dahle et al. 2013), the

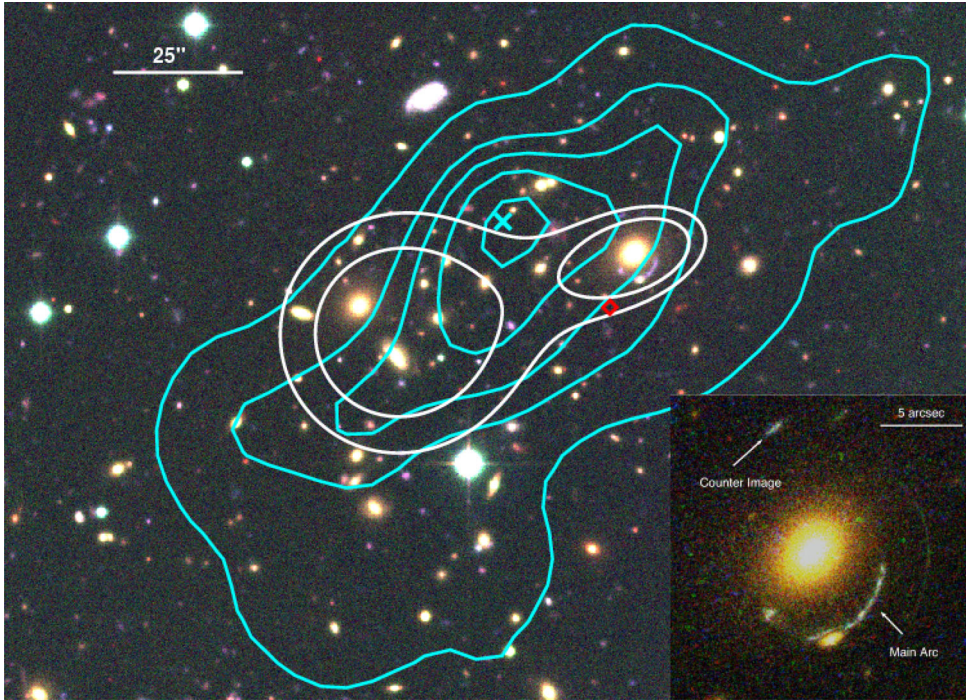


Figure 3. Composite CFHTLS g,r,i colour image of the group SL2S J08544-0121, with a size of 3×2 arcmin corresponding to $891 \text{ kpc} \times 594 \text{ kpc}$ at the redshift of the object, $z = 0.351$. Overlaid in white are the mass contours derived from the SL model, showing where the projected mass density equals $(1.5, 2.0) \times 10^{10} M_{\odot} \text{ arcsec}^{-2}$. The X-ray contours from the *XMM* observation are overplotted in cyan, showing the clear displacement between the X-ray peak, marked by the cyan x point, and the lensing mass, centred at the coordinates of the galaxy populating the lens (see inset). The red diamond point marks the position of the excluded point source discussed in the text. The inset in the bottom-right corner shows the *HST* image with the main arc and its counter image, revealing the particular asymmetric configuration.

currently known smallest mass system showing a bullet-cluster-like configuration.

Using the data of SL2S J08544-0121, we can derive another independent order-of-magnitude estimate for the self-interaction cross-section of DM. We follow the first argument of M04 and assume that the NW subcluster has passed once close to the centre of the SE subcluster, and that the direction of motion is very nearly in the plane of the sky. The offset between the DM centroid of the NW subcluster and the peak of the X-ray gas, which is assumed to belong originally to the same structure, indicates that the scattering depth of the DM subcluster with respect to the collisions of the DM particle stream is lower than 1. If this would not be the case, the DM would behave as a fluid showing ram pressure stripping as the gas. We further assume that the surface mass density along the collision direction is similar to that along the line of sight: this is a conservative estimate given the best-fitting ellipticity of the halo from SL (0.50 ± 0.04 ; Limousin et al. 2010). The scattering depth of DM in the SL subcluster is therefore

$$\tau = \frac{\sigma}{m} \Sigma < 1, \quad (1)$$

where σ is the DM collision cross-section, m is its particle mass and Σ is the DM surface density of the NW subcluster associated with the lens.

The choice of the radius where to calculate the average DM surface density in previous studies has been selected to provide conservative constraints and a comparison between different cluster systems. A radius of 150 kpc was used for the subcluster of the Bullet cluster given the available lensing data at that time (M04), and then used as a reference in following studies. If we calculate Σ at the position of the SL peak averaged over a radius of 150 kpc,

we obtain 0.06 g cm^{-2} and therefore an estimate for the upper limit on the scattering cross-section of $\sigma/m \lesssim 17 \text{ cm}^2 \text{ g}^{-1}$. If instead we use a radius smaller than the measured separation of 124 kpc, in particular 100 kpc, we get 0.10 g cm^{-2} and an upper limit of $\sigma/m \lesssim 10 \text{ cm}^2 \text{ g}^{-1}$.

The detection of DM–baryons separation in SL2S J08544-0121 provides further evidence for the collisionless DM model and an independent upper limit on its interaction cross-section. Systems with mass of $1\text{--}2 \times 10^{14} M_{\odot}$ like the Bullet Group are 10^3 times more numerous than massive clusters of $1 \times 10^{15} M_{\odot}$ like the Bullet Cluster and therefore examples of DM–baryons separation are not as rare as usually assumed (Amendola et al. 2013). Indeed, numerical simulations already suggested a fair number of ‘bullets’ at every mass scale to be present in the adopted cosmological scenario (e.g. Forero-Romero et al. 2010), in particular the number of bullet groups is three times larger than the one of bullet clusters (Fernandez-Trincado et al. 2014). Upcoming lensing surveys (e.g. with the *Euclid* satellite) and X-ray surveys (with the *eROSITA* telescope on the *Spektrum–Roentgen–Gamma Mission*) should therefore provide hundreds of similar examples allowing the properties of DM to be studied in a statistical manner (Massey, Kitching & Nagai 2011).

5 CONCLUSIONS

SL2S J08544-0121 is a really remarkable object because it is an SL-selected group, its lensing image configuration already provided evidence of a bimodal mass configuration, and the X-ray follow-up showed evidence of baryons–DM separation down to at least a mass scale of few times $10^{14} M_{\odot}$. It might be considered as a proof of

concept of the potential of upcoming deep lensing and X-ray surveys of discovering many similar examples allowing a statistical study of the properties of DM. Deeper X-ray observations with *Chandra* and optical spectroscopy of an increased number of member galaxies are needed for a better understanding of the merger geometry of this system.

ACKNOWLEDGEMENTS

FG is supported by INAF-ASI through grant I/023/05/0, I/088/06/0 and I/032/10/0. AF is supported by INAF through VIPERS grants PRIN 2008/2010. VM acknowledges the support of FONDECYT 1120741. RM acknowledges the support of FONDECYT 3130750. RC, GF, ML, VM acknowledge the support of ECOS-CONICYT C12U02. TV acknowledges support from CONACYT through grant 165365 and 203489. MM acknowledges financial contribution from the agreement ASI/INAF/ I/023/12/0 and from INFN project PD51.

REFERENCES

- Amendola L. et al., 2013, *Living Rev. Relativ.*, 16, 6
- Arnaud K. A., 1996, in Jacoby G. H., Barnes J., eds, *ASP Conf. Ser. Vol. 101, Astronomical Data Analysis Software and Systems V*. Astron. Soc. Pac., San Francisco, p. 17
- Arnaud M., Pointecouteau E., Pratt G. W., 2005, *A&A*, 441, 893
- Ashman K. M., Bird C. M., Zepf S. E., 1994, *AJ*, 108, 2348
- Bradač M., Allen S. W., Treu T., Ebeling H., Massey R., Morris R. G., von der Linden A., Applegate D., 2008, *ApJ*, 687, 959
- Cabanac R. A. et al., 2007, *A&A*, 461, 813
- Dahle H. et al., 2013, *ApJ*, 772, 23
- Dawson W. A., 2013, *ApJ*, 772, 131
- Dawson W. A. et al., 2012, *ApJ*, 747, L42
- Fernandez-Trincado J. G., Forero-Romero J. E., Foëx G., Verdugo T., Motta V., 2014, *ApJ*, preprint ([arXiv:1404.5636](https://arxiv.org/abs/1404.5636))
- Foëx G., Motta V., Limousin M., Verdugo T., More A., Cabanac R., Gavazzi R., Muñoz R. P., 2013, *A&A*, 559, A105
- Forero-Romero J. E., Gottlöber S., Yepes G., 2010, *ApJ*, 725, 598
- Freeman P. E., Doe S., Siemiginowska A., 2001, in Harnden F. R., Jr, Primi F. A., Payne H. E., eds, *ASP Conf. Ser. Vol. 238, Astronomical Data Analysis Software and Systems X*. Astron. Soc. Pac., San Francisco, p. 483
- Furlanetto S. R., Loeb A., 2002, *ApJ*, 565, 854
- Grevesse N., Sauval A. J., 1998, *Space Sci. Rev.*, 85, 161
- Guainazzi M., 2013, EPIC Status of Calibration and Data Analysis, XMM-SOC-CAL-TN-0018 (<http://xmm.vilspa.esa.es/docs/documents/CAL-TN-0018.pdf>)
- Hou A., Parker L. C., Harris W. E., Wilman D. J., 2009, *ApJ*, 702, 1199
- Kalberla P. M. W., Burton W. B., Hartmann D., Arnal E. M., Bajaja E., Morras R., Pöppel W. G. L., 2005, *A&A*, 440, 775
- Limousin M. et al., 2010, *A&A*, 524, A95
- Markevitch M., Gonzalez A. H., Clowe D., Vikhlinin A., Forman W., Jones C., Murray S., Tucker W., 2004, *ApJ*, 606, 819 (M04)
- Massey R., Kitching T., Nagai D., 2011, *MNRAS*, 413, 1709
- Merten J. et al., 2011, *MNRAS*, 417, 333
- More A., Cabanac R., More S., Alard C., Limousin M., Kneib J.-P., Gavazzi R., Motta V., 2012, *ApJ*, 749, 38
- Moretti A., Campana S., Lazzati D., Tagliaferri G., 2003, *ApJ*, 588, 696
- Muñoz R. P. et al., 2013, *A&A*, 552, A80
- Rasia E., Mazzotta P., Evrard A., Markevitch M., Dolag K., Meneghetti M., 2011, *ApJ*, 729, 45
- Shan H., Qin B., Fort B., Tao C., Wu X.-P., Zhao H., 2010, *MNRAS*, 406, 1134
- Smith R. K., Brickhouse N. S., Liedahl D. A., Raymond J. C., 2001, *ApJ*, 556, L91
- Snowden S. L. et al., 1997, *ApJ*, 485, 125
- Snowden S. L., Mushotzky R. F., Kuntz K. D., Davis D. S., 2008, *A&A*, 478, 615

This paper has been typeset from a $\text{\TeX}/\text{\LaTeX}$ file prepared by the author.

Combining strong lensing and dynamics in galaxy clusters: integrating MAMPOSSt within LENSTOOL

I. Application on SL2S J02140-0535^{★,★★}

T. Verdugo^{1,2}, M. Limousin³, V. Motta², G. A. Mamon⁴, G. Foëx⁵, F. Gastaldello⁶, E. Jullo³, A. Biviano⁷, K. Rojas²,
R. P. Muñoz⁸, R. Cabanac⁹, J. Magaña², J. G. Fernández-Trincado¹⁰, L. Adame¹¹, and M. A. De Leo¹²

¹ Instituto de Astronomía, Universidad Nacional Autónoma de México, Apdo. postal 106, CP 22800, Ensenada, B.C, Mexico
e-mail: tomasv@astro.unam.mx

² Instituto de Física y Astronomía, Universidad de Valparaíso, Avenida Gran Bretaña 1111, Valparaíso, Chile

³ Laboratoire d'Astrophysique de Marseille, Université de Provence, CNRS, 38 rue Frédéric Joliot-Curie,
13388 Marseille Cedex 13, France

⁴ Institut d'Astrophysique de Paris (UMR 7095: CNRS & UPMC), 98bis Bd Arago, 75014 Paris, France

⁵ Max-Planck Institute for Extraterrestrial Physics, Giessenbachstrasse, 85748 Garching, Germany

⁶ INAF-IASF Milano, via E. Bassini 15, 20133 Milano, Italy

⁷ INAF-Osservatorio Astronomico di Trieste, via G. B. Tiepolo 11, 34143 Trieste, Italy

⁸ Instituto de Astrofísica, Facultad de Física, Pontificia Universidad Católica de Chile, Av. Vicuña Mackenna 4860, 7820436 Macul,
Santiago, Chile

⁹ Laboratoire d'Astrophysique de Toulouse-Tarbes, Université de Toulouse, CNRS, 57 avenue d'Azereix, 65 000 Tarbes, France

¹⁰ Institut Utinam, CNRS UMR 6213, Université de Franche-Comté, OSU THETA Franche-Comté-Bourgogne,
Observatoire de Besançon, BP 1615, 25010 Besançon Cedex, France

¹¹ Facultad de Ciencias Físico-Matemáticas, Universidad Autónoma de Nuevo León, San Nicolás de los Garza, Mexico

¹² Department of Physics and Astronomy, University of California, Riverside, CA 92521, USA

Received 2 April 2016 / Accepted 11 August 2016

ABSTRACT

Context. The mass distribution in galaxy clusters and groups is an important cosmological probe. It has become clear in recent years that mass profiles are best recovered when combining complementary probes of the gravitational potential. Strong lensing (SL) is very accurate in the inner regions, but other probes are required to constrain the mass distribution in the outer regions, such as weak lensing or studies of dynamics.

Aims. We constrain the mass distribution of a cluster showing gravitational arcs by combining a strong lensing method with a dynamical method using the velocities of its 24 member galaxies.

Methods. We present a new framework in which we simultaneously fit SL and dynamical data. The SL analysis is based on the LENSTOOL software and the dynamical analysis uses the MAMPOSSt code, which we integrated into LENSTOOL. After describing the implementation of this new tool, we applied it to the galaxy group SL2S J02140-0535 ($z_{\text{spec}} = 0.44$), which we had previously studied. We used new VLT/FORS2 spectroscopy of multiple images and group members, as well as shallow X-ray data from XMM.

Results. We confirm that the observed lensing features in SL2S J02140-0535 belong to different background sources. One of these sources is located at $z_{\text{spec}} = 1.017 \pm 0.001$, whereas the other source is located at $z_{\text{spec}} = 1.628 \pm 0.001$. With the analysis of our new and our previously reported spectroscopic data, we find 24 secure members for SL2S J02140-0535. Both data sets are well reproduced by a single NFW mass profile; the dark matter halo coincides with the peak of the light distribution, with scale radius, concentration, and mass equal to $r_s = 82^{+44}_{-17}$ kpc, $c_{200} = 10.0^{+1.7}_{-2.5}$, and $M_{200} = 1.0^{+0.5}_{-0.2} \times 10^{14} M_{\odot}$ respectively. These parameters are better constrained when we fit SL and dynamical information simultaneously. The mass contours of our best model agrees with the direction defined by the luminosity contours and the X-ray emission of SL2S J02140-0535. The simultaneous fit lowers the error in the mass estimate by 0.34 dex, when compared to the SL model, and in 0.15 dex when compared to the dynamical method.

Conclusions. The combination of SL and dynamics tools yields a more accurate probe of the mass profile of SL2S J02140-0535 up to r_{200} . However, there is tension between the best elliptical SL model and the best spherical dynamical model. The similarities in shape and alignment of the centroids of the total mass, light, and intracluster gas distributions add to the picture of a non-disturbed system.

Key words. gravitational lensing: strong – galaxies: groups: general – galaxies: groups: individual: SL2S J02140-0535

* SL2S: Strong Lensing Legacy Survey.

** Based on observations obtained with MegaPrime/MegaCam, a joint project of CFHT and CEA/IRFU, at the Canada-France-Hawaii Telescope (CFHT) which is operated by the National Research Council (NRC) of Canada, the Institut National des Science de l'Univers of the Centre National de la Recherche Scientifique (CNRS) of France, and the University of Hawaii. This work is based in part on data products produced at Terapix available at the Canadian Astronomy Data Centre as part of the Canada-France-Hawaii Telescope Legacy Survey, a collaborative project of NRC and CNRS. Also based on *Hubble* Space Telescope (HST) data, VLT (FORS 2) data, and XMM data.

1. Introduction

The Universe has evolved into the filamentary and clumpy structures (dubbed the cosmic web, Bond et al. 1996) that are observed in large redshift surveys (e.g., Colless et al. 2001). Massive and rich galaxy clusters are located at the nodes of this cosmic web, which are fed by accretion of individual galaxies and groups (e.g., Frenk et al. 1996; Springel et al. 2005; Jauzac et al. 2012). Galaxy clusters are the most massive gravitationally bound systems in the Universe, thus constituting one of the most important and crucial astrophysical objects to constrain cosmological parameters (see for example Allen et al. 2011). Furthermore, they provide information about galaxy evolution (e.g., Postman et al. 2005). Also, galaxy groups are important cosmological probes (e.g., Mulchaey 2000; Eke et al. 2004b) because they are tracers of the large-scale structure of the Universe, but also because they are probes of the environmental dependence of the galaxy properties, galactic content of dark matter haloes, and clustering of galaxies (Eke et al. 2004a). Although there is no clear boundary in mass between groups of galaxies and clusters of galaxies (e.g., Tully 2015), it is commonly assumed that groups of galaxies lie in the intermediate mass range between large elliptical galaxies and galaxy clusters (i.e., masses between $\sim 10^{13} M_{\odot}$ to $\sim 10^{14} M_{\odot}$).

The mass distribution in both galaxy groups and clusters has been studied extensively using different methods, such as the radial distribution of the gas through X-ray emission (e.g., Sun 2012; Ettori et al. 2013, and references therein), the analysis of galaxy-based techniques that employs the positions, velocities, and colors of the galaxies (see Old et al. 2014, 2015, for a comparison of the accuracies of dynamical methods in measuring M_{200}), or through gravitational lensing (e.g., Limousin et al. 2009, 2010; Kneib & Natarajan 2011, and references therein). Each probe has its own limitations and biases, which in turn impact the mass distribution measurements. Strong lensing (hereafter SL) analysis provides the total amount of mass and its distribution with no assumptions on either the dynamical state or the nature of the matter producing the lensing effect. Nevertheless, the analysis has its own weakness; for example, it can solely constrain the two-dimensional projected mass density and it is limited to small projected radii. On the other hand, the analysis of galaxy kinematics does not have such limitations, but assumes local dynamical equilibrium (i.e., negligible rotation and streamings motions) and spherical symmetry.

In this paper, we put forward a new method to overcome one of the limitations of the SL analysis, namely, the impossibility of constraining large-scale properties of the mass profile. Our method combines SL (in a parametric fashion, see Sect. 2) with the dynamics of the group or the cluster galaxy members, fitting both data sets simultaneously. Strong lensing and dynamics are both well-recognized probes, the former providing an estimate of the projected two-dimensional mass distribution within the core (typically a few dozens of arcsecs at most), whereas the latter is able to study the density profile at larger radii, using galaxies as test particles to probe the host potential.

There are several methods to constrain the mass profiles of galaxy clusters from galaxy kinematics. One can fit the second and fourth moments of the line-of-sight (hereafter LOS) velocities in bins of projected radii (Łokas & Mamon 2003). One can assume a profile for the velocity anisotropy and apply mass inversion techniques (e.g., Mamon & Boué 2010; Wolf et al. 2010; Sarli et al. 2014). Both methods require binning of the data. An alternative is to fit the observed distribution of galaxies in projected phase space (projected radii and LOS velocity, hereafter

PPS), which does not involve binning the data. This can be performed by assuming six-dimensional distribution functions (DFs), expressed as function of energy and angular momentum (e.g., Wojtak et al. 2009; who used DFs derived by Wojtak et al. 2008, for Λ CDM halos), but the method is very slow, as it involves triple integrals for every galaxy and every point in parameter space. An accurate and efficient alternative is to assume a shape of the velocity DF, as in the method called Modelling Anisotropy and Mass Profiles of Observed Spherical Systems (MAMPOSSt) of Mamon et al. (2013), which has been used to study the radial profiles of mass and velocity anisotropy of clusters (Biviano et al. 2013, 2016; Munari et al. 2014; Guennou et al. 2014). For the aims of the present study, MAMPOSSt is ideal as it 1) is accurate for and very rapid a dynamical model, a valuable asset, since lensing modeling has become time demanding, see, for example the discussion in Jauzac et al. (2014) about the computing resources when modeling a SL cluster with many constraints; 2) produces a likelihood, as does the LENSTOOL¹ code used here for SL (see Sect. 2); and 3) can run with the same parametric form of the mass profile as used in LENSTOOL.

The idea of combining lensing and dynamics is not new. So far, dynamics have been used to probe the very center of the gravitational potential, through the measurement of the velocity dispersion profile of the central brightest cluster galaxy (Sand et al. 2002, 2004; Newman et al. 2009, 2013). However, the use of dynamical information at large scale (velocities of the galaxy members in a cluster or a group), together with SL analysis has not been fully explored. Through this approach, Thanjavur et al. (2010) showed that it is possible to characterize the mass distribution and the mass-to-light ratio of galaxy groups. Biviano et al. (2013) analyzed the cluster MACSJ1206.2-0847, constraining its mass, velocity-anisotropy, and pseudo-phase-space density profiles, finding a good agreement between the results obtained from cluster kinematics and those derived from lensing. Similarly, Guennou et al. (2014) compared the mass profile inferred from lensing with different profiles obtained from three methods based on kinematics, showing that they are consistent among themselves.

This work follows the analysis of Verdugo et al. (2011), hereafter VMM11, where we combined SL and dynamics in the galaxy group SL2S J02140-0535. In VMM11, dynamics were used to constrain the scale radius of a NFW mass profile, which is a quantity that is not accessible to SL constraints alone. These constraints were used as a prior in the SL analysis, allowing VMM11 to probe the mass distribution from the center to the virial radius of the galaxy group. However, the fit was not simultaneous. In this work we propose a framework aimed at fitting SL and dynamics simultaneously, combining the likelihoods obtained from both techniques in a consistent way. Our paper is arranged as follows: in Sect. 2 the methodology is explained. In Sects. 3 and 4 we present the observational data images, spectroscopy, and the application of the method to the galaxy group SL2S J02140-0535. We summarize and discuss our results in Sect. 5. Finally in Sect. 6, we present the conclusions. All our results are scaled to a flat, Λ CDM cosmology with $\Omega_M = 0.3$, $\Omega_{\Lambda} = 0.7$ and a Hubble constant $H_0 = 70 \text{ km s}^{-1} \text{ Mpc}^{-1}$. All images are aligned with WCS coordinates, i.e., north is up, east is left. Magnitudes are given in the AB system.

¹ The LENSTOOL software is publicly available at <https://projets.lam.fr/projects/lenstool/wiki>

2. Methodology

In this section we explain how the SL and dynamical likelihoods are computed in our models.

2.1. Strong lensing

The figure-of-merit function, χ^2 , which quantifies the goodness of the fit for each trial of the lens model, has been introduced in several works (e.g., Verdugo et al. 2007; Limousin et al. 2007; Jullo et al. 2007), therefore, we summarize the method here. Consider a model whose parameters are θ , with N sources, and n_i the number of multiple images for source i . We compute, for every system i , the position in the image plane $x^j(\theta)$ of image j , using the lens equation. Therefore, the contribution to the overall χ^2 from multiple image system i is

$$\chi_i^2 = \sum_{j=1}^{n_i} \frac{[x_{\text{obs}}^j - x^j(\theta)]^2}{\sigma_{ij}^2}, \quad (1)$$

where σ_{ij} is the error on the position of image j , and x_{obs}^j is the observed position. Thus, we can write the likelihood as

$$\mathcal{L}_{\text{Lens}} = \prod_i \frac{1}{\prod_j \sigma_{ij} \sqrt{2\pi}} e^{-\chi_i^2/2}, \quad (2)$$

where it is assumed that the noise associated with the measurement of each image position is Gaussian and uncorrelated (Jullo et al. 2007). This is not true in the case of images that are very close to each other, but it is a reasonable approximation for SL2S J02140-0535. In this work we assume that the error in the image position is $\sigma_{ij} = 0.5''$, which is slightly greater than the value adopted in VMM11, but is half the value that has been suggested by other authors in order to take into account systematic errors in lensing modeling (e.g., Jullo et al. 2010; D'Aloisio & Natarajan 2011; Host 2012; Zitrin et al. 2015).

2.2. Dynamics

The MAMPOSSt (Mamon et al. 2013) method performs a maximum likelihood fit of the distribution of observed tracers in PPS. Mamon et al. (2013) provide a detailed description and we present a summary of this method. The MAMPOSSt method assumes parameterized radial profiles of mass and velocity anisotropy and a shape for the three-dimensional velocity distribution (a Gaussian 3D velocity distribution); MAMPOSSt fits the distribution of observed tracers in PPS. The method has been tested in cosmological simulations, showing the possibility to recover the virial radius, tracer scale radius, and dark matter scale radius when using 100 to 500 tracers (Mamon et al. 2013). Moreover, Old et al. (2015) found that the mass normalization M_{200} is recovered with 0.3 dex accuracy for as few as ~ 30 tracers.

The velocity anisotropy is defined through the expression

$$\beta(r) = 1 - \frac{\sigma_\theta^2(r) + \sigma_\phi^2(r)}{2\sigma_r^2(r)}, \quad (3)$$

where, in spherical symmetry, $\sigma_\phi(r) = \sigma_\theta(r)$. We adopt a constant anisotropy model with $\sigma_r/\sigma_\theta = (1 - \beta)^{-1/2}$, assuming spherical symmetry (see Sect. 4).

The 3D velocity distribution is assumed to be Gaussian,

$$f_v = \frac{1}{(2\pi)^{3/2} \sigma_r \sigma_\theta^2} \exp \left[-\frac{v_r^2}{2\sigma_r^2} - \frac{v_\theta^2 + v_\phi^2}{2\sigma_\theta^2} \right], \quad (4)$$

where v_r , v_θ , and v_ϕ are the velocities in a spherical coordinate system. This Gaussian distribution assumes no rotation or radial streaming, which is a good assumption inside the virial radius, as has been shown by numerical simulations (Prada et al. 2006; Cuesta et al. 2008). The Gaussian 3D velocity model is a first-order approximation, which can be improved (see Beraldo e Silva et al. 2015).

Thereby, MAMPOSSt fits the parameters using maximum likelihood estimation, i.e., by minimizing

$$-\ln \mathcal{L}_{\text{Dyn}} = -\sum_{i=1}^n \frac{\ln q(R_i, v_{z,i} | \bar{\theta})}{C(R_i)}, \quad (5)$$

where q is the probability density of observing an object at projected radius R with LOS velocity v_z , for a N -parameter vector $\bar{\theta}$. And $C(R_i)$ is the completeness of the data set (see Sect. 3.2).

2.3. Combining likelihoods

In order to combine SL and dynamical constraints, we compute their respective likelihoods. The SL likelihood is computed via LENSTOOL code. This software implements a Bayesian Monte Carlo Markov chain (MCMC) method to search for the most likely parameters in the modeling. This code has been used in a large number of clusters studies and characterized in Jullo et al. (2007). The likelihood coming from dynamics of cluster members is computed using the MAMPOSSt code (Mamon et al. 2013), which has been tested and characterized on simulations. Technically, we incorporated the MAMPOSSt likelihood routine into LENSTOOL.

The SL likelihood (see Eq. (2)) depends on the image positions of the arcs and their respective errors. On the other hand, the MAMPOSSt likelihood is calculated through the projected radii and LOS velocity (Eq. (5)). The errors on the inputs for the strong lensing, on one hand, and MAMPOSSt, on the other, should not be correlated; in other words, the joint lensing-dynamics covariance matrix should be diagonal. So, we can write

$$\mathcal{L}_T = \mathcal{L}_{\text{Lens}} \times \mathcal{L}_{\text{Dyn}}, \quad (6)$$

where \mathcal{L}_{Dyn} is given by Eq. (5) and $\mathcal{L}_{\text{Lens}}$ is calculated through Eq. (2). This definition of a total likelihood, where the two techniques (lensing and dynamics) are considered independent, is not new, and has been used previously at different scales by other authors (e.g., Sand et al. 2002, 2004); we are using the dynamics to obtain constraints in the outer regions. In this sense, the main difference from previous works, as for example Biviano et al. (2013), Guennou et al. (2014), or VMM11, is that in this work we do a joint analysis, searching for a solution that is consistent with both methods that maximizes a total likelihood. Additionally, we assume the same weight of the SL and dynamics on the total likelihood, however, this cannot be the case, for example, when combining SL and weak lensing (see the discussion in Umetsu et al. 2015).

2.4. NFW mass profile

We adopt the NFW mass density profile that has been predicted in cosmological N -body simulations (Navarro et al. 1996, 1997),

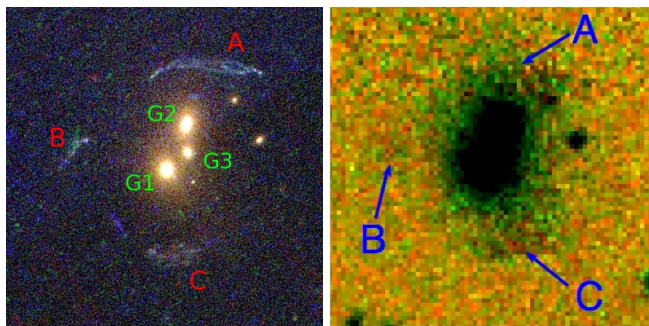


Fig. 1. Images of the group SL2S J02140-0535 at $z_{\text{spec}} = 0.44$. *Left:* composite HST/ACS F814, F606, and F475 color image ($22'' \times 22'' = 125 \times 125 \text{ kpc}^2$) showing the central region of the group (from VMM11). *Right:* composite WIRCam J, K_s color image ($22'' \times 22''$).

given by

$$\rho(r) = \frac{\rho_s}{(r/r_s)(1+r/r_s)^2}, \quad (7)$$

where r_s is the radius that corresponds to the region where the logarithmic slope of the density equals the isothermal value, and ρ_s is a characteristic density. The scale radius is related to the virial radius r_{200} through the expression $c_{200} = r_{200}/r_s$, which is the so-called concentration. Where the radius r_{200} is the radius of a spherical volume inside of which the mean density is 200 times the critical density at the given redshift z , $M_{200} = 200 \times (4\pi/3)r_{200}^3\rho_{\text{crit}} = 100H^2r_{200}^3/G$. The mass contained within a radius r of the NFW halo is given by

$$M(r) = 4\pi r_s^3 \rho_s \left[\ln(1+r/r_s) - \frac{r/r_s}{1+r/r_s} \right]. \quad (8)$$

Although other mass models (e.g., Hernquist or Burkert density profiles) have been studied within the MAMPOSSt formalism (see Mamon et al. 2013), and LENSTOOL allows to probe different profiles, we adopt the NFW profile to compare our results with those obtained in VMM11. The NFW profile is a spherical density profile and the MAMPOSSt formalism can only model spherical systems. The initial profile is spherical with LENSTOOL, however, but is transformed into a pseudo-elliptical NFW (see Golse & Kneib 2002), as is explained in Jullo et al. (2007), to perform the lensing calculations. Although the simultaneous modeling shares the same spherical parameters, the difference between the pseudo-elliptical and the spherical framework could influence our methodology (see Sect. 4.3).

3. Data

In this section, we present the group SL2S J02140-0535, briefly reviewing our old data sets. Also, we present new data that we have obtained since VMM11. From space, the lens was followed up with the X-ray Multi-Mirror Mission (*XMM-Newton* Space Telescope). Additionally, a new spectroscopic follow up of the arcs and group members were carried out with the Very Large Telescope (VLT).

3.1. SL2S J02140-0535

This group, located at $z_{\text{spec}} = 0.44$, is populated by three central galaxies. We label them as G1 (the brightest group galaxy, BGG), G2, and G3 (see left panel of Fig. 1). The lensed images consist of three arcs surrounding these three galaxies: arc A,

situated north of the deflector, composed by two merging images; a second arc in the east direction (arc B), which is associated with arc A, whereas a third arc, arc C, situated in the south, is singly imaged. SL2S J02140-0535 (first reported by Cabanac et al. 2007) was studied previously using strong lensing by Alard (2009) and both strong and weak lensing by Limousin et al. (2009), and also kinematically by Muñoz et al. (2013).

SL2S J02140-0535 was observed in five filters (u^*, g', r', i', z') as part of the CFHTLS (Canada-France-Hawaii Telescope Legacy Survey)² using the wide-field imager MEGAPRIME (Gwyn 2011), and in the infrared using WIRCam (Wide-field InfraRed Camera, the near-infrared mosaic imager at CFHT) as part of the proposal 07BF15 (P.I. G. Soucail); see Verdugo et al. (2014) for more information. In the right panel of Fig. 1 we show a false-color image of SL2S J02140-0535, combining the two bands J and K_s . Arcs A and C appear mixed with the diffuse light of the central galaxies, and arc B is barely visible in the image. SL2S J02140-0535 was also followed up spectroscopically using FORS 2 at VLT (VMM11).

From space, the lens was observed with the *Hubble* Space Telescope (HST) in snapshot mode (C 15, P.I. Kneib) using three bands, with the ACS camera (F814, F606, and F475).

3.2. New spectroscopic data

Selecting members. We used FORS 2 on VLT with a medium resolution grism (GRIS 600RI; 080.A-0610; P.I. V. Motta) to target the group members (see Muñoz et al. 2013) and a low resolution grism (GIRS 300I; 086.A-0412; P.I. V. Motta) to observe the strongly lensed features. In the later observation, we use one mask with 2×1300 s on-target exposure time. Targets (other than strongly lensed features) were selected via a two-step process. First, we use the T0005 release of the CFHTLS survey (November, 2008) to obtain a photometric redshift-selected catalog, which includes galaxies within ± 0.01 of the redshift of the main lens galaxy. The galaxies in this catalog have colors within $(g-i)_{\text{lens}} - 0.15 < g-i < (g-i)_{\text{lens}} + 0.15$, where $(g-i)_{\text{lens}}$ is the color of the brightest galaxy within the Einstein radius. From this sample, we selected those candidates that were not observed previously. More details will be presented in a forthcoming publication (Motta et al., in prep.).

The spectroscopic redshifts of the galaxies were determined using the Radial Velocity SAO package (Kurtz & Mink 1998) within the IRAF software³. By visual inspection of the spectra, we identify several emission and absorption lines. Then, we determine the redshifts (typical errors are discussed in Muñoz et al. 2013) via cross-correlation between a spectrum and the template spectra of known velocities. To determine the group membership of SL2S J02140-0535, we follow the method presented in Muñoz et al. (2013), which in turn adopted the formalism of Wilman et al. (2005). The group members are identified as follows: we assume initially that the group is located at the redshift of the main bright lens galaxy, z_{lens} , with an initial observed-frame velocity dispersion of $\sigma_{\text{obs}} = 500(1+z_{\text{lens}}) \text{ km s}^{-1}$. After computing the required redshift range for group membership (see Muñoz et al. 2013) and applying a biweight estimator (Beers et al. 1990), the iterative process

² <http://www.cfht.hawaii.edu/Science/CFHLS/>

³ IRAF is distributed by the National Optical Astronomy Observatory, which is operated by the Association of Universities for Research in Astronomy (AURA) under cooperative agreement with the National Science Foundation.

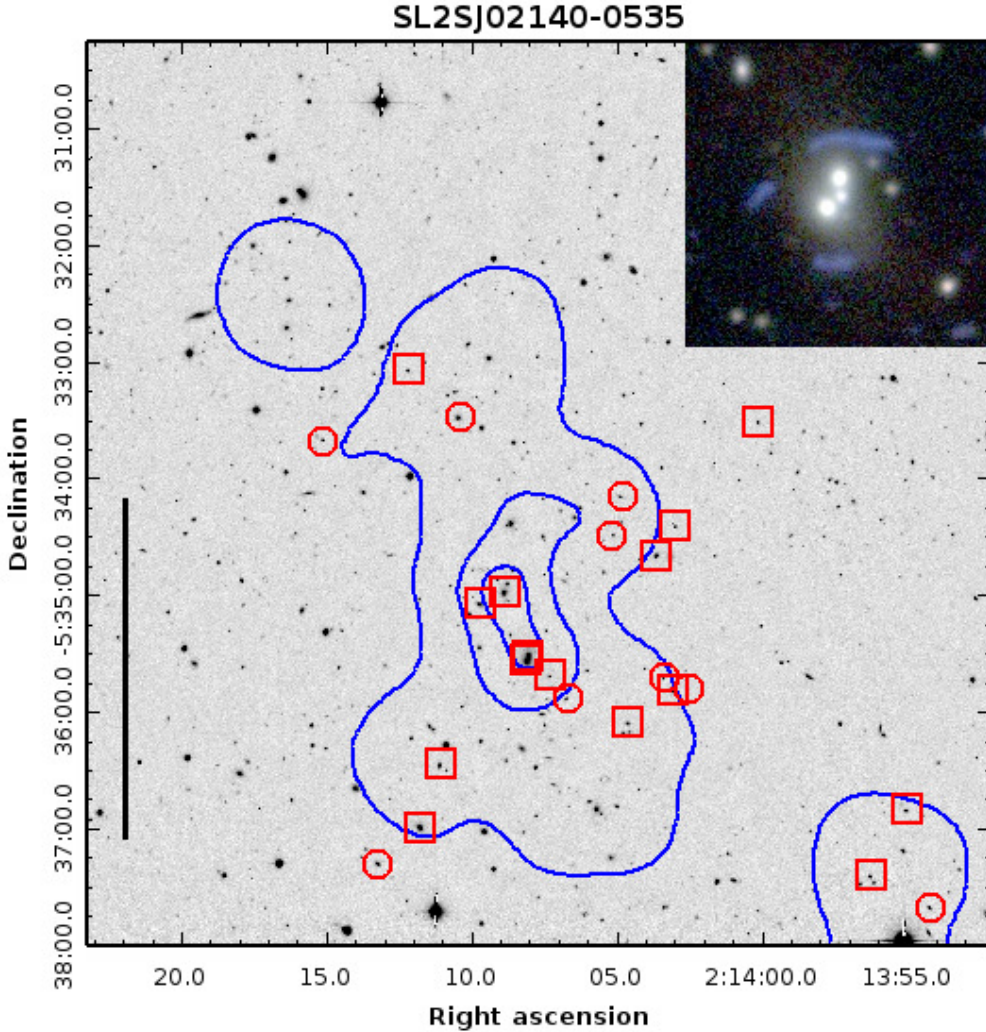


Fig. 2. CFHTLS *i*-band image with the luminosity density contours for SL2S J02140-0535. They represent 1×10^6 , 5×10^6 , and $1.0 \times 10^7 L_{\odot} \text{ kpc}^{-2}$ from outermost to innermost contour, respectively. The red squares and circles show the location of the 24 confirmed members of the group, the squares represent the galaxies previously reported by Muñoz et al. (2013), and the circles represent the new observations. The black vertical line on the left represents 1 Mpc at the group rest frame. The inset in the top-right corner shows a $30'' \times 30''$ CFHTLS false color image of the system.

reached a stable membership solution with 24 secure members and a velocity dispersion of $\sigma = 562 \pm 60 \text{ km s}^{-1}$. These galaxies are shown with red squares and circles in Fig. 2, and their respective redshifts are presented in Table A.1. The squares in Fig. 2 represent the galaxies previously reported by Muñoz et al. (2013). Figure 2 also shows the luminosity contours, which are calculated according to Foëx et al. (2013). Fitting ellipses to the luminosity map, using the task *ellipse* in IRAF, we find that the luminosity contours have position angles equal to $99^{\circ} \pm 9^{\circ}$, $102^{\circ} \pm 2^{\circ}$, and $109^{\circ} \pm 2^{\circ}$, from outermost to innermost contour respectively.

Completeness. Muñoz et al. (2013) presented the dynamical analysis of seven SL2S galaxy groups, including SL2S J02140-0535. They estimated the completeness within 1 Mpc of radius from the center of the group to be 30%. In the present work, as we increased the number of observed galaxies in the field of SL2S J02140-0535, and thus increasing the number of confirmed members (hereafter gal_{spec}), a new calculation is carried out to estimate the completeness as a function of the radius. We first define the color-magnitude cuts to be applied to the photometric catalog of the group, i.e., $0.7 < (r - i) < 0.92$ and $21.44 < m_i < 21.47$. These values correspond to the photometric

properties of the gal_{spec} . We exclude one galaxy because of its color, $(r - i) = 0.45$. Then, we select all the galaxies falling within the photometric ranges (hereafter gal_{phot}), and we estimate the density of field galaxies within the $15' \times 15'$ square arcminutes after excluding a central region of radius 1.3 Mpc, which is the largest distance from the center of the group of gal_{spec} . This density is then converted into an estimated total number of galaxies N_{field} over the full field of view.

Given gal_{spec} , we bin the data and define $N_{\text{spec}}(r_i)$ as the number of confirmed members in the i th radial bin. Thus, the radial profile of the completeness is given by

$$C(r_i) \equiv \frac{N_{\text{spec}}(r_i)}{N_r(r_i) - N_{\text{field},r}(r_i)}, \quad (9)$$

where $N_{\text{field},r}(r_i)$ is the number of field galaxies in the i th bin, and $N_r(r_i)$ is the total number of gal_{phot} present in the i th bin, i.e., its value is the sum of the number of group members and field galaxies. To estimate $N_{\text{field},r}(r_i)$, a Monte Carlo approach is adopted. We randomly draw the positions of the N_{field} galaxies over the whole field of view, and then count the corresponding number of galaxies $N_{\text{field},r}(r_i)$ falling in each bin. Thus, each

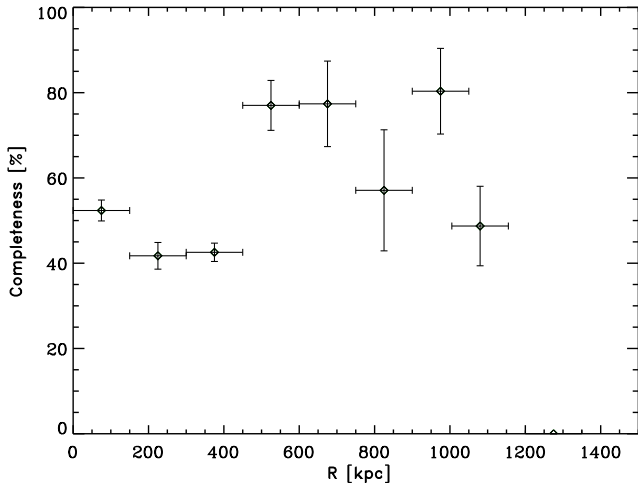


Fig. 3. Completeness as a function of the radius in SL2S J02140-0535. $C \sim 60\%$ roughly constant up to 1 Mpc.

Monte Carlo realization leads to an estimate of the completeness. Finally, we average the $C(r_i)$, after excluding the realizations for which we obtain $N_t(r_i) < N_r(r_i)$ or $C(r_i) > 1$. In Fig. 3 we present the resulting profile and its estimated 1σ deviation, showing a completeness $C \sim 60\%$ that is consistent with a constant profile up to 1 Mpc.

3.3. Multiple images: confirming two different sources

Spectroscopic redshifts. In VMM11 we reported a strong emission line at 7538.4 \AA in the spectra of arc C, that we associated with $[\text{OII}]\lambda 3727$ at $z_{\text{spec}} = 1.023 \pm 0.001$. We obtained new 2D spectra for the arcs consisting in two exposures of 1300 s each. Because of the closeness of the components (inside a radius of $\sim 8''$), the slit length is limited by the relative position of the arcs, making sky-subtraction difficult (see bottom panel of Fig. 4). Most of the 2D spectra show a poor sky subtraction compared to that which we would have obtained using longer slits. However, our new 2D spectra also show the presence of $[\text{OII}]\lambda 3727$ spectral feature and additionally another emission line appears in the spectrum, $[\text{OIII}]\lambda 4958.9$. In the same Fig. 4 (top right panel) we show the spectrum and indicated some characteristic emission lines, along with a few sky lines. We compare the spectrum with a template of a starburst galaxy from Kinney et al. (1996), shifted at $z = 1.02$. After performing a template fitting using RVSAO, we obtain $z_{\text{spec}} = 1.017 \pm 0.001$, confirming our previously reported value.

On the other hand, in our previous work, we did not find any spectroscopic features in the arcs A and B owing to the poor signal to noise. In the top left panel of Fig. 4 we show the new obtained spectrum of arc A. It reveals a weak (but still visible) emission line at 9795.3 \AA . This line probably corresponds to $[\text{OII}]\lambda 3727$ at $z \sim 1.6$. We do not claim a clear detection, as this region of the spectrum is affected by sky emission lines (as we discuss above), but it is worth noting that the photometric redshift estimate supports this detection (see Fig. 5). Assuming emission from $[\text{OII}]\lambda 3727$ and applying a Gaussian fitting, we obtain $z_{\text{spec}} = 1.628 \pm 0.001$. This feature is not present in the spectrum of arc B, since arc B is almost one magnitude fainter than arc A. Furthermore, this line is not present in the spectrum of arc C, which confirms the previous finding of VMM11, i.e., system AB and arc C come from two different sources.

Photometric redshifts. As a complementary test, and to extend the analysis presented in VMM11, we calculate the photometric redshifts of arcs A, B, and C using the HyperZ software (Bolzonella et al. 2000), adding the J and K_s -bands to the original bands (u^* , g' , r' , i' , z'). The photometry in J and K_s -bands was performed with the IRAF package *apphot*. We employed polygonal apertures to obtain a more accurate flux measurement of the arcs. For each arc, the vertices of the polygons were determined using the IRAF task *polymark*, and the magnitudes inside these apertures were computed by the IRAF task *polyphot*. The results are presented in Table A.2.

It is evident in the right panel of Fig. 1 that the gravitational arcs are contaminated by the light of the central galaxies. To quantify the error in our photometric measurements, in the J and K_s -bands we proceed as follows. We subtract the central galaxies of the group and follow the procedure described in McLeod et al. (1998), that is, we fit a galaxy profile model convolved with a point spread function (PSF); de Vaucouleurs profiles were fitted to the galaxies with synthetic PSFs. After the subtraction, we run the IRAF task *polyphot* again. The errors associated with the fluxes are defined as the quadratic sum of the errors on both measurements.

The photometric redshifts for the arcs were estimated from the magnitudes reported in Table A.2, and those reported in VMM11. We present the output probability distribution function (PDF) from HyperZ in Fig. 5. We note in the same figure that the K_s -band data do not match with the best-fit spectral energy distribution; this is probably related to the fact that the photometry of the arcs is contaminated by the light of the central galaxies. Arc C is constrained to be at $z_{\text{phot}} = 0.96 \pm 0.07$, which is in good agreement with the $z_{\text{spec}} = 1.017 \pm 0.001$ reported above. The multiple imaged system constituted by arcs A and B have $z_{\text{phot}} = 1.7 \pm 0.1$ and $z_{\text{phot}} = 1.6 \pm 0.2$, respectively. The photometric redshift of arc A is in agreement with the identification of the emission line as $[\text{OII}]\lambda 3727$ at $z_{\text{spec}} = 1.628 \pm 0.001$.

To summarize, the spectroscopic and photometric data both confirm the results of VMM11, namely, the system formed by arcs A and B, and the single arc C, originate from two different sources, the former at $z_{\text{spec}} = 1.628$ and the latter at $z_{\text{spec}} = 1.017$.

3.4. X-ray data

We observed SL2S J02140-0535 with XMM as part of an X-ray follow-up program of the SL2S groups to obtain an X-ray detection of these strong-lensing selected systems and to measure the X-ray luminosity and temperature (Gastaldello et al., in prep.). SL2S J02140-0535 was observed by XMM for 19 ks with the MOS detector and for 13 ks with the pn detector. The data were reduced with SAS v14.0.0, using the tasks *emchain* and *epchain*. We considered only event patterns 0–12 for MOS and 0–4 for pn, and the data were cleaned using the standard procedures for bright pixels, hot columns removal, and pn out-of-time correction. Periods of high backgrounds due to soft protons were filtered out leaving an effective exposure time of 11 ks for MOS and 8 ks for pn.

For each detector, we create images with point sources in the 0.5–2 keV band. The point sources were detected with the task *edetect_chain*, and masked using circular regions of $25''$ radius centered at the source position. The images were exposure corrected and background subtracted using the XMM-Extended Source Analysis Software (ESAS). The XMM image in the 0.5–2 keV band of the field of SL2S J02140-0535 is shown in Fig. 6.

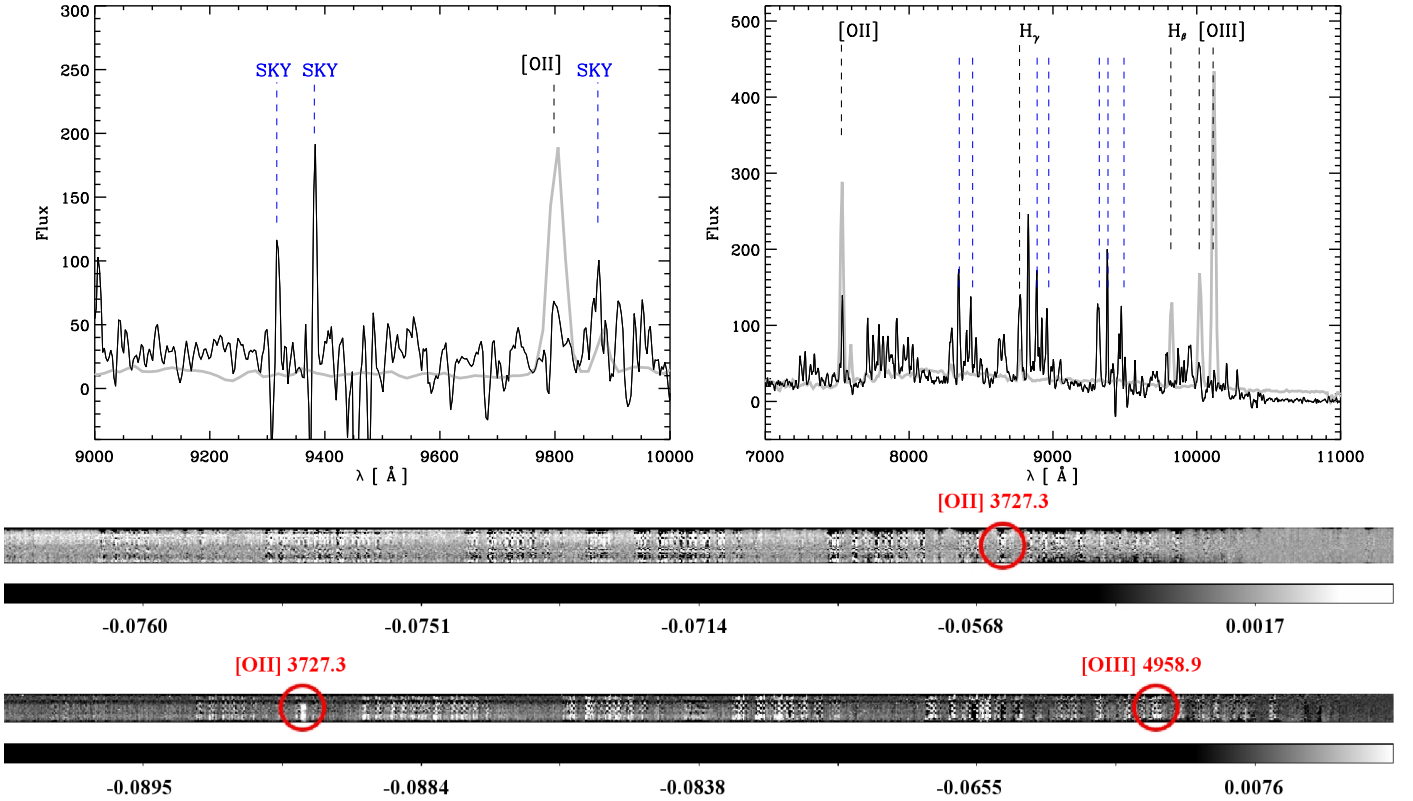


Fig. 4. *Top panel:* as mentioned in Sect. 3.3, the slit length was limited by the position of the arcs, hence producing poor sky subtraction. *Left:* observed spectrum of arc A (black continuous line). In gray we depict a starburst template from Kinney et al. (1996) shifted at $z = 1.628$, and we indicate a possible [OII] λ 3727 emission line, and some sky lines, in blue (see Sect. 3.3). *Right:* observed spectrum of arc C (black continuous line), as before we depicted in gray the starburst template from Kinney et al. (1996), but shifted at $z = 1.02$. We indicated some characteristic emission lines, along with the sky lines in blue, but we omit for clarity the labels of the last lines. *Bottom panel:* two-dimensional spectra of arc A (with a color bar in arbitrary units). We note the [OII] λ 3727 emission line. Below, we show the two-dimensional spectra of arc C, with two emission lines clearly identified: [OII] λ 3727, and [OIII] λ 4958.9.

The X-ray peak is spatially coincident with the bright galaxies inside the arcs, and the X-ray isophotes are elongated in the same direction as the optical contours (see discussion in Sect. 5). The quality of the X-ray snapshot data is not sufficient for a detailed mass analysis assuming hydrostatic equilibrium (e.g., Gastaldello et al. 2007). In this case, the mass can only be obtained adopting a scaling relation, such as a mass-temperature relation (e.g., Gastaldello et al. 2014). Therefore this mass determination is not of the same quality as that obtained with our lensing and dynamical information. In addition, as we discuss in Sect. 5, we need to be very cautious when assuming scaling relations for strong lensing clusters. We only make use of the morphological information provided by the X-ray data hereinafter.

4. Results

In this Section, we apply the formalism outlined in Sect. 2 on SL2S J02140-0535, using the data presented in Sect. 3. In the subsequent analysis, SL model refers to the SL modeling, Dyn model to the dynamical analysis, and SL+Dyn model to the combination of both methods.

4.1. SL model

As we discussed in VMM11, the system AB shows multiple sub-components (surface brightness peaks) that can be conjugated as different multiple image systems, increasing the number of constraints as well as the degrees of freedom (for a fixed number of

free parameters). Thus, the AB system is transformed into four different systems, conserving C as a single-image arc (see Fig. 4 in VMM11). In this way, our model has five different arc systems in the optimization procedure, leading to 16 observational constraints. Based on the geometry of the multiple images, the absence of structure in velocity space, and the X-ray data, we model SL2S J02140-0535 using a single large-scale mass clump accounting for the dark matter component. This smooth component is modeled with a NFW mass density profile, characterized by its position, projected ellipticity, position angle, scale radius, and concentration parameter. The position, (X, Y) ranges from $-5''$ and $5''$, the ellipticity from $0 < \epsilon < 0.7$, and the position angle from 0 to 180 deg. The parameters r_s and c_{200} are free to range between $50 \text{ kpc} \leq r_s \leq 500 \text{ kpc}$, and $1 \leq c_{200} \leq 30$, respectively.

Additionally, we add three smaller-scale clumps that are associated with the galaxies at the center of SL2S J02140-0535. We model them as follows: as in VMM11, we assume that the stellar mass distribution in these galaxies follows a pseudo-isothermal elliptical mass distribution (PIEMD). A clump modeled with this profile is characterized by the following seven parameters: the center position, (X, Y) , the ellipticity ϵ , the position angle θ , and the parameters, σ_0 , r_{core} , and r_{cut} (see Limousin et al. 2005; Elíasdóttir et al. 2007, for a detailed discussion of the properties of this mass profile). The center of the profiles, ellipticity, and position angle are assumed to be the same as for the luminous components. The remaining parameters in the small-scale clumps, namely, σ_0 , r_{core} , and r_{cut} , are scaled as a function of their galaxy luminosities (Limousin et al. 2007),

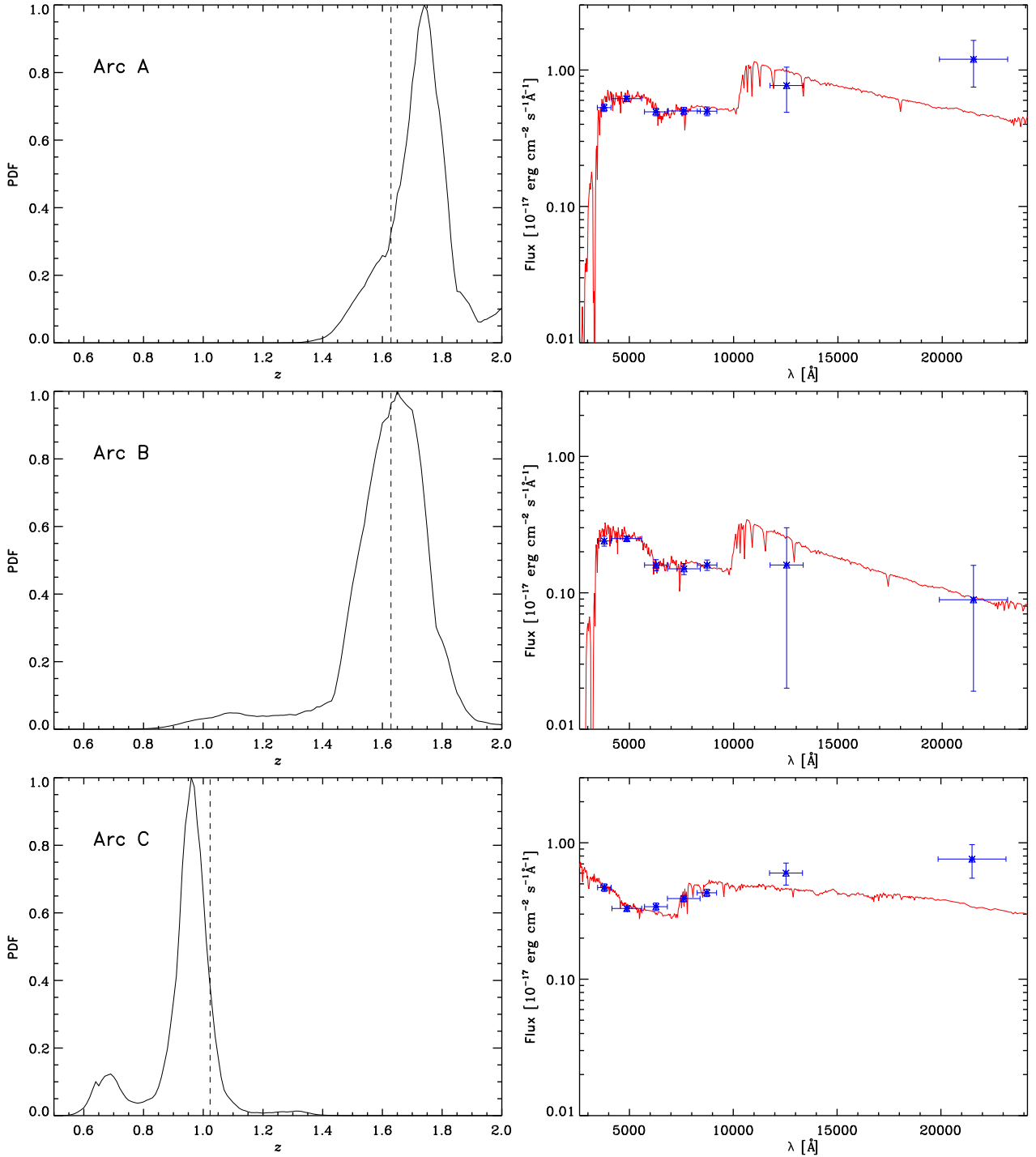


Fig. 5. *Left column:* photometric redshift PDF for the selected arcs (see text). The dashed vertical lines correspond to the spectroscopic value. *Right column:* best-fit spectral energy distribution. Points represent the observed CFHTLS broadband magnitudes, and J and K_s from WIRCam. Vertical and horizontal error bars correspond to photometric error and wavelength range of each filter, respectively.

using as a scaling factor the luminosity L^* associated with the g -band magnitude of galaxy G1 (see Fig. 1),

$$r_{\text{core}} = r_{\text{core}}^* \left(\frac{L}{L^*} \right)^{1/2},$$

$$r_{\text{cut}} = r_{\text{cut}}^* \left(\frac{L}{L^*} \right)^{1/2},$$

$$\sigma_0 = \sigma_0^* \left(\frac{L}{L^*} \right)^{1/4},$$
(10)

setting r_{core}^* and σ_0^* to be 0.15 kpc and 253 km s^{-1} , respectively. This velocity dispersion is obtained from the LOS velocity dispersion of galaxy G1, with the use of the relation reported by Elíasdóttir et al. (2007). This LOS velocity dispersion has a value of $\sigma_{\text{los}}^* = 215 \pm 34 \text{ km s}^{-1}$, which is computed from the G -band absorption line profile (see VMM11). The last parameter, r_{cut}^* , is constrained from the possible stellar masses for galaxy G1 (VMM11), which in turn produce an interval of 1–6 kpc.

Our model is computed and optimized in the image plane with the seven free parameters discussed above, namely

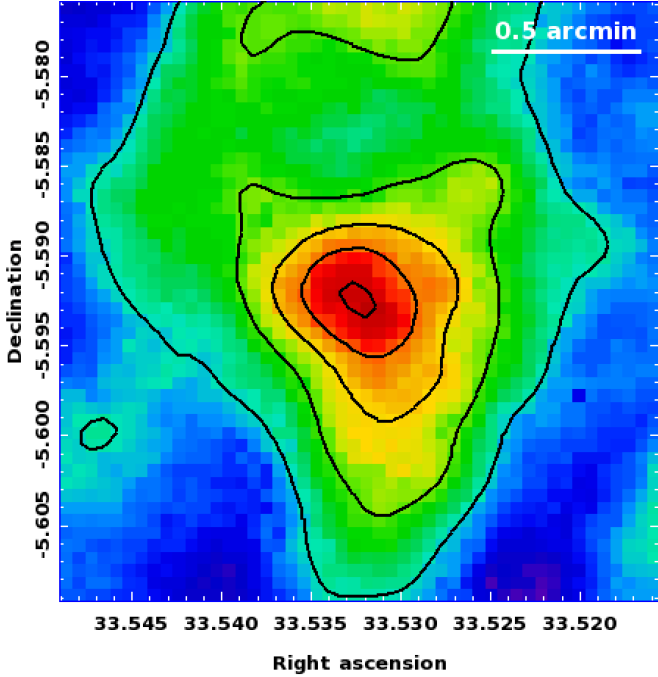


Fig. 6. Adaptively smoothed image of SL2S J02140-0535 in the 0.5–2.0 keV band. The X-ray contours in black are linearly spaced from 5 to 20 cts/s/deg².

$\{X, Y, \epsilon, \theta, r_s, c_{200}, r_{\text{cut}}^*\}$. The first six parameters characterize the NFW profile, and the last parameter is related to the profile of the central galaxies. All the parameters are allowed to vary with uniform priors. We show the results (the PDF) of the SL analysis *only* in top panel of Fig. 7, and the best-fit parameters are given in Table 1. Additionally, in Fig. 8 we show the plots of r_s vs. r_{200} , since these plots provide us with a better understanding of how unconstrained is the lens model at large scale (see next section), and also to be consistent with the form in which the plots are presented in Mamon et al. (2013). Figure 9 shows the results for the concentration and M_{200} , from which we can gain insight for the mass constraint.

4.2. Dyn model

Since we only have 24 group members, we assume that the group has an isotropic velocity dispersion (i.e., $\beta = 0$ in Eq. (3)). This parameter β might influence the parameters of the density profile (r_s and c_{200}), however, it is not possible to constrain β with only 24 galaxies. Besides, it is beyond the scope of this work to analyze its effect over the parameters. We defer this analysis to a forthcoming paper, in which we apply the method to a galaxy cluster with a greater number of members.

The Jeans equation of dynamical equilibrium, as implemented in MAMPOSSt, is only valid for values of $r \lesssim 2r_{\text{vir}} \approx 2.7r_{200}$ (Falco et al. 2013). Thus, before running MAMPOST, we estimate the virial radius, r_{200} , of SL2S J02140-0535. From the scale radius and the concentration values reported in VMM11 we find the virial radius to be $r_{200} = 1 \pm 0.2$ Mpc. This value is considerably smaller than the previously reported value of 1.42 Mpc by Lieu et al. (2016)⁴. Table A.1 shows that there are 3 galaxies with $1 \text{ Mpc} < R < 1.4 \text{ Mpc}$, i.e., within $1.4r_{200}$, which seems sufficiently small to keep in our analysis. The galaxy members lie between 7.9 kpc to 1392.3 kpc with a mean distance of

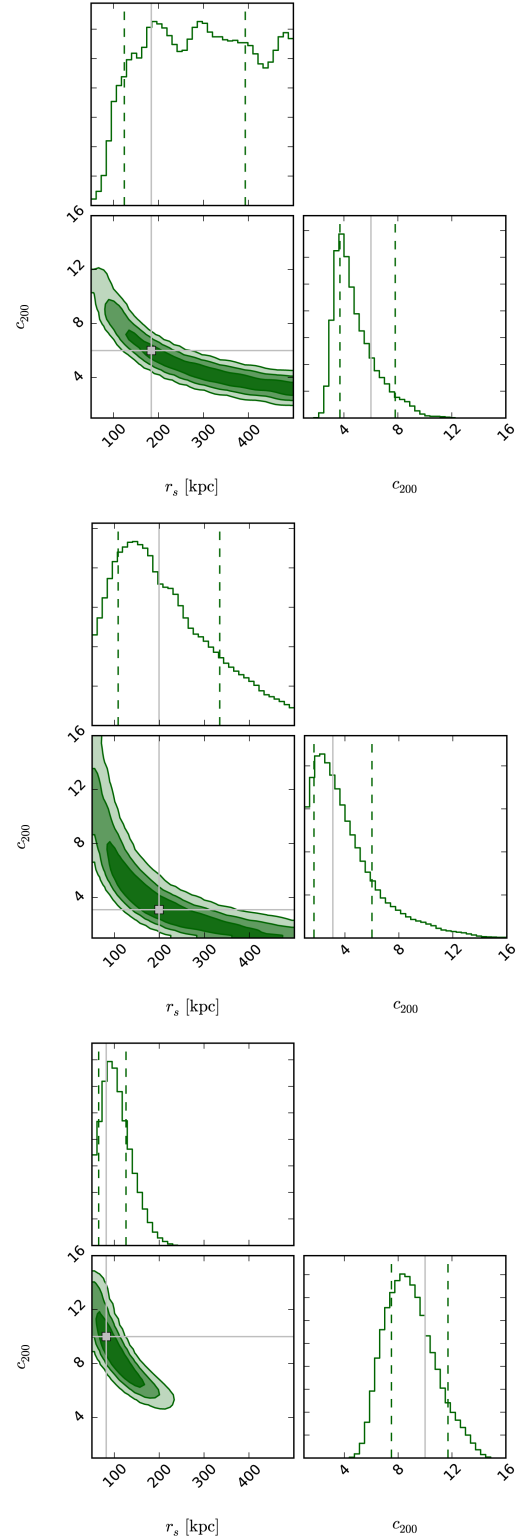


Fig. 7. PDFs and contours of the parameters c_{200} and r_s . The three contours stand for the 68%, 95%, and 99% confidence levels. The values obtained for our best-fit model are indicated with a gray square and with vertical lines in the 1D histograms; the asymmetric errors are presented in Table 1. *Top panel:* results from the SL model. *Middle panel:* results from the Dyn model. *Bottom panel:* results from the SL+Dyn model.

650 kpc from the center. Given the scarce number of members in SL2S J02140-0535 we keep this galaxy in our calculations.

⁴ SL2S J02140-0535 is identified as XLSSC 110 in the XXL Survey.

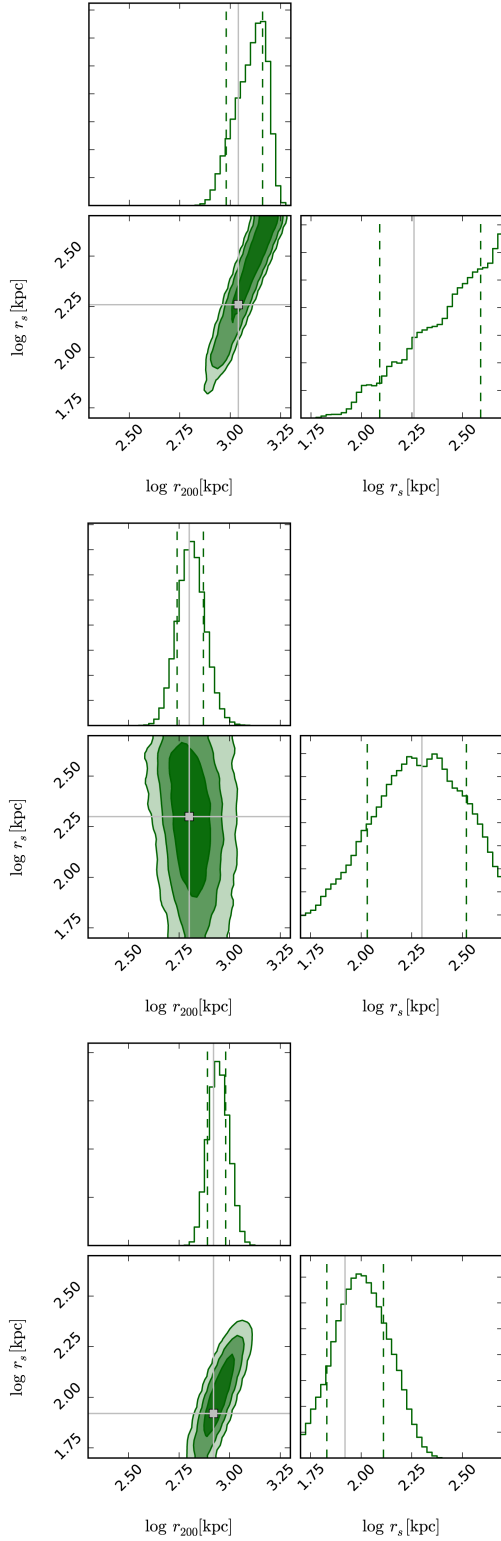


Fig. 8. PDFs and contours of the parameters $\log r_s$ and $\log r_{200}$. The three contours stand for the 68%, 95%, and 99% confidence levels. The values obtained for our best-fit model are indicated with a gray square and with vertical lines in the 1D histograms; the asymmetric errors are presented in Table 1. *Top panel:* results from the SL model. *Middle panel:* results from the Dyn model. *Bottom panel:* results from the SL+Dyn model.

To further simplify our analysis, we assume that the completeness, as a function of the radius, is a constant (see Sect. 3.2). Also, we assume that both the tracer scale radius (r_v in

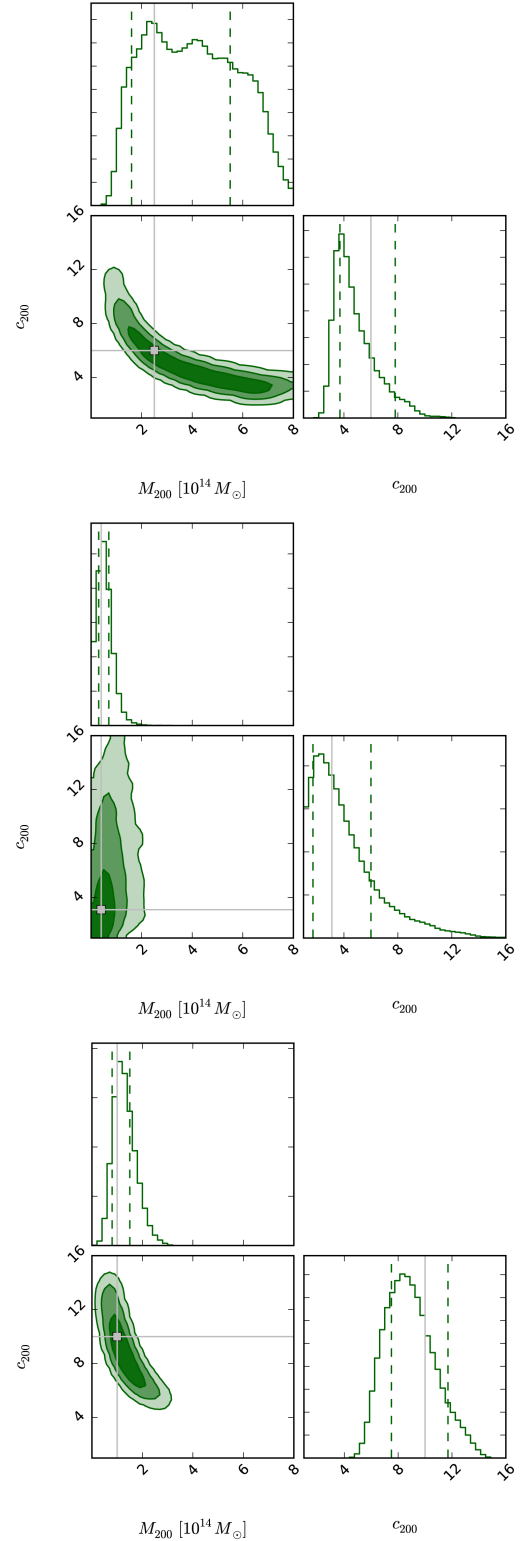


Fig. 9. PDFs and contours of the parameters c_{200} and M_{200} . The three contours stand for the 68%, 95%, and 99% confidence levels. The values obtained for our best-fit model are shown with a gray square and with vertical lines in the 1D histograms; the asymmetric errors are presented in Table 1. *Top panel:* results from the SL model. *Middle panel:* results from the Dyn model. *Bottom panel:* results from the SL+Dyn model.

Mamon et al. 2013) and the dark matter scale radius r_s are the same, that is, the total mass density profile is forced to be proportional to the galaxy number density profile: *we assume that*

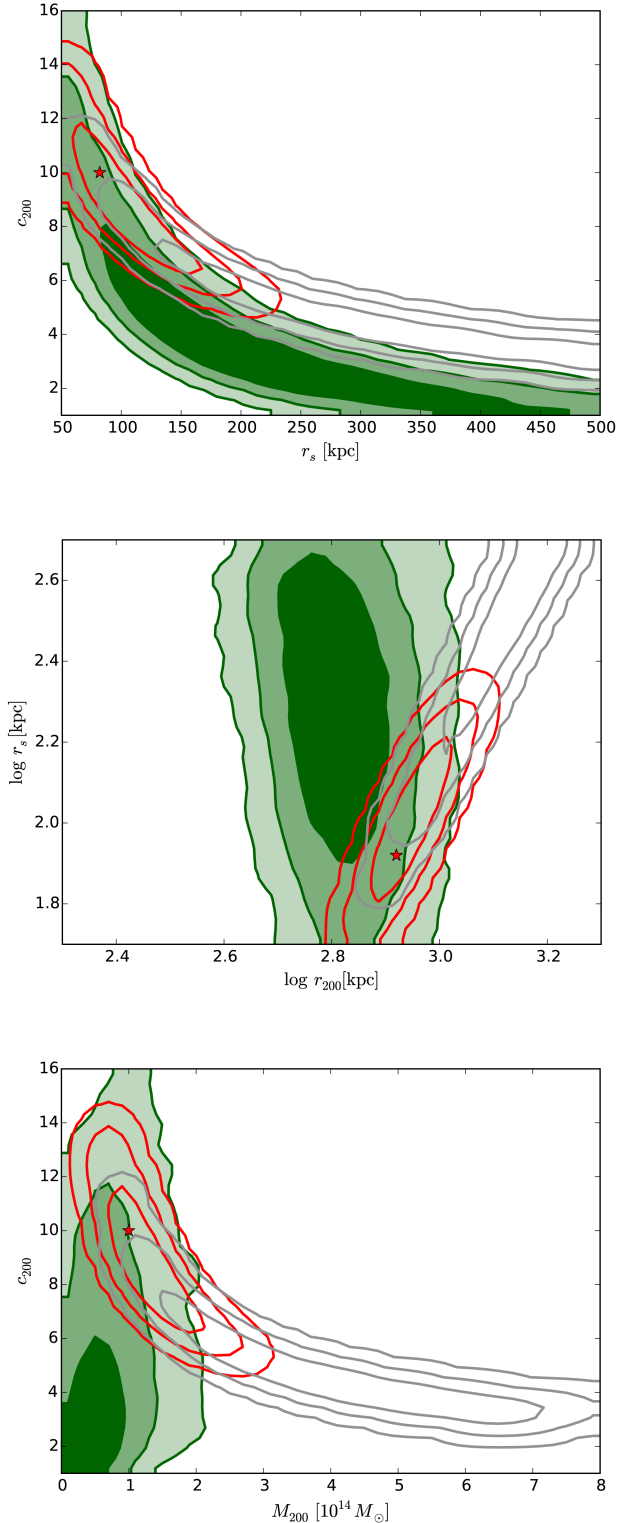


Fig. 10. Joint distributions. *Top panel:* scale radius and concentration. *Middle panel:* $\log r_s$ and $\log r_{200}$. *Bottom panel:* concentration and M_{200} . Green-filled contours are 1, 2, and 3σ regions from the Dyn model. Gray contours stand for the 68, 95, and 99% confidence levels for the SL model. Red contours is the result of the SL+Dyn model with the best solution depicted with a red star.

mass follows light. As we see in the next section, this is not a bad assumption. Therefore our model only has two free parameters, namely, the scale radius, r_s , and the concentration, c_{200} . These parameters have broad priors with $50 \text{ kpc} \leq r_s \leq 500 \text{ kpc}$ and

$1 \leq c_{200} \leq 30$. The middle panels of Figs. 7–9 show the PDF for this model; the best values of the fit are presented in Table 1.

4.3. SL+Dyn model

The main difference of our work, when compared to previous works (e.g., Biviano et al. 2013; Guennou et al. 2014) is that we apply a joint analysis, seeking a solution that is consistent with both the SL and the dynamical methods, maximizing the total likelihood. In the bottom panels of Figs. 7–9, we show the PDF of this combined model. The best-fit values are presented in Table 1.

From the figures it is clear that tension exists between the results from the SL model and the Dyn model; the models are in disagreement at 1σ level. The discrepancy is related to the oversimplified assumption of the spherical Dyn model. Although in some cases it is expected to recover a spherical mass distribution at large scale (e.g., Gavazzi 2005), at smaller scale, i.e., at strong lensing scales, the mass distribution tends to be aspherical. In order to investigate such tension between the results, we construct a strong lensing spherical model with the same constrains as before. We show the results in the left panel of Fig. B.1. It is clear that in this case the model is not well constrained, a natural result given the lensing images in SL2S J02140-0535. However, the comparison between the joint distributions in the top panel of Fig. 10 and the one in the right panel of Fig. B.1 shows that the change in the contours is small, which indicates that the assumption of spherical symmetry has little impact on the final result (the agreement between contours is related to the shallow distribution from LENSTOOL, which produces a joint distribution that follows the top edge of the narrower MAMPOSSt distribution). Also, the combined model has a bimodal distribution (see right panel of Fig. B.1), with higher values of concentration inherited from the lensing constraints.

A possible way to shed more light on the systematic errors of our method is to test it with simulations. For example, we can compare spherical and non spherical halos or quantify the bias when a given mass distribution is assumed and the underlying mass distribution is different. Such an analysis is out of the scope of the present work, however, it could be performed in the near future since the state-of-the-art simulations on lensing galaxy clusters have reached an incredible quality (e.g., Meneghetti et al. 2016).

5. Discussion

5.1. Lensing and dynamics as complementary probes

From Figs. 7 and 8, it is clear that SL model is not able to constrain the NFW mass profile. This result is expected since SL constraints are available in the very central part of SL2S J02140-0535, whereas the scale radius is generally several times the SL region. The degeneracy between c_{200} and r_s (or r_s and r_{200}), which is related to the mathematical definition of the gravitational potential, was previously discussed in VMM11. This degeneracy commonly occurs in lensing modeling (e.g., Jullo et al. 2007). From the SL model we obtain the following values: $r_s = 184_{-60}^{+209} \text{ kpc}$ and $c_{200} = 6.0_{-2.3}^{+1.8}$. Thus, the model is not well constrained (similarly, we obtain a value of $\log r_{200} = 3.04_{-0.06}^{+0.12} \text{ kpc}$ for the virial radius). Moreover, the mass M_{200} is not constrained in the SL model (see Fig. 9).

The same conclusion holds when considering dynamics only, i.e., in the Dyn model the constraints are so broad that both parameters (r_s and c) can be considered as unconstrained (see

Table 1. Best-fit model parameters.

Parameter	SL model		Dyn model		SL+Dyn model	
	group	L^*	group	L^*	group	L^*
X^\dagger ["]	$1.2^{+0.2}_{-0.4}$	–	–	–	0.9 ± 0.2	–
Y^\dagger ["]	$0.7^{+0.9}_{-0.4}$	–	–	–	$1.5^{+0.4}_{-0.3}$	–
$\epsilon^{\dagger\dagger}$	$0.23^{+0.04}_{-0.05}$	–	–	–	$0.298^{+0.002}_{-0.045}$	–
θ [°]	$111.2^{+1.6}_{-1.3}$	–	–	–	$111.1^{+1.4}_{-1.3}$	–
r_s [kpc]	184^{+209}_{-60}	–	199^{+135}_{-91}	–	82^{+44}_{-17}	–
$\log r_{200}$ [kpc]	$3.04^{+0.12}_{-0.06}$	–	$2.80^{+0.07}_{-0.06}$	–	$2.92^{+0.06}_{-0.03}$	–
c_{200}	$6.0^{+1.8}_{-2.3}$	–	$3.1^{+2.9}_{-1.4}$	–	$10.0^{+1.7}_{-2.5}$	–
M_{200} [$10^{14} M_\odot$]	$2.5^{+3.0}_{-0.9}$	–	$0.4^{+0.3}_{-0.1}$	–	$1.0^{+0.5}_{-0.2}$	–
r_{core} [kpc]	–	[0.15]	–	–	–	[0.15]
r_{cut} [kpc]	–	$2.6^{+2.1}_{-1.1}$	–	–	–	$2.4^{+2.1}_{-1.0}$
σ_0 [km s $^{-1}$]	–	[253]	–	–	–	[253]
$\chi^2_{\text{d.o.f.}}$	–	0.1	–	–	–	0.9

Notes. ^(†) The position in arc seconds relative to the BGG. ^(††) The ellipticity is defined as $\epsilon = (a^2 - b^2)/(a^2 + b^2)$, where a and b are the semimajor and semiminor axis, respectively, of the elliptical shape. The first column identifies the model parameters. In Cols. 2–10 we provide the results for each model, using square brackets for those values which are not optimized. Columns L^* indicate the parameters associated to the small-scale clumps. Asymmetric errors are calculated following [Andrae \(2010\)](#) and [Barlow \(1989\)](#).

middle panel of Fig. 7 and middle panel of Fig. 8). In this case we obtained a scale radius of $r_s = 199^{+135}_{-91}$ kpc, and a concentration of $c_{200} = 3.1^{+2.9}_{-1.4}$. However, in this case the scale radius is slightly more constrained when compared to the value obtained with the SL model. This is due to employing the distribution of the galaxies to estimate the value when using MAMPOSSt. Furthermore, the virial radius r_{200} is even more constrained with $\log r_{200} = 2.80^{+0.07}_{-0.06}$ kpc. These weak constraints are related to the small number of galaxy members (24) in the group. Nonetheless, even with the low number of galaxies, the error in our mass M_{200} (see Table 1 and Fig. 9) is approximately a factor of two, i.e., ~ 0.3 dex, which is consistent with the analysis of [Old et al. \(2015\)](#).

Interestingly, when combining both probes into the SL+Dyn model, it is possible to constrain both the scale radius and the concentration parameter. The SL model is sensitive to the mass distribution at inner radii (within 10"), whereas the dynamics provide constraints at larger radius (see bottom panels of Figs. 7 and 8). For this model, we find the values $r_s = 82^{+44}_{-17}$ kpc, $c_{200} = 10.0^{+1.7}_{-2.5}$, and $M_{200} = 1.0^{+0.5}_{-0.2} \times 10^{14} M_\odot$. The errors in the mass, although large, are smaller when compared to the two previous models, by a factor of 2.2 (0.34 dex) and by a factor of 1.4 (0.15 dex), for the SL model and Dyn model, respectively.

To highlight how the combined SL+Dyn model is better constrained than both the SL model and the Dyn model, we show in Fig. 10 the 2D contours for $c_{200} - r_s$, $\log r_s - \log r_{200}$, and $c_{200} - M_{200}$, for the three models discussed in this work. We note the overlap of the solutions of the SL model and the Dyn model, and the stronger constraints of the SL+Dyn model. The shift in the solutions for the SL+Dyn model shown in Fig. 7, i.e., r_s is much lower (greater c_{200}) than the values for the SL model and Dyn model, can be understood in light of the discussion presented in Sect. 4.3, and additionally explained with the analysis of Fig. 10. On the one hand, the tension between both results (lack of agreement between solutions at 1σ) is the result of assuming a spherical mass distribution in the Dyn model. On the

other hand, the joint solution of SL+Dyn model (red contours) is consistent with the region where both the SL model and the Dyn model overlap.

5.2. Mass, light, and gas

We find that the center of the mass distribution coincides with that of the light (see Fig. 11). In [VMM11](#) we showed that the position angle of the halo was consistent with the orientation of the luminosity contours and the spatial distribution of the group-galaxy members. In the present work we confirm these results. The measured position angles of the luminosity contours presented in Figs. 2 and 11 (the values are equal to $109^\circ \pm 2^\circ$, $102^\circ \pm 2^\circ$, and $99^\circ \pm 9^\circ$, from innermost to outermost contour), agree with the orientation of the position angle of $111.1^{+1.4}_{-1.3}$ deg of the halo.

In addition to the distribution of mass and light, Fig. 11 shows the distribution of the gas component of SL2S J02140-0535, which was obtained from our X-ray analysis. The agreement between these independent observational tracers of the three group constituents (dark matter, gas, and galaxies) is remarkable. This supports a scenario in which the mass is traced by light and argues in favor of a non-disturbed structure, i.e., the opposite from a disturbed structure, where the different tracers are separated, such as in the Bullet Group ([Gastaldello et al. 2014](#)) or as in the more extreme cluster mergers (e.g., [Bradač et al. 2008](#); [Randall et al. 2008](#); [Menanteau et al. 2012](#)).

5.3. Comparison with our previous work

In [VMM11](#) we analyzed SL2S J02140-0535 using the dynamical information to constrain and build a reliable SL model for this galaxy group. However, it is not expected to have a perfect agreement between the best value of the parameters computed in the former work and the values reported in the present paper, mainly because of the difference in methodologies, and the new

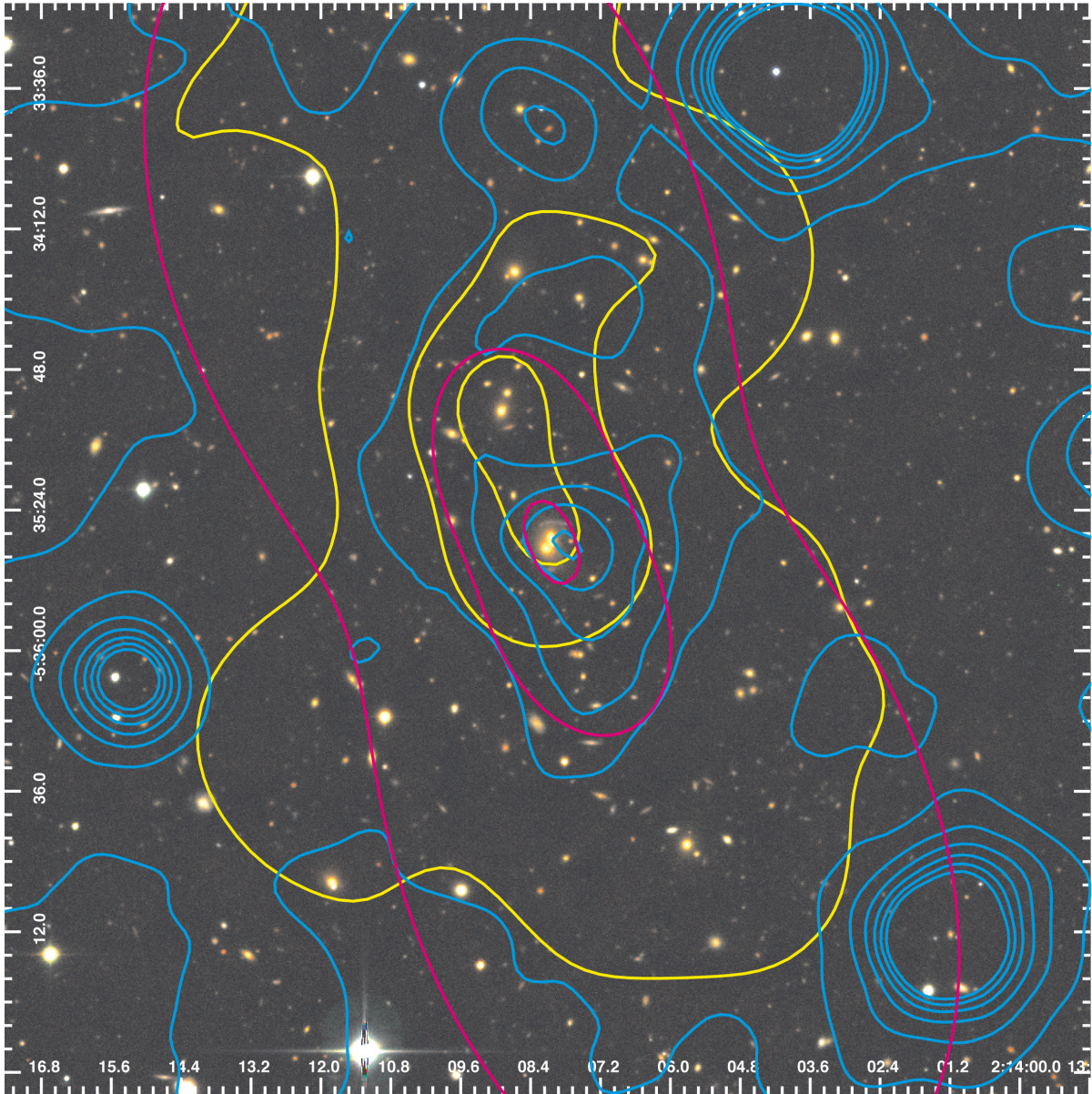


Fig. 11. Distribution of mass, gas, and galaxies in SL2S J02140-0535, as reflected by the total mass derived from the combined lensing and dynamics analysis (magenta), the adaptively smoothed i -band luminosity of group galaxies (yellow), and the surface brightness from XMM observations (blue). The lensing mass contours (magenta lines) correspond to projected surface densities of 0.2×10^9 , 1.2×10^9 , and $7.4 \times 10^9 M_{\odot} \text{arcsec}^{-2}$. The size of the image is 1.5×1.5 Mpc.

spectroscopic number of members reported in this work. For example, in [VMM11](#) we found the values $c_{200} = 6.0 \pm 0.6$, and $r_s = 170 \pm 18$ kpc, whereas for our SL+Dyn model, we find the values $c_{200} = 10.0^{+1.7}_{-2.5}$, and $r_s = 82^{+44}_{-17}$ kpc. However, the latter values lie within the range predicted by [VMM11](#) with dynamics (cf. $2 < c_{200} < 8$, and $50 \text{ kpc} < r_s < 200 \text{ kpc}$). Furthermore, those ranges need to be corrected using the new velocity dispersion. This correction shifts the confidence interval to higher values in c_{200} , and lower values in r_s , thus improving the agreement between both works.

Additionally, as presented in Sect. 3, we found the velocity dispersion to be $\sigma = 562 \pm 60 \text{ km s}^{-1}$ with the 24 confirmed members. This velocity dispersion is in good agreement with the velocity reported in [VMM11](#), $\sigma = 630 \pm 107 \text{ km s}^{-1}$, which was computed with only 16 members, and it is also in agreement with the value obtained from weak lensing analysis ($\sigma = 638^{+101}_{-152} \text{ km s}^{-1}$, [Foëx et al. 2013](#)). Besides, the projected

virial radius, $\tilde{R}_v = 0.9 \pm 0.3 \text{ Mpc}$ (the projected harmonic mean radius, e.g., [Irgens et al. 2002](#)), is also consistent with the value reported in our previous work, $\tilde{R}_v = 0.8 \pm 0.3 \text{ Mpc}$, which was used in [VMM11](#) to estimate the priors in the SL modeling.

5.4. An over concentrated galaxy group?

The concentration value of SL2S J02140-0535 is clearly higher than the expected from Λ CDM numerical simulations. Assuming a dark matter halo at $z = 0.44$ with $M_{200} \approx 1 \times 10^{14} M_{\odot}$, the concentration is $c_{200} \approx 4.0$ (computed with the procedures of [Duffy et al. 2008](#)). SL2S J02140-0535 was also studied by [Foëx et al. \(2014\)](#), who were able to constrain the scale radius and concentration parameters of galaxy groups using stacking techniques. SL2S J02140-0535, with an Einstein radius of $\sim 7''$, belongs to their stack “R3”, which was characterized to have

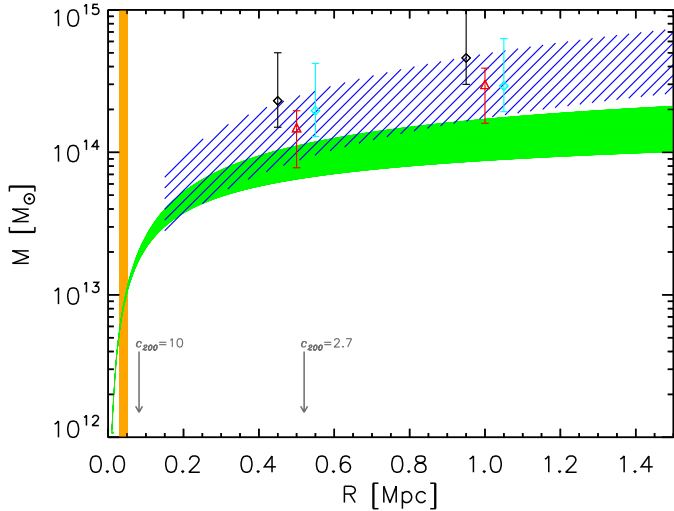


Fig. 12. Two-dimensional projected mass as a function of the radius measured from the BGG. The green and blue shaded areas corresponds to the mass profile within 1σ errors for the SL+Dyn model and the weak lensing model reported in VMM11, respectively. The orange-shaded region shows the area where the arc systems lie. The two red triangles with error bars show two estimates (at 0.5 and 1 Mpc) of the weak lensing mass from Foëx et al. (2013). Black diamonds (shifted in $r-0.05$ for clarity) show the predicted mass calculated from the work of Lieu et al. (2016). Cyan diamonds (shifted in $r+0.05$ for clarity) are the masses calculated from Lieu et al. (2016) data, but assuming $c_{200} = 10$ (see text). We also depict with two arrows, our best r_s (for $c_{200} = 10$), and the r_s (for $c_{200} = 2.7$) reported in Lieu et al. (2016).

$c_{200} \sim 10$ and $M_{200} \sim 10^{14} M_{\odot}$. Those values are in agreement with our computed values. As discussed thoroughly in Foëx et al. (2014), this high concentration seems to be due to an alignment of the major axis with the LOS. Even in the case in which a cluster displays mass contours elongated in the plane of the sky, the major axis could be near the LOS (see for example Limousin et al. 2007, 2013).

Finally, Fig. 12 shows the comparison between the mass obtained from our SL+Dyn model with the weak lensing mass previously obtained by VMM11. Both models overlap up to ~ 1 Mpc; this is consistent with the scarce number of galaxies located at radii larger than 1 Mpc. Therefore, the dynamic constraints are not strong, also the weak lensing mass estimate can be slightly overestimated at large radii, since the mass is calculated assuming a singular isothermal sphere. The red triangles in Fig. 12 show two estimates (at 0.5 and 1 Mpc) of the weak lensing mass, which are calculated using the values reported in Foëx et al. (2013). Those values are also consistent with the above-mentioned measurements. For comparison, we show the predicted mass (at 0.5 and 1 Mpc) derived from Lieu et al. (2016) in black diamonds. The discrepancy between these values and our values calculated from lensing arises from the fact that Lieu et al. (2016) set the cluster concentration from a mass-concentration relation derived from N-body simulations, thus obtaining the values $c_{200} = 2.7$ and $r_s = 0.52$ Mpc. To prove this assertion, we performed a simple test. We used the values of M_{200} and c_{200} from Lieu et al. (2016), and then we generated a shear profile with their same radial range and number of bins. We fitted their data seeking the best M_{200} value, assuming a concentration value of $c_{200} = 10$. The projected mass from this estimate is shown as cyan symbols in Fig. 12. This change in concentration not only solves the difference in mass estimates, but also explains why SL2S J02140-0535 (XLSSC 110) is an outlier

in the sample of Lieu et al. (2016). This highlights the risk of assuming a $c - M$ relation for some particular objects, such as strong lensing clusters. The discussion of the bias and the effect on the $M-T$ scaling relation will be discussed in a forthcoming publication (Foëx et al., in prep.).

6. Conclusions

We have presented a framework that allows us to simultaneously fit SL and dynamics. We apply our method to probe the gravitational potential of the lens galaxy group SL2S J02140-0535 on a large radial range, by combining two well-known codes, namely MAMPOSSt (Mamon et al. 2013) and LENSTOOL (Jullo et al. 2007). We performed a fit adopting a NFW profile and three galaxy-scale mass components as perturbations to the group potential, as previously carried out by VMM11, but we include the dynamical information in a new consistent way. The number of galaxies increased to 24, when new VLT (FORSS2) spectra were analyzed. This new information was included to perform the combined strong lensing and dynamics analysis. Moreover, we studied the gas distribution within the group from X-ray data obtained with XMM.

We list our results below:

1. Our new observational data set confirms the results presented previously in VMM11. We also present supporting X-ray analysis.
 - Our spectroscopic analysis confirms that the arcs AB and the arc C of SL2S J02140-0535 belong to different sources, the former at $z_{\text{spec}} = 1.017 \pm 0.001$ and the latter at $z_{\text{spec}} = 1.628 \pm 0.001$. These redshift values are consistent with the photometric redshift estimation.
 - We find 24 secure members of SL2S J02140-0535 from the analysis of our new and previously reported spectroscopic data. The completeness $C \sim 60\%$ is roughly constant up to 1 Mpc. We also computed the velocity dispersion, obtaining $\sigma = 562 \pm 60 \text{ km s}^{-1}$, which is a value that is comparable to the previous estimate of VMM11.
 - The X-ray contours show an elongated shape that is consistent with the spatial distribution of the confirmed members. This argues in favor of an unimodal structure since the X-ray emission is unimodal and centered on the lens.
2. Our method simultaneously fits strong lensing and dynamics, allowing us to probe the mass distribution from the center of the group up to its virial radius. However, there is a tension between the results of the Dyn model and the SL model, which is related to the assumed spherical symmetry of the former. While our result shows that deviation from spherical symmetry can in some cases induce a bias in the MAMPOSSt solution for the cluster $M(r)$, this does not need to be the rule. In another massive cluster at $z = 0.44$, Biviano et al. (2013) found good agreement between the spherical MAMPOSSt solution and the non spherical solution from strong lensing. In addition, MAMPOSSt has been shown to provide unbiased results for the mass profiles of cluster-sized halos extracted from cosmological simulations (Mamon et al. 2013).
 - Models relying solely on either lensing (SL model) or dynamical information (Dyn model) are not able to constrain the scale radius of the NFW profile. We obtain a scale radius of $r_s = 184_{-60}^{+209} \text{ kpc}$ for the best SL model, whereas we obtain a value of $r_s = 199_{-91}^{+135} \text{ kpc}$ for the

best Dyn model. We find that the concentration parameter is unconstrained as well.

- However, it is possible to constrain both the scale radius and the concentration parameter when combining both lensing and dynamics analysis (as previously discussed in VMM11). We find a scale radius of $r_s = 82^{+44}_{-17}$ kpc, and a concentration value of $c_{200} = 10.0^{+1.7}_{-2.5}$. The SL+Dyn model reduces the error in the mass estimation in 0.34 dex (a factor of 2.2), when compared to the SL model, and in 0.15 dex (a factor of 1.4), compared to the Dyn model.
- Our joint SL+Dyn model allows us to probe, in a reliable fashion, the mass profile of the group SL2S J02140-0535 at large scale. We find a good agreement between the luminosity contours, mass contours, and X-ray emission. This result confirms that the mass is traced by light.

The joint lensing-dynamical analysis presented in this paper, applied to the lens galaxy group SL2S J02140-0535, aims to show a consistent method to probe the mass density profile of groups and clusters of galaxies. This is the first paper in a series in which we extend our methodology to the galaxy clusters, for which the number of constraints is larger both in lensing images and in galaxy members. Therefore, we should be able to probe more parameters, such as the anisotropy parameter and the tracer radius (Verdugo et al., in prep.), with our new method.

Acknowledgements. The authors thank the anonymous referee for invaluable remarks and suggestions. T.V. thanks the staff of the Instituto de Física y Astronomía of the Universidad de Valparaíso. M.L. acknowledges the Centre National de la Recherche Scientifique (CNRS) for its support. V. Motta gratefully acknowledges support from FONDECYT through grant 1120741, ECOS-CONICYT through grant C12U02, and Centro de Astrofísica de Valparaíso. M.L. and E.J. also acknowledge support from ECOS-CONICYT C12U02. A.B. acknowledges partial financial support from the PRIN INAF 2014: “Glittering kaleidoscopes in the sky: the multifaceted nature and role of galaxy clusters” P.I.: M. Nonino. K. Rojas acknowledges support from doctoral scholarship FIB-UV/2015 and ECOS-CONICYT C12 U02. J.M. acknowledges support from FONDECYT through grant 3160674. J.G.F-T is currently supported by Centre National d’Études Spatiales (CNES) through Ph.D. grant 0101973 and the Région de Franche-Comté and by the French Programme National de Cosmologie et Galaxies (PNCG). M. A. De Leo would like to thank the NASA-funded FIELDS program, in partnership with JPL on a MUREP project, for their support.

References

- Alard, C. 2009, *A&A*, 506, 609
- Allen, S. W., Evrard, A. E., & Mantz, A. B. 2011, *ARA&A*, 49, 409
- Andrae, R. 2010, ArXiv e-prints [arXiv:1009.2755]
- Barlow, R. 1989, *Statistics. A guide to the use of statistical methods in the physical sciences* (New York: Wiley)
- Beers, T. C., Flynn, K., & Gebhardt, K. 1990, *AJ*, 100, 32
- Beraldo e Silva, L., Mamon, G. A., Duarte, M., et al. 2015, *MNRAS*, 452, 944
- Biviano, A., Rosati, P., Balestra, L., et al. 2013, *A&A*, 558, A1
- Biviano, A., van der Burg, R. F. J., Muzzin, A., et al. 2016, *A&A*, 594, A51
- Bolzonella, M., Miralles, J.-M., & Pelló, R. 2000, *A&A*, 363, 476
- Bond, J. R., Kofman, L., & Pogossyan, D. 1996, *Nature*, 380, 603
- Bradač, M., Allen, S. W., Treu, T., et al. 2008, *ApJ*, 687, 959
- Cabanac, R. A., Alard, C., Dantel-Fort, M., et al. 2007, *A&A*, 461, 813
- Colless, M., Dalton, G., Maddox, S., et al. 2001, *MNRAS*, 328, 1039
- Cuesta, A. J., Prada, F., Klypin, A., & Moles, M. 2008, *MNRAS*, 389, 385
- D’Aloisio, A., & Natarajan, P. 2011, *MNRAS*, 411, 1628
- Duffy, A. R., Schaye, J., Kay, S. T., & Dalla Vecchia, C. 2008, *MNRAS*, 390, L64
- Eke, V. R., Baugh, C. M., Cole, S., et al. 2004a, *MNRAS*, 348, 866
- Eke, V. R., Frenk, C. S., Baugh, C. M., et al. 2004b, *MNRAS*, 355, 769
- Eliásdóttir, Á., Limousin, M., Richard, J., et al. 2007, ArXiv e-prints [arXiv:0710.5636]
- Ettori, S., Donnarumma, A., Pointecouteau, E., et al. 2013, *Space Sci. Rev.*, 177, 119
- Falco, M., Mamon, G. A., Wojtak, R., Hansen, S. H., & Gottlöber, S. 2013, *MNRAS*, 436, 2639
- Foëx, G., Motta, V., Limousin, M., et al. 2013, *A&A*, 559, A105
- Foëx, G., Motta, V., Jullo, E., Limousin, M., & Verdugo, T. 2014, *A&A*, 572, A19
- Frenk, C. S., Evrard, A. E., White, S. D. M., & Summers, F. J. 1996, *ApJ*, 472, 460
- Gastaldello, F., Buote, D. A., Humphrey, P. J., et al. 2007, *ApJ*, 669, 158
- Gastaldello, F., Limousin, M., Foëx, G., et al. 2014, *MNRAS*, 442, L76
- Gavazzi, R. 2005, *A&A*, 443, 793
- Golse, G., & Kneib, J.-P. 2002, *A&A*, 390, 821
- Guennou, L., Biviano, A., Adami, C., et al. 2014, *A&A*, 566, A149
- Gwyn, S. D. J. 2011, ArXiv e-prints [arXiv:1101.1084]
- Host, O. 2012, *MNRAS*, 420, L18
- Irgens, R. J., Lilje, P. B., Dahle, H., & Maddox, S. J. 2002, *ApJ*, 579, 227
- Jauzac, M., Jullo, E., Kneib, J.-P., et al. 2012, *MNRAS*, 426, 3369
- Jauzac, M., Clément, B., Limousin, M., et al. 2014, *MNRAS*, 443, 1549
- Jullo, E., Kneib, J.-P., Limousin, M., et al. 2007, *New J. Phys.*, 9, 447
- Jullo, E., Natarajan, P., Kneib, J.-P., et al. 2010, *Science*, 329, 924
- Kinney, A. L., Calzetti, D., Bohlin, R. C., et al. 1996, *ApJ*, 467, 38
- Kneib, J.-P., & Natarajan, P. 2011, *A&ARv*, 19, 47
- Kurtz, M. J., & Mink, D. J. 1998, *PASP*, 110, 934
- Lieu, M., Smith, G. P., Giles, P. A., et al. 2016, *A&A*, 592, A4
- Limousin, M., Kneib, J.-P., & Natarajan, P. 2005, *MNRAS*, 356, 309
- Limousin, M., Richard, J., Jullo, E., et al. 2007, *ApJ*, 668, 643
- Limousin, M., Cabanac, R., Gavazzi, R., et al. 2009, *A&A*, 502, 445
- Limousin, M., Jullo, E., Richard, J., et al. 2010, *A&A*, 524, A95
- Limousin, M., Morandi, A., Sereno, M., et al. 2013, *Space Sci. Rev.*, 177, 155
- Łokas, E. L., & Mamon, G. A. 2003, *MNRAS*, 343, 401
- Mamon, G. A., & Boué, G. 2010, *MNRAS*, 401, 2433
- Mamon, G. A., Biviano, A., & Boué, G. 2013, *MNRAS*, 429, 3079
- Menanteau, F., Hughes, J. P., Sifón, C., et al. 2012, *ApJ*, 748, 7
- Meneghetti, M., Natarajan, P., Coe, D., et al. 2016, *MNRAS*, submitted [arXiv:1606.04548]
- Mulchaey, J. S. 2000, *ARA&A*, 38, 289
- Munari, E., Biviano, A., & Mamon, G. A. 2014, *A&A*, 566, A68
- Muñoz, R. P., Motta, V., Verdugo, T., et al. 2013, *A&A*, 552, A80
- Navarro, J. F., Frenk, C. S., & White, S. D. M. 1996, *ApJ*, 462, 563
- Navarro, J. F., Frenk, C. S., & White, S. D. M. 1997, *ApJ*, 490, 493
- Newman, A. B., Treu, T., Ellis, R. S., et al. 2009, *ApJ*, 706, 1078
- Newman, A. B., Treu, T., Ellis, R. S., et al. 2013, *ApJ*, 765, 24
- Old, L., Skibba, R. A., Pearce, F. R., et al. 2014, *MNRAS*, 441, 1513
- Old, L., Wojtak, R., Mamon, G. A., et al. 2015, *MNRAS*, 449, 1897
- Postman, M., Franx, M., Cross, N. J. G., et al. 2005, *ApJ*, 623, 721
- Prada, F., Klypin, A. A., Simonneau, E., et al. 2006, *ApJ*, 645, 1001
- Randall, S. W., Markevitch, M., Clowe, D., Gonzalez, A. H., & Bradač, M. 2008, *ApJ*, 679, 1173
- Sand, D. J., Treu, T., & Ellis, R. S. 2002, *ApJ*, 574, L129
- Sand, D. J., Treu, T., Smith, G. P., & Ellis, R. S. 2004, *ApJ*, 604, 88
- Sarli, E., Meyer, S., Meneghetti, M., et al. 2014, *A&A*, 570, A9
- Springel, V., White, S. D. M., Jenkins, A., et al. 2005, *Nature*, 435, 629
- Sun, M. 2012, *New J. Phys.*, 14, 045004
- Thanjavur, K., Crampton, D., & Willis, J. 2010, *ApJ*, 714, 1355
- Tully, R. B. 2015, *AJ*, 149, 54
- Umetsu, K., Sereno, M., Medezinski, E., et al. 2015, *ApJ*, 806, 207
- Verdugo, T., de Diego, J. A., & Limousin, M. 2007, *ApJ*, 664, 702
- Verdugo, T., Motta, V., Muñoz, R. P., et al. 2011, *A&A*, 527, A124
- Verdugo, T., Motta, V., Foëx, G., et al. 2014, *A&A*, 571, A65
- Wilman, D. J., Balogh, M. L., Bower, R. G., et al. 2005, *MNRAS*, 358, 71
- Wojtak, R., Łokas, E. L., Mamon, G. A., et al. 2008, *MNRAS*, 388, 815
- Wojtak, R., Łokas, E. L., Mamon, G. A., & Gottlöber, S. 2009, *MNRAS*, 399, 812
- Wolf, J., Martinez, G. D., Bullock, J. S., et al. 2010, *MNRAS*, 406, 1220
- Zitrin, A., Fabris, A., Merten, J., et al. 2015, *ApJ*, 801, 44

Appendix A: Spectroscopic and photometric data

Table A.1. Spectroscopic data of the confirmed members of the group.

RA	Dec	z_{spec}	R [kpc]
33.533779	-5.592632	0.4446 [†]	–
33.533501	-5.591930	0.4449 [†]	7.9
33.530430	-5.594814	0.4474 [†]	79.8
33.527908	-5.597961	0.4443	161.0
33.536942	-5.582868	0.4430 [†]	204.3
33.540424	-5.584474	0.4427 [†]	210.7
33.519188	-5.601521	0.4459 [†]	349.6
33.546135	-5.607511	0.4436 [†]	398.0
33.514061	-5.595108	0.4455	405.4
33.521729	-5.574636	0.4462	439.8
33.512676	-5.596797	0.4473 [†]	440.5
33.510559	-5.596503	0.4442	480.4
33.515137	-5.577593	0.4442 [†]	486.3
33.519920	-5.569031	0.4449	556.8
33.548912	-5.616460	0.4426 [†]	580.2
33.512367	-5.573329	0.4440 [†]	586.5
33.543442	-5.557844	0.4424	735.2
33.555248	-5.621617	0.4471	745.7
33.563099	-5.561144	0.4465	883.5
33.550777	-5.551144	0.4438 [†]	916.6
33.500538	-5.558484	0.4459 [†]	976.6
33.484375	-5.623324	0.4436 [†]	1194.2
33.479259	-5.613928	0.4435 [†]	1201.0
33.475819	-5.627750	0.4438	1392.3

Notes. ^(†) Previously reported in [Muñoz et al. \(2013\)](#). Columns (1) and (2): right ascension and declination. Column (3): redshift. Column (4): the projected radius measured with respect to the BGG.

Table A.2. Results from photometry in arc A.

ID	J	K_s	z_{phot}	z_{spec}
<i>A</i>	19.9 ± 0.4	18.2 ± 0.4	1.7 ± 0.1	1.628 ± 0.001
<i>B</i>	21.6 ± 1.0	21.1 ± 0.9	1.6 ± 0.2	–
<i>C</i>	20.2 ± 0.2	18.7 ± 0.3	0.96 ± 0.07	1.017 ± 0.001

Notes. Column 1 lists the identification for each object as in Fig. 1. Columns (2) and (3) are the WIRCam magnitudes. Columns (4) and (5) list the photometric and spectroscopic redshifts, respectively.

Appendix B: Spherical lensing model

To compare the spherical Dyn model with a spherical lensing model, we construct an additional model using LENSTOOL. We set the ellipticity and position angle equal to zero, and we use the same constraints as those used in the elliptical case. Since lensing spherical models tend to be poorly constrained, the parameter c_{200} is free to range between $1 \leq c_{200} \leq 16$, avoiding large unphysical values and reducing the possible solutions in the r_s - c_{200} parameter space. Finally we also set $\sigma_{ij} = 3''$, to obtain a reduced χ^2 near unity. We show the result in Fig. B.1. For clarity, the colors are reversed with respect to the plots in the main text, gray-filled contours depict the result of the spherical SL model, and green contours depict the result of the Dyn model.

To highlight further the result of the comparison between models, we present in Fig. B.2 the solutions in the $\log c_{200}$ - $\log r_{200}$ space. A clear tendency to greater values of concentration exists in the SL model with a bimodal distribution in r_{200} . The $\log c_{200}$ - $\log r_{200}$ parameter space also makes evident the existence of a possible bimodal solution in the combined model, which is consistent with the result depicted in the right panel of Fig. B.1.

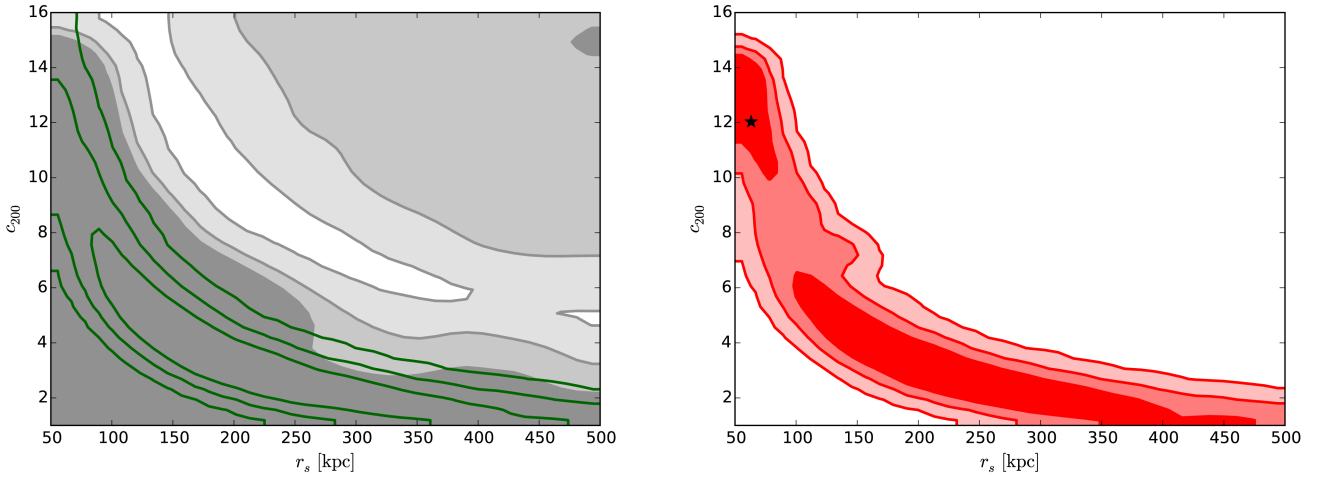


Fig. B.1. Joint distributions (scale radius and concentration) for the spherical model. *Left panel:* from dark to white gray-filled contours are 1, 2, and 3σ regions from the SL model, and green contours stand for the 68, 95, and 99% confidence levels for the Dyn model. *Right panel:* red-filled contours is the result of the SL+Dyn model, with the best solution depicted with a black star.

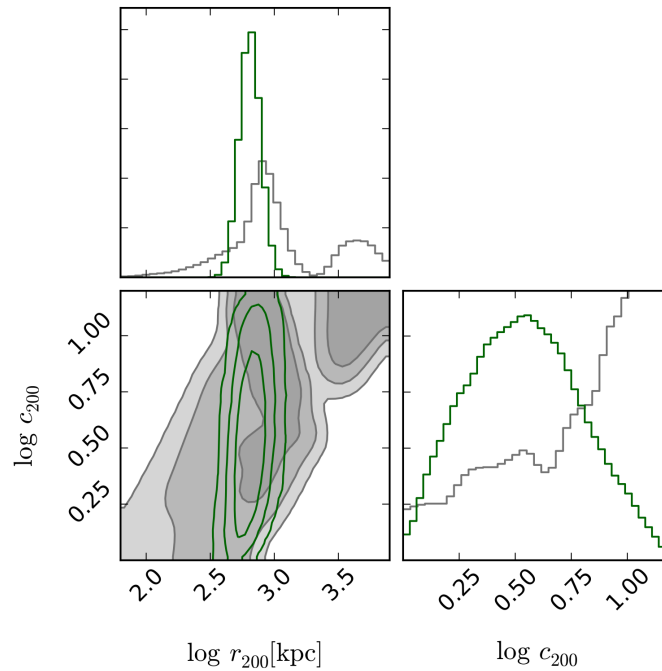


Fig. B.2. PDFs and contours of the parameters $\log c_{200}$ and $\log r_{200}$. From dark to white gray-filled contours are 1, 2, and 3σ regions from the SL model, and green contours stand for the 68, 95, and 99% confidence levels for the Dyn model.

Chapitre 4

Perspectives de recherches

Les avancées de recherche présentées dans ce manuscrit ouvrent de riches perspectives de recherche pour les prochaines années. C'est l'objet de la présente section. Le thème majeur de mon programme de recherche est l'étude des groupes de galaxies avec effet de lentilles, comprendre leur formation, leur évolution et leur rôle dans la construction des structures à grande échelles de l'univers, des filaments aux amas de galaxies.

4.1 Programmes d'observations des groupes de galaxies avec les grands observatoires au sol et missions spatiales de la prochaine décade

A la somme des observatoires d'aujourd'hui (ALMA, GRMT, VLA, NEOMA, VLT, GTC, Gemini, Keck, Subaru, CFHT, PanSTARR, VISTA, XMM / Chandra, eROSITA / SPECTRUM-ROETGEN-GAMMA) vont s'ajouter dans les prochaines années de nouveaux instruments¹ dédiés à l'étude du ciel profond de notre univers dans pratiquement tous les domaines de l'électromagnétisme, des hautes énergies vers les basses : Athena (Mission ESA X), Vera Rubin Observatory (LSST visible/infrarouge proche), European Extremely-Large Telescope (ESO visible/infrarouge), Euclid (Mission ESA visible/infrarouge proche), Nancy-Grace-Roman Telescope (Mission NASA infrarouge), James Web Space Telescope (Mission NASA infrarouge), Square Kilometer Array (International, radio).

Au delà des télescopes eux-mêmes qui fixent le plafond de sensibilité d'une instrumentation associée, c'est également une progression parallèle fulgurante de la performance des instruments aux foyers des télescopes qui jouent sur notre capacité à analyser les objets du ciel profond.² Dans le domaine de l'observation astronomique des groupes de galaxies, c'est sans contredit l'avènement de spectrographes 3D ou intégraux sur des champs (en jargon Integral Field Unit Spectrograph) de quelques dizaines d'arcmin² qui feront à l'avenir la différence. Aujourd'hui, c'est MUSE au VLT³ qui représente le meilleur exemple de

1. Je ne mentionne ici que les instruments dont les astronomes européens auront l'usage. Les instruments financés par des agences étrangères ou privées, e.g. Giant Magellan Telescope, Large Binocular Telescope, sont volontairement tenus à l'écart.

2. J'emploie souvent la métaphore *oeil-cerveau* \equiv *télescope-instrument* pour expliquer au grand public du Pic du midi la synergie symbiotique entre la surface collectrice d'un télescope et la capacité d'analyse de son instrumentation.

3. <https://www.eso.org/public/france/teles-instr/paranal-observatory/vlt/vlt-instr/muse/> et la page du VLT <https://www.eso.org/sci/facilities/paranal/instruments/muse.html> et publications consortium

ce type d'instrument. Le champ de vision de MUSE (1 arcmin²) est petit, mais acceptable pour l'étude des groupes de galaxies à $z \geq 0.2$ (e.g. Husemann et al. 2016; Bielby et al. 2017; Epinat et al. 2018) Le Tableau 3.2 donne une vision synoptique des observatoires d'intérêt cosmologique à venir et de leur instrumentation. Nous décrivons rapidement par ordre d'arrivée les observatoires et les instruments qui auront un impact probablement important sur la science des groupes de galaxies.

James Webb Space Telescope JWST 2021 : cette mission spatiale qui remplacera le télescope spatial Hubble, arrivera (enfin!) fin 2021. Ce télescope de 6 m de diamètre est optimisé pour le visible et proche infrarouge, il sera en orbite L2, comme la plupart des missions scientifiques contemporaines. Sa panoplie d'instruments couvrent un large spectre d'applications servant une communauté large. Les extragalacticiens utiliseront le spectro-imageur infrarouge MIRI, 4.9 à 28.8 μm , sur un champ de 1×2 arcmin², idéal pour sonder la formation stellaire des proto-amas, le spectro-imageur NIRISS, 0.5-5 μm , sur un champ de 2×2 arcmin², pour l'imagerie des objets à redshift intermédiaire, le spectrographe multi-objet NIRSPEC, 0.6-5.3 μm , sur un champ de 3.6×3.4 arcmin², sera idéal pour les études dynamiques et chimiques des groupes de galaxies, et enfin NIRCAM, 0.6-5 μm , $2 \times 132'' \times 132''$ dans son mode grand champ, sera une machine à étudier les champs sur-denses à tous les redshifts. Les instruments du JWST sont assez proches les uns des autres sur les fonctions basales de spectro-imageurs pour assurer une redondance maximale en cas de panne en L2. Seul MIRI donne accès au gaz froid à très haut décalage spectral. Mahler et al. (2019) donnent quelques éléments prospectifs sur le potentiel de JWST dans le cadre du projet Reionization Lensing Cluster Survey (RELICS) HST Treasury program, GO14096 (PI : Coe), 13 amas-lentilles massifs vont être suivis sur les 4 instruments promettant une riche moisson de données. Je poursuis avec mes collaborateurs Brenda Frye (University of Arizona, Stewart Observatory), Hervé Dole (Institut d'Astrophysique Spatiale, Orsay), Matt Lehnert (Institut d'Astrophysique de Paris) et al. un programme de demande de temps de télescope suivi de proto-amas détectés avec le satellite Herschell de façon à mettre en lumière les premiers moments de formation stellaires et d'effondrements il y a 10 milliards d'années.

Euclid (2022) : cette mission spatiale de l'ESA est sans contredit la plus importante mission à venir jusqu'à Nancy-Grace-Roman Telescope / WFIRST pour la recherche en cosmologie et l'ensemble des données héritage qui en découleront. Euclid est un télescope de 1.2 m de diamètre, dont la mission est résumée dans la page Euclid Mission Summary tirée du Red Book d'Euclid. Euclid est équipé de deux instruments grand champ, une caméra visible VIS à une seule bande large 0.55-0.9 μm de 1 deg², de résolution 0.1 arcsec/pix et une caméra infrarouge NISP avec deux canaux, un canal imageur avec 3 bandes YJH de 0.3''/pix en J et un canal spectroscopique sans fente, 1-2 μm , Résolution 250. Euclid est conçu comme une expérience scientifique et non comme un observatoire avec de multiples programmes sur appel d'offre.

Le consortium Euclid a conçu un programme dans le but de comprendre l'origine de l'expansion accélérée de l'univers. Il va utiliser des sondes cosmologiques pour scruter la nature de l'énergie sombre, de la matière sombre et de la gravité en traçant leur signature observationnelle sur la géométrie de l'univers et sur l'histoire cosmique de la formation des structures à grande échelle. Euclid va construire une carte des structures à grande échelle

sur une durée cosmique couvrant les derniers 10 milliards d'années. La mission est optimisée pour deux sondes cosmologiques primaires : l'effet de lentillage faible (en jargon Weak gravitational Lensing WL) et les oscillations acoustiques de la matière baryonique (en jargon Baryonic Acoustic Oscillations ; BAO). le WL exige une excellente qualité d'image sur des échelles inférieures à la seconde d'arc⁴ pour les mesures de forme des galaxies et une photométrie fine en visible et infrarouge pour mesurer les redshifts photométriques jusqu'à $z \approx 2$. Le BAO quant à lui exige de mesurer des redshifts spectroscopiques jusqu'à $z \approx 0.7$. Les deux sondes exigent de plus de couvrir la plus grande partie du ciel extragalactique.

Pour comprendre la nature de l'énergie sombre, son équation d'état (cf chapitre 2) doit être déterminée. Euclid utilise les WL et BAO pour mesurer la constante et les termes variables temporellement de l'équation d'état avec une précision de 0.02 et 0.1 (erreur d' 1σ). Euclid va également tester la validité de la relativité générale en mesurant le taux d'augmentation des structures (l'exposant γ de cette loi) à 0.02 (erreur d' 1σ), suffisant pour différencier la RG avec des lois alternatives. Euclid pourra mesurer le spectre de puissance des fluctuations à 1% près et, en combinaison avec les données de Planck, tester l'hypothèse de "gaussianité" de ces fluctuations.

Pour répondre à ces questions, la mission Euclid sera envoyée pour un lent pavage du ciel de 5 ans au point de Lagrange L2 et construira un sondage large de $15\,000\text{ deg}^2$ jusqu'à une limite de sensibilité de $\simeq 1\ \mu\text{J}$ ou $VIS_{\text{mag}} \leq 24$ et un sondage profond de 40 deg^2 jusqu'à une limite de sensibilité de $\simeq 0.15\ \mu\text{J}$ ou $VIS_{\text{mag}} \leq 26$. Le spectrographe sans fente atteindra, quant à lui, une sensibilité de $3 \times 10^{-19}\text{ W}\cdot\text{m}^{-2}$.

Une autre particularité d'Euclid, pour dire les choses avec euphémisme, est que les buts scientifiques ne pourront être atteints sans un complément indispensable de photométrie fournie par un ensemble de télescopes au sol, déjà en fonction ((CFHT-CFIS ; Ibata et al. 2017, DES ; Collaboration : et al. 2016). ou en construction (LSST ; Capak et al. 2019, J-PAS <http://j-pas.org/>). En effet, les compléments photométriques en bande u, g, r, i, z pour une mesure du redshift à 0.03 (avec moins de 1% d'erreurs supérieure à 0.1) sont indispensables.

Le sondage final d'Euclid va produire un ensemble de données héritage sans équivalent dans le paysage de l'astronomie contemporaine pour de nombreuses disciplines dont, particulièrement, les effets de lentille forts à toutes les échelles. Le groupe de travail *Euclid Strong Lensing Science* a calculé (papier in prep) que le sondage large d'Euclid avait le potentiel de fournir ca. 100 000 lentilles galaxies-galaxies et autour de ca. 10 000 lentilles de groupes de galaxies en reportant les statistiques de $\sim 1.3\text{ lentille}\cdot\text{deg}^{-2}$ du SL2S. La figure 3.4 donne la fonction de sélection des amas et groupes lentilles ainsi que la distribution finale attendue en fonction du redshift de leur densité numérique. Euclid a donc le potentiel de multiplier par trois ordres de grandeur le nombre de lentilles connues à toutes les échelles. C'est un changement de paradigme pour reprendre les termes de Thomas Kuhn, pour lequel la communauté se prépare activement.

4. cette qualité d'image était plus facilement atteignable avec un design optique sans obstruction comme l'ont montré Singaravelu & Cabanac (2014). C'est également le choix technique de l'équipe chinoise pour le Chinese Space Station Optical Survey (Gong et al. 2019) et le projet Messier (Lombardo et al. 2019), mais le choix optique Korsch TMA pour Euclid était dicté par un contexte économique interdisant tout développement augmentant le risque de la mission. Euclid a été choisie en grande partie parce que la mission ne présentait pas de difficultés techniques.

Euclid Mission Summary

Main Scientific Objectives					
Understand the nature of Dark Energy and Dark Matter by:					
<ul style="list-style-type: none"> Reach a dark energy $FoM > 400$ using only weak lensing and galaxy clustering; this roughly corresponds to 1 sigma errors on w_p and w_a of 0.02 and 0.1, respectively. Measure γ, the exponent of the growth factor, with a 1 sigma precision of < 0.02, sufficient to distinguish General Relativity and a wide range of modified-gravity theories Test the Cold Dark Matter paradigm for hierarchical structure formation, and measure the sum of the neutrino masses with a 1 sigma precision better than 0.03eV. Constrain n_s, the spectral index of primordial power spectrum, to percent accuracy when combined with Planck, and to probe inflation models by measuring the non-Gaussianity of initial conditions parameterised by f_{NL} to a 1 sigma precision of ~ 2. 					
SURVEYS					
	Area (deg ²)	Description			
Wide Survey	15,000 (required) 20,000 (goal)	Step and stare with 4 dither pointings per step.			
Deep Survey	40	In at least 2 patches of $> 10 \text{ deg}^2$ 2 magnitudes deeper than wide survey			
PAYLOAD					
Telescope	1.2 m Korsch, 3 mirror anastigmat, $f=24.5 \text{ m}$				
Instrument	VIS	NISP			
Field-of-View	$0.787 \times 0.709 \text{ deg}^2$	$0.763 \times 0.722 \text{ deg}^2$			
Capability	Visual Imaging	NIR Imaging Photometry			NIR Spectroscopy
Wavelength range	550– 900 nm	Y (920-1146nm),	J (1146-1372 nm)	H (1372-2000nm)	1100-2000 nm
Sensitivity	24.5 mag 10 σ extended source	24 mag 5 σ point source	24 mag 5 σ point source	24 mag 5 σ point source	3 $10^{-16} \text{ erg cm}^{-2} \text{ s}^{-1}$ 3.5 σ unresolved line flux
Detector Technology	36 arrays 4k \times 4k CCD	16 arrays 2k \times 2k NIR sensitive HgCdTe detectors			
Pixel Size	0.1 arcsec	0.3 arcsec			0.3 arcsec
Spectral resolution					R=250
SPACECRAFT					
Launcher	Soyuz ST-2.1 B from Kourou				
Orbit	Large Sun-Earth Lagrange point 2 (SEL2), free insertion orbit				
Pointing	25 mas relative pointing error over one dither duration 30 arcsec absolute pointing error				
Observation mode	Step and stare, 4 dither frames per field, VIS and NISP common FoV = 0.54 deg^2				
Lifetime	7 years				
Operations	4 hours per day contact, more than one ground station to cope with seasonal visibility variations;				
Communications	maximum science data rate of 850 Gbit/day downlink in K band (26GHz), steerable HGA				
Budgets and Performance					
	Mass (kg)		Nominal Power (W)		
industry	TAS	Astrium	TAS	Astrium	
Payload Module	897	696	410	496	
Service Module	786	835	647	692	
Propellant	148	232			
Adapter mass/ Harness and PDCU losses power	70	90	65	108	
Total (including margin)	2160		1368	1690	

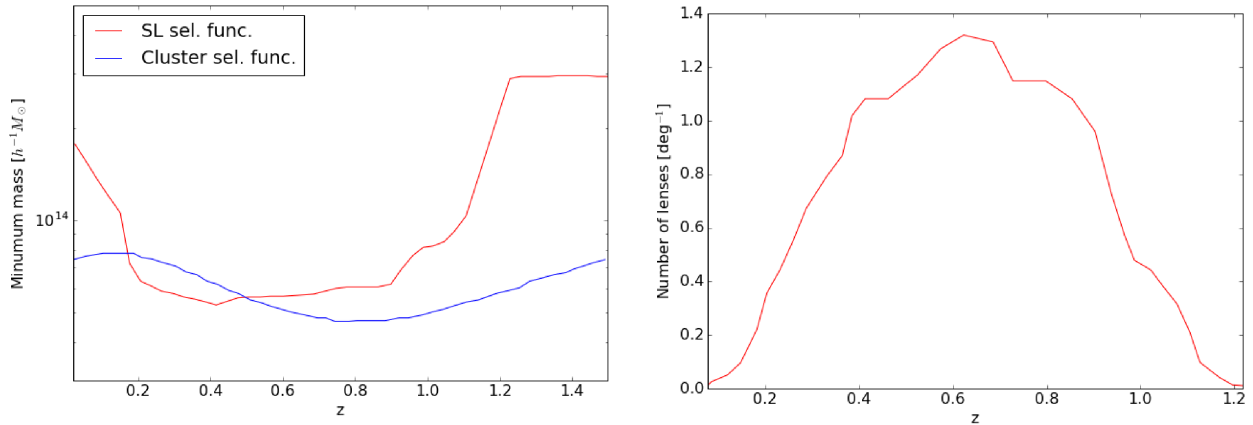


FIGURE 4.1 – Droite : Masse minimale détectable par leur effet de lentille de groupes et amas dans le sondage large d’Euclid (ligne rouge). La masse limite des groupes et amas lentilles (i.e. qui développent des lignes critiques plus grandes que 5 arcsec) est montrée en fonction du redshift. La ligne bleue montre la fonction de sélection calculée par Sartoris et al. (2016) pour une population globale de groupes et d’amas. La fonction de sélection des lentilles est la combinaison de la fonction de sélection de lentilles et des sources d’arrière-plan. Gauche : Densité numérique (deg^{-2}) des amas et groupes détectés dans le sondage large d’Euclid par effet de lentille en fonction du redshift. Tiré de Meneghetti (priv. com.)

Vera Rubin Observatory LSST (2022) : Le projet contrepartie d’Euclid au sol est le Large Synoptic Survey Telescope de l’Observatoire Vera Rubin (Ivezic et al. 2019) en cours de construction au Cerro Pachon, près de La Serena, Chili. Ce télescope de 8.4m de diamètre, d’un design optique original (Paul Baker modifié avec surface effective d’un miroir de 6.4m) admet un très grand champ (≈ 3.5 deg de diamètre). La caméra qui pave ce grand champ de 63 cm de diamètre, 3.2 milliards de pixels de 0.2 arcsec. 5 filtres sur 6 de bandes u, g, r, i, z, y sont montés en tout temps. Le LSST a une cadence phénoménale qui lui permet de couvrir le ciel de l’hémisphère sud en 4 nuits. Le programme d’observation consiste à poursuivre un sondage de tout le ciel à des cadences diverses pour capturer les événements transitoires à différentes échelles temporelles, les variations positionnelles sur des époques variables et sur dix ans d’atteindre une sensibilité en magnitude sur une pose et sur 10 ans de u : 23.9, 26.1, g : 25.0, 27.4, r : 24.7, 27.5, i : 24.0, 26.8, z : 23.3, 26.1 et y : 22.1, 24.9. C’est-à-dire qu’en quelques nuits le LSST fournira les données d’appui nécessaire à Euclid sur son sondage large. Les synergies entre les deux projets sont évidentes (Rhodes et al. 2017). Dans le domaine du lentillage fort, la propriété la plus importante est la finesse d’image. Euclid est donc absolument essentiel au LSST qui peut apporter une photométrie précise des candidats lentilles.

Square Kilometer Array (2021-2030) : Le grand projet international dans le domaine radio est le Square Kilometre Array (site SKA pour les astronomes, tous les documents clefs se trouvent sur le site [www](http://www.skatelescope.org) du SKA, il n’y a pas de publication majeure sur ADS hormis un rapport d’étape de la phase SKA1 présenté à SPIE; McPherson et al. 2018). L’ambition de ce projet force l’admiration. Situé sur deux sites géographiques, site Boolardy (Ouest Australie) qui accueillera 512 stations de plus de 130 000 antennes et site Karoo (Afrique du Sud) qui accueillera 197 paraboles pour les hautes fréquences, SKA offrira un télescope radio couvrant toutes les techniques d’imagerie par synthèse d’ouverture du centimétrique au décimétrique avec une sensibilité de quelques μJy une résolution ultime à 1.4 GHz (raie de HI) de 0.01 arcsec et une rapidité de relevé 10 à

1000 fois plus rapide que les grands radiotélescopes actuels. Le véritable défi de SKA est la capacité de calcul et de transfert de données à atteindre pour corrélérer les signaux des milliers d'antennes et de paraboles. Le livre du programme scientifique de SKA (Volume 1 et Volume 2) couvre tous les domaines de l'astrophysique contemporaine. Le chapitre sur le lentillage fort (McKean et al. 2014 Strong Lensing with SKA) expose les cas scientifiques où SKA apportera des données uniques. La connaissance des contenus en gaz froid des systèmes lentilles et leurs sources magnifiées à haute résolution sur 100 000 lentilles galaxie-galaxie dont on commence à voir l'impact de données ALMA aujourd'hui e.g. Hezaveh et al. (2016); Spilker et al. (2016); Wong et al. (2017). C'est l'extrême sensibilité de SKA qui donnera une vision nouvelle du gaz froid à tous les redshifts et notamment dans les groupes de galaxies.

European Extremely Large Telescope (2025) : Le projet Européen de télescope géant de 39 m de diamètre E-ELT a pris de l'avance sur son alter-ego nord-américain, le Thirty-Meter Telescope qui a un peu de mal à convaincre la population Hawaïenne de l'utilité d'un nouveau télescope au sommet du Mauna Kea malgré des efforts soutenus (get-the-facts). L'E-ELT sera équipé de systèmes d'optique adaptative natifs (dont MAORY corrigeant la turbulence atmosphérique dans le proche infrarouge. Il offrira une batterie de cinq instruments. HIRES est le seul instrument "classique" de l'E-ELT, il s'agit d'un spectrographe de résolution 100 000 couvrant 0.4-1.8 μm , avec ou sans optique adaptative. HARMONI est un spectrographe 3D ou IFU d'une dizaine d'arcsec de champ de vision à la VLT/MUSE, mais sur un intervalle de longueur d'onde plus large, 0.4-2.4 μm et des résolutions de 500 à 20 000. Cet instrument est pensé pour des applications larges de l'étude de systèmes exo-planétaires à la l'étude de galaxies (et groupes de galaxies!) à haut redshift. METIS est un spectro-imageur infrarouge moyen (3-14 μm) de résolution 500 à 100 000, un mode IFU (0.5" de côté), un champ de vision de 11 \times 11arcsec², un mode coronographique. METIS a été pensé pour étudier la physique des objets compacts (étoiles proches, planètes, trous noirs, AGN, objets compacts extragalactiques). MICADO, comme METIS, est un spectro-imageur limité par la diffraction (6-12 milliarcsec) grâce à un double étage d'optique adaptative avec une possibilité de spectroscopie à fente de résolution de 8000 et une couverture spectrale de 0.8-2.4 μm . MICADO est plutôt conçu pour l'étude morphologique d'objets de quelques secondes d'arc. MOSAIC est un spectrographe multi objets (en jargon Multi-Object Spectrograph MOS) entre 0.4-1.8 μm , résolution de 5000 à 15000, sur un champ de vision de 6.4 arcmin, une capacité multiplex de 200 objets en visible (fibre de 0.8 arcsec) et 100 en infrarouge (fibre de 0.6 arcsec), un mode IFU de 10 \times 2 \times 2 arcsec². C'est cet instrument le plus adapté à l'étude dynamique et chimique des groupes de galaxies à haut redshift. Comme tous les grands télescopes, l'E-ELT va servir une communauté large, son mode opératoire est encore discuté, mais il est peu probable que le télescope se lance dans des projets de longue haleine dès le début de ses observations. Il fonctionnera probablement sur un modèle proche du VLT qui a établi les plus hauts standards d'efficacité de l'astronomie observationnelle du XXIe siècle.

Nancy-Grace-Roman Telescope WFIRST (\geq 2025) : Après Euclid, NGR WFIRST sera une mission infrarouge équipée d'un miroir de 2.4 m et d'une caméra fournissant un champ de vision de 45 \times 23 arcmin² (0.28 deg²), sensible de 0.5 à 2 μm . Le télescope pourra fonctionner en quatre modes :

1. un mode imagerie,
2. un mode spectroscopique sans fente (GRISM),

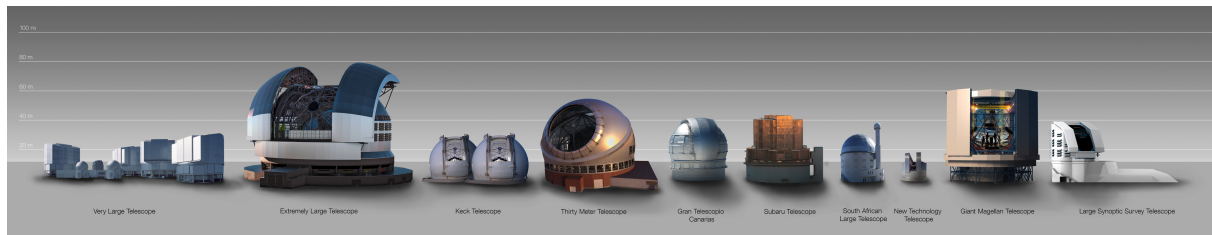


FIGURE 4.2 – ce bandeau illustre les grands télescopes actuels et ceux qui vont être construits dans les 10 prochaines années. Crédits ESO

3. un mode spectroscopique et
4. un mode coronographique.

Ces modes correspondent à des projets scientifiques bien définis. Les modes 1 et 2 serviront un sondage profond de 2000 deg^2 , Wide-Field-Instrument High-Latitude Survey, dans les bandes Y, J, H et $F184$, jusqu'à une limite de $J = 26.7 AB$ ($0.076 \mu\text{Jy}$). La spectroscopie de 15 millions d'objets sera extraite entre $1.1 < z < 2.8$, fournissant un excellent complément à Euclid sur l'étude des composantes sombres de l'univers. Le mode 3 est spécifiquement orienté à la mesure des supernovas de type Ia pour une dérivation du paramètre de Hubble dans trois intervalles de redshifts ($< 0.4, < 0.8 < 1.7$) pour un total anticipé de ≈ 2700 SN Ia. Deux programmes d'études exoplanétaires sont également prévus, un de découverte par méthode de micro-lentille et un de suivi de planètes avec le coronographe du mode 4. A la différence d'Euclid, NGR WFIRST ne sera pas réservé à ces grands sondages, mais il est prévu d'offrir le télescope aux programmes visiteurs sur appel d'offre.

ATHENA (2031) : La dernière mission à arriver sera le Advanced Telescope for High-ENergy Astrophysics ATHENA, mission L2 de l'ESA, héritière de L'observatoire XMM-Newton. Le miroir d'ATHENA permettra d'atteindre une résolution meilleure que 5 arcsec sur un champ de vision de $40 \times 40 \text{ arcmin}^2$, sur une bande passante de $0.5\text{-}15 \text{ keV}$, à une limite en flux de $10^{-17} \text{ erg/cm}^2/\text{s}$. ATHENA offrira deux instruments, XIFU, un spectrographe 3D de 2.5 eV de résolution spectrale, 5 arcsec de résolution spatiale, une bande passante de $0.2\text{-}12 \text{ keV}$, sur un champ total de 5 arcmin , absolument idéal pour étudier le gaz chaud dans les groupes de galaxies et la physique de la rétroaction AGN. L'instrument WFI est un imageur grand champ de résolution 5 arcsec (pixel de 2.2 arcsec), une bande passante de $0.5\text{-}15 \text{ keV}$, sur un champ de vision de $40 \times 40 \text{ arcmin}^2$. ATHENA sera un fantastique outil d'étude de l'univers chaud.

TABLE 4.1 – Table synoptique des grands observatoires à venir

Nom	Longueur d'onde	Sensibilité [μ Jy]	Année	Instruments	Science
JWST	0.6 à 30	0.01 à 1000	2021	MIRI, NIRISS, NIRCAM, NIRSPEC	JWST science ré-ionisation, premiers étoiles, galaxies, amas
VRO LSST	0.33 à 1 μ m	0.040	2022	imageur grand champ	sondage profond du ciel, astronomie variable.
Euclid	0.4-1.8 μ m	0.65	2022	VIS, NISP	Euclid Science étude des composantes sombres de l'univers.
SKA	0.05 - 15.3 GHz	1.2 à 25	>2021	synthèse d'ouverture, corrélateurs	SKA science le gaz HI dans l'univers, magnétisme cosmique, l'âge sombre
E-ELT	0.4-14 μ m	1 (spectro R 100 000)	2025	HARMONI, HIRES, MICADO, METIS, MOSAIC	ELT science les premières étoiles, origine des galaxies
NGR WFIRST	0.5 - 2 μ m	0.02/1.3 img/spec	2025	WFI	WFIRST science sondage du ciel infrarouge.
ATHENA	0.2-12 KeV	10^{-17} erg/cm ² /s	2031	XIFU , WFI	ATHENA science le gaz chaud, Trous noirs, AGN

4.2 Projets de recherches spécifiques

4.2.1 Recherches avec le Strong Lensing Legacy Survey

Comme indiqué à la section précédente, le Strong Lensing Legacy survey offre un échantillon homogène d'une centaine de groupes de galaxies de masses intermédiaires et larges. L'étude complète de la distribution de matière sombre par effet de lentille nécessite un suivi haute résolution (possible jusqu'à maintenant uniquement avec les données du Télescope spatial). Les télescopes mentionnés dans la section précédente offriront autant de possibilités de sonder la matière sombre (Euclid), la formation stellaire (NGR WFIRST), l'environnement (VRO LSST), le contenu en gaz froid (SKA) et chaud (ATHENA). Un projet particulièrement intéressant me semble l'analyse de la composition chimique des galaxies membres de groupes comme comme sonde temporelle et spatiale de l'enrichissement (métallicité, gradients, synthèse de population stellaire) et des facteurs dynamiques en jeu. Ces mesures spectroscopiques de moyennes résolutions ($R = 5000-20\,000$) sont à la portée des spectrographes multi-objets des VLT/GTC/Keck/Gemini/Subaru et bien entendu des futurs grands instruments.

4.2.2 Recherches sur les techniques de détection

Nous l'avons vu au chapitre précédent, les techniques de détection contemporaines se tournent résolument vers des solutions semi-automatiques en préparation des grands relevés qui fourniront des centaines de milliers, voire des millions de candidats lentilles à filtrer. Les derniers travaux collaboratifs sur les meilleurs algorithmes de filtrage, dont le papier Metcalf et al. (2019) reproduit dans le manuscrit, pointent systématiquement vers les méthodes d'apprentissage profond, que ce soient des réseaux de neurones convolutifs, des analyses PCA ou des méthodes vectorielles SVM (Hartley et al. 2017). Comme nous l'avons mentionné les réseaux de neurones convolutifs sont des méthodes supervisées. D'une part, l'étiquetage de dizaines de milliers de lentilles est impraticable et d'autre part, la fabrication de simulations fussent-elles les plus réalistes possibles, biaisera forcément la détection des candidats, empêchant même la découverte de candidats lentilles rares, donc non présents dans l'échantillon simulé. Il est probable que les réseaux de neurones non-supervisés de type auto-encodeur seront de plus en plus utilisés pour la classification de données réelles (Cheng et al. 2020) car ils permettent d'éviter un étiquetage initial. C'est un des domaines de recherche que je compte explorer dans les prochaines années.

4.2.3 Recherches avec l'échantillon de groupes d'Euclid

Euclid avec sa moisson de 100 000 galaxies, 10 000 groupes de galaxies et 5000 amas découverts par effet de lentille, nous offrira d'ici 5 ans, un échantillon absolument inégalable d'étude des lentilles fortes dans un intervalle de redshift $0 < z < 1.5$. Je suis membre du consortium Euclid et je participe activement à la préparation des données avec mes collègues du groupe Strong Lensing Work Legacy Survey. Nous avons élaboré une stratégie de recherche de l'échantillon de lentilles fortes à toutes les échelles dans Euclid à travers une série de projets clefs approuvés par le board, que nous mèneront au fur et à mesure des publications internes des données observées à partir de 2023 jusqu'en 2030, un white paper est en cours de rédaction par le Strong Lensing Working Group (Strong lensing with Euclid, 2020 in prep).

4.2.4 Recherches instrumentales

Je n'ai pas du tout abordé dans ce manuscrit tout un pan de mes recherches instrumentales menées dès ma thèse (Astronomie avec Miroir Liquides, 1998) et poursuivies avec la thèse de mon étudiant (évoqués section 4.1). Ces dernières années, du fait de mes tâches de service comme directeur du Télescope Bernard Lyot, j'ai été amené à participer au projet de renouvellement de son instrumentation Narval en fonction depuis 2007, par une nouvelle instrumentation. L'instrument Neo-Narval (Neo-Narval) dont je suis le Co-PI PI Torsten Böhm) est actuellement en cours de commissioning au TBL. Le projet Neo-Narval consiste en une stabilisation en vitesse radiale et une jouvence générale du spectropolarimètre Narval. Le but scientifique de Neo-Narval est de répondre à trois questions astrophysiques majeures : i) étudier les étoiles géantes hôtes d'exoplanètes et comprendre les phases finales d'évolution des systèmes planétaires encore très mal connues et inobservées : quelle influence ont les champs magnétiques au moment crucial où l'atmosphère des étoiles absorbe leur cortège de planètes ? Peut-on observer ces événements majeurs directement ? ii) Etudier les cycles d'activité des étoiles de type solaire et établir leur occurrence et variation en fonction de l'intensité et de la topologie magnétique de l'étoile, afin de mieux comprendre la dynamo magnétique stellaire. iii) Etudier en profondeur le magnétisme stellaire à travers le diagramme HR pour comprendre le rôle que jouent les différents paramètres stellaires fondamentaux dans la génération des champs magnétiques. Une partie de mon temps de recherche des prochaines années sera dédié à la finalisation des capacités de Neo-Narval et à la participation aux programmes scientifiques de l'instrument, en particulier le suivi des Jupiter chauds dans les systèmes stellaires en fin de vie.

Chapitre 5

Conclusion

Ce manuscrit avait pour but de décrire l'état de nos connaissances sur les groupes de galaxies et d'apporter la petite brique de l'étude des effets de lentilles à l'édifice de nos connaissances actuelles. La somme des connaissances cumulées par des générations de naturalistes d'abord, puis d'astronomes, puis de physiciens et enfin d'astrophysiciens depuis trois cents ans est impressionnante. Quand on songe que nous ne savions pas, au début du XXe siècle, si notre univers se limitait à notre Voie Lactée et si les nébuleuses spirales et elliptiques faisaient partie de notre galaxie ou non. Alors qu'aujourd'hui la finesse de nos observations nous permet de proposer un scénario plausible d'histoire de l'Univers de ses tous premiers instants jusqu'à aujourd'hui, 13.8 milliards d'années plus tard, à quelques pourcents d'erreur sur les paramètres des modèles cosmologiques les plus probables.

Ainsi nous savons que notre univers était en expansion décélérée jusqu'à il y a environ 5 milliards d'années et en expansion accélérée depuis. Nous pensons que cette accélération provient d'une énergie sombre dominant aujourd'hui le budget énergétique de l'Univers à 70%. Nous savons que l'univers contenait à sa naissance une soupe de plasma chaud, homogène, seulement parcouru par d'infimes fluctuations aléatoires d'un dix-millièmes à un cent-millième de sa température et densité moyennes. Nous pensons que ce fluide cosmique est composé à 90% d'une matière étrange non-collisionnelle qui n'interagit pas avec le 10% restant de matière normale (les protons, neutrons ou baryons et les électrons) autrement qu'à travers la gravité. Nous pensons que ce fluide cosmique s'est effondré dans les zones de sur-densité pour former les premières étoiles, les premiers trous noirs et autour d'eux des proto-galaxies (l'apparition des trous noirs super-massifs reste une énigme aujourd'hui).

Nous savons qu'avant même que les étoiles ne commencent à se créer et à ioniser le milieu neutre ambiant, ce fluide cosmique s'est refroidit et s'est structuré pendant quelques millions d'années, sous l'action de la gravité, en objets de plus en plus grands physiquement et de plus en plus massifs. L'observation de cette période de l'espace-temps qu'on appelle l'âge sombre reste encore très difficile, même aujourd'hui avec nos puissants moyens, mais sera à la portée de l'observatoire radio Square Kilometer Array.

Aux très grandes échelles, la distribution des galaxies recèle l'empreinte des effets cosmologiques dans l'évolution des structures, cette empreinte rejoint celle laissée par le rayonnement de corps noir émis 380 000 ans après le Big Bang. Les effets cosmologiques expliquent l'apparition des grandes structures et des amas de galaxies dont le nombre dépend du modèle cosmologique. Aux échelles plus petites l'effondrement devient non-linéaire, ce sont les effets de la physique baryonique qui permettent de mieux expliquer

la formation des galaxies, des groupes de galaxies et un certain nombre d'effets observés dans les amas. Les groupes de galaxies qui contiennent l'immense majorité des galaxies de l'univers. Ils sont aussi les blocs de base de la construction des amas de galaxies par fusions progressives au cours du temps. Ces groupes de galaxies sont à la frontière des effets cosmologiques et des effets de la physique baryonique. Comprendre la physique qui gouverne leur formation et leur évolution, c'est comprendre le chaînon reliant l'univers local à l'univers cosmologique.

Par ailleurs, nous observons que l'histoire de la formation des étoiles à l'échelle de l'Univers a connu un pic de formation commençant il y a 12 milliards d'années et un plateau d'une durée de 2 milliards d'années. Puis, pour une raison que l'on ne comprend pas encore très bien, l'efficacité de cette formation d'étoiles a graduellement diminué dans l'univers jusqu'à pratiquement zéro, aujourd'hui. Pendant ce temps, les zones sur-denses se sont hiérarchiquement assemblées pour former d'immenses ensembles de galaxies et d'amas de galaxies via des réseaux de feuilles et de filaments, eux-mêmes trop faibles pour être visibles, mais nécessaires selon les simulations numériques, pour acheminer le carburant (le gaz) dans les galaxies, lieux de formation des étoiles.

Avec l'augmentation des concentrations de matière baryonique, les phénomènes physiques décrivant les interactions au sein des galaxies se sont complexifiés. Les étoiles ont changés chimiquement, les métaux ont enrichi le milieu interstellaire, la poussière et les composantes froides ont été créés. La physique décrivant la vie des étoiles est suffisamment comprise aujourd'hui pour interpréter les observations de la plupart des objets de notre Univers proche, des plus denses (les trous noirs, pulsars, étoiles à neutron) aux plus diffus (le gaz chaud du milieu intra-amas), des plus jeunes (nuages moléculaires pouponnières d'étoiles) aux plus anciens (naines blanches), des plus froids aux plus chauds.

Pourtant, de cet ensemble relativement cohérent, émergent des zones d'ombre, voire d'obscurité. Nous ne comprenons toujours pas bien la formation des amas, groupes de galaxies et galaxies-même. Une tension a récemment émergée dans les mesures reliant la densité de l'univers et le taux de formation des structures. Tension entre les données provenant du rayonnement de fond cosmologique, provenant donc dans l'Univers jeune, et les données provenant de la distribution des galaxies, donc dans de l'espace-temps proche de nous. Pourquoi cette tension ? Cela annonce-t-il une crise de la cosmologie ou est-ce explicable par des modifications mineures du modèle standard (e.g. Di Valentino et al. 2020) ?

La formation d'étoiles dans les galaxies semble être passée d'une phase extrêmement efficace il y a 10 milliards d'année, à une phase extrêmement inefficace aujourd'hui. Les raisons de cette évolution restent obscures. Est-ce à mettre à l'actif des processus de rétroactions divers des étoiles elles-mêmes, des noyaux de galaxies actifs ? Est-ce causé par des effets de balayages dynamiques lors de la création des amas et des groupes ? Est-ce dû à des effets non-linéaires de marées gravitationnelles au sein des groupes de galaxies ?

Plus énigmatiques encore sont les composantes sombres. La matière sombre non-baryonique fait l'objet de recherches actives depuis bientôt 60 ans sans succès pour l'instant. Quelles sont ses propriétés hormis celles, assez vagues, imposées par les modèles de formation ? Pourquoi n'observe-t-on qu'un nombre de galaxies naines très inférieur (d'un facteur trois à dix) au nombre prédit par les simulations à n -corps ?

Les simulations hydrodynamiques font des efforts louables pour introduire de la physique dans les particules simulées sur des échelles allant de quelques kiloparsecs à celles du cosmos. Mais ces simulations manquent de résolution aux échelles les plus petites. Pour

pallier ces limites, les simulations introduisent des recettes largement phénoménologiques imitant la physique baryonique des échelles non-résolues. Malheureusement ce sont à ces échelles non-résolues, celles des zones denses de gaz froid où se forment les étoiles et celles des zones à proximité des trous noirs super-massifs, que se joue toute la physique des rétroactions.

Les premières tentatives pour assembler des échantillons conséquents de groupes de galaxies sur la base de leur détections en X ou par effets de lentilles nous limitent encore aux groupes les plus massifs. Ces efforts présentés en partie dans ce manuscrit montrent que les analyses combinées d'effet de lentille et de dispersion de vitesses sont des outils puissants pour distinguer les composantes en interaction physique, établir des profils sur de grands rayons en combinant les effets de lentilles forts et faibles, tester les lois d'échelles dans les groupes de galaxies. Ils montrent en outre, la complexité dynamique de ses groupes lentilles fortes, dont certains sont très perturbés et certains relativement simples, en apparence, à modéliser. Ces travaux soulignent l'importance d'inclure un maximum d'observations dans toutes les gammes de longueurs d'onde pour séparer les effets cosmologiques des effets baryoniques.

Dans les travaux de recherches poursuivis jusqu'à aujourd'hui sur le SL2S, aucune analyse chimique des membres des groupes, d'études de gradients de métallicité et d'âge de populations stellaires n'ont été faites. Ces éléments seraient une excellente source d'information indépendante sur l'évolution de la formation stellaire, l'âge des sursauts de formation. On sent malgré tout qu'il sera difficile d'établir des lois robustes sur la base d'une centaine de groupes bien caractérisés.

Il est donc essentiel de poursuivre la détection d'échantillons importants de groupes de galaxies que permettront les prochaines missions et les prochains observatoires au sol. Euclid et l'observatoire Vera Rubin (sondage LSST) sont certainement les plus prometteurs pour découvrir des milliers de nouveaux groupes de galaxies par effet de lentille. Les années qui viennent nous promettent donc des avancées importantes dans notre connaissance de l'histoire du cosmos à travers ces objets si communs, si divers, et parfois si complexes, ces objets qui recèlent la clef de l'évolution des structures à la frontière de la physique baryonique et de la cosmologie : les groupes de galaxies.

Bibliographie

- Abadi, M. G., Moore, B., & Bower, R. G. 1999, MNRAS, 308, 947
- Abazajian, K. N., Adelman-McCarthy, J. K., Agüeros, M. A., et al. 2009, ApJ Sup. Ser., 182, 543
- Abbott, B. P., Abbott, R., Abbott, T. D., et al. 2016, PRL, 116, 061102
- Abell, G. O. 1958, The Astrophysical Journal Supplements, 3, 211
- Adam, R., Vannier, M., Maurogordato, S., et al. 2019, A&A, 627, A23
- Aguerri, J. A. L., Girardi, M., Boschini, W., et al. 2011, A&A, 527, A143
- Alatalo, K., Appleton, P. N., Lisensfeld, U., et al. 2015, The Astrophysical Journal, 812, 117
- Anguita, T., Barrientos, L. F., Gladders, M. D., et al. 2012, The Astrophysical Journal, 748, 129
- Auger, M. W., Treu, T., Brewer, B. J., & Marshall, P. J. 2011, Monthly Notices of the Royal Astronomical Society : Letters, 411, L6
- Avila-Rese, V. 2006, in Lectures given at the IV Mexican School of Astrophysics, July 18-25, 2005, 48
- Ayromlou, M., Nelson, D., Yates, R. M., Kauffmann, G., & White, S. D. M. 2019, MNRAS, 487, 4313
- Baldry, I. K., Driver, S. P., Loveday, J., et al. 2012, MNRAS, 421, 621
- Balona, L. A., Henrichs, H. F., & Medupe, R., eds. 2003, Astronomical Society of the Pacific Conference Series, Vol. 305, Magnetic Fields in O, B and A Stars : Origin and Connection to Pulsation, Rotation and Mass Loss
- Barchi, P. H., de Carvalho, R. R., Rosa, R. R., et al. 2019, arXiv e-prints, arXiv :1901.07047
- Bardeen, J., Steinhardt, P., & Turner, M. S. 1983, Phys. Rev. D, 28
- Barnes, D. J., Kay, S. T., Bahé, Y. M., et al. 2017, Monthly Notices of the Royal Astronomical Society, 471, 1088
- Barnes, J. E. 1989, Nature, 338, 123
- Bartelmann, M. 2010, Classical and Quantum Gravity, 27, 233001

- Bartelmann, M. & Maturi, M. 2017, *Scholarpedia*, 12, 32440
- Bartolo, N., Komatsu, E., Matarrese, S., & Riotto, A. 2004, *Phys. Reports*, 402, 103
- Bayliss, M. B., Gladders, M. D., Oguri, M., et al. 2011, *The Astrophysical Journal*, 727, L26
- Behroozi, P. S., Wechsler, R. H., & Conroy, C. 2013, *ApJ*, 770, 57
- Bekenstein, J. D. 2011, *Philosophical Transactions of the Royal Society A : Mathematical, Physical and Engineering Sciences*, 369, 5003
- Bellagamba, F., Roncarelli, M., Maturi, M., & Moscardini, L. 2017, *Monthly Notices of the Royal Astronomical Society*, 473, 5221
- Bernardeau, F., Colombi, S., Gaztañaga, E., & Scoccimarro, R. 2002, *Physics, Reports*, 367, 1
- Betoule, M., Kessler, R., Guy, J., et al. 2014, *A&A*, 568, A22
- Bielby, R., Crighton, N. H. M., Fumagalli, M., et al. 2017, *Monthly Notices of the Royal Astronomical Society*, 468, 1373–1386
- Birrer, S. & Amara, A. 2018, *Physics of the Dark Universe*, 22, 189–201
- Blandford, R. D., Kochanek, C. S., Kovner, I., & Narayan, R. 1989, *Science*, 245, 824
- Blandford, R. D. & Narayan, R. 1992, *Annual Review of Astronomy and Astrophysics*, 30, 311
- Bolton, A. S., Burles, S., Koopmans, L. V. E., Treu, T., & Moustakas, L. A. 2006, *The Astrophysical Journal*, 638, 703
- Bom, C., Poh, J., Nord, B., Blanco-Valentin, M., & Dias, L. 2019
- Boquien, M., Burgarella, D., Roehlly, Y., et al. 2019, *Astronomy and Astrophysics*, 622, A103
- Boucaud, A., Huertas-Company, M., Heneka, C., et al. 2019, *arXiv e-prints*, arXiv :1905.01324
- Brownstein, J. R., Bolton, A. S., Schlegel, D. J., et al. 2012, *Astrophysical Journal*, 744
- Bruzual, G. & Charlot, S. 2003, *Monthly Notices of the Royal Astronomical Society*, 344, 1000
- Burke, C. J., Aleo, P. D., Chen, Y.-C., et al. 2019, *arXiv e-prints*, arXiv :1908.02748
- Cabanac, R. A., Alard, C., Dantel-Fort, M., et al. 2007, *A&A*, 461, 813
- Cabanac, R. A., Valls-Gabaud, D., Jaunsen, A. O., Lidman, C., & Jerjen, H. 2005, *A&A*, 436, L21
- Canameras, R., Schuldt, S., Suyu, S. H., et al. 2020, *arXiv e-prints*, arXiv :2004.13048
- Capak, P., Cuillandre, J.-C., Bernardeau, F., et al. 2019, *arXiv e-prints*, arXiv :1904.10439

- Carroll, S., Press, W., & Turner, M. S. 1992, *Annual Review of Astronomy and Astrophysics*, 30, 499
- Carroll, S. M., Press, W. H., & Turner, E. L. 1992, *ARAA*, 30, 499
- Cayatte, V., Kotanyi, C., Balkowski, C., & van Gorkom, J. H. 1994, *AJ*, 107, 1003
- C  lerier, M. N. 2012, *A&A*, 543, A71
- Chabrier, G. 2003, *Publications of the Astronomical Society of the Pacific*, 115, 763
- Chand, H., Srianand, R., Petitjean, P., & Aracil, B. 2004, *A&A*, 417, 853
- Cheng, T.-Y., Li, N., Conselice, C. J., et al. 2020, *Monthly Notices of the Royal Astronomical Society*, 494, 3750
- Chevallard, J. & Charlot, S. 2016, *Monthly Notices of the Royal Astronomical Society*, 462, 1415
- Chiu, I., Saro, A., Mohr, J., et al. 2016, *MNRAS*, 458, 379
- Chollet et al., F. 2018, *Keras : The Python Deep Learning library*
- Cid Fernandes, R., Mateus, A., Sodr  , L., Stasi  nska, G., & Gomes, J. M. 2005, *Monthly Notices of the Royal Astronomical Society*, 358, 363
- Coc, A. & Vangioni, E. 2017, *International Journal of Modern Physics E*, 26, 1741002
- Cole, S., Aragon-Salamanca, A., Frenk, C. S., Navarro, J. F., & Zepf, S. E. 1994, *Monthly Notices of the Royal Astronomical Society*, 271, 781
- Cole, S., Lacey, C. G., Baugh, C. M., & Frenk, C. S. 2000, *MNRAS*, 319, 168
- Collaboration :, D. E. S., Abbott, T., Abdalla, F. B., et al. 2016, *Monthly Notices of the Royal Astronomical Society*, 460, 1270
- Colless, M., Dalton, G., Maddox, S., et al. 2001, *Monthly Notices of the Royal Astronomical Society*, 328, 1039
- Corsini, E. M., Morelli, L., Zarattini, S., et al. 2018, *Astronomy & Astrophysics*, 618, A172
- Cosmai, L., Fanizza, G., Sylos Labini, F., Pietronero, L., & Tedesco, L. 2019, *Classical and Quantum Gravity*, 36, 045007
- Cousin, M., Guillard, P., & Lehnert, M. D. 2019, *Astronomy and Astrophysics*, 627, A131
- Dalla Vecchia, C. & Schaye, J. 2012, *MNRAS*, 426, 140
- Davis, T. M. & Lineweaver, C. H. 2004, *PASA*, 21, 97
- Dekel, A. & Silk, J. 1986, *ApJ*, 303, 39
- dell'Antonio, I. P. & Tyson, J. A. 1996, *The Astrophysical Journal*, 473, L17
- Di Valentino, E., Anchordoqui, L. A., Ali-Haimoud, Y., et al. 2020, 1

- Díaz-Giménez, E., Zandivarez, A., & Taverna, A. 2018, *A&A*, 157, 1
- Diehl, H. T., Buckley-Geer, E. J., Lindgren, K. A., et al. 2017, *The Astrophysical Journal Supplement Series*, 232, 15
- Dobbels, W., Krier, S., Pirson, S., et al. 2019, *Astronomy and Astrophysics*, 624, A102
- Domínguez Sánchez, H., Huertas-Company, M., Bernardi, M., Tuccillo, D., & Fischer, J. L. 2018, *Monthly Notices of the Royal Astronomical Society*, 476, 3661
- Donati, J. F. & Landstreet, J. D. 2009, *Annual Review of Astronomy and Astrophysics*, 47, 333
- D’Onghia, E., Sommer-Larsen, J., Romeo, A. D., et al. 2005, *ApJ Let.*, 630, L109
- Duarte, M. & Mamon, G. A. 2015, *MNRAS*, 453, 3848
- Dubois, Y., Pichon, C., Welker, C., et al. 2014, *Monthly Notices of the Royal Astronomical Society*, 444, 1453
- Ebeling, H., Edge, A. C., & Henry, J. P. 2001, *ApJ*, 553, 668
- Ebeling, H., Stephenson, L. N., & Edge, A. C. 2014, *ApJ Let*, 781, L40
- Ebrahimpour, L., Viana, P. T. P., Manolopoulou, M., et al. 2018, arXiv e-prints, arXiv :1805.03465
- Efstathiou, G. 1992, *MNRAS*, 256, 43P
- Ellis, G. 2008, *Nature*, 452, 158
- Epinat, B., Contini, T., Finley, H., et al. 2018, *Astronomy & Astrophysics*, 609, A40
- Estrada, J., Annis, J., Diehl, H. T., et al. 2007, *The Astrophysical Journal*, 660, 1176
- Fabian, A. C. 1994, *ARA&A*, 32, 277
- Fabian, A. C. 2012, *ARA&A*, 50, 455
- Farhang, M., Bond, J. R., & Chluba, J. 2011, arXiv.org, 1110, 4608
- Faure, C., Kneib, J., Covone, G., et al. 2008, *The Astrophysical Journal Supplement Series*, 176, 19–38
- Fischer, J. L., Domínguez Sánchez, H., & Bernardi, M. 2019, *Monthly Notices of the Royal Astronomical Society*, 483, 2057
- Foëx, G., Motta, V., Limousin, M., et al. 2013, *A&A*, 559, A105
- Fort, B., Mellier, Y., Kneib, J. P., Pelló, R., & Bonnet, H. 1993, in *Astronomical Society of the Pacific Conference Series*, Vol. 51, *Observational Cosmology*, ed. G. L. Chincarini, A. Iovino, T. Maccacaro, & D. Maccagni, 419
- Frieman, J. A., Turner, M. S., & Huterer, D. 2008, *ARAA*, 46, 385
- Furlanetto, C., Santiago, B. X., Makler, M., et al. 2013, *Monthly Notices of the Royal Astronomical Society*, 432, 73

- Gaia Collaboration, Brown, A. G. A., Vallenari, A., et al. 2018, *A&A*, 616, A1
- Gaia Collaboration, Prusti, T., de Bruijne, J. H. J., et al. 2016, *A&A*, 595, A1
- Gallagher, J. S. 1978, *ApJ*, 223, 386
- Gaspari, M., Brighenti, F., D’Ercole, A., & Melioli, C. 2011a, *Monthly Notices of the Royal Astronomical Society*, 415, 1549
- Gaspari, M., Melioli, C., Brighenti, F., & D’Ercole, A. 2011b, *Monthly Notices of the Royal Astronomical Society*, 411, 349
- Gastaldello, F., Limousin, M., Foex, G., et al. 2014, *MNRAS*, 442, L76
- Gaudi, B. S. 2012, *Annual Review of Astronomy and Astrophysics*, 50, 411
- Giodini, S., Lovisari, L., Pointecouteau, E., et al. 2013, *Space Science Reviews*, 177, 247
- Giovanelli, R. & Haynes, M. P. 1985, *ApJ*, 292, 404
- Girardi, M., Manzato, P., Mezzetti, M., Giuricin, G., & Limboz, F. 2002, *ApJ*, 569, 720
- Gladders, M. D., Yee, H. K. C., McCarthy, P. J., et al. 2002, in *American Astronomical Society Meeting Abstracts*, Vol. 201, 59.06
- Gong, Y., Liu, X., Cao, Y., et al. 2019, *The Astrophysical Journal*, 883, 203
- González, R. E., Muñoz, R. P., & Hernández, C. A. 2018, *Astronomy and Computing*, 25, 103
- González Delgado, R. M., Cerviño, M., Martins, L. P., Leitherer, C., & Hauschildt, P. H. 2005, *Monthly Notices of the Royal Astronomical Society*, 357, 945
- Gorbunov, A. A., Isaev, E. A., & Samodurov, V. A. 2017, *Russian Radio Physics and Radio Astronomy*, 22, 270
- Gozaliasl, G., Finoguenov, A., Khosroshahi, H. G., et al. 2014, *Astronomy & Astrophysics*, 566, A140
- Guérou, A., Emsellem, E., Krajnović, D., et al. 2016, *Astronomy and Astrophysics*, 591, A143
- Gunn, J. E. & Gott, J. Richard, I. 1972, *ApJ*, 176, 1
- Guo, Q., White, S., Boylan-Kolchin, M., et al. 2011, *MNRAS*, 413, 101
- Hansson, J. 2015, *International Journal of Modern Physics and Applications*, 1, 12
- Hartley, P., Flamary, R., Jackson, N., Tagore, A. S., & Metcalf, R. B. 2017, *MNRAS*, 471, 3378
- Hausen, R. & Robertson, B. 2019, *arXiv e-prints*, arXiv :1906.11248
- Heavens, A., Panter, B., Jimenez, R., & Dunlop, J. 2004, *Nature*, 428, 625
- Henden, N. A., Puchwein, E., Shen, S., & Sijacki, D. 2018, *MNRAS*, 479, 5385

- Hester, J. A. 2006, *The Astrophysical Journal*, 647, 910
- Hezaveh, Y. D., Dalal, N., Marrone, D. P., et al. 2016, *ApJ*, 823, 37
- Hezaveh, Y. D., Levasseur, L. P., & Marshall, P. J. 2017, *Nature*, 548, 555–557
- Hickson, P. 1982, *ApJ*, 255, 382
- Hickson, P. 1994 (Gordon and Breach Science Publishers S.A.), 221
- Ho, M., Rau, M. M., Ntampaka, M., et al. 2019, arXiv e-prints, arXiv :1902.05950
- Hopkins, A. M. & Beacom, J. F. 2006, *ApJ*, 651, 142
- Hopkins, A. M., Driver, S. P., Brough, S., et al. 2013, *Monthly Notices of the Royal Astronomical Society*, 430, 2047
- Horner, D. J. 2001, PhD thesis, University of Maryland College Park
- Huchra, J. P. & Geller, M. J. 1982, *ApJ*, 257, 423
- Huertas-Company, M., Gravet, R., Cabrera-Vives, G., et al. 2015, *The Astrophysical Journal Supplement Series*, 221, 8
- Huertas-Company, M., Rodriguez-Gomez, V., Nelson, D., et al. 2019, arXiv e-prints, arXiv :1903.07625
- Husemann, B., Bennert, V. N., Scharwächter, J., Woo, J. H., & Choudhury, O. S. 2016, *MNRAS*, 455, 1905
- Husemann, B. & Harrison, C. M. 2018, *Nature Astronomy*, 2, 196
- Ibata, R. A., McConnachie, A., Cuillandre, J.-C., et al. 2017, *ApJ*, 848, 128
- Inada, N., Oguri, M., Shin, M.-S., et al. 2012, *The Astronomical Journal*, 143, 119
- Irwin, J. A., Dupke, R., Carrasco, E. R., et al. 2015, *ApJ*, 806, 268
- Ishiyama, T., Prada, F., Klypin, A. A., et al. 2020, 18, 1
- Ivezić, Ž., Kahn, S. M., Tyson, J. A., et al. 2019, *The Astrophysical Journal*, 873, 111
- Jachym, P., Kenney, J. D. P., Sun, M., et al. 2019, arXiv e-prints, arXiv :1905.13249
- Jackson, N., Rampadarath, H., Ofek, E. O., Oguri, M., & Shin, M. S. 2012, *Monthly Notices of the Royal Astronomical Society*, 419, 2014
- Jacobs, C., Collett, T., Glazebrook, K., et al. 2019, *The Astrophysical Journal Supplement Series*, 243, 17
- Jaelani, A. T., More, A., Oguri, M., et al. 2020, 17, 1
- Jankov, V. & Prochaska, J. X. 2018, *Publications of the Astronomical Society of the Pacific*, 130, 094501
- Jauzac, M., Richard, J., Jullo, E., et al. 2015, *Mon. Not. R. Astron. Soc.*, 452, 1437

- Jones, D. H., Read, M. A., Saunders, W., et al. 2009, *MNRAS*, 399, 683
- Jones, L. R., Ponman, T. J., Horton, A., et al. 2003, *Monthly Notices of the Royal Astronomical Society*, 638, 627
- Jullo, E. & Kneib, J. P. 2009, *MNRAS*, 395, 1319
- Jullo, E., Kneib, J. P., Limousin, M., et al. 2007, *New Journal of Physics*, 9, 447
- Kaiser, N. 1986, *MNRAS*, 222, 323
- Karachentsev, I. D. & Kashibadze, O. G. 2006, *Astrophysics*, 49, 3
- Kay, S. T., Pearce, F. R., Frenk, C. S., & Jenkins, A. 2002, *Monthly Notices of the Royal Astronomical Society*, 330, 113
- Keeton, C. R. 2001, arXiv e-prints, astro
- Keller, B. W. & Kruijssen, J. M. D. 2020, arXiv e-prints, arXiv :2004.03608
- Keller, B. W., Wadsley, J., Benincasa, S. M., & Couchman, H. M. 2014, *Monthly Notices of the Royal Astronomical Society*, 442, 3013
- Kennicutt, R. C. 1998, *The Astrophysical Journal*, 498, 541
- Kennicutt, R. C. & Evans, N. J. 2012, *ARAA*, 50, 531
- Khan, A., Huerta, E. A., Wang, S., et al. 2019, *Physics Letters B*, 795, 248
- Khandai, N., Di Matteo, T., Croft, R., et al. 2015, *Monthly Notices of the Royal Astronomical Society*, 450, 1349
- King, L., Browne, I., Marlow, D., Patnaik, A., & Wilkinson, P. 2002, *Monthly Notices of the Royal Astronomical Society*, 307, 225
- Kneib, J. P., Ellis, R. S., Smail, I., Couch, W. J., & Sharples, R. M. 1996, *ApJ*, 471, 643
- Kneib, J.-P. & Natarajan, P. 2011, *Astronomy and Astrophysics Review*, 19, 47
- Kochanek, C. S., Falco, E. E., Impey, C. D., et al. 1999, in *American Institute of Physics Conference Series*, Vol. 470, *After the Dark Ages : When Galaxies were Young (the Universe at $2 < Z < 5$)*, ed. S. Holt & E. Smith, 163–175
- Kolb, E. W. & Turner, M. S. 1990, *The Early Universe (Addison-Wesley)*, 547
- Kravtsov, A. V. & Borgani, S. 2012, *ARAA*, 50, 353
- Kroupa, P. 2002, *Science*, 295, 82
- Kubo, J. 2007, PhD thesis, Brown University
- Kubo, J. M., Allam, S. S., Annis, J., et al. 2009, *The Astrophysical Journal*, 696, L61
- Kubo, J. M., Allam, S. S., Drabek, E., et al. 2010, *The Astrophysical Journal*, 724, L137
- Kundert, A., D’Onghia, E., & Aguerri, J. A. L. 2017, *ApJ*, 845, 45

- Kundert, A., Gastaldello, F., D'Onghia, E., et al. 2015, *MNRAS*, 454, 161
- Lanusse, F., Ma, Q., Li, N., et al. 2018, *Monthly Notices of the Royal Astronomical Society*, 473, 3895
- Lefor, A. T., Futamase, T., & Akhlaghi, M. 2013, *New Astronomy Reviews*, 57, 1
- Lemon, C. A., Auger, M. W., & McMahon, R. G. 2019, *MNRAS*, 483, 4242
- Leung, H. W. & Bovy, J. 2019, *Monthly Notices of the Royal Astronomical Society*, 483, 3255
- Li, C. & White, S. D. M. 2009, *MNRAS*, 398, 2177
- Limousin, M., Cabanac, R., Gavazzi, R., et al. 2009, *A&A*, 502, 445
- Limousin, M., Jullo, E., Richard, J., et al. 2010, *Astronomy and Astrophysics*, 524, 1
- Limousin, M., Richard, J., Kneib, J. P., et al. 2008, *A&A*, 489, 23
- Lin, Y.-T., Stanford, S. A., Eisenhardt, P. R. M., et al. 2012, *The Astrophysical Journal Letters*, 745, L3
- Lombardo, S., Muslimov, E., Valls-Gabaud, D., et al. 2019, in *Society of Photo-Optical Instrumentation Engineers (SPIE) Conference Series*, Vol. 11180, *International Conference on Space Optics — ICSO 2018*, 111802W
- Lotz, J. M., Koekemoer, A., Coe, D., et al. 2017, *The Astrophysical Journal*, 837, 97
- Lucas, W. E., Bonnell, I. A., & Dale, J. E. 2020, *Monthly Notices of the Royal Astronomical Society*, 493, 4700–4710
- Madau, P. & Dickinson, M. 2014, *ARAA*, 52, 415
- Madau, P., Ferrara, A., & Rees, M. J. 2001, *ApJ*, 555, 92
- Mahler, G., Sharon, K., Fox, C., et al. 2019, *ApJ*, 873, 96
- Makarov, D. & Karachentsev, I. 2011, 2520, 2498
- Malmquist, K. G. 1922, *Meddelanden fran Lunds Astronomiska Observatorium Serie I*, 100, 1
- Mamon, G. A. 1986, *ApJ*, 307, 426
- Mandelbaum, R. 2018, *Annual Review of Astronomy and Astrophysics*, 56, 393
- Mantz, A. B., Allen, S. W., Morris, R. G., & Schmidt, R. W. 2016, *Monthly Notices of the Royal Astronomical Society*, 456, 4020
- Marshall, P. J., Hogg, D. W., Moustakas, L. A., et al. 2009, *ApJ*, 694, 924
- Mathis, H., Charlot, S., & Brinchmann, J. 2006, *Monthly Notices of the Royal Astronomical Society*, 365, 385
- McDonald, M., Gaspari, M., McNamara, B. R., & Tremblay, G. R. 2018, *ApJ*, 858, 45

- McKean, J. P., Jackson, N., Vegetti, S., et al. 2014, 1
- McNamara, B. R. & Nulsen, P. E. J. 2012, *New Journal of Physics*, 14, 055023
- McPherson, A. M., McMullin, J., Stevenson, T., et al. 2018, in *Society of Photo-Optical Instrumentation Engineers (SPIE) Conference Series*, Vol. 10700, *Ground-based and Airborne Telescopes VII*, 107000Y
- Mehrtens, N., Romer, A. K., Hilton, M., et al. 2012, *MNRAS*, 423, 1024
- Mellier, Y. 1999, *Annual Review of Astronomy and Astrophysics*, 37, 127
- Mendes de Oliveira, C. L. & Carrasco, E. R. 2007, *ApJ Letter*, 670, 93
- Metcalf, R. B., Meneghetti, M., Avestruz, C., et al. 2019, *A&A*, 625, A119
- Meylan, G., Jetzer, P., North, P., et al., eds. 2006, *Gravitational Lensing : Strong, Weak and Micro*
- Milgrom, M. 1983, *ApJ*, 270, 365
- Milgrom, M. 2019, *Phys. Rev. D*, 99, 044041
- Milgrom, M. & Sanders, R. H. 2016
- Moore, B., Katz, N., Lake, G., Dressler, A., & Oemler, A. 1996, *Nature*, 379, 613
- More, A., Cabanac, R., More, S., et al. 2012, *ApJ*, 749, 38
- More, A., Jahnke, K., More, S., et al. 2011, *Astrophysical Journal - ASTROPHYS J*, 734
- More, A., Verma, A., Marshall, P. J., et al. 2016, *MNRAS*, 455, 1191
- Muñoz, R. P., Motta, V., Verdugo, T., et al. 2013, *A&A*, 552, A80
- Mulchaey, J. S. 2000, *ARA&A*, 38, 289
- Mulchaey, J. S. & Zabludoff, A. I. 1999, *The Astrophysical Journal*, 514, 133
- Muthukrishna, D., Parkinson, D., & Tucker, B. 2019, arXiv e-prints, arXiv :1903.02557
- Myers, S. T., Jackson, N. J., Browne, I. W. A., et al. 2003, *Monthly Notices of the Royal Astronomical Society*, 341, 1
- Nagai, D., Vikhlinin, A., & Kravtsov, A. V. 2007, *The Astrophysical Journal*, 655, 98
- Navarro, J. F. & White, S. D. 1993, *Mon. Not. R. Astron. Soc.*, 265, 271
- Negrello, M., Amber, S., Amvrosiadis, A., et al. 2017, *MNRAS*, 465, 3558
- Nightingale, J. W., Dye, S., & Massey, R. J. 2018, *Monthly Notices of the Royal Astronomical Society*, 478, 4738–4784
- Nottale, L. 2011, *Scale Relativity and Fractal Space-Time : a New Approach to Unifying Relativity and Quantum Mechanics*
- Ntampaka, M., ZuHone, J., Eisenstein, D., et al. 2019, *The Astrophysical Journal*, 876, 82

- Oguri, M. 2006, *Monthly Notices of the Royal Astronomical Society*, 367, 1241
- Ohlin, L., Renaud, F., & Agertz, O. 2019, *MNRAS*, 485, 3887
- Old, L., Skibba, R. A., Pearce, F. R., et al. 2014, *Monthly Notices of the Royal Astronomical Society*, 441, 1513
- Old, L., Wojtak, R., Mamon, G. A., et al. 2015, *Monthly Notices of the Royal Astronomical Society*, 449, 1897
- Osmond, J. P. & Ponman, T. J. 2004, *Monthly Notices of the Royal Astronomical Society*, 350, 1511
- Osterbrock, D. E. & Ferland, G. J. 2006, *Astrophysics of gaseous nebulae and active galactic nuclei*
- Pacaud, F., Pierre, M., Adami, C., et al. 2007, *Monthly Notices of the Royal Astronomical Society*, 382, 1289
- Paczynski, B. 1996, *Annual Review of Astronomy and Astrophysics*, 34, 419
- Padmanabhan, T. 1993, *Structure Formation in the Universe*, 499
- Peacock, J. A. 1999, *Cosmological Physics*
- Pearson, W. J., Wang, L., Trayford, J. W., Petrillo, C. E., & van der Tak, F. F. S. 2019, *Astronomy and Astrophysics*, 626, A49
- Peebles, P. J. E. 1993, *Principles of Physical Cosmology*
- Peebles, P. J. E. & Yu, J. T. 1970, *ApJ*, 162, 815
- Percival, W. J., Cole, S., Eisenstein, D. J., et al. 2007, *MNRAS*, 381, 1053
- Perlmutter, S., Aldering, G., Goldhaber, G., et al. 1999, *ApJ*, 517, 565
- Peter, P. & Uzan, J.-P. 2012, *Cosmologie primordiale 2e Edition* (Belin Education)
- Petrillo, C. E., Tortora, C., Chatterjee, S., et al. 2019, *Monthly Notices of the Royal Astronomical Society*, 482, 807
- Petrillo, C. E., Tortora, C., Vernardos, G., et al. 2019, *Monthly Notices of the Royal Astronomical Society*, 484, 3879
- Planck Collaboration, Ade, P. A. R., Aghanim, N., et al. 2016, *A&A*, 594, A13
- Planck Collaboration, Ade, P. A. R., Aghanim, N., et al. 2014, *A&A*, 24
- Planck Collaboration, Aghanim, N., Akrami, Y., et al. 2018, 1
- Poggianti, B. M., Moretti, A., Gullieuszik, M., et al. 2017, *ApJ*, 844, 48
- Ponman, T. J., Allan, D. J., Jones, L. R., et al. 1994, *Nature*, 369, 462
- Ponman, T. J., Sanderson, A. J. R., & Finoguenov, A. 2003, *MNRAS*, 343, 331
- Postman, M., Coe, D., Benítez, N., et al. 2012, *ApJ Suppl.*, 199, 25

- Pratt, G. W., Croston, J. H., Arnaud, M., & Böhringer, H. 2009, *Astronomy and Astrophysics*, 498, 361
- Proctor, R. N., Oliveira, C. M. D., Azanha, L., Dupke, R., & Overzier, R. 2015, *Mon. Not. R. Astron. Soc.*, 449, 2345
- Pyne, T. & Birkinshaw, M. 1996, *ApJ*, 458, 46
- Rafferty, D. A., McNamara, B. R., & Nulsen, P. E. J. 2008, *The Astrophysical Journal*, 687, 899
- Raouf, M., Khosroshahi, H. G., & Dariush, A. 2016, *ApJ*, 824, 140
- Reddy, N. A., Pettini, M., Steidel, C. C., et al. 2012, *The Astrophysical Journal*, 754, 25
- Refregier, A. 2003, *Annual Review of Astronomy and Astrophysics*, 41, 645
- Renaud, F. 2018, *New Astronomy Reviews*, 81, 1
- Rhodes, J., Nichol, R. C., Aubourg, É., et al. 2017, *The Astrophysical Journal Supplement Series*, 233, 21
- Riess, A. G., Filippenko, A. V., Challis, P., et al. 1998, *AJ*, 116, 1009
- Robson, D. & Dav, R. 2020, 17, 1
- Rotermund, K. M., Chapman, S. C., & Vieira, J. D. 2020, submitted to *Mon. Not. R. Astron. Soc*
- Sadr, A. V., Vos, E. E., Bassett, B. A., Oozeer, N., & Lochner, M. 2018, 15, 1
- Salpeter, E. E. 1955, *The Astrophysical Journal*, 121, 161
- Santos, W. A., Mendes de Oliveira, C., & Sodr e, Laerte, J. 2007, *The Astronomical Journal*, 134, 1551
- Sartoris, B., Biviano, A., Fedeli, C., et al. 2016, *MNRAS*, 459, 1764
- Scharf, C., Jones, L., Ebeling, H., et al. 1997, *ApJ*, 477, 79
- Schaye, J., Crain, R. A., Bower, R. G., et al. 2015, *Monthly Notices of the Royal Astronomical Society*, 446, 521
- Schaye, J., Vecchia, C. D., Booth, C. M., et al. 2010, *Monthly Notices of the Royal Astronomical Society*, 402, 1536
- Schneider, P., Ehlers, J., & Falco, E. E. 1992, *Gravitational Lenses*
- Sharon, K., Bayliss, M. B., Dahle, H., et al. 2019, arXiv e-prints, arXiv :1904.05940
- Shen, A. X. & Bekki, K. 2020, *MNRAS*
- Sheth, R. K., Mo, H. J., & Tormen, G. 2001, *Monthly Notices of the Royal Astronomical Society*, 323, 1
- Shu, Y., Bolton, A. S., Kochanek, C. S., et al. 2016, *The Astrophysical Journal*, 824, 86

- Silk, J. 1968, *ApJ*, 151, 459
- Silk, J. & Rees, M. J. 1998, *A&A*, 331, L1
- Singaravelu, B. & Cabanac, R. A. 2014, *PASP*, 126, 386
- Smith, M. C., Sijacki, D., & Shen, S. 2018, *Monthly Notices of the Royal Astronomical Society*, 478, 302
- Smith, M. J. & Geach, J. E. 2019, arXiv e-prints, arXiv :1904.10286
- Smith, N. 2014, *Annual Review of Astronomy and Astrophysics*, 52, 487
- Soker, N. 2016, *New Astronomy*, 75, 1
- Somerville, R. S. & Primack, J. R. 1999, *MNRAS*, 310, 1087
- Soucail, G., Fort, B., Mellier, Y., & Picat, J. P. 1987, *Astronomy and Astrophysics*, 172, L14
- Spilker, J. S., Marrone, D. P., Aravena, M., et al. 2016, *ApJ*, 826, 112
- Spiniello, C., Agnello, A., Napolitano, N. R., et al. 2018, *Monthly Notices of the Royal Astronomical Society*, 480, 1163
- Springel, V. 2010, *Monthly Notices of the Royal Astronomical Society*, 401, 791
- Springel, V. & Hernquist, L. 2003, *MNRAS*, 339, 289
- Stark, D. P., Auger, M., Belokurov, V., et al. 2013, *Monthly Notices of the Royal Astronomical Society*, 436, 1040
- Steidel, C. C., Adelberger, K. L., Shapley, A. E., et al. 2003, *The Astrophysical Journal*, 592, 728
- Steinhauser, D., Schindler, S., & Springel, V. 2016, *Astronomy & Astrophysics*, 591, A51
- Stinson, G., Seth, A., Katz, N., et al. 2006, *MNRAS*, 373, 1074
- Stinson, G. S., Bovy, J., Rix, H. W., et al. 2013, *Monthly Notices of the Royal Astronomical Society*, 436, 625
- Sylos Labini, F., Montuori, M., & Pietronero, L. 1998, *Phys. Rev.*, 293, 61
- Tago, E., Saar, E., Tempel, E., et al. 2010, *Astronomy & Astrophysics*, 514, A102
- Tegmark, M., Blanton, M. R., Strauss, M. A., et al. 2004, *The Astrophysical Journal*, 606, 702
- Tempel, E., Tuvikene, T., Kipper, R., & Libeskind, N. I. 2017, *A&A*, 100, 1
- Tessore, N., Bellagamba, F., & Metcalf, R. B. 2016, *Monthly Notices of the Royal Astronomical Society*, 463, 3115
- Teyssier, R. 2015, *ARAA*, 53, 325

- Tollet, E., Cattaneo, A., Macciò, A. V., Dutton, A. A., & Kang, X. 2019, *Monthly Notices of the Royal Astronomical Society*, 485, 2511–2531
- Treu, T. 2010, *Annual Review of Astronomy and Astrophysics*, 48, 87
- Treu, T., Agnello, A., Baumer, M. A., et al. 2018, *Monthly Notices of the Royal Astronomical Society*, 481, 1041
- Treu, T., Dutton, A. A., Auger, M. W., et al. 2011, *Monthly Notices of the Royal Astronomical Society*, 417, 1601–1620
- Tuccillo, D., Huertas-Company, M., Decencière, E., et al. 2018, *Monthly Notices of the Royal Astronomical Society*, 475, 894
- Tully, R. B. 2015, *The Astronomical Journal*, 149, 171
- Tully, R. B., Courtois, H., Hoffman, Y., & Pomarède, D. 2014, *Nature*, 513, 71
- Turner, E. L. & Gott, III, J. R. 1976, *ApJ Sup. Ser.*, 32, 409
- Valls-Gabaud, D. 2009, in *Astronomical Society of the Pacific Conference Series*, Vol. 409, *Cosmology Across Cultures*, ed. J. Rubiño-Martín, J. Belmonte, F. Prada, & A. Alberdi, 57
- Verdugo, T., Limousin, M., Motta, V., et al. 2016, *A&A*, 595, A30
- Verdugo, T., Motta, V., Foëx, G., et al. 2014, *A&A*, 571, A65
- Verdugo, T., Motta, V., Muñoz, R. P., et al. 2011, *A&A*, 527, A124
- Verlinde, E. 2017, *SciPost Physics*, 2, 016
- Vogelsberger, M., Genel, S., Sijacki, D., & et al. 2013, *MNRAS*, 436
- Vogelsberger, M., Genel, S., Springel, V., et al. 2014, *MNRAS*, 444, 1518
- Voit, G. M. 2005, *Rev. Mod. Phys.*, 77, 207
- Vollmer, B., Cayatte, V., Balkowski, C., & Duschl, W. J. 2001, *ApJ*, 561, 708
- von Benda-Beckmann, A. M., D’Onghia, E., Gottlöber, S., et al. 2008, *MNRAS*, 386, 2345
- Walsh, D., Carswell, R. F., & Weymann, R. J. 1979, *Nature*, 279, 381
- Wambsganss, J. 1998, *Living Reviews in Relativity*, 1, 12
- Wang, L., Dutton, A. A., Stinson, G. S., et al. 2015, *Monthly Notices of the Royal Astronomical Society*, 454, 83–94
- Wardlow, J. L., Cooray, A., Bernardis, F. D., et al. 2012 *arXiv* :1205.3778v2
- Weisberg, J. M. & Taylor, J. H. 2004, 1
- Wiesner, M. P., Lin, H., Allam, S. S., et al. 2012, *ApJ*, 761, 1
- Willis, J. P., Hewett, P. C., Warren, S. J., Dye, S., & Maddox, N. 2006, *Monthly Notices of the Royal Astronomical Society*, 369, 1521

- Wisotzki, L., Koehler, T., Groote, D., & Reimers, D. 1996, *ApJ Supp. Ser.*, 115, 227
- Wong, K. C., Ishida, T., Tamura, Y., et al. 2017, *ApJ Letters*, 843, L35
- Yoshida, M., Yagi, M., Komiyama, Y., et al. 2008, *ApJ*, 688, 918
- Zarattini, S., Barrena, R., Girardi, M., Boschini, W., & Aguerri, J. A. L. 2014, *Astronomy & Astrophysics*, 565, A116
- Zhang, X., Zhao, G., Yang, C. Q., Wang, Q. X., & Zuo, W. B. 2019, *Publications of the Astronomical Society of the Pacific*, 131, 094202
- Zhang, Z.-Y., Romano, D., Ivison, R. J., Papadopoulos, P. P., & Matteucci, F. 2018, *Nature*, 558, 260
- Zhao, Y., Ge, J., Yuan, X., et al. 2019, *Monthly Notices of the Royal Astronomical Society*, 487, 801
- Zhu, L., Romanowsky, A. J., van de Ven, G., et al. 2016, *Monthly Notices of the Royal Astronomical Society*, 462, 4001

Curriculum Vitae

Rémi André CABANAC

2 septembre 2020

Données personnelles

51 ans, marié, 6 enfants, citoyen Français et Canadien rcabanac@irap.omp.eu
Domicile: 7 Rue de la Collégiale, 65420 IBOS, France +33 5 62 34 26 33
Travail: 57 Avenue d'Azereix, 65000 TARBES +33 5 62 34 26 33
portable +33 6 84 88 33 93
ORCID: 0000-0001-6679-2600

Études

- **Université Laval** Québec, Canada
Doctorat en physique (PhD) 1998
 - Titre: Astronomie avec miroirs liquides.
 - Superviseur, Pr. Ermanno F. Borra. Boursier du Conseil de Recherches en Sciences Naturelles et en Génie du Canada (CRSNG).
 - Thèse faite en partie à l'Université de Colombie Britannique (UBC) avec P. Hickson.
 - Bourse d'excellence du Conseil de Recherches en Sciences Naturelles et en Génie du Canada (CRSNG).
- **Université Laval** Québec, Canada
Maîtrise en physique (MSc) 1992
 - Bourse d'excellence du Conseil de Recherches en Sciences Naturelles et en Génie du Canada (CRSNG).
- **Université Laval** Québec, Canada
Baccalauréat en physique (MSc) 1991
 - Bourse d'excellence du Conseil de Recherches en Sciences Naturelles et en Génie du Canada (CRSNG).
- **Secondaire et Primaire** Québec, Canada / Lyon, France
Baccalauréat C 1976-1987

Travail post-académique

- **Université de Toulouse 3 Paul Sabatier** Toulouse, France
Astronome Adjoint Hors Classe (Conseil National des Astronomes et Physiciens) depuis 2013
 - Tâches de service CNAP: Direction SNO3 TBL (de 2013 à 2016), SNO4 Euclid (depuis 2016).
 - Directeur Adjoint of Observatoire Midi Pyrénées au Pic du midi et à Tarbes par intérim (2015-2016)

- Responsable scientifique du Pic du midi, co-responsable scientifique SNO TBL par intérim (2019-2020)
- Directeur Adjoint de l’Observatoire Midi Pyrénées en Bigorre, Responsable scientifique du Pic du midi, co-responsable scientifique SNO TBL par intérim (depuis 2020)

- **Université de Toulouse 3 Paul Sabatier** Toulouse, France
Astronome Adjoint (Conseil National des Astronomes et Physiciens) 2009-2013
 - Tâches de service CNAP: Direction SNO3 TBL
 - Responsable scientifique Pic du midi & OMP Tarbes, Directeur Télescope Bernard Lyot, USR 5026 CNRS
- **Université de Toulouse 3 Paul Sabatier** Toulouse, France
CDD CNRS 2007-2009
 - Directeur Télescope Bernard Lyot, USR 5026 CNRS (2007-2008)
 - Responsable scientifique Pic du midi & OMP Tarbes, Directeur Télescope Bernard Lyot, USR 5026 CNRS (2009)
- **Canada-France-Hawaii Telescope** Hawaï, EU
Astronome résident NRC 2003-2006
 - Responsable scientifique instrument Espadons
 - Astronome support observations de service
 - Responsable Education and Public Outreach
- **European Southern Observatory** Vitacura, Chili
ESO Fellow 2000-2002
 - Science Operation: VLT Paranal, Astronome support visiteur et observations de service sur tous les instruments de UT1 à UT4 (2000-2001)
 - Post-doc Pontificia Universidad Catolica de Chile, Santiago, Campus San Joaquin (2002)
- **Institut d’Astrophysique de Paris** Paris, France
Post-doctorat du Fonds pour les Chercheurs et l’Aide à la Recherche (Québec) 1998-1999
 - Collaboration avec Valérie de Lapparent et Paul Hickson (UBC), préparation scientifique du Large Zenith Telescope (miroir liquide 6m en construction à UBC)

Enseignement et encadrement

- **Université de Toulouse 3 Paul Sabatier** Tarbes, France
Licence Physique, Chimie, Astrophysique, Météorologie, Énergie (L3 PCAME) depuis 2016
 - Relativité restreinte et notion de relativité générale S5
 - Astronomie extragalactique et cosmologie S6
 - Projets tutorés de recherche S6, 3 mois
 - TP d’observations astronomiques au Pic du Midi (une semaine), également donnés au Master 2 ASEP, Toulouse, M2 Univ. Bordeaux et M2 Univ. Franche Comté.
- **NEONS** Brno, Slovaquie
Summer school in modern astronomy 3-10 sept 2016
 - Cours invité: Telescope Bernard Lyot/Narval: The Observatory of Stellar Magnetism
- **Université de Toulouse 3 Paul Sabatier** Tarbes, France
Encadrements 2007-2020

- Post-doc ANR projet SL2S: Marceau LIMOUSIN (2007-2008), Anupreta MORE (2009)
- Thésitif: BALASUBRAMANIAN SINGARAVELU. Thèse intitulée *Modélisation de lentilles gravitationnelles et Design de télescopes non-obstrués pour les sondages grands champs* soutenue en nov 2014. (2012-2014)
- Stage M2 offert, mais effectué en stage M1(3 mois): Joshua GONNET, Univ Lyon: Euclid: cluster detection, impact of masking on AMICO and PZWAV. (2020)
- Stages d'été découverte de la recherche:
 - * Lucas FUSTER 1ère Année, Magistère Physique Fondamentale, Orsay (été 2017),
 - * Aritra ROY Stage de fin d'étude Indian Institute of Science Education and Research (IISER), Kolkata, India (2017),
 - * Nils CANDEBAT 1ère Année de Magistère Physique Fondamentale, Orsay (été 2019),
 - * Hugues EVARD LPCAME (2019).

- **Institut Supérieur de l'Aéronautique et de l'Espace (ISAE Supaero)** Toulouse, France
Cours sur les grands projets internationaux d'observatoires astronomiques au sol 2012-2016
- **Université Laval** Québec, Canada
Département de physique 1998
 - Cours de Science et Société adressés aux futurs enseignants du secondaire

Contrats de recherche

- COST: Polarization as a tool... , PI Hervé LAMY, Belg. Inst. for Space Aeronomy. (2012-2015)
- ANR: Strong Lensing Legacy Survey, PI B. Fort (2006-2009)

Sociétés savantes

- Canadian Astronomical Society Canadienne d'Astronomie (1992-2006)
- Société Française d'Astronomie et d'Astrophysique (depuis 2003)
- European Astronomical Society (depuis sa fondation)
- International Astronomical Union (Co-chairman of IAU Commission C.C4 (2015-2016 et 2020...))

Comités

- Membre CFHT TAC (Depuis 2018)
- Observatoire Midi Pyrénées: Comité scientifique (2007-2016, et depuis 2019)
- Observatoire Midi Pyrénées Conseil (2007-2016 et depuis 2019)
- Observatoire Midi Pyrénées Comité des Directeurs (2007-2016 et depuis 2019)
- OMP UMS 831 Conseil (2008-2016 et depuis 2019)
- Comité d'allocation de temps des télescopes nationaux (2007-2016 et depuis 2019))

- European Tran-National Access Program OPTICON Directors Forum (2007-2016 et depuis 2019))
- Conseil du Centre Universitaire Tarbes-Pyrénées (2007-2016) et depuis 2019)
- IUT Tarbes comité scientifique (2007-2016)
- Ecole Supérieure d'Art des Pyrénées comité scientifique (. Depuis 2015)
- Expert FNRS Belgique (Depuis 2009)
- Expert INSU exercices de prospective 2009 et 2013

Recherche

Depuis le début de ma carrière, mes intérêts de recherche ont été assez ouverts. Après une thèse d'instrumentation sur l'utilisation des télescopes à miroir liquide en l'astronomie, j'ai poursuivi dans la continuité de ma thèse la préparation du grand télescope à miroir liquide de 6 m (Large Zenith Telescope) construit par P. Hickson dans la forêt de Maple Ridge (University of British Columbia). J'ai étudié les techniques automatiques de classification de millions d'objets mesurés avec des filtres à bandes moyennes (Résolution = 40) que promettait cet instrument géant (Post-doctorat IAP, avec V. de Lapparent, (Cabanac, et al. 2000, 2002).

Après les miroirs liquides, j'ai décidé d'approfondir ma connaissance des télescopes traditionnels et des instruments de pointe de l'astronomie contemporaine et je suis parti faire un post-doc à l'ESO à Vitacura, Chili. A l'époque, les post-doc ESO se passaient en deux temps, 2 ans de tâches de service (pour moi VLT/Paranal: observations de service et soutien aux observateurs, sur toute l'instrumentation 1ere génération FORS1/2, UVES, ISAAC, HAWK-I, FLAMES, VIMOS, NAOS-CONICA, SINFONI, VISIR) et 1 an de post-doc dans une université Chilienne (j'ai choisi la Pontificia Universidad Catolica de Chile, pour son équipe extragalactique). Cette période a été l'occasion de faire évoluer mes intérêts de recherche dans plusieurs directions en lien avec l'effervescence scientifique de l'ESO. J'ai développé la première bibliothèque haute résolution d'étoiles brillantes du ciel avec UVES (UVES Paranal Observatory Program: PI Bagnulo, Bagnulo et al. 2003). J'ai commencé à m'intéresser aux galaxies à sursaut de formation d'étoiles très jeune (Cabanac et al. 2005), j'ai étudié les alignements du signal polarimétrique des quasars avec D. Hutsemekers (Hutsemekers et al. 2005) et enfin j'ai fortuitement découvert deux objets fort rares, le premier, un peu anecdotique en ce qui me concerne, un météore (Jenniskens et al. 2004), dont l'identification et l'analyse sur un spectre infrarouge de FORS2 ont été passionnants, et surtout une lentille gravitationnelle exceptionnelle à l'époque, un anneau d'Einstein très lointain ($z_{\text{lens}} = 0.98$ et $z_{\text{src}} = 3.77$), l'étude des protogalaxies via amplification gravitationnelle (Cabanac et al. 2005, 2008) qui m'a orienté vers l'étude des effets de lentilles forts.

Pendant ma dernière année à l'ESO, j'ai commencé à m'intéresser au sondage CFHT Legacy Survey en préparation à Hawaï. J'ai décidé de partir à Hawaï pour participer à son élaboration, en tant qu'astronome résident sur un poste du National Research Council du Canada. Mes travaux de recherche actuels sont en lien avec mes années passées à Hawaï, pendant lesquelles j'étais responsable d'une part de l'instrument Echelle SpectroPolarimetric Device for the Observation of Stars (ESPaDONs), en charge des observations de services pour mes tâches de services et bien sur très impliqué dans le CFHT Legacy Survey que j'ai commencé à exploiter en cherchant des candidats lentilles fortes. De ce travail est issu le Strong Lensing Legacy Survey (SL2S: Cabanac et al. 2007, More et al. 2012) et l'étude des groupes de galaxies par effet de lentille (voir la bibliographie sur le SL2S et le manuscrit HDR). Le SL2S a, en outre, été un projet de recherche propice pour préparer les missions spatiales à venir, notamment pour développer et tester des méthodes semi-automatiques de détection de lentilles,

En lien avec les lentilles fortes, au CFHT puis en arrivant au Laboratoire d'Astrophysique de Toulouse et Tarbes (maintenant Institut de Recherche en Astrophysique et Planétologie), d'abord en poste rouge

(2006), puis CDD CNRS (2007-2008) et finalement AA CNAP (depuis 2009), je me suis intéressé aux missions spatiales proposées pour leur potentiel de *découvreurs en série* de candidats lentilles fortes (SNAP puis DUNE puis Euclid). J'ai utilisé le temps libre que me laissait la direction du Télescope Bernard Lyot et du Pic du Midi, c'est-à-dire en réalité fort peu, pour m'impliquer dans la mission Euclid, étudiant un design optique optimal pour un télescope spatial optimisé en haute résolution et stabilité de la PSF (Thèse de Balasubramanian Singaravelu 2014).

Mes tâches de service SO4 EUCLID après 2016 m'ont permis de passer davantage de temps sur la recherche extragalactique au service de la mission, avec l'étude des techniques automatiques de classification et de filtrage de données par réseau de neurones convolutifs (apprentissage profond), les tests des algorithmes de détection et de mesure des paramètres physiques des amas de galaxies, et le développement de la pipeline de mesure des paramètres morphologiques sur les objets du catalogue final de la mission Euclid.) Projets sur lesquels j'ai supervisé des 4-5 étudiants (la plupart M1 et quelques L3 brillants).

Le dernier volet de mes recherches, est un peu un retour aux sources, avec le développement instrumental du Télescope Bernard Lyot, qui a abouti au financement puis à la réalisation de la nouvelle instrumentation du TBL: Neo-Narval (et mon retour aux commandes du Pic du midi en 2019).

Recherches actuelles: lentilles gravitationnelles fortes, proto-amas

Depuis 2019, j'ai repris l'étude de lentilles gravitationnelles: deux études m'occupent sur le CFHT-LS SL2S. D'une part la répartition de l'échantillon complet de lentilles d'échelle de groupes $3 \text{ arcsec} < R_{\text{eins}} < 10 \text{ arcsec}$ pour des masses totales (Halo CDM + Baryon) $10^{12}-10^{13} M_{\odot}$ et l'étude de sources à redshifts intermédiaires ($2 < z < 4$) fortement amplifiés, ces deux projets devraient mener à des publications dans les mois à venir. Je participe également à des demandes de temps pour le JWST sur des proto-amas de galaxies observés avec Planck, demandes ST-EXUPERY et PROTEUS (PI Brenda Frye, H. Dole), ainsi que des suivis 4-MOST de (futurs) lentilles fortes Euclid (PI T. Collett). Les demandes de temps JWST pour l'instant infructueuses nous ont cependant permis de développer une collaboration riche avec nos collègues américains et de mieux connaître JWST. Enfin, le groupe de travail Strong Lensing d'Euclid a développé des techniques de détections automatiques de lentille sur les champs Euclid (Metcalf et al; 2019) auquel j'ai activement participé.

Recherches actuelles: Neo-Narval

Depuis 2013, j'ai également participé au développement de Neo-Narval (500 Keuros) comme co-PI de l'instrument (Torsten Böhm PI), ce développement instrumental consiste à stabiliser en température et en pression les composants de Narval sensibles aux variations d'indice de réfraction, à injecter une troisième voie de calibration avec un Fabry-Perot stabilisé, à remplacer le détecteur par une nouvelle caméra et à installer des fibres octogonales stabilisant la pupille. Ces améliorations permettent d'ouvrir le domaine de la vélocimétrie au TBL à 2m/s sur le long terme et d'explorer les systèmes exo-planétaires de Jupiter chauds, notamment les phases ultimes de vie stellaire, quand les planètes sont absorbés dans la phase de géante rouge. Un avantage de Neo-Narval est sa sensibilité sur un intervalle large de longueur d'onde 400nm-1 μ m et bien entendu sa sensibilité spectropolarimétrique. Neo-Narval est arrivé en septembre 2019 dans une première phase d'intégration sur le télescope, qui a permis de récupérer les capacités spectropolarimétriques de Narval avec un gain d'efficacité sur le ciel permis par la caméra. Une deuxième phase d'intégration est prévue à l'automne 2020 pour installer le Fabry-Perot stabilisé (fabrication Observatoire de Genève, F. Pepe) et commencer la carrière vélocimétrique de Neo-Narval.

Bibliographie

H-index = 25 (2020)

Publications arbitrées

1. Euclid Collaboration, 2020, *The Complete Calibration of the Colour-Redshift Relation survey: VLT/KMOS observations and data release*, 2020arXiv200702631G
2. Euclid Collaboration, 2019, *Euclid preparation: VII. Forecast validation for Euclid cosmological probes*, A&A.
3. Metcalf, R.B., et al., 2019 *The strong gravitational lens finding challenge*, A&A.
4. Ibata, et al., 2017, *Chemical Mapping of the Milky Way With The Canada-France Imaging Survey: A Non-parametric Metallicity-Distance Decomposition of the Galaxy*, accepted in ApJ.
5. Ibata et al., 2017, *The Canada-France Imaging Survey: First results from the u-band component*, accepted in ApJ.
6. Verdugo, et al., 2016, *Combining strong lensing and dynamics in galaxy clusters: integrating MAM-POSSt within LENSTOOL. I. Application on SL2S J02140-0535*, A&A, 595, 30
7. Verdugo, et al., 2014, *Characterizing SL2S galaxy groups using the Einstein radius*, A&A, 571, 65.
8. Gastaldello et al., 2014 *Dark matter-baryons separation at the lowest mass scale: the Bullet Group*, MNRAS, 442, 76
9. Singaravelu & **Cabanac, R.**, 2014, *Obstructed Telescopes Versus Unobstructed Telescopes for Wide Field Survey? A Quantitative Analysis*, PASP, 126, 386
10. Smoker, et al., 2014, *Early-type stars observed in the ESO UVES Paranal Observatory Project - IV. Studies of CN, CH+ and CH in the interstellar medium*, MNRAS, 438, 1127.
11. Muñoz, et al., 2013, *Dynamical analysis of strong-lensing galaxy groups at intermediate redshift*, A & A, 552, 80
12. Foex, et al., 2013 *SARCS strong-lensing galaxy groups. I. Optical, weak lensing, and scaling laws*, A & A, 559, 105
13. More et al., 2012, *The CFHTLS-Strong Lensing Legacy Survey (SL2S): Investigating the group-scale lenses with the SARCS sample*, ApJ, 749, 38 – Verdugo et al., 2011A&A *Gravitational lensing and dynamics in SL2S J02140-0535: probing the mass out to large radius*, 527A.124V
14. Smoker, J et al., 2011 *Early-type stars observed in the ESO UVES Paranal Observatory Project - III. Sub-parsec and au-scale structure in the interstellar medium*, MNRAS.414...59
15. Vidal-Madjar, Alfred et al., 2010, *The Earth as an extrasolar transiting planet: Earth's atmospheric composition and thickness revealed by Lunar eclipse observations*, A&A 523, 57.
16. Morin et al., 2010, *exploring topology of M stars*, 2010arXiv1009.2589M.
17. Konstantinova-Antova, et al., 2010, *Direct detection of a magnetic field in the photosphere of the single M giant EK Boo: How common is magnetic activity among M giants?* 2010arXiv1009.2001K
18. Verdugo et al., 2010, *Grav. Lensing and Dynamics in SL2S,J02140-0535: Probing the mass out to large radius*, 2010arXiv1005.1566V
19. Hutsemékers et al. , 2010, *Optical circular polarization in quasars*

20. Auriere et al., 2009, the magnetic field of Pollux, *A&A*, 504 231.
21. Limousin, **Cabanac, R.**, et al., 2009, submitted to *A&A*, *A New Window of Exploration in the Mass Spectrum: Strong Lensing by Galaxy Groups in the SL2S*.
22. Tu Hong, **Cabanac, R.**, Fort, B., Gavazzi, R., Kneib, et al., 2009, *The SL2S: dark matter vs luminous matter in SL2SJ021737-051329*, accepted in *New Physics Reviews*.
23. Morin, J.; Donati, J.-F.; Petit, P.; Delfosse, X.; Forveille, T.; Albert, L.; Aurière, M.; **Cabanac, R.**; et al., 2008, *Large-scale magnetic topologies of mid M dwarfs*, *MNRAS* 390 567.
24. Donati, J.-F.; Morin, J.; Petit, P.; Delfosse, X.; Forveille, T.; Aurière, M.; **Cabanac, R.** et al., 2008, *Large-scale magnetic topologies of early M dwarfs*, *MNRAS* 390 545
25. Limousin, M. et al., 2008 *Strong lensing in Abell 1703: constraints on the slope of the inner dark matter distribution* *A&A* 489 23
26. **Cabanac, R.**, Valls-Gabaud, D., Lidman, C., 2008, *FORJ0332-3557: medium-resolution spectroscopy of a post-starburst galaxy at $z=3.8$.*, *MNRAS* 386, 2065-2074.
27. Konstantinova-Antova, R., et al., 2008, *The detection of a magnetic Field in V390*, *A&A*, in press.
28. Hickson, P., Pfrommer, D., **Cabanac, R.**, et al., 2007, *The LZT: a 6-m LMT*, *PASP*, 119, 444.
29. **Cabanac, R.**, et al., 2007, *The CFHTLS Strong Lensing Legacy Survey (SL2S): I. Survey overview and T0002 release sample*, *A&A*, 461, 813.
30. Hunter, I, Smoker, J.V., Keenan, F.P., Ledoux C., Jehin, E., **Cabanac, R.**, Melo, C., Bagnulo, S., 2006, *Early-type stars observed in the ESO UVES Paranal Observatory Project: I – Interstellar Na I UV, Ti II and Ca II K observations*, *MNRAS*, 367, 1478.
31. Stutz, C., Bagnulo, S., Jehin, E., Ledoux, C., **Cabanac, R.**, Melo, C., 2006, *Abundance analysis of 5 early type stars in the young open cluster IC2391*, accepted in *A&A*.
32. Sluze, D., Claeskens, J.F., Altieri, B., **Cabanac, R.**, Garcet, O., Hutsemékers, D., Jean, C., Smette, A., Surdej, J., 2006, *Multi-wavelength study of the gravitational lens system RXS J113155.4-123155: I. Multi-epoch optical and near infrared imaging*, accepted in *A&A*.
33. Hutsemékers, **Cabanac, R.**, Lamy, H., Sluze, D., 2005, *Mapping extreme-scale alignments of quasar polarization vectors: Evidence for photon-pseudoscalar mixing on cosmological scales?* *A&A* 441, 915.
34. Meech, K. J., et al., (203 authors), 2005, *Deep Impact: Observations from a Worldwide Earth-Based Campaign*, *Science* 310, 265.
35. **Cabanac, R.**, Vanzi, Leo, Sauvage, M., 2005, *A fresh view on Henize 2-10 with VLT/NAOS-CONICA*, *ApJ* 631, 252.
36. **Cabanac, R.**, Valls-Gabaud, D., Jaunsen, A.O., Lidman, C., Jerjen, H., 2005, *Discovery of a high redshift Einstein ring*, *A&A* 436, 21
37. Sluze, D., Hutsemékers, D., Lamy, H., **Cabanac, R.**, Quintana, H., 2005, *New optical polarization measurements of quasi-stellar objects*, *A&A* 433, 757.
38. Jenniskens, P., Jehin, E., **Cabanac, R.**, Laux, O., & Boyd, I., 2004, *Spectroscopic anatomy of a meteor trail cross section with the European Southern Observatory Very Large Telescope*, *Meteoritics & Planetary Science* 39, 4.
39. **Cabanac, R.**, de Lapparent, V., & Hickson, P., 2002, *Classification and redshift estimation by principal component analysis*, *A&A* 389, 1090.

40. **Cabanac, R.**, de Lapparent, V., Hickson, P., 2000, *Evolution of faint galaxy clustering. The 2-point angular correlation function of 20,000 galaxies to $V < 23.5$ and $I < 22.5$* , A&A **364**, 349.
41. **Cabanac, R.**, E.F. Borra, M. Beauchemin, 1998, *A Search for Peculiar Objects with the NASA Orbital Debris Observatory 3-m Liquid Mirror Telescope*, ApJ **509**, 309.
42. **Cabanac, R.**, Borra, E. F., *A study of Cross-Correlation and Breakfinding Algorithms Applied to the Measurements of redshifts in Very-Low-Resolution Spectra*, Publications of the Astronomical Society of the Pacific **108**, 271-276, 1996.
43. Hickson, P., Borra, E. F., **Cabanac, R.**, Content, R., Gibson, B., Walker, G., *UBC/LAVAL 2.7-m Liquid Mirror Telescope*, ApJ **436**, L201-204, 1994.

Autres publications

1. Bagnulo, S., Jehin, E., Ledoux, C., **Cabanac, R.**, Melo, C., Gilmozzi, R., & and the ESO Paranal Science Operations Team, 2003, *The UVES Paranal Observatory Project: A Library of High-Resolution Spectra of Stars across the Hertzsprung-Russell Diagram*, Messenger, 114, 10.
2. **Cabanac, R.**, Astronomie avec Miroirs Liquides, Ph.D. Thesis, Université Laval, 198 pages, 1998.
3. **Cabanac, R.**, Prolégomènes au projet LIMITS, Maitrise ès science, Université Laval, 130 pages, 1992.
4. Masetti, N., et al., 2002, GRB020405: VLT observations of the OT environment, GRB Coordinates Network 1375, 1 2002.
5. Tholen, D. J. et al., 2005, Minor Planet Observations [568 Mauna Kea], MPC 54972, 13.
6. **Cabanac, R.**, chapitre sur l'Hindouisme, in *Le bonheur et les morales des grandes religions. Regards de scientifiques*, PUL, eds Cabanac M., Bonniot M.-C., 240 pages.
7. Treu, et, al., 2013 *Dark energy with gravitational lens time delays*, 2013arXiv1306.1272T
8. Cabanac, *Notre Belle Langue*, 2016, eds Mélibée, ISBN : 9782362526152

Communications

1. Kümmel, et al., 2019, Euclid Detections and Science Challenge 3, ASPC 521
2. Kümmel, et al., 2017, Data Challenges for the Euclid Cataloging Pipeline, ASPC 512
3. **Cabanac, R.**, 2016, Telescope Bernard Lyot: operation, instrumentation, perspectives, SF2A 237
4. Kummel, et al., 2015, Source Detection and Classification in Euclid, ASPC, 495, 249
5. **Cabanac, R.**, 2014, Frontier of Science invited talk: Secrets of the Universe, exoplanets and Dark Matter, Tapei, June 2014.
6. **Cabanac, R.**, 2014, Telescope Bernard Lyot beyond Narval: Neo-Narval and SPIP, SF2A conf 151
7. Gastaldello, et al., 2014, The Bullet Group, xru conf E, 79
8. More, et al., 2014, 2014, The CFHTLS-Strong Lensing Legacy Survey (SL2S): Investigating the group-scale lenses with the SARCS sample, JPhCS, 484, 2041
9. Konstantinova, et al., 2013, Magnetic activity in stars on the giant branches: Twenty years of observations BlgAJ, 19, 14
10. **Cabanac, R.**, 2012, Lensing in clusters, SF2A-2012, 443-448
11. Hu et al., 2011ASPC..446..137T

12. Verdugo et al., 2011, Constraining strong lensing models with dynamics, RMxAC..40..104V
13. Limousin et al., 2008, Oz Lens, Sydney
14. Hutsemékers et al., *Quasar polarization alignment on large scales*, 2008, Polarization in Astronomy, Québec
15. Jehin, E., et al., 2007, *Spectroscopic anatomy of a meteor with the very large telescope (ESO)*, AdSpR, 39, 550
16. Vanzi et al., 2007, *Infrared Observation of Extragalactic Young Massive Clusters*, Venise, Octobre 2006, ASPC, 374, 299
17. Smoker, J., et al., 2007, *Small Scale Structure in the ISM towards IC 2391 and NGC 6475*, ASPC, 365, 82
18. Valls-Gabaud, D., **Cabanac, R.**, Lidman, C., Diego, Saha, P., 2006, *Non-parametric mass profiles of a unique elliptical galaxy at redshift of 1*, in IAP Meeting: Mass Profiles and Shapes of Cosmological Structures, G. Mamon, F. Combes, Deffayet, B. Fort eds.
19. Jehin, E., Bagnulo, S., Melo, C., Ledoux, C., **Cabanac, R.**, 2005, *The UVES Paranal Observatory Project: a public library of high resolution stellar spectra*, IAU Symp. 228, Paris, eds. Hill, François, Primas.
20. **Cabanac, R.**, Valls-Gabaud, D., Jaunsen, A.O., Lidman, C., Jerjen, H., 2004, *A new highly magnified star-forming galaxy in an Einstein ring configuration at $Z=3.77$* , IAU Symp. 225, Lausanne, eds. Mellier, Y., Meylan, G.
21. **Cabanac, R.**, Hutsemekers, D., Sluse., D., Lamy, H., 2004, *Large scale correlations of quasar polarization vectors: Hints of extreme scale structures?*, in Astronomical Polarimetry - Current Status and Future Directions, Waikoloa, ed. Adamson, A.
22. Mason, E., Bagnulo, S., Szeifert, T., **Cabanac, R.**, Jehin, E., Ledoux, C., 2004, *Observation of polarimetric standard stars with FORS1 at the ESO VLT*, in Astronomical Polarimetry - Current Status and Future Directions, Waikoloa, ed. Adamson, A.
23. Cuby, J.-G., Barriga, P., **Cabanac, R.**, Castillo, R., Gavignaud, I., Gillet, G., Haddad, N., Kieckbusch, M., Marchesi, M., Mardones, P., 2002, *Instrumentation activities at Paranal Observatory*, SPIE 4844, 35.
24. **Cabanac, R.**, de Lapparent, V., Hickson, 2002, *The Different Clustering of Red and Blue Galaxies: A Robust Signal from $\omega(\theta)$* , in a New Era in Cosmology, ASP Conf. Ser., 283, eds Metcalfe, Shanks, Durham.
25. **Cabanac, R.**, de Lapparent, V., Hickson, 2002, *The Large Zenith Telescope: A Deep Survey Using a 6-m Liquid Mirror Telescope*, in a New Era in Cosmology, ASP Conf. Ser., 283, eds Metcalfe, Shanks, Durham.
26. **Cabanac, R.**, de Lapparent, V., Hickson *The Large Zenith Telescope: Redshifts and Physical Parameters of Faint Objects from a Principal Component Analysis*, in Galaxy Clustering at High Redshift, ASP Conf. Ser., 200, eds V. Lebrun, O. LeFevre, A. Mazure, Marseilles, 1999.
27. Cabanac, M., **Cabanac, R.**, *The Fifth influence*, ISSS 99129, Proc. of the 43rd Annual meeting of the Int. Soc. Systems Science, Asilomar, 1999.
28. Hickson, P., Borra, E.F., Walker, G.H., **Cabanac, R.**, Chapman, S., Mulrooney, M., de Lapparent, V., Proc. SPIE, Vol. 3356, *Advance Technology Optical/IR Telescopes VI: Large Zenith Telescope Project: a 6-m mercury-mirror telescope*, Kona, 1998.

29. **Cabanac, R.**, *the NODO Season 1996*, in ASP Conf. Ser. 147, Abundance Profiles: Diagnostic Tools for Galaxy history, Québec, 1997, eds. Friedli, Edmunds, Robert, Drissen.
30. Hickson, P., Walker, A. H., Borra, E. F., **Cabanac, R.**, Proc. SPIE, Vol. 2199, *Advance Technology Optical telescope V: A 2.7-m Liquid-Mirror Telescope*, p922-927, 1994.
31. **Cabanac, R.**, *The UBC-Laval Liquid Mirror Observatory*, International Space University Alumni Conference, Barcelona, 1994.
32. **Cabanac, R.**, *Liquid Mirrors at Université Laval*, International Space University Summer Session, Huntsville, Alabama, 1993.

A Tarbes le 2 septembre 2020



A Toulouse le 3 septembre 2020

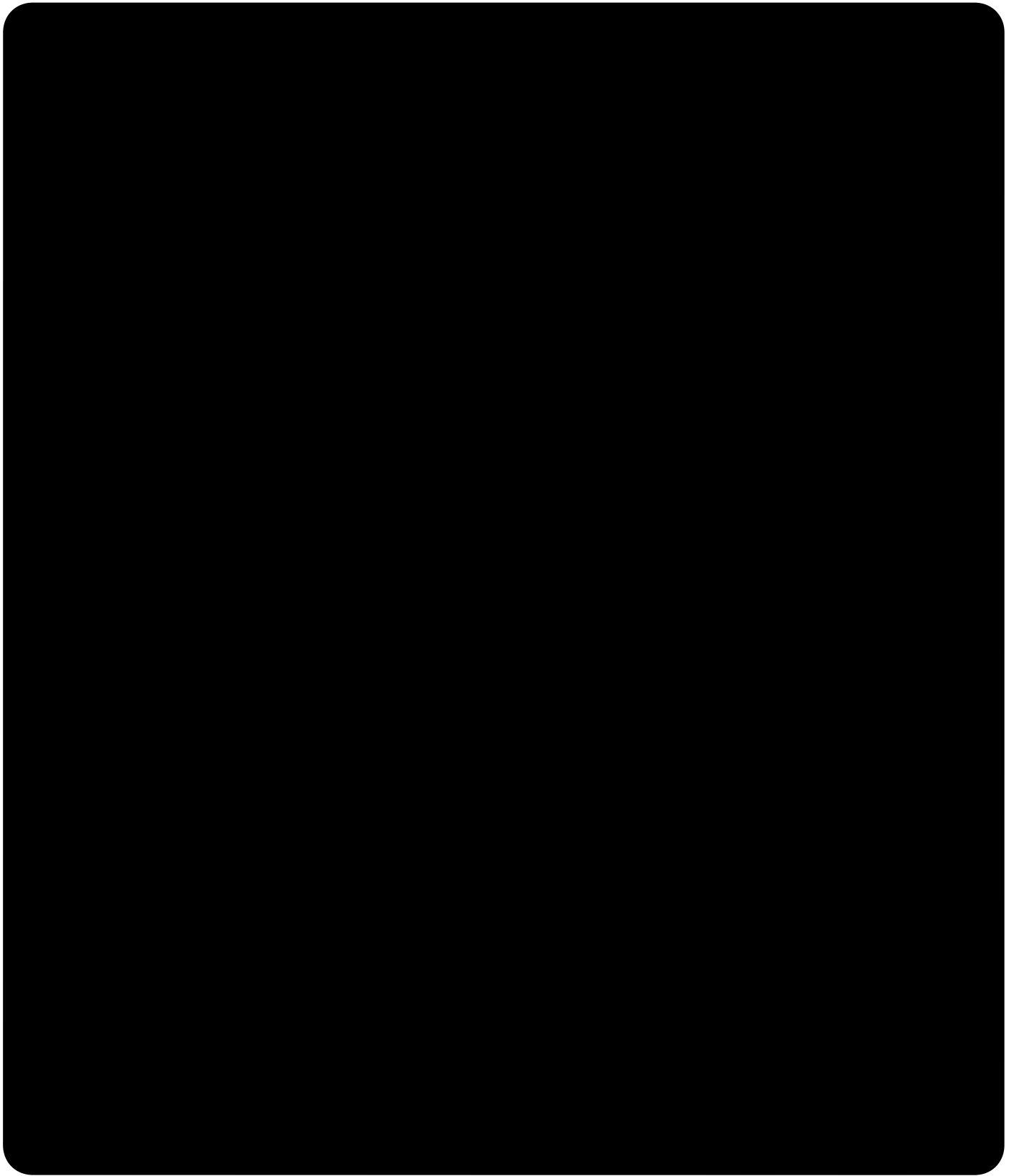


Geneviève SOUCAÏL
Directrice de l'École Doctorale
"Sciences de l'Univers,
de l'Environnement et de l'Espace"

Date: 15/12/2020

Page: 1 / 2

Heure: 16:50:33



Le Président de l'Université de Toulouse et le Président de Toulouse III attestent que

l' Habilitation à Diriger des Recherches de l'Université de Toulouse
a été décernée à

Monsieur CABANAC REMI

né le 24 août 1969 à LA TRONCHE (038)

au titre de l'année universitaire 2020/2021

Date de soutenance : 3 décembre 2020

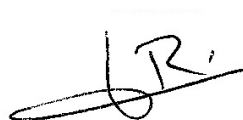
Etablissement soutenance : UNIVERSITE TOULOUSE III

Jury : Mme GENEVIEVE SOUCAIL, Président du jury, ASTRONOME
UNIVERSITE TOULOUSE III
Mme FLORENCE DURRET, Rapporteur du jury, ASTRONOME
UNIVERSITE PARIS 6
M. EMERIC LE FLOCH, Rapporteur du jury, INGENIEUR CEA
UNIVERSITE PARIS 7
M. MATHIAS SCHULTHEIS, Rapporteur du jury, ASTRONOME
UNIVERSITE DE NICE
M. THIERRY CONTINI, Membre du jury, DIRECTEUR DE RECHERCHE CNRS
UNIVERSITE TOULOUSE III
Mme ROSER PELLO, Membre du jury, ASTRONOME
UNIVERSITE TOULOUSE III

Ecole doctorale : Ecole Doctorale de Sciences de l'Univers, de l'Environnement et de l'Espace - UPS

Fait à TOULOUSE, le 15 décembre 2020

Le Président de Toulouse III



Jean-Marc BROTO

N° étudiant : 22016657